Displacement of oil by waterflooding in fractured chalk

Lykke, Miriam Mølgaard

Publication date:
2005

Document Version
Publisher's PDF, also known as Version of record

Miriam M. Lykke

Displacement of oil by waterfloding in fractured chalk

BYG·DTU

DANMARKS
TEKNISKE
UNIVERSITET

Rapport
BYG·DTU
R-128
2005
ISSN 1601-2917
ISBN 87-7877-198-6

Displacement of Oil by Waterflooding in Fractured Chalk

Miriam M. Lykke

Ph.D. Thesis

Department of Civil Engineering
Technical University of Denmark

2005

Displacement of Oil by Waterflooding in Fractured Chalk

Printed by
Department of Civil Engineering
Technical University of Denmark
87-7877-198-6
1601-2917

Preface

This Ph.D. thesis is the written documentation of the Ph.D. project "Displacement of Oil by Waterflooding in Fractured Chalk". The Ph.D. project was carried out at the Department of Civil Engineering (BYG•DTU), DTU under supervision of Director of Research Niels Foged, BYG•DTU, DTU and co-supervision of Chief Engineer Helle F. Christensen, GEO.

The Ph.D. project was coordinated with and partly financed by a Danish Energy Research Programme (EFP) project 2000. The title of this project is "Displacement and Deformation Processes in Fractured Reservoir Chalk" (Christensen 2003), and the main objective was to quantify the displacement processes in fractured reservoir chalk. The research partners were: Danish Geotechnical Institute (GEO), Geological Survey of Denmark and Greenland (GEUS), Department of Environment and Resources (ER), DTU and Department of Civil Engineering (BYG•DTU), DTU. The industrial partners were: BP Norway and Mærsk Olie og Gas AS.

Lyngby, April 2005

Miriam M. Lykke

Acknowledgements

I thank my supervisor Director of Research Niels Foged, BYG•DTU for his enthusiasm and excellent guidance especially in relation to the waterflooding tests. I am grateful to my co-supervisor Chief Engineer Helle F. Christensen, GEO for her excellent guidance and her ability to keep her surroundings on the ground and on the right track.

Further, I thank Research Assistant Katrine A. Olufsen, BYG•DTU for good collaboration during preparation and testing of a single specimen and for her work on the TDR probes. Appreciations to Reader Leif Fuglsang and Associate Professor Gunnar Bagge for fruitful discussions about centrifuge equipment and testing, and to Associate Professor Anette Krogsbøll for support and discussions in general, all BYG•DTU. Many thanks to technicians Linnert Christiansen and Vita Larsen, BYG•DTU for their help and hard work especially during the waterflooding tests performed in the centrifuge.

Senior Research Geologist Finn Jakobsen, GEUS is acknowledged for help and supervision during description of the Hillerslev outcrop chalk.

BP Norway in general and Senior Petroleum Engineer Tron G. Kristiansen and Lead Reservoir Engineer Roar M. Kjelstadli in particular are acknowledged for a pleasant stay at BP Norway and for fruitful discussions about oil recovery and insight into reservoir simulation. Further, I wish to thank BP Norway for providing data from the Valhall Tor formation. The financing by BP Norway of the waterflooding tests performed in the oedometer cell is gratefully acknowledged.

I am grateful to Rogaland Research, Norway for letting me perform capillary pressure measurements on Hillerslev outcrop chalk specimens at their premises. I thank Research Engineer Jan Erik Iversen, Rogaland Research, and Engineer Egil Boye Petersen, earlier working at Rogaland Research, for help and supervision during the tests.

Furthermore, I thank Professor Rasmus Risnes, Professor Tor Austad, Post Doctor Dag C. Standnes and Professor Svein Skjæveland at Stavanger College, Norway for fruitful discussions about wettability and capillary pressure. Stavanger College, Norway is acknowledged for a pleasant stay there.

The co-financing of the Ph.D. project by the Danish Energy Authority, Mærsk Olie og Gas AS and BP Norway is gratefully acknowledged.

I am deeply grateful to Kurt Jager Sørensen for invaluable support and discussions, and to Astrid Jager Lykke just for being there.

Abstract

Displacement of oil by waterflooding in fractured chalk reservoirs has been considered a risk of flow of water mainly in the fractures, resulting in early water breakthrough and inefficient sweep.

In order to study if the presence of fractures in a chalk reservoir impose a risk of flow of water mainly in the fractures, waterflooding tests were performed on seven large ($D \approx 50$ cm, $H = 43$-50 cm), oil-saturated, naturally fractured Hillerslev outcrop chalk specimens. Five of the specimens were tested in a centrifuge to be able to model the capillary imbibition and to facilitate up-scaling to reservoir scale. The remaining two specimens were tested in an oedometer cell at a higher stress level. Six of the specimens were strongly water-wet, whereas a single specimen was altered to a fractional-wet state before testing in the centrifuge.

At $N = 80$ times the gravitational acceleration in the centrifuge, water was injected into the specimens by a falling hydraulic pressure difference. During testing, pore pressure transducers were used to measure inflow and outflow pressures, keep track of produced volumes and detect water breakthrough. Further, TDR (Time Domain Reflectometry) probes were used for indication of the position of the waterfront in the matrix and the water in the fractures during testing.

Similarly at 1 g, water was injected into the specimens in the oedometer cell by a falling hydraulic pressure difference. During testing, pore pressure transducers were used to measure inflow and outflow pressures. Further, LVDTs (linear variable displacement transducers) were used to measure axial deformations during testing.

Based on test observations it is evaluated that oil displacement by waterflooding is very efficient in strongly water-wet chalk with a well-connected fracture network with many branches.

Even though water breakthrough was successfully obtained by flow of water in the fractures in four of the water-wet specimens tested in the centrifuge, the capillary imbibition potential of the water-wet matrix was so strong that the flow of water in the fractures in the three most fractured water-wet specimens were more or less absorbed. For the least fractured water-wet specimen, flow of water in the fractures continued after water breakthrough, resulting in simultaneous production of oil and water. This is explained by the water running in a single, almost vertical fracture continuing from the lower horizontal fracture plane to the top of the specimen. In the other three water-wet specimens, capillary imbibition took over, resulting in a high oil production.

It is evaluated that the centrifuge can be used for modelling and up-scaling of waterflooding tests on the large, naturally fractured Hillerslev outcrop chalk specimens. Centrifuge scaling factors were derived for the specimens.

In the oedometer tests, the oil displacement was dominated by capillary imbibition resulting in a waterfront moving up through the specimens. The yield stress was reduced in the specimens due to water weakening upon waterflooding. There was a distinct effect of waterflooding above the yield stress. This was seen as a significant deformation during waterflooding, i.e. oil was also displaced due to water-induced compaction. It was seen that creep is highly dependent on the water saturation, but this evaluation is affected by varying stresses in the specimen due to side friction.

The displacement processes are depending mainly on the fracture network and not just on the degree of fracturing. The displacement processes are also affected by the wettability as a continued flow of water in the fractures was observed in the fractional-wet, extensively fractured specimen. Finally, the displacement processes are affected by the flow rate.

Resumé

Fortrængning af olie ved vandinjektion i sprækkede kalk reservoirer kan udgøre en risiko for strømning af vand hovedsageligt i sprækkerne, resulterende i tidlig vandgennembrud og ineffektiv fortrængning.

For at undersøge om sprækker i et kalk reservoir udgør en risiko for strømning af vand i sprækkerne er der udført vandinjektionsforsøg på syv store ($D \approx 50$ cm, H = 43-50 cm), olie-mættede, naturligt sprækkede kalk prøver. Forsøg på fem af prøverne er udført i en centrifuge for at kunne modellere den kapillare imbibition og muliggøre opskalering til reservoir skala. Der er desuden udført forsøg på to prøver i en oedometer celle ved et højere spændingsniveau. Seks af prøverne var stærkt vand-våde, mens wettabiliteten af en enkelt prøve var ændret til "fractional"-våd.

Ved $N = 80$ gange tyngdeaccelerationen i centrifugen blev vandet injiceret ind i prøverne ved hjælp af en faldende hydraulisk trykniveauforskel. Der blev anvendt poretryksmålere under forsøgene til måling af indløbs og udløbs tryk, holde styr på producerede voluminer og registrere vandgennembrud. Desuden blev der anvendt TDR prober for at få en indikation af positionen af vandfronten i matricen og vandet i sprækkerne under forsøgene.

Vand blev tilsvarende injiceret ind i prøverne i oedometer cellen ved hjælp af en faldende hydraulisk trykniveauforskel ved 1 g. Der blev anvendt poretryksmålere til måling af indløbs og udløbs tryk. Desuden blev der anvendt LVDT'ere til måling af lodrette deformationer under forsøgene.

Baseret på forsøgsresultaterne er det evalueret at fortrængning af olie ved vandinjektion er meget effektiv i stærkt vand-vådt kalk med et sammenhængende sprækkenetværk med mange forgreninger.

Selv om der blev opnået vandgennembrud ved strømning af vand i sprækkerne i forsøgene på de fire vand-våde prøver i centrifugen, var det kapillare opsugningspotentiale af den vand-våde matrice så stort, at strømningen af vand i sprækkerne i de tre mest sprækkede prøver blev mere eller mindre absorberet. I den mindst sprækkede prøve fortsatte strømningen af vand i sprækkerne efter vandgennembrud, resulterende i samtidig produktion af olie og vand. Dette forklares ved at vandet løber i en enkelt, nærmest lodret sprække, der er gennemgående fra det nedre vandrette sprækkeplan til toppen af prøven. I de øvrige tre vand-våde prøver overtog kapillar opsugning, resulterende i en høj olie produktion.

Det er evalueret at centrifugen kan anvendes til modellering og opskalering af vandinjektionsforsøg på store, naturligt sprækkede Hillerslev kalk prøver. Der er udledt centrifuge skaleringsfaktorer for prøverne.

Fortrængningen af olie i oedometer forsøgene var domineret af kapillar opsugning. Det resulterede i en vandfront op gennem prøverne. Prøvernes flydespænding blev reduceret på grund af en svækkelse af kalken ved vandmætning. Der var en tydelig effekt af at injicere vand over flydespændingen. Dette blev observeret som en signifikant deformation af prøverne ved vandinjektion, det vil sige at der også blev fortrængt olie ved vand-induceret kompaktion. Det blev observeret at krybning er stærkt afhænging af vandmætningen, men denne vurdering påvirkes af varierende spændinger i prøven på grund af sidefriktion.

Fortrængningsprocesserne er hovedsageligt afhængige af sprækkemønstret og ikke kun af graden af sprækkethed. Fortrængningsprocesserne påvirkes også af wettabiliteten idet en fortsat strømning af vand i sprækkerne blev observeret i den "fractional"-våde, massivt sprækkede prøve. Endelig er fortrængningsprocesserne påvirket af strømningsraten.

Table of Contents

List of Adjacent Reports

Report 1

Lykke, M. M. (2005). Hillerslev Outcrop Chalk. BYG•DTU. Report no. R-020. Rev. 1. ISSN 1601-2917. ISBN 87-7877-075-0. DTU.

Report 2

Lykke, M. M. (2005). Wettability and Capillary Pressure Measurements on Hillerslev Outcrop Chalk. BYG•DTU. DTU.

Chapter 1

Introduction

1.1 Background

The main part of the recovery of oil from the North Sea takes place from fractured chalk reservoirs with low matrix permeability. Allan and Quing Sun (Allan & Quing Sun 2003) evaluated twenty fractured oil reservoirs of the type that most commonly occur in ductile rocks such as chalk, diatomite and siliceous shale. This type of reservoir has a high matrix porosity and a low matrix permeability, and it is believed that the matrix provides the storage capacity and the fractures provide the fluid-flow pathways. The evaluation showed that the application of secondary recovery such as waterflooding or enhanced oil recovery (EOR) techniques is essential for maximizing oil recovery in this type of fractured oil reservoirs. In fact, none of these types of fractured oil reservoirs are produced to final depletion without using some type of secondary or EOR techniques. The recovery factor in the reservoirs is affected by rock and fluid properties, particularly matrix permeability, wettability and fracture intensity. Fractured reservoirs that have been properly developed have ultimate recoveries that compare favorable with many conventional sandstone and carbonate reservoirs. All of the well-fractured, water-wet reservoirs have ultimate recovery factors larger than 25%, whereas all of the well-fractured, oil-wet reservoirs have ultimate recovery factors below 25%. The reason for the difference in recovery factors between water-wet and oil-wet reservoirs is that water can penetrate micro-pores in water-wet reservoirs by capillary imbibition, and thus provide an efficient recovery mechanism, while this is not the case for oil-wet reservoirs. Consequently, waterflooding into the water-wet reservoirs is far more efficient than in the oil-wet reservoirs. However, in poorly fractured reservoirs, in which bypassed oil is commonly left behind in the matrix blocks, the ultimate recovery factors are less than 20% regardless of wettability, implying the importance of fracture intensity.

Originally, a low oil recovery factor around 15% was obtained by primary production through conventional wells in the Valhall field, which is a chalk reservoir with low matrix permeability located 290 km offshore at 70 m water depth in the Norwegian sector of the North Sea (Leonard & Munns 1987). Most of the recovery was achieved by compaction drive (Ruddy et al. 1989). Later, drilling of horizontal wells and improved well completion has resulted in more than double the production rate of a typical conventional well (Ali & Alcock 1992). Recently initiated waterflooding in the highly fractured, neutral to slightly

oil-wet/slightly water-wet Tor formation of the Valhall field is expected to improve the oil recovery factor from 31 to 38% (Offshore Technology 2004).

The initial recovery factor under depletion drive was around 10% for oil production from conventional wells in the Dan field, which is a chalk reservoir with low matrix permeability located in the Danish sector of the North Sea at 40 m water depth some 200 km from the Danish coast. Development within drilling and completion techniques has resulted in horizontal wells producing on average 5-6 times more than conventional wells located in the same area (Wodka 1992). Today, oil recovery in the major part of the much less fractured, water-wet Dan field is successfully based on high rate waterflooding (Larsen et al. 1997). High rate waterflooding is used to induce fractures in the reservoir (hydraulic fracturing) in order to enhance the effective permeability of the reservoir. According to the Danish Energy Authority (Energistyrelsen 2004), the accumulated oil production in the Dan field since 1972 was 69.48 mio. m^3 and the oil reserves were 62.5 mio. m^3 per 1/1-2004.

On the other hand, Putra and Schechter (Putra & Schechter 1999) reported that initial waterflooding in the low permeable, fractured, weakly water-wet Spraberry field located in West Texas (mainly low-porosity sandstone) was only moderately successful. The oil recovery factor for primary production was less that 10%, and after more than 40 years of waterflooding, the oil recovery factor was still less than 12%, even though a waterflood pilot proved successful. Failure of the waterflooding has been assigned to the low matrix permeability and extensive fracturing. Further, rock wettability and stress-sensitive permeability appear to have a dominant effect on reservoir performance, and it was evaluated that more has to be understood about the matrix capillary imbibition transfer mechanism and stress-sensitive permeability. The present waterflood was initiated in 1995. In contrast to the earlier waterflooding field experience, Chowdhury et al. (Chowdhury et al. 2003) reported that the oil recovery factor for this waterflood has exceeded 25%. Before this waterflood, placing of injection and production wells along the same fracture orientation (on-trend wells) was avoided under the assumption of early water breakthrough. However, on-trend wells probably have been responsible for most of the oil recovery by waterflooding in the Spraberry field. It was found that the success of this waterflood depends on the knowledge of fracture orientation and properly positioning of injectors and producers.

Laboratory tests have shown that displacement of oil by waterflooding is a very efficient recovery mechanism in chalk. Waterflooding tests performed by Christensen (Christensen 2003) on small chalk specimens ($D = 5$ cm, $H = 10$ cm) have shown oil recovery factors of 45-74%.

However, in 1984, subsidence of approximately 3 m due to reservoir compaction was encountered in the Ekofisk field, which is an oil-producing, naturally fractured reservoir comprising Maastrichtian and Danian chalk with low matrix permeability located in the Norwegian sector of the North Sea (Sylte et al. 1999). This compaction was believed mainly to be due to reduction in pore pressure, and subsequent increase in effective stresses. A stepwise increase of waterflooding for the purpose of pressure maintenance and enhanced recovery was expected to slow and eventually stop the subsidence. However, as pressures stabilized in 1993-94, the subsidence rate remained essentially unchanged through 1998, with cumulative subsidence approaching 7.8 m. The continued subsidence

after 1994, together with laboratory and other field data, indicated that water induced compaction had become the primary mechanism for compaction in the field.

The main reasons for waterflooding oil-bearing chalk reservoirs is to increase the recovery of oil and maintain the pore pressure. However, oil displacement by waterflooding in fractured chalk is affected by many factors. For example pore geometry, fluid distribution, saturation history, relative permeability, wettability, waterflooding rate and viscosity ratio (Viksund 1998). The factors listed below are evaluated to have the greatest influence on the displacement processes of oil recovery by waterflooding in fractured reservoir chalk:

- Wettability
- Fractures
- Water weakening
- Water induced compaction

Wettability influences multi-phase flow properties such as capillary pressure, relative permeability, and waterflooding by controlling the location, flow and distribution of fluids in a reservoir (Anderson 1986*e*).

Water movement during waterflooding is significantly affected by the presence of fractures, especially since the matrix permeability of the fractured chalk reservoirs is low. The main matrix-fracture fluid exchange mechanisms for oil displacement by waterflooding are gravity drainage, capillary imbibition, molecular diffusion and viscous forces (Andersen 1995).

The saturating fluid affects the mechanical strength of the chalk. Injection of water into an oil-saturated chalk reduces the mechanical strength of the chalk in terms of a lower yield stress and lower consolidation moduli, when additional stress is applied (Christensen et al. 2000).

Injection of seawater into chalk during compaction tests has indicated that the changes in rock properties are localized to a zone around the oil/water interface. This causes a stress redistribution and may be an important local drive mechanism as the injection gives rise to a local increase in the rock compressibility (Foged et al. 1996). The additional compaction initiated by the waterflooding seems to be related to a shift in pore collapse stress (yield) caused by the increased water saturation, i.e. water weakening (Christensen 2003). Vanggard (Vanggard 1993) reported that waterflooding above the yield stress leads to significant compaction, while no major compaction is induced by waterflooding below the yield stress.

1.2 Literature Overview

Over the years, oil displacement by waterflooding has been the subject of many studies, both theoretically and experimentally. To obtain information relevant for this Ph.D. project, a short literature overview is included with more details provided for the more recent studies.

1.2.1 Wettability and Waterflooding

Earlier, flow of water in the fractures from a waterflood causing early water breakthrough and resulting in lower oil recovery was believed to be inevitable in extensively fractured sandstone reservoirs. In 1952, Brownscombe and Dyes introduced the concept of capillary imbibition, and the idea of oil production based on capillary imbibition of water from the water-filled fractures occurred ((Aguilera 1984), and references therein).

Brown and Fatt (Brown & Fatt 1956) reported the existence of fractional wettability in reservoir rocks, i.e. where different areas of the reservoir rock have different wettabilities due to the difference in adsorption of crude oil.

Mattax and Kyte (Mattax & Kyte 1962) introduced the term "critical rate" of the vertical water advance in fractured, strongly water-wet reservoirs. At the critical rate, the water in the fractures reach the top of the matrix blocks, when the capillary imbibition process has completed in the matrix. Above the critical rate, the water level in the fractures move ahead of the water in the matrix resulting in earlier water breakthrough. However, laboratory tests showed that the capillary imbibition could proceed even after water breakthrough, where the matrix was completely surrounded by water-filled fractures.

Mungan (Mungan 1966) found that waterflooding of strongly oil-wet rocks resulted in much lower recoveries at water breakthrough and a long period of simultaneous production of oil and water compared to strongly water-wet rocks. In fact, it was found that recovery of oil by waterflooding into strongly oil-wet rocks is inefficient. However, the recovery can be made more efficient by a) reducing the interfacial tension between oil and water, b) increasing the viscosity of the injected water, and c) changing the matrix wettability to water-wet. These findings were based on waterflooding tests on synthetic cores.

Mannon and Chilingar (Mannon & Chilingar 1972) established a relationship in the laboratory between the rate of water injection into a simulated fracture-matrix reservoir model and the rate of water capillary imbibition. In a series of waterflooding tests on strongly water-wet Berea sandstone cores surrounded by fractures, it was discovered that, under proper conditions, the higher the waterflooding rate, the higher the capillary imbibition rate, and the greater the indicated ultimate oil recovery. This may be explained by the concept that a higher injection rate would more easily break loose the oil droplets on the matrix surface, expelled by imbibition of water into the matrix, resulting in free oil channels to produce at a faster rate.

Rathmell et al. (Rathmell et al. 1973) conducted imbibition and waterflooding tests on Berea cores, where the wettability was altered to a weakly water-wet state. They found that waterflooding rocks characterized as weakly water-wet may result in lower residual oil saturations both at water breakthrough and ultimately, than for strongly water-wet rocks.

Salathiel (Salathiel 1973) introduced the term "mixed-wettability" for a special type of fractional wettability in which the oil-wet surfaces form continuous paths through the larger pores. The smaller pores remain water-wet and contain no oil.

Kleppe and Morse (Kleppe & Morse 1974) investigated the quantitative effects of

fracture flow capacity and production rate on the production performance and ultimate oil recovery of a fractured oil reservoir produced by waterflooding. Tests were performed on a Berea sandstone core surrounded by fractures. At low production rates, almost piston-like displacement was seen, whereas earlier water breakthrough followed by additional oil production was observed at higher production rates. Further, ultimate oil recovery from fractured reservoirs was highly affected by production rate at conductivity ratios higher than 1, where the conductivity ratio is defined as the ratio of the total vertical flow capacity of the fractures to the total vertical flow capacity of the matrix. For fracture flow capacities in the order of 1/10 of the matrix flow capacities, the effect of production rate on oil recovery is negligible. However, they found that oil is not lost because of an initial high production rate, but can be recovered by reducing the rate.

Morrow et al. (Morrow et al. 1984) conducted imbibition and waterflooding tests on strongly water-wet Berea sandstone cores and similar cores of a mixed wettability condition induced by crude oil. It was found that the mixed-wet cores showed water-wet imbibition behavior, resulting in improved displacement efficiency compared to the strongly water-wet cores. Further, clean water breakthrough and low relative permeability to water at residual oil saturation was observed in the mixed-wet cores.

In 1989, Monjoie and Schroeder ((Risnes & Flaageng 1999) and references therein) found that water has a pronounced weakening effect on chalk. Oil-saturated samples were found to be 2-3 times stronger than water-saturated samples.

Morrow (Morrow 1990) concluded that reservoir wettability can cover a wide range of conditions. Further, systems of intermediate or mixed wettability are quite common, whereas strongly water-wet systems may be rare. He also concluded that for a crude-oil/brine/rock system, the oil recovery is optimum at near neutral-wettability.

Jadhunandan and Morrow (Jadhunandan & Morrow 1991) carried out spontaneous imbibition and waterflooding tests on Berea sandstone cores, where the wettability was altered by crude oil. They found that systems which weakly imbibe water give higher oil recovery by waterflooding than very strongly water-wet systems.

As part of his master thesis, Vanggard (Vanggard 1993) performed waterflooding tests in an oedometer cell on strongly water-wet Stevns outcrop chalk specimens ($D \approx 54$ mm, $H \approx 108$ mm) with a porosity of 46.5% from Stevns Klint, Denmark. He reported that the effect of waterflooding on Stevns chalk is mainly influenced by the two factors: the yield stress and the saturation of the chalk. Waterflooding above the yield stress leads to significant compaction and accelerated strain rate in the 98% oil-saturated chalk specimens, while no major compaction or accelerated strain rate is induced by waterflooding below the yield stress or in chalk specimens above the yield stress containing 17% initial water. The compaction occurred locally at the waterfront. Further, he performed strength tests (Brazil, simple compression and triaxial), and found that the 98% oil-saturated specimens showed higher strength characteristics than specimens containing 17% initial water and fully water-saturated specimens.

Cuiec et al. (Cuiec et al. 1994) performed experimental studies of spontaneous imbibition of water in low-permeable, strongly water-wet outcrop chalk. They concluded that

spontaneous imbibition is controlled by counter-current flow mechanisms.

Waterflooding fractured chalk impose a risk of flow of water in the fractures resulting in early water breakthrough and less efficient oil recovery. Water injection tests carried out by Babadagli (Babadagli 1994) have shown that the water injection rate is an important parameter on the capillary imbibition transfer in fractured systems. In fact, it was found that above a critical water injection rate, an inefficient capillary imbibition transfer occurs. These findings were based on water injection tests on strongly water-wet, artificially fractured rock samples. The test material was Berea sandstone, Austin chalk and Colton sandstone. The tests revealed that at an increase in the injection rate, fracture pattern becomes an effective parameter on the matrix saturation distribution. As the rate is lowered, however, the system behaves like a homogeneous system showing a frontal displacement regardless of fracture configurations. Slower rates allow water to contact the matrix for a longer period of time resulting in stronger capillary imbibition. The obtained recovery curves imply that once the capillary imbibition initiates, the imbibition continues until the recoverable amounts of oil in the matrix is displaced. The capillary imbibition transfer is governed by the wettability and the permeability of the matrix. Above the critical rate, the injected water does not contact the matrix long enough to initiate capillary imbibition. No matter how much water is injected, only oil in the fracture is produced. This was observed in a test on a Colton sandstone sample, where no capillary imbibition took place in the matrix. A capillary fracture number was proposed for fractured rock, instead of the traditional capillary number for un-fractured rock. Beyond a limiting capillary fracture number, the capillary imbibition dominated displacement in fractured rock can be considered as an inefficient process. Based on experimental and numerical studies, the limiting value of injection rate is defined as a function of matrix capillary pressure and matrix permeability for an efficient capillary imbibition transfer.

Pratap et al. (Pratap et al. 1997) performed a simulation study of the effect of vertical capillary continuity for oil recovery by water displacement in a fractured, mixed-wet chalk reservoir simulated by vertical stacks of matrix blocks. They found that for mixed-wet fractured rock, the oil recovery is significantly enhanced even with a moderate areal contact between the matrix blocks. However, in strongly water-wet rock where capillary imbibition controls the oil recovery, the effect of capillary continuity is not significant.

Based on laboratory and field measurements, Sylte et al. (Sylte et al. 1999) reported that water weakening has been established as an important compaction mechanism for the Ekofisk field in the Norwegian sector of the North Sea. The surface subsidence since 1971 of over 7.8 m for the naturally fractured chalk reservoir is a result of reservoir compaction, which is considered primarily to be due to pressure depletion until the early 1990s and water weakening thereafter.

Graue et al. (Graue et al. 1999a) and Standnes and Austad (Standnes & Austad 2000a) developed reproducible methods to create homogenous oil-wet chalk material wettability. This was done by aging chalk cores saturated with crude oil for different time intervals at different temperatures. Further, Standnes and Austad (Standnes & Austad 2000b) presented results from a study regarding wettability alteration from oil-wet to water-wet chalk using water soluble surfactants. They found that some cationic surfactants are able

to alter the wettability in an irreducible way.

Pooladi-Darvish and Firoozabadi (Pooladi-Darvish & Firoozabadi 2000) performed water injection experiments in fractured porous media composed of a stack of water-wet Austin chalk and Berea sandstone blocks. The blocks experienced an advancing fracture-water level (FWL), and were compared with single-block immersion-type tests. It was found that the dominant recovery mechanism changed from co-current, i.e. no production below FWL, to counter-current imbibition, when the boundary conditions changed from advancing FWL to immersion-type. Further, co-current imbibition led to faster and more efficient recovery. They defined that a low rate of water injection will result in advancing FWL, whereas an infinitely high injection rate is equivalent to immersing a block in water. The concept of an advancing FWL is considered more representative for field behavior during waterflooding.

In the Joint Chalk Research, Phase V (Christensen et al. 2000), a conceptual model for intact chalk was proposed on basis of tests on Stevns outcrop Maastrichtian chalk with porosities in the range of 43-45%, and later verified on high porosity (40-45%) Tyra Maastrichtian chalk. The suggested conceptual model offers a simple way to model the chalk-water interaction as a change in basic compaction behavior related to the initial saturation, the porosity, the pore collapse stress and the wettability. The model is based on the observation that fully oil-saturated and fully water-saturated chalk have different compaction curves. Fully water-saturated chalk has a significantly lower pore collapse (yield) stress than fully oil-saturated chalk. When chalk is waterflooded, the compaction behavior shifts from the "oil compaction curve" to the "water compaction curve". In the plastic stress regime, this results in an accelerated strain rate and additional compaction. Chalk with low initial water saturation shows a similar response, while chalk with an initial water saturation above approximately 20% shows no or minor effect. There is an indication that for high porosity Maastrichtian chalk (porosity above 40%), the difference in pore collapse stress is reduced with decreasing porosity. Waterflooding under elastic stress conditions has very little or no effect in terms of stress relaxation and accelerated strain. However, the increased water saturation leads to a weakening of the chalk, which is seen as a lower yield stress and lower elastic and plastic consolidation moduli while loading to higher stresses. It was concluded that chalk-water interaction is a modification of the time-dependent behavior of chalk, i.e. creep.

Homand and Shao (Homand & Shao 2000) found that chalk behavior is clearly sensitive to water. The plastic yield stress is dramatically reduced, when chalk is saturated with water, and additional strains due to waterflooding are clearly localized. These findings are based on an experimental investigation. First, conventional hydrostatic and triaxial compression tests were carried out on water- or oil-saturated samples. Then, waterflooding tests were conducted on initially oil-saturated samples. The tests were performed on small samples ($D = 36$ mm, $H = 72$ mm) of outcrop chalk from Upper Campanian age called Lixhe chalk, which is sampled in the CBR quarry near Liège, Belgium. The chalk has a mean porosity of 43% and a mean matrix permability of 1.2 mD. The fluids used were Soltrol 170$^{\text{TM}}$ (oil) and distilled water mixed with crushed chalk.

As part of her master thesis, Larsen (Larsen 2000) performed a waterflooding test on

a single, large (D = 50 cm, H = 50 cm), naturally fractured Hillerslev outcrop chalk specimen with a porosity of 47% from the Hillerslev outcrop chalk quarry, Denmark. The specimen was strongly water-wet, and fully oil-saturated with the laboratory oil Isopar-L. The test was performed in a triaxial cell. After only a small part of the specimen was waterflooded, the specimen collapsed presumably due to water weakening effects. During the waterflooding test, a combination of flow of water in the fractures and capillary imbibition were observed.

Graue et al. (Graue et al. 1999b) reported that the oil production in fractured chalk reservoirs generally was believed to result from spontaneous imbibition of water from the fractures and subsequent movement of the expelled oil through the fractures to the producing wells. However, recent waterflooding tests performed by Graue et al. (Graue et al. 1999b) and (Graue et al. 2001a) revealed that viscous displacement of oil in a less than strongly water-wet chalk matrix could provide an alternate path for movement of the expelled oil to the producing wells. They studied the effect of embedded and interconnected fractures and wettability on the movement and recovery of oil during waterflooding. This study was based on waterflooding tests on eight larger (15-20 cm $\times$ 10-13 cm $\times$ 5-6 cm) low permeable Roerdal outcrop chalk blocks from the Portland quarry, Denmark.

The chalk blocks had a mean porosity and absolute matrix permeability of 45-48% and 2-4 mD, respectively. The chalk blocks were artificially fractured, and reassembled to produce "closed" fractures, i.e. with matrix blocks in contact, both perpendicular and parallel to the flow, and a single open fracture of 2 mm perpendicular to the flow. Four blocks were strongly water-wet (Amott water wetting index of WWI = 1.0) while the wettability of three of the blocks was altered to a moderately water-wet state (WWI = 0.6-0.8), and a single block was altered to a near neutral-wet state (WWI = 0.3) using crude oil. The blocks were prepared with an initial water saturation S_{wi} of 22-28%. First the whole blocks were waterflooded, then driven back to S_{wi} and fractured, and then waterflooded again. 2D nuclear tracer imaging was used to monitor waterflooding of the chalk blocks.

The oil recovery mechanisms involved with waterflooding fractured chalk blocks were found to depend on the wettability of the chalk and contact between adjacent blocks. Both the "closed" embedded and interconnected fractures significantly affected the fluid movement in the strongly water-wet blocks, but only had minor effect in the less water-wet blocks. However, the open fracture affected the flow in all the blocks, by impeding and redirecting the flow. At strongly water-wet conditions, water flow stopped at each fracture until the spontaneous imbibition endpoint water saturation $S_{w,if}$ was reached in the preceding matrix block. Then water filled the fractures, and entered the next matrix block gradually from both the perpendicular and parallel fractures. At less water-wet conditions, water moved across the "closed" fractures almost as if they were not there. For the strongly and moderately water-wet blocks, the oil recovery was similar before and after fracturing when the permeability increase after fracturing was low. A slightly lower recovery was observed after fracturing in the less water-wet blocks. Total oil recovery was observed to decrease with a decrease in water wetness. A clean water breakthrough was observed in the strongly water-wet blocks, both whole and with embedded fractures,

whereas an additional oil recovery after water breakthrough was seen in the less water-wet blocks, and indicated in the strongly water-wet blocks with interconnected fractures. Even at fairly low flow rates, more oil was mobilized by waterflooding at less water-wet conditions than recovered by spontaneous imbibition. The recovery mechanisms changed towards more viscous dominant flow at less water-wet conditions for both the whole and the fractured blocks. The reduced effect of the fractures on the less water-wet blocks is believed to be due to a reduced capillary hold-up of the wetting phase at the fractures, and/or formation of water bridges across the fractures.

Tang and Firoozabadi (Tang & Firoozabadi 2001) reported a study of the effect of wettability and initial water saturation on spontaneous imbibition and waterflooding in low permeable Kansas outcrop chalk samples, both un-fractured and fractured. The fractured samples consisted of cylindrical blocks stacked together and surrounded by fractures. The porosity of the samples was approximately 30% and the permeability was approximately 0.5 mD. The wettability of some of the samples was altered by use of stearic acid to a mixed-wet state showing weakly water-wet imbibition behavior. Estimated capillary pressure curves show higher recovery at less water-wet conditions, but at higher differential pressures. The waterflooding of the un-fractured cores showed that with an increase in pressure gradient, the oil recovery efficiency can increase substantially in a mixed-wet chalk. The same behavior is expected in a mixed-wet, fractured chalk. They found that the effect of initial water saturation S_{wi} on oil recovery depends on the wettability. For a strongly water-wet sample, oil recovery by waterflooding can decrease mildly with an increase in S_{wi}. However, for the mixed-wet samples, oil recovery by waterflooding can increase significantly with an increase in S_{wi}. Finally, they conclude that the recovery of oil by waterflooding in chalk reservoirs may be nearly independent of wettability.

Recently, waterflooding tests were reported by Graue et al. (Graue et al. 2001b), Aspenes et al. (Aspenes et al. 2002) and Graue et al. (Graue et al. 2003) on the impact of flow rate, fracture width and wettability for waterflooding tests on chalk. The tests were performed on six core plugs ($H \approx 6$ cm, $D \approx 3.8$ cm) of Roerdal ourcrop chalk, Denmark. The core plugs had a mean porosity of 46% and a mean matrix permeability of 4 mD. The wettability of four of the core plugs was altered towards less water-wet conditions. The chalk cores were cut into two half plugs, and then the two halves were stacked horizontally, i.e. separated by a fracture perpendicular to the flow direction. Magnetic resonance imaging was used to monitor the waterflooding of the stacked cores. The tests were thus performed on two strongly water-wet ($WWI = 1.0$), three moderately water-wet ($WWI = 0.5$-0.7) and a single near neutral-wet ($WWI = 0.3$) stacked core plugs. The plugs had an initial water saturation S_{wi} of approximately 25%. The tests were run with fracture widths of 1 mm, 2.3 mm and 3.5 mm using flow rates of 0.4 cm^3/h and 2.0 cm^3/h.

At strongly water-wet conditions, water did not cross the fracture before the spontaneous imbibition endpoint water saturation $S_{w,if}$ was reached in the inlet plug, even at the high flow rate. When water entered the fracture, gravity segregation resulted in displacement of oil from the bottom of the fracture and upward. The oil production was dominated by capillary forces, which caused the inlet plug to reach $S_{w,if}$ before water could leave the matrix and enter the fracture. The fracture crossing mechanism was hy-

draulic displacement of oil upward at the rate of the water injection. At less water-wet conditions, water droplets formed on the outlet face of the inlet plug, which formed bridges across the fracture and provided a path for water movement into the outlet plug, while the oil phase was still being produced from the inlet plug. The wetting phase bridges were formed before $S_{w,if}$ was reached in the inlet plug. As the bridges increased in size, gravity caused the bridges to sag downward, and slowly fill the fracture from the bottom. At less water-wet conditions, less capillary imbibition contributed to the oil displacement. Due to the capillary continuity of the wetting phase across the fracture provided by the bridges, a viscous pressure drop was established across the stacked core plug, suggesting a viscous component contributing to the total oil recovery in the fractured chalk for less water-wet conditions. At nearly neutral-wet conditions, bridges appeared to form earlier allowing the water to cross even wider fractures. The fractures significantly affected the water movement during waterflooding at strongly water-wet conditions, but not at less water-wet conditions, where capillary continuity of the wetting phase was established across the fractures. This bridging effect on the wetting phase was shown to depend on the wetting conditions, the fracture width and the flow rate. The mechanism controlling the formation of wetting phase bridges and thus the ability of wetting phase fracture crossing is an interaction between the viscous pressure, which controls the growth of water droplets, the interfacial tension between the water and the oil, and the wettability at the exit face controlling the droplet contact angle. The possibility of forming bridges is dependent on fracture width, with bridges more likely to form at smaller widths and not forming beyond a critical fracture width. The width that the bridges could cross was dependent on the rate of water injection, with wider bridges at the higher rate.

Recent waterflooding tests performed by Christensen (Christensen 2003) on five medium scale (D = 10 cm, $H \approx$ 20 cm), cylindrical chalk specimens showed that fractured and un-fractured chalk respond differently to waterflooding. The tests were performed on four specimens from the Dan field and a single specimen from the Valhall Tor formation. In the Dan field specimens with no visible fractures, piston-like displacement was observed, whereas flow of water in the fractures was observed in both Dan and Valhall Tor formation specimens with visible fractures. The specimens from the Dan field was from the Maastrichtian M1, M2 and M3 formation with low porosities in the range of 20-25%. The single specimen from the Tor formation of the Valhall field had a high porosity of approximately 40%. Before testing, the Dan specimens were cleaned in methanol and toluene. The Valhall specimen was tested without cleaning. The specimens were fully saturated with Isopar-L oil, and the waterflooding rate was 10-14 cm^3/h.

To sum up, the reservoir wettability ranges from water-wet over fractional-wet to oil-wet. It is possible to obtain a homogeneous wettability alteration of test specimens by wettability alteration methods. Oil recovery by waterflooding in fractured reservoirs depends strongly on the wettability and the presence of fractures. Capillary continuity between adjacent matrix blocks affects the displacement processes. Similarly, the displacement processes depend on the wettability and the fractures. However, more has to be understood about the displacement processes, especially the effect of naturally fractures on the displacement processes. The possibility of the existence of a critical waterflooding rate in fractured reservoirs is discussed. However, no consistent conclusions can be drawn

based on the included references, and further studies of the concept of a critical rate are necessary. Oil recovery by waterflooding is also effected by water weakening and water induced compaction, when waterflooding above the yield stress. A model for the mechanical behavior of intact, high porosity Maastrichtian chalk during waterflooding has been proposed. However, it would be interesting to study the chalk-water interaction in naturally fractured chalk.

1.2.2 Up-scaling of Waterflooding Tests

Scaling laws for up-scaling of laboratory tests observations to reservoir scale are important in order to be able to predict the behavior during waterflooding of a fractured chalk reservoir.

Mattax and Kyte (Mattax & Kyte 1962) proposed a scaling law for scaling of small laboratory imbibition tests on fractured samples to be used for prediction of imbibition oil recovery behavior for large fractured reservoirs. It was shown that the time required to recover a given amount of oil from a matrix block by imbibition is proportional to the square of the distance between the fractures. However, the proposed scaling law requires that the shape of the laboratory model is identical to the matrix block and the water-to-oil viscosity ratio is similar. Further, initial fluid distribution, wettability and pore geometry must result in identical relative permeability curves for the model and the reservoir matrix block, and the capillary pressure curves must be related by direct proportionality between the model and the reservoir matrix block. The scaling law was later modified by many authors. See Babadagli and Zeidani (Babadagli & Zeidani 2004) for a systematic overview of the modifications.

Kyte (Kyte 1970) introduced a new method to predict oil recovery behavior for matrix blocks in a fractured reservoir. Centrifuge tests were carried out on preserved core samples from a slightly water-wet consolidated sandstone reservoir to scale the effects of both gravity and capillarity in order to simulate a water-oil displacement in a reservoir. The method requires that the selected core has the same shape as the prototype reservoir matrix block. Further, the wettability, porosity and permeability must be identical in the core and the prototype reservoir matrix block. It was shown that the centrifuge tests properly scale the capillary and gravity forces that are important in recovering oil from a water-drive reservoir. Another advantage of the centrifuge method is that the boundary effects can be properly scaled. It was evaluated that centrifuge tests on preserved reservoir cores, or on cores with restored wettability, represents the most reliable method available for prediction of matrix block recovery behavior in fractured reservoirs.

Illangasekare et al. (Illangasekare et al. 1991) performed centrifuge tests on infiltration of a light nonaqueous phase liquid (LNAPL) into a fine sand column with and without initial water saturation. Prototype testing was conducted in a long plexiglas sand column with similar boundary conditions as in the centrifuge model tests. Good agreement between the two types of experiment verified the derived scaling relations for the flow processes of the advance of a LNAPL wetting front in fine sand. However, due to the limited height of the sand column, only the initial part of the infiltration was duplicated in the prototype test. They concluded that the results demonstrate the feasibility of using

the geotechnical centrifuge to model stable LNAPL infiltration in unsaturated media.

Petersen and Cooke (Petersen & Cooke 1994) expressed scaling concerns for immiscible multiphase flow in porous media based on results on scaling analysis of unstable LNAPL infiltration into sand. The analysis of fingering indicates that at increased gravities, fewer fingers will form, and those that do form, will be larger and propagate faster than would be required for modelling similitude. However, this wetting front instability with formation of gravity fingers was observed for gravity-driven flow in sand.

Knight and Mitchell (Knight & Mitchell 1996) performed modelling of models tests on LNAPL infiltration into a sectioned sand column with a water table and capillary water above the water table, i.e. modelling of three phase flow. After centrifuging, the saturation was determined in the sections of the sand column. They concluded that the work demonstrated the usefulness of centrifuge modelling for producing three-fluid flow data in fine sand. However, care must be taken to ensure that deficiency in similitude is minimized by the use of appropriate materials and scales.

Culligan et al. (Culligan et al. 1996) reported that geotechnical centrifuge modelling is a technique that has proven useful in the study of LNAPL infiltration in unsaturated media. Since LNAPL will preferentially wet a solid with respect to air, the infiltration of LNAPL in the vadose zone (area between the ground surface and the water table) involves a wetting front displacement. Tests were performed in the centrifuge of LNAPL infiltration into an initially dry sand medium comprising two sand layers and a water table. It was concluded that scaling of gravity-driven LNAPL fingering into the vadose zone, i.e. unstable LNAPL infiltration, is possible using the geotechnical centrifuge.

Further, centrifuge tests on remediation of LNAPL by hydraulic flushing (waterflooding) was carried out on sand samples initially saturated with LNAPL, with water displacing the LNAPL upwards. When the extraction of LNAPL is performed by hydraulic flushing, discontinuous blobs of LNAPL can become entrapped in the porous media behind the wetting (water) front. The degree of entrapped non-wetting phase after test was determined at various g-levels and various wetting phase displacement velocities. The work demonstrated the influence of buoyancy and viscous forces on capillary entrapment.

Cooke (Cooke 2000) performed tests in the centrifuge on LNAPL infiltration into a column of fine sand. As the effect of the capillary and Bond numbers on multiphase flow processes is manifested in the degree of residual entrapment of a displaced fluid, these effects would not be apparent in the infiltration of a LNAPL into dry sand, except at the trailing edge of a LNAPL, i.e. unless the LNAPL was allowed to be completely depleted during the test period. Consequently, the tests were run at different g-levels for a limited amount of LNAPL allowing a trailing edge. The results indicate that modelling of LNAPL infiltration, where the LNAPL passes through the soil leaving behind residual LNAPL, cannot be reliable carried out in the centrifuge. It is assumed that the main problem is lack of similitude in the residual entrapment process, which is influenced by the capillary and Bond numbers. A tendency towards decreasing residual entrapment with increasing g-level was observed.

Pantazidou et al. (Pantazidou et al. 2000) experimentally investigated the migration potential of dense nonaqueous phase liquids (DNAPLs) in water-saturated soils using the

centrifuge. The stable infiltration of a high viscosity DNAPL in saturated homogeneous media was shown to be properly modelled in the centrifuge. This was based on tests on model soil samples constructed with sand-size and silt-size glass beads. The model tests were continued until no further movement of the DNAPL front could be observed. However, some DNAPL remained in the source. After centrifuging, the soil samples were dissected to examine the final DNAPL distribution in the samples. Normalized capillary entry pressures (to 1 g) were close to unity, confirming the assumption that the relative magnitude of governing forces, i.e. gravity and capillary forces in this case, can be preserved in the centrifuge. Further, modelling of models, i.e. tests on models that correspond to the same prototype, but at different g-levels, were carried out confirming the validity of the centrifuge scaling. Finally, the centrifuge results were compared with predictions of a numerical model, which further support the usefulness of the centrifuge for modelling DNAPL transport.

Christensen (Christensen 2001) provided suggestions regarding up-scaling of strength and deformation properties based on tests on Hillerslev and Stevns outcrop chalk specimens (Havmøller & Krogsbøll 2001). The tests revealed that at higher stress levels (close to the pore collapse stress level), and/or at higher confining stresses, the conventional scale tests can be applied directly without up-scaling.

Within the frame of the NECER program, Bagge et al. (Bagge et al. 2002) investigated the scaling of capillary phenomena in a centrifuge by cross-testing at several laboratories, using similar samples and the same Congleton sand. Capillary rise and drainage of water in sand was measured after the test and in-flight measurement of water content was also attempted, using radiotracers and tensiometers as well as TDR probes and pore pressure transducers. The results indicate that it is possible to model the entire capillary zone for Congleton sand in a centrifuge with the vertical dimension reduced by the g-factor N. This is due to that the capillary imbibition potential is reduced by the factor N in the model. Further, time dependent phenomena appear to be reduced by the factor N^2 in the model.

To sum up, up-scaling of laboratory test results on oil displacement by waterflooding in fractured chalk specimens to reservoir scale is affected by the presence of fractures. However, it seems that strength and deformation properties in conventional scale tests at stress levels close to the pore collapse stress and/or at higher confining stresses can be applied directly to reservoir scale. It seems possible to use the centrifuge to model the displacement processes during waterflooding. Especially since the capillary imbibition potential is reduced by the g-factor N. However, due to inconsistency in similarity between model and prototype, it may be questionable to use the centrifuge for modelling total oil recovery. In other words, the possible inconsistency in capillary and Bond number caused by a high centrifuge acceleration and a corresponding high flow velocity may result in a higher oil recovery by waterflooding, i.e. a lower residual entrapment as would be expected in the prototype. Further, gravity-driven flow in the centrifuge can cause wetting front instability, which may lead to scaling problems. The main part of the published work on centrifuge modelling is performed on NAPL infiltration into sand. To the authors knowledge, no centrifuge studies are published on large-scale tests of oil displacement by

waterflooding in naturally fractured chalk specimens.

1.3 Objectives of the Ph.D. Project

To optimize waterflooding in fractured reservoir chalk and thereby increase the recovery factor, more has to be understood about the displacement processes, especially the effect of wettability and fractures on the displacement processes. Further, more has to be understood about chalk-water interaction at higher stress levels (above yield stress), especially the effect of fractures on the interaction. More work is also required in relation to up-scaling of laboratory test observations to reservoir scale.

The main objectives of the Ph.D. project were to study the displacement processes for displacement of oil by waterflooding in naturally fractured chalk, the effect of wettability and especially the effect of fractures on the displacement, and also the effect of chalk-water interaction, i.e. water weakening and water-induced compaction during waterflooding. The secondary objectives were to study the correlation between matrix and effective permeability, and centrifuge scale factors to facilitate the up-scaling of laboratory test observations to reservoir scale.

The study was based on oil permeability and waterflooding tests on seven large ($D \approx$ 50 cm, $H =$ 43-50 cm), naturally fractured Hillerslev outcrop chalk specimens. The tests on five of the specimens were performed at low mean stress levels in a centrifuge. The tests on the remaining two specimens were performed at higher mean stress levels in an oedometer cell.

The purpose of the oil permeability tests was to investigate the influence of stress on the permeability. The study of effective permeability stress dependency was only conducted for information on Hillerslev outcrop chalk, and no literature overview on this subject is thus included.

Given sufficient time and water, oil displacement by waterflooding results in high oil recovery for strongly water-wet chalk. To determine whether the presence of fractures in strongly water-wet chalk impose a risk of flow of water in the fractures, leading to early water breakthrough and an inefficient matrix-fracture transfer, the waterflooding tests were performed at a high rate in a centrifuge suppressing the capillary imbibition potential. The aim of the waterflooding tests in the centrifuge was to obtain water breakthrough caused by flow of water in the fractures ahead of the waterfront and possibly continued water production. Thereby the interrelation between the two displacement processes: viscous displacement and capillary imbibition, and the concept of a critical waterflooding rate could be studied, i.e. the effect of fractures on the displacement processes. Further, the wettability of a single specimen was altered towards less water-wet to a fractional-wet state to perform waterflooding on as close an analogue to the Tor formation of the Valhall field as possible, and to investigate the effect of wettability on the displacement processes.

The aim of the waterflooding tests in the oedometer cell was to study the displacement processes and the chalk-water interaction at higher stresses (stresses above yield) during waterflooding of naturally fractured chalk.

The study of the effect of wettability and fractures on the displacement processes and chalk-water interaction is believed to be improved, when large, naturally fractured chalk specimens are used, as they are considered more representative for field scale as the effect

of complex groups of natural fractures are included.

The centrifuge was used to facilitate the modelling and up-scaling of the displacement processes during waterflooding of fractured chalk. The modelling and up-scaling is believed to be improved, when centrifuge tests are conducted on these large, fractured chalk specimens. Further, the capillary imbibition potential is reduced by the g-factor N making the test specimens more representative for reservoir scale. Since less than one pore volume of water was injected into the specimens during centrifuging, these test evaluations are based on displacement processes and not on total recovery. Further, the flow was opposite the direction of the artificial gravity field, i.e. not gravity-driven.

1.4 Overview of the Experimental Work in the Ph.D. Project

A schematic overview of the experimental work in the Ph.D. project is shown in Figure 1.1. In the following, the experimental work is briefly described, including details on which part of the work that was carried out by the author and others involved.

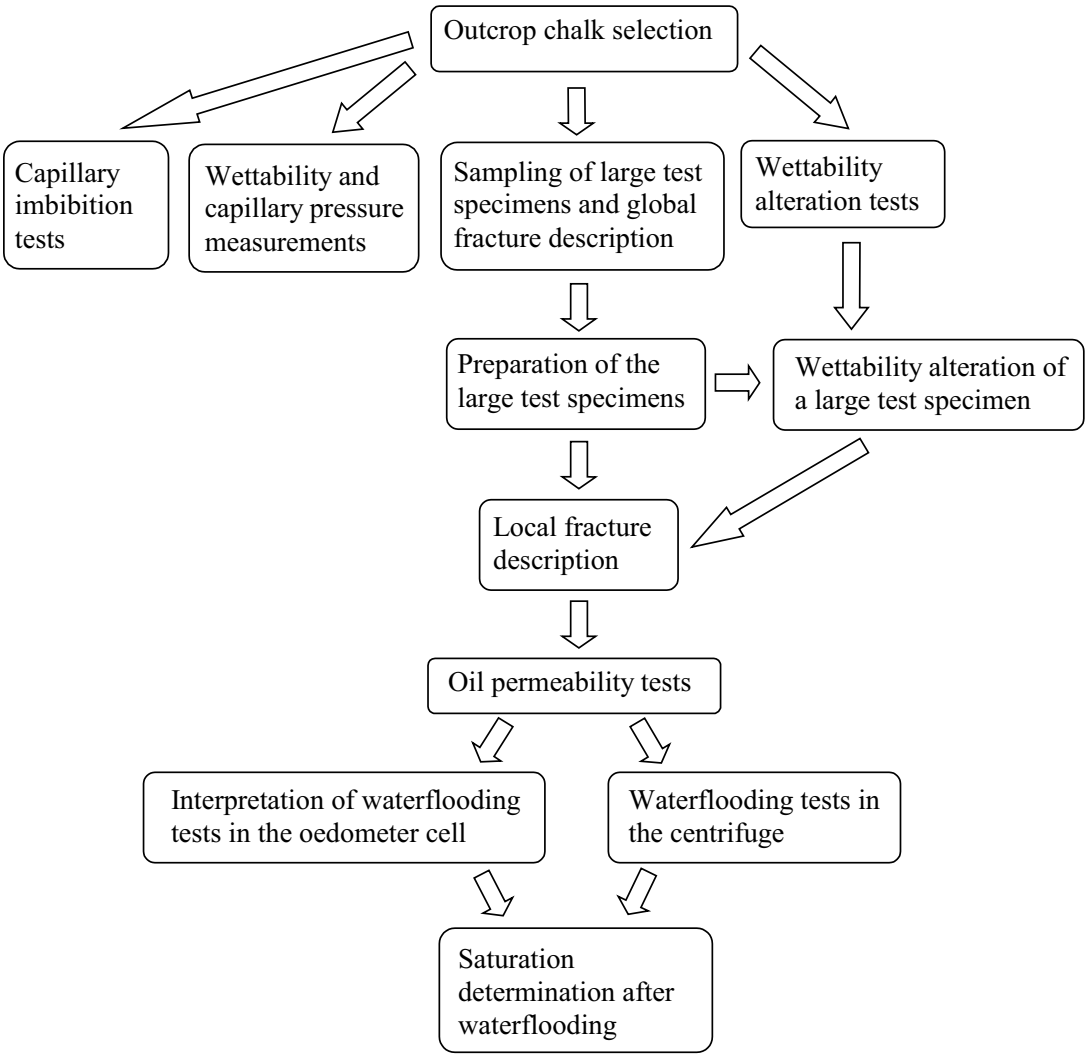

Figure 1.1 *Schematic overview of the experimental work in the Ph.D. project.*

Wettability and Capillary Pressure Measurements

Measurement of wettability and subsequent establishment of capillary pressure curves was carried out for three small (D = 38 mm, H = 50 mm) Hillerslev outcrop chalk specimens. This was done by utilizing Amott cups and an automated Beckmann centrifuge at the premises of Rogaland Research, Stavanger, Norway. Two of the specimens tested

were originally water-wet, while the wettability of a single specimen was altered to a homogenous, neutral to slightly oil-wet state.

The tests were planned and carried out by the author with help and supervision from Research Engineer Jan Erik Iversen, Rogaland Research, and Engineer Egil Boye Petersen, earlier working at Rogaland Research. The data processing, evaluation and reporting was carried out by the author.

Capillary Imbibition Tests

Measurement of spontaneous imbibition of water were carried out on three small ($D \approx 54$ mm, $H \approx 27$ mm) Hillerslev outcrop chalk specimens. The author planned the tests, and technician Vita Larsen, BYG•DTU carried out the tests. The data was processed, evaluated and reported by the author.

Sampling of Large Test Specimens

A field trip was made to the Hillerslev outcrop chalk quarry located in the northern part of Jutland, Denmark. Here, twelve large specimens ($D \approx 50$ cm, $H \approx 50$ cm) were sampled. A group of five including the author performed the sampling of the large specimens. However, the drilling of the specimens by use of a mobile drilling rig was performed by GEO, and staff at the Hillerslev quarry performed the rough excavation by use of a backhoe. A (global) fracture description was carried out mainly by the author. The processing and evaluation of the fracture data was performed by the author. The presentation of the fracture data by use of the program SpheriStat was carried out at GEUS with help and supervision from Senior Research Geologist Finn Jakobsen, GEUS.

Preparation of the Large Test Specimens

Before the waterflooding tests, seven of the twelve sampled large test specimens were trimmed, measured and cast with gypsum. Then a (local) fracture description of the specimens was carried out. The specimens were then oven-dried and oil-saturated. The author performed this work on the five specimens intended for the centrifuge tests. For the two test specimens used in the oedometer cell, GEO prepared the specimens, and the author assisted with the fracture description.

As part of her master thesis, Inge Larsen prepared two large, fractured Hillerslev outcrop chalk specimens to use for waterflooding tests. These specimens were recovered during the earlier research project "Fractures and Rock Mechanics", phase 2 (Jakobsen 2001). Inge Larsen only had time to test one of the specimens, so the author took over the specimen not used for testing. This specimen was trimmed, measured and cast with gypsum by Inge Larsen. Further, a fracture description of the specimen was carried out, and the specimen was oven-dried and oil-saturated. The specimen was thus prepared by Inge Larsen. However, the author helped with the preparation of the specimen tested by Inge Larsen and co-supervised Inge Larsen during her master thesis.

Eight specimens were intended to be used for waterflooding. However, one of these specimens were not used due to that liquid rubber mass entered the fractures in the specimen during mounting in the centrifuge set-up.

Wettability Alteration Tests

Wettability alteration tests were performed on small pieces of Hillerslev outcrop chalk by adding 0.1 weight%, 0.5 weight% or 1.0 weight% Dodekane acid to the laboratory oil Isopar-L, then saturate the chalk pieces with this mixture and leave them in the mixture at 20° C, 40° C or 90° C for 1 week, 20 days or as long as 1 month. This work was planned by the author and performed by the laboratory at BYG•DTU. The data processing, evaluation and reporting was performed by the author.

Development of Test Equipment

Two test set-ups were developed for the permeability and waterflooding tests in the centrifuge. The design and planning was done by the author in cooperation with Director of Research Niels Foged, BYG•DTU. The actual manufacturing of the equipment was performed by technicians at GEO and at BYG•DTU. During instrumentation, mounting and testing, different issues occurred which was solved by further development on the equipment and by improving the specimen handling as well as the test procedures. This was done by the author.

GEO designed and manufactured the equipment used for the tests in the oedometer cell.

Wettability Alteration of a Large Test Specimen

The wettability of a single large test specimen was altered towards less water-wet. The wettability alteration was done by adding 0.5 weight% Dodekane acid to the Isopar-L, then saturate the specimen with this mixture and leave it in the mixture for aging at room temperature. Due to problems with the liquid rubber mass entering the fractures in the specimen, this specimen was not used for testing. Consequently, the wettability of another specimen was altered towards less water-wet following the same procedure.

The wettability alteration was planned by the author and carried out by help of technicians at BYG•DTU.

Permeability and Waterflooding Tests in the Centrifuge

Oil permeability and waterflooding centrifuge tests were carried out on five large, naturally fractured Hillerslev outcrop chalk specimens. Four of the specimens were instrumented with TDR probes. Initially, oil permeability tests were run, and then the waterflooding was performed in the centrifuge. After testing, small samples were taken out of the large test specimens for determination of mean saturation. The author did the planning of the tests for all five specimens.

A single test specimens was used in Katrine A. Olufsens master thesis. Katrine A. Olufsen instrumented the specimen with TDR probes. Together, the author and Katrine A. Olufsen performed the mounting, permeability tests and waterflooding test. She performed the determination of saturation after test. The data processing, evaluation and reporting on the shared specimen was done differently, and thus separately. However, the author helped and co-supervised Katrine A. Olufsen during her master thesis.

For the four other test specimens, the author performed the instrumentation, mounting, permeability tests and waterflooding test, and the determination of saturation after test. Further, the author performed the data processing, evaluation and reporting.

Interpretation of Permeability and Waterflooding Tests in the Oedometer Cell

Tests including consolidation and creep phases, permeability measurements and waterflooding were carried out on two large, naturally fractured Hillerslev outcrop chalk specimens in an oedometer cell. The tests were carried out by GEO. The author participated in the test procedure design. Further, the author performed the data processing, evaluation and reporting.

1.5 Content of the Ph.D. Thesis

The main objective of this Ph.D. thesis was to provide the overall findings of the Ph.D. project. The overall content of the following chapters are outlined below.

Chapter 2 describes the theoretical aspects of oil displacement by waterflooding in fractured chalk. This spans from description of a fractured chalk reservoir and general reservoir behavior, over pure waterflooding theory to centrifuge modelling theory, and finally the mechanical behavior of chalk.

Chapter 3 elaborates on the basis for the experimental work and the overall choices made in connection with this work.

Chapter 4 provides the general properties of Hillerslev outcrop chalk. This includes a description of chalk type, wettability, capillary pressure and fractures. Further, a comparison of the chalk from the Tor formation of the Valhall field and the Hillerslev outcrop chalk is included.

Chapter 5 includes a description of the test specimens used for the tests in the centrifuge and the oedometer cell, i.e. a description of the fracture patterns, and the wettability alteration of a single specimen. Further an absolute oil permeability study of Hillerslev outcrop chalk is presented.

Chapter 6 includes a description of the waterflooding tests in the centrifuge. Initially, the planning and modifications of the centrifuge tests are described. Then a description of the waterflooding test set-up, procedure and results are included. The displacement processes observed during waterflooding are described, and the influence of wettability and fractures on these displacement processes are evaluated. Finally, an interpretation of the centrifuge modelling is included.

Chapter 7 presents a short description and discussion of the simulations performed by Gudbjerg (Christensen 2003) on two of the waterflooding tests performed in the centrifuge.

Chapter 8 includes a description of the test set-up, procedure and results for the waterflooding tests in the oedometer cell. The displacement processes observed during waterflooding are described. Further, the chalk-water interaction observations during waterflooding are included. Finally, the waterflooding test observations in the centrifuge and the oedometer cell are compared.

Chapter 9 presents the waterflooding field evidence of the Tor formation of the Valhall field. The present waterflooding test observations are compared to the waterflooding field

evidence.

Chapter 10 contains the main conclusions on the displacement processes and the effect of wettability and fractures on the displacement processes based on the experimental work. Further, the main conclusions on the effect of the chalk-water interaction on the waterflooding is included.

Chapter 11 provides an overall perspective of the work on oil displacement by waterflooding in fractured chalk performed in a centrifuge and an oedometer cell.

1.6 Content of the Adjacent Reports

Two reports prepared during the Ph.D. project are adjacent to this Ph.D. thesis for reference to theory and calculated data and also for details not necessary for the conclusions in this Ph.D. thesis.

Report 1 "Hillerslev Outcrop Chalk" includes a fracture description at the Hillerslev outcrop chalk quarry, a description of the sampling of the large specimens at the quarry, and finally a fracture description of the specimens used for the waterflooding tests. Report 2 "Wettability and Capillary Pressure Measurement on Hillerslev Outcrop Chalk" is prepared including measurements of two-phase flow properties such as wettability indices and capillary pressure curves for Hillerslev outcrop chalk.

Chapter 2

Theoretical Aspects of Waterflooding Fractured Chalk

2.1 Geology of Fractured Chalk Reservoirs

This Section includes a short description of the geology of fractured chalk reservoirs in the North Sea based on Andersen (Andersen 1995).

The chalk fields of the North Sea are located in the Norwegian and Danish sectors of the Central Graben area, and lie along a line almost midway between Norway, Denmark and the United Kingdom. Generally, the fields are characterized as fractured, overpressured, high porosity chalk. The porosities ranges up to 50%, while the matrix permeability is low ranging from 1-10 mD. The productive chalk formations comprise the Ekofisk, Tor and Hod formations. The Ekofisk formation is Danien in age (Paleocene), the Tor formation is mainly Maastrichtian in age (Late Cretaceous), and the Hod formation is Turonian through Campanian in age (Late Cretaceous).

Chalk is a pelagic sediment, formed in the open sea, and deposited as a slow rain of algal remains. North Sea chalks mainly consist of coccolith fragments or aggregates of coccolith platelets, see Figure 2.1. The particles of chalk originate as skeletons of algae that are called coccosperes (30 μm), which are formed by coccoliths (3-15 μm) enclosing the soft part of the algal organism. The coccoliths are formed into assemblages of rings and rosettes by calcite plates (0.5-2.5 μm). The chalk in the fields ranges from very pure chalk containing primarily calcite coccoliths (>98%) to chalk contaminated by silica and clay or calcite overgrows between the coccoliths. The pure chalk is mechanically very weak, in many cases there is little to no cementation. The impure chalk has greater mechanical strength from the cementation provided by the silica or calcite overgrowth.

Chalk from the Central Graben area underwent downslope movements. This reworked chalk is termed allochthonous. Sediments that has not moved are termed autochthonous.

The structures, i.e. the hydrocarbon traps, where the hydrocarbon accumulates can amongst others be formed by folding or diapirism providing less permeable layers, i.e. seals. Folding occurs when the regional stresses are compressive, causing the layers to buckle or fold. Diapirism is intrusion of salt from below the formation. Both folding and diapirism can cause the chalk formation to fracture.

Fractures are important for reservoir performance since the matrix permeability is

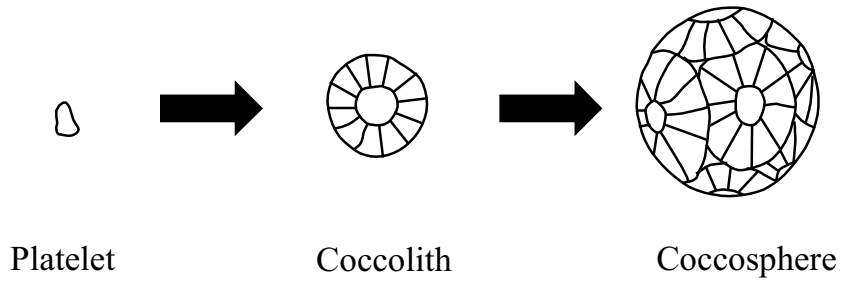

Figure 2.1 *Calcite platelet, coccolith and coccoshere.*

low. An examination of cores from wells from four fields identified four fracture types: tectonic, stylolite-associated, irregular, and healed fractures. Tectonic fractures are shear or extensional fractures, formed from deformation of the sediment by fault movement, diapirism, or regional extension or compression fields. The tectonic fractures contribute most to the increase in fracture permeability. The stylolites are common in North Sea chalks, and are thought to result from pressure solution and differential movement. The stylolites neither help nor hinder the permeability, but stylolite-associated fractures can enhance the permeability. Irregular fractures locally enhance permeability, but are poorly connected. The origin of healed fractures is strictly conjecture. They could have formed pathways for oil migration, but now they are found filled with a calcite material.

The source of the oil in the North Sea chalk fields is the organic-rich shales of Upper Jurrasic in age, the Mandal formation or Kimmeridge clay. The oil migration to the hydrocarbon traps is mainly provided by the fractures induced by folding or diapirism.

2.2 Wettability and Capillary Effects

2.2.1 Wettability

Wettability is the preference of a solid to be in contact with, i.e. wetted by, one immiscible fluid in comparison to another. The term wetting means that the fluid spreads over the solid surface and non-wetting means that the fluid tends to ball up and run off the surface. Wettability is only used for the wetting preference of the solid, it does not necessarily refer to the fluid in contact with the solid. In an oil/water/chalk system, water-wet means that the chalk surface prefers water in the presence of oil.

Wettability can be explained by the question of which state is energetically more favorable, having fluid A or fluid B in contact with the solid. If both fluids are available to wet the solid surface, the fluids will rearrange to give the lower energy state (Andersen 1995). In Figure 2.2, the preferential wetting of a solid surface is illustrated.

The sum of forces acting on the element of the contact line between the three phases must be equal to zero, see Figure 2.2(b). By projecting the forces onto the surface, the Young formula is obtained:

$$\cos\theta = \frac{\sigma_{SB} - \sigma_{SA}}{\sigma_{AB}} \tag{2.1}$$

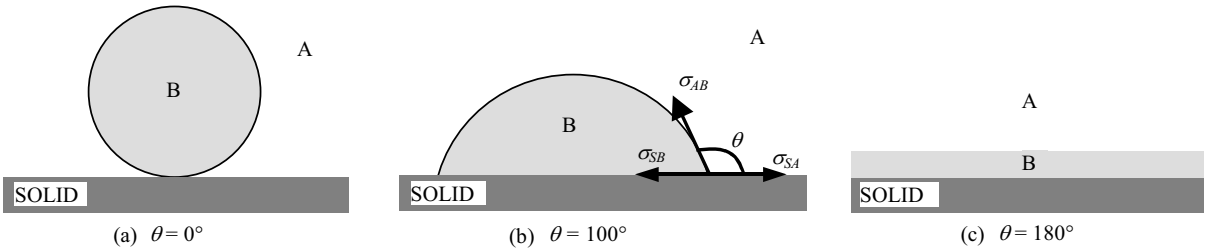

Figure 2.2 *(a) complete wetting of fluid A (spreading of fluid A), (b) equal wetting of the two fluids, and (c) complete wetting of fluid B (spreading of fluid B).*

where σ_{SA} and σ_{SB} are the surface tensions between the fluids and the solid, σ_{AB} is the interfacial tension between the two fluids and θ is the contact angle here measured through fluid A. By convention, the contact angle in an oil/water/chalk system is measured through the water.

The value of θ may lie anywhere between 0° and 180°. For the range $0° \leq \theta < 75°$ fluid A is preferentially wetting with the corresponding degree of wetting decreasing towards 75°, whereas for the range $105° < \theta \leq 180°$ fluid A is preferentially non-wetting with the corresponding degree of nonwetting increasing moving away from 105°. Equal wetting (neutral wettability) corresponds to the range $75° \leq \theta \leq 105°$ (Anderson 1986*a*).

Types of Wettability

Various types of wettability exist. In oil/water/chalk systems, wettability can cover a broad spectrum of wetting conditions that range from strongly water-wet to strongly oil-wet. A water-wet solid surface is covered by a film of water, and attracts only water and repels other fluids. An oil-wet solid surface is covered with an oil film and attracts only oil, and repels other fluids. A neutral-wet solid surface has no strong preference for either oil or water, and neither fluid is attracted spontaneously, whereas it attracts and repels involved fluids equally under force. An intermediate-wet solid surface spans over slightly oil-wet, neutral-wet, and slightly water-wet (Cuiec 1987). The degree of wetness results in a corresponding degree of attraction.

Within the range from strongly water-wet to strongly oil-wet, fractional-wet conditions exist. These non-homogeneous wet systems have portions of the surface, which are water-wet, while the rest are oil-wet. A fractional-wet solid surface is also termed Dalmatian-, speckled- or spotted-wet. Salathiel (Salathiel 1973) introduced the term "mixed-wettability" for a special type of fractional wettability in which the oil-wet surfaces form continuous paths through the larger pores. The smaller pores remain water-wet and contain no oil. The main distinction between mixed- and fractional-wettability is that the latter neither imply specific locations for the oil-wet and water-wet surfaces nor continuous oil-wet paths. Fractional- or mixed-wet material may attract both oil and water spontaneously.

Oil Migration

Before oil migration, a reservoir chalk is fully saturated with water and assumed strongly water-wet (Anderson 1986*d*). However, the reservoir chalk may in fact be less than strongly water-wet due to original coating of the coccoliths with organic films (Baldwin 1988). When oil migrates into the reservoir, the water is displaced. As the oil accumulates, the reservoir is filled from the top down, because the density of the oil is less than the density of the water and due to the less permeable layer overlaying the reservoir providing a seal. This density difference becomes a pressure difference gradient with depth, acting as a driving pressure for forcing the nonwetting oil into the pores (Andersen 1995). The pressure difference between the invading phase pressure (oil) and the displaced phase pressure (water) defines the capillary pressure P_c. The (minimum) capillary pressure that first causes the nonwetting oil to enter the largest pores is called the capillary entry pressure P_{ce}. Water is displaced first from the larger interconnected pores. When these larger pores are filled with oil and the capillary pressure increases further, the smaller pores and pore volumes connected through these are also filled with oil. Except at very high capillary pressures, the smallest pores will be the last, if ever, to be filled with oil. After the oil migration, the reservoir is left at the residual water saturation termed the connate water saturation S_{wc}. At S_{wc}, the water phase is immobile. The water tends to occupy small pores and be in contact with the main part of the chalk surface in form of a continuous water film, while the oil will be located in the center of larger pores (Anderson 1986*d*). As a film of water remains on the pore walls, the reservoir will be oil-saturated, but stay water-wet.

The distribution of fluids in a fractured chalk reservoir may be different from an unfractured chalk reservoir. In a fractured reservoir, the majority of the oil migration occurs along faults and fractures. If the height of a matrix block in the matrix-fracture system is less than the capillary entry pressure P_{ce}, water will not be displaced from the matrix block, except if there is capillary continuity between adjacent blocks. Consequently, lower matrix blocks will contain more water than higher matrix blocks.

Wettability Alteration

The original water-wetness of chalk reservoirs can be altered by adsorption of polar compounds and/or deposition of organic material present in the crude oil. The surface-active agents (surfactants) in the oil are generally believed to be polar compounds containing oxygen, nitrogen and/or sulfur. These surfactants contain both a polar and a hydrocarbon end. The polar end adsorbs on the surface, exposing the hydrocarbon end and making the surface more oil-wet. Experiments have shown that some of these surfactants are sufficiently soluble in water to adsorb onto the solid surface after passing through a water film (Anderson 1986*a*).

The natural surfactants are more prevalent in the heavier fractions of crude oil such as resins and asphaltenes. However, experimental data so far show no clear correlation between the asphaltene/resin content and the ability of crude oil to make the chalk surface oil-wet, other than that these must be present in the crude oil. Standnes and Austad (Standnes & Austad 2000a) reported that the wettability induced by crude oils on chalk surfaces is related to the amount of acidic components in the crude oil, i.e. crude oils

with high acid numbers (AN) have a greater potential to turn the chalk oil-wet. The crude oil must have an AN in the order of 0.5-1.0 mg KOH/g oil if the chalk wettability is to be altered towards oil-wet (personal communication with Professor Tor Austad, Stavanger College, Norway). In addition to the oil composition, the degree of wettability alteration by the natural surfactants is also determined by the pore roughness, water saturation, history of the fluid exposed to the chalk surface, surface mineralogy, the microscopic distribution of fluids, pressure, temperature, and water chemistry, including ionic composition, salinity and pH (Viksund 1998).

In an extreme case, a chalk reservoir could be altered to strongly oil-wet, still oil-saturated, but with a residual water saturation of the same size as S_{wc}. However, since a film of oil now covers the pore walls, the residual water is considered mainly to exist as disconnected "blobs". In strongly oil-wet chalk, oil is generally found in the smaller pores and as films, and water is located in the center of larger pores. The location of connate water in strongly oil-wet reservoirs is somewhat uncertain. It is not known to what extend the water may be displaced from its original positions by oil, particularly in smaller pores that were initially fully water saturated (Rathmell et al. 1973). The wettability alteration may also result in an intermediate- or mixed-wet chalk reservoir.

In order to obtain a homogeneously altered wetting state in a test specimen, Standnes and Austad (Standnes & Austad 2000a) recommend to flush the specimen with crude oil in each direction. After flushing, the specimen should be aged in a container, where it is surrounded by crude oil. This results in the outermost layer being more oil-wet due to the mechanism of adsorption. Another issue is the capillary end effect related to the saturation procedure used to establish an irreducible water saturation S_{wir} in a water-wet specimen before aging. In case of capillary end effect, the outermost part of a water-wet specimen appears to be more water-wet. These outermost effects make the removal of at least 2 mm of the outermost layer necessary.

Wettability alteration can affect the results of most specimen analysis. However, the wettability measured on cores taken from a reservoir may be different from the wettability of the reservoir. Unfortunately, many factors can significantly alter the wettability of the specimen. These factors can be divided into two general categories: (1) those that influence specimen wettability before testing, such as drilling fluids, packing, preservation and cleaning, and (2) those that influence wettability during testing, such as test fluids, temperature and pressure. In addition, the pressure and temperature drop that occurs as the specimen is brought to the surface may also change the wettability as it results in expelling of fluid and changes the spatial distribution of the fluids. Generally, specimens run at atmospheric conditions are more oil-wet than those run at reservoir conditions (Anderson 1986*a*).

Measuring Methods for Wettability

Wettability can be measured in the laboratory. Three quantitative methods are generally used: (1) contact angle method, (2) the Amott test, and (3) the U. S. Bureau of Mines (USBM) test. The contact angle method measures the wettability of a specific surface, while the Amott and USBM tests measure the average wettability of a specimen. The two latter methods are also used in a combined test referred to as the modified USBM

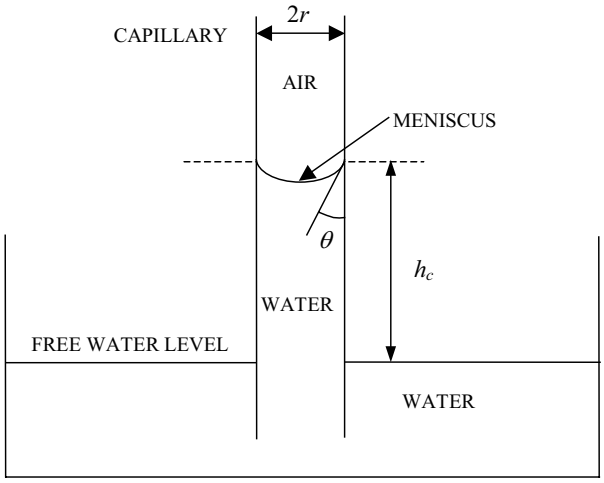

Figure 2.3 *Water rise above the free water level by capillary forces in a capillary with radius r.*

test (Anderson 1986*b*). A detailed description of these methods are included in Report 2.

2.2.2 Capillary Pressure

Capillary Pressure Curves

Information on capillary pressure of chalk reservoirs are necessary in order to estimate the waterflooding behavior. Capillary pressure curves are obtained in the laboratory on small, un-fractured chalk specimens. A capillary pressure curve represents the relationship between the capillary pressure and the degree of saturation of the chalk. However, for a fractured chalk reservoir, the capillary pressure curves only provide information on the behavior of the matrix blocks.

Capillary pressure is caused by interfacial tension (IFT) between oil, water and rock, i.e. a result of the attractive forces (adhesion and adsorption) between a fluid and solid particles and the cohesive forces between fluid molecules. In a capillary, a balance between the weight of the fluid and the cohesive and adhesive forces exist (Senneset et al. 1995). In Figure 2.3, a cylindrical capillary with radius r is placed in a container with water. The adhesive forces between the capillary tube and the water will cause the water to rise until equilibrium is reached between the capillary forces (directed upwards) and the gravitational forces (directed downwards), creating a meniscus. The capillary rise of the water is inversely proportional to the radius of the capillary, i.e. the smaller the radius, the higher the capillary rise. The height of the capillary rise above the free water level is termed the capillary pressure head h_c. A capillary can be used as a simple model for a pore in a porous medium.

Capillary pressure P_c [Pa] defines the pressure difference between the wetting fluid and the nonwetting fluid, and is given by the Young-Laplace equation:

$$P_c = \Delta P = \frac{2\sigma_i \cos\theta}{r} \tag{2.2}$$

where ΔP [Pa] is the pressure between the two fluids, σ_i [N/m] is the interfacial tension

between the two fluids, θ [deg.] is the contact angle between the fluid and the pore throat and r [m] is the radius of the pore throat. The radii of curvature of the interface, and hence the capillary pressure are determined by local pore geometry, wettability, saturation and saturation history. By convention the capillary pressure in an oil/water/chalk system is defined as $P_c = P_o - P_w$. Thus, the capillary pressure may be either positive or negative. When the interface is flat, the capillary pressure is zero. When fluids other than oil and water are used, the capillary pressure is defined as $P_c = P_{nonwetting} - P_{wetting}$ (Anderson 1986*c*). The capillary pressure head h_c [m] is determined as:

$$P_c = \Delta\rho g h_c \tag{2.3}$$

where $\Delta\rho$ [kg/m^3] is the density difference between the two fluids and g [m/s^2] is the gravitational acceleration. In an oil/water/chalk system, $\Delta\rho = \rho_w - \rho_o$, and for systems with other fluids than oil and water, $\Delta\rho = \rho_{wetting} - \rho_{nonwetting}$.

The capillary pressure is inversely related to the size of the pore throat. Since a porous medium has a distribution of pore throat sizes (modelled simplified by capillaries with different radii), there will be a distribution of capillary pressures within the porous medium. The curvature of a capillary pressure curve provides information about the distribution of the pores accessible through the pore throats in the medium. A very sharp curvature indicates a very narrow distribution of pore throat sizes, while a more gradual curve indicates a wide distribution.

Imbibition and Drainage

Imbibition and drainage describe the mechanisms of a fluid being driven into or expelled from a porous medium by capillary, viscous or gravity forces. Imbibition implies that the wetting phase is increasing while drainage is the opposite. A capillary pressure curve can thus either be a drainage curve or an imbibition curve.

In spontaneous (capillary) imbibition the process of displacing the nonwetting fluid from the pore goes to completion without any outside interference required. When the wetting fluid is placed under a higher pressure than the nonwetting fluid resulting in displacement, there is a case of forced imbibition. This is opposite for drainage, where the spontaneous and forced drainage is due to displacement of the wetting fluid. Larger pores emptying before smaller pores characterize drainage. Smaller pores filling before larger pores characterize spontaneous imbibition. Milter (Milter 1996) reported that the rate and amount of capillary imbibition depend highly on the wettability. Other factors thought to affect capillary imbibition in chalk reservoirs are porosity, permeability, the geometric shape of the chalk blocks, temperature, initial fluid saturations, fluid properties like density, viscosity, interfacial tension and composition of oil and water.

Schematic capillary pressure curves are shown for a water-wet chalk specimen and a chalk specimen altered to an oil-wet state in Figure 2.4, and for a chalk specimen altered to a mixed-wet state in Figure 2.5. For the water-wet chalk specimen, the primary drainage by oil is performed on a 100% water-saturated chalk specimen to the irreducible water saturation S_{wir}. At S_{wir}, the water phase is immobile and may be located in the smaller pores and as a continuous film covering the surface of the pore walls, i.e. corresponding to S_{wc} for the reservoir. For the water-wet chalk specimen, the primary drainage is followed

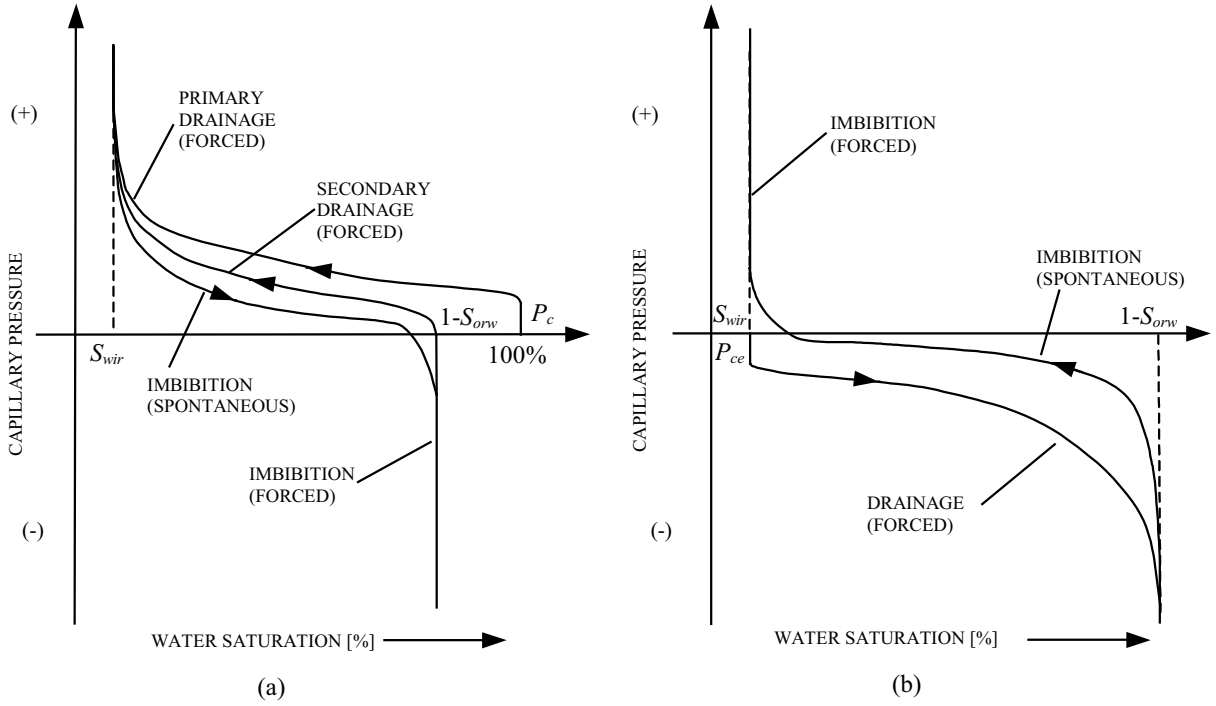

Figure 2.4 *Schematic of capillary pressure curves for (a) a water-wet chalk specimen and (b) an oil-wet chalk specimen.*

by imbibition to the residual oil saturation S_{orw} (the index w refers to displacement by water), where the oil phase is immobile and considered mainly to exist as disconnected "blobs" surrounded by water in the larger pores. Then secondary drainage back to S_{wir} follows.

For the oil-wet chalk specimen, the primary drainage and subsequent wettability alteration (not shown) is followed by drainage to S_{orw} and imbibition back to S_{wir}. For the mixed-wet chalk specimen, the primary drainage and subsequent wettability alteration (not shown) is followed by imbibition to S_{orw} and drainage back to S_{wir}. However, due to the wettability alteration, the initial water saturation after alteration in an oil-wet or a mixed-wet chalk specimen may be differently distributed than the irreducible water saturation in a water-wet chalk specimen.

The spontaneous imbibition of water into a strongly water-wet chalk specimen is so strong that the specimen is left at the residual oil saturation S_{orw}, and no forced imbibition takes place. Similarly, a strongly oil-wet system is left at the irreducible water saturation S_{wir} after spontaneous imbibition of oil, and no forced imbibition takes place.

The imbibition and drainage curves differ from each other. This is called hysteresis. Hysteresis can be explained by the amount of water contained in a non-uniform capillary tube illustrating the geometrical characteristics of many pores being larger than their pore throats, see Figure 2.6. In the tube of capillary rise (imbibition), the water will not rise beyond the height h_1 above the free water level corresponding to the largest radius. On the other hand, during drainage of a water-filled tube to a free water level, the tube will remain full of water to a height h_2 above the free water level corresponding to the

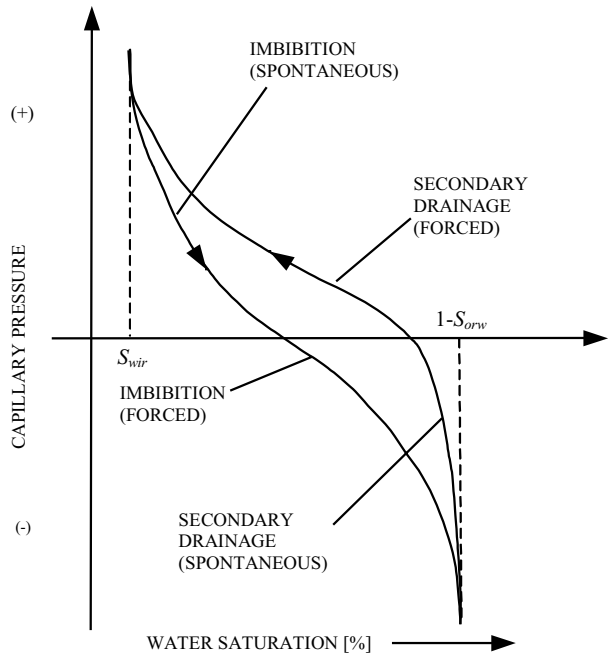

Figure 2.5 *Schematic of a capillary pressure curve for a mixed-wet chalk specimen.*

minimum radius of the tube.

Chalk is characterized by relatively high capillary entry pressures P_{ce} and relatively low irreducible water saturations S_{wir} due to the small pore throats and the narrow pore throat distribution. Further, chalk is characterized by a significant capillary hysteresis (Albrechtsen et al. 2001).

Saturation vs. height in the reservoir generally resembles a drainage capillary pressure curve. In Figure 2.7, the distribution of oil and water in three capillaries with different radii is shown. The capillary transition zone is indicated. The transition zone contains both oil and water. The point of fully water saturation for the largest capillary defines the lower bound of the transition zone and the point of fully oil saturation for the smallest

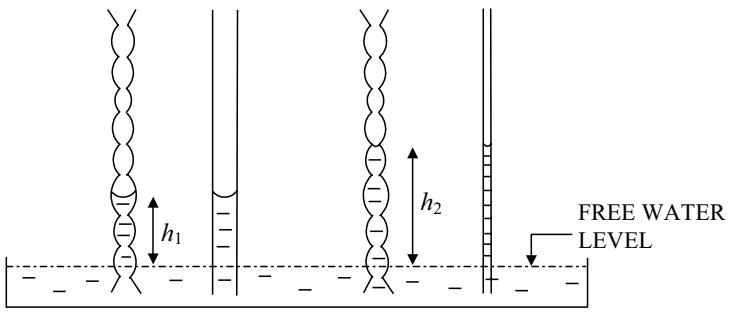

Figure 2.6 *Hysteresis in the amount of water contained in a non-uniform capillary tube for (a) imbibition and (b) drainage.*

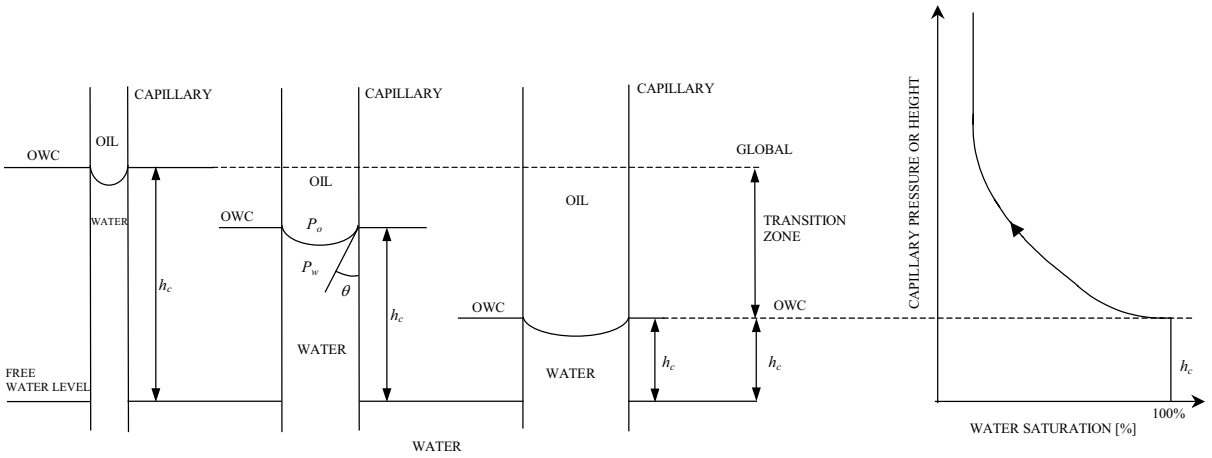

Figure 2.7 *Capillary pressure head h_c and transition zone for a simplified reservoir model and the corresponding drainage capillary pressure curve.*

capillary defines the upper bound of the transition zone. The lower bound is also denoted the oil-water contact OWC which is found at the point of the 100% water saturated zone. In the transition zone both oil and water are mobile. However, fractured chalk reservoirs lack transition zones due to the high permeability of the fracture network providing a mechanism for rapid re-equilibration of fluid contacts (Allan & Quing Sun 2003).

Measuring Methods for Capillary Pressure

Capillary pressure can be measured in the laboratory by at least three different techniques. (1) the mercury injection method. As mercury is a nonwetting fluid for reservoir rock, drainage capillary pressure curves can be obtained. (2) the porous plate method. The specimen is placed on a diaphragm wet by the fluid to be displaced from the specimen. During increase in the displacing pressure, the corresponding saturation is determined. (3) the centrifuge method. Here the pressure difference between the fluids results from the density difference, as in the gravity-driven process in the field.

According to Christoffersen (Christoffersen 1995) the porous plate method is considered the most accurate, whereas the mercury injection method and the centrifuge method are much faster to perform. An obvious disadvantage of the mercury injection method is that a different fluid system is used. The porous plate method directly measures the capillary pressure curve, while the centrifuge method is an indirect method and additional data processing is required to obtain a capillary pressure curve. A detailed description of the centrifuge method is included in Report 2.

2.3 Fracture Effects

Fractures in reservoir chalk are a great benefit to production of oil by waterflooding, since the matrix permeability of oil-bearing chalk reservoirs in the North Sea is low. Without natural or induced fractures to enhance the effective permeability, it would be marginally economic to produce from many of these reservoirs (Andersen 1995). For some fractured

North Sea chalk reservoirs, the effective permeability is 10 to 100 times larger than the matrix permeability (Viksund 1998).

Naturally fractured reservoirs behave in a different manner than un-fractured reservoirs due to the existence of two media, the matrix and the fractures. The fractures are characterized by a very high permeability compared to the surrounding matrix. Oil is primarily stored in the matrix, but flows primarily in the fractures. If a formation has an incomplete fracture network, flow must pass through the matrix to get from one subnetwork of fractures to another. This means that both matrix permeability, fracture permeability and effective permeability are important (Viksund 1998).

Increasing stress levels in the reservoir may affect the fracture network. Stress components normal to a fracture tend to close the fracture resulting in reduction in fracture permeability. Shear stresses may increase the permeability and even generate new fractures (Sulak & Danielsen 1989).

The efficiency and cost of waterflooding are characterized both by the injection pressure and the injection rate. Water should be injected at a pressure above the fracture propagation pressure to ensure fracturing in the reservoir and at the same time prevent fracturing in the layers above the reservoir. If the reservoir is oil-wet, the water should be injected at a pressure above the capillary entry pressure. In water-wet reservoirs, water should be injected at a rate facilitating imbibition.

2.3.1 Permeability

Absolute, Matrix Permeability

The absolute permeability (single-phase flow) is a measure of the ability of a porous medium to conduct a fluid provided that the porous medium is completely saturated with that fluid. Slow, one-phase fluid flow through a porous medium can be described by Darcy's law as:

$$Q = kAi \tag{2.4}$$

where Q [m^3/s] is the volumetric flow rate, k [m/s] is the hydraulic conductivity, A [m^2] is the cross sectional area and i [-] is the hydraulic gradient, which is defined as $\Delta h/H$, where Δh [m] is the hydraulic pressure expressed in fluid height and H [m] is the flow path. The hydraulic conductivity k can be expressed as:

$$k = \frac{K\rho g}{\mu} \tag{2.5}$$

where K [m^2] is the intrinsic permeability (1 D = $9.869 \cdot 10^{-13} m^2$), ρ [kg/m^3] is the fluid density, g [m/s^2] is the gravitational acceleration and μ [Pa·s] is the dynamic viscosity of the fluid.

The equations (2.4) and (2.5) can be rewritten into an expression for the absolute, intrinsic permeability K as (Dullien 1991):

$$K = \frac{Q\mu H}{A\Delta P} \tag{2.6}$$

where ΔP [Pa] is the hydraulic pressure difference over the flow path. The absolute permeability is not affected by wettability (Anderson 1986*d*).

The Darcy flow domain is valid for the Reynolds number Re lower than a limit value varying between 1 and 10, depending on materials and authors (Garnier et al. 2000). The Reynolds number is found as:

$$Re = \frac{\rho v b}{\mu} \tag{2.7}$$

where v [m/s] is the flow velocity and b [m] is a characteristic dimension of the flow, here the fracture aperture.

At low Reynolds numbers, the flow is laminar. Above $Re = 10$, the flow regime enters a transition zone from laminar to turbulent flow. The turbulent flow regime is entered around Re in the range of 100. The value of the Reynolds number thus categorizes the manner by which fluid flows through a medium.

Absolute, Fracture Permeability

The most common model for fluid flow through a single fracture is the cubic law, which is the adjustment of Darcy's law to flow through a fracture. A fracture is represented by two plane plates separated by a constant aperture b [m]. The cubic law for one-dimensional fluid flow in a single fracture is given by:

$$Q_f = \frac{\rho g}{\mu} \frac{b^3}{12} wi \tag{2.8}$$

where Q_f [m^3/s] is the volumetric flow rate through the fracture and w [m] is the fracture length.

The intrinsic fracture permeability K_f [m^2] for flow in a single fracture assuming the fracture is being formed by two smooth parallel plates is then given by:

$$K_f = \frac{b^2}{12} \tag{2.9}$$

Gudbjerg (Gudbjerg 2003) reports that experimental studies have shown that natural fracture walls are rough, and that the fractures behave more like a porous medium, and modelling of the fractures are necessary to obtain the fracture permeability. The parallel plate approach cannot be used for natural fractures, as $K_{parallel} >> K_{rough}$. In spite this statement, the parallel plate approach is used in this thesis to obtain qualitative estimates of the fracture permeability for evaluation of the consequence of closing of fractures on the fracture permeability, i.e. the estimates are only used relative to each other, see Section 5.3.1.

Absolute, Effective Permeability

The measure of permeability determined in fractured formations is termed the effective permeability K_{eff}. It includes the flow capacity of both the fracture and the surrounding matrix, and the entire cross-section of the matrix and fractures is used in the calculation of the permeability. However, the contribution of fractures to the effective permeability

of the reservoir may be of the same order of magnitude as that of the matrix blocks, even though the permeability of the individual fracture is large compared to the matrix permeability (using subscript m for matrix and f for fractures):

$$K_{eff} = \frac{K_m \cdot A_m + K_f \cdot A_f}{A_m + A_f} \tag{2.10}$$

where K [m^2] is the intrinsic permeability and A [m^2] is the cross-sectional area.

Relative Permeability

Relative permeability can be described as a direct measure of the ability of the porous system to conduct one fluid in the presence of one or more fluids, i.e. each fluid has its own permeability depending on the saturation of each fluid. The terminology indicates that the permeability of one fluid is measured in the presence of another fluid. These flow properties are the composite effect of pore geometry, wettability, fluid distribution, and saturation history (Anderson 1986*d*). However, for a fractured chalk reservoir, the relative permeability curves only provide information on the behavior of the matrix blocks.

At the irreducible water saturation S_{wir}, where the water phase is immobile, the permeability of the water phase is zero, and the permeability of the oil phase is termed the end-point oil permeability. The permeability of the water phase increases as the water saturation increases, and when the porous medium is 100% water saturated, the permeability of the water is by definition equal to the absolute permeability. At the residual oil saturation S_{orw}, where the oil phase is immobile, the oil permeability is zero, and the permeability of water is termed the water end-point permeability. When the oil saturates the porous media completely the oil permeability equals the absolute permeability.

The permeability of each phase is often normalized by the value of the absolute permeability to produce the relative permeability. The maximum relative permeability of oil and water that can naturally occur during displacement are called end-point relative permeability. The point at which the relative permeabilities are equal is called the crossover point (Dake 1997).

Wettability has a strong effect on relative permeability. For a strongly water-wet core at S_{wir}, the water is located in the small pores and as a film on the surface, where it has very little effect on the oil flow, i.e. the relative oil permeability is high. In contrast, the relative water permeability is low at S_{orw} because some of the oil is trapped in the center of the larger pores. This means that oil displacement almost totally cease after passing of the waterfront. In a strongly oil-wet core, the position of the two fluids is reversed. The relative oil permeability at S_{wir} is relatively low because the water blocks the oil flow. The relative water permeability is high at S_{orw} because the oil is located in the small pores and as a film on the surface, and has thus little effect on the flow of water. This means that oil displacement can continue at a very low rate over a long period of time. Relative permeability curves are shown for a strongly water-wet sandstone specimen and a strongly oil-wet sandstone specimen in Figure 2.8.

Essentially all reservoirs are affected by the interactions between capillary pressure and relative permeability at various wettability conditions. Fractured chalk reservoirs

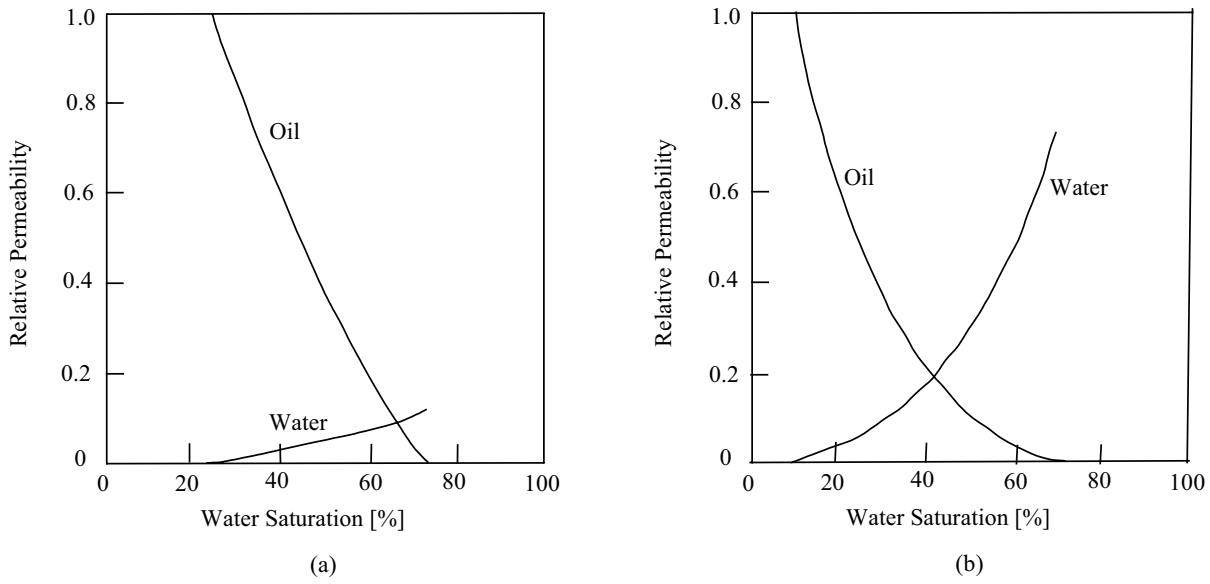

Figure 2.8 *Relative permeability curves for (a) a strongly water-wet sandstone specimen and (b) a strongly oil-wet sandstone specimen, after (Anderson 1986*d*).*

with very low matrix permeability are in particular sensitive to these interactions (Graue et al. 1999).

2.3.2 Critical Waterflooding Rate

Waterflooding fractured chalk with a well-connected fracture network may impose a risk of flow of water mainly in the fractures resulting in early water breakthrough and less efficient oil recovery. If the water does not displace oil in the matrix, the waterflood will fail, and the water will travel directly from the injection well to the production well through the fracture system, i.e. the result would be recycled water.

For fractured reservoir chalk, the efficiency of oil displacement by waterflooding can be studied by a critical waterflooding rate. Mattax and Kyte (Mattax & Kyte 1962) reported that the most efficient displacement and thus the highest recovery is obtained when the waterfront progresses almost simultaneously in the fractures and the matrix (plug flow), i.e. with the lowest water production. A critical waterflooding rate may exist above which the displacement shifts from plug flow to a scenario, where the water in the fractures moves critically long ahead of the water in the matrix (water fingering) leading to an inefficient matrix-fracture transfer, resulting in earlier water breakthrough and less efficient oil recovery.

In a strongly water-wet, fractured chalk, the flow may change from fingering to plug flow due to capillary imbibition from the water-filled fractures into the oil-filled matrix. This means that the dominant recovery mechanism changes from co-current to counter-current imbibition. However, co-current imbibition has been shown to lead to faster and more efficient oil recovery (Pooladi-Darvish & Firoozabadi 2000). Babadagli (Babadagli 1994) reported that above the critical rate, the injected water may not contact the matrix long enough to initiate the capillary imbibition, i.e. no matter how much water is injected,

only oil in the fractures is produced. However, the capillary imbibition may proceed even after water breakthrough, where the matrix is completely surrounded by water-filled fractures (Mattax & Kyte 1962). On the other hand, Mannon and Chilingar (Mannon & Chilingar 1972) found that a higher waterflooding rate may result in a higher capillary imbibition rate, and a greater ultimate oil recovery. This may be explained by a higher injection rate would more easily break loose the oil droplets on the matrix surface, expelled by imbibition of water into the matrix, resulting in free oil channels to produce at a faster rate.

In less than strongly water-wet, fractured chalk, the capillary imbibition is not as strong, and forced imbibition/drainage is necessary to obtain an efficient oil recovery. In this case, a high rate facilitating forced imbibition/drainage may also lead to fingering.

2.4 Displacement Processes

Oil displacement by waterflooding results from a simultaneous competition between capillary, viscous and gravity forces (Bognø et al. 2001).

During waterflooding of a fractured chalk reservoir, water is injected into the fractures, decreasing the capillary pressure by increasing the pressure in the water phase, exposing the chalk to water. The oil displacement processes involved with waterflooding fractured chalk are found to depend on the wettability of the chalk and capillary continuity between adjacent matrix blocks. Water movement during waterflooding is affected by the presence of fractures, especially since the matrix permeability of the chalk reservoirs is low. The main matrix-fracture fluid exchange mechanisms for oil displacement by waterflooding are gravity drainage, capillary imbibition, molecular diffusion (spreading of an agent at the molecular level caused by the random thermal motion of the molecules) and viscous forces (Andersen 1995).

If the chalk is water-wet, water from the fractures will be sucked into the chalk by capillary forces and increase the water saturation until the capillary pressure becomes zero, i.e. until equilibrium is reached between the capillary forces and the gravitational forces. This is called spontaneous (capillary) imbibition. In fractured, strongly water-wet chalk, capillary forces dominate the matrix-fracture transfer mechanism, and spontaneous imbibition of water from the fractures into the matrix is the major recovery mechanism. This dominance of capillary forces is due to the water-wetness, the narrow pore throats and the low matrix permeability of chalk (Graue et al. 1999a). The concept of oil production by spontaneous imbibition of water in a fractured rock is illustrated for a rock with a single horizontal fracture in Figure 2.9. Water is injected into the fracture only. Part of the injected water imbibes into the matrix due to capillary forces and releases oil, which becomes part of the flowing string in the fracture. In the case where the imbibition rate is greater than the rate of injection, all the water will imbibe into the matrix and only oil will reach the end of the fracture. With time, the capillary imbibition rate will decrease, water will travel longer distances in the fracture, and eventually it will reach the producing well, and water production will start ((Aguilera 1984), and references therein).

In strongly water-wet chalk, Graue et al. (Graue et al. 2001a) found that water imbibition stopped at each fracture, even with matrix blocks in contact, until the spontaneous imbibition endpoint water saturation $S_{w,if}$ was reached in the preceding matrix block.

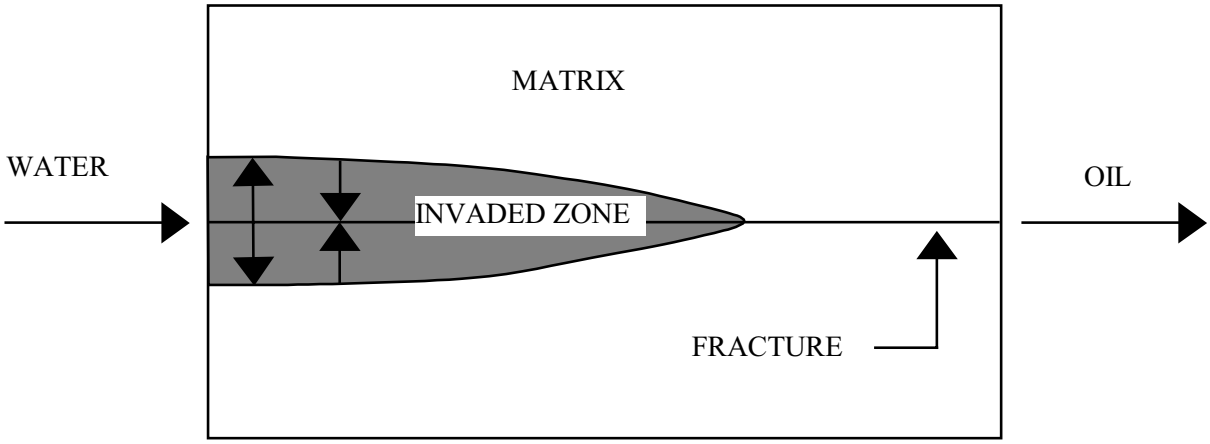

Figure 2.9 *Illustration of oil production by spontaneous imbibition of water, after ((Aguilera 1984) and references therein).*

Then water filled the fractures, and entered the next matrix block. Open fractures transverse to the flow impeded and redirected the flow.

When waterflooding naturally fractured chalk reservoirs, an important recovery mechanism is gravity drainage. In fractured chalk, capillary forces in the fracture network are negligible compared to gravitational forces, and gravity segregation of fluids in open fractures occurs (Viksund 1998). The driving force in gravity driven displacement is the density difference between the fluid in the matrix (oil) and the fluid in the fractures (water). The density difference results in production of oil until the gravitational forces are equalized by the capillary retaining forces (Christoffersen 1995).

A density driven process or applied pressure gradients creates viscous forces on the matrix block and thereby displaces the oil in place (Eltvik et al. 1990), i.e. forced imbibition. At increasing flow rates, viscous forces become stronger causing the fluids to flow through the more highly permeable layers of the chalk. High rate waterflooding may lead to viscous displacement in the fractures. However, if there is sufficient capillary contact between the chalk matrices on either side of a fracture in a less than strongly water-wet chalk, the oil may also move through the matrix, i.e. the matrix pore network could provide an alternate path for viscous oil displacement. This can be provided by wetting phase bridges across the fractures (Graue et al. 1999b).

The efficiency of the viscous forces depends on the wettability. Viscous forces are small in the matrix compared to capillary forces when the rock is water-wet (Milter 1996). Therefore, although the actual flow is driven by gravitational forces or a pressure gradient, the capillary forces determine the flow paths at the pore scale.

Capillary and Bond number

The capillary number N_C and the Bond number N_B are dimensionless numbers that can be used to evaluate if gravitational, capillary or viscous forces dominate, i.e. characterize the displacement processes in homogeneous rock.

The capillary number N_C represents the ratio of viscous to capillary forces at pore level, and is defined as (Milter 1996):

$$N_C = \frac{\mu_w v}{\sigma_i \cos\theta} \tag{2.11}$$

where μ_w [Pa·s] is the viscosity of the water (displacing fluid), v [m/s] is the velocity, σ_i [N/m] is the interfacial tension (IFT) between the fluids, and θ [deg] is the contact angle.

The dimensionless Bond number N_B describes the ratio of gravitational to capillary forces at pore level (Skauge & Poulsen 2000):

$$N_B = \frac{Kg\Delta\rho}{\sigma_i} \tag{2.12}$$

where K [m^2] is the absolute, intrinsic permeability, g [m/s^2] is the gravitational acceleration and $\Delta\rho$ [kg/m^3] is the fluid density difference. This expression transforms into the centrifugal gravity-to-capillary Bond number $N_{B,cen}$ by replacing the gravitational acceleration g with the centrifugal acceleration $\omega^2 R$, where ω [sec.$^{-1}$] is the angular velocity and R [m] is the radius from the center of the specimen to the rotational axis.

The degree of residual entrapment of a displaced fluid is a function of the dimensionless capillary and Bond numbers. The capillary forces which cause trapping or resist mobilization of residual saturations can be overcome by a viscous pressure gradient or gravity forces. Above a certain upper critical capillary or Bond number, no capillary trapping occurs, and the residual nonwetting phase saturation is close to zero. Conversely, below a certain lower critical capillary or Bond number, the trapping is dominated by capillary forces, and the residual nonwetting phase saturation reaches a constant maximum value. Between these two extremes, the residual nonwetting phase saturation depends upon the combined effects of capillary, viscous and gravity forces (Lake 1989).

For the centrifuge waterflooding tests, a mean capillary number ranging from $N_C = 7.3\cdot10^{-8} - 1.6\cdot10^{-7}$ is estimated. This estimate is based on flow of water in the matrix, i.e. displacement of oil by water in the matrix, and a mean matrix permeability of 2.8 mD, see Section 5.3.1. The velocity of the water in the matrix is estimated based on equation (2.6), and inserted in (2.11) together with an interfacial tension between Isopar-L and artificial seawater of 60 mN/m and a contact angle of 30° (according to GEUS).

A mean centrifuge Bond number for the waterflooding tests in the centrifuge is estimated to $N_{B,cen} = 8.7 \cdot 10^{-9}$. This estimation is based on a matrix permeability of 2.8 mD, and an interfacial tension of 60 mN/m using equation (2.12) with $\omega^2 R$ replacing g.

Similarly, a mean capillary number ranging from $N_C = 7.0 \cdot 10^{-12} - 6.1 \cdot 10^{-10}$ and a mean Bond number of $N_B = 1.2 \cdot 10^{-10}$ are estimated for the waterflooding tests in the oedometer cell.

However, the author has located no critical values for capillary or Bond numbers for oil displacement by waterflooding in chalk.

Capillary End Effect

There is a phenomenon seen in laboratory tests referred to as capillary end effect, which also is important for fractures in a test specimen as well as in the field. Since saturation

of a porous medium is dependent on the capillary pressure at the outflow surface, the pressure in the two phases are required to be the same. At such a zero capillary pressure, the wetting phase is retained and accumulates inside. As the pressure builds up, the wetting phase breaks through the outflow surface, and the wetting phase is displaced. In a dynamic displacement test, this effect can result in the wetting phase saturation being higher at the outflow surface of the specimen than in the middle. Flow across a fracture indicates complete capillary contact (capillary continuity) across the fracture. Therefore the capillary end effect may only be present at the outflow surface for fractured chalk with matrix blocks in contact (Andersen 1995).

It is normally assumed that capillary end effects are negligible in centrifuge displacement tests. At low centrifugal speed, the flow regime is capillary dominated thus the wetting phase is retained near the outflow surface of the specimen. Above a critical centrifuge Bond number (the critical value of rotational speed), at which centrifugal forces dominate over capillary forces, the end effect seems to become negligible. Skauge et al. (Skauge et al., 1997) found the critical centrifuge Bond number for avoiding end effect in small-scale centrifuge gas-oil displacement tests for sandstone to depend on permeability, i.e. increasing critical centrifuge Bond number with increasing permeability.

The author has located no critical centrifuge Bond number for avoiding capillary end effect during oil displacement by waterflooding in chalk. However, since the test specimens are large, the impact of capillary end effects is assumed negligible (Graue et al. 2001b).

2.5 Centrifuge Modelling

Physical modelling of processes in soil and rock is a special challenge since material properties are stress dependent and behavior is stress path dependent. However, the essence of centrifuge modelling is the ability to reproduce soil self-weight stress distributions, i.e. stress dependent behavior can be modelled. When a model at 1:N is rotated to a radial acceleration of N times Earth's gravity in the centrifuge, the axial stresses in the rotating model are equivalent to the vertical gravitational stresses in a prototype of N times larger geometric dimensions than the model, i.e. the stress distribution is the same in the model and the full scale prototype. Soil models in a model container have a free unstressed upper surface and within the soil body the magnitude of stress increases with depth at a rate related to the soil density and the acceleration field. If the same soil is used in the model and the prototype, then for the model subjected to a centrifugal acceleration field of N times Earth's gravity, the vertical stress at depth h_m will be identical to that in the corresponding prototype at depth $h_p = N \cdot h_m$ (using subscript m for model and p for prototype), see Figure 2.10.

Similarity conditions and subsequent model laws for centrifuge modelling should be derived either through dimensional analysis or from differential equations governing the phenomenon in question. Langhaar (Langhaar 1951) has described the principles of dimensional analysis, while Roscoe (Roscoe 1968) used differential equations to derive scaling relations for soil properties. Fuglsang and Krebs Ovesen (Fuglsang & Krebs Ovesen 1988) illustrated the use of these two methods in a simple geotechnical problem. Fuglsang and Krebs Ovesen conclude that distorted test results may appear in granular soils due to particle size-effects, and also in flow problems due to time-effects (creep).

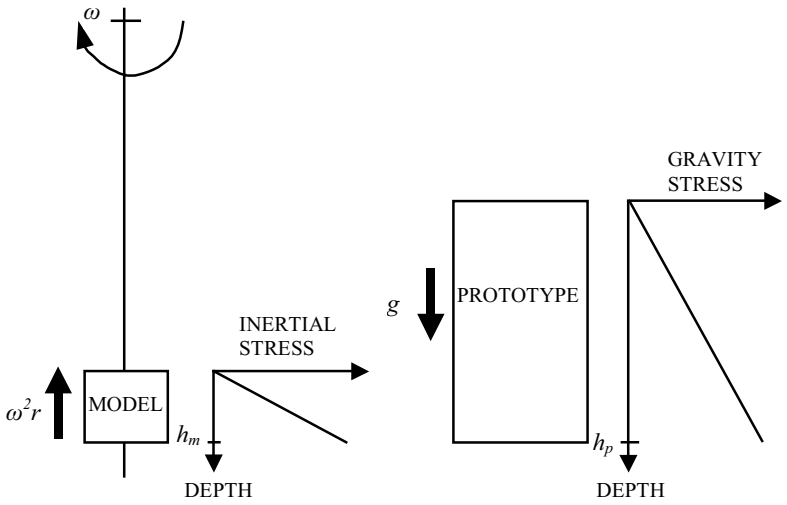

Figure 2.10 *Inertial stresses in a centrifuge model induced by rotation about a fixed axis correspond to gravitational stresses in the corresponding prototype, after (Taylor 1995).*

Dimensional Analysis

In this thesis, dimensional analysis based on (Fuglsang & Krebs Ovesen 1988) is used to derive the similarity requirements and subsequently the scaling factors for the centrifuge tests. In dimensional analysis, a model law is established based on the actual parameters that characterize the event:

$$f(x_1, x_2, x_3, x_4, x_5...) = 0 \tag{2.13}$$

These parameters are then written on dimensionless form, and are referred to as dimensionless numbers or Π-products:

$$f^*(\Pi_1, \Pi_2, ...) = f^*(\frac{x_1 \cdot x_2}{x_3 \cdot x_4}, \frac{x_5}{x_3}, ...) = 0 \tag{2.14}$$

The Buckingham Π theorem is a key theorem in dimensional analysis. According to the Buckingham Π theorem, the functional dependence between a certain number (e.g. n) of parameters can be reduced by the number (e.g. m) of independent dimensions occurring in those parameters to give a set of $s = n - m$ independent dimensionless numbers. The dimensionless numbers directly give the model requirements. Similarity between model and prototype is attained, when each dimensionless number has the same value in the model and the prototype. The similarity requirements can be written as:

$$(\Pi)_{model} = (\Pi)_{prototype} \tag{2.15}$$

If the scaling factor F_x of a parameter x is defined as the model value over the prototype value of that parameter, similarity for each dimensionless number leads to a relation between the scaling factors of the parameters in that dimensionless number:

$$F_x = \frac{x_m}{x_p} \tag{2.16}$$

When scaling factors are established for basic soil parameters, dimensionless numbers are given for all the parameters, and similarity conditions (requirements) are expressed in terms of N-values. This is done under the assumption that the magnitude of the field of acceleration is scaled at N, model heights are scaled at N^{-1}, and the prototype soil is used in the model. Utilizing the similarity requirement (2.15) and the scaling relation (2.16) on Π_1 given in (2.14) results in:

$$\begin{aligned} (\Pi_1)_{model} &= (\Pi_1)_{prototype} \\ \frac{x_{1,m} \cdot x_{2,m}}{x_{3,m} \cdot x_{4,m}} &= \frac{x_{1,p} \cdot x_{2,p}}{x_{3,p} \cdot x_{4,p}} \\ \frac{x_{1,m}}{x_{1,p}} &= (\frac{x_{2,m}}{x_{2,p}})^{-1} \cdot \frac{x_{3,m}}{x_{3,p}} \cdot \frac{x_{4,m}}{x_{4,p}} \\ F_{x_1} &= (F_{x_2})^{-1} \cdot F_{x_3} \cdot F_{x_4} \end{aligned} \tag{2.17}$$

The assumption that the prototype soil is used in the model implies that parameters like soil density and particle size are scaled at a factor of 1. However, the scaling factor for particle size should be that of the model height, that is N^{-1}. So the use of the prototype soil in the model introduces a conflicting scaling factor on particle size which may result in distorted test results, i.e. scale effects. Other parameters may also introduce conflicting scaling factors which may result in scale effects. This should be checked by means of tests at different model scales, i.e. tests at different values of N.

In summary, the first step of centrifuge modelling is to establish a centrifuge model either through dimensional analysis or from the governing differential equations. Then conflicting scaling factors should be found, i.e. deviations from the centrifuge model. Finally, the consequence of the conflicting scaling factors should be evaluated, i.e. the significance of the deviations.

Centrifuge Model of the Actual Problem with Prototype Material

In the centrifuge, the test specimens were exposed to an acceleration field N times the gravitational acceleration g. A centrifuge model was established for the fluid flow tests on fractured chalk specimens through dimensional analysis, i.e. for both the oil permeability tests and the waterflooding tests. Initially, all the relevant, independent parameters describing the fluid flow through fractured chalk were identified, and included in Table 2.1 and 2.2. The use of dimensional analysis is illustrated for a few of the identified parameters.

Parameters: $$f(a, H, \rho, P, v, ...) = 0$$

where a is the centrifuge acceleration, H is the test specimen height (model height), ρ is the density, P is the pressure and v is the flow velocity.

The function $f(a, H, \rho, P, v, ...)$ was expressed on dimensionless form.

Dimensionless numbers: $$f^*(\Pi_1, \Pi_2, ...) = f^*(\frac{P}{a \cdot H \cdot \rho}, \frac{v \cdot \mu}{K \cdot a \cdot \rho \cdot i}, ...) = 0$$

where Π_1 expresses P on dimensionless form, and Π_2 expresses v on dimensionless form. μ is the dynamic viscosity, i is the hydraulic gradient and K is the intrinsic permeability.

Finally, the similarity requirements were set up and the scaling factors were obtained from each dimensionless number. The scaling factors were obtained under the assumption that the centrifuge acceleration is scaled at N, model heights are scaled at N^{-1}, and the same soil and fluids are used in the model and the prototype, i.e. are scaled at 1.

$$\begin{aligned} \text{Similarity requirements:} \qquad F_P &= F_a \cdot F_H \cdot F_\rho = 1 \\ F_v &= F_K \cdot F_a \cdot F_\rho \cdot F_i \cdot F_\mu^{-1} = N \\ &etc. \end{aligned}$$

This means that the dimensionless numbers $\Pi_1 = \frac{P}{a \cdot H \cdot \rho}$ and $\Pi_2 = \frac{v \cdot \mu}{K \cdot a \cdot \rho \cdot i}$ have the same value in the model and the prototype, i.e. there is similarity between model and prototype, when the parameter P is scaled at 1 and the parameter v is scaled at N.

The assumed centrifuge scaling factors for the flow tests are summarized in Table 2.1, and the derived scaling factors are given in Table 2.2.

Parameter	Symbol	Similarity Requirement	Scaling Factor
Centrifuge acceleration	a	F_a	N
Model dimensions	H, $D, \Delta h$	F_{model}	N^{-1}
Material parameters	d, r, b, l, α, ρ, ϕ, K	F_{mat}	1
Fluid parameters	ρ, μ, ν, σ_i	F_{fluid}	1
Contact angle	θ	F_θ	1
Saturation	S	F_S	1

Table 2.1 *Assumed scaling factors for flow through fractured chalk.*

The model dimensions include test specimen height H, diameter D and hydraulic pressure difference expressed in fluid height Δh. The material parameters include particle size d, size of voids between the particles described by the radius of pore throat r, fracture aperture b, length l and inclination α, matrix block dimensions, density ρ, porosity ϕ and intrinsic permeability K (2.6) both for matrix and fractures. The fluid parameters include density ρ, dynamic viscosity μ, kinematic viscosity ν and interfacial tension σ_i.

All the model dimensions are scaled similar to the model heights since the model scales in space, i.e. in all directions. At a chosen acceleration of N, the test specimens can thus be considered to model the *behavior* of a reservoir block of N times the geometric dimensions of the test specimens, see Figure 2.11. This scaling implies that the scaled mean parameters for the test specimen for instance the intrinsic permeability apply to the whole reservoir block, and the inclination of the fractures are similar for model and prototype. Further, the scaling ensures that the prototype soil is used in the model. This means that the capillary continuity, and the capillary imbibition potential of the fractures are similar in the model and the prototype, i.e. the fracture spacing and the apertures of the fractures are scaled at 1. A scaling of all the dimensions of the model results in scaling factors of N^{-2} for the cross sectional area A and N^{-3} for the volume V of the model.

Parameter	Symbol	Dim. less Number	Similarity Requirement	Scaling Factor
Model cross-sectional area	A	$\frac{A}{\frac{1}{4}\cdot\pi\cdot D^2}$	$F_A = (F_D^{-1})^2$	N^{-2}
Model volume	V	$\frac{V}{\frac{1}{4}\cdot\pi\cdot D^2\cdot H}$	$F_V = (F_D^{-1})^2 \cdot F_H^{-1}$	N^{-3}
Stress	σ	$\frac{\sigma}{aH\rho}$	$F_\sigma = F_a \cdot F_H \cdot F_\rho$	1
Pressure	P	$\frac{P}{aH\rho}$	$F_P = F_a \cdot F_H \cdot F_\rho$	1
Hydraulic gradient	i	$\frac{\Delta h}{H}$	$F_i = F_{\Delta h} \cdot F_H^{-1}$	1
Flow velocity	v	$\frac{v\mu}{Ka\rho i}$	$F_v = F_K \cdot F_a \cdot F_\rho \cdot F_i \cdot {F_\mu}^{-1}$	N
Flow time	t	$\frac{tv}{H}$	$F_t = F_H \cdot F_v^{-1}$	N^{-2}
Volumetric flow rate	Q	$\frac{Q}{vA}$	$F_Q = F_v \cdot F_A$	N^{-1}
Hydraulic conductivity	k	$\frac{k\cdot\mu}{K\cdot\rho\cdot a}$	$F_k = F_K \cdot F_\rho \cdot F_a \cdot F_\mu^{-1}$	N
Capillary imbibition pot.	h_c	$\frac{h_c r\Delta\rho a}{2\sigma_i\cos\theta}$	$F_{h_c} = F_{\sigma_i} \cdot F_\theta \cdot F_r^{-1} \cdot F_\rho^{-1} \cdot F_a^{-1}$	N^{-1}

Table 2.2 *Derived scaling factors for flow through fractured chalk.*

The volumetric flow rate Q_p through the reservoir block is N times the flow rate Q_m through the specimens. The scaling factors for flow velocity v, flow time t, and volumetric flow rate Q were derived assuming that the intrinsic permeability K scale at 1 like the material parameters. The hydraulic conductivity k (2.5) is defined as a function of the properties of the material and the fluid, and the centrifuge acceleration, and scales at N.

The vertical stress distribution is the same in the model and the prototype since the model at 1:N is subjected to N times the gravitational acceleration in the centrifuge. According to the elasticity theory, the horizontal stress will increase with an increase in the vertical stress, i.e. the stress is scaled at the same scaling factor $F_\sigma = 1$ in all directions. Similarly, the distribution of fluid pressure is the same in the model and the prototype. This can also be explained by the fluid particles being heavier during centrifuge testing. Consequently, capillary pressure defined as the pressure difference between the two fluids (in this case oil and water, where $P_c = P_o - P_w$) is scaled at the same scaling factor $F_P = F_{P_c} = 1$ in all directions.

The scaling factors are obtained to ensure that each dimensionless number has the same value in the model and the prototype, i.e. that similarity between model and prototype is attained. This implies that if the actual processes work in all directions, the scaling factors apply in all directions.

Using similar arguments, all fluid transport processes are scaled at the same scaling factor in all directions. For clarification, the scaling of (viscous) flow is derived for a model test with inclined flow in Appendix A. The scaling can be explained by the flow velocity being N times faster in the model and the flow path being N times shorter (the model heights are scaled at N^{-1}) resulting in N^2 times faster flow.

Rezzoug (Rezzoug 1999) has shown theoretically based on the Navier-Stokes flow equations and by experimental verification that the capillary imbibition potential scales at N^{-1}, the imbibition velocity dh_c/dt scales at N and imbibition time at N^{-2}. This has also been verified from centrifuge tests performed by Bagge et al. (Bagge et al. 2002).

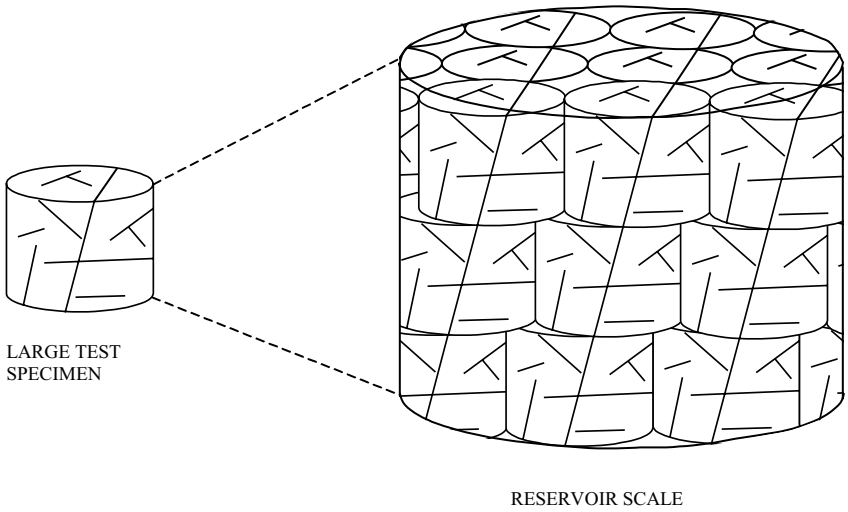

Figure 2.11 *Principle sketch of the up-scaling of a large, fractured test specimen to reservoir scale.*

Lord (Lord 1999) investigated theoretically the scaling of the time for capillary flow (imbibition and drainage) in unsaturated soil, i.e. two-phase flow (air and water). This was done assuming the same soil in the model and the prototype, treating the unsaturated soil as a "bundle of capillaries", and using a simple Poiseuille's capillary flow approach. This approach gives a N^{-2} time dependence for flow in the centrifuge for:

1. Capillary rise at an arbitrary angle to the horizontal
2. Horizontal capillary flow
3. Downward capillary flow at an arbitrary angle to the horizontal
4. Vertical capillary drainage

This implies that capillary imbibition and drainage scale at the same scaling factor in all directions, which is consistent with the fact that these processes take place in all directions. The scaling can be explained by the imbibition flow velocity being N times faster in the model, and the flow path being and N times shorter (capillary imbibition potential scale at N^{-1}) resulting in N^2 times faster capillary imbibition. This also means that the ratio between fracture flow and capillary flow is the same in the model and the prototype.

Even though the oil and water in the flow tests are flowing in the opposite direction as the direction of the artificial gravity field, the flow velocity is still N times faster in the model. This is because the flow is driven by a hydraulic pressure difference Δh, i.e. the drive is scaled similarly for injection into the top and bottom of the specimen, see Figure 2.12.

Numerous authors have established scaling laws for flow phenomena in the centrifuge see for example (Culligan-Hensley & Savvidou 1995). These scaling laws are in agreement with the scaling factors included in Table 2.1, 2.2 and 2.3.

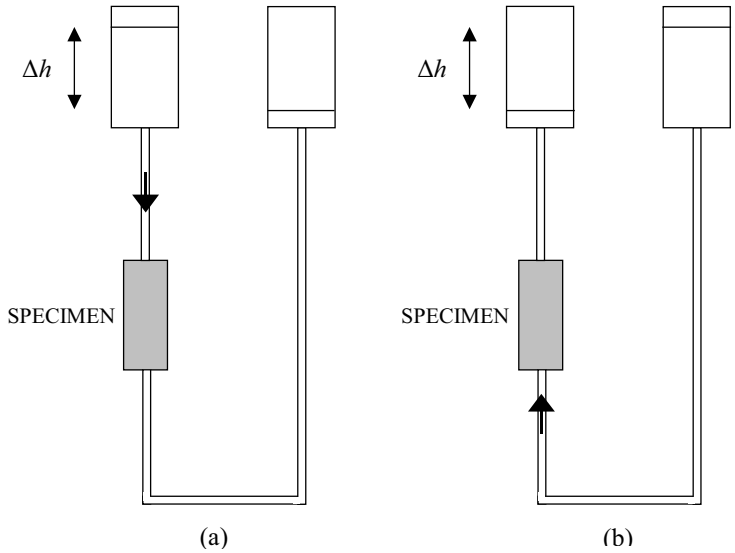

Figure 2.12 *Schematic set-up for flow driven by a hydraulic pressure difference Δh (a) into the top of the specimen (with the direction of gravity) and (b) into the bottom of the specimen (opposite the direction of gravity).*

Problems with Centrifuge Modelling of Two-Phase Flow in Chalk

Some authors (see for instance (Petersen & Cooke 1994)) express scaling concerns with regard to centrifuge modelling of two-phase flow as it was observed that the wetting front may become unstable and break into gravity fingers during gravity-driven flow. Further, it was observed that at increased gravities, fewer fingers will form, and those that do form, will be larger and propagate faster than would be required for modelling similitude. However, in the waterflooding tests performed in this Ph.D. project, the water was injected opposite the direction of the artificial gravity field to obtain a stabile wetting front. Consequently, it is assumed that there were no problems with an unstable wetting front due to gravity because the flow was driven by a falling hydraulic pressure difference, and not gravity-driven.

Another issue is the problems related to centrifuge modelling of the material chalk. Prior to the large-scale centrifuge tests, capillary pressure measurements were performed on three small chalk specimens in a Beckmann centrifuge, see Section 4.2. For these tests, centrifuge modelling of capillary pressure curves for Hillerslev chalk was shown to be unsuitable due to the low mechanical strength of chalk, as well as the high capillary pressure making it difficult to obtain the necessary high rotational speed, i.e. problems with centrifuge speed limitations. However, since the waterflooding tests were conducted at low mean stress levels $p' \leq 0.22$ MPa, no problems were encountered with the low mechanical strength, see Section 3.4. Further, no capillary pressure measurements were performed on the large test specimens in the centrifuge, i.e. it was not necessary to obtain higher rotational speed than the applied $N = 80$ times the gravitational acceleration at the bottom of the specimens, which is the limitation for the centrifuge. However, it would have been interesting to apply a higher rotational speed to obtain higher mean stress levels.

Model Deviations

The assumption that the prototype soil is used in the model implies that model material dimensions like particle size, fracture aperture and density are scaled at a factor of 1. However, the scaling factor for particle size should be that of the model height, that is N^{-1}. So the use of the prototype material in the model introduces a conflicting scaling factor on particle size which may result in distorted test results, i.e. scale effects.

If the particle size was in fact scaled at N^{-1}, the particle size would be significant compared to prototype dimensions. Consequently, a coarser soil type than the prototype soil would be modelled, i.e. clay in the model would represent fine sand in the prototype etc. Further, it is unlikely that the model would mobilize the same stress-strain curve in the soil as would be the case in the prototype.

In order that the same principles of conservation and transport govern both a centrifuge model and the prototype, certain conditions need to be observed. Throughout the previous centrifuge modelling, it has been assumed that Darcy's law could be used to describe the fluid flow in both the model and the prototype. Thus, it is always necessary to confirm that the flow is laminar during centrifuge testing.

For the oil permeability tests, the highest mean value of Reynold's number for flow of oil in the fractures was estimated to $Re \leq 0.1$, i.e. the flow in these tests are evaluated to be laminar. Reynold's number is estimated assuming that the fractures take up 1% of the cross-sectional area of the specimens. This assumption is used in equation (2.10) together with a mean matrix permeability of 2.8 mD to obtain a fracture permeability, which is then used to estimate the velocity of the oil in the fractures based on equation (2.6). Finally, this fracture velocity is inserted in equation (2.7) to obtain an estimate of Reynold's number. A fracture aperture of $b = 0.1$ mm ($b \leq 100$ μm is representative of Hillerslev chalk, see Section 4.3.3). Similarly, the highest mean value of Reynold's number for flow of water in the fractures was estimated to $Re \leq 0.2$ for the waterflooding tests, i.e. the flow in these tests are also evaluated to be laminar.

It is also necessary to evaluate the dimensionless Reynolds number Re (2.7) used to categorize the type of flow (laminar vs. turbulent etc.), the capillary number N_C (2.11) and the Bond number N_B (2.12) used to evaluate if gravitational, capillary or viscous forces dominate, i.e. categorize the displacement processes. The centrifuge scaling factors for the three dimensionless numbers are included in Table 2.3.

Name	Symbol	Dim. less Number	Similarity Requirement	Scaling Factor
Reynolds number	Re	$\frac{\rho v b}{\mu}$	$F_{Re} = F_\rho \cdot F_v \cdot F_b \cdot {F_\mu}^{-1}$	N
Capillary number	N_C	$\frac{\mu v}{\sigma_i \cos\theta}$	$F_{N_C} = F_\mu \cdot F_v \cdot {F_{\sigma_i}}^{-1} \cdot {F_\theta}^{-1}$	N
Bond number	N_B	$\frac{Ka\Delta\rho}{\sigma_i}$	$F_{N_B} = F_K \cdot F_a \cdot F_\rho \cdot {F_{\sigma_i}}^{-1}$	N

Table 2.3 *Centrifuge scaling factors for the dimensionless numbers categorizing the flow and flow processes of flow through fractured chalk.*

For strict similitude between the centrifuge model and the prototype, the dimensionless numbers Re, N_C and N_B should be identical in model and prototype. However, model and prototype similitude of the Reynolds number is not achieved because the velocity in

the model is N times greater than in the prototype resulting in the Reynolds number being N times greater in the model. The degree of residual entrapment is a function of the dimensionless capillary and Bond numbers, both of which vary with N, see Section 2.4. The velocity in the model is N times greater than in the prototype resulting in the capillary number N_C being N times greater in the model than in the prototype, and because the centrifuge model acceleration is N times larger in the model, the Bond number N_B is N times greater in the model than in the prototype. Similitude between model and prototype is thus not achieved for any of these two numbers. High values of N_C and N_B implies a domination of viscous forces or gravity forces since the capillary number N_C represents the ratio of viscous to capillary forces, and the Bond number N_B describes the ratio of gravitational to capillary forces. Consequently, the magnitude of residual oil saturation can be reduced due to viscous forces and/or gravity forces on residual oil for the waterflooding tests on the fractured chalk specimens.

However, in certain cases, the same principles of behavior will govern the model and the prototype even when similitude is not achieved. Knight and Mitchell (Mitchell 1998) argue that by relaxing similitude requirements, overall similitude can still be achieved under a particular set of modelling constraints. The relaxation of the Reynolds number should not have a significant impact provided that the flow in the model is laminar. Further, when centrifuge models use fluids with a low density difference, low accelerations (low N), and a relatively high capillary porous medium (such as silt, chalk etc.), N_C and N_B will be limited and the magnitude of centrifuge residual mobilization may be minimized. In other words, below a certain critical capillary or Bond number, similitude in these numbers will not be significant. However, according to Cooke (Cooke 2000), it may be questionable to use the centrifuge for modelling total oil recovery due to inconsistency in similarity between model and prototype. This is based on the observation of a tendency towards decreasing residual entrapment with increasing g-level in fine sand. The test evaluations in the Ph.D. project are based on displacement processes and not on total recovery.

In the commercially used techniques to establish capillary pressure curves in small centrifuges, de-saturation effects, i.e. reduction in residual saturation, is avoided by conducting the tests below a certain critical Bond number.

Evaluation of Scale Effects (Model Deviations)

Experimental evidence is needed to justify that the deviations from complete similarity are insignificant. In this case, the consequence of the conflicting scaling factor for the particle size is evaluated. Further, the relaxation in similitude for F_{Re}, F_{N_C} and F_{N_B} is evaluated.

It is possible to evaluate the significance of the scale effects for particle size by performing modelling of models, i.e. tests on models corresponding to the same prototype, but at different g-levels, i.e. different stress levels. In Figure 2.13 is illustrated the concept of modelling of models on the prototype material at $N = 10$, 20, 40 and 80. At each scaling factor of N, the grey area of the model is corresponding to the same prototype, i.e. the geometrically reduced models (models of the model) represent the same prototype at N times the geometrical dimensions.

The volumetric flow Q through the models can be found from:

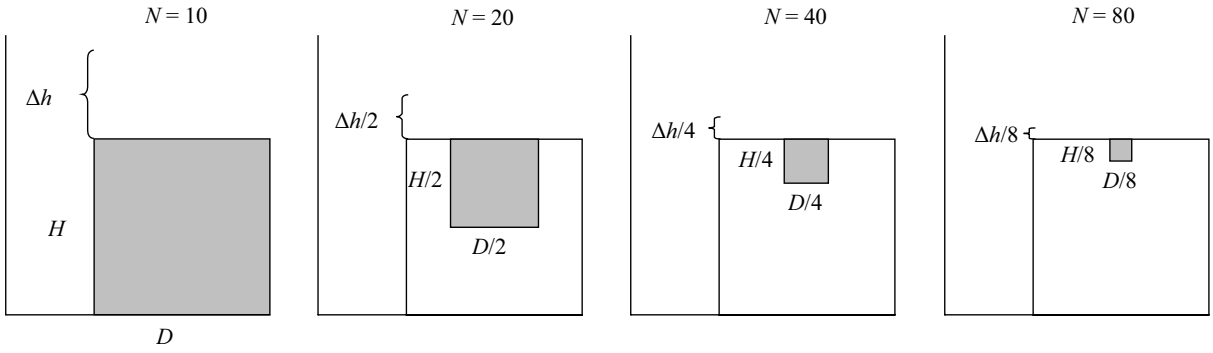

Figure 2.13 *The concept of modelling of models at N = 10, 20, 40 and 80.*

$$Q = KA\frac{\rho}{\mu}\, a\frac{\Delta h}{H} = K\pi(\frac{D}{2})^2\frac{\rho}{\mu}\, Ng\frac{\Delta h}{H} = CKD^2N\frac{\Delta h}{H} \tag{2.18}$$

where the constant C is given by $C = \frac{\pi}{4}\frac{\rho g}{\mu}$.

In Table 2.4, the volumetric flow Q for N = 10, 20, 40 and 80 are included based on equation (2.18) and Figure 2.13.

	$N = 10$	$N = 20$	$N = 40$	$N = 80$
Q	$CKD^2\frac{\Delta h}{H} \cdot 10$	$CK(\frac{D}{2})^2\frac{\Delta h}{H} \cdot 20$ $= CKD^2\frac{\Delta h}{H} \cdot 5$	$CK(\frac{D}{4})^2\frac{\Delta h}{H} \cdot 40$ $CKD^2\frac{\Delta h}{H} \cdot 2.5$	$CK(\frac{D}{8})^2\frac{\Delta h}{H} \cdot 80$ $CKD^2\frac{\Delta h}{H} \cdot 1.25$

Table 2.4 *Volumetric flow Q for the models at N = 10, 20, 40 and 80.*

From Table 2.4 it is found that:

$$Q_i = CK_iD_i^2\frac{\Delta h_i}{H_i} \cdot n_i \tag{2.19}$$

On dimensionless form, the volumetric flow Q_{dim} can be expressed as:

$$Q_{dim} = \frac{Q_i}{CK_iD_i^2\frac{\Delta h_i}{H_i}n_i} \tag{2.20}$$

If Q_{dim} is similar at N = 10, 20, 40 and 80, then the tests are models of each other, and therefore the single test is a model of the prototype, i.e. the same soil is used in the model and the prototype. Q_{dim} is only similar in the tests if the hydraulic conductivity K is constant in the tests, i.e. if K scales at 1 as assumed, see Table 2.1. Consequently, oil permeability tests were performed at N = 10, 20, 40 and 80 to determine the intrinsic permeability K, which is a function of particle shape, diameter and packing, i.e. the geometry of the material. The evaluation of the results of the oil permeability tests at different scale factors of N is included in Section 6.6.

Since the flow in these large-scale centrifuge tests are evaluated to be laminar, the relaxation of the Reynolds number should not have a significant impact. For the waterflooding tests in the centrifuge, a mean capillary number ranging from $N_C = 7.3 \cdot 10^{-8}$ to $1.6 \cdot 10^{-7}$, and a mean centrifuge Bond number of $N_{B,cen} = 8.7 \cdot 10^{-9}$ were estimated, see Section 2.4.

However, the author has located no critical capillary or Bond number for oil displacement by waterflooding in chalk, i.e. no definition of low fluid density difference or low acceleration (low N). However, since chalk is used, a high capillary porous medium is used. Due to the lack of critical capillary and Bond numbers, it cannot be concluded whether the inconsistency in similarity between model and prototype for these two numbers have a significant impact on the test results. However, since the lack of similitude was assumed to be the main problem with modelling of LNAPL infiltration into fine sand (Cooke 2000), the impact may be less in the high capillary chalk. Further, only the displacement processes and not final recovery are evaluated. It is thus considered possible to use the centrifuge for modelling of the displacement processes in the waterflooding tests.

Variation in the Acceleration Field

The scaling factor N vary linearly along the large test specimens, and can be found from:

$$N \cdot g = \omega^2 \cdot R \tag{2.21}$$

where ω [sec.$^{-1}$] is the angular velocity, and R [m] is the distance from the center of rotation. For the permeability tests, $N = 10$, 20, 40 and 80 was chosen at the bottom of the specimen, and for the waterflooding tests, $N = 80$ was also chosen at the bottom of the specimen ($R_{bottom} = 2.565$ m).

The effective vertical stress varies non-linearly with depth in the model due to the fact that the inertial acceleration field comes from rotational acceleration given by $\omega^2 R$. This is referred to as a centrifugal effect. The distributions of vertical stress in the model and the corresponding prototype are compared directly in Figure 2.14, where the non-linear variation of stress in the model is shown exaggerated for clarity.

In the prototype, the vertical stress at depth $h_p = Nh_m$ is given by $\sigma_{vp} = \rho g h_p = \rho g N h_m$. If the radius to the top of the model is R_t, then the vertical stress at depth z in the model can be determined from (Taylor 1995):

$$\sigma_{vm} = \int_0^z \rho\omega^2(R_t + z)dz = \rho\omega^2 z(R_t + \frac{z}{2}) \tag{2.22}$$

The vertical stress in the model and the prototype will be identical at a chosen depth $z = h_i$, when the corresponding effective centrifuge radius is $R_e = R_t + 0.5 \cdot h_i$. The constant scale factor N used for up-scaling from model to prototype should be calculated using the effective centrifuge radius R_e such that $N \cdot g = \omega^2 \cdot R_e$. For the flow tests, $h_i = h_m$ is chosen, i.e. the height of the test specimens. This results in the vertical stress in the model and the prototype being identical at the specimen bottom, with a maximum difference in stress level of 5% at the middle of the specimen, i.e. at R_e, see Figure 2.14. This choice is based on the fact that the stress levels used for the calculations are the maximum stress levels, i.e. at the specimen bottom. For the flow tests, the effective

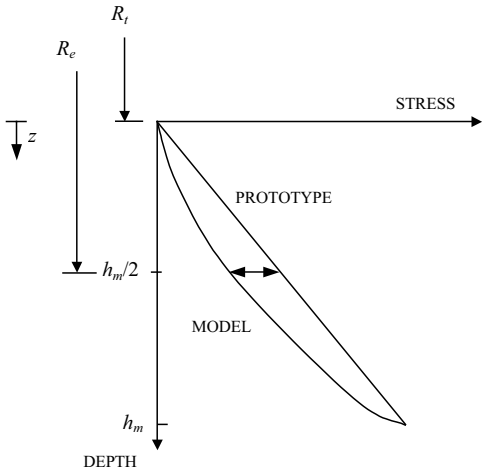

Figure 2.14 *Comparison of stress variation with depth in a centrifuge model and its corresponding prototype, after (Taylor 1995).*

radius $R_e = 2.315$ m for $h_m = 0.5$ m results in a constant factor for scaling from model to prototype of $N = 72$. In other words, identical vertical stresses are obtained at the bottom of the model and the prototype, when $N = 80$ is chosen at the bottom of the specimen resulting in a constant scaling factor of $N = 72$ for the whole specimen.

Actually, the distance R_b from the center of rotation to the bottom of the specimen consists of the length of the centrifuge arm R_0 and the length of the centrifuge model container hinged to the centrifuge arm R_1, see Figure 2.15.

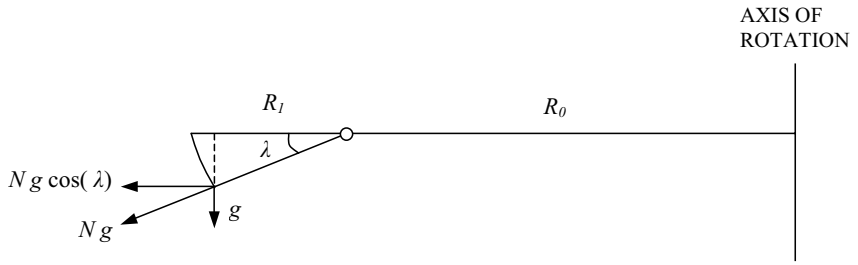

Figure 2.15 *Sketch of the centrifuge arm and hinged model container at an angle λ with horizontal during centrifuging.*

The angle λ of the inclined centrifuge model container is found as:

$$\lambda = \arctan(\frac{g}{a}) = \arctan(\frac{g}{(2\pi\omega)^2(R_0 + R_1 cos(\lambda)}) \tag{2.23}$$

However, for centrifuge accelerations at $N \geq 10$, the centrifuge model container is assumed to be horizontal, i.e. there is no angle of inclination. The measurements of the flow tests in this Ph.D. project are only used for $N \geq 10$, and (2.23) is thus not used.

While a centrifuge is a convenient method of generating an artificial high gravitational acceleration field, problems are created by the rotation about a fixed axis. The inertial radial acceleration is proportional to the radius which leads to a variation with depth

in the model - discussed above. Also, this acceleration is directed away from the center of rotation and hence in the horizontal plane, there is a change in its direction relative to vertical across the width of the model. There is therefore a lateral component of acceleration, i.e. the centrifugal field in a centrifuge experiment is not one-dimensional, but has a radial component. This is significant if there is a major area of activity near a side wall of the model container, see Figure 2.16. In the central region of the model, the error due to the radial nature of the acceleration field is small. For the model having a half width of $R = 0.25$ m and an effective radius of $R_e = 2.315$ m, the lateral acceleration has a maximum value of $0.25/2.065 \approx 0.12$ times the "vertical" acceleration.

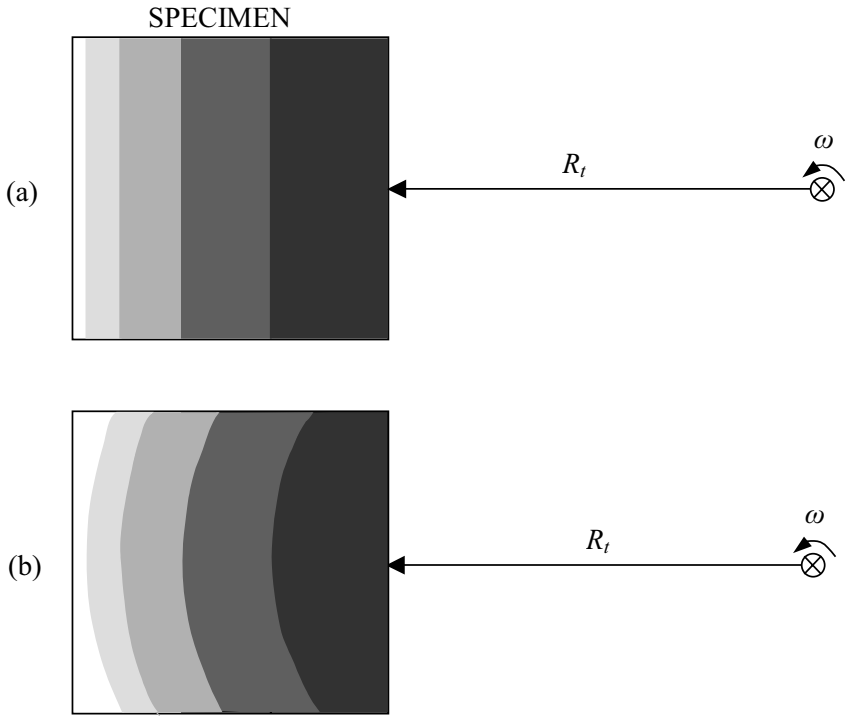

Figure 2.16 *(a) Assumption of a one-dimensional distribution of the centrifugal field, and (b) radial distribution of the centrifugal field, after (Forbes et al. 1994). The different colors correspond to different fluid saturations.*

Finally, there is an effect of gravity on the centrifugal field referred to as gravity degradation, see Figure 2.17. This effect results in an inclined acceleration field at low centrifuge speed. The angle γ of the inclined acceleration field is given by (Ruth & Chen 1995):

$$\gamma = \arctan(\frac{g}{a}) = \arctan(\frac{g}{\omega^2 R_p}) \tag{2.24}$$

The higher ω, the smaller γ, i.e. the less inclined acceleration field, and thus the less significance of gravity degradation. At the bottom of the test specimens, where $N = 80$ and $R_{bottom} = 2.565$ m, the effect of gravity degradation only results in an inclination of $\gamma = 0.72$ deg., i.e. the effect of gravity degradation is insignificant in these flow tests.

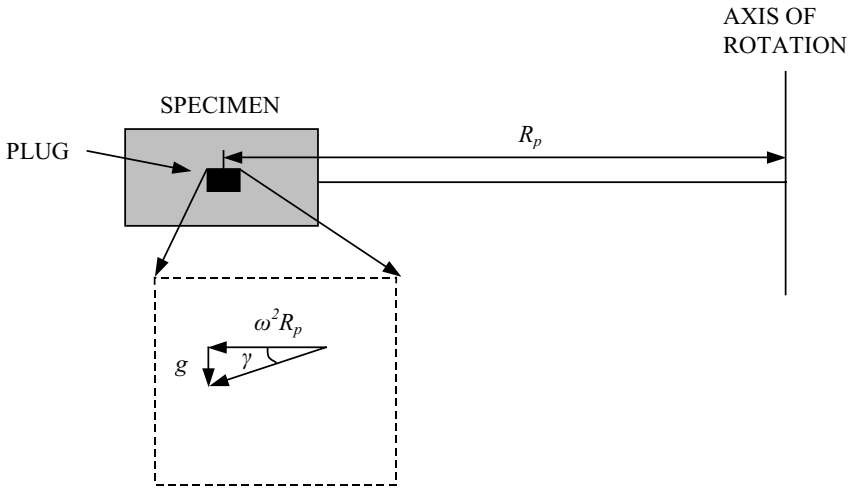

Figure 2.17 *Effect of gravity degradation shown for a small plug with distance R_p from the axis of rotation, after (Ruth & Chen 1995).*

2.6 Chalk-Water Interaction

An interesting aspect of waterflooding is the chalk-water interaction during waterflooding, i.e. water-weakening and water-induced compaction.

The effect of waterflooding chalk is dependent on wettability, water saturation, porosity and stress level (Christensen et al. 2000). In order to understand the behavior of chalk during waterflooding, it is necessary to understand the basic mechanical behavior of oil-saturated chalk. To obtain information on the possible stress states of chalk, a rock mechanics model should be established.

A rock mechanics model includes both elastic and plastic behavior, see Figure 2.18. The elastic area is enveloped by tensile and shear failure criteria and a yield surface. If the chalk experiences large shear stresses, it may reach a failure criterion and failure will occur. If the chalk undergoes compaction along a stress path with minor shear stresses it may reach the yield surface resulting in irreversible deformation (pore collapse). The strength and deformation parameters which characterize and form the outer limits of the elastic and plastic behavior needs to be defined.

2.6.1 Mechanical Behavior of Chalk

Chalk vary from mechanically weak, high porosity chalk, to well-cemented low porosity chalk. Weak chalks are characterized by a high porosity (35-45%) and a low silica content ($< 5\%$) (Risnes & Flaageng 1999).

When a material is subjected to sufficiently large stresses, it will experience failure. For a porous material like chalk, there are three different main types of failure: tensional failure, shear failure and pore collapse (matrix compaction). The latter introduces a shift from an elastic to a plastic state.

Fluid pressures in the reservoir partly carry the loads, which are transmitted by the surrounding rock, particularly the overburden, to the reservoir. Reduction in pore pressure due to oil production leads to increased effective stresses, and subsequent compaction of

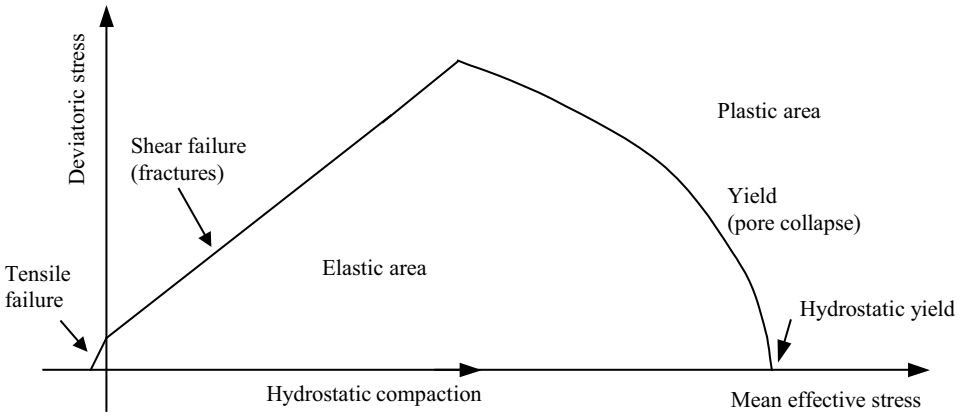

Figure 2.18 *Typical yield or failure model for chalks.*

the chalk matrix. This apparent failure, called pore collapse, adds a drive force for expelling more fluid from the formation. It also means that the reservoir as a whole compacts and reduces in thickness. This compaction is then transferred to the seabed as subsidence. Due to pore collapse, compaction causes reduction in the porosity and the permeability of the chalk. The following factors are believed to determine the magnitude of compaction drive: stress state, deformability of the reservoir rock, and changes in loads (or effective stresses) (Gutierrez & Hansteen 1994). The effective stresses σ' for incompressible pore fluids are found as:

$$\sigma' = \sigma - u \tag{2.25}$$

where σ are the total stresses and u is the pore pressure. Biot principle for reservoir conditions takes into account the compressibility of a solid and fluid phases:

$$\sigma' = \sigma - \alpha_B \cdot u \tag{2.26}$$

where α_B is the Biot factor. The Biot factor gives the relationship between the compressibility of mineral grains and the total compressibility of the material. For materials with porosities larger than 25%, the Biot factor is close to 1.0 (Malmin 1998).

Strength Parameters

Chalk is described by the tensile strength σ_t, the unconfined compressive strength σ_c and the yield stress σ_y.

The tensile failure criterion is the boundary of the elastic regime in the low stress region, in fact where the stress becomes negative. The tensile failure criterion connects with the shear failure criterion. Both criteria are also the boundaries for physically possible stress states, i.e. chalk cannot experience stresses beyond these stress limits. The yield surface envelopes the elastic state, and introduces a shift into the plastic state.

Deformation Parameters

Chalk is described by the consolidation modulus K, the coefficient of earth pressure at rest K_0, Young's modulus E and Poisson's ratio ν.

The consolidation modulus K is defined as the ratio between the changes of axial stress and strain measured under the conditions of no radial deformations, i.e. at uniaxial strain conditions:

$$K = \frac{\Delta\sigma_1}{\Delta\varepsilon_1} = \frac{1}{c} \tag{2.27}$$

where σ_1 is the axial stress, ε_1 is the axial strain, and the slope of the compaction curve is the compressibility c of the chalk matrix.

The coefficient of earth pressure at rest K_0 is defined as the ratio between horizontal and vertical stress in the condition of no radial deformations:

$$K_0 = \frac{\Delta\sigma_3}{\Delta\sigma_1} \tag{2.28}$$

where σ_3 is the radial stress.

Young's modulus E is defined as the ratio between the changes of axial stress and strain measured under the conditions of $\Delta\sigma_3 = 0$:

$$E = \frac{\Delta\sigma_1}{\Delta\varepsilon_1} \tag{2.29}$$

Poisson's ratio ν is defined as the ratio between radial strain and axial strain under the condition of no radial stress:

$$\nu = -\frac{\varepsilon_3}{\varepsilon_1} \tag{2.30}$$

where ε_3 is the radial strain.

Pure high porosity chalk consists of intact coccoliths and greater and smaller fragments giving the chalk a rather open structure, where the dimensions of the pore space may be considerably greater than the dimensions of the individual grains (Risnes & Flaageng 1999). Mechanically, high porosity chalk behaves as frictional materials, i.e. the dominant deformation mechanism is mechanical translation and rotation of coccolith fragments and calcite grains. However, the open structure enhance the failure mechanism referred to as pore collapse or compaction, where chalk grains are forced into the pore space. Compaction is actually a large-scale measure of the axial strain upon loading.

High porosity North Sea chalk is rate-sensitive in compaction, i.e. the amount of compaction depends on the rate at which the material is loaded. The rate-dependency is based on a breakdown of the structure made up by coccolith fragments, see Section 2.1. Each pore is protected by structures referred to as "beams" and "arches" made up by many chalk particles, and these particles are very poorly cemented. When the pore pressure is reduced due to oil production, the load is shifted to the chalk structure, where it exceeds the ability of these weak structures to support it, and the chalk fails. There is a macroscopic yield point, but each support structure has its own failure condition

(Andersen et al. 1992). There is a cascade of failure, which reaches a steady-state under forced loading. When the loading rate changes, the deformation response changes to a new steady-state condition, but that change is not instantaneous.

Chalk has a time-dependent behavior above the yield stress referred to as creep, which is compaction that continues after loading stops. In the Joint Chalk Research, Phase V (Christensen et al. 2000) it was concluded that chalk-water interaction is a modification of the time-dependent behavior of chalk, i.e. creep. High porosity North Sea chalk is also rate-sensitive in creep. The creep behavior displays a logarithmic dependence on time, see Figure 2.19.

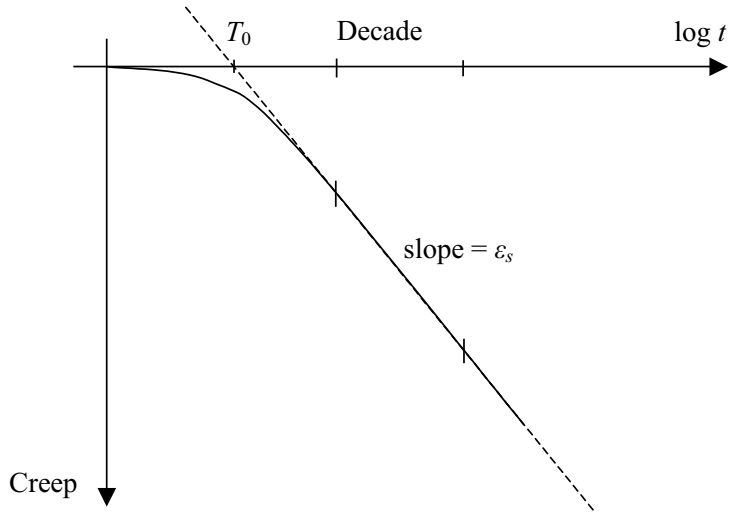

Figure 2.19 *Schematic time curve.*

After a certain time at constant stress, the time curve shows a linear slope on the log-linear plot of strain (creep) vs. time giving the creep parameter ε_s [%/time decade], which is the additional strain per time decade during creep:

$$\varepsilon_s = \frac{d\varepsilon_z}{d\log t} \tag{2.31}$$

By linear extrapolation of this slope to zero additional creep ($\Delta\varepsilon_{creep} = 0$), a base time T_0 can be established. The additional creep at time $t > T_0$ may be calculated by:

$$\Delta\varepsilon_{creep} = \varepsilon_s \log \frac{t}{T_0} \tag{2.32}$$

The total amount of creep ε_t is found as:

$$\varepsilon_t = \varepsilon_0 + \Delta\varepsilon_{creep} \tag{2.33}$$

where the initial creep ε_0 is included in the total initial deformation measured in the laboratory experiment.

The strain rate $\dot{\varepsilon}_{creep}$ can be calculated as the derivative of $\Delta\varepsilon_{creep}$ with respect to time (Ruddy et al. 1989):

$$\dot{\varepsilon}_{creep} = \frac{d(\Delta\varepsilon_{creep})}{dt} = \frac{\varepsilon_s}{ln10 \cdot t} = \frac{\varepsilon_s \cdot 0.434}{t} \tag{2.34}$$

where the prime denotes the time derivative.

Often a creep parameter ε_s of 0.1% strain/hour is applied in the laboratory, whereas a parameter of 0.0001% strain/hour ($\approx$ 10 cm compaction per 10 m of the reservoir per year) is estimated in the field (Havmøller 1998).

Water Weakening

Mechanical properties of high porosity chalk has shown to be strongly dependent on the type of fluid in the pores. Water-saturated chalk is considerably weaker than oil-saturated chalk. This effect is often referred to as a water-weakening effect (Madland et al. 2002).

Waterflooding, i.e. increased water saturation, under elastic stress conditions leads to a significant weakening of the chalk, which is seen as a lower yield stress (Havmøller 1998) and lower plastic consolidation moduli while loading to higher stresses. Further, the elastic consolidation modulus decrease as the chalk change from oil-saturated to water-saturated. However, the failure criterion does not seem to be affected by the change in saturation fluid.

Water-Induced Compaction

Waterflooding above yield leads to significant compaction, while no major compaction is induced by waterflooding below the yield stress (Christensen & Vanggard 1994). There is an indication that the final compaction due to pore collapse is comparable for primary production and waterflooding. However, it takes considerably longer time to obtain the final compaction for primary production.

When oil-filled chalk is waterflooded at a stress level above the pore collapse stress, extensive compaction is observed to follow the waterfront locally through the chalk. In Figure 2.20, a waterflood front moving away from a wellbore is indicated. Ahead of the flood front, the pore pressure has increased due to the waterflood. The waterflood repressurizes the formation, so the oil ahead of the flood front is repressurized. This makes it behave more elastic (i.e. stiffer). Behind the flood front there is a zone of chalk possibly altered by the flood front passage. Behind the flood front is fractured chalk that is also behaving elastically (except for stress redistribution caused by the fractures). In the front zone, the chalk is actively compacting and fracturing, resulting in an enhanced permeability zone in the waterflooded zone. The compaction zone at the flood front is bounded above and below by unmoving formations and ahead by a stiff elastic body (Andersen 1996).

2.6.2 Conceptual Model for High Porosity Maastrichtian Chalk

In the Joint Chalk Research, Phase V (Christensen et al. 2000), a simple conceptual model was proposed for the mechanical behavior of intact chalk during waterflooding on basis of tests on Stevns outcrop Maastrichtian chalk with porosities in the range of 42.9-44.5%.

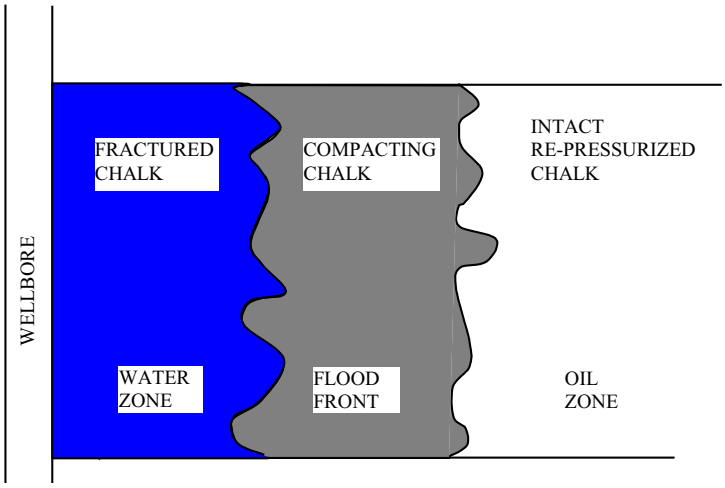

Figure 2.20 *Compacting chalk at the waterflood front, after (Andersen 1996).*

The model was later verified on high porosity (40-45%) Tyra Maastrichtian chalk. The conceptual model was proposed to be used for prediction of the consequences of chalk-water interaction. A sketch of the conceptual chalk model is shown in a mean effective stress - deviatoric stress - compaction plot in Figure 2.21.

The mean effective stress p' is defined as:

$$p' = (\sigma_1' + \sigma_2' + \sigma_3')/3 \tag{2.35}$$

The deviatoric stress q is defined as:

$$q = ((\sigma_1 - \sigma_2)^2 + (\sigma_2 - \sigma_3)^2 + (\sigma_3 - \sigma_1)^2)^{\frac{1}{2}} \cdot \frac{1}{\sqrt{2}} \tag{2.36}$$

The conceptual model offers a simple way to model chalk-water interaction as a change in basic compaction behavior related to the initial saturation, the porosity, the pore collapse stress (yield) and the wettability. The model is based on the observation that fully oil- and fully water-saturated chalk have different compaction curves, i.e. fully water-saturated chalk has a significantly lower pore collapse stress level than fully oil-saturated chalk. When oil-saturated chalk is waterflooded, the compaction behavior shifts from the "oil compaction curve" to the "water compaction curve", see Figure 2.21. In the plastic stress regime, this results in a temporary accelerated strain rate and additional final compaction.

The initial water saturation is a key parameter, influencing the magnitude of compaction during waterflooding. Chalk with low initial water saturation results in a pore collapse effect when waterflooded, while chalk with an initial water saturation above approximately 20% shows no or minor effect when waterflooded, see Figure 2.22.

For high porosity Maastrichtian chalk (porosity above 40%), the difference in pore collapse stress seem to be reduced with decreasing porosity.

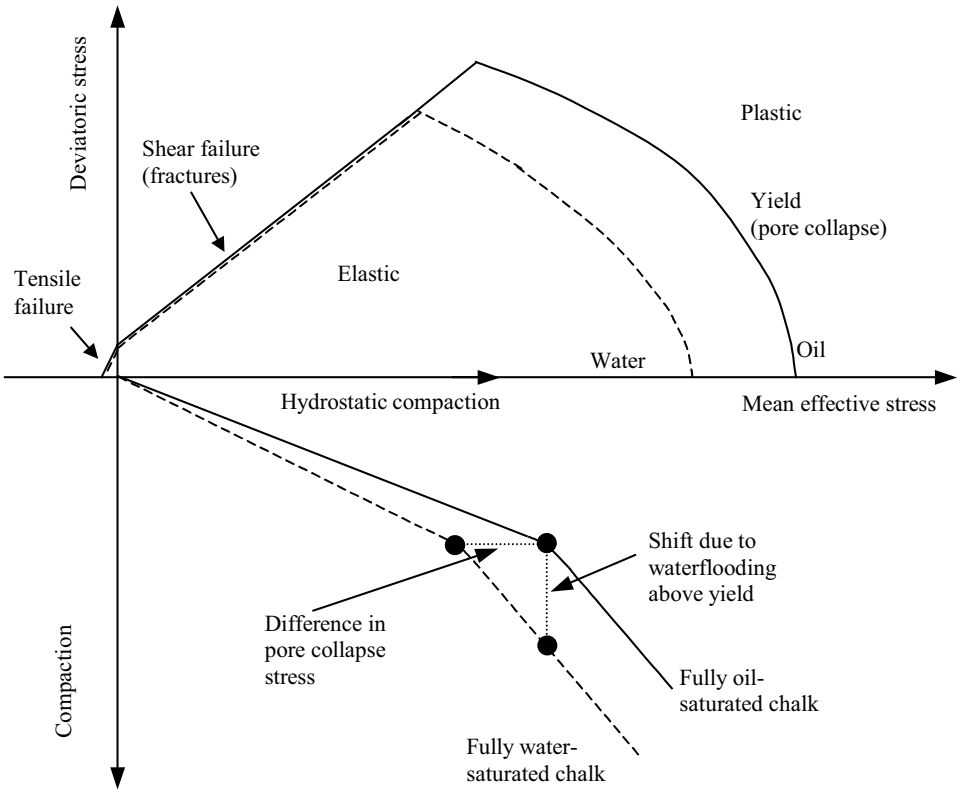

Figure 2.21 *Sketch of the conceptual model for intact chalk, based on (Christensen et al. 2000).*

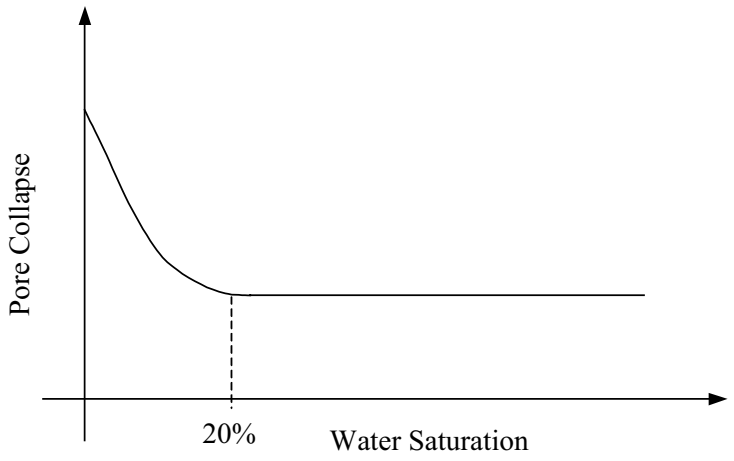

Figure 2.22 *The influence on initial water saturation on pore collapse.*

The chalk-water interaction has been explained by capillary pressure effects (oil-water), cohesive forces caused by the water film in partly saturated chalk, chemical and mechanical changes near the grain-to-grain contacts and dissolution of chalk. One explanation is that capillary forces are strong at low initial water saturation giving chalk mechanical strength, i.e. capillary forces are known to induce an apparent cohesion between chalk grains. Any increase in the water saturation reduces the capillary forces and results in an, at least temporarily, weaker chalk which compacts (Christensen et al. 2000).

Chapter 3

Experimental Basis

The overall choices made in connection with the waterflooding tests in the Ph.D. project are described in this Chapter. Further, the experimental work performed prior to the waterflooding tests to obtain information on wettability, capillary pressure, fractures and permeability are described.

Initially, the choice of chalk material and fluids are explained. Then follows a description of the wettability and capillary pressure measurements, and the fracture description including oil permeability tests. Further, the advantages of using a centrifuge for the waterflooding tests are described. Finally, the relevance of the waterflooding tests on Hillerslev outcrop chalk in relation to field conditions are discussed.

3.1 Chalk Material and Fluids

Hillerslev outcrop chalk was used because this chalk is highly fractured and available for sampling of large test specimens. Further, the chalk can be regarded as a close analogue to the oil-producing Tor formation of the Valhall field, see Section 4.4.

It was chosen to use large, naturally fractured specimens for testing as they are considered more representative for field scale as the effect of complex groups of natural fractures are included. Further, the reason for using large test specimens is to investigate, at a larger scale, the displacement processes, and to reduce capillary end effects.

It was chosen to use the light laboratory oil Isopar-L with a density of $\rho = 0.763$ g/cm^3 and a dynamic viscosity of $\mu = 1.41$ mPa·s, both at 22° C because this oil is easier to handle at room temperature than crude oil, and since many of the existing waterflooding tests are performed on specimens saturated with Isopar-L. Further, due to the composition of Isopar-L, the wettability of the specimens are not altered. To resemble the conditions of a North Sea chalk reservoir in the best possible way, the water used for waterflooding was saline (artificial seawater) with a salinity of 34 g NaCl/l water. To avoid dissolution of chalk during testing, chalk pieces were dissolved in the water resulting in a density of $\rho = 1.025$ g/cm^3 and a dynamic viscosity of $\mu = 1.0$ mPa·s, both at room temperature.

3.2 Wettability Considerations

Wettability measurements were carried out on two small Hillerslev outcrop chalk specimens to obtain knowledge of the wettability. Based on the measurements, it was concluded that Hillerslev outcrop chalk is strongly water-wet, see Section 4.2. In contrast, the Valhall Tor formation is reported to be neutral to slightly oil-wet (Andersen 1995) or neutral to slightly water-wet (Eltvik et al. 1990). However, after the waterflooding tests were completed, BP Norway provided data from recently performed laboratory tests on Valhall Tor formation specimens (communication with BP Norway 2004). In these tests it was found that at reservoir condition waterfloods, there were strong indications of water-wet behavior, but there were also indications of some oil-wet surfaces, i.e. a fractional-wettability, see Section 4.4.

Capillary imbibition tests were carried out on three small ($D = 54$ mm, $H = 27$ mm) Hillerslev chalk specimens. The tests showed spontaneous imbibition of water in the range of 71-72%, see Appendix C. These tests also revealed a high capillary imbibition rate as 96-98% of the imbibition was completed within 1-1$\frac{1}{2}$ hours.

The possibility of altering the wettability towards less water-wet using crude oil added 1 weight% Dodekane acid was tested on a single small Hillerslev outcrop chalk specimen. The wettability alteration was performed to learn how to alter the wettability in order to be able to alter the wettability of a single of the large test specimens used for waterflooding. The wettability of the small specimen was altered to a neutral to slightly oil-wet state, i.e. the wettability of the strongly water-wet Hillerslev chalk can be altered towards a less water-wet state using crude oil added Dodekane acid, see Section 4.2. However, the wettability alteration method affected the chalk of the small specimen, making it more brittle and the periphery of the specimen slightly uneven.

Consequently, additional wettability alteration tests were performed on small pieces of Hillerslev outcrop chalk using Isopar-L added Dodekane acid, see Section 5.2.1. The wettability alteration did not seem to affect the chalk. The effect on the chalk for the small chalk specimen is thus assumed to be related to the use of crude oil added with Dodekane acid, since the laboratory oil Isopar-L was used in the wettability alteration tests on the small chalk pieces. Based on these tests, it was chosen to alter the wettability of a single of the large test specimens using Isopar-L added 0.5 weight% Dodekane acid.

Water-oil capillary pressure curves were established for the two strongly water-wet Hillerslev outcrop chalk specimens and the single Hillerslev chalk specimen altered to a neutral to slightly oil-wet state, see Section 4.2.

Six of the large specimens used in the waterflooding tests were strongly water-wet, while the wettability of a single specimen was altered towards less water-wet. The wettability alteration of the single large test specimen was performed in order to be able to perform a waterflooding test on a specimen as close an analogue to the Valhall Tor formation as possible.

The specimen was left for aging in 8 months. An effect of the wettability alteration procedure on the chalk was in fact seen, making the chalk brittle, and the gypsum "toothpaste-like". This was assumed to be due to the long period of aging. Due to problems during mounting of the specimen in the centrifuge test set-up (Section 5.2.1), this specimen was not used for testing. Consequently, the wettability of a second test speci-

men was altered towards less water-wet following the same procedure. The specimen was only left for aging in 1 week. The assumption that the long period of aging affected the chalk seem valid, since fortunately, the wettability alteration was not observed to affect the chalk in this specimen. The wettability alteration of the single large specimen resulted in the specimen being fractional-wet, see Section 5.2.1.

3.3 Fracture Considerations

To study the effect of fractures on the displacement processes, it is important to obtain knowledge of the fractures in the chalk. For this purpose, a (global) fracture description was carried out at the Hillerslev outcrop chalk quarry located in the northern part of Jutland, see Section 4.3. Here, twelve chalk specimens ($D \approx 50$ cm, $H \approx 50$ cm) were sampled. A (local) fracture description of the specimens tested was carried out. The local and the global fracture descriptions were in accordance, i.e. the fracture system in the specimens represents the major part of the Hillerslev outcrop chalk fracture pattern, see Section 5.3.

The mean matrix permeability for Hillerslev outcrop chalk was measured on two small specimens to 2.6-2.9 mD using synthetic Valhall formation water, see Section 5.3.1.

Absolute oil permeability tests were performed on the large test specimens to study the effect of fractures and stress level on permeability, see Section 5.3.1. A significant influence of fractures on permeability was seen. The tests showed that the presence of fractures increased the matrix permeability with a factor of up to 100-130. Both constant permeability and permeability reduction was observed with increasing mean stress. The different scenarios are believed to be due to different fracture orientations. It was concluded that the permeability stress dependency was mainly characterized by the fracture pattern and not just by the degree of fracturing.

3.4 Centrifuge Modelling

In the centrifuge, the test specimens were exposed to an acceleration field of N times the gravitational acceleration g. This implies that at the chosen acceleration of $N = 72$, the 50×50 cm blocks of chalk can be considered to model the *behavior* of 36×36 m blocks in a reservoir, see Section 2.5. Further, in the centrifuge, the flow time including the time for capillary imbibition is reduced by N^2, which means that the tests are considerably faster to perform than tests at $N = 1$.

Another advantage of the centrifuge is that the height of the capillary imbibition is reduced by N. In a chalk reservoir with similar properties as Hillerslev chalk, the saturation profile resulting from spontaneous imbibition of water will in principle be as shown in Figure 3.1. In the centrifuge, the specimen saturation profile above the free water level will follow the curves in Figure 3.1 up to 36 m represented by the specimen height of 50 cm at $N = 72$. The saturation profile for a specimen at $N = 1$ is not representative for reservoir scale as the modelled prototype height at $N = 1$ is 50 cm.

Given sufficient time and water, the test specimens can spontaneously imbibe around 70% at 1 g due to capillary forces, see Figure 3.2(a). When these test specimens are used as models in the centrifuge under application of 72 g, a water saturation profile as

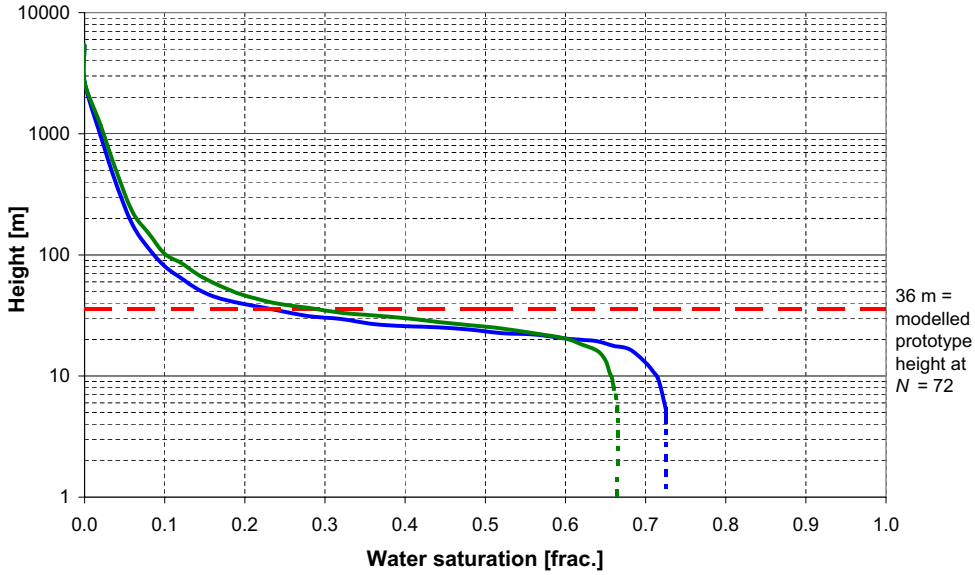

Figure 3.1 *Two calculated water-oil capillary imbibition curves for Hillerslev outcrop chalk, see Section 4.2.1.*

illustrated in Figure 3.2(b) will be obtained after spontaneous imbibition of water. During waterflooding, the waterfront will move up in the model, and the water saturation profile will move up accordingly, see Figure 3.2(c). As the waterfront reaches approximately 35 cm above the specimen bottom, a capillary imbibition of around 70% is possible in the whole specimen, similar to the specimen at 1 g. However, until the waterfront has reached 35 cm above the specimen bottom, the capillary imbibition potential is suppressed, and consequently, a larger part of the capillary pressure curve for the Hillerslev outcrop chalk can be represented. This means that the centrifuge tests makes it possible to follow the waterfront up through the specimen.

The reduction in capillary imbibition potential facilitates flow of water in the fractures. The capillary imbibition time is reduced by N^2, but since the flow time is reduced similarly, the ratio between capillary imbibition time and the flow time remains the same, i.e. the ratio between flow of water in the fractures and capillary imbibition is the same in the model and the prototype.

Problems with the Low Mechanical Strength of Chalk

The high capillary pressure of chalk makes it difficult to obtain the necessary high rotational speed to establish capillary pressure curves for chalk in the centrifuge. At the same time, the low mechanical strength of chalk implies that the centrifuge speed must be limited to ensure that fractures are not induced in the chalk.

These problems with centrifuge modelling of chalk were experienced during testing of three small, unfractured Hillerslev outcrop chalk specimens in a Beckmann centrifuge prior to the centrifuge tests performed on the large, fractured Hillerslev chalk specimens, see Section 4.2. In the Beckmann centrifuge, capillary pressure curves were established for the three small specimens 1A, 2 and 3. First, the specimens were centrifuged in

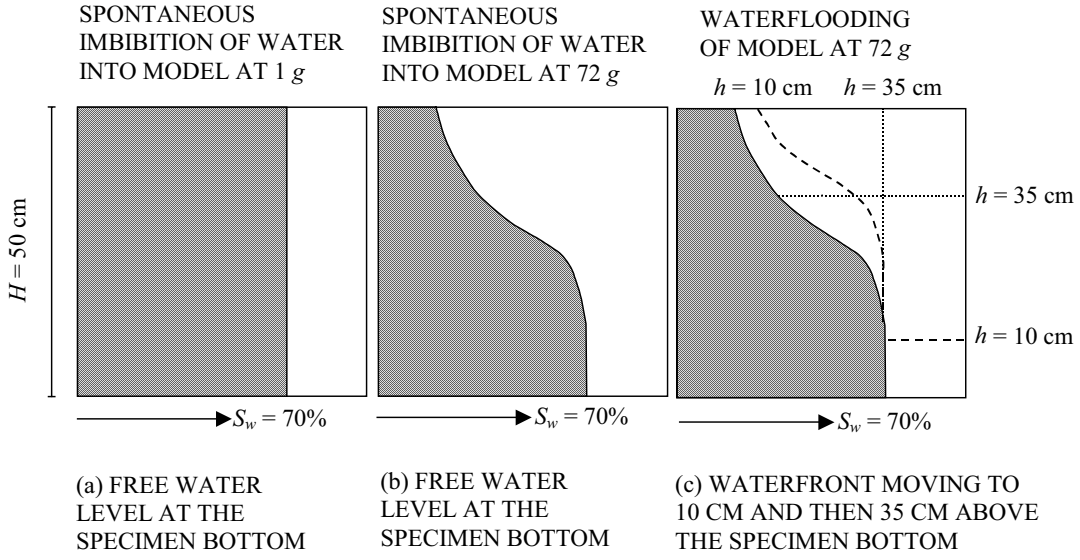

Figure 3.2 *Illustration of water saturation profiles for a large Hillerslev outcrop chalk specimen at $N = 1$ and 72 times the gravitational acceleration. The saturation profile for $N = 72$ is moving up through the specimen following the waterfront.*

water and then in oil. During the centrifuging in water, distinct fractures were induced in specimens 1A and 3. The maximum effective, vertical stress σ'_v at the bottom of these specimens were obtained at the last step of the centrifuging in water, i.e. at 7700 RPM. The maximum effective stresses are calculated for the two specimens using equation (2.22) reduced for pore pressure. The calculated values of σ'_v for the two specimens are included in Table 3.1 along with specimen height H, and effective centrifuge radius R_e.

Specimen	H [cm]	R_e [cm]	σ'_v [MPa]
1A	3.62	14.82	2.88
3	5.0	14.13	3.85

Table 3.1 *The specimen height H, effective centrifuge radius R_e, and effective vertical stress at the specimen bottom σ'_v for specimens 1A and 3.*

The calculated values of σ'_v are compared with the estimated unconfined compressive strength $\sigma'_{ci} = 2.4$ MPa of intact Hillerslev chalk (Havmøller & Krogsbøll 2001). For both specimens, the estimated σ'_{ci} is exceeded, which is consistent with the fact that fractures were induced. Specimen 2 experiences approximately the same stress levels as specimen 3, and thus fractures are presumed to have been induced, however less distinct.

The low mechanical strength of chalk is thus a problem for establishing capillary pressure curves for Hillerslev chalk in the centrifuge. Further, the speed limitation of 8000 RPM for the Beckmann centrifuge is a problem for establishing capillary pressure curves. Especially the centrifuging in oil was not completed. To be able to establish capillary pressure curves for Hillerslev outcrop chalk, a centrifuge of larger capacity must be used. However, a centrifuge of larger capacity would induce more fractures in the

chalk. Consequently, capillary pressure curves cannot be obtained for Hillerslev outcrop chalk in the centrifuge, see Section 4.2.

For the centrifuge tests on the large, fractured Hillerslev chalk test specimens, only oil permeability tests and waterflooding tests were performed. This implies that no problems were encountered in relation to the high capillary pressure of Hillerslev chalk for the centrifuge tests in this Ph.D. project.

To investigate the mechanical strength of chalk test specimens, Havmøller and Krogsbøll (Havmøller & Krogsbøll 2001) used a model suggested by Papamichos et al. ((Havmøller & Krogsbøll 2001) and references therein) developed for collapsible soil to be used for chalk-water interaction. This model was later modified to:

$$F = \sqrt{J_2} \cdot (\cos\theta_L + \frac{\sin\varphi \cdot \sin\theta_L}{\sqrt{3}}) - (p' + \sigma_t) \cdot \sin\varphi \cdot \sqrt{\frac{\sigma_y - p'}{\sigma_y - \sigma_t}} \tag{3.1}$$

where σ_y is the hydrostatic pore collapse stress (yield), σ_t is the tensile stress, p' is the mean effective stress, φ is the peak angle of friction, θ_L is Lode's angle (θ_L = -30° for stress path in standard triaxial test) and J_2 is the 2^{nd} invariant of deviatoric stress related to von Mises stress q by $\sqrt{J_2} = q/\sqrt{3}$. For shear failure and pore collapse stress surface, $F = 0$ and:

$$q = \sqrt{3} \cdot \frac{(p' + \sigma_t) \cdot \sin\varphi \cdot \sqrt{\frac{\sigma_y - p'}{\sigma_y - \sigma_t}}}{(\cos\theta_L + \frac{\sin\varphi \cdot \sin\theta_L}{\sqrt{3}})} \tag{3.2}$$

Havmøller and Krogsbøll (Havmøller & Krogsbøll 2001) determined model parameters from tests on both fractured and un-fractured, normal-scale (D = 5.4 cm) specimens and fractured, block (D = 50 cm, H = 50 cm) specimens of water-saturated Hillerslev outcrop chalk. The model parameters are included in Table 3.2.

Surface	φ [deg.]	σ_c [MPa]	σ_t [MPa]
Surface 1	45	7	0.5
Surface 2	45	5	0.2
Surface 3	45	3	0.01

Table 3.2 *Model parameters for water-saturated Hillerslev chalk, from (Havmøller and Krogsbøll 2001). Surface 1 is for intact chalk specimens, with increasing degree of fracturing for surface 2 and surface 3.*

Figure 3.3 illustrates the model applied to the test series on water-saturated Hillerslev outcrop chalk specimens. HF and HU refers to normal-scale tests on fractured and un-fractured Hillerslev chalk specimens, respectively. Surface 1 is for intact chalk specimens, with increasing degree of fracturing for surface 2 and surface 3.

The centrifuge tests were performed at low mean stress levels since the specimens were not subjected to any vertical stress other than the self-weight in the gravitational field. The mean effective stress p' and the deviator stress q were calculated at the bottom of the specimens at the end of the waterflooding using equation (2.22) reduced for pore

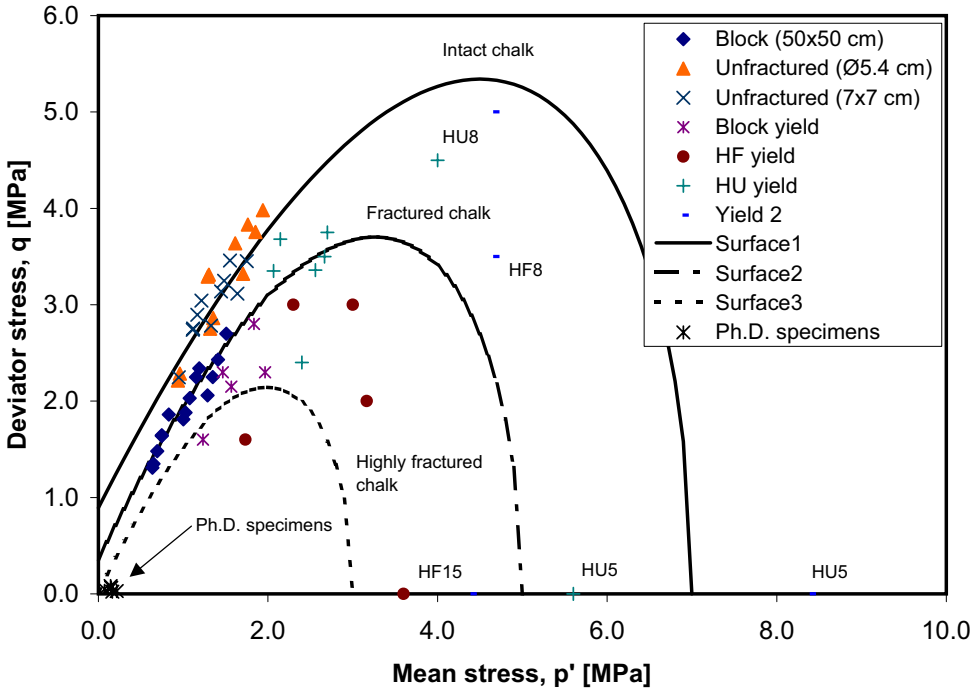

Figure 3.3 *Combined yield and failure surface for water-saturated Hillerslev chalk, from (Havmøller & Krogsbøll 2001).*

pressure, mean weights for the specimens containing water, and simple measurements of the fluid levels. Here, the centrifuge is spinning at 167.1 RPM. The data for the large-scale centrifuge tests are included in Figure 3.3, referred to as Ph.D. specimens. As seen in the figure, the stress level for all the specimens tested in the centrifuge in this Ph.D. project are below the shear failure line, i.e. there were no problems with the low mechanical strength in these tests.

3.5 Field Relevance

Waterflooding a fractured chalk reservoir with a well-connected fracture network throughout the reservoir has been considered a risk of flow of water mainly in the fractures. The purpose of the waterflooding tests in the centrifuge was to study whether the presence of fractures in a chalk reservoir impose a risk of flow of water in the fractures when waterflooded, leading to early water breakthrough and an inefficient sweep.

The tests were performed on large, naturally fractured chalk specimens representative for reservoir scale. Further, the capillary imbibition potential was reduced in the centrifuge making the test specimens more representative for reservoir scale.

The waterflooding tests in the centrifuge were performed at a high rate. In the field, high rate waterflooding is carried out to induce fractures in the reservoir (hydraulic fracturing) to enhance the effective permeability.

Hillerslev outcrop chalk specimens were used as this chalk is regarded a close analogue to the Valhall Tor formation, with comparable lithology, porosity, permeability and fracture sets, i.e. the specimens represented Valhall Tor chalk flow properties.

The centrifuge tests were conducted at low stress levels. At high stress levels fractures may close, resulting in a reduction in permeability or even porosity, i.e. a change in the flow properties. Tests were thus carried out in the oedometer cell at higher stress levels. The purpose of the initial oil permeability tests was to investigate the influence of stress on the permeability. The oedometer tests were also conducted to study the effect of chalk-water interaction above yield, which is observed in chalk reservoirs.

Hillerslev outcrop chalk is strongly water-wet. The wettability of a single test specimen was altered to fractional-wet. This made the specimen a closer analogue to the Valhall Tor formation since the most recent analysis indicate that Valhall Tor chalk exhibit water-wet behavior, with indications of some oil-wet surfaces, i.e. a fractional-wettability.

Testing in the area constant cell in the centrifuge and the oedometer cell results in more field representative boundary conditions as lateral expansion is prevented

In the field, waterflooding is normally performed by horizontal/inclined injectors. However, in both the centrifuge and the oedometer tests, water was injected into the bottom of the specimens against the gravity field, i.e. corresponding to a vertical injector in the field.

Chapter 4

Hillerslev Outcrop Chalk Properties

This Chapter includes a general description of the chalk in the Hillerslev outcrop chalk quarry. Further, earlier established capillary pressure curves are included along with results of laboratory measurements of wettability and capillary pressure curves for Hillerslev outcrop chalk carried out during the Ph.D. project. These measurements are included in Report 2, and for detailed information the reader is referred to this report. The fracture system at the Hillerslev outcrop chalk quarry is described, and for detailed information the reader is referred to Report 1. Finally, the chalk at the quarry is compared to the chalk from the Tor formation of the Valhall field, as these chalks are considered analogues.

4.1 General Hillerslev Outcrop Chalk Description

The Hillerslev outcrop chalk quarry is located near Thisted in the northwestern part of Jutland. The location of the Hillerslev chalk quarry and the Norwegian offshore oil bearing chalk field Valhall is indicated on Figure 4.1. The Hillerslev chalk quarry is a quarry in operation located on the eastern half of the top of the Thisted dome, which is a salt-induced dome. The size of the quarry is approximately 500 m $\times$ 200 m. The chalk at the Hillerslev quarry is heavily fractured. The fracturing of the quarry is assumed to be related to the structural growth of the salt-induced dome and partly to glacial disturbance at the top. The general tilt in the Hillerslev area is 4 degrees towards ESE (Jakobsen 2001).

The chalk in the quarry is of Late Maastrichtian age. It is a soft, greyish white, weakly cemented mudstone/wackestone. It is composed almost exclusively of coccolithic material with subordinate amounts of skeletal material (foraminifera, bryozoans, echinoderms and molluscs) (Krogsbøll et al. 1997).

Analysis of more than 200 specimens sampled along a horizontal profile in the quarry shows a porosity variation of 44-52% with an average of 47%. The average gas permeability is 8.1 mD, ranging from 5.1-13.4 mD. The average distribution of pore throat radius is 0.6 μm. The content of insoluble residue (silica, clay minerals and pyrite) is low, around 4%. Analysis of the specimens indicate that the chalk is more affected by compaction (mechanical diagenesis) than chemical diagenesis. Flint concretions in the chalk only amount to a small part of the total sediment volume (Krogsbøll et al. 1997).

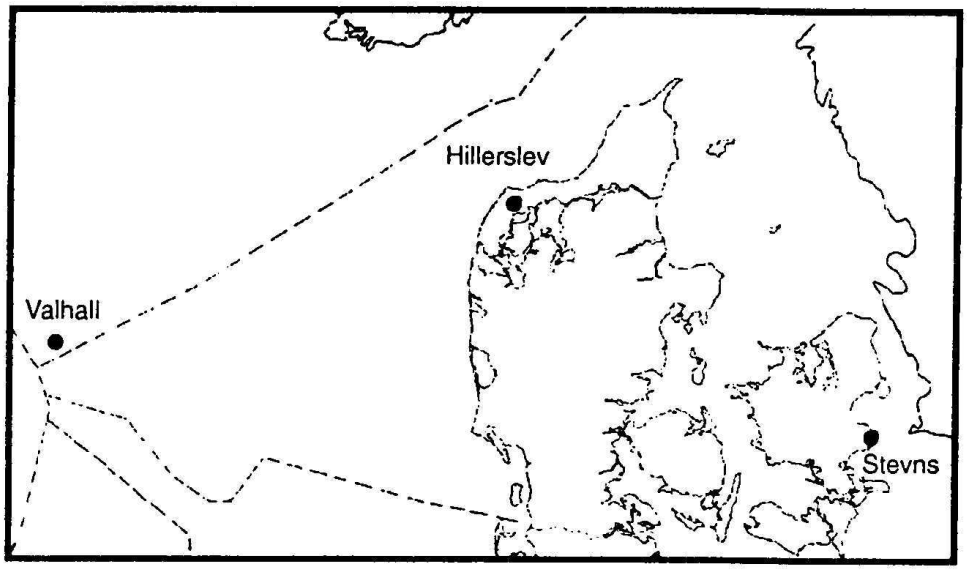

Figure 4.1 *Location of the Hillerslev chalk quarry and the oil bearing chalk field Valhall.*

4.2 Wettability and Capillary Pressure

4.2.1 Earlier Research Project, Phase 1

In the earlier research project "Fractures and Rock Mechanics", phase 1 (Krogsbøll et al. 1997), mercury-gas capillary pressure curves were established for two small Hillerslev chalk specimens, see Appendix B. These curves are converted to oil-water capillary pressure curves, and included in Figure 4.2. The conversion between the capillary pressure from one fluid pair $(P_c)_1$ to another fluid pair $(P_c)_2$ is performed as follows:

$$\frac{(P_c)_1}{(P_c)_2} = \frac{\sigma_{i1}}{\sigma_{i2}}$$

where σ_i [mN/m] is the interfacial tension (IFT) between the two fluids. No correction for contact angle is applied since the chalk is strongly water-wet. The conversion from the fluid pair gas-mercury (laboratory) to the fluid pair brine-Isopar-L (laboratory) can be performed by use of the values listed in Table 4.1.

Fluid pair	[mN/m]
Brine-Isopar-L (lab.)	60
Gas-mercury (lab.)	480

Table 4.1 *Values of interfacial tension for fluid pairs (according to GEUS).*

The method used to obtain the capillary pressure curves results in a 100% displacement of gas by mercury even though a residual gas saturation is expected. This means that the converted capillary pressure curves show a 100% displacement of water by oil even

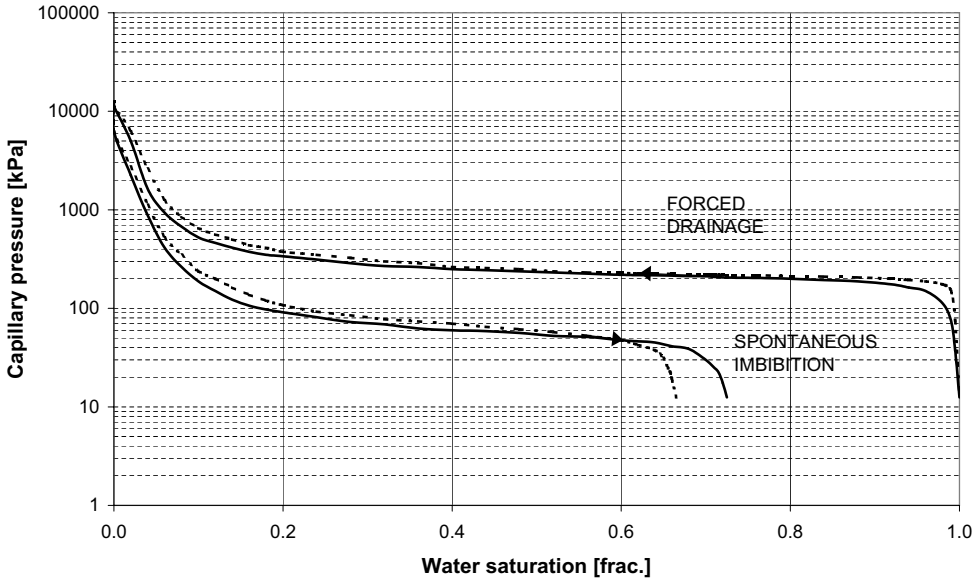

Figure 4.2 *Oil-water capillary pressure curves for two Hillerslev outcrop chalk specimens converted from mercury-gas capillary pressure curves (Krogsbøll et al. 1997).*

though an irreducible water saturation S_{wir} is expected. Further, the capillary pressures in the mercury-gas capillary pressure curves are plotted from 1 bar in a logarithmic scale resulting in capillary pressures in the converted oil-water capillary pressure curves from approximately 13 kPa.

The converted capillary pressure curves reveal a total spontaneous water imbibition potential in the range of 66-73%.

Earlier experimental work by Nørgaard et al. (Nørgaard et al., 1999) has shown that capillary pressure curves obtained by mercury injection lie significantly below curves obtained by the centrifuge method on the same specimen of North Sea Chalk. The reason for this may lie in problems with conversion, i.e. scaling the interfacial tension (IFT) and contact angle of the mercury liquid - mercury vapor system to the oil-water system (Anderson 1986*c*). Consequently, the converted curves are affected by the method used to obtain the tests, the conversion and the values of IFT.

4.2.2 Ph.D. Project

Wettability Determination

Measurement of wettability and subsequent establishment of capillary pressure curves was carried out for three small Hillerslev chalk specimens during the Ph.D. project (Report 2). This was done by utilizing Amott cups and an automated Beckmann centrifuge at Rogaland Research, Stavanger, Norway. The three specimens were taken from a small block of Hillerslev outcrop chalk material from the research project "Fractures and Rock Mechanics", phase 2 (Jakobsen 2001). The dimensions of the specimens were $D = 38$ mm and $H = 50$ mm. The fluids used were synthetic Valhall formation water with a density of $\rho = 1.05$ g/cm^3 and a dynamic viscosity of $\mu = 1.0$ mPa·s, both at room temperature, and the laboratory oil Isopar-L with a density of $\rho = 0.763$ g/cm^3 and a dynamic viscosity

of $\mu = 1.41$ mPa·s, both at 22° C.

Prior to the wettability measurement, it was known that Hillerslev outcrop chalk is water-wet, but the wettability measurement was carried out to determine the degree of water-wetness. Two of the specimens tested were originally water-wet, whereas the wettability of a single specimen was altered towards less water-wet using crude oil added 1 weight% Dodekane acid to obtain as close an analogue to the Valhall Tor formation as possible. Based on information available at the time of the wettability alteration, the wettability of the Valhall Tor formation was believed to be neutral to slightly oil-wet or neutral to slightly water-wet, see Section 4.4. The wettability alteration affected the chalk, and the specimen broke in one end. Consequently, a new diameter and height was obtained, i.e. $D = 37.9$ mm and $H = 36.2$ mm.

The modified U. S. Bureau of Mines (USBM) method (Anderson 1986*b*) was used to determine the wettability and subsequently establish capillary pressure curves for the three specimens. The method consists of five steps: (1) initial oil drive, (2) spontaneous imbibition of water, (3) water drive, (4) spontaneous imbibition of oil, and (5) oil drive. The initial oil drive to the initial water saturation S_{wi} was performed by flow. The spontaneous imbibition steps were performed utilizing Amott cups and the secondary drive steps were performed using an automated Beckmann centrifuge.

The centrifuge is a Beckman L8-55M/P Ultra centrifuge using a rotor with standard or inverted buckets. Three 1.5" diameter cylindrical specimens can be centrifuged simultaneously in the Beckman centrifuge. The centrifuge is automated so that there is automatic reading of produced volumes, evaluation of equilibrium, and change of speed. The centrifuge is equipped with a strobe light assembly in the rotor chamber door. The strobe flashes once during each revolution of the rotor, so measurement of extracted volume can be made without stopping the centrifuge. The strobe can be adjusted to shine through a slit in any one of the rotor buckets. The extracted fluid is collected in a tube. A camera reads the produced fluid volume and a stroboscope light ensures that the camera obtains stable recordings in the rotation cup.

In the centrifuge, multi-step tests were performed, i.e. where the angular velocity is increased in steps. The produced volumes at each step were read initially every 1-2 seconds, but as the production slowed down, the readings were every 5 minutes. At each step, the centrifuge was spun until hydrostatic equilibrium was reached. In the tests, equilibrium was defined as the point at each step for each specimen where the fluid production was ≤ 0.03 cm^3 over a 5 min. period. However, the data processing revealed that the hydrostatic equilibrium may have been defined at too high a fluid production level, as the production curves were not constant in every step, i.e. a small production of 0.03 cm^3 or less went on for a long period of time in some of the specimens at some of the steps. These steps should have been allowed to carry on for a longer period of time, i.e. to a lower fluid production level.

The Amott-Harvey wettability index was calculated to 1 for both water-wet specimens with initial water saturations of $S_{wi} = 29\%$ and $S_{wi} = 0$. It was not possible to calculate the USBM wettability index for neither of the two specimens, since the minimum capillary pressure required to force oil into the specimen was higher than the upper boundary of 70 kPa defined for the USBM wettability index calculation (Anderson 1986*b*). Spontaneous imbibition of water into the two water-wet specimens was in the range of 71-73%. The

water imbibed rapidly, and approximately 88% of the spontaneous imbibition was completed within an hour. No water could be forced into the specimens after spontaneous imbibition. Based on this, Hillerslev outcrop chalk is described as strongly water-wet.

For the single wettability-altered specimen with initial water saturation of $S_{wi} = 13\%$, the Amott-Harvey wettability index was calculated to -0.02, and the USBM wettability index was calculated to -0.77. A small amount of oil (0.12 cm^3) imbibed spontaneously, whereas no water imbibed spontaneously. Based on this it was evaluated that the Hillerslev chalk specimen was altered to a homogeneous neutral to slightly oil-wet state.

Wettability Alteration

The crude oil used for the wettability alteration of the single Hillerslev outcrop chalk specimen was oil from the Snorre field located in the Norwegian part of the North Sea. However, it was not possible to obtain information about the acid number (AN) for the Snorre oil. To ensure the ability of the crude oil to alter the wettability towards less water-wet, it was decided to add 1 weight% Dodekane acid ($C_{11}H_{23}COOH$) to the oil (personal communication with Professor Tor Austad, Stavanger College, Norway).

In order to obtain a homogenous wettability state throughout the specimen, it was flushed in each direction with 100 ml of the Snorre oil added 1 weight% Dodekane acid. After flushing, the specimen was aged in the mixture for 5 weeks at 90° C and 8 bar. Only the end surfaces of the specimen were surrounded by the mixture as a shrink fix sleeve was wrapped around the specimen periphery. During removal of the specimen after aging, it broke in one end. After removal, the crude oil was displaced by Isopar-L. Then the broken end was cut to an even surface, and approximately 2 mm of the other end was removed to prevent outermost effects related to establishment of S_{wi} and the aging in the crude oil.

The wettability alteration method affected more than the wettability of the specimen. The aging made the specimen brittle, and the color changed from light grey to dark brown. Further, the displacement of the crude oil by Isopar-L made the periphery of the specimen slightly uneven.

It was concluded that the wettability of the strongly water-wet Hillerslev chalk can be altered to a homogenous neutral to slightly oil-wet state using crude oil added 1 weight% Dodekane acid. However, this wettability alteration method affect the chalk as well.

Capillary Pressure Curves

The oil-water capillary pressure curves for the two strongly water-wet specimens are included in Figure 4.3, and the oil-water capillary pressure curves for the neutral to slightly oil-wet specimen are included in Figure 4.4. Only the centrifugal part of the capillary pressure curves are included, i.e. forced imbibition and forced drainage.

The small initial increase in S_w seen on the forced imbibition part of the capillary pressure curves for the strongly water-wet specimens is due to water displacing air during the initial centrifuging.

The form of the capillary pressure curves for all three specimens implies that the centrifuge test was ended at too low a capillary pressure. In other words, the capillary pressure curves were not fully completed even though the Beckman centrifuge was run

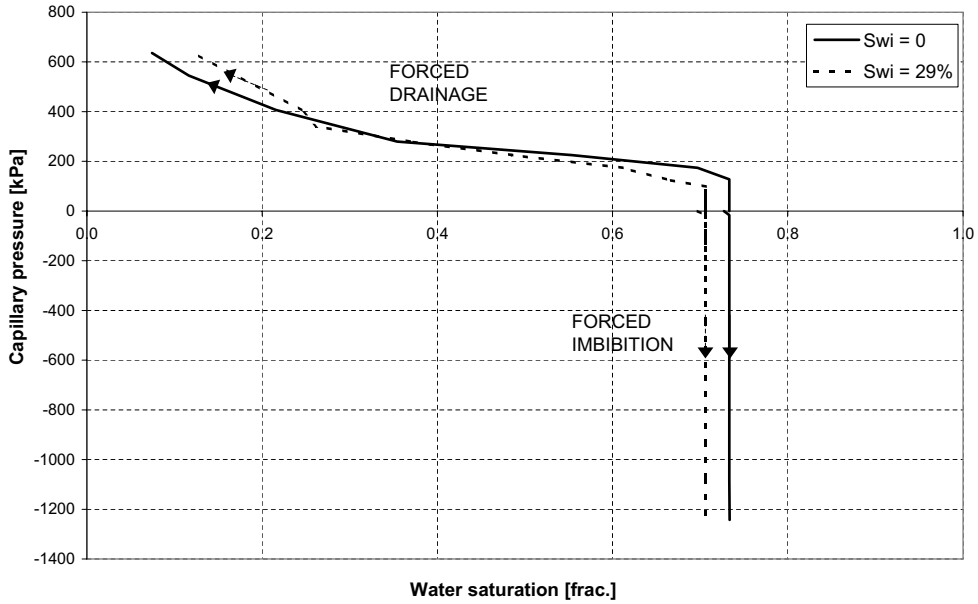

Figure 4.3 *Oil-water capillary pressure curves for two strongly water-wet Hillerslev outcrop chalk specimens.*

to its maximum capacity of 8000 RPM. This means that the irreducible water saturation S_{wir} was not obtained in any of the specimens at the end of the test. However, for the strongly water-wet specimens, the residual oil saturation S_{orw} is in the order of 0.27-0.29 as expected. For the neutral to slightly oil-wet specimen, a S_{orw} of 0.34 was obtained, and seem reliable based on the form of the forced drainage curve.

There were no visible fractures in the specimens before the measurement, but distinct fractures were induced in one of the strongly water-wet specimens and in the single wettability-altered specimen during the centrifuging in water. Further, less distinct fractures may have been induced in the other strongly water-wet specimen. This changes the fluid flow properties such as permeability of the chalk specimens, and may explain the slight difference in the capillary pressure curves for the two strongly water-wet specimens. This also means that the capillary pressure curves were obtained on slightly fractured specimens.

In centrifuge measurements, sources of error consist of data acquisition and not waiting long enough to obtain a good estimate of equilibrium average saturation at each centrifuge step. At some of the centrifuge steps, hydrostatic equilibrium was defined at too high a production level resulting in poor data sets for the capillary pressure curves, affecting the form of the capillary pressure curves. Further, interpretation of centrifuge measurement for capillary pressure curves requires a number of assumptions regarding core homogeneity and boundary conditions.

The high capillary pressure of chalk makes it difficult to obtain the necessary high rotational speed to establish capillary pressure curves for chalk in the centrifuge. To be able to establish capillary pressure curves for Hillerslev outcrop chalk, a centrifuge of larger capacity must be used. At the same time, the low mechanical strength of the chalk implies that the centrifuge speed must be limited to ensure that fractures are not induced

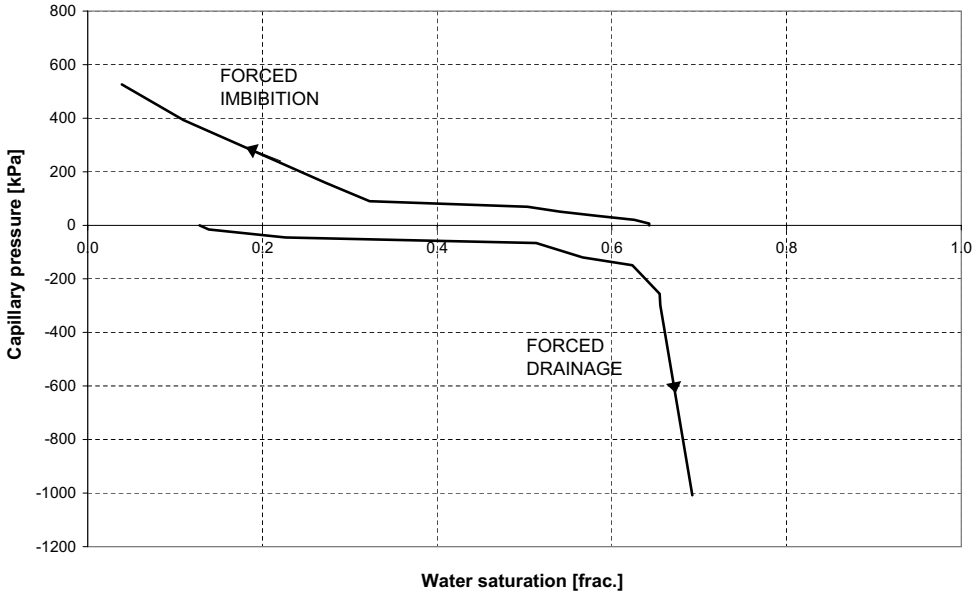

Figure 4.4 *Oil-water capillary pressure curves for a single Hillerslev outcrop chalk specimen altered to a neutral to slightly oil-wet state.*

in the chalk.

This is consistent with the fact that conventional methods used for determination of saturation functions are mainly developed for rocks of lower capillary pressure and higher mechanical strength than chalk. This means that these methods may not apply for chalk. Bech (Bech, 2000) states that especially the centrifuge method is unsuitable due to the low mechanical strength of chalk, as well as the difficulty in obtaining the necessary high rotational speed.

Based on the form of the capillary pressure curves, the fact that the capillary pressure curves were obtained on slightly fractured specimens, and the fact that the capillary pressure curves were not fully completed, it is evaluated that the obtained capillary pressure curves are not fully representative for the specimens. However, a good estimate of the residual oil saturation S_{orw} is obtained, especially for the strongly water-wet specimens.

Based on the fact that the capillary pressure curves were not fully completed due to centrifuge limitations, and that fractures were induced (Section 3.4) in the specimens even at these lower centrifuge speeds, it is evaluated that complete capillary pressure curves for Hillerslev outcrop chalk cannot be obtained in the centrifuge.

Capillary Imbibition Potential

The rate and amount of capillary imbibition depend highly on the wettability. The amount is also affected by porosity and permeability, whereas the rate also depends on viscosity of oil and water, interfacial tension between oil and water, pore structure and initial water saturation (Anderson 1986*c*).

The capillary imbibition potential of the strongly water-wet Hillerslev outcrop chalk is strong as large amounts of water imbibe at a high rate.

Spontaneous water imbibition tests carried out on small ($D = 54$ mm, $H = 27$ mm)

Hillerslev chalk specimens, see Appendix C, showed spontaneous imbibition of water in the range of 71-72%. These tests also revealed a high capillary imbibition rate as 96-98% of the imbibition was completed within 1-1$\frac{1}{2}$ hours. Spontaneous imbibition of water into the two strongly water-wet specimens with initial water saturation of $S_{wi} = 29\%$ and $S_{wi} = 0$, resulted in final average water saturations in the range of 71-73%, and it was not possible to further increase the water saturation by forced imbibition during centrifuging. There is no clear evidence of an effect of different initial water saturations S_{wi} on the final average saturation after spontaneous (and forced) water imbibition in strongly water-wet Hillerslev outcrop chalk.

The strong capillary imbibition potential of Hillerslev outcrop chalk is due to the narrow pore throats, the chalk being strongly water-wet and the low matrix permeability.

4.3 Fracture Description

4.3.1 Earlier Research Project, Phase 1

Earlier, a detailed description of the fracture system of the Hillerslev chalk quarry was carried out, and the main conclusions are given in the research project "Fractures and Rock Mechanics", phase 1 (Krogsbøll et al. 1997). In the northern part of the Hillerslev quarry a chalk wall (approximately 4 m high and 45 m long) was excavated. A fracture description including amongst other fracture density and fracture orientations (strike/dip) were carried out along a horizontal profile (approximately 31 m long) along the wall supplemented with measurements from other locations in the quarry. The fracture description was associated with a series of one inch core plugs sampled along the horizontal profile.

The measured fracture densities indicate almost random spacing of fractures. A high proportion of the fractures are oriented ENE-WSW with NNW-SSE as another important direction. The majority of the fractures are steeply dipping with a dominance of almost vertical fractures.

Three different lithotypes have been recognized along the profile. The most common is burrowed massive chalk mudstone. Locally, burrowed laminated chalk mudstone is also seen and in the eastern part of the profile pebbly massive chalk mudstone (and skeletal wackestone) is dominating.

4.3.2 Earlier Research Project, Phase 2

In the earlier research project "Fractures and Rock Mechanics", phase 2 (Jakobsen 2001) supplementary fracture system descriptions were carried out along a new horizontal profile along a re-excavation of the same wall section as described in phase 1. Thus, information on the fractures was obtained along the same horizontal profile, except for the length. The new profile was only approximately 25 m of the originally approximately 31 m. The chalk profile was excavated 2 m further into the wall with a temporary formation of a plateau for sampling of ten cylindrical block specimens (Havmøller & Krogsbøll 2001).

The measured fracture densities indicate almost random spacing of fractures. Many of the fractures are oriented ENE-WSW and SSE-NNW with NNE-SSW and SE-NW as secondary directions. Horizontal bedding is seen, and horizontal bedding parallel fractures

are common. The majority of the fractures are steeply dipping with a dominance of almost vertical fractures.

Based on the specimens, two chalk types were identified, a soft, greyish white bioturbated chalk mudstone characterized by a weakly laminated structure partly disturbed by burrowing organisms, and a sparse biomicritic chalk wackestone.

4.3.3 Ph.D. Project

In the Ph.D. project (Report 1) a fracture description was carried out by the author along horizontal profiles in the northern part of the quarry just west of the location used for fracture description and sampling in the research projects "Fractures and Rock Mechanics", phase 1 and 2.

A chalk wall (approximately 4 m high and 25 m long) was excavated. A horizontal plateau (approximately 1.5 m high, 25 m long and 2 m deep) referred to as the chalk bench was made by further excavation (approximately 2 m) into the wall for sampling of twelve cylindrical block specimens.

Fracture descriptions were carried out along horizontal profiles along the freshly excavated wall (referred to as wall), along the front of the bench (referred to as bench), and finally along twelve horizontal profiles, one behind each of the sampled specimens (referred to as behind the specimens), resulting in three fracture data sets.

Horizontal bedding with beds of hardened chalk and horizontal bedding parallel fractures are seen in all three fracture data sets. These fractures may be surface parallel tensional fractures due to unloading since the area has been subjected to uplift and subsequent erosion during the geological history (Jakobsen 2001). Conjugate shear fracture sets are also seen. "Crushing zones", i.e. zones with brittle chalk are seen as well.

The measured fracture densities indicate almost random spacing of fractures. Along the wall, a high proportion of fractures (strike) are oriented NNE-SSW and ENE-WSW with NNW-SSE and WNW-ESE as secondary directions, see Figure 4.5 (a). Along the bench, a high proportion of fractures are oriented NNE-SSW and ESE-WNW with NNW-SSE as a secondary direction, see Figure 4.5 (b). Behind the specimens, a high proportion of fractures are oriented NNE-SSW and ESE-WNW with ENE-WSW and NNW-SSE as secondary directions, see Figure 4.5 (c). A comparison shows that the main orientation NNE-SSW, and the secondary orientation NNW-SSE is found in all three fracture data sets. For all three fracture data sets, it is seen that the majority of fractures are steeply dipping with a dominance of almost vertical fractures.

When comparing the measured Joint Roughness Coefficient (JRC) and fracture aperture for all three sets of fracture data, it is evaluated that some of the fractures along the chalk wall are disturbed which apart from the influence of excavation may be due to weathering near the chalk wall. For the fractures along the wall, apertures between ≤ 0.1 to 0.5 mm and 1 to 2 mm are seen, i.e. both closed to very narrow fractures and very open fractures are seen. The closed to very narrow fractures are dominating, but some very open fractures are seen. For the fractures both along the chalk bench and behind the specimens, it is primarily apertures ≤ 1 mm, which are seen, i.e. the number of closed fractures are dominant and only very few very open fractures are observed.

Overall, the three fracture data sets in the Ph.D. project are evaluated to be similar.

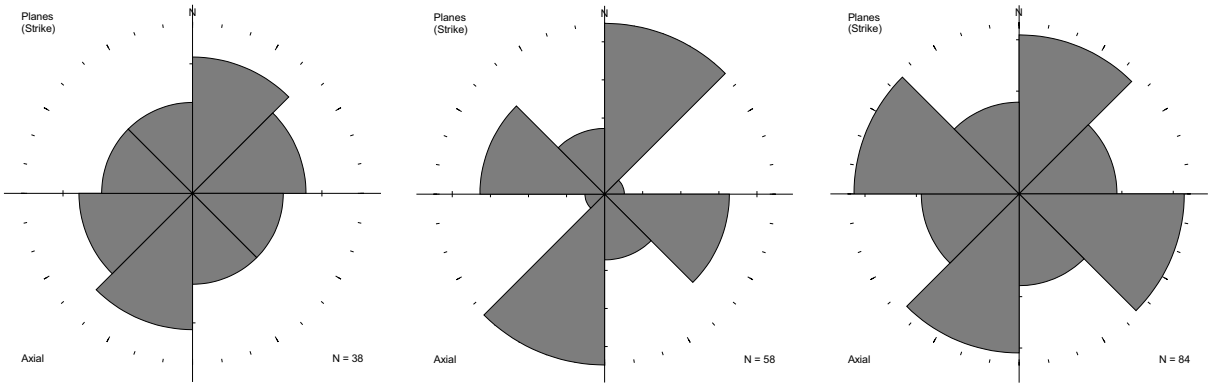

(a) (b) (c)

Figure 4.5 *Rose diagram of strike orientations for all measured fractures (a) along the chalk wall, (b) along the chalk bench and (c) behind the twelve sampled large specimens.*

Based on the twelve sampled large specimens, the chalk was identified as chalk mudstone.

Comparison of the Three Research Projects

The main and secondary orientations of the measured fractures (strike) for the three research projects are included in Table 4.2.

	"Fractures and Rock Mechanics"				Ph.D. project					
	Phase 1		Phase 2		Wall		Bench		Behind specimens	
Main orientations	ENE-WSW	NNW-SSE	SSE-NNW	ENE-WSW	NNE-SSW	ENE-WSW	NNE-SSW	ESE-WNW	ESE-WNW	NNE-SSW
Secondary orientations	-	-	SE-NW	NNE-SSW	NNW-SSE	WNW-ESE	NNW-SSE	-	ENE-WSW	NNW-SSE

Table 4.2 *Main and secondary fracture orientations for the research projects "Fractures and Rock Mechanics", phase 1 and 2 and the Ph.D. project.*

A comparison shows that the main orientation ENE-WSW is found in the "Fractures and Rock Mechanics", phase 1 and 2, and along the wall in the Ph.D. project. This orientation is also found as a secondary orientation behind the specimens. The main orientation NNE-SSW found in all three fracture data sets in the Ph.D. project is also found as a secondary orientation in phase 2.

In all three fracture data sets in the Ph.D. project and in "Fractures and Rock Mechanics", phase 2, horizontal beds are observed, and horizontal bedding parallel fractures are common. The fracture density for all the measured fractures in the Hillerslev chalk quarry indicate almost random spacing of the fractures. The majority of all the measured fractures in the Hillerslev chalk quarry are steeply dipping with a dominance of almost vertical fractures. Based on the comparison it is evaluated that overall, the fracture descriptions for the three research projects are similar.

4.4 Hillerslev Outcrop Chalk Field Analogy

Hillerslev outcrop chalk is regarded as a close analogue to the Tor formation of the Valhall field (Havmøller & Krogsbøll 1997).

The crestal area of the Valhall field has two productive chalk formations, the Tor and the Hod. The Tor formation is of Late Campanian to Maastrictian age and the Hod formation is Turonian in age. The main reservoir, the Tor formation, has a high porosity around 42-50%, and even exceeding 50% i some places, and a low matrix permeability around 1-10 mD. A 1000 m thick Tertiary claystone section of primarily Paleocene, Eocene and Miocene age overlie the chalk section providing the top seal (Barkved et al. 2003).

The fracture sets of the Valhall Tor formation and the Hillerslev chalk quarry are considered comparable. In both cases, the chalk was uplifted, and the fracturing is assumed to be related to this structural development. The Hillerslev quarry is uplifted due to salt dome activity, while the uplift of the Tor formation is due to structural displacements in underburden clay (Ali & Alcock 1992).

Hillerslev chalk can be described as autochthonous pelagic chalk (burrowed massive chalk mudstone), while Valhall Tor chalk can be described as allochthonous mud flows/slumps ((burrowed) massive chalk mudstone). Lithologically the Hillerslev chalk is correlative of the Valhall Tor chalk as they are both related to the Maastrichtian Tor formation or time equivalent formations. The comparison shows two different overall types of depositional situations but more or less the same lithotype (Krogsbøll et al. 1997).

The actual depth of burial in the Valhall field is approximately 2400 m. Compaction and subsequent dissolution of the chalk, however, have been reduced by pore pressure support (overpressure) reducing the effective vertical stress acting on the formation and leaving a soft medium consolidated and highly porous chalk. The effective stress on the formation was less than 3450 kPa at discovery (Ali & Alcock 1992). Only weak indications on pressure dissolution are seen (dissolution seams and stylolites). The degree of cementation is relatively low. This is comparable with Hillerslev chalk, which is highly porous and weakly compacted with a relatively sparse cementation.

Due to the high excess pore pressures, the (effective) stress acting on the Tor formation corresponds to an effective depth of burial much smaller than the actual depth (Havmøller & Krogsbøll 1997). The effective depth of burial is of the same order for the Tor formation (390 m) and the Hillerslev chalk (>300 m) and the same conditions seem to have prevailed these areas.

The Tor chalk specimens have a high density of hairline fractures whereas very few are seen in Hillerslev chalk. Stylolites are seen in the Valhall Tor formation but they are absent in Hillerslev. Stylolite associated fractures are not observed in Valhall Tor, but many small fractures are present. The presence of stylolites seems to have only minor influence on the strength and deformation properties (Havmøller & Krogsbøll 1997). The Valhall field is a double plunging NNW-SSE trending anticline, see Figure 4.6.

The wettability of fresh state Valhall Tor formation plugs was evaluated (Springer et al. 1996) to be neutral based on the measured Amott-Harvey wettability index ranging from -0.008 to -0.0031, and the USBM wettability index ranging from -0.31 to 0.03. The plugs used for the determinations were taken from preserved full core Valhall Tor formation and then substitution cleaned, i.e. flushed at 60° C with 20-30 pore volumes of Isopar-L

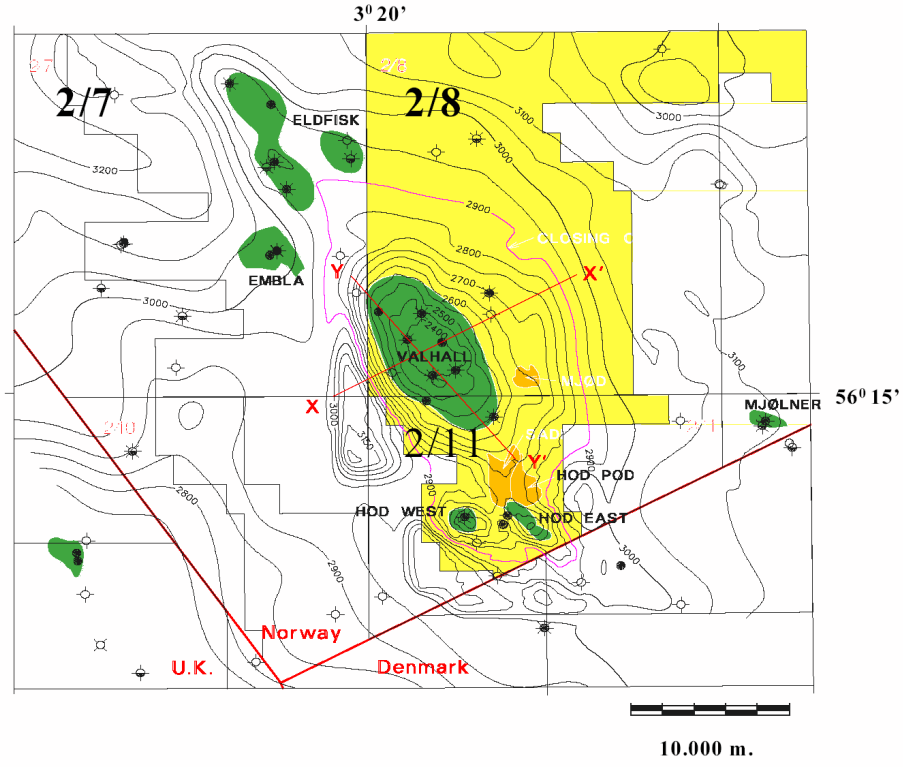

Figure 4.6 *The Valhall field is a double plunging NNW-SSE trending anticline, from (Barkved et al. 2003).*

until the effluent was visually clear. Oil-water capillary pressure curves for a single fresh state Valhall Tor formation plug are shown in Figure 4.7. Only the centrifugal parts are included, i.e. forced imbibition (B) and forced drainage (D). Another wettability study evaluates the Valhall Tor formation to be neutral to slightly oil-wet with an Amott-Harvey wettability index in the range of 0 to -0.37 (Andersen 1995). Later tests on cores from the waterflood pilot at Valhall indicated spontaneous water imbibition as high as 20%, and tests on the same core material showed a neutral to weakly water-wet system (Eltvik et al. 1990). In contrast, Hillerslev outcrop chalk is strongly water-wet, see Section 4.2.

Recently, laboratory tests were performed on Valhall Tor formation samples to obtain further information on imbibition capillary pressure characteristics, relative permeability and behavior during waterflooding (personal communication with BP Norway 2004). This was done prior to the recently initiated waterflooding of the Valhall Tor formation. The tests were split in two phases. In phase 1, waterflooding tests were performed on Valhall Tor formation M2 samples with "as received" effective oil permeabilities of approximately 3 mD. In phase 2, waterflooding tests were conducted, and imbibition capillary pressure curves and relative permeability curves were established on Valhall Tor formation M1, M2 and M3 with porosities ranging from 41.0-43.4%. The waterfloods were carried out at a low flow rate of 4 ml/hour ($1.1 \cdot 10^{-3}$cm^3/s) equivalent to a typical reservoir advance rate of 1 ft/day (30.5 cm/day) and at a high flow rate of 400 ml/hour (0.11cm^3/s).

It was found that preserved core samples at ambient conditions exhibit moderate oil-

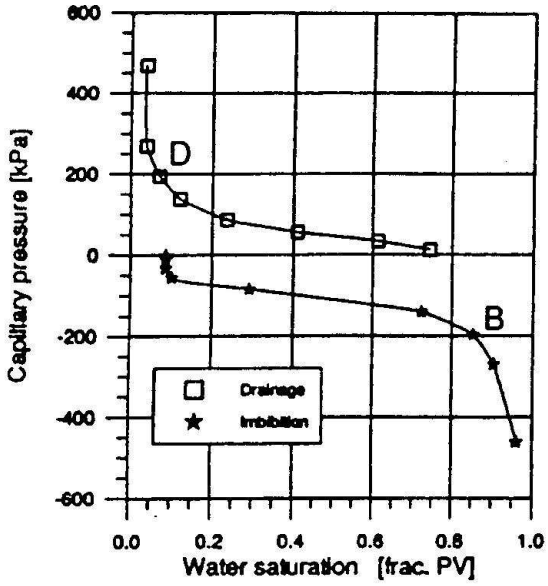

Figure 4.7 *Oil-water capillary pressure curves for a fresh state, substitution cleaned Valhall Tor formation plug, from (Springer et al. 1996).*

wet character upon waterflooding. Whereas cleaned core samples (solvent cleaned using cold toluene and methanol) at ambient conditions exhibit strongly water-wet character upon waterflooding. However, at reservoir conditions, preserved and restored characteristics were similar. The reservoir conditions comprise a temperature of 90°, a confining pressure of 40.0 MPa, pore pressures of 27.2 MPa and live crude oil. At reservoir condition waterfloods there were strong indications of water-wet behavior, but there were also indications of some oil-wet surfaces, i.e. a fractional-wettability. The low rate waterfloods were capillary dominated, whereas the high rate waterfloods were viscous dominated and drained down to a relatively low S_{or}. It was evaluated that low rate waterfloods should be used for describing fluid flow in the reservoir away from the near well bore region, and high rate waterfloods should be used to describe the near well bore behavior.

The established imbibition capillary pressure curves are shown in Figure 4.8. The initial water saturations were $< 10\%$ and the spontaneous water saturation increased to 28-33% (cross-over) for all samples tested. Remaining oil saturation at the end of the imbibition capillary pressure tests ranged from 15-16% for all the samples.

The reason for the different wettability and capillary pressure characteristics for the Valhall Tor formation is due to that wettability measured on cores taken from a reservoir may be different from the wettability of the reservoir. As discussed in Section 2.2.1, many factors can significantly alter the wettability of the specimen, for instance pressure and temperature. Further, specimens run at ambient conditions are generally found to behave more oil-wet than those at reservoir conditions (Anderson 1986*a*).

The established, interpreted relative permeability curves are shown in Figure 4.9. The initial water saturations were $< 10\%$. The breakthrough saturations ranged from 59-63%. Ultimate residual oil saturations to waterflood were 12-15%, and the end point water relative permeabilities ranged from 60-66%.

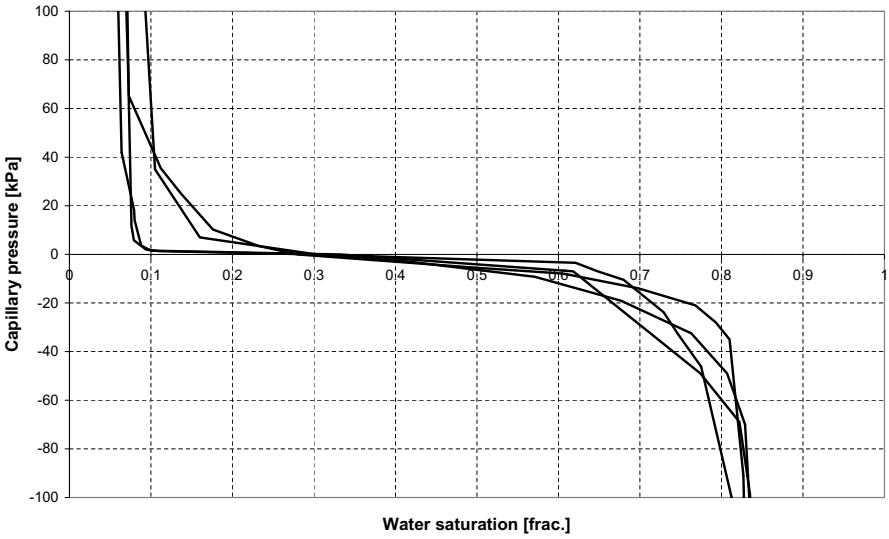

Figure 4.8 *Reservoir condition imbibition oil-water capillary pressure curves for Valhall Tor plugs (personal communication with BP Norway 2004).*

To sum up, Hillerslev outcrop chalk is regarded as a close analogue to the Valhall Tor formation, with comparable lithology, porosity, permeability and fracture sets, but different wettability. Mechanically, however, the Valhall Tor chalk is stronger than Hillerslev outcrop chalk (Havmøller & Krogsbøll 2001).

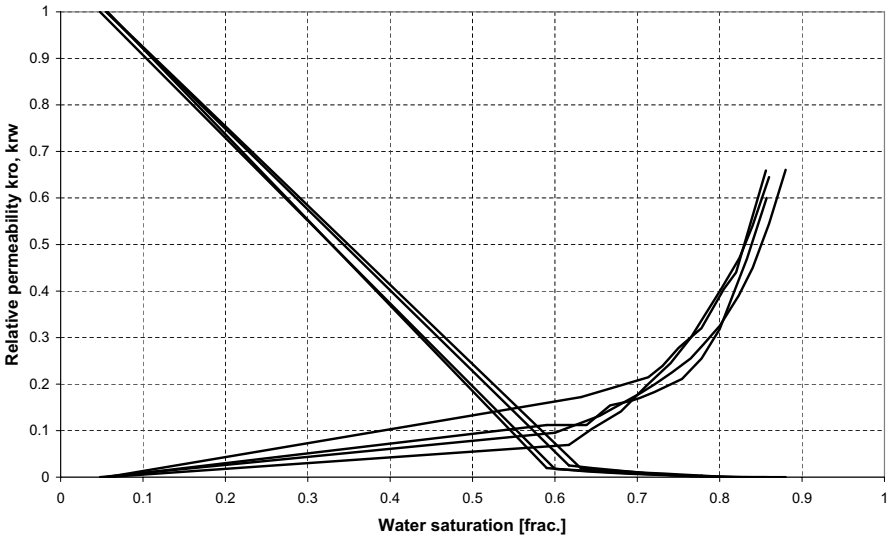

Figure 4.9 *Interpreted water/oil relative permeability curves for Valhall Tor formation plugs (personal communication with BP Norway 2004).*

Chapter 5

Hillerslev Outcrop Chalk Test Specimens

This Chapter includes a description and classification of the tested large specimens, wettability alteration tests on Hillerslev outcrop chalk pieces and the subsequent wettability alteration of two large test specimens (only one of these were used for testing). Finally, the evaluation of stress dependency on the effective, absolute oil permeability of the fractured Hillerslev outcrop chalk specimens is included.

5.1 Sampling of the Large Specimens

At the Hillerslev chalk quarry, twelve cylindrical block specimens with the dimensions $D \approx 50$ cm and $H \approx 50$ cm were sampled. A detailed description of the sampling and the fracture pattern at the location of the sampling at the Hillerslev outcrop chalk quarry is included in Report 1.

A chalk wall (approximately 4 m high and 25 m long) was excavated. A horizontal plateau (approximately 1.5 m high, 25 m long and 2 m deep) referred to as the chalk bench was made by further excavation (approximately 2 m) into the wall. The bench was made for sampling of the twelve cylindrical block specimens.

Drilling was performed using a mobile drilling rig. Water was added during drilling to cool the drill bit and flush away cuttings. Drilling was performed at a speed lower than 50 rpm using a light vertical pressure. After drilling, a metal shield was inserted into the trace left by the drill bit. A backhoe was used to perform the rough excavation around the specimen to a distance of approximately 20 cm from the metal shield and to a depth of 30-50 cm below the specimen bottom. The distance to the metal shield was maintained to avoid possible fracturing induced by the backhoe. As the chalk is highly fractured, most of the chalk surrounding the specimen was removed by hand using hammer and chisel or an electrical hammer.

After removal of the surrounding chalk, the metal shield was removed. A rubber membrane was pulled down around the specimen, and an additional rubber blanket and the metal shield were wrapped around the specimen. Two steel belts were fastened around the shield. The top surface was trimmed roughly by use of a chain saw. Then a plastic cap was placed on the top surface of the specimen. The top of the membrane was fitted

Figure 5.1 *View of the wall and the bench. The chalk is removed around most of the twelve specimens, which are wrapped in metal shields. In the front, the first sampled specimen is seen.*

around the cap, and a steel belt was fastened around the membrane.

The backhoe was used to hold onto the specimen via lifting equipment while the specimen was cut free at the bottom by use of a chain saw. The backhoe was then used to lift the specimen and turn it upside down for a rough trimming of the bottom surface by use of a chain saw. The specimens were trimmed to a height a little higher that 50 cm, since the final trimming should be performed in the laboratory. A plastic cap was then placed on the bottom surface. The bottom of the membrane was fitted around the cap, and a steel belt was fastened around the membrane.

5.2 Specimen Preparation and Description

Waterflooding tests were carried out on seven naturally fractured Hillerslev outcrop chalk specimens (specimens 2, 5, 7, 8, 9, 10 and 11). One of these specimens (specimen 11) was sampled earlier (Havmøller & Krogsbøll 1997). The other six were sampled during the Ph.D. project, as described above. It was intended to use an additional specimen 3 for testing in the centrifuge, but due to problems with liquid rubber mass, see Section 5.2.1, specimen 3 was described (Report 1), but not used for testing.

The specimens were described as light grey (chalk mudstone) with areas of a darker

Figure 5.2 *A specimen equipped with a lifting arrangement for turning the specimen upside down in the laboratory.*

grey color (clay). Spots of rust were seen on the surfaces. There were voids at the surface (material missing) on all the specimens to a higher or lesser degree. Small pieces of flint were seen in specimens 2, 7 and 8. Few fossils were found in specimen 2 and many in specimen 8.

The specimens used for testing in the centrifuge (specimens 2, 5, 7, 8 and 11) were trimmed and measured. The trimming of these large specimens were time consuming, as it was done by hand using a chisel and a steel ruler. Further, the specimens had to be trimmed at both ends, i.e these heavy specimens had to be turned upside down. The turning was performed using a crane, with the specimens equipped with a lifting arrangement, see Figure 5.2. During the trimming period, the specimens were covered with plastic overnight to reduce the drying, since this made the trimming more difficult. After trimming, the specimens were dried at 105° C in an oven. The specimens were weighed on an almost daily basis until the weight was constant. The specimens were moved in and out of the oven and placed on a balance using a pallet truck. The drying took 9-18 days. After drying, the specimens were saturated with the laboratory oil Isopar-L to an oil saturation S_o of 97-99% before testing, see Table 5.1. Specimen 11 had been prepared similarly in an earlier project (Larsen 2000). The procedure and equipment used for the oil saturation of the specimens is included in Appendix D.

The specimens used for testing in the oedometer cell (specimens 9 and 10) were trimmed and measured by GEO. Before drying, the specimens were wrapped in soft plastic foil, and placed in the oedometer cell. Then liquid gypsum was poured into the

Figure 5.3 *Specimen 2 with the ring of gypsum (left) and the layer of sand laid out within the ring of gypsum (right). The specimen is instrumented with TDR probes.*

oedometer cell to fill the excess space between the foil-wrapped specimen and the oedometer cell. The specimens were wrapped in soft plastic foil to prevent liquid gypsum from entering the fractures. Approximately 44.3 kg liquid gypsum was poured into the excess space between the oedometer cell and specimen 9. For specimen 10 the amount of liquid gypsum used was approximately 37.6 kg. Then the specimens were dried in an oven at 95° C. The drying took a long time 22-26 days, since the specimens cast with gypsum were dried in the oedometer cell in the oven. The specimens were weighed regularly until the weight was constant. After drying, the oedometer cell was mounted in the set-up, and the specimens were oil saturated prior to testing.

In the field, gypsum was cast on top of specimen 2, and it was necessary to remove the gypsum in the middle of the specimen top to ensure a flow through the specimen. To avoid a large dead volume at the specimen top, a gypsum ring was left to contain a filter layer of Leighton-Buzzard laboratory sand, which is very coarse and thus prevents a reduction in the permeability of the specimen. An amount of 4.48 kg dry Leighton-Buzzard sand was laid out with a loose density estimated to $\rho_{sand} \approx 1500$ kg/m^3 corresponding to a layer of sand with a mean height of $H_{sand} \approx 2$ cm within the ring of gypsum with a mean width of $W_{gypsum} \approx 2.5$ cm, see Figure 5.3. As can be seen on Figure 5.3, the estimated height of the sand layer is very rough, since some areas of the specimen have a layer of sand of up to 7 cm, whereas other areas barely are covered by sand. The estimate is thus for an evenly distributed layer of sand.

In the laboratory, specimen 2 was again cast with gypsum to stabilize it before trimming. Specimen 7 was cast with gypsum after drying and specimens 9 and 10 before drying to fill voids at the periphery and stabilize the top and bottom. Specimen 11 was cast with gypsum earlier to fill voids (Larsen 2000). Approximately 1.8 kg was cast onto the periphery of specimen 2. However, it was not possible to measure the amount of gypsum in the ring left to contain the sand. The height of the gypsum ring was measured to range from $H_{gypsum} = 4$ - 7 cm, see Figure 5.3. Based on the measurements of the

gypsum ring and a measured mean dry density of the gypsum of $\rho_{gypsum} = 1.85$ g/cm^3, the amount of dry gypsum was estimated to 2.7 kg for $H_{gypsum} = 4$ cm and 4.8 kg for $H_{gypsum} = 7$ cm. The estimated amount of gypsum used on specimen 2 is thus 4.5-6.6 kg. The amount of gypsum used to prepare specimen 9 before it was placed in the oedometer cell was not weighed.

The initial parameters for the test specimens before testing are listed in Table 5.1 along with the amounts of dry gypsum used.

Specimen	D [cm]	H [cm]	M_{dry} [kg]	M_{gypsum} [kg]	BV [cm^3]	PV [cm^3]	M_{oilsat} [kg]	S_o [%]
2	49.4	49.5	124.80	4.5-6.6	87212	40990	155.95	99.6
5	48.9	48.8	128.245	-	89619	42121	159.65	97.7
7	48.9	48.8	132.38	2.0	92509	43479	164.52	96.9
8	49.1	48.8	131.06	-	91586	43045	162.86	96.8
9	49.6	45.7	no data	no data	88302	41502	no data	-
10	49.8	43.0	no data	5	83756	39365	no data	-
11	49.1	49.0	130.68	2.99	91321	42921	162.863	98.3

Table 5.1 *Initial parameters for the seven tested specimens. The weights of specimens 2, 7 and 11 include gypsum. The weights of specimen 2 is without the sand.*

The diameter D [cm], height H [cm], dry weight M_{dry} [kg] and oil-saturated weight M_{oilsat} [kg] are measured. Prior to the drying, the height of specimen 9 was 47.0 cm, but after drying the height was reduced by 1.3 cm to 45.7 cm. The gypsum weight M_{gypsum} [kg] is based on both measurements and estimation. The bulk volume BV [cm^3] is calculated as $M_{dry}/(\rho_s \cdot 10^{-3})/(1-\phi)$, where the grain density is $\rho_s = 2.70$ g/cm^3. An average matrix porosity of $\phi = 47\%$ is assumed for the test specimens, see Section 4.1. The bulk volume is not based on the diameter and height of the centrifuge specimens since these parameters are uncertain. However, it was necessary to determine the bulk volume based on diameter and height for specimens 9 and 10, since the weights for these specimens were not available. The pore volume PV [cm^3] is calculated as $\phi \cdot BV$. The oil saturation S_o [%] is based on the oil uptake, i.e. $(M_{oilsat} - M_{dry}) \cdot 1000/\rho_o/PV \cdot 100$. As specimens 9 and 10 were not weighed after oil saturation, it was not possible to determine the initial oil or air saturation in the specimens before testing.

The dry density is calculated as M_{dry}/BV to $\rho_{dry} = 1.431$ g/cm^3 and the void ratio is calculated as $\rho_s/\rho_{dry} - 1$ to $e = 0.887$ for all the centrifuge specimens.

The gypsum affect the saturation, the permeability and the flow pattern of the specimens. To quantify the effect of the gypsum on the specimens, an estimation was made of the ratio between the part of the cross-sectional area containing gypsum if the amount of gypsum was evenly distributed on the specimen periphery and the cross-sectional area of the specimen, i.e. $A_{gypsum}/A_{specimen}$. This results in a ratio of 3.6% (for 6.6 kg gypsum), 1.2% and 1.6% for specimens 2, 7 and 11, respectively. As the estimated ratios are small, the gypsum will not have a significant effect on neither the saturation, the permeability nor the flow pattern of the specimens. Only a small amount of gypsum was cast on the top and bottom to stabilize specimens 9 and 10. However, the large amount of gypsum used for specimens 9 and 10 results in a ratio of at least 6.5% and 7.2% for specimens 9

and 10, respectively, since the inner diameter of the oedometer cell is 51.5 cm compared to the diameters of the specimens, see Table 5.1 (no density of the liquid gypsum was available). The gypsum may have an effect on the saturation, the permeability or the flow pattern of the specimens.

The sand layer will in fact reduce the actual height of specimen 2. Using the mean height of 2 cm corresponding to an evenly distributed layer of sand, the height will be reduced to $H = 47.5$ cm. This will have an effect on the permeability calculation, see Section 5.3.1.

5.2.1 Wettability Alteration

The wettability of two large test specimens were altered towards less water-wet in order to be able to perform waterflooding on a specimen as close an analogue to the Valhall Tor formation as possible. At the time of the wettability alteration, the wettability of the Valhall Tor formation was believed to be neutral to slightly oil-wet or neutral to slightly water-wet, see Section 4.4.

Earlier it was found that the wettability of the strongly water-wet Hillerslev chalk can be altered towards a less water-wet state using crude oil added Dodekane acid, see Section 4.2. This was found as the wettability of a single small Hillerslev outcrop chalk specimen ($D = 38$ mm, $H = 50$ mm) was altered to a homogeneous neutral to slightly oil-wet state using crude oil from the Snorre field added 1 weight% Dodekane acid ($C_{11}H_{23}COOH$), see Section 4.2. The wettability alteration by adding Dodekane acid was based on personal communication with Professor Tor Austad, Stavanger College, Norway. However, the wettability alteration of the small specimen affected the chalk, making it more brittle and the periphery of the specimen slightly uneven.

Consequently, additional wettability alteration tests were performed on small pieces of Hillerslev outcrop chalk by adding 0.1 weight%, 0.5 weight% or 1.0 weight% Dodekane acid to the Isopar-L, then saturate the chalk pieces with this mixture and leave them in the mixture at 20° C, 40° C or 90° C for 1 week, 20 days or as long as 1 month.

The tests revealed no major wettability alteration effect of adding 0.1 weight% neither for aging at 20° C nor 40° C for 1 week. In contrast, adding 0.1 weight% for aging at 20° C for a period of 1 month resulted in almost no spontaneous imbibition of water, i.e. the chalk was altered towards less water-wet. The increase in aging period seemed to increase the wettability alteration effect. Similarly, adding 1.0 weight% for aging at 20° C or 40° C for 1 month resulted in no spontaneous imbibition. The temperature increase seemed to reduce the wettability alteration effect. Adding 0.5 weight% for aging at 90° C for 20 days resulted in only a small spontaneous imbibition of water.

The wettability alteration tests on the small chalk pieces did not seem to affect the chalk. The effect on the chalk for the single small chalk specimen is thus assumed to be related to the use of crude oil added with Dodekane acid, since the laboratory oil Isopar-L was used in the wettability alteration tests on the small chalk pieces.

Based on this, and the fact that it was not possible to alter the large specimens at temperatures higher than room temperature at the premises, the wettability of test specimen 3 was altered by adding 0.5 weight% Dodekane acid to the Isopar-L, then saturate the specimen with this mixture and leave it in the mixture for aging at room tempera-

Figure 5.4 *Photograph of the fractional-wet specimen 2 after test with drops of water on the oil-wet surfaces.*

ture. For various reasons, the specimen was left for aging in 8 months. Due to that liquid rubber mass entered the fractures during mounting of the specimen in the centrifuge test set-up (Section 6.2), specimen 3 was not used for testing. Consequently, the wettability of test specimen 2 was altered towards oil-wet to a fractional-wet state following the same procedure. However, the specimen was only left for aging in 1 week.

An effect of the wettability alteration procedure on the chalk was in fact seen in specimen 3 as it resulted in the chalk becoming brittle, and the gypsum becoming "toothpaste-like". However, since this was not observed in the tests on the small chalk pieces, the effect is assumed to be due to the long period of aging. Due to the relatively few large specimens available for testing, it was intended to use specimen 3 for testing in spite the effect on the chalk. The assumption that the long period of aging affected the chalk seem valid, since fortunately, the wettability alteration was not observed to affect the chalk in specimen 2.

A photograph of the wettability-altered specimen 2 after waterflooding is shown in Figure 5.4. Light areas looking wet and darker areas looking less wet were seen. Drops of water were observed on the darker areas whereas water spontaneously imbibed into the light areas implying a fractional-wet state of specimen 2. However, this is only based on inspection, since no tests were carried out to determine the wettability. The non-homogeneous wet state of specimen 2 is considered to be due to that it was not possible to flush the specimen with the Isopar-L added 0.5 weight% Dodekane acid, but only to

saturate and leave it for aging in the mixture.

The wettability alteration of specimen 2 made this specimen a closer analogue to the Valhall Tor formation since recently performed laboratory tests revealed that at reservoir condition waterfloods, there were strong indications of water-wet behavior, but there were also indications of some oil-wet surfaces, i.e. a fractional-wettability, see Section 4.4.

5.3 Fracture Description

A (local) fracture description was carried out the on the seven Hillerslev chalk specimens 2, 3, 5, 7, 8, 9 and 10. The fractures, voids at the surface, crushed zones and gypsum were indicated on pieces of plastic matching the top, bottom and periphery of the specimens. The fracture description of specimen 11 was performed earlier (Larsen 2000). Photographs of this are included in Report 1. Due to problems with the liquid rubber mass, specimen 3 was not used for testing, and is omitted in the following. Sketches of the specimens used for testing with fractures, crushed zones and gypsum indicated on the top, bottom and periphery are included in Appendix E.

All the specimens were fractured to a higher or lesser degree. It was observed that some fractures opened after the specimens were unwrapped and exposed to air (drying), and due to specimen handling. Specimen 5 contained so-called crushed zones where the chalk was brittle, and almost plastified (reworked). In these zones, it was difficult to see fractures. Zones with brittle chalk as seen in specimens 2 and 5 were also seen along all the horizontal profiles at the Hillerslev quarry.

In four of the specimens, horizontal fracture planes were present, two continuing ones in specimen 8, see Figure 5.6, a continuing one in specimen 5, two in specimen 7 and one in specimen 9. This is in accordance with the global fracture observations in the Hillerslev chalk quarry.

The fracture density in the specimens are similar to the observations in the Hillerslev chalk quarry indicating almost random spacing of fractures. The most dominant fractures in the periphery of the specimens were very steeply dipping and seemed almost vertical. This is consistent with the overall picture from the global fracture description concluding that the majority of fractures are steeply dipping with a dominance of almost vertical fractures.

Based on the extensive fracture description in the Hillerslev outcrop chalk quarry, see Section 4.3, and the fracture description of the specimens used for testing, it was concluded that overall, the local and the global fracture descriptions were in accordance, i.e. the fracture system in the specimens represents the major part of the Hillerslev outcrop chalk fracture pattern. Further, since the Hillerslev outcrop chalk is regarded as a close analogue to the Valhall Tor formation, with comparable lithology, porosity, permeability and fracture sets, the specimens represent Valhall Tor chalk flow properties, except for wettability.

It was considered to perform CT-scanning of the specimens to obtain a better description of the fractures inside the specimens. However, it was not evaluated possible for such large specimens.

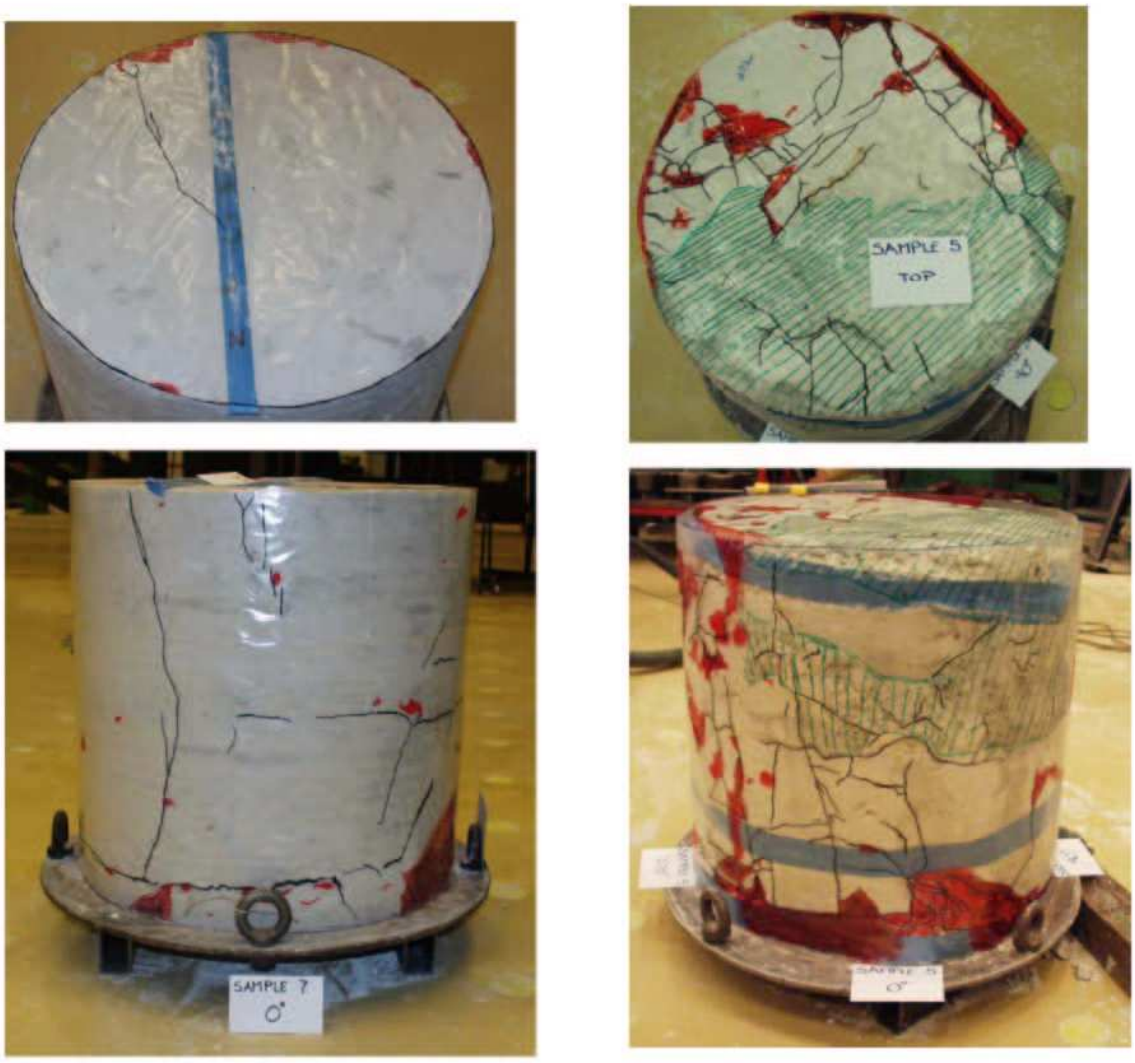

Figure 5.5 *Indication of fractures (black), voids at the surface (red) and "crushed zones" (green) for specimen 7 (left) and specimen 5 (right).*

5.3.1 Permeability

The mean absolute matrix permeability for Hillerslev outcrop chalk was measured to $K = 2.8$ mD, ranging from 2.6-2.9 mD using synthetic Valhall formation water (Report 2). This permeability is in the range of the matrix permeability measured to around 4 mD in the highly permeable crestal area of the Valhall Tor formation, where a waterflood pilot was carried out from 1990 to 1993, see Section 9.1.

Absolute oil permeability tests were performed in the centrifuge and the oedometer cell to study the effect of fractures and stress level on permeability for Hillerslev chalk. Further, permeability data was extracted and calculated from earlier work on water-saturated Hillerslev chalk (Havmøller & Krogsbøll 2001). These data are compared with the data from this Ph.D. project.

Figure 5.6 *Photograph of the lower of the two horizontal fracture planes in specimen 8 after test.*

Centrifuge

The permeability measurements on specimens 7 and 11 were conducted in the old test set-up, and the tests on specimens 2, 5 and 8 in the new test set-up, see Figure 5.7. Both set-ups are sketched in Appendix F, and described in detail in Section 6.2.

The inlet container was used for oil flushing, and the outlet container was used for produced oil. The production to the outlet container flowed through an overflow tube. Five pore pressure transducers (PPTs) were included in both test set-ups, see Figure 5.7. To avoid flow along the side between the membrane and the specimen, liquid rubber mass was cast around the specimen between the specimen and the membrane, and a confining pressure was applied on the membrane through a water-filled tube on the form. An automated magnet valve was included at the bottom to control start and end of flow of oil through the specimens.

The specimens were flushed with oil to remove air entrapped during specimen handling after oil-saturation and fill the dead volumes with oil. Further, entrapped air was evacuated in the specimens using a vacuum pump connected to a receiving bottle, which was connected to the overflow tube in the outlet container.

Initially, 1 g permeability measurements were performed in the set-ups. Then the set-ups were mounted in the centrifuge, and permeability measurements were performed during centrifuging.

The absolute oil permeability at $N = 1$ g was determined by flowing oil from the inlet container to the specimen bottom, up through the specimen, through a tube connected to the overflow tube in the outlet container, and finally to a container placed on a balance. The calculation of the permeabilities are carried out using equation (2.6) based on the

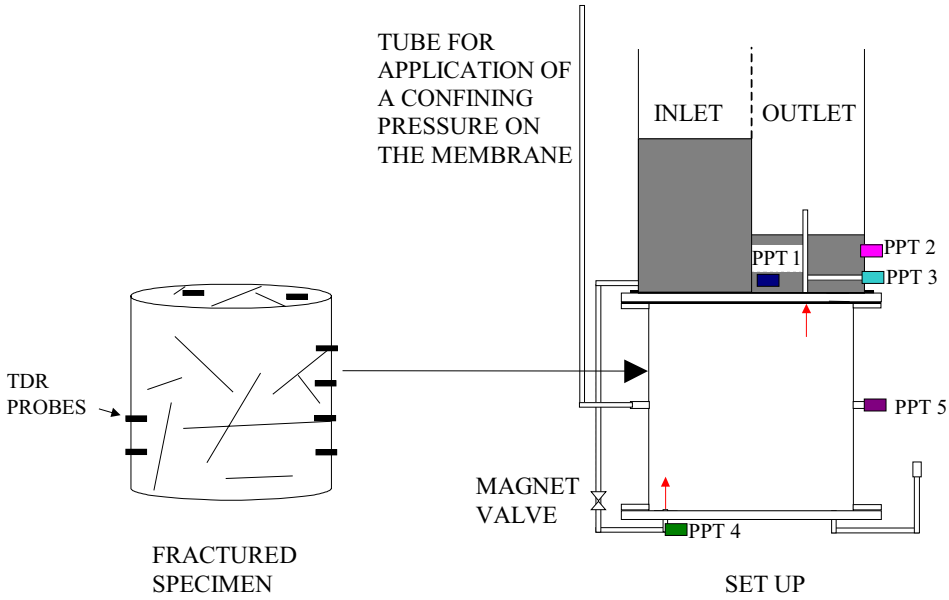

Figure 5.7 *Specimen to be mounted in the new test set-up.*

measurements of the oil outflow on the balance over time, and the initial fluid level difference, which was relatively constant during testing. The mean permeabilities are included in Table 5.2 along with the standard deviations (in parentheses).

Then, the centrifuge was rotated resulting in application of $N = 10$, 20, 40 and 80 times the gravitational acceleration at the specimen bottom corresponding to a centrifuge speed of 59.1 RPM, 83.6 RPM, 118.2 RPM and 167.1 RPM, respectively. When the centrifuge had reached the desired speed, the magnet valve was opened, and flow initiated. Testing of the specimens was intended done applying a constant hydraulic pressure difference by use of the Mariotte principle in the inlet container and the overflow tube in the outlet container. A tube was placed in the inlet container in order for it to act as a Mariotte bottle, where a pressure of 1 atm. is maintained at the lower end of the tube in the inlet container by air being pulled into the tube due to fluid volume being expelled.

Initially, the test on specimen 11 was performed applying a constant hydraulic pressure difference, but it was seen that the pore pressures measured by the PPT in the inlet container was decreasing instead of being constant, i.e. the Mariotte principle did not function. Since the PPT measurements were not following the fluid level in the inlet container either, the tube was removed from the inlet container, and new permeability tests were conducted applying a falling hydraulic pressure difference resulting from the difference in inlet and outlet (overflow tube) oil levels at $N = 10$, 20, 40 and 80.

The test on specimen 7 was run utilizing the Mariotte principle. The test also showed that the Mariotte principle was not working. It was decided to perform the oil permeability measurements on the remaining specimens applying a falling hydraulic pressure difference.

The centrifuge oil permeabilities are determined using equation (2.6) based on the inflow and outflow pressures measured by the PPTs, and the produced volumes of oil

obtained from the calculated fluid height based on the PPT measurements in the outlet container during testing.

As the gravitational acceleration g varies along the set-up during centrifuging, the fluid height H [m] corresponding to the fluid level above the PPT (measured by the PPT) is calculated as:

$$H = R \pm \sqrt{R^2 - \frac{P}{\rho \cdot \omega^2}} \tag{5.1}$$

where P [Pa] is the fluid pressure measured by the PPT, R [m] is the distance from the centrifuge axis to the PPT, ρ [kg/m^3] is the fluid density and ω [sec.$^{-1}$] is the angular velocity. At accelerations below 10 g the calculated fluid heights may be extreme as the hinged arm is not perpendicular to the axis, i.e. the centrifuge container is not horizontal, see Section 2.5.

The fluid height corresponding to the filled overflow tube is calculated to check the pore pressure measurements. Similarly, the fluid height above the bottom PPT (inlet pressure) is calculated. The calculated fluid heights based on the PPT measurements and equation (5.1) was compared to the corresponding fluid heights measured by use of a measuring tape in the inlet and outlet containers at the start and end of the permeability tests, and the measured height of the overflow tube. This comparison revealed that the calculated and measured heights in some cases differed up to 6 cm. The PPTs were clearly not precise enough. However, since the relative PPT measurements during testing seem reliable, it was chosen to use the PPT measurements corrected according to the measured heights at the start of the permeability tests, and a reasonable match with the measured heights at the end of the tests was obtained.

For specimen 7, the PPT measurements for 10, 20 and 40 g were following the fluid level in the inlet container, and it was evaluated that even though the Mariotte principle was not working, the measurements for these centrifuge steps could be used. However, at 80 g the bottom PPT measurements did not match the measured fluid heights. This could not be corrected properly. As a consequence, the permeability measurement for specimen 7 at 80 g is not included.

For specimen 5, a large difference was observed between the measured and the calculated fluid heights based on the bottom PPT. The calculated height increased due to opening of the magnet valve, but not as high as corresponding to the fluid height in the inlet container. In fact, it was found that the bottom PPT was following the trend of the overflow tube, i.e. when the overflow tube was overflown at 20 and 40 g, the same increase in pressure seen on the PPT in the overflow tube was observed on the bottom PPT. The odd measurements may be due to some kind of blocking of the magnet valve. It was attempted to correct the bottom PPT measurements, but this could not be done properly. Consequently, the permeability measurements for specimen 5 are not included.

The permeability is determined assuming a constant hydraulic pressure difference at each PPT measuring step occurring every 10 sec. during centrifuging. Based on these values, the mean absolute permeabilities K [mD] are determined at each centrifuge step, and included in Table 5.2. The values in parentheses are the standard deviation from the mean permeabilities.

Permeability determinations based on an equation for falling hydraulic pressure difference at each PPT measuring step could not be used as the results were too scattered. The method and the results are thus not included. However, for PPT measurements every 10 sec., the hydraulic pressure difference is close to constant, and it is evaluated that the permeability can be calculated using equation (2.6). Further, the mean value of Reynold's number for flow of oil in the fractures is estimated to $Re \leq 0.1$ for each centrifuge step corresponding to the permeability calculations, see Section 2.5. Based on the estimation of Reynold's number, the flow in these tests is evaluated to be laminar.

Fracturing	Specimen	Permeability (st.dev.(permeability)) [mD]				
		1 g	10 g	20 g	40 g	80 g
1	2	206 (-)	340 (197)	364 (88)	325 (70)	235 (21)
2	5	249 (83)	-	-	-	-
3	8	227 (18)	301 (189)	299 (118)	359 (36)	344 (21)
4	11	31* (2)	18 (41)	18 (20)	18 (14)	19 (6)
5	7	8 (3)	7 (31)	6 (9)	7 (4)	-

Table 5.2 *The absolute oil permeabilities at N = 1, 10, 20, 40 and 80. The * indicates possible side flow. The specimens are listed after degree of fracturing based on inspection with the most fractured specimen first.*

The layer of sand is included in the permeability calculation for specimen 2, see Table 5.2. If this sand layer is assumed to have an infinite permeability, the permeability of the specimen should be calculated based on the reduced height of specimen 2, i.e. $H = 47.5$ cm, see Section 5.2. The permeability for a reduced height of specimen 2 is included in Table 5.3. These permeabilities are used to describe the specimen in the following.

Permeability (st.dev.(permeability)) [mD]				
1 g	10 g	20 g	40 g	80 g
198 (-)	326 (189)	349 (84)	312 (67)	226 (21)

Table 5.3 *The absolute oil permeabilities at N = 1, 10, 20, 40 and 80 for specimen 2 with reduced height.*

It was not possible to check if there was side flow during testing at 1 g, since the data needed for the calculation was incomplete. However, for specimen 11, the 1 g permeability implies side flow. This is probably the case, since liquid rubber mass was not poured into the excess space between the specimen and the rubber membrane for the 1 g test, see Section 6.2. Membrane leakage occurred at the end of the 1 g test, and a new membrane was applied and liquid rubber mass was poured into the excess space between the specimen and the membrane before the tests in the centrifuge.

Due to that the PPT measurements were not very precise, the measurements cannot be used to check the confining pressure during testing. Instead the confining pressure and the pore pressure in the specimens are calculated based on the measured fluid heights, and compared. The comparison showed that the confining pressure on the specimens was higher than the pore pressures in the specimens, i.e. no indications of side flow.

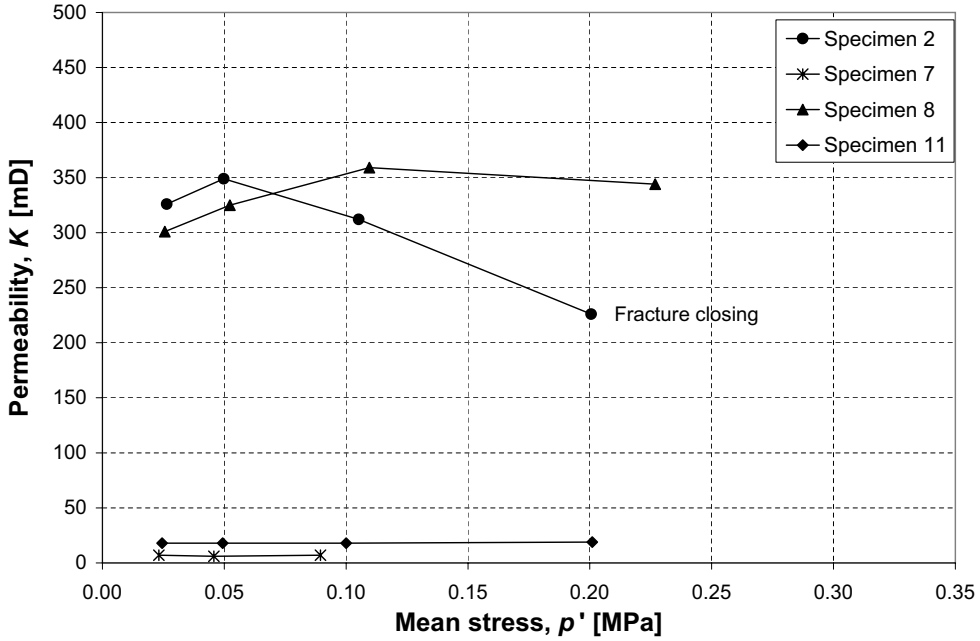

Figure 5.8 *Absolute permeability vs. effective mean stress p' for the tests in the centrifuge at N = 10, 20, 40 and 80.*

The permeability at 1 g cannot be directly compared to the centrifuge permeabilities as the mean stress levels at 1 g are evaluated to be higher than at 10 g (at least) due to high confining pressures at 1 g. However, due to incomplete data, the mean stress levels at 1 g cannot be calculated.

For the permeability test at 1 g on specimen 2, leakage occurred in the overflow container, i.e. not all the fluid reached the container on the balance. It was not possible to correct properly for this leakage, and instead the permeability was based on estimates for flow of oil overnight through the specimen after mounting in the centrifuge.

It was found that not all the air had been evacuated from specimens 2 and 8, i.e. a larger volume of oil was injected than produced. This means that the permeabilities at 1, 10 and 20 g are too low, whereas no difference in inflow and outflow was observed for 40 and 80 g.

The relatively high standard deviations are due to the limited flow in the short measuring periods of 10 seconds. The standard deviations are seen to decrease as a function of increasing g. This is probably due to the higher flow at higher g, where the PPT measurements were more accurate.

A significant influence of fractures on permeability was seen. The absolute oil permeability tests showed that the presence of fractures increased the matrix permeability with a factor of up to 100-130.

The centrifuge permeabilities are plotted vs. effective mean stress in Figure 5.8. The specimens clearly fell into two groups, the two most fractured specimens 2 and 8 with high permeabilities in the range of 250-350 mD, and the two least fractured specimens 7 and 11 with low permeabilities in the range of 5-20 mD.

The absolute oil permeability tests were performed at low effective mean stress levels

($p' \leq 0.25$ MPa) as the specimens were not subjected to any vertical stress other than the self-weight in the gravitational field.

The permeability of specimen 2 is decreasing for increasing mean stress levels at 40 and 80 g. It is evaluated that this trend would have been followed from even higher values at 10 and 20 g, if air had not been present in the specimen. Closing of some of the fractures may explain the permeability reduction. However, after the fracture closure, the permeabilities were still very high, which is probably due to the low mean stress levels.

The permeability of specimen 8 is slightly increasing for increasing mean stress levels at 10, 20 and 40 g, but from 40 to 80 g, a small decrease in permeability is seen for increasing mean stress. It is evaluated that the permeabilities at 10 and 20 g would have been higher, if no air was present, i.e. the permeability would either have been approximately constant or decreasing from even higher values at 10 and 20 g.

The permeability of the two least fractured specimens 7 and 11 was approximately constant with increasing mean stress.

Both constant permeability and permeability reduction was observed with increasing mean stress. The high permeability specimen 2 shows a distinct dependency on mean stress. The difference in stress dependency between the low and high permeability specimens is believed to be mainly due to the degree of fracturing.

The different scenarios between the two high permeability specimens are believed to be mainly due to different fracture patterns. Besides being the most fractured specimen, specimen 2 contained zones of brittle chalk. Figure 5.9 shows an "intense" interconnected fracture pattern for specimen 2. Specimen 8 contained a much "cleaner" fracture pattern than specimen 2, see Figure 5.10. Further, due to the fracture orientation in specimen 2, the fractures there must have been easier to close than in specimen 8.

It is concluded that the permeability stress dependency is mainly characterized by the fracture pattern and not just the degree of fracturing.

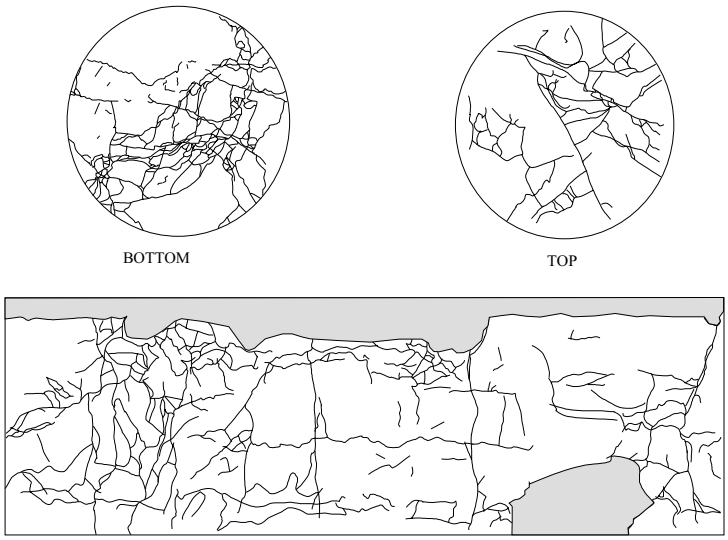

Figure 5.9 *Fractures (black lines) and gypsum (grey area) are indicated on the top, bottom and periphery of specimen 2.*

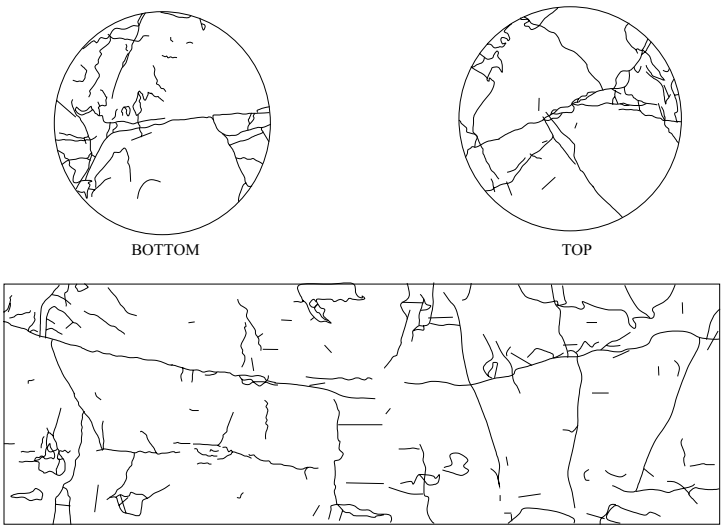

Figure 5.10 *Fractures (black lines) are indicated on the top, bottom and periphery of specimen 8.*

Oedometer Cell

Absolute oil permeability tests were carried out in the oedometer cell on specimens 9 and 10. The specimens were mounted in the test set-up sketched in Figure 5.11 and shown in a photo in Figure 8.2. The test set-up is described in detail in Section 8.1.

During testing, axial stress was applied to the specimens by a load piston. An inlet container was used for oil flushing and an outlet container was used for produced oil. The inlet container was placed on a balance (weight U1) and the outlet container was placed on another balance (weight U2). The injected and produced oil was measured during testing. The test set-up included two pore pressure transducers (PPTs), Ubot and Utop. Ubot was used to measure the inlet pressure and Utop was used to measure the outlet pressure during testing.

Initially, the dry specimens were flushed with oil to saturate the specimens and fill the dead volumes with oil. The oil was flushed from the inlet container to the specimen bottom, up through the specimen, and to the outlet container. Prior to the permeability measurements, air entrapped in the specimens was evacuated using a vacuum pump, see Figure 5.11.

To avoid flow along the side between the oedometer cell and the specimen, gypsum was cast around the specimen, between the specimen and the oedometer cell.

The loading procedure is plotted as axial stress vs. time of testing for specimen 9 in Figure H.1 and for specimen 10 in Figure H.2, Appendix H. Specimen 9 was flushed with oil during uploading, with constant stress levels only at 0.5 MPa and 4.7 MPa. For specimen 10, the stress level was kept constant at 0.25 MPa, 0.5 MPa, 1 MPa, 2 MPa, 3 MPa and 4.7 MPa where oil was flushed through the specimen. The oil permeability measurements were performed applying a falling hydraulic pressure difference resulting from the difference in oil levels in the inlet and outlet containers.

The calculation of the absolute oil permeabilities is carried out using equation (2.6) based on measurements of the oil inflow on the balance (weight U1) and the inflow and

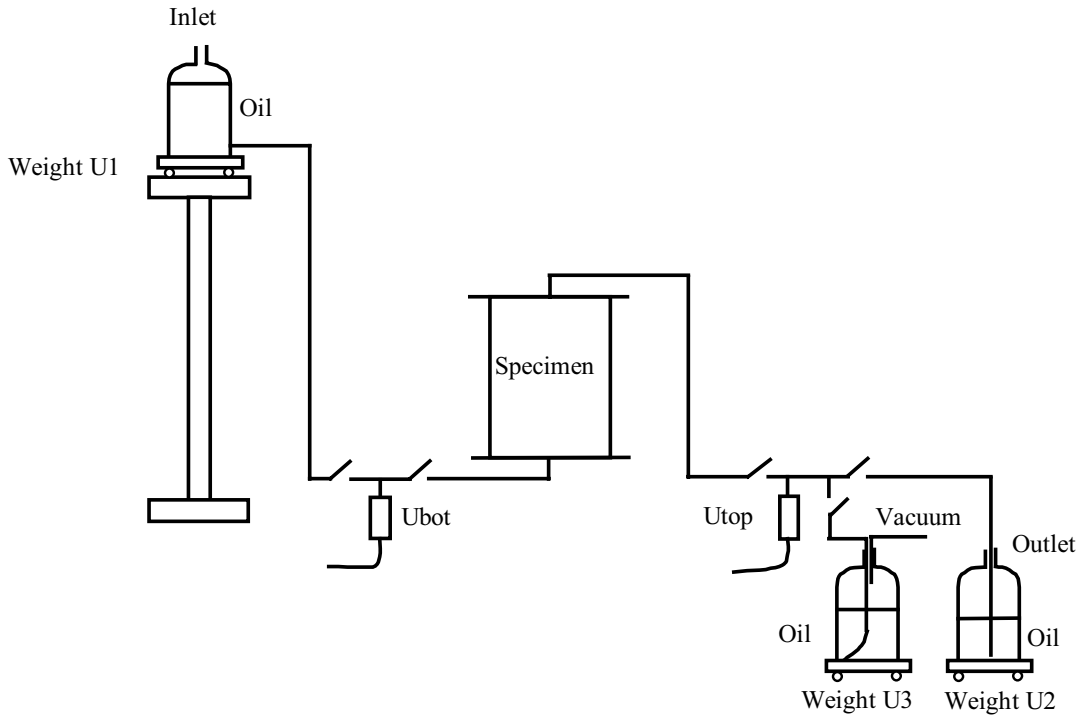

Figure 5.11 *Sketch of the set-up for oil permeability tests.*

outflow pressures measured by the pore pressure transducers Ubot and Utop, respectively. The permeability is determined assuming a constant hydraulic pressure at each measuring step as the oil level difference in the inlet and outlet containers were small at each measuring step.

The mean values of Reynold's number for flow of oil in the fractures is estimated to $Re \leq 0.06$ for each measuring step. Reynold's number is estimated as described in Section 2.5 for the centrifuge permeabilities. Based on the estimation of Reynold's number, the flow in these tests is evaluated to be laminar.

The mean permeabilities are included in Table 5.4 along with the standard deviations (in parentheses).

Fracturing	Specimen	Permeability (st.dev.(permeability)) [mD]				
		0.25 MPa	0.5 MPa	3 MPa	3.9 MPa	4.7 MPa
1	9	-	45 (2)	-	33 (1)	2 (0.4)
2	10	6 (1)	5 (1)	5 (0.5)	-	5 (1)

Table 5.4 *The absolute oil permeabilities vs. axial stress for specimens 9 and 10.*

The standard deviations from the mean values of the permeabilities are low. The uncertainty in the permeabilities are mainly due to the uncertainty in the flow calculation,

which is based on the measurement on weight U1. The weight has a precision of ± 12 g.

It was only possible to obtain permeabilities for an axial stress of 0.5 MPa, 3.9 MPa and 4.7 MPa for specimen 9 due to the test procedure with oil flushing during uploading. For specimen 10, it was possible to obtain more permeabilities as the axial stress was kept constant during oil flushing at more stress levels. However, it was not possible to obtain a representative permeability at 1 MPa and 2 MPa. At 1 MPa, the hydraulic pressure difference was too low to obtain a precise enough flow for the permeability calculation. At 2 MPa, the time period for keeping the stress level constant was too short in order for the permeability to stabilize.

The oedometer permeabilities are plotted vs. effective mean stress in Figure 5.12. Since the stresses in the lateral direction are unknown in an oedometer test, the mean effective stress p' and the deviatoric stress q is found assuming that the chalk specimen is at rest, i.e. that the following is valid:

$$\sigma_3' = K_0 \cdot \sigma_1' \tag{5.2}$$

where K_0 is the earth pressure at rest defined in equation (2.30).

Expressions for p' and q are then obtained by inserting equation (5.2) into equations (2.35) and (2.36). The mean effective stress p' is found as:

$$p' = \frac{1}{3} \cdot \sigma_1' \cdot (1 + 2K_0) \tag{5.3}$$

The deviatoric stress q is found as:

$$q = \sigma_1 \cdot (1 - K_0) \tag{5.4}$$

It is not possible to determine K_0 in the oedometer test since only axial stress is applied. However, Havmøller and Krogsbøll (Havmøller & Krogsbøll 2001) evaluated K_0 based on triaxial tests on large ($D \approx 50$ cm, $H \approx 50$ cm), naturally fractured, water-saturated Hillerslev chalk specimens. They found a mean value of K_0 at the highest axial stress levels in these tests (σ_1 = 3.5-4 MPa) to $K_{0,max} = 0.28$ with a standard deviation of 0.024, which is used generally in this evaluation.

The most fractured specimen 9 had a relatively high permeability in the range of 35-45 mD, whereas the lesser fractured specimen 10 had a low permeability around 5 mD. The permeability for specimen 9 was decreasing for increasing mean stress. Closing of some of the fractures may explain the permeability reduction. Closing of fractures along with apparatus effects and rearrangement of chalk lumps is seen as an axial strain upon loading during testing, see Figure 8.3.

The permeability for specimen 10 was approximately constant for increasing mean stress. However, closing of fractures along with apparatus effects and rearrangement of chalk lumps is also seen as an axial strain upon loading during testing, see Figure 8.6. So even though the degree of fracturing based on inspection is almost similar for specimens 9 and 10, and a higher axial strain is seen in specimen 10 than 9 upon loading to the same axial stress level, the closing of fractures in specimen 10 does not contribute to a permeability reduction as seen specimen 9.

Specimen 10 was similar to specimen 7. Both specimens contained few fractures, and had a single, almost vertical fracture continuing from the bottom to the top. Both

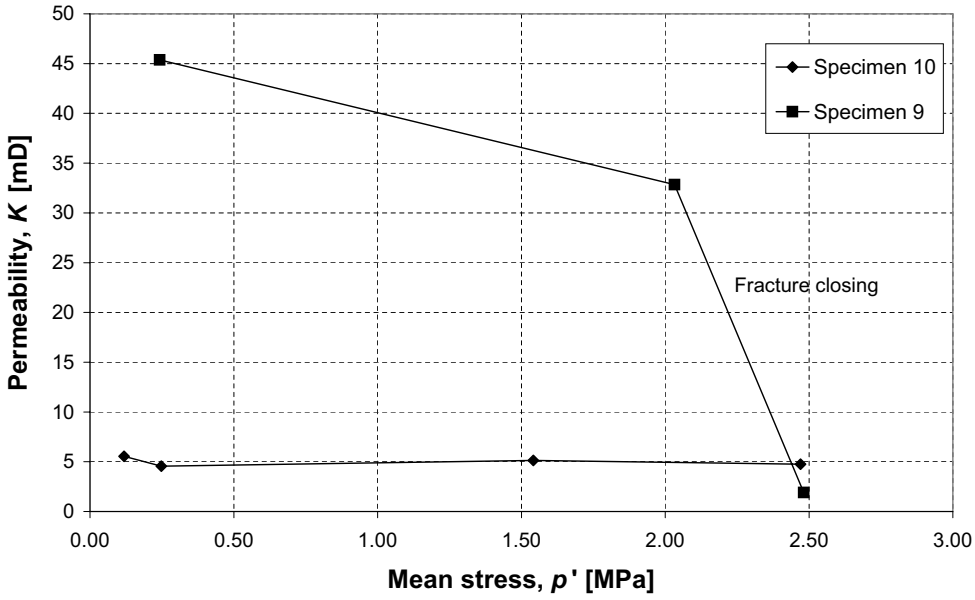

Figure 5.12 *Absolute permeability vs. effective mean stress p' for the tests in the oedometer cell.*

specimens had a constant permeability with increasing mean stress of 5 mD for specimen 10 and 8 mD for specimen 7. The constant permeability was seen at high mean stress levels for specimen 10, and it is evaluated that this would also have been the case for specimen 7 at higher mean stress levels.

Both constant permeability and permeability reduction was observed with increasing mean stress. The relatively high permeability specimen 9 showed a distinct dependency on mean stress. The difference in stress dependency between the two specimens is believed to be mainly due to different fracture patterns.

Extracted Permeability Data

Permeability data was extracted from earlier multiple triaxial tests on large ($D \approx 50$ cm, $H \approx 50$ cm) fractured, water-saturated Hillerslev chalk specimens at high effective mean stress levels, $p' \leq 1.4$ MPa (Havmøller & Krogsbøll 2001), see Figure 5.13.

These block specimens clearly fell into two similar permeability groups as the centrifuge and the oedometer tests. The low permeabilities remained constant for increase in mean stress level, even to high mean stress levels. The high permeabilities were decreasing to similar values as the low permeabilities as the effective mean stress level increased. Increasing mean stress caused the permeability reduction for the high permeability block specimens as fracture closure occurred. These tests showed large initial permeabilities, reflecting that the fractures that opened during sampling and laboratory handling were not closed at the low initial stresses. The initial permeability drop at constant stress for two of the block specimens may be explained by specimen disturbance from sampling and handling.

The centrifuge permeability data and the oedometer permeability data are included in Figure 5.13.

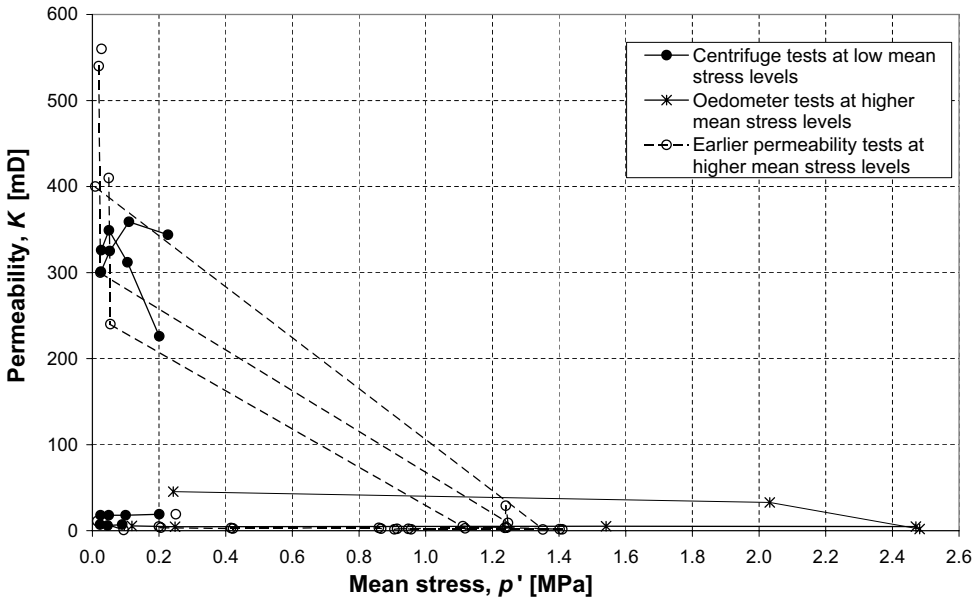

Figure 5.13 *Absolute permeability vs. effective mean stress level for the earlier permeability tests (Havmøller & Krogsbøll 2001), the centrifuge tests and the oedometer tests.*

Fracture Permeability

Using the parallel plate approach (equation (2.11)) on a chalk specimen ($D = 50$ cm, $H = 50$ cm) with a single, vertical continuous fracture with a fracture aperture of $b = 0.1$ mm ($b \leq 100$ μm is representative of Hillerslev chalk, see Section 4.3.3) results in a fracture permeability of $K_f \approx 844$ D. The corresponding effective fracture permeability is $K_f^{eff} \approx 215$ mD using:

$$K_f^{eff} = K_f \frac{A_f}{A} = K_f \frac{bD}{\pi/4D^2} \tag{5.5}$$

The effective permeability for the whole chalk specimen with a matrix permeability of $K_m = 2.8$ mD is $K_{eff} \approx 218$ mD based on equation (2.10).

Reducing the fracture aperture by 10% results in a relatively high effective fracture permeability reduction of 27%, and a relatively high effective permeability reduction of 27% for the whole specimen.

Chapter 6

Centrifuge Modelling of Waterflooding Hillerslev Chalk

This Chapter includes a description of the waterflooding tests in the centrifuge. Initially, the planning and modifications of the centrifuge tests are described. Then a description of the waterflooding test set-up, procedure and results are included. The displacement processes observed during waterflooding are described, and the influence of wettability and fractures on these displacement processes are evaluated, including an evaluation of the concept of a critical rate. Finally, an interpretation of the centrifuge modelling is included.

6.1 Design of the Waterflooding Tests

The waterflooding tests in the centrifuge were coordinated with and partly financed by a Danish Energy Research Programme (EFP) project 2000. The title of this project is "Displacement and Deformation Processes in Fractured Reservoir Chalk" (Christensen 2003), and the main objective was to quantify the displacement processes in fractured reservoir chalk. The waterflooding tests in the centrifuge were part of the EFP project to provide knowledge on large-scale waterflooding, i.e. include the effect of more complex fracture systems, and up-scaling of flow in the centrifuge. The main advantage of the coordination was that two of the waterflooding tests were simulated, see Chapter 7, and that the very expensive sampling and testing of these large specimens were partly financed. However, the coordination also meant a limited time frame for conducting the tests.

During specimen handling, instrumentation, mounting and testing, different issues occurred which was solved by further development on the equipment and by improving the specimen handling as well as the test procedures. This is described in the following along with the planning of the tests.

6.1.1 Old Waterflooding Test Set-up

Initially, a test set-up (referred to as the old set-up) was developed for the waterflooding tests, see Figure 6.1. Five pore pressure transducers (PPTs) and a magnet valve were included in the set-up. Due to the limited time frame and economics, the inlet and outlet containers were manufactured at DTU from materials found at the premises. These

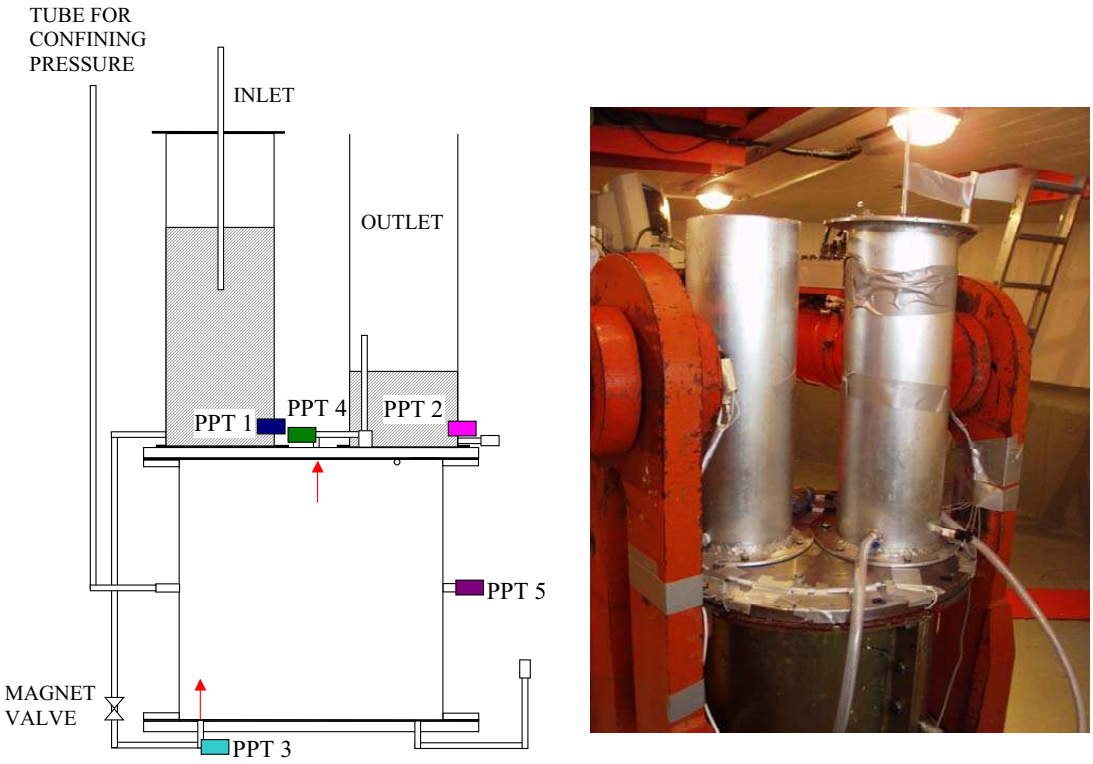

Figure 6.1 *Sketch of the old test set-up (left) and photograph of the set-up mounted in the centrifuge (right).*

containers could only contain 17.1 l each. However, the containers could not have been any higher due to the limited space between the centrifuge model container and the centrifuge arm, when the model container swings to horizontal during centrifuging. With specimen pore volumes of 41-43.5 l, these containers were not large enough to contain enough water to allow matrix displacement throughout the specimens. However, since the aim of these tests was to study the processes during waterflooding and not final recovery, it was evaluated that the containers could be used for testing. The old set-up was used for testing first on specimen 11 and then specimen 7.

To prevent flow along the side between the specimen and the membrane during testing, it was decided to apply a confining pressure on the membrane placed around the specimen.

Testing of the specimens was intended done applying a constant hydraulic pressure difference over the specimens by use of the Mariotte principle in the inlet container and an overflow tube in the outlet container, see Figure 6.1.

Specimen 11

A 1 *g* oil permeability test was run on specimen 11 in the old set-up. Unfortunately the membrane leaked, and some of the water used for application of a confining pressure on the membrane was let into the specimen. It was chosen to continue testing on specimen 11 with a small but unknown initial water saturation. It was decided to cast liquid rubber mass around the specimen between the specimen and the membrane to reduce the risk

of membrane leakage and also the risk of side flow, i.e. with the membrane not directly contacting the fairly rough specimen periphery, and reducing the excess space between the specimen and the membrane.

Oil permeability tests were performed in the centrifuge. It was seen that the pore pressures measured by the PPT located in the inlet container was decreasing, i.e. the Mariotte principle did not function. The tube was removed from the inlet container, and new oil permeability tests were conducted applying a falling hydraulic pressure difference.

The waterflooding test on specimen 11 was run. Water breakthrough occurred after injection of approximately 1.8 l (not corrected for dead volumes). After testing it was observed that a few of the fractures were filled with rubber mass. However, as this only affected few of the fractures at the specimen periphery, it was chosen to continue casting rubber around the remaining specimens. Further, the high oil permeability encountered at 1 g without rubber compared to the permeabilities found during centrifuging with rubber indicated side flow, confirming the advantage of casting rubber.

Based on the work by Olufsen (Olufsen 2002*a*), it was decided to instrument the remaining specimens with TDR probes.

Specimen 7

Initially, a very fast flow of oil was seen in the 1 g oil permeability test on specimen 7. The top pressure head was removed, and it was verified that the fast flow was due to oil travelling in the safety tubes used to protect the TDR probes. Silicone grease was injected 5 cm down the safety tubes. The exit of the tubes was covered with silicone sealant acting as a plug. The oil flushing was re-established and it was observed that the oil was now travelling through the fractures and the matrix of the specimen.

The oil permeability tests in the centrifuge was run utilizing the Mariotte principle. During the test, PPT 2 went malfunctioning, and a new PPT was ordered. Further, the lead to the magnet valve was torn during centrifuging, resulting in an emergency stop. After this was repaired, the tests were continued. The tests showed that the Mariotte principle was not working. However, the PPT measurements at 10, 20 and 40 g did not seem to be affected by this, whereas the PPT measurements at 80 g differed from the measured fluid heights. This could not be properly corrected. It was decided to test the principle in the waterflooding test.

The waterflooding test on specimen 7 was run. Since water breakthrough was not observed after injection of approximately 5 l water (not corrected for dead volumes), it was considered necessary to stop the test and add water to the inlet container and let oil out of the outlet container. Water breakthrough was observed shortly after the test was continued. It was found that the Mariotte principle did not function well at 80 g, and it was decided to run tests on the remaining specimens applying a falling hydraulic pressure difference.

Two TDR probes were installed vertically in the specimen top. After testing, a high water saturation was encountered in the top of the specimen as water from the top dead volume entered due to gravity forces and imbibition. It was evaluated that the dead volume in the top could be flowing down into the holes drilled for the TDR probes as well. Based on this, it was decided to place the TDR probes horizontally approximately

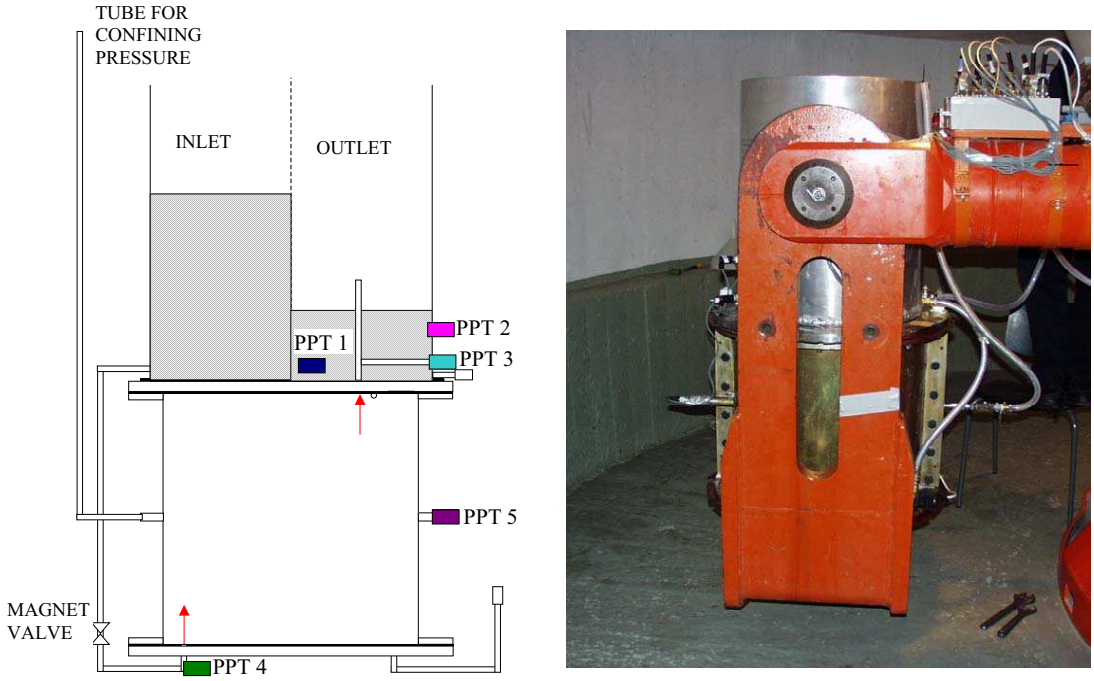

Figure 6.2 *Sketch of the new test set-up (left) and photograph of the set-up mounted in the centrifuge (right).*

0.5-1 cm into the specimen top, and cover the probes with a mix of pulverized chalk and Isopar-L. The probes placed in the chalk matrix were further covered with a piece of plastic to prevent downwards flow to the probes.

6.1.2 New Waterflooding Test Set-up

Due to the concerns with the amount of water available for testing, it was decided to develop new and larger inlet and outlet containers for the set-up. This set-up is referred to as the new set-up, see Figure 6.2. These containers could maximum contain 52 l each. The containers are actually made by separating a cylindrical container into two by a vertical plate. Again, the height of the containers are maximum possible in relation to the limited space. By mistake, PPT 3 and PPT 4 were switched around in the new set-up. However, this had no implications for the tests, as the two PPTs cover the same range. It was decided to remove PPT 1 from the inlet container, in order to have two PPTs in the outlet container. This was done to be able to check the PPT measurements at different positions. Looking back, no new information was obtained by this, and instead measurements were missing from the inlet container. The new set-up was first intended used for testing on specimen 3, and then it was used for testing on specimens 5, 8 and 2.

Specimen 3

The wettability of specimen 3 was altered towards less water-wet using Dodekane acid. During cast of rubber around the wettability altered specimen 3, rubber entered some of the fractures, and blocked the main part of the porous filter. Even though the specimen

was trimmed, dried, oil-saturated and mounted in the set-up, it was decided not to use the specimen for testing. Further, it was decided to wrap the remaining specimens in soft plastic foil before casting with liquid rubber mass to prevent liquid rubber mass from entering the fractures. Further, silicone sealant was put on the edge of the porous plate along the periphery of the foil-wrapped specimen to prevent liquid rubber mass from blocking the porous plate.

The wettability alteration of specimen 3 affected the chalk as well. Based on observations from small scale wettability alteration tests, it was evaluated that the reason for the wettability alteration to affect the chalk was the long period of aging. Since specimen 3 was not used for testing, it was decided to alter the wettability of specimen 2, however, at a shorter aging period.

Specimen 5

During the oil permeability test on specimen 5 in the centrifuge, PPT 5 went malfunctioning, and a new PPT was ordered. The centrifuge permeability tests at 10, 20 and 40 g were performed with an overflow tube of 10 cm. However, the tube was overflown during testing at 20 and 40 g. The overflow tube was replaced with one of 30.5 cm, and this was used in the test on this specimen and on the two remaining specimens.

Waterflooding on specimen 5 was run. Water breakthrough occurred after injection of approximately 7.9 l (not corrected for dead volumes). After the tests it was found that the measured inlet pressures were odd, which may be due to some kind of blocking of the magnet valve. The magnet valve was cleaned.

It was decided to carry out an initial water capillary imbibition phase prior to the actual waterflooding on the remaining two specimens. This was decided in order to let the specimens obtain an initial water saturation profile to further suppress the capillary imbibition potential in the centrifuge. It was evaluated that there was not enough water available for an initial water imbibition phase followed by high rate waterflooding. It was thus decided to mount an additional container (the inlet container from the old set-up) near the centrifuge axis to be used to fill water into the new inlet container during testing, see Figure 6.3.

Specimen 8

The test on specimen 8 was run in the new set-up utilizing the additional container. When it was evaluated that there was no significant fluid level difference during waterflooding, the capillary imbibition phase was ended, and approximately 15.3 l water from the additional container was let into the inlet container. Water breakthrough was observed at the end of the capillary imbibition phase after injection of approximately 21 l (not corrected for dead volumes).

Specimen 2

Then the wettability-altered specimen 2 was tested in the new set-up utilizing the additional container. When it was evaluated that there was no significant fluid level difference during waterflooding, the capillary imbibition phase was ended, and approximately 12.4 l

Figure 6.3 *Photograph of the additional container mounted near the centrifuge axis.*

water from the additional container was let into the inlet container. Water breakthrough was observed in the capillary imbibition phase after injection of approximately 7 l (not corrected for dead volumes).

6.2 Waterflooding Tests Set-up

Both the old and the new test set-up includes a cylindrical form providing an area constant "oedometer cell" with two plates (top and bottom). The form consists of two half shells bolted together along the flanges. Both half shells have double walls, and the inner walls are porous, see Figure 6.4. A porous filter plate ($D = 50$ cm) was adjoined to both plates. The porous filters were punched from 600 $\times$ 1200 mm Dynapore TWM-20 five-layer filter media plates of AISI type 316L stainless steel. The fine-masked side face the specimen, and the rough-masked side face the top and bottom plates to distribute the fluids evenly. A sketch of the new test set-up is shown in Figure 6.5, and a sketch of both test set-ups are shown in Appendix F.

In the old set-up, two cylindrical containers were bolted onto the top plate. In the new set-up, a larger cylindrical container separated into two by a vertical plate was also bolted onto the top plate. The inlet container was used for waterflooding, and the outlet container was used for displaced oil and produced water. The production to the outlet container flowed through an overflow tube. To avoid flow along the side between the membrane and the specimen, liquid rubber mass was cast around the specimen between the specimen and the membrane, and a confining pressure was applied on the membrane

Figure 6.4 *Photographs of the cylindrical form used in both test set-ups*

through a water-filled tube on the form. An automated magnet valve was included at the bottom to control start and end of flow of water through the specimens.

In the old set-up the containers can maximum contain 17.1 l each, whereas the containers in the new set-up can maximum contain 52 l each. The inlet container from the old set-up was used as additional container for the waterflooding of specimens 2 and 8. The inflow of water from the additional container to the inlet container during testing was controlled by a magnet valve.

Five pore pressure transducers (PPTs) were included in both test set-ups. In the old set-up, PPT 1 (inlet) and PPT 2 (outlet) was used to keep track of injected and produced volumes, respectively. PPT 3 was used to measure the inlet pressure and PPT 4 (overflow tube) was used to detect water breakthrough and to measure the outlet pressure. In the new set-up, PPT 1 and PPT 2 (both outlet) were used to keep track of produced volumes. PPT 3 and PPT 4 was switched around, so PPT 3 (overflow tube) was used to detect water breakthrough and to measure the outlet pressure, while PPT 4 was used to measure the inlet pressure. In both test set-ups, PPT 5 was used to check the confining pressure. A description and calibration of the PPTs is included in Appendix G. In all the tests, the PPTs measure in a 10 sec. cycle with a delay of 4.5-4.9 msec. between each measurement.

Eight TDR (Time Domain Reflectometry) probes (probe 1-6, 8 and 10) were placed along the periphery and in the top of specimens 2, 5, 7 and 8. The TDR probes measure the dielectric properties both of the surrounding material and their own core. A TDR probe has an effective measuring volume of 180 mm^3, and the probe takes up approximately half of this, i.e. the TDR probes provide point measurements (Olufsen 2002*a*). Due to the difference in electrical conductivity for water and oil, a significant increase in the dielectric constant was observed as water reached a probe. The dielectricity constant is around 2 for Isopar-L and around 80 for water (artificial seawater). For the chalk saturated with Isopar-L, the dielectricity constant was in the range of 1.5-3. Based on the work by Olufsen (Olufsen 2002*b*), it was evaluated that at this point, there are no consis-

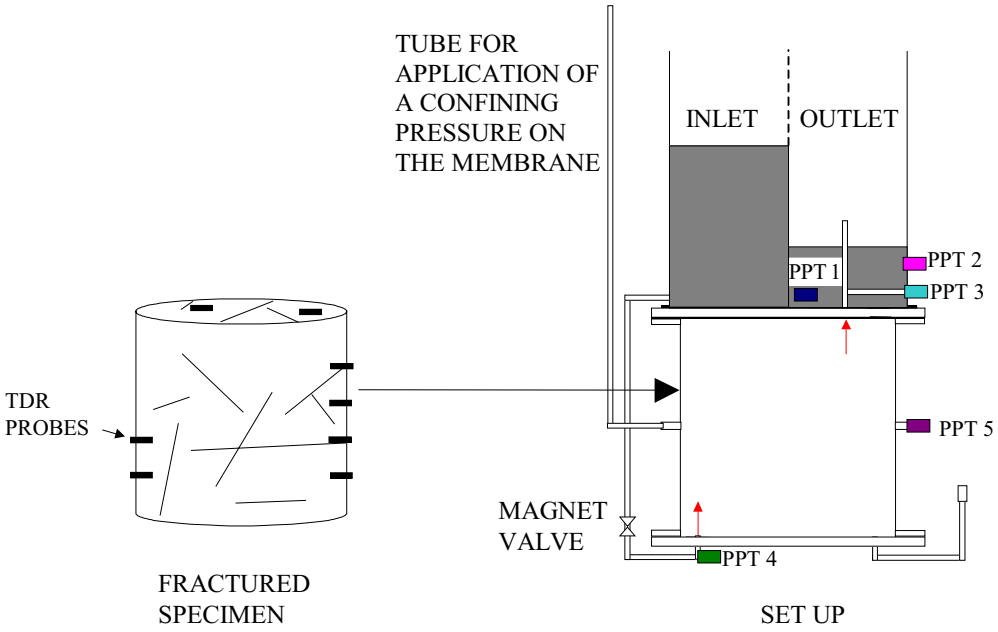

Figure 6.5 *Specimen instrumented with TDR probes to be mounted in the new test set-up.*

tent correlation between the dielectric constant and the water saturation in the vicinity of a TDR probe. The TDR probes were thus only used for indication of the position of the waterfront in the matrix and the water in the fractures during testing. A photograph of a TDR probe along with a description and calibration of the TDR probes is included in Appendix I. In all the tests, the TDR probes measure in a 31.05 sec. cycle with a delay of 100 msec. between each measurement.

6.2.1 Instrumentation and Mounting of the Specimens

The trimmed, oil-saturated specimen was placed on the porous filter on the bottom plate, see Figure J.1, Appendix J.

Holes were drilled in the specimen for the probes, and Isopar-L was injected into the holes using a syringe, see Figure J.2, Appendix J.

Soft plastic foil was wrapped around the specimen. Silicone sealant was put on the edge of the porous plate along the periphery of the foil-wrapped specimen. Then the TDR probes were placed in the holes, a few cm inside the specimen periphery. A mix of pulverized chalk and Isopar-L was filled into the holes. Silicone sealant was used to seal off the holes made for the TDR probes in the soft plastic foil. Plastic tubes were put around the leads from the TDR probes for protection from the liquid rubber mass, and taken along the periphery (inside the membrane) and out between the membrane and the form, see Figure 6.6. Both the soft plastic foil and the silicone sealant were used to prevent liquid rubber mass from entering the specimen and the porous plate.

A precast two-component rubber membrane was placed around the specimen. The two halves of the form were bolted together. The lower membrane flange was slit (cut open) between each bolt hole "to be made in the lower membrane flange" corresponding to the bolt holes in the lower flange of the form. Then holes were made in the membrane

Figure 6.6 *Photograph of specimen 8 with TDR probes mounted along the periphery (left). On the right, a photograph of liquid rubber mass being poured into the excess space between the specimen and the membrane.*

for the bolts with a chop pipe. Four steering bolts were placed, and the form was lowered down around the specimen using a crane. After the form was in place, it was bolted together with the bottom plate. Then the upper membrane flange was slit between each bolt hole "to be made in the upper membrane flange", and holes were made for the bolts with a chop pipe. Bolts were put into the holes to keep the membrane at place during cast of liquid rubber mass, see Figure J.4, Appendix J.

Liquid rubber mass was poured into the excess space between the specimen and the rubber membrane, see Figure 6.6. After hardening of the rubber mass overnight, TDR probes were mounted in the top of the specimen. In specimen 7, the TDR probes were placed vertically in the specimen top, whereas the TDR probes were placed horizontally in the specimen top of specimens 2, 5 and 8.

The horizontally placed TDR probes were placed in a fracture in the top of the specimen, or just below the surface in a trail made by a use of a chisel 0.5-1 cm down into the matrix part of the top. The probes were covered with a mix of pulverized chalk and Isopar-L. The probes placed in the chalk matrix were then covered with plastic fastened with silicone grease in order to prevent water from from the top dead volume from flowing down to the probes, see Figure J.6, Appendix J.

The plastic safety tubes for the TDR probes were sealed off with silicone sealant to prevent flow through these tubes during testing, see Figure J.7, Appendix J. The top plate with a porous filter was mounted.

6.2.2 The Centrifuge

The centrifuge is located in a 2 m deep underground construction with a diameter of 6 m at DTU. The control room is placed on the ground floor. The centrifuge is hydraulically

Figure 6.7 *Photograph of the new test set-up mounted in the centrifuge.*

driven. The rotor turns in a horizontal plane and the model container and the counterweight are hinged to the rotor. The radius from the center of rotation to the specimen bottom was 2.565 m during centrifuging, when the model container was horizontal. On the axis of rotation, slip rings are mounted to transfer voltage supply and electrical measurements. A photograph of the new test set-up mounted in the centrifuge is seen in Figure 6.7. The maximum centrifuge capacity is approximately 80 times the gravitational acceleration g. A centrifuge rotation applying 80 g at the specimen bottom corresponds to a centrifuge speed of 167.1 RPM.

After mounting of the test set-up in the model container, all the TDR probe leads and the leads from the pore pressure transducers were secured before the centrifuge tests. The leads were fastened with tape and strips to ensure that they were not torn during centrifuging due to the model container swinging to horizontal or due to the exposure to an artificial gravity field, see Figure 6.8.

6.3 Waterflooding Test Procedure

At $N = 80$ times the gravitational acceleration at the specimen bottom, water was injected into the bottom of the specimens using a falling hydraulic pressure difference resulting from the difference in inlet and outlet fluid heights and fluid densities at $N = 80$. Testing of specimen 7 was conducted by use of the Mariotte principle in the inlet container and

Figure 6.8 *Photograph of leads from the TDR probes and the PPTs secured with tape and strips before centrifuge testing in the new test set-up.*

the overflow tube in the outlet container as it was intended to apply a constant hydraulic pressure difference over the specimen. However, a constant hydraulic pressure difference could not be maintained at 80 g.

Water was injected into the bottom of the specimen, i.e. against the artificial gravity field to prevent wetting front instability with formation of gravity fingers, which can form during gravity-driven flow, and may result in scaling problems.

An initial water capillary imbibition phase was carried out before the waterflooding for the water-wet specimen 8 and the fractional-wet specimen 2. The aim was to let the specimens obtain an initial water saturation profile to suppress the capillary imbibition potential. In specimen 8, water was allowed to imbibe into the specimen before the waterflooding by opening the magnet valve for periods of 1 min. and letting small amounts of water into the specimen. After each of the 1 min. periods of water inflow, there was a 1 min. pause for imbibition. In total, 53 periods of 1 min. water inflow and 1 min. pause were conducted. For every 10 periods, pauses of 10-30 min. were held. The reason for the short periods of water inflow was to prevent flow of water in the fractures resulting in water breakthrough in the imbibition phase. However, water breakthrough was observed at the end of the water imbibition phase.

The test on specimen 2 was following the same principle as specimen 8. Since the specimen was fractional-wet and thus consisted of both oil-wet and water-wet surfaces, the periods for water inflow were reduced to 0.5 min. in an attempt to prevent flow of water in the fractures resulting in water breakthrough during the imbibition phase. After

each of the 0.5 min. periods of water inflow, there was a 1.5 min. pause for imbibition. In total, 40 periods of 0.5 min. water inflow and 1.5 min. pause were conducted. For every 10 periods, pauses of 10-30 min. were held. In spite the short water inflow periods, water breakthrough was observed in the imbibition phase.

For both specimens 2 and 8, a high rate for the waterflooding was obtained by adding water from the additional container placed near the centrifuge axis into the inlet container, where the fluid height had decreased during the initial water imbibition.

The waterflooding tests were performed at low effective mean stress levels ($p' \leq 0.22$ MPa) as the specimens were not subjected to any vertical stress other than the self-weight in the gravitational field.

6.4 Waterflooding Test Results

The displacement processes for waterflooding the fractured, oil-saturated chalk specimens were investigated based on:

- Injected and produced volumes of fluids
- Position of the waterfront and water in the fractures during testing
- Mean saturations before and after test
- Saturation profiles after test

The measured volumes of injected water and produced oil and water is included in Table 6.1. The time until water breakthrough (wbt) after start of waterflooding (wf), i.e. after the water reaches the specimen bottom is included along with the time period for the waterflooding. The total volumes of injected and produced fluids are calculated based on simple measurements of the fluid heights in the inlet and outlet containers by use of a measuring tape before and after waterflooding. After test, the amount of produced volumes was measured as well using measuring glasses. The waterflooding test data are corrected for dead volumes.

The relatively short time to water breakthrough for specimen 11 is due to that the magnet valve was leaking during this test.

It is believed that the dead volume between the specimen top and the top plate initially filled with oil is displaced by water before water breakthrough in the overflow tube. After test on specimen 8, it was estimated that approximately half of this water enters the specimen top during and after testing due to gravity forces and imbibition. For specimen 7 this also took place during the pause. The entering of water from the top was also seen as a high water saturation at the top of the specimens after test. The dead volumes for the set-ups are estimated based on simple measurements and calculations. The dead volume at the bottom and the top of the set-up (tubes etc.) is estimated to 193 cm^3 and 127 cm^3, respectively. The total dead volumes between the specimen top and the top plate are included in Table 6.2.

Since approximately half of the dead volume between the specimen top and the top plate consists of oil after waterflooding, only half of these dead volumes are used to correct for dead volumes.

Specimen	Injected water [cm^3]	Produced oil [cm^3]	Produced water [cm^3]	Time to wbt after start of wf	Time period for wf
2	24782	14682	10100	42.0 min (during water imbibition)	118 min. water imbibition and 34 min. wf
5	19445	19051	394	3.66 min.	32.83 min.
8	25904	24084	1820	197.83 min. (during water imbibition)	205.83 min. water imbibition and 44.17 min. wf
11	5793	5578	215	4.66 min.	39.0 min.
7	7142	5854	1288	100.97 min. (incl. a pause of 27 min.)	140.83 min.

Table 6.1 *Waterflooding test data corrected for dead volumes. The pore volumes were around 41-43.5 l. The specimens are listed after degree of fracturing based on inspection with the most fractured specimen first.*

Specimen	2	5	8	11	7
Dead volume [cm^3]	384	1690	1704	1326	1690

Table 6.2 *Total dead volumes between the specimen top and the top plate for all five tested specimens.*

For specimen 2, the dead volume in the sand is estimated to 356 cm^3.

Due to the pause in the waterflooding of specimen 7, it was problematic to correct water breakthrough for dead volumes, and water breakthrough at the top of the specimen was instead based on the reaction of TDR probe 8 in the top detecting water.

The maximum volume of injected water was 25.9 l compared to the specimen pore volume of 41-43.5 l, i.e. less than one pore volume was injected during waterflooding.

Interpretation and Evaluation of the PPT Measurements

The pressures measured by use of the five PPTs are plotted vs. time of testing for each of the specimens, and is included in Appendix K. The different N levels: 10, 20, 40 and 80 can be observed as "pressure plateaus" on the plots.

The PPT placed at the bottom of the set-up, i.e. PPT 3 (old set-up) or PPT 4 (new set-up) change from measuring the fluid height from the bottom PPT through the specimen to the top of the overflow tube in the outlet container to measuring the fluid height from the bottom PPT to the fluid level in the inlet container, when opening the magnet valve. As a result, an increase in pressure is seen. However, this is not the case for specimen 11 as the magnet valve does not close properly resulting in some flow of water into the specimen before the start of the waterflooding.

In the old set-up, the fluid height during testing is calculated from the pore pressures measured by PPT 1 in the inlet container and PPT 2 in the outlet container. In the new set-up, the fluid height during testing is calculated from the pore pressures measured by PPT 1 and PPT 2 placed in two different positions in the outlet container. For both set-ups, the inlet pressure is calculated as a fluid height above the bottom PPT, i.e. PPT

3 (old set-up) or PPT 4 (new set-up). The bottom PPT calculations were performed to check the pore pressure measurements compared to the volumes measured in the inlet container especially for the new test set-up.

If the overflow tube is filled, and the fluid height in the outlet container is below the overflow tube, then the pressure measured by PPT 4 (old set-up) or PPT 3 (new set-up) should be constant during the test corresponding to the height of the overflow tube. Water breakthrough in the overflow tube was observed as an increase in pressure due to the density change as water entered the oil-filled overflow tube. The fluid height in the overflow tube is calculated from the pore pressures using the oil density throughout the test as this calculated fluid height then distinctly shows water breakthrough, and if flow of water in the fractures continues after water breakthrough or is diminished.

The calculated fluid height for the produced fluids in the outlet container is based on the oil density, i.e. the height is not the actual height, but indicates the production during testing. This is due to that it is only possible to determine the total amount of oil and water produced during testing, not the fractions. For the inlet container, the calculated fluid height is based on the density of the artificial sea water. Initially, the calculated fluid height corresponding to the inlet pressure (bottom PPT) is based on the density of the oil, but shortly after the magnet valve is open, the calculated height is based on the density of the artificial sea water.

As the gravitational acceleration g varies along the set-up during centrifuging, the fluid height corresponding to the fluid level above the PPTs (measured by the PPTs) is calculated using equation (5.1). At accelerations below 10 g the calculated fluid heights may be extreme as the centrifuge model container is not horizontal, see Section 2.5.

The calculated fluid heights based on the PPT measurements and equation (5.1) and the corresponding fluid heights measured by use of a measuring tape in the inlet and outlet containers at the start and end of the waterflooding test, and the measured height of the overflow tube was compared. This comparison revealed that the calculated and measured fluid heights in some cases differed up to 6 cm, and for specimen 7 the bottom PPT (PPT 3) differed 9.6 cm. In this test, the Mariotte principle did not function, but it was possible to correct the PPT measurements.

For the interpretation of the waterflooding tests, the pore pressure transducers were mainly used to detect water breakthrough, and to evaluate the tests. Only for calculation of the waterflooding rate during testing, see Section 6.4.3, the calculated fluid heights for the bottom PPT was used. Since the relative PPT measurements during testing seem reliable, it was chosen to use the PPT measurements corrected according to the measured heights. The flow calculations for specimen 7 may however be more uncertain than for the other specimens. The odd measurements by the bottom PPT during the permeability tests on specimen 5 may be due to some kind of blocking of the magnet valve. This was seen again during waterflooding, and consequently the waterflooding flow rate could not be calculated.

Due to that the PPT measurements are not very precise, the PPT 5 measurements cannot be used to check the confining pressure during waterflooding. Instead the confining pressure and the pore pressure in the specimens are calculated based on the measured fluid heights, and compared. The comparison showed that the confining pressure on the specimens was higher than the pore pressures in the specimens, i.e. no indications of

side flow. Further, if side flow occurred during testing, this would be observed on the saturations of the small samples taken from the specimens after test, see Section 8.3.1. Approximately five small samples were taken out at five different levels in the specimen, four close to the periphery and one in the middle. Since the saturation of the small samples from the middle of the specimen was consistent with the saturation of the small samples close to the periphery, it was evaluated that there was no side flow during testing.

In the following, plots of the calculated fluid height based on measurements of the PPTs during testing are shown. These plots are only used to show the behavior during testing, and especially water breakthrough.

6.4.1 Displacement Processes

Overview

Both a waterfront, flow of water in the fractures ahead of the waterfront and capillary imbibition from the fractures were observed for all five specimens, i.e. both displacement processes: viscous displacement in the fractures and in the matrix (forced imbibition) and capillary imbibition into the chalk matrix were seen. The indications of flow of water in the fractures are the relatively small volumes of water injected at the time of water breakthrough detected by the PPTs, and the observed drop in some TDR probe output after test. The indication of capillary imbibition from the fractures is the high water saturation encountered up through the specimens after testing, and the observed drops in TDR output. The indication of a waterfront is the observed higher constant output from some of the TDR probe(s) after test, implying that the waterfront has reached at least the TDR probe(s) in question. Further, this was based on the water saturation after test. A drop in the TDR probe output corresponds to water retraction from a probe due to imbibition into the surrounding chalk implying flow of water in the fractures. Further, flow of water in the fractures ahead of the waterfront was possible for all five tested specimens, since there was a fracture system connected from the bottom to the top, see Appendix E. If no fractures were encountered at the bottom, the water should first imbibe through the matrix until a fracture was reached, and the flow of water would then be to slow to feed flow of water in the fractures. The evaluation of the displacement processes observed in the waterflooding tests are summarized in Table 6.3.

Specimen	Fracturing	Flow of water in the fractures	Imbibition
2	1	continued	some
5	2	low	dominating
8	3	low	dominating
11	4	low	dominating
7	5	continued	low

Table 6.3 *The displacement processes observed in the waterflooding tests.*

Water breakthrough was obtained by flow of water in the fractures in all four water-wet specimens 5, 7, 8 and 11, but the imbibition potential of the matrix was so strong

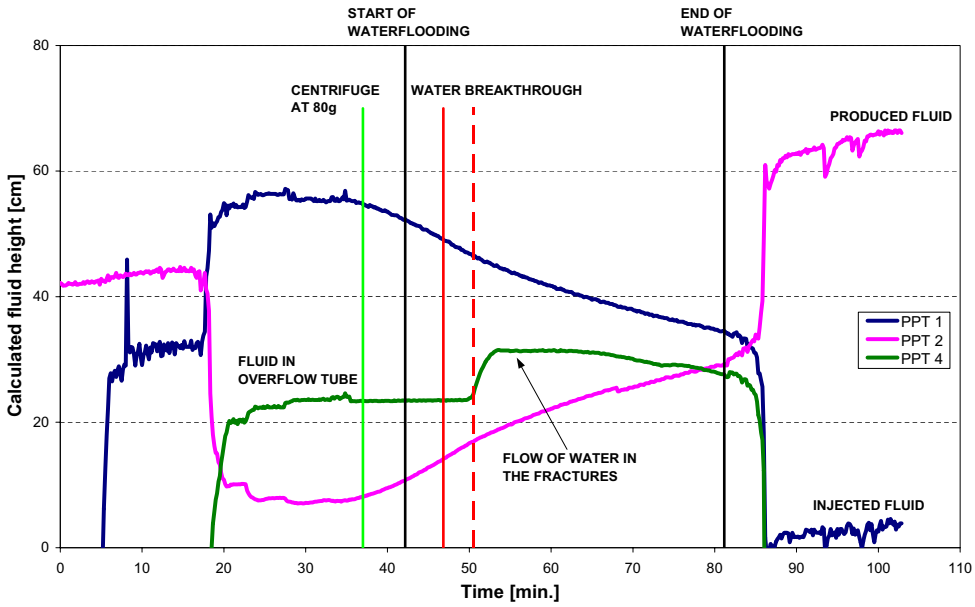

Figure 6.9 *Calculated fluid height vs. time of testing for specimen 11. The full red line corresponds to water breakthrough at the specimen top.*

that the flow of water in the fractures in the three most fractured, water-wet specimens 5, 8 and 11 were diminished or even absorbed during the test period. For the least fractured, water-wet specimen 7, flow of water in the fractures continued after water breakthrough, resulting in simultaneous production of oil and water. In the other three specimens, imbibition more or less took over, resulting in a high oil production. For these specimens, the high imbibition rate may be due to the specimens being strongly water-wet, heavily fractured, and the fractures being well interconnected. The diminished flow of water in the fractures ahead of the waterfront due to the reduced waterflooding rate resulting in a shift from flow of water in the fractures to imbibition from the fractures into the surrounding matrix. A distinct waterfront was observed in all four specimens.

For specimen 2, a continued flow of water in the fractures was observed. This is considered to be mainly due to the specimen being fractional-wet, as the specimen was highly fractured and the fractures were well connected. After water breakthrough, mainly water with oil slugs was produced.

In the test on specimens 2 and 8, water breakthrough occurred during the initial water capillary imbibition phase, i.e. before the waterflooding.

Specimen 11

The calculated fluid height based on measurements of PPT 1 (inlet), PPT 2 (outlet) and PPT 4 (overflow tube) vs. time of testing for specimen 11 is shown in Figure 6.9. The dotted red line in Figure 6.9 corresponds to water breakthrough in the overflow tube. The full red line line corresponds to water breakthrough corrected for dead volumes, i.e. water breakthrough at the specimen top. This is similar for all the plots in the following.

For specimen 11, the calculated fluid height based on the pressure measured in the overflow tube (PPT 4) was at a constant level before water breakthrough corresponding

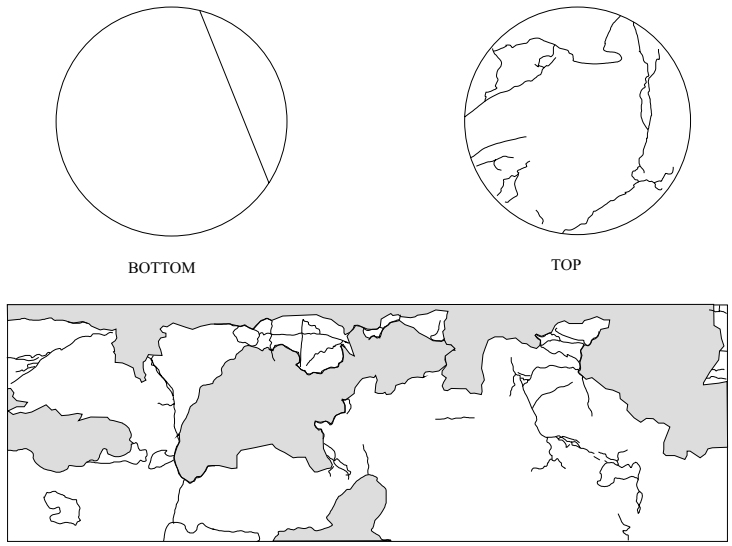

Figure 6.10 *Fractures (black lines) and gypsum (grey areas) are indicated on the top, bottom and periphery of specimen 11.*

to the height of the overflow tube. Water breakthrough was indicated by an apparent increase in fluid height in the overflow tube corresponding to that the water entering the overflow tube is denser than the oil, and the fluid height was calculated based on the oil density, see Figure 6.9. The fluid height increased to a higher approximately constant level. This higher level was maintained for approximately 8 min. and then the fluid height decreased again. Since a relatively small volume of water was injected at water breakthrough, the water breakthrough must be due to flow of water in the fractures. This means that initially oil was produced, then after water breakthrough mainly water was produced with oil slugs, i.e. water and oil was produced simultaneously. After approximately 8 min., the oil production increased, and the flow of water in the fractures was diminished, i.e. mainly oil with slugs of water was produced. This shift was due to the reduction in hydraulic pressure difference over the specimen.

The fact that the overflow tube was overflown by 2.8 cm may mask the actual time, the flow of water in the fractures diminish. Further, if only oil was produced at the end of the test, the fluid height should only be 2.8 cm higher. However, the calculated fluid height at the end of the tests confirms production of oil with slugs of water.

The magnet valve was leaking resulting in flow of water into the specimen before the start of the waterflooding. This is seen as an decrease in the fluid height calculated based on PPT 1 and an increase in the fluid height calculated based on PPT 2 from before the centrifuge reached 80 g.

Flow of water in the fractures is possible since the fracture pattern in specimen 11 is connected from bottom to top. A sketch of the fracture pattern for specimen 11 is shown in Figure 6.10. However, the fractures at the periphery of the specimen top is not shown, as gypsum was cast here.

Specimen 7

The calculated fluid height based on measurements of PPT 1 (inlet), PPT 2 (outlet) and PPT 4 (overflow tube) during testing vs. time of testing for specimen 7 is shown in Figure 6.11.

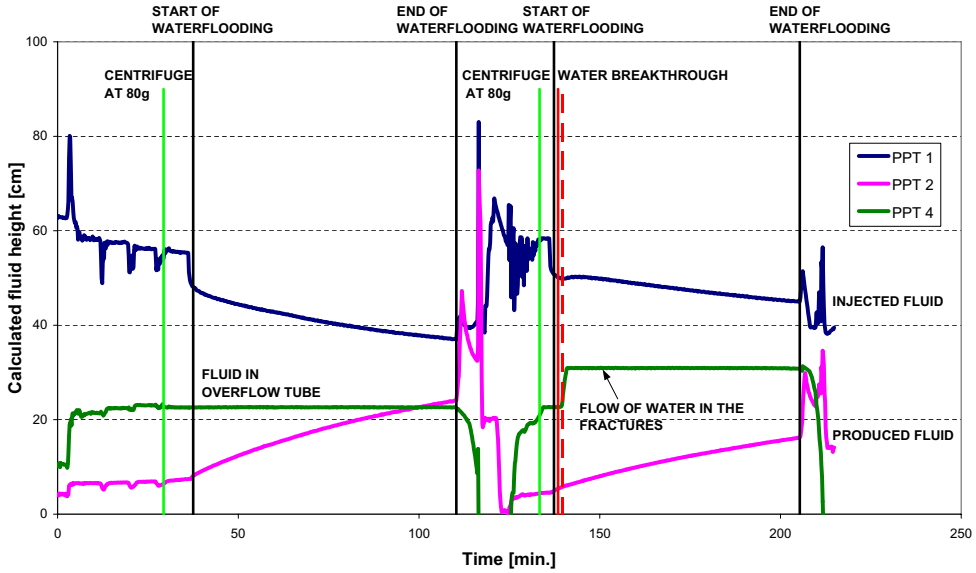

Figure 6.11 *Calculated fluid height vs. time of testing for specimen 7. The full red line corresponds to water breakthrough at the specimen top.*

After approximately 73 min. of waterflooding, the centrifuge was stopped to fill water into the inlet container and remove oil from the outlet container. The pause was approximately 27 min. This pause is believed to cause imbibition of the water from the upper dead volume into the specimen top and from the fractures into the surrounding matrix. Due to the pause, it was problematic to correct water breakthrough for dead volumes, and the corrected water breakthrough is instead based on reaction of TDR probe 8 located in the top.

The calculated fluid height based on the pressure measured by PPT 4 in the overflow tube was at a constant level corresponding to oil production before water breakthrough and increased to a higher constant level after water breakthrough implying production of mainly water with oil slugs, i.e. water and oil was produced simultaneously. Since a relatively small volume of water was injected at water breakthrough, the water breakthrough must be due to flow of water in the fractures. Flow of water in the fractures continued from water breakthrough until the test was ended.

For specimen 7, a reaction was seen on three TDR probes, probe 1, 5 and 8. These probes are colored in Figure 6.12 (right). TDR probe 1 and 5 were positioned opposite each other 5 cm from the bottom in the lower horizontal fracture plane, and probe 8 was in a fracture in the top. Probe 1 and 5 reacted shortly after start of waterflooding. During the pause, a drop in the measured dielectric constant (probe output) for all three probes implies imbibition of water into the matrix, i.e. the waterfront has not reached any of these probes. After the pause, probe 1 and 5 reacted again, and probe 8 reacted

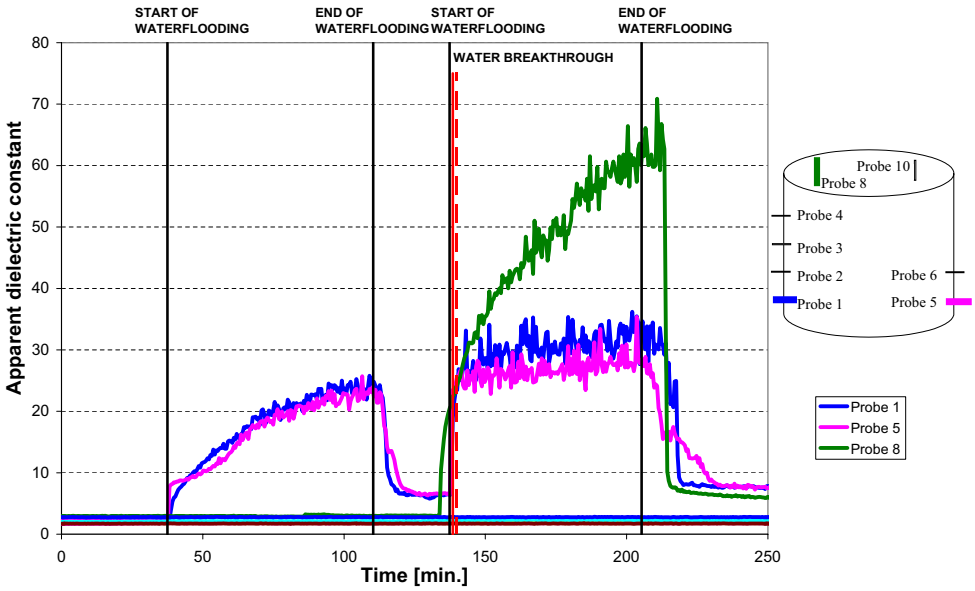

Figure 6.12 *Apparent dielectric constant measured by the TDR probes vs. time of testing for specimen 7. The full red line corresponds to water breakthrough at the specimen top. The location of the TDR probes is shown to the right.*

indicating water breakthrough. The water detected by the probes must be due to flow of water in the fractures as the probe output drops when closing the magnet valve at the end of the test. The waterfront has not reached probe 1 and 5, i.e. the waterfront has not reached 5 cm above the specimen bottom.

The remaining five probes, probe 2, 3, 4, 6 and 10 did not react. Except for probe 3, these probes were placed in the matrix higher than 5 cm above the specimen bottom. Probe 2 and 6 were positioned opposite each other 15 cm from the bottom. Probe 3 and 4 were positioned 25 cm and 35 cm above the specimen bottom, respectively. Probe 10 was placed in the matrix top. Probe 3 was placed in the upper horizontal fracture plane.

For specimen 7, flow of water in the fractures continued after water breakthrough, even though the specimen was water-wet and fractured. A sketch of the fracture pattern for specimen 7 is shown in Figure 6.13. On the sketch is indicated that specimen 7 contained two horizontal fracture planes. Further, a single, almost vertical fracture was seen above the lower horizontal fracture plane, approximately 5 cm above the specimen bottom. This fracture plane was connected by a fracture to the specimen bottom. Before water breakthrough, water mainly imbibed into the matrix below the lower horizontal fracture plane. After water breakthrough, a continued flow of water was seen in the single, almost vertical fracture continuing from the lower horizontal fracture plane to the top. The continued flow of water in the fractures dominated over the imbibition of water from the fractures into the surrounding matrix. Hence, if more water was injected at the same flow rate, flow of water in the fractures may have been able to continue, followed by a distinct waterfront. The second horizontal fracture plane approximately at the middle of the specimen, may have been closed during centrifuging. This is supported by the fact that probe 3 placed in the upper horizontal fracture plane did not react.

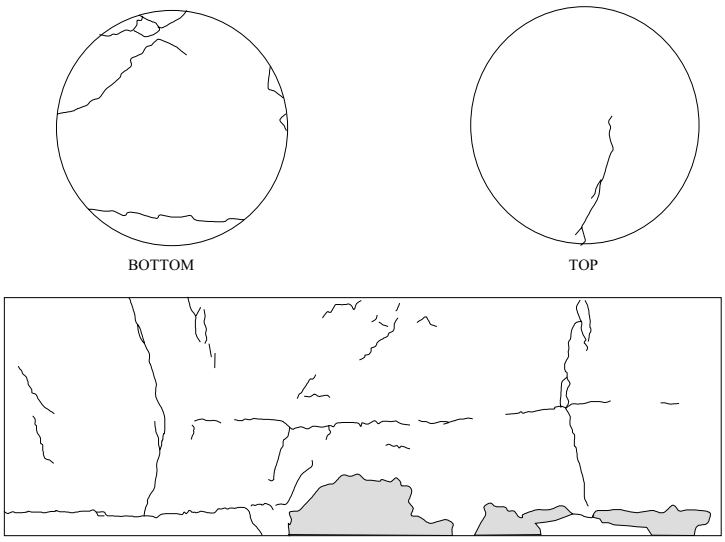

Figure 6.13 *Fractures (black lines) and gypsum (grey areas) are indicated on the top, bottom and periphery of specimen 7.*

Specimen 5

The calculated fluid height based on measurements of PPT 1 (outlet), PPT 2 (outlet) and PPT 3 (overflow tube) vs. time of testing for specimen 5 is shown in Figure 6.14.

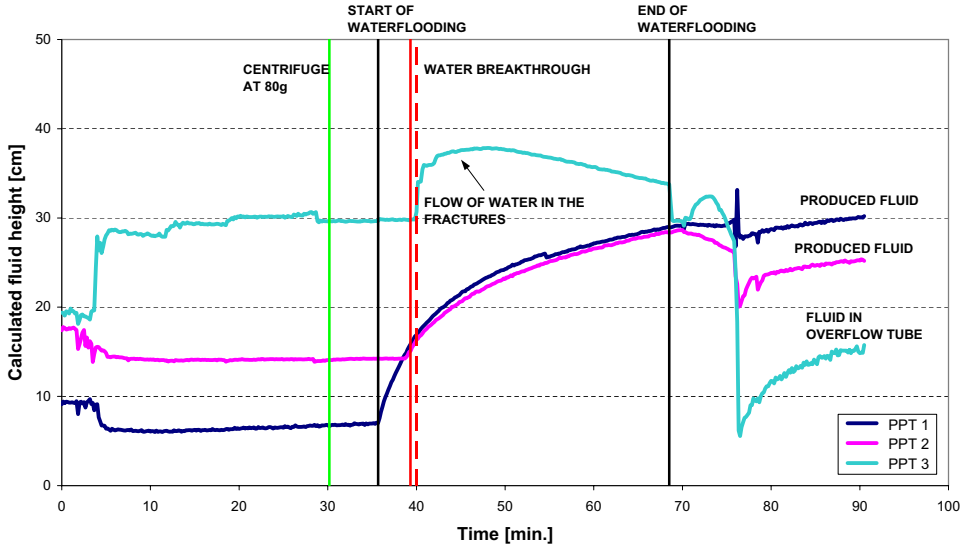

Figure 6.14 *Calculated fluid height vs. time of testing for specimen 5. The full red line corresponds to water breakthrough at the specimen top.*

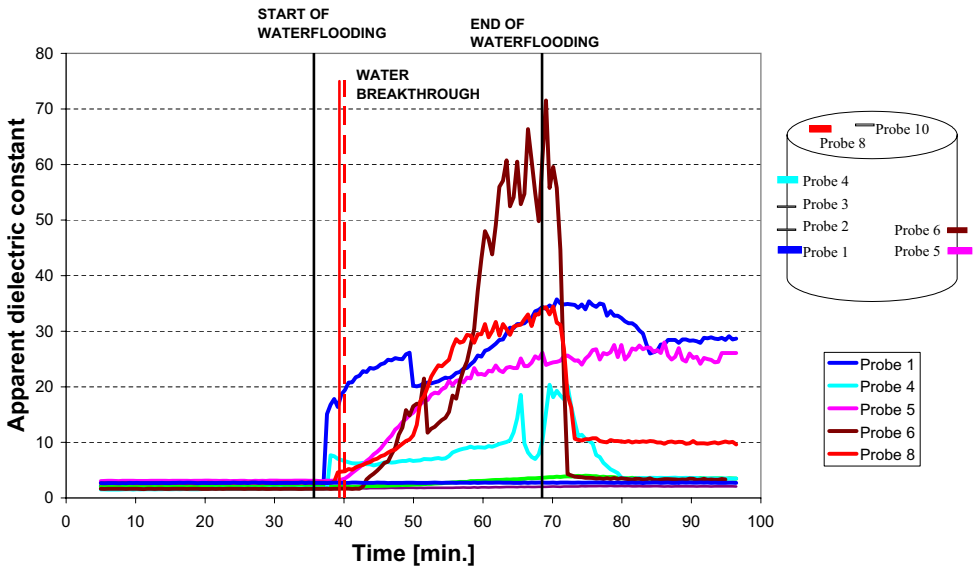

Figure 6.15 *Apparent dielectric constant measured by the TDR probes vs. time of testing for specimen 5. The full red line corresponds to water breakthrough at the specimen top. The location of the TDR probes is shown to the right.*

For specimen 5, the fluid height in the overflow tube calculated from the pressures measured by PPT 3 was constant before water breakthrough corresponding to the overflow tube being oil-filled, i.e. only production of oil initially. After water breakthrough, the fluid height increased, i.e. mainly water was produced with slugs of oil. The relatively small volume of water injected at the time of water breakthrough indicates flow of water in the fractures. After approximately 10 min., the fluid height decreased slowly implying a production of oil with slugs of water, i.e. a simultaneous production of oil and water. The shift was due to the reduction in hydraulic pressure difference over the specimen.

A reaction was seen on five TDR probes during waterflooding on specimen 5, i.e. probe 1, 4, 5, 6 and 8, see Figure 6.15. The reacting probes are colored in the sketch in Figure 6.15 (right). Probe 1 and 5 were positioned opposite each other 10 cm from the bottom, probe 4 and 6 were opposite and 35 cm and 17 cm from the bottom and probe 8 was in the top. Probe 1, 2, 4, 5 and 8 were in fractures. Probe 1, 4 and 8 reacted shortly after start of waterflooding indicating flow of water in the fractures and a well connected fracture system. The output drop for probe 4, 6 and 8 after test supported this indication. Probe 5 and 6 reacted shortly after water breakthrough. As the output for probe 1 and 5 stabilized at a higher level after test, the waterfront must have reached (at least) this height above the specimen bottom, i.e. at least 10 cm above the bottom.

Probe 10 did not react since it was placed in the matrix at the specimen top. Probe 2 did not react even though it was placed in a fracture opposite probe 6, which did react even though it was placed in the matrix above the waterfront. Probe 2 and 6 were placed opposite each other 17 cm from the specimen bottom. The reaction on probe 6 must be due to imbibition from a fracture into the surrounding matrix since the probe was placed near a fracture. The fracture that probe 2 was placed in may not have been connected to the part of the fracture network, where water was running, or the fracture may have

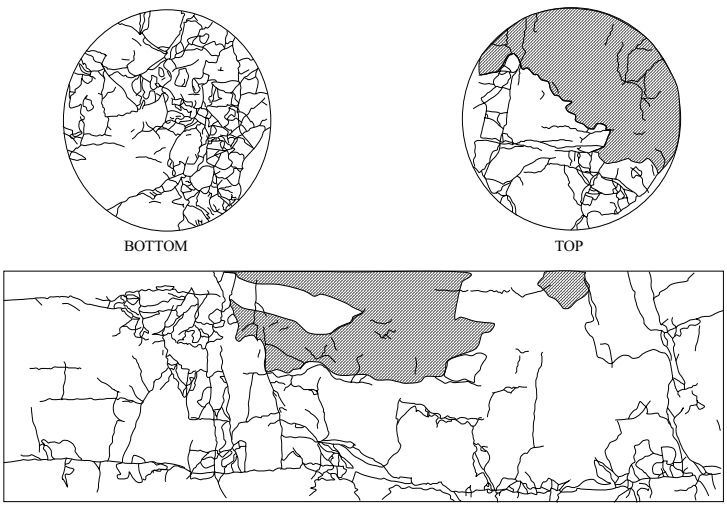

Figure 6.16 *Fractures (black lines) and crushed zones (hatched areas) are indicated on the top, bottom and periphery of specimen 5.*

been closed during centrifuging.

There is a small difference of 0.7 min. between the corrected water breakthrough and the reaction of the TDR probe 8 in the top. This difference is in accordance with the fact that the probe is placed 0.5-1 cm into the specimen top, and thus is expected to react shortly before water breakthrough at the top.

A sketch of the fracture pattern for specimen 5 is shown in Figure 6.16. On the sketch is indicated that specimen 5 contained a horizontal fracture plane near the specimen bottom. Further, the horizontal fracture plane was well-connected both to the specimen bottom and to the top. The flow of water in the fractures dominated over the imbibition of water from the fractures into the surrounding matrix for approximately 10 min. This could be due to water running in almost vertical fractures continuing from the horizontal fracture plane to the top. The shift when the flow rate decreased is due to the very well connected fracture network in the specimen.

Specimen 8

The calculated fluid height based on measurements of PPT 1 (outlet), PPT 2 (outlet) and PPT 3 (overflow tube) vs. time of testing for specimen 8 is shown in Figure 6.17.

For specimen 8, a similar displacement pattern was seen as for specimen 5 in spite the initial water imbibition phase. This imbibition phase was believed to increase the possibility of flow of water in the fractures. The calculated fluid height based on the pressure measured in the overflow tube (PPT 3) was at a constant level before water breakthrough (oil production) and increased after water breakthrough (water in the overflow tube), but then after approximately 25. min. it decreased again. The relatively small volume of water injected at the time of water breakthrough indicates flow of water in the fractures. The shift was due to the reduction in hydraulic pressure difference over the specimen.

The fact that the overflow tube was overflown by 5.2 cm may mask the time, the flow of water in the fractures diminish. Further, if only oil was produced at the end of the

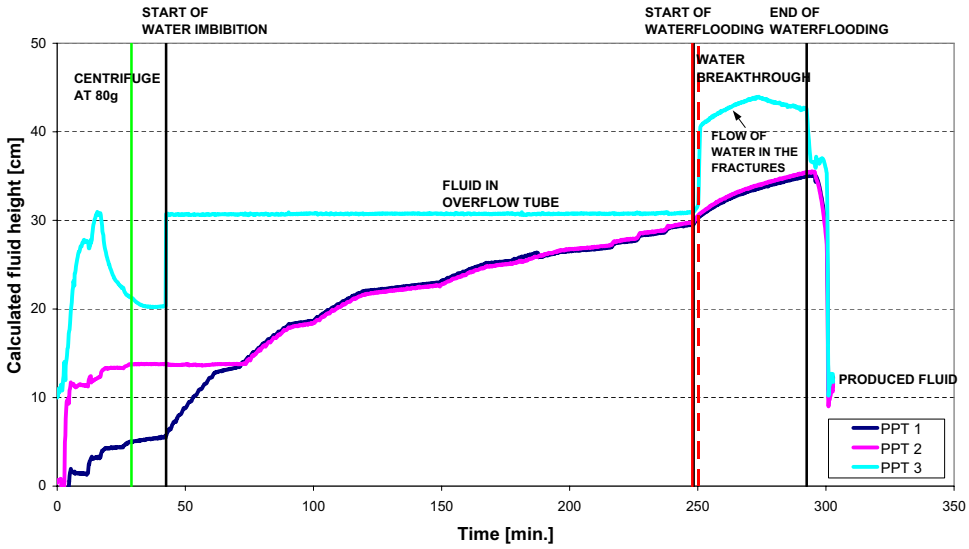

Figure 6.17 *Calculated fluid height vs. time of testing for specimen 8. The full red line corresponds to water breakthrough at the specimen top.*

test, the fluid height should only be 5.2 cm higher. However, the calculated height at the end of the test confirms production of oil with slugs of water.

A reaction was seen on seven of the eight TDR probes in specimen 8, only probe 6 did not react, see Figure 6.18. These probes are colored in Figure 6.18 (right). Probe 10 and 5 were positioned 10 cm from the bottom, probe 1 and 6 were 20 cm from the bottom, probe 3 and 4 were positioned 30 cm and 40 cm from the bottom, respectively. Probe 2 and 8 was placed in the specimen top. Probe 10, 1, 3, 4 and 8 were at the same side opposite probe 5, 6 and 2. Only probe 2 was placed in a fracture. The order of reaction is probe 10, 5, 3, 4, 2, 8 and 1. The probes all react during the initial water imbibition phase. The fluctuations in most probe output in the water imbibition phase are due to that the small amounts of water entering when the magnet valve was opened reached these probes. However, the water imbibed into the surrounding matrix when the magnet valve was closed. The probes continued to react in the waterflooding phase. Water breakthrough was detected at the top of the specimen during the imbibition phase, especially by probe 8, which was placed in the matrix. Probe 10 stabilized at a higher value in the water imbibition phase, and is the only probe that distinctly shows presence of water after end of waterflooding. This indicates that the waterfront has reached at least probe 10, i.e. at least 10 cm above specimen bottom. The output for the rest of the probes drops implying flow of water in the fractures. Only a little reaction was seen on probe 2 placed in a fracture in the top. This reaction was approximately constant from 10 min. before water breakthrough throughout the waterflooding phase, implying that water was present in the fracture, but that the water breakthrough did not occur through this fracture. Instead, the higher reaction on probe 8 seen at the time of water breakthrough in the overflow tube implies that the flow of water in the fractures may be in the vicinity of probe 8. The reaction on probe 8 is thus due to imbibition of water from the fracture.

The reaction on probe 8 in the top is seen at the same time as the water breakthrough is observed in the overflow tube. This support the evaluation that the reaction on probe

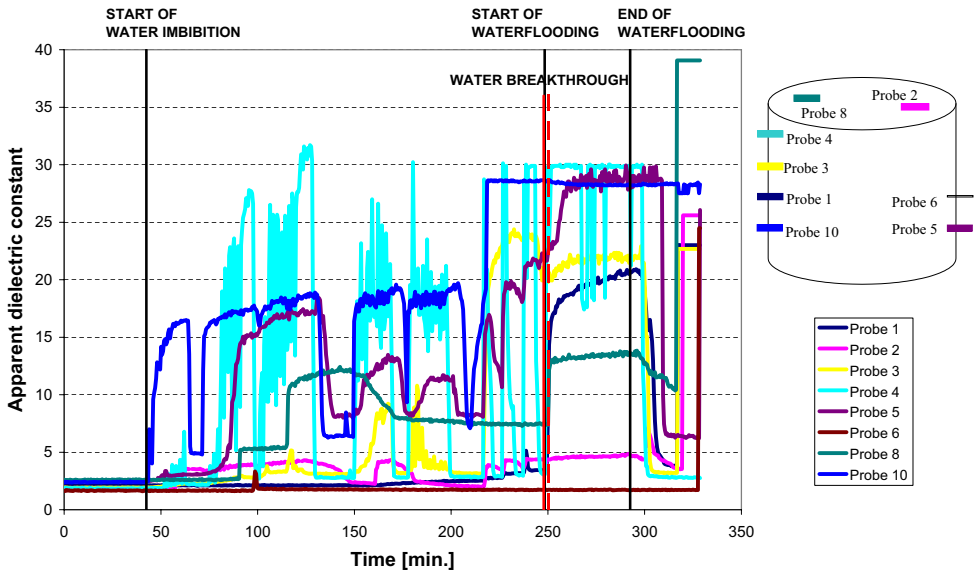

Figure 6.18 *Apparent dielectric constant measured by the TDR probes vs. time of testing for specimen 8. The full red line corresponds to water breakthrough at the specimen top. The location of the TDR probes is shown to the right.*

8 is due to imbibition from a fracture since water breakthrough at the overflow tube first occur when the dead volume is filled with water, i.e. the time for filling this dead volume is also the time for imbibition at probe 8.

A sketch of the fracture pattern for specimen 8 is shown in Figure 6.19. On the sketch is indicated the two horizontal fracture planes in specimen 8. The two horizontal fracture planes were well-connected both to the specimen bottom and to the top. The flow of water in the fractures dominated initially over the imbibition of water from the fractures into the surrounding matrix. This could be due to water running in the almost vertical fractures continuing from the bottom to the top. The shift when the flow rate decrease is due to the very well connected fracture network in the specimen. The reason for a shift in spite the initial water imbibition phase may be due to that water was distributed more into the fracture network due to the two horizontal fracture planes.

Specimen 2

The calculated fluid height based on measurements of PPT 1 (outlet), PPT 2 (outlet) and PPT 3 (overflow tube) vs. time of testing for specimen 2 is shown in Figure 6.20.

The calculated fluid height based on the pressure measured in the overflow tube for waterflooding (PPT 3) was at a constant level (oil production) before water breakthrough and increased to a higher constant level after water breakthrough implying production of mainly water with oil slugs, i.e. water and oil was produced simultaneously. The relatively small volume of water injected at the time of water breakthrough indicates flow of water in the fractures. The flow of water in the fractures continued throughout the test. The water breakthrough was seen early in the water imbibition phase. The fluctuations seen for the calculated fluid height in the imbibition phase after water breakthrough are due

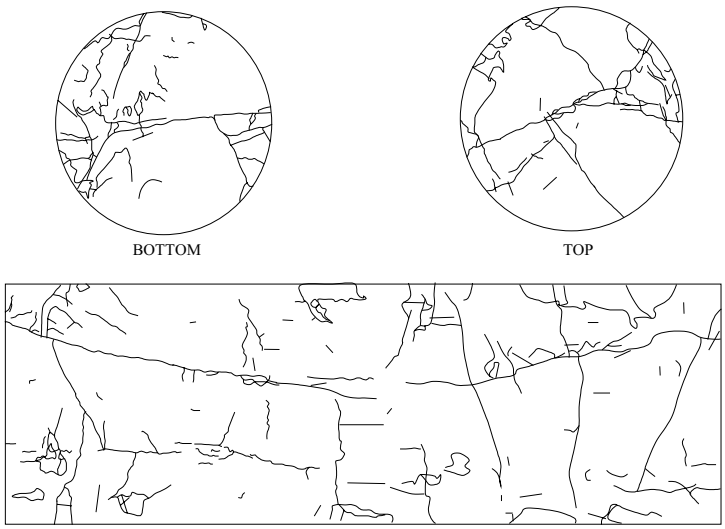

Figure 6.19 *Fractures (black lines) are indicated on the top, bottom and periphery of specimen 8.*

to that water slugs enter the overflow tube when the magnet valve was opened.

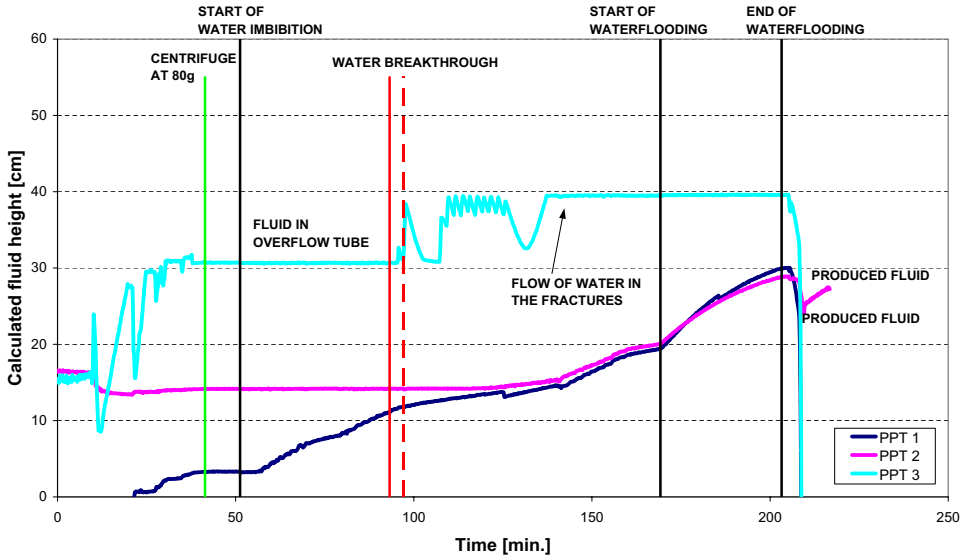

Figure 6.20 *Calculated fluid height vs. time of testing for the fractional-wet specimen 2. The full red line corresponds to water breakthrough at the specimen top.*

For specimen 2, a reaction is seen on six of the seven TDR probes, only probe 3 did not react (probe 2 was malfunctioning), see Figure 6.21. These probes are colored in Figure 6.21 (right). Probe 10, 1, 5, 6 and 3 were positioned 6 cm, 10 cm, 15 cm, 25 cm and 35 cm from the bottom, respectively. Probe 4 and 8 were in the top. TDR probe 5, 6 and 8 were in fractures. Probe 4 was in the sand layer on top of the specimen. The order of reaction is probe 10, 1, 6, 5, 8 and 4. Only a minor reaction was seen on probe 5 and 6. The probes all react during the initial water imbibition phase, and continued

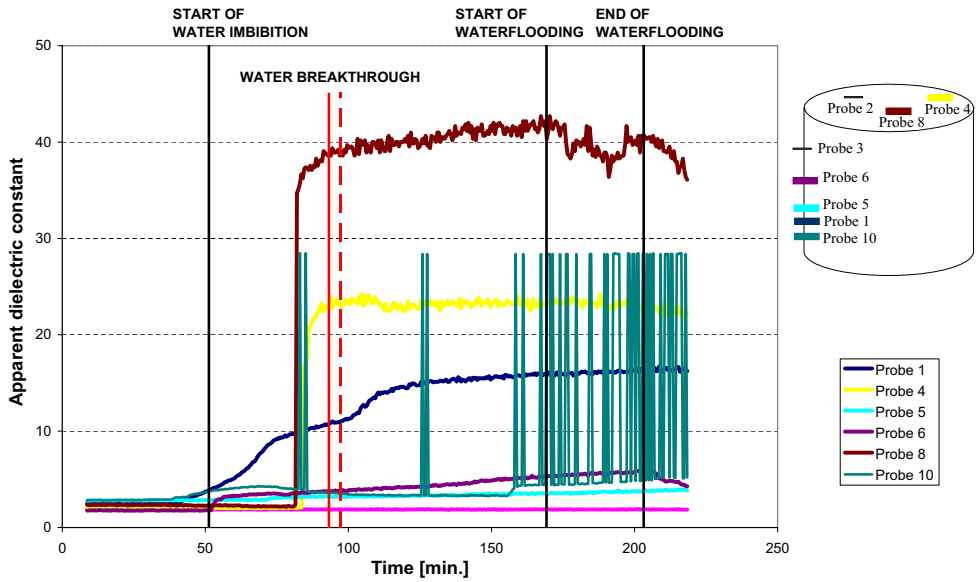

Figure 6.21 *Apparent dielectric constant measured by the TDR probes vs. time of testing for the fractional-wet specimen 2. The full red line corresponds to water breakthrough at the specimen top. The location of the TDR probes is shown to the right.*

to react in the waterflooding phase. In fact, most of the probes react before start of the waterflooding, i.e. the magnet valve must be slightly leaking in this test. In contrast to the probe reactions in specimen 8, fluctuations were not seen in the probe outputs for specimen 2 during the imbibition phase, except for probe 10. Instead the output from probe 1, 4 and 8 were stabilized at a higher value in the imbibition phase after water breakthrough. The water does thus not retract from these probes as the magnet valve is closed. This continues after end of waterflooding implying the waterfront has reached these probes. Since both probe 4 and 8 are placed in the top, this is not the case. The presence of water here may be due to the sand layer containing water and also to the fractional-wet state of the specimen. The fracture in which probe 8 was placed may have been oil-wet enabling water to "accumulate" there. The output for probe 10 shows peaks from a very low value to a relatively high value. As this was also seen after end of waterflooding, it is evaluated that probe 10 was malfunctioning, see Figure 6.22. The higher dielectric constant measured for probe 1 after test indicate that the waterfront has reached at least probe 1, i.e. at least 10 cm above specimen bottom.

In Figure 6.22 (right), a plot of the TDR probe outputs from the end of the waterflooding test to approximately 12.5 hours later. The specimen remained in the set-up after testing with the magnet valve closed, i.e. only the fluids inside the form were allowed to redistribute overnight. The output for probe 4 drops indicating that the water in the sand layer imbibes into the chalk matrix. The output for probe 1 remains constant at a high level confirming that the waterfront must have reached at least this probe. The output for probe 8 decreases to a constant relatively high level confirming that the fracture in which the probe was placed may have been oil-wet enabling water to "accumulate" there. Overall, the plot confirms that redistribution takes place over time after testing.

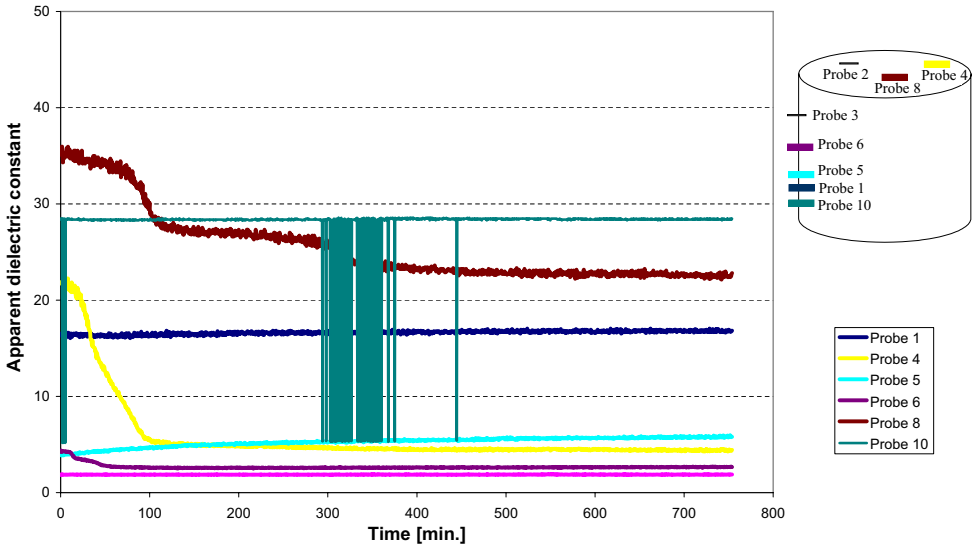

Figure 6.22 *Apparent dielectric constant measured by the TDR probes vs. time after testing for the fractional-wet specimen 2. The location of the TDR probes is shown to the right.*

For specimen 2, flow of water in the fractures continued after water breakthrough, even though the specimen was highly fractured. A sketch of the fracture pattern for specimen 2 is shown in Figure 6.23.

On the sketch is indicated that specimen 2 contained distinct, almost vertical fractures from approximately 5 cm above the specimen bottom. These fractures were connected to the bottom via other fractures. The continued flow of water in the fractures dominated over the imbibition of water from the fractures into the surrounding matrix. This could be due to water running in these almost vertical fracture continuing from the bottom to the top. Further, the continued flow of water in the fractures is believed to be due to the fractional-wet state of the specimen, i.e. water did not imbibe into the oil-wet parts of the matrix. It is likely that the oil-wet parts were especially present in the fractures due to the wettability alteration method.

Saturations Before and After Waterflooding

Based on the dry and oil-saturated weights of the specimens before test (Section 5.2) and the water up-take, i.e. the water volume present in the specimens after test, the mean fluid saturations for each specimen before and after waterflooding are determined and included in Table 6.4. The saturations after test are based on the assumption that the amount of air present in the specimens is the same before and after waterflooding. Air was evacuated by use of a vacuum pump prior to the oil permeability tests, and air was also displaced by oil during the centrifuging. However, it was not possible to determine the amount of air in the specimens after testing, and further, most of the air evacuated and displaced was probably due to specimen handling after oil saturation.

In specimens 2, 5 and 8 a high overall mean water saturation was seen. This was caused by imbibition from the extensive fracture network into the surrounding chalk matrix, and

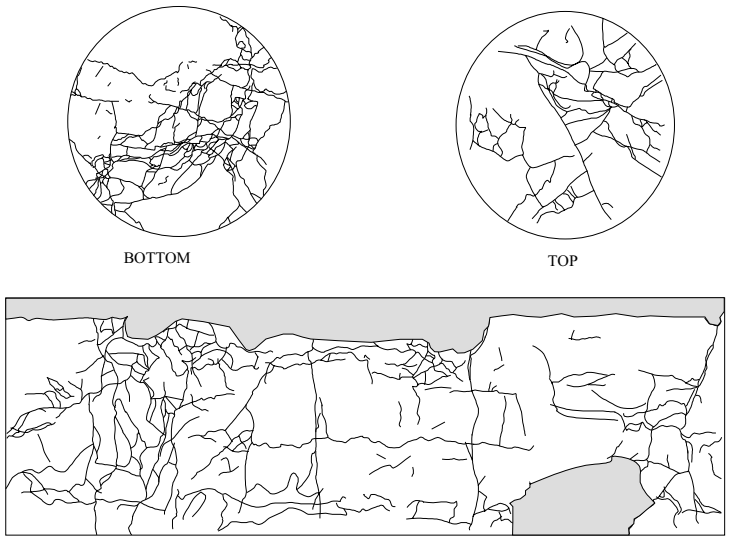

Figure 6.23 *Fractures (black lines) and gypsum (grey areas) are indicated on the top, bottom and periphery of specimen 2.*

	Before waterflooding			After waterflooding		
Specimen	S_o [%]	S_w [%]	S_g [%]	S_o [%]	S_w [%]	S_g [%]
2	99.6	-	0.4	64.7	34.9	0.4
5	97.7	-	2.3	52.5	45.2	2.3
8	96.8	-	3.2	40.8	56.0	3.2
11	≤ 98.3	$S_{wi} \geq 0$*	1.7	85.3	13.0	1.7
7	96.9	-	3.1	83.4	13.5	3.1

Table 6.4 *Mean fluid saturation of the specimens before testing (based on weight) and after testing (based on volumes) corrected for dead volumes. *During the 1 g permeability measurement on specimen 11, membrane leakage occurred and a small amount of water entered the specimen.*

for specimens 2 and 8 it was also due to the water imbibition phase. The fact that the overall mean water saturation is lower for specimen 2 than for specimens 5 and 8 is mainly due to the fractional-wet state resulting in continued flow of water in the fractures and a higher production of water for specimen 2 than for specimens 5 and 8. The low mean water saturation for specimens 7 and 11 is mainly due to the lower amount of injected water, but for specimen 7 it is also due to the continued flow of water in the fractures.

The water saturations are not to be compared to final recovery since the injected volumes are less than one PV.

Distribution of Fluids after Waterflooding

After waterflooding, the specimens were disassembled, and 25-36 small samples were taken from each of the five tested specimens using hammer and chisel for determination of mean saturations using Archimedes' principle for volume determination. Five samples

Figure 6.24 *Photo of the set-up for measuring the submerged weight of the small samples.*

were taken at 5-6 different levels along the specimens. The samples were taken at the specimen periphery at $0°, 90°, 180°, 270°$ and at the center of the specimens. Further, samples were taken at the location of the tip of the TDR probes. After a sample was cut free, it was wrapped in tinfoil and placed in a small plastic sample bag, which was closed with tape. Specimens 2 and 11 were disassembled the day after the waterflooding whereas specimens 5, 7 and 8 were disassembled shortly after testing. In Appendix L, the disassembling of the specimens is illustrated by photographs.

Initially, the small samples were weighed. Then thin wires were placed around the samples, and they were submerged into Isopar-L, where they were weighed on an electronic balance, see Figure 6.24. Finally, the samples were dried in an oven at 105°C and weighed again. Only for specimen 7, data was obtained for the small samples the same day as the waterflooding. The data on the small samples from specimens 2 and 11 was obtained the next day after disassembling. The small samples from specimens 5 and 8 were left in the sample bags overnight, and data was obtained the next day.

The volumes of oil V_o [cm^3] and water V_w [cm^3] present in the samples after waterflooding are determined from the weight of oil and water M_{o+w} [g] present in the small samples as:

$$V_w = \frac{M_{o+w} - \rho_o \cdot PV \cdot (1 - S_{air}/100)}{(\rho_w - \rho_o)} \tag{6.1}$$

$$V_o = \frac{M_{o+w} - \rho_w \cdot PV \cdot (1 - S_{air}/100)}{-(\rho_w - \rho_o)} \tag{6.2}$$

where M_{o+w} [g] is the weight of oil and water present in the samples, ρ_o [g/cm^3] is the oil density, ρ_w [g/cm^3] is the water density, PV [cm^3] is the pore volume and S_{air} [%] is the saturation of air in the samples. The saturations are based on the assumption that the amount of air present in the small samples are the same as in the large specimens. However, for specimen 2, the saturation of air $S_{air} = 0.4\%$ in the specimen resulted in a few negative water saturations, and the air saturation was adjusted to $S_{air} = 0.9\%$

Specimen	ρ_d [g/cm^3]	e [-]	ϕ (std(ϕ)) [%]	S_o [%]	S_w [%]	S_{air} [%]
2	1.458	0.853	46.0 (1.25)	72.2	26.9	0.9
5	1.471	0.837	45.5 (1.38)	41.6	56.1	2.3
8	1.443	0.872	46.6 (1.0)	39.3	57.5	3.2
11	1.435	0.882	46.8 (1.10)	74.3	24.0	1.7
7	1.437	0.880	46.8 (0.89)	80.7	16.5	3.1

Table 6.5 *Bulk fluid saturations based on mean values of the small samples taken out after waterflooding.*

corresponding to the lowest air saturation with only positive water saturations. This means that the air saturation of 0.4% determined for specimen 2 may be too low.

The weight of oil and water M_{o+w} is found from the saturated and the dry weight of the samples. The pore volume PV is found from the saturated and the submerged weight of the samples, i.e. the buoyancy on the samples, and the porosity of the samples. The bulk fluid saturations based on mean values of the small samples are included in Table 6.5. Further, the mean values of dry density, void ratio and porosity of the small samples are included in Table 6.5, along with the standard deviations from the mean values of the porosity (in parentheses).

The bulk mean water saturations are only qualitative values for the specimens. However, more interesting are the mean saturations for each of the small samples, which are used to obtain saturation profiles for the specimens.

The mean saturation vs. the distance to the specimen bottom are shown in Figure 6.25 for all five specimens, and in Appendix M for each of the five specimen.

Saturation profiles are sketched for each specimen based on the mean saturations resulting from the imbibition, see Figure 6.25. The high water saturation encountered in the top of the specimens are due to approximately half of the dead volume of water at the top going back into the specimens during and after testing due to gravity forces and imbibition. The high water saturations above the sketched saturation profiles are due to imbibition of water from the fractures. The saturation profile for specimen 2 is dotted as the waterfront sketched at 20 cm is not distinct, in fact a saturation profile could be sketched at 10 cm as well.

The saturation profiles resulting from imbibition are principally similar to the imbibition capillary pressure curves in Figure 3.1, supporting that the capillary imbibition potential is reduced in the specimens during centrifuging.

The saturation profile for specimen 7 shows that a high water saturation was encountered in the lower 5 cm of the specimen, i.e. below the horizontal fracture plane. Above this horizonal fracture plane, a low water saturation was encountered. This means that only a small amount of water imbibed from the almost vertical fracture into the surrounding matrix during the continued flow of water in the fractures. Specimen 7 contained a further horizontal fracture plane approximately at the middle of the specimen. However, since a higher water saturation was not observed here, this fracture plane may have been closed during centrifuging.

The mean water saturation was approximately the same for specimens 7 and 11,

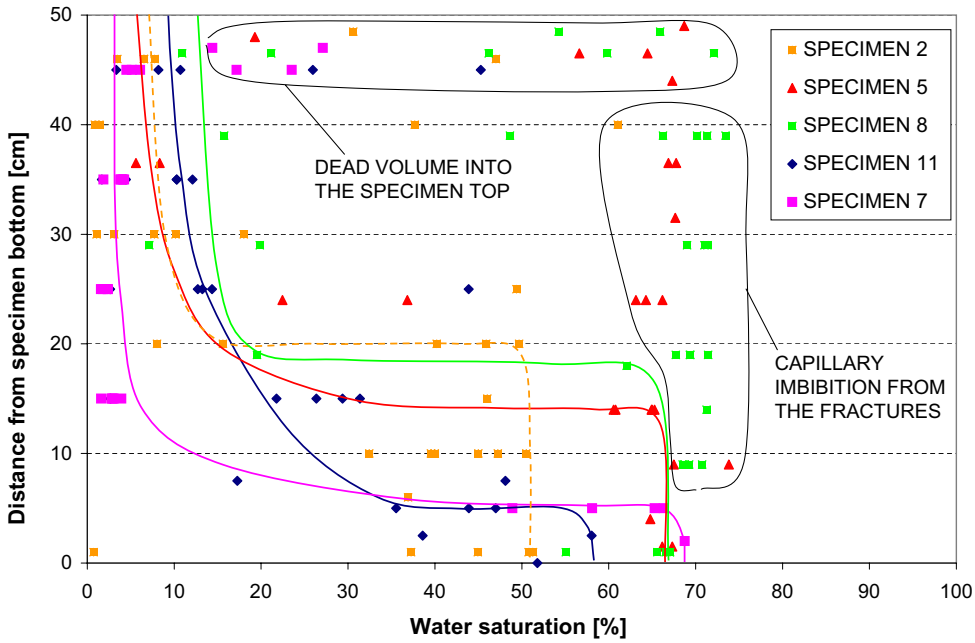

Figure 6.25 *Sketched saturation profiles based on mean saturation measured on the small samples taken from the specimens after test.*

however, the saturation profiles are different. The waterfront reached approximately the same level in the two specimens, but the water saturation at the waterfront is lower for specimen 11 than for specimen 7. Further, a higher water saturation was encountered up through specimen 11 than in specimen 7. The difference in saturation distribution between the two specimens is due to the difference in fracture pattern. The higher water saturation at the waterfront for specimen 7 is explained by a more well-connected fracture pattern at the lower 5 cm of the specimen and a horizontal fracture plane, whereas the higher saturation above the 5 cm for specimen 11 is due to a more well-connected fracture pattern above the 5 cm.

The water saturation profiles for specimens 5 and 8 are similar, except for the higher water saturation in specimen 8, which is due to that more water was injected into specimen 8 than 5. A high water saturation above the sketched saturation profiles due to imbibition of water from the fractures was seen for both specimens, which were extensively fractured with well-connected fracture networks. This was not the case for specimen 2, even though flow of water in the fractures continued throughout the test, and that the specimen was highly fractured. This difference must be due to the fractional-wet state of specimen 2.

The saturation profiles seem to be depending on the fracture system and whether the fractures are well connected or not. This is explained by the capillary imbibition into the matrix from the fractures being strong, and whether there is an extensive fracture network.

The mean water saturations are not higher than the expected around 73%, see Section 4.2, i.e. there are no indications of de-saturation effects in the specimens. This means that there are no indications of problems with too high capillary number N_c and Bond number N_B, see Section 2.5.

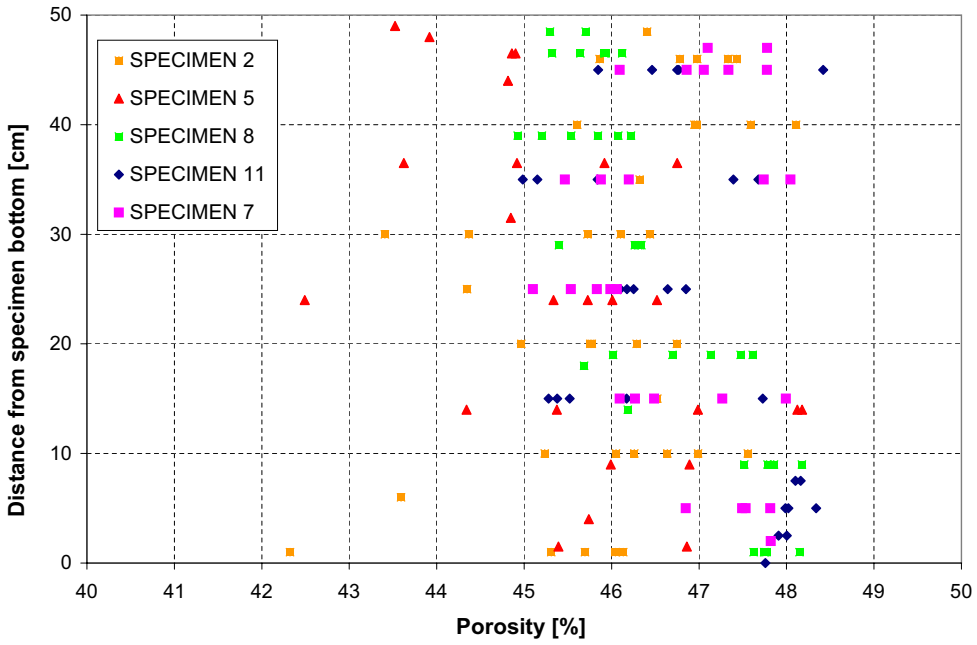

Figure 6.26 *Mean porosities based on the small samples taken from the specimens after test.*

The mean porosity determined on basis of the small samples taken out after waterflooding is slightly lower than the mean matrix porosity of 47% used in the calculations on the large specimens, see Section 5.2. In Figure 6.26 porosity vs. distance to the specimen bottom is shown for all five tested specimens.

The determined porosities are scattered, and no clear evidence of compaction is seen. This means that the assumed porosity of 47% of the specimens may have been too high. However, the standard deviations from the mean porosities on the small samples are too large to make any final conclusions on the initial porosity of the specimens. Further, the major part of the porosities are found in the range of 45-47%.

The maximum height of the waterfront during testing based on the TDR probe measurements is listed in Table 6.6. Here is also included the estimated height of the waterfront and the mean water saturation S_w behind this waterfront based on the saturation profiles.

The maximum height of the waterfront evaluated from the TDR probe measurements are in agreement with the estimated heights after test based on the saturation profiles.

High overall water saturations behind the waterfront are seen for specimens 5, 7 and 8. A relatively high water saturation is also seen behind the waterfront in specimen 2 considering the fractional-wet state.

In Table 6.7 the injected amount of water is listed along with the fraction of this water used for flow of water in the fractures, and for estimated imbibition both above and below the waterfront. The fraction used for flow of water in the fractures is determined from the injected and produced amount of water, and the remaining water is imbibed. The fraction of water imbibition below the waterfront is based on the estimated height of the waterfront and the water saturation behind the waterfront based on the saturation

Specimen	Waterfront based on TDR probes [cm]	Waterfront based on the saturation profiles [cm]	S_w behind the waterfront based on the saturation profiles [%]
2	10-15	20	51
5	10-17	14	67
8	10-20	18	67
11	-	5	58
7	0-5	5	69

Table 6.6 *Estimates of the waterfront and the water saturation corrected for dead volumes. Specimen 11 was not instrumented with TDR probes.*

profiles in Table 6.6. The remainder is imbibition above the waterfront.

Specimen	Injected water [l]	Flow of water in the fractures [%]	Imbibition above the waterfront [%]	Imbibition below the waterfront [%]
2	24.8	41	22	37
5	19.4	2	55	43
8	25.9	7	52	41
11	5.8	4	51	45
7	7.1	18	39	43

Table 6.7 *The water volumes and fractions of the water volumes involved in the waterflooding tests corrected for dead volumes.*

From the values in Table 6.7 it is seen that the largest fraction of the imbibition takes place above the waterfront for the specimens with well-connected fracture systems, i.e. specimens 5 and 8. For specimen 2 the estimated imbibition above the waterfront is smaller than below the waterfront probably due to that the water above the waterfront runs in fractures, i.e. only the part of the matrix surrounding the fractures may imbibe water. The fractures may however be more oil-wet. The imbibition below the waterfront takes place both from the fractures, but also from the specimen bottom, i.e. through the matrix. For specimens 2 and 7 with continued flow of water in the fractures, the fraction of flow of water in the fractures is high compared to the other specimens.

6.4.2 Effect of Wettability

The displacement processes are affected by wettability. In spite the fact that both specimens 2 and 8 were extensively fractured, with well-connected fracture networks, and that the waterflooding procedures were similar for the two specimens, a continued flow of water in the fractures was observed in the fractional-wet specimen 2, whereas flow of water in the fractures diminished in the strongly water-wet specimen 8. As drainage is assumed to be relatively low in the oil-wet parts, flow of water in the fractures may have been able to continue, but imbibition was dominating in the water-wet parts of the specimen. Forced drainage, resulting from the applied hydraulic pressure difference, may have increased the

water saturation to some degree in the oil-wet parts. This is based on the fact that within the first 20 cm above the specimen bottom, a water saturation of less than 10% was only found in a single sample taken from the specimen after test. On the other hand, the water saturation behind the waterfront was relatively low. Overall, a high water saturation was obtained in the specimen.

The estimated imbibition above the waterfront is smaller than below the waterfront. This probably due to that the water above the waterfront runs in fractures, and only the part of the matrix surrounding the fractures may imbibe water. The fractures may thus be more oil-wet. The imbibition below the waterfront takes place both from the fractures, but also from the specimen bottom, i.e. through the matrix.

The initial water imbibition phase may also have contributed to a continued flow of water in the fractures.

6.4.3 Effect of Fractures

The displacement processes in the water-wet chalk specimens were affected by the fracture network and not just the degree of fracturing. The more extensively fractured, and the more interconnected the fracture system was, the more imbibition from the fractures into the surrounding matrix dominated in the specimens. For the water-wet specimens, flow of water in the fractures only continued in specimen 7 containing a single almost vertical fracture with few branches, which were not well-connected above the lower horizontal fracture plane.

Critical Waterflooding Rate

Waterflooding fractured chalk with a fracture network connected throughout the chalk has been considered a risk of flow of water mainly in the fractures leading to early water breakthrough and less efficient oil displacement. In all the centrifuge tests, flow of water in the fractures ahead of the waterfront was observed, leading to early water breakthrough, but at and after water breakthrough, oil and water was produced simultaneously, with more oil produced than water. However, for three of the four water-wet specimens, flow of water in the fractures diminished, i.e. the amount of water produced compared to oil diminished as the hydraulic pressure difference decreased. Flow of water in the fractures continued in a single of the four water-wet specimens. For all the specimens, a distinct waterfront was observed at the lower part of the specimens.

For specimens 5, 8 and 11, the flow of water in the fractures diminished, as imbibition from the water-filled fractures into the oil-filled matrix increased. This was seen as a higher water saturation up through these specimens above the waterfront. This is explained by an increase in imbibition as the waterflooding rate decreased due to the falling hydraulic pressure difference. At a lower waterflooding rate, water is allowed more time to contact the matrix, and the imbibition increase. If the waterflooding on specimens 5, 8 and 11 had been continued, it is evaluated that a further decrease in the flow rate would result in production of only oil, i.e. an efficient displacement of oil by waterflooding. However, it is believed that the efficiency of this displacement is due to that the water running in the fractures are imbibed into the matrix displacing oil, and that this displacement pattern is followed by a waterfront, i.e. imbibition dominated flow.

For specimen 7, flow of water in the fractures continued after water breakthrough, even though the specimen was water-wet and fractured. The low water saturation encountered above the waterfront imply that the water imbibition from the vertical fracture may be reduced due to the flow of water in the fractures, however, imbibition is seen in. If more water was injected at the same flow rate, flow of water in the fractures may have been able to continue, followed by a distinct waterfront. On the other hand, a continued decrease in the flow rate is believed to diminish the flow of water in the fractures.

Babadagli (Babadagli 1994) reported that when waterflooding strongly water-wet, artificially fractured rock samples above a critical water injection rate, the injected water does not contact the matrix long enough to initiate capillary imbibition. No matter how much water is injected, only oil in the fracture is produced. Slower rates allow water to contact the matrix for a longer period of time resulting in stronger capillary imbibition.

If a critical waterflooding rate is defined as the inflow rate where only water is running in the fractures ahead of the waterfront after water breakthrough, it is clear that the waterflooding rate was below a critical waterflooding rate in all the centrifuge tests since mainly oil was produced at and after water breakthrough. It is not possible to evaluate if a higher waterflooding rate in the centrifuge tests would cause the injected water not to contact the matrix long enough to initiate capillary imbibition. However, it was found in the present tests that capillary imbibition proceeded after water breakthrough as seen by Mattax and Kyte (Mattax & Kyte 1962). At a lower waterflooding rate, water is allowed more time to contact the matrix, and the imbibition increase.

The flow rates for the waterflooding tests are shown in Table 6.8, i.e. the injection flow rates at the start of the waterflooding Q_{init} [cm^3/s], at the time when the effect of the flow of water in the fractures diminished $Q_{diminish}$ [cm^3/s], and at the end of the waterflooding Q_{end} [cm^3/s].

Specimen	Q_{init} [cm^3/s]	$Q_{diminish}$ [cm^3/s]	Q_{end} [cm^3/s]
2	4.0	*	1.2
5	-	-	-
8	1.8	1.1	1.0
11	3.9	1.7	1.2
7	0.5	*	0.4

Table 6.8 *Waterflooding flow rates at the start and end of waterflooding, and at the time when the flow of water in the fractures diminished. The * indicates continued flow of water in the fractures after water breakthrough.*

The waterflooding flow rates during testing are based on the calculated fluid heights for the bottom PPT, i.e. the inflow rate. The calculated fluid heights were corrected according to the measured heights.

The Mariotte principle did not function in the waterflooding test on specimen 7, but it was possible to correct the PPT measurements. The flow calculations for this specimen may however be more uncertain than for the other specimens. For specimen 5, the odd measurements by the bottom PPT during waterflooding may be due to some kind of blocking of the magnet valve. Consequently the flow rate is not included.

It is only possible to compare the flow rates for specimens 7 and 11, since these tests were conducted in a similar way. The tests on specimens 2 and 8 were also conducted in a similar way, but the wettability of the two specimens differed. The waterflooding of specimens 2 and 8 included an initial water imbibition phase, but the waterflooding phase of specimens 2, 7, 8 and 11 are comparable

A comparison of the flow rates for waterflooding of specimens 7 and 11 shows that the flow of water in the fractures continued in specimen 7 at a much lower waterflooding rate than the waterflooding rate where the flow of water in the fractures diminished in specimen 11, i.e. the flow rate $Q_{diminish}$ seems to be higher for more interconnected fracture network. This can be explained by looking at flow in the different fracture networks sketched in Figure 6.27.

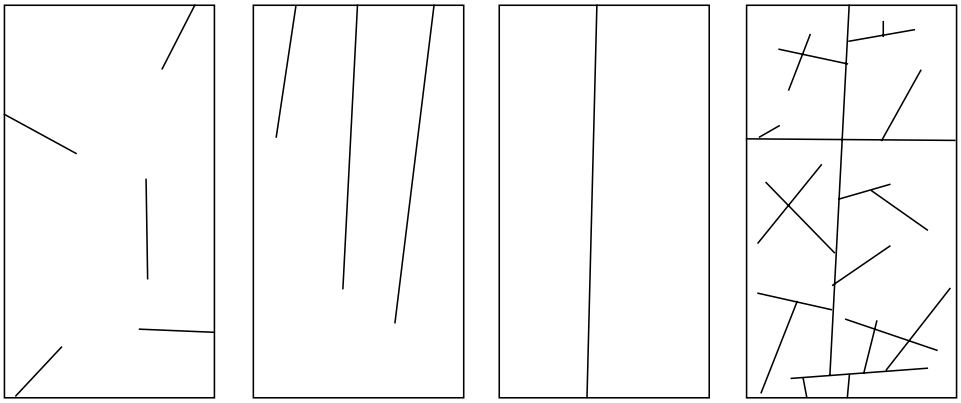

Figure 6.27 *Chalk specimens with different fracture networks.*

For the fracture networks in Figure 6.27 (a) and (b), the fracture network is not connected from the specimen bottom to the top. This means that flow of water in the fractures is not possible no matter the flow rate, except of course for hydraulic fracturing. This is due to that water should first imbibe through the matrix until a fracture is reached, and the flow of water would then be to slow to feed flow of water in the fractures. Waterflooding reservoirs with fracture networks as shown in (a) and (b) without hydraulic fracturing would be time consuming, and probably not economical. For the fracture networks in Figure 6.27 (c) and (d), flow of water in the fractures is possible, since there is a fracture system connected from the bottom to the top. If a similar waterflooding rate (inflow rate) was used to waterflood these two fracture networks, the flow rate in the single fractures would be lower for (d) than for (c) due to that water is spread more out in the well-connected fracture network shown in (d). A shift from a domination of flow of water in the fractures to imbibition domination when the flow rate decrease is seen at a higher flow rate in a specimen with a well-connected fracture network with many branches. This means that only a well-connected (almost) vertical fracture network with

few branches could impose a risk of continued flow of water in the fractures, as seen in specimen 7.

For specimen 8, the water imbibition phase was assumed to suppress the capillary imbibition potential. The outflow production rate shows that this may be the case as the waterflooding rate where the flow of water in the fractures diminish is lower for this specimen than for specimen 11, even though specimen 8 was more fractured with a well-connected fracture network.

For specimen 2, the continued flow of water in the fractures could be due to the fractional-wet state but also due to the water imbibition phase. The imbibition above the waterfront is smaller than below the waterfront probably due to that the water above the waterfront runs in fractures, i.e. only the part of the matrix surrounding the fractures may imbibe water. These parts may be more oil-wet.

The up-scaled values of the waterflooding rates are included in Section 6.6, and compared with a field relevant flow rate.

6.5 Evaluation of the Test Results

Initially, viscous displacement of oil in the fractures dominated over capillary imbibition of water from the fractures into the surrounding matrix in the four water-wet specimens. Water breakthrough was obtained by flow of water in the fractures, i.e. water (and oil) running in the fractures ahead of the waterfront. However, for the three most fractured specimens, a combination of a strong capillary imbibition potential of the chalk matrix, a well-connected fracture network with many branches, and a reduction in the flow rate, resulted in a shift from a domination of flow of water in the fractures to a domination of capillary imbibition, i.e. a diminished flow of water in the fractures. A distinct waterfront was observed in the specimens due to the strong capillary imbibition potential/forced imbibition.

For the least fractured, water-wet specimen, a domination of flow of water in the fractures continued after water breakthrough due to water running in a single, almost vertical fracture with limited branching, continuing from the lower horizontal fracture plane to the top of the specimen. However, a distinct waterfront was seen in the most fractured part of the specimen due to the strong capillary imbibition potential/forced imbibition.

For the four water-wet specimens, the ultimate recovery factor is considered to be similar, after injection of more volumes of water in the least fractured specimen than in the other three. The main matrix-fracture transfer mechanism in all four water-wet specimens was dominated by capillary forces, whereas viscous forces dominated in the fractures. Forced imbibition also took place in the matrix driven by the hydraulic pressure difference over the specimens.

In the fractional-wet specimen, a domination of flow of water in the fractures was seen, which continued throughout the test mainly due to the wettability of the specimen. Viscous forces dominated in the fractures and in the oil-wet parts, whereas capillary forces dominated in the water-wet parts of the specimen, where forced imbibition also took place.

The displacement processes were thus influenced both by the fracture network and the wettability, but also the flow rate.

The evaluation of the displacement processes during waterflooding of the five test specimens is mainly based on measurements by the pore pressure transducer in the overflow tube and the TDR probes in the specimens. Due to the large scale of the test specimens, and the limitations in the test set-up, it was not possible to monitor these specimens by etc. CT-scanning during testing. This means that the evaluation of the present displacement processes is on a macro-scale.

As reported by Graue et al. (Graue et al. 1999b), the displacement processes with waterflooding fractured chalk in the centrifuge tests were found to depend on the wettability of the chalk. Further, the fracture network was found to affect the displacement mechanisms. In the centrifuge tests, it was not possible to monitor if the fractures affected the water movement during waterflooding. However, the observations in specimen 7 could be explained by observations at micro-scale reported by Graue et al. (Graue et al. 1999b). They observed that at strongly water-wet conditions, water flow stopped at each fracture until the spontaneous imbibition endpoint water saturation was reached in the preceding matrix block. A relatively large volume of water was injected into specimen 7 before water breakthrough (approximately 5 l), and a continued flow of water in the fractures after water breakthrough was observed. This could be explained by the end-point water saturation below the lower horizontal fracture plane should be reached before enough water accumulated in the fracture plane to feed flow of water in the single almost vertical fracture above the fracture plane. This is consistent with the high water saturation encountered at the waterfront, i.e. below the lower fracture plane, and the low water saturation above the fracture plane. Even though water was running in the horizontal fracture plane as detected by the TDR probes, this water did not imbibe into the matrix above the horizontal fracture plane before the end-point water saturation was reached in the matrix below. The fracture plane was connected by a fracture from the bottom, but the water running in this fracture must only have distributed into the fracture plane and imbibed into the surrounding matrix.

In all the centrifuge tests, flow of water in the fractures was observed, leading to early water breakthrough and less efficient oil displacement by waterflooding.

Based on the centrifuge test observations it is evaluated that oil displacement by waterflooding is very efficient in strongly water-wet chalk with a well-connected fracture network continuing from the bottom to the top with many branches. Waterflooding strongly water-wet chalk containing a single almost vertical, well-connected fracture with limited branching may impose a risk of continued flow of water in the fractures resulting in less efficient oil displacement. On the other hand, waterflooding fractional-wet chalk may also impose a risk of continued flow of water in the fractures resulting in less efficient oil displacement, even with the chalk containing a well-connected fracture network continuing from the bottom to the top with many branches.

Strongly water-wet:

- Well-connected fracture network, many branches
  - Flow of water in the fractures diminished during waterflooding due to falling hydraulic pressure difference
  - Decreasing water production after water breakthrough

- Well-connected fracture network, few branches
  - Continued flow of water in the fractures during waterflooding
  - Approximately constant water production after water breakthrough

Fractional-wet:

- Well-connected fracture network, many branches
  - Continued flow of water in the fractures during waterflooding
  - Approximately constant water production after water breakthrough

6.6 Interpretation of the Modelling

Most laboratory waterflooding tests are carried out on small specimens (D = 2.5-10 cm, H = 5-20 cm) often without fractures. Laboratory measurements on small specimens cannot be applied directly to reservoir scale due to the effect of capillary forces and the absence of fractures. Normally, the effect of fractures has to be considered by means of analytical methods when waterflooding test results are up-scaled to reservoir scale. The centrifuge tests were performed on large specimens that are considered more representative for field scale as the effect of complex groups of natural fractures are included.

In the centrifuge, the specimens were exposed to an acceleration field of N times the gravitational acceleration g. At an acceleration of N, the test specimens can be considered to model the *behavior* of a reservoir block of N times the geometric dimensions of the test specimens. This scaling means that the scaled mean parameters for the test specimen for instance the intrinsic permeability apply to the whole reservoir block. Further, the displacements processes observed in the model specimens during waterflooding will be similar in the full-scale reservoir prototype. A constant scaling factor of $N = 72$ apply for the whole specimen, see Section 2.5, i.e. the identified parameters can thus be scaled by use of $N = 72$.

Evaluation of the Conflicting Scaling Factor on Particle Size

The significance of the conflicting scaling factor for particle size was evaluated by performing modelling of models, i.e. tests on models corresponding to the same prototype, but at different stress levels, see Section 2.5. Oil permeability tests were performed at N = 10, 20, 40 and 80 to determine the intrinsic permeability K. The results of the oil permeability tests at increasing mean stress (increasing scale factors of N) is included in Figure 5.8 in Section 5.3.1.

From Figure 5.8 it is clear that the absolute permeability is approximately constant for increasing mean stress, i.e. K scale at 1 for specimens 7 and 11, and possibly for specimen 8. Based on these test results, is was concluded that the assumed and derived centrifuge scaling factors apply for these specimens, i.e. the same soil is used in the model and the prototype. However, the test on the highly fractured specimen 2 revealed that the intrinsic permeability does not scale at 1 for this specimen. This may at first hand be interpreted as a scale effect. However, it can be explained as a change in the

material due to fracture closure at high stresses, i.e. a different model material is obtained. Consequently, the assumed and derived centrifuge scaling factors cannot be used directly for specimen 2. However, the reduced scaling factor of $F_K < 1$ can be used directly to obtain valid centrifuge scaling factors for the physically changed material.

Modelling of models for waterflooding was not performed, but must be expected to be similar to the oil flow tests.

Consequently, it is evaluated that the centrifuge can be used for modelling and up-scaling of waterflooding tests on the large Hillerslev outcrop chalk specimens.

Accounting for the Variation in the Acceleration Field

The variation in the gravitational field along the specimen in the centrifuge is accounted for in the calculation of the fluid heights during testing using equation (5.1).

Similarly, the influence of a non-uniform acceleration field is taken into account in the calculation of the stress level using equation (2.22).

Up-scaling of the Test Observations to Field Scale

The centrifuge test observations for the waterflooding of specimens 7 and 11 were up-scaled to reservoir scale. The displacement processes observed in the waterflooding tests on these specimens are thus representative for the displacement of oil by waterflooding in a reservoir of N times the dimensions of the test specimens, and under the same conditions. A constant scaling factor of $N = 72$ is used for the whole specimen. A few parameters for specimens 7 and 11 are included in Table 6.9, and these parameters are up-scaled in Table 6.10.

Specimen	H [m]	D [m]	K [mD]	Q_{init} [cm^3/s]	$Q_{diminish}$ [cm^3/s]	Q_{end} [cm^3/s]	Time to wbt [min.]
7	0.49	0.49	7	0.5	*	0.4	74 min. (ex. pause)
11	0.49	0.49	18	3.9	1.7	1.2	4.66

Table 6.9 *Parameters for specimens 7 and 11. The * indicates continued flow of water in the fractures.*

Reservoir block	H [m]	D [m]	K [mD]	Q_{init} [cm^3/s]	$Q_{diminish}$ [cm^3/s]	Q_{end} [cm^3/s]	Time to wbt [min.]
7	35.3	35.3	7	36	*	28.8	383616 (266 days)
11	35.3	35.3	18	280.8	122.4	86.4	24157 (17 days)

Table 6.10 *Up-scaled parameters from specimens 7 and 11 to reservoir blocks 7 and 11. The * indicates continued flow of water in the fractures.*

The calculated flow rates for the reservoir blocks, Table 6.10, are equivalent to an advance rate of 0.7-5.3 cm/day assuming plug flow and a porosity of 47%. In comparison, a typical reservoir advance rate is 1 ft/day (30.5 cm/day) (personal communication with BP Norway 2004).

Chapter 7

Simulation of the Centrifuge Waterflooding Tests

As part of the Danish Energy Research Programme (EFP) project 2000 "Displacement and Deformation Processes in Fractured Reservoir Chalk" (Christensen 2003), Gudbjerg performed numerical modelling of two of the waterflooding tests performed in the centrifuge by the author. His report "Numerical Modeling of Oil Displacement by Water Injection in Fractured Chalk" (Gudbjerg 2003) was the contribution to the EFP project from the Department of Environment and Resources (ER), DTU, and is included in the report for the EFP project (Christensen 2003).

This Chapter includes a short description of the simulations and a discussion of the simulations compared to the aim of the centrifuge tests and the test results. For detailed information, the reader is referred to Gudbjerg's report (Gudbjerg 2003).

7.1 Numerical Model

Gudbjerg performed the simulations with the numerical code T2VOC, which is a member of the TOUGH family of codes developed to simulate multi-dimensional, non-isothermal, multi-phase flow and transport in porous media. The code considers simultaneous flow of up to three phases (water, gas and oil) according to a multi-phase extension of Darcy's law. The capillary pressure-saturation relationship was based on Van Genuchten and the relative permeability-saturation relationship was based on Brooks and Corey ((Gudbjerg 2003) and references therein). Some modifications to T2VOC were necessary to model flow in a centrifugal field. This included adding the centrifugal acceleration to the gravitational acceleration g, which is an input parameter, i.e. a straightforward increase in g.

Modelling Assumptions

Modelling of multi-phase flow in fractured porous media is complex due to the heterogeneity introduced by the fractures. Gudbjerg assumed that flow in fractures can be modelled in the same way as flow in a porous medium, i.e. by using macroscopic descriptions such as capillary pressure/relative permeability-saturation curves.

In the model, Gudbjerg assumed that the fractures had the same properties and were equally spaced. Further, he assumed that the fractures were parallel or perpendicular to

the flow direction and that the circular chalk specimens could be represented by a square. These assumptions made it possible to describe the system with a 2-D model containing only one fracture in the flow direction.

The centrifuge tests on specimens 5 and 7 were simulated using a mixed equivalent porous medium approach. In this approach, the equivalent porous medium was used in parts of the model and the traditional discretization was used in the remainder. For the equivalent porous media, the fractures and the matrix were lumped into one volume, which was given effective hydraulic parameters. This was done since the interaction between fractures and matrix was fast compared to the overall flow regime so local equilibrium existed within a gridblock. For the traditional discretization, the individual fractures and the matrix between the fractures were discretized. In this way the grid blocks directly represented the difference in permeabilities and there were no integration over media with varying hydraulic properties.

To sum up, a model was set up where the fracture and the first 2 mm of the matrix were assumed to be at equilibrium. Thus, the fracture was modelled as a 2 mm thick equivalent porous medium. A discretized matrix was attached to the fracture and the width of the matrix was determined by the fracture spacing. It was possible to further divide the matrix by fractures perpendicular to the flow direction.

An initial oil saturation of 95% in the specimens was modelled since T2VOC requires that a small amount of water is present in the gridblocks.

Based on a simulation performed by Gudbjerg for drainage of a large ($H = 48$ cm) hypothetical chalk specimen, he assumed a constant g-level along the specimens in the simulation of the centrifuge tests.

Numerical Modelling of the Tests on Specimens 5 and 7

The water inlet was modelled as a constant pressure boundary, and at the top, outflow occurred when the pressure in a phase exceeded atmospheric pressure. In contrast, the centrifuge tests were run with a falling hydraulic pressure difference.

Both chalk specimens were modelled with a height of 48 cm and a radius of 24 cm. However, for both specimen 5 and 7, the height was actually measured to 48.8 cm, and the diameter to 48.9 cm.

Since complete capillary pressure or relative permeability data were not available for the Hillerslev chalk specimens, and only sparse information was available on the fracture properties, Gudbjerg used data from a small, artificially fractured, cylindrical chalk plug ($D = 3.795$ cm, $H = 5.87$ cm). Earlier, a displacement test was carried out on this chalk plug (Olsen et al. 2001), and the test was simulated by Gudbjerg (Gudbjerg 2003). The matrix permeability of the plug was $1.6 \cdot 10^{-15}\text{m}^2$ (1.6 mD), which is lower than the mean matrix permeability measured for Hillerslev outcrop chalk to 2.8 mD, see Section 5.3.1. The fracture permeability was $2.9 \cdot 10^{-11}\text{m}^2$ (29 D). The porosity was 32%, which is low compared to the mean porosity of 47% for Hillerslev outcrop chalk, see 4.1. The capillary pressure curve for the small plug determined by (Olsen et al. 2001) are included in Figure 7.1 along with a capillary pressure curve ("New curve") modified by Gudbjerg. The modified capillary pressure curve provided a much better match in the simulation of the displacement in the small plug. According to both capillary pressure curves, a higher

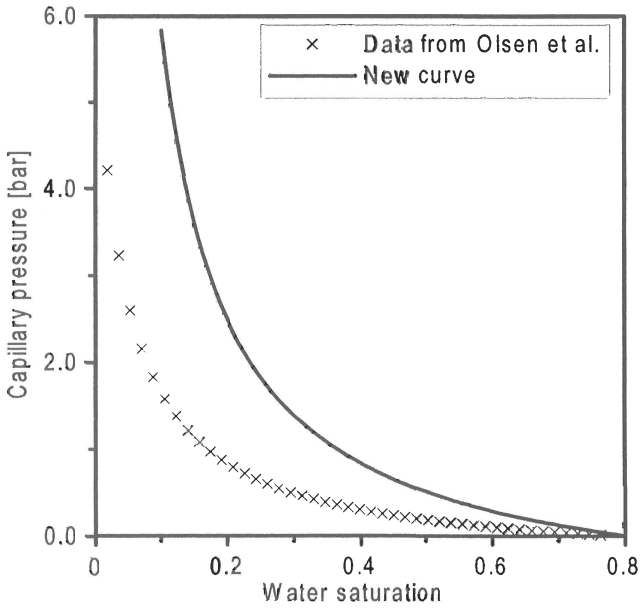

Figure 7.1 *Reference and new capillary pressure curve for the chalk matrix, from (Gudbjerg 2003).*

water saturation is obtainable in the small plug (80%) than in Hillerslev outcrop chalk (73%, see Section 4.2).

The relative permeability curves for the small plug determined by (Olsen et al. 2001) are included in Figure 7.2 along with the relative permeability curves ("Adjusted") modified by Gudbjerg.

The capillary pressure curve and relative permeability curves are included in Figure 7.3 for the fractures. At a saturation of 0.03 the capillary pressure in the fracture was equal to the initial capillary pressure in the matrix, i.e. the minimum saturation in the fracture. Above a saturation of 0.5 there was no capillary pressure in the fracture. The modelling of the fractures and the inlet/outlet containers were similar.

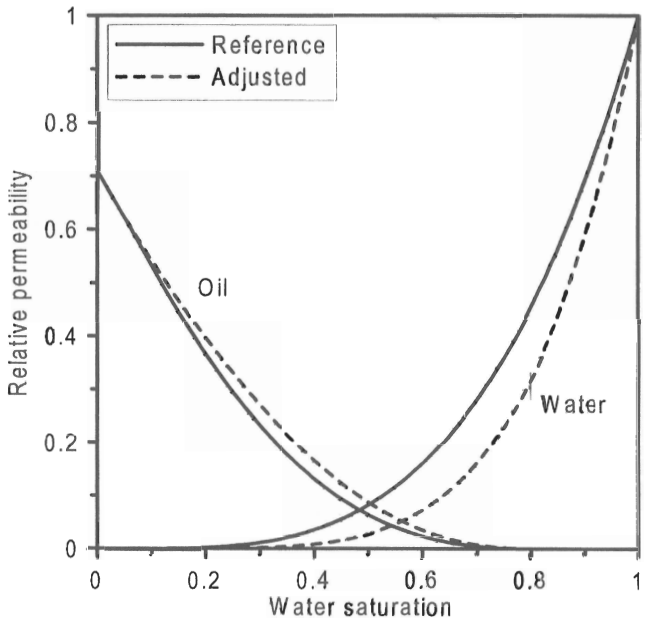

Figure 7.2 *Reference and adjusted relative permeability curves for the chalk matrix, from (Gudbjerg 2003).*

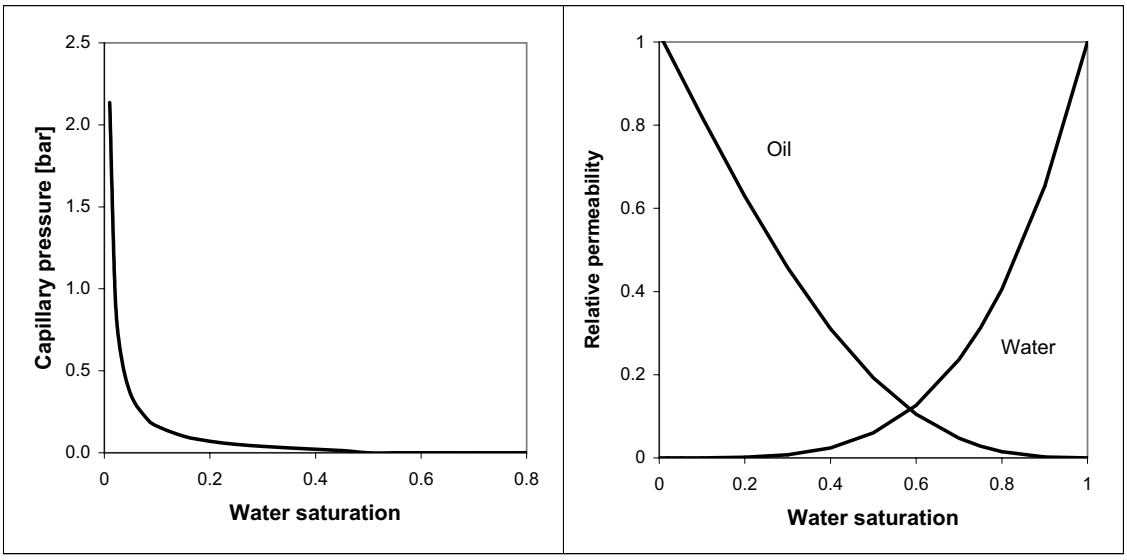

Figure 7.3 *Capillary pressure curve for the fractures (left) based on van Genuchten and relative permeability curves for the fractures (right) based on Brooks and Corey, based on (Gudbjerg 2003).*

Specimen 7

Specimen 7 only contained a few fractures, see Figure 7.4. Gudbjerg used the effective permeability 8 mD ($8 \cdot 10^{-15}$ m^2) measured on the specimen at 1 g, see Section 5.3.1. The specimen was modelled with a single fracture connected to a 20 cm wide matrix. This corresponds to a chalk specimen with a single fracture down the middle.

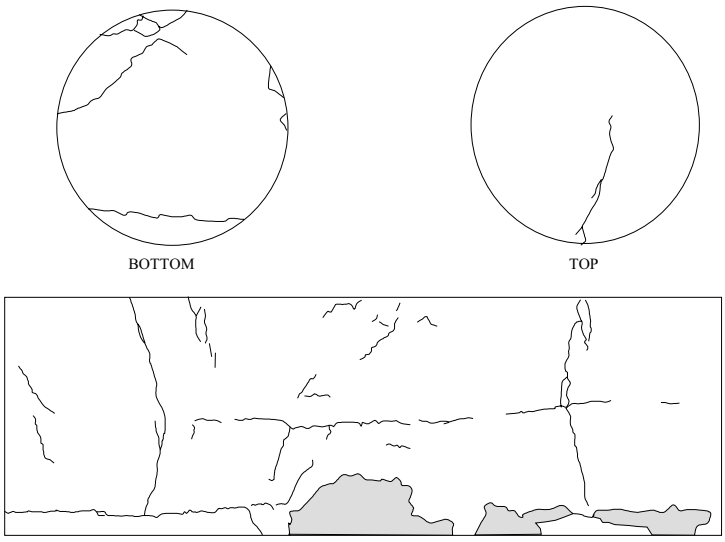

Figure 7.4 *Fractures (black lines) and gypsum (grey areas) are indicated on the top, bottom and periphery of specimen 7.*

The matrix permeability was assumed to be equal to the matrix permeability of the small plug, i.e. $K_m = 1.6 \cdot 10^{-15}$ m^2 (1.6 mD), i.e. lower than the measured mean matrix permeability of 2.8 mD. The fracture permeability was adjusted to $K_f = 5 \cdot 10^{-11}$ m^2 (50 D). The effective relative permeability for the equivalent porous medium was determined to $k_r = 390k_{r,f} + 0.99k_{r,m}$.

Specimen 5

Specimen 5 was highly fractured, see Figure 7.5. Gudbjerg used the effective permeability of 249 mD ($249 \cdot 10^{-15}$ m^2) measured on the specimen at 1 g, see Section 5.3.1. The specimen was modelled with a fracture spacing of 5 cm in both vertical and horizontal direction.

The matrix permeability was adjusted to $K_m = 5 \cdot 10^{-16}$ m^2 (0.5 mD), which is much smaller than the measured mean matrix permeability of 2.8 mD. The fracture permeability was adjusted to $K_f = 2.5 \cdot 10^{-10}$ m^2 (250 D). The effective relative permeability for the equivalent porous medium was determined to $k_r = 6250k_{r,f} + 0.99k_{r,m}$.

7.2 Numerical Modelling Results

The amount of input data was very limited and it was therefore not possible to provide an accurate simulation of the centrifuge displacement tests. Instead some simulations

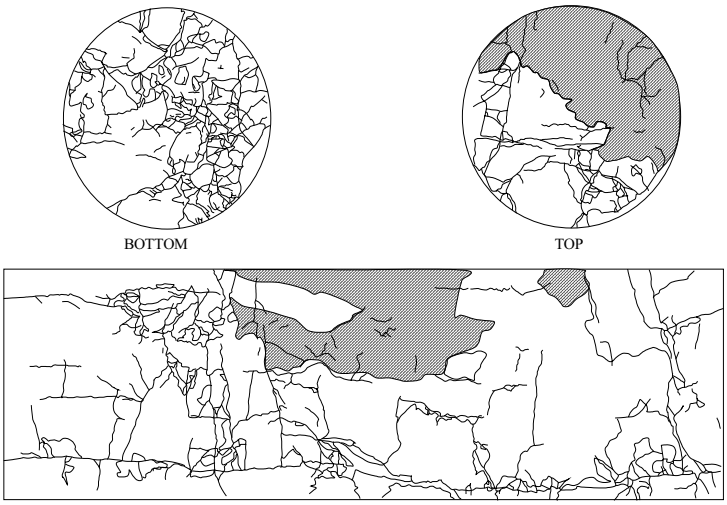

Figure 7.5 *Fractures (black lines) and crushed zones (hatched areas) are indicated on the top, bottom and periphery of specimen 5.*

were performed that qualitatively show the effects of varying different parameters and configurations on the recovery curve.

Specimen 7

Figure 7.6 shows the simulated saturation at various times for specimen 7 based on the data from the small plug (referred to as the reference case) with the adjusted fracture permeability. In Figure 7.6 D (right), a horizontal fracture is inserted 5 cm from the inlet.

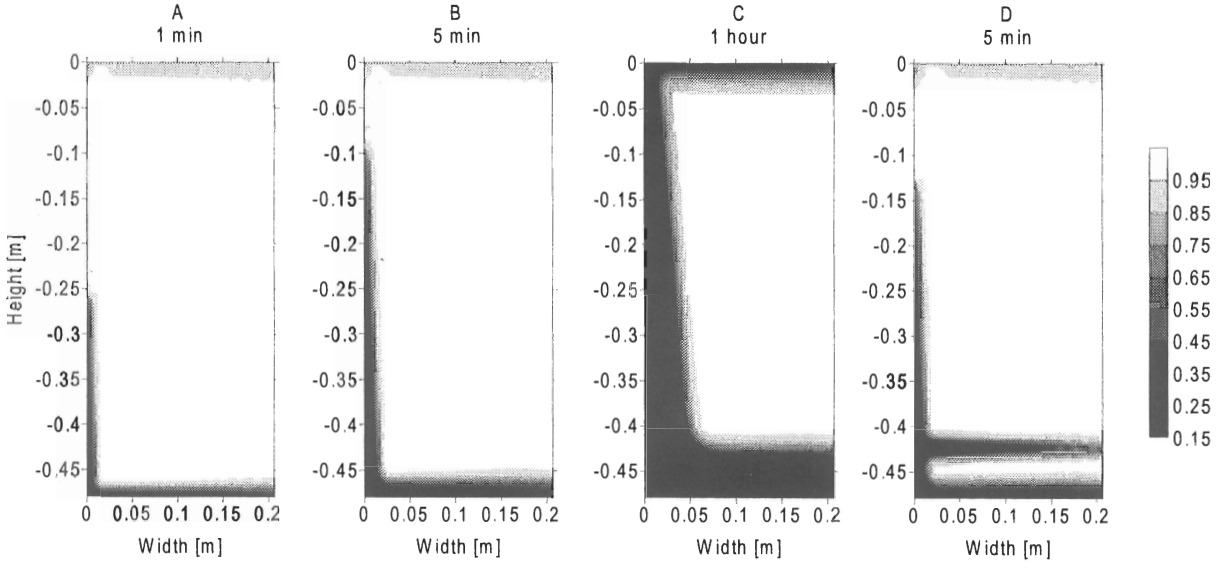

Figure 7.6 *Simulated oil saturation at different times. In plot D (right) a horizontal fracture is inserted 5 cm from the inlet, from (Gudbjerg 2003).*

From Figure 7.6 A to C, it is seen that water rises rapidly in the fracture and imbibes

into the matrix. The water runs in the fracture ahead of the waterfront, i.e. flow of water in the fractures resulting in early water breakthrough is seen, which is similar to the observations in the test on specimen 7. However, the imbibition from the fracture may be faster than observed in the test. Outflow of water is not observed until the flow of water through the fracture exceeds the imbibition rate from the outlet container.

It is observed that the imbibition in the simulation takes place both from the inlet and outlet container. This is due to that water can easily displace oil close to the outlet container since the oil can escape to the outlet container.

Gudbjerg reported the following seven different simulations of recovery of the centrifuge test on specimen 7, and compared them to the observed recovery, which is referred to as "Experimental data":

- Reference case
- Capillary pressure
- Fracture perm.
- Relative permeability
- Horizontal fracture
- No fracture
- No connect

Figure 7.7 compares the observed recovery curve ("Experimental data") for specimen 7 with the simulated ("Reference") curve, and also the results from the other simulations are included.

In Figure 7.7 (left), the curve termed "Capillary pressure" is a simulation where the capillary pressure curve of the matrix has been changed from ("Data from Olsen et al." (Olsen et al. 2001)) used in the "Reference" simulation to the modified curve ("New curve"), see Figure 7.1. With a larger capillary drive more water is imbibed and consequently more oil is produced. The oil production is faster, and water breakthrough occurs earlier.

When the fracture permeability is fixed at the lower value 29 D used for the small plug and the matrix permeability is increased instead to 4.4 mD, the oil production is faster as indicated by the curve termed "Fracture perm.". This is due to that the increased matrix permeability increases the water imbibition. Water breakthrough occurs later, which is because more water imbibes and water moves slower through the fracture at the lower permeability.

In the curve termed "Relative permeability", the change of the relative permeability curve from ("Reference") to ("Adjusted") as shown in Figure 7.2, reduced the oil production rate. This is because the relative permeability to water is reduced and this is not balanced by the increased relative permeability to oil.

In Figure 7.7 (right) the curve termed "Horizontal fracture" shows the recovery from the simulation with a horizontal fracture inserted 5 cm from the inlet. The simulated

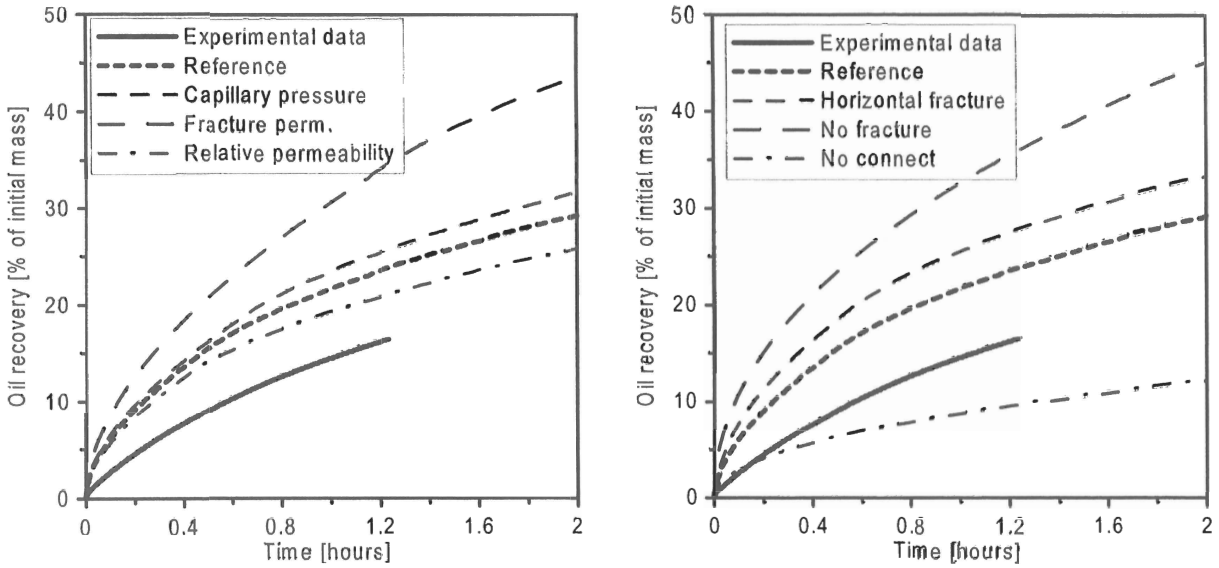

Figure 7.7 *Simulated recovery for different parameters and model configurations, from (Gudbjerg 2003).*

saturation after 5 minutes is shown in Figure 7.6 D. In this case the recovery is much faster because the matrix area available to imbibition is larger. Further, water breakthrough occurs earlier. A model with a horizontal fracture inserted 5 cm from the inlet is more representative for specimen 7, since a horizontal fracture plane was found approximately 5 cm above the specimen bottom, see Figure 7.4. However, the imbibition from the horizontal fracture seems to be similar above and below the fracture, which is believed to be different from the test observations, see Section 6.5.

For the curve termed "No fracture", the chalk specimen is considered as a matrix only with the measured effective permeability of 8 mD. This gives the fastest recovery, however, a matrix with such high permeability is unrealistic. The simulation only serves to show the effect of ignoring the fracture system. In this case, the displacement occurs as a sharp front (plug flow) moving through the matrix and there is no early water breakthrough.

In the last simulation termed "No connect", the fracture does not penetrate the matrix completely. The lower 5 cm close to the inlet are given matrix properties and this results in a slow recovery. Again the water moves as a sharp front and there is no early water breakthrough. The significance of the fracture is very limited even after the waterfront reaches it. This is because water cannot flow fast enough through the matrix to create rapid flow in the fracture. Thus there is no water in the fracture moving ahead of the waterfront in the matrix.

In the present test, water breakthrough occurred after 100.97 min. inclusive a pause of 27 min., i.e. after approximately 74 minutes, and flow of water in the fractures continued. Oil and water was produced simultaneously after water breakthrough. The time to water breakthrough for the test on specimen 7 (Experimental data) is included in Table 7.1, along with water breakthrough times for some of the simulations described above.

	Time to water breakthrough
Test (Experimental data)	74
Reference case	31
Capillary pressure	42
Fracture permeability	82
Relative permeability	27
Horizontal fracture	35

Table 7.1 *Time to water breakthrough for simulations with different parameters and model configurations, from (Gudbjerg 2003).*

Specimen 5

Figure 7.8 (left) representing a highly fractured system shows how the water distributes rapidly into the fracture system and then more slowly imbibes into the matrix. In this simulation, water is evenly distributed in each matrix block due to the fracture configuration, i.e. no waterfront is seen.

In specimen 5, water breakthrough occurred after approximately 4 min. and only a small amount of water was produced after water breakthrough. The recovery in the test is faster than in the simulation of the test, see Figure 7.8 (right). This may be because the density of the fractures is underestimated in the model or because some of the properties in the model do not correspond to the properties in the test (e.g. porosity, residual oil saturation, permeability, capillary pressure etc.). Water breakthrough in the simulation occurred after 3 min. compared to 4 min. in the test. After water breakthrough, water and oil were produced simultaneously in the simulation, which did not occur in the test. This is because the injection pressure decreased in the test due to the falling hydraulic pressure difference, whereas it was kept constant in the simulation. As seen in Figure 7.8 (right), the recovery of approximately 45% for the present test on specimen 5 (Block 5) is much lower than the shown recovery of approximately 70% for Block 5. One reason for this may be that a lower porosity of 32% was used for the specimen instead of the mean porosity of 47% for Hillerslev outcrop chalk. However, the recovery of 14% for the present test on specimen 7 (Block 7) is comparable to the shown recovery for Block 7.

7.3 Discussion of the Numerical Modelling

The aim of the waterflooding tests in the centrifuge was to obtain water breakthrough caused by flow of water in the fractures ahead of the waterfront and possibly continued water production. Thereby the interrelation between flow of water in the fractures and imbibition from the fractures, and the concept of a critical waterflooding rate was studied.

A simulation of the centrifuge tests is very relevant, especially since it was not possible to monitor the displacement processes during waterflooding inside the specimens other than by use of the TDR probes and the detection of water breakthrough by the PPT in the overflow tube. A simulation of the centrifuge tests can provide more knowledge about the displacement processes involved during testing. Further, a simulation can allow for a better understanding of the concept of a critical waterflooding rate.

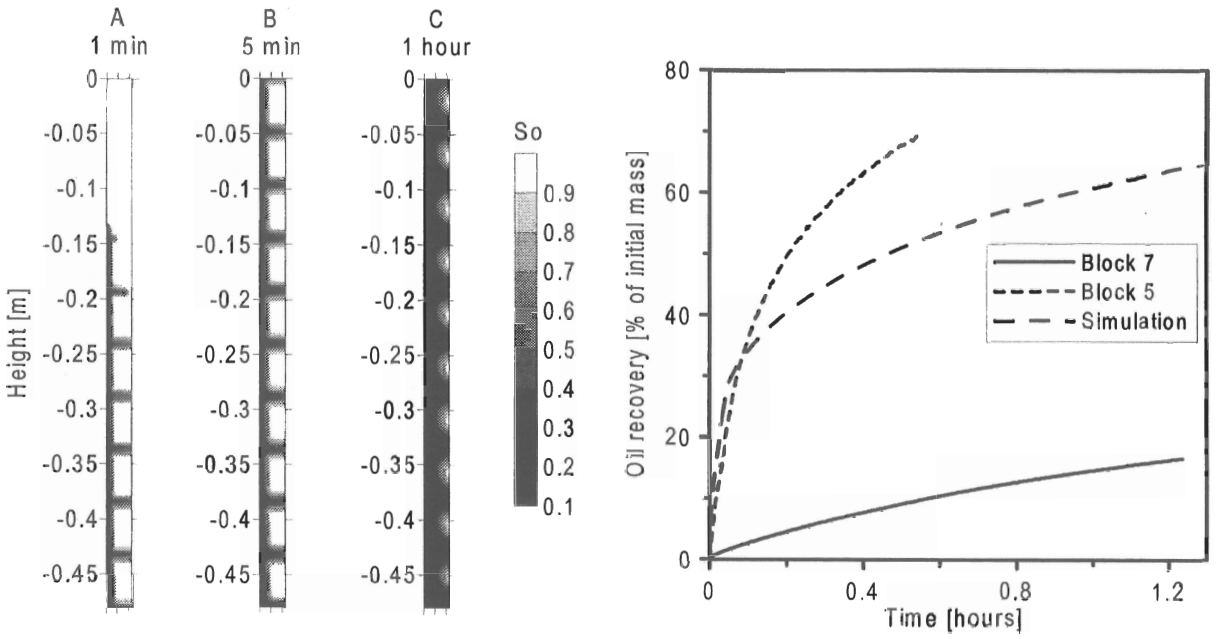

Figure 7.8 *Simulated oil saturation and recovery for the highly fractured model compared to the recovery for specimen 5 (Block 5). The recovery for specimen 7 (Block 7) is shown for comparison, from (Gudbjerg 2003).*

Gudbjerg simulated the saturation at different times and the oil recovery for specimens 5 and 7, i.e. for a highly fractured and a much lesser fractured numerical model.

For specimen 7, the simulation of the saturation at different times based on data from the small plug showed that water was running in the fracture ahead of the waterfront. Flow of water in the fractures resulting in early water breakthrough was seen, and water from the fracture imbibed into the surrounding matrix. Further, a distinct waterfront was seen due to imbibition from the inlet. The displacement processes involved during waterflooding represent the observations in the test on specimen 7. However, the imbibition from the vertical fracture seems to be faster in the model than in the test. Further, the imbibition above and below the inserted horizontal fracture in the model may be different from the interpretation of the test.

For specimen 5, the simulation of the saturation at different times based on data from the small plug showed that water was running in the fractures. However, since the water was distributed rapidly into the fracture system, from where it imbibed into the surrounding matrix, a distinct waterfront was not seen. In fact, the imbibition from the fractures into the surrounding matrix resulted in an evenly distribution of water in the matrix blocks. The saturation, i.e the displacement processed involved during waterflooding are different for the simulations and the observations in the test on specimen 5.

Despite the stated differences in boundary conditions and matrix/fracture parameters, no further modelling was carried out.

7.4 Perspective of the Numerical Modelling

Gudbjergs's simulations of the centrifuge tests focus on oil recovery instead of the displacement processes during testing. Further, as Gudbjerg concluded, the amount of input data was in fact very limited and consequently, he was not able to provide an accurate simulation of the centrifuge displacement tests. Instead, he presented simulations that qualitatively show the effects of varying different parameters and configurations on the oil recovery curve. From these simulations it can be concluded that (at least) the following parameters/configurations have a significant impact on the simulation of the recovery:

- Capillary pressure-saturation relationship
- Relative permeability-saturation relationship
- Matrix and fracture permeability
- Degree of fracturing and the fracture connectivity

If more representative data was available/used in the simulations of the specimens, the author believes that more representative simulations could be obtained, which would improve the understanding of the displacement processes during waterflooding. However, the model should probably be modified to take into account that at strongly water-wet conditions, water flow stop at each fracture until the spontaneous imbibition endpoint water saturation is reached in the preceding matrix block (Graue et al. 1999b). Further, it is not possible to study the concept of a critical waterflooding rate in the simulations of the two centrifuge tests in a similar way as in the actual tests unless a falling hydraulic pressure difference is implemented.

Chapter 8

Waterflooding Hillerslev Chalk during Uniaxial Compaction

This Chapter includes a description of the waterflooding tests in the oedometer cell. Initially, a description of the waterflooding test set-up, procedure and results are included. The displacement processes observed during waterflooding are described. Further, the effect of chalk-water interaction, i.e. water weakening and water induced compaction during waterflooding is described. Finally, the centrifuge and oedometer waterflooding test results are compared.

8.1 Waterflooding Tests Set-up

The waterflooding tests on specimens 9 and 10 were carried out in an oedometer cell. The test set-up consists of an oedometer cell, which is mounted in the MARK-2 set-up. The oedometer cell is a cylindrical form with a bottom plate. At the top, a load piston fits into the form. The load piston is mounted in the MARK-2 set-up. During testing, the load piston was pushed down onto the specimen top by the MARK-2 hydraulic load frame. The maximum capacity of the load frame is 1000 kN, i.e. the maximum vertical stress is approximately 5 MPa. A porous filter plate (D = 50 cm) was adjoined to both the bottom plate and the load piston. The porous filters were punched from 600 × 1200 mm Dynapore TWM-20 five-layer filter media plates of AISI type 316L stainless steel. The fine-masked side face the specimen, and the rough-masked side face the bottom plate and the load piston to distribute the fluids evenly. A sketch of the waterflooding test set-up without the MARK-2 set-up is shown in Figure 8.1, and a photo of the whole set-up is show in Figure 8.2.

An inlet container and two outlet containers were used. The inlet container was used for waterflooding, and the outlet containers were used for displaced oil and produced water. All the containers were placed on balances. The inlet container was placed on weight U1, and the outlet containers were placed on weight U2 and weight U3. The displaced fluids were recorded on a double-balance system, see Figure 8.1 and Figure N.1 in Appendix N. The displaced fluids flow to the outlet container placed on weight U3. This container is a constant volume reservoir measuring the displaced water. When a fluid volume enters the constant volume reservoir, the same volume of oil is displaced to

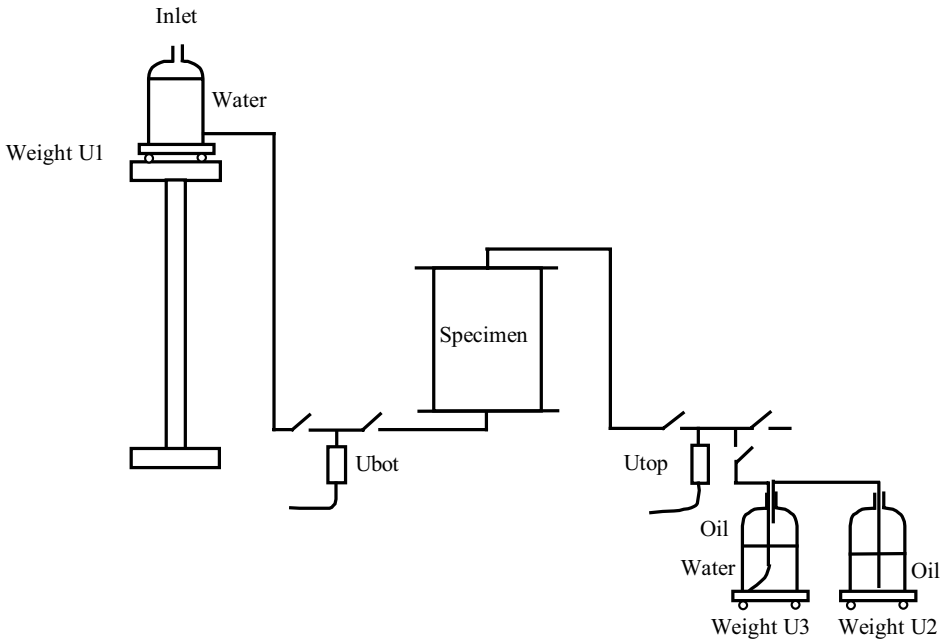

Figure 8.1 *Sketch of the set-up for the waterflooding tests.*

the outlet container placed on weight U2. Due to the difference in the density of oil and water, the displaced volume of water from the specimen is found on basis of a weight increase on weight U3. The outlet container placed on weight U2 is for the total volume of displaced oil. The total volume of injected water is found from weight U1. The volume of oil displaced from the specimen due to waterflooding is found as the total volume of displaced oil minus the volume of produced water.

Water breakthrough into the outlet container placed on weight U3 was detected as an increase on weight U3.

To avoid flow along the side between the cylindrical form and the specimen, gypsum was cast around the specimen, between the specimen and the form.

Two pore pressure transducers (PPTs) were included in the test set-up, Ubot and Utop, to measure the pore pressures during testing. Ubot was used to measure the inlet pressure and Utop was used to measure the outlet pressure, see Figure N.2 and Figure N.3 in Appendix N. The axial deformations were measured by two linear variable displacement transducers (LVDTs). The two LVDTs were placed opposite each other on top of the oedometer cell, treading down on the load piston, measuring the external, axial deformations, see Figure N.4 in Appendix N.

8.1.1 Mounting of the Specimens

Before drying, the trimmed specimen was placed on the porous filter on the bottom plate and wrapped in soft plastic foil. The cylindrical form was placed down around the specimen, and the bottom plate and the cylindrical form were bolted together. Then

Figure 8.2 *Photo of the oedometer cell mounted in the MARK-2 set-up. The inlet container is seen elevated to the left.*

liquid gypsum was poured into the oedometer cell to fill the excess space between the specimen and the oedometer cell. The plastic foil was used to prevent liquid gypsum from entering the fractures of the specimen. The specimen was then dried inside the form in an oven. After drying, the cell was mounted in the MARK-2 set-up, where the load piston was lowered down to the specimen top. The specimen was oil saturated prior to testing by combined vacuum and flow of Isopar-L through the specimen and the equipment.

8.2 Waterflooding Test Procedure

The specimen was loaded to approximately 4.7 MPa at a strain rate of 0.2%/hour by use of the load piston. The loading procedure for the entire test is plotted as axial stress vs. time of testing for specimen 9 in Figure H.1 and for specimen 10 in Figure H.2, Appendix

H. At the desired stress level, the stress was kept constant, and water was injected into the bottom of the specimen.

The waterflooding was performed applying a falling hydraulic pressure difference resulting from the difference in fluid densities and fluid heights in the inlet and outlet containers. Specimen 10 was tested first, then followed the test on specimen 9.

8.3 Waterflooding Test Results

The displacement processes and the effect of the chalk-water interaction during waterflooding of the fractured, oil-saturated chalk specimens were investigated based on:

- Injected and produced volumes of fluids
- Axial deformation measurements
- Saturations and porosities after test

The measured volumes of injected water and produced oil and water are included in Table 8.1. The time until water breakthrough (wbt) at the specimen top after start of waterflooding (wf), i.e. after the water reaches the specimen bottom is included along with the time period for the waterflooding. The total volumes of injected and produced fluids are calculated based on measurements of the weight of the fluids in the inlet and outlet containers during waterflooding. The waterflooding test data are corrected for dead volumes.

Specimen	Injected water [cm^3]	Produced oil [cm^3]	Time to wbt after start of wf	Injected water at wbt [cm^3]	Time period for wf
9	29498	29572	-	-	11479 min.
10	63806	no data	1394 min.	26670	2927 min. incl. a pause of 720 min.

Table 8.1 *Waterflooding test data corrected for dead volumes.*

The displaced volume of water from the specimen is found on basis of weight U3. The total volume of injected water is found from weight U1. The total volume of displaced oil is found from weight U2. The three weights U1, U2 and U3 have a precision of $\pm$ 12 g.

The dead volumes at the bottom (inflow) and the top (outflow) of the test set-up (tubes etc.) are estimated to 1179.85 cm^3 and 239.65 cm^3, respectively.

The volume of injected water into specimen 9 was 29498 cm^3 compared to the specimen pore volume of 41502 cm^3 (before waterflooding), i.e. approximately 0.7 pore volume of water was injected during waterflooding. Water breakthrough was not obtained in specimen 9.

The volume of injected water into specimen 10 was 63806 cm^3 compared to the specimen pore volume of 39365 cm^3 (before waterflooding), i.e. approximately 1.6 pore volume was injected during waterflooding. No oil was displaced after water breakthrough. The volume of produced oil could not be obtained due to problems with the weight U3.

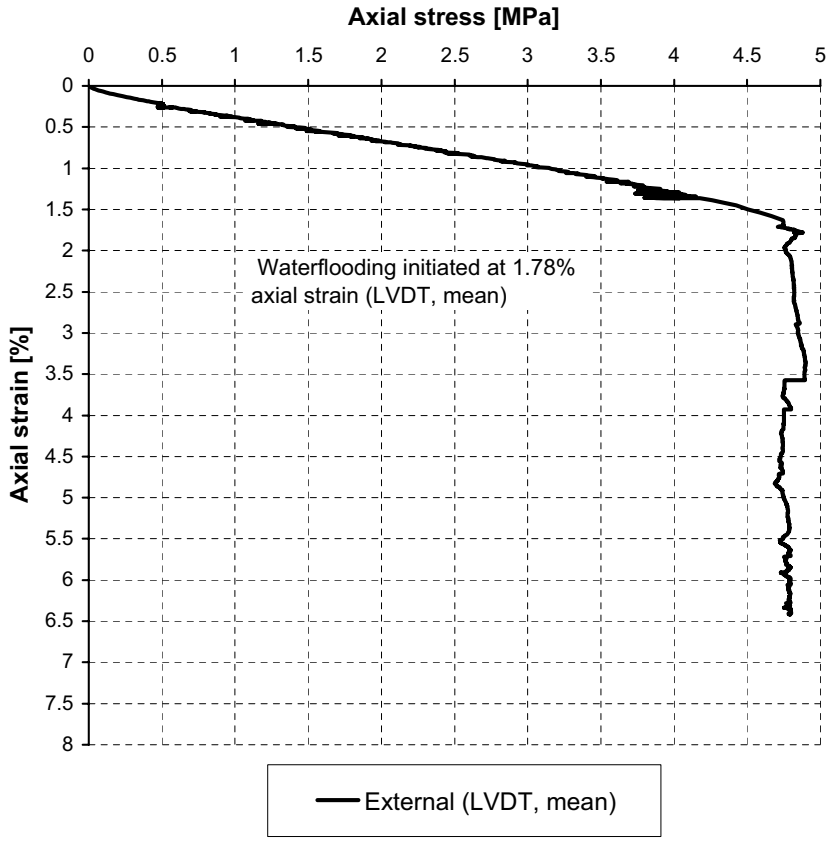

Figure 8.3 *Axial stress vs. axial strain for specimen 9.*

8.3.1 Waterflooding above the Yield Stress

Overview

For both specimens 9 and 10, the oil displacement was dominated by capillary imbibition resulting in a waterfront moving up through the specimens. After water breakthrough in specimen 10 no more oil was produced. Water breakthrough was not obtained in specimen 9.

The imbibition potential of the chalk matrix was so strong that waterflooding resulted in a relatively homogeneous water saturation of approximately 71% throughout both specimens.

There was a distinct effect of waterflooding above the yield stress since significant deformations were seen upon waterflooding.

Specimen 9

The axial stress vs. axial strain during testing is plotted in Figure 8.3. The axial strain is a mean value of the axial strain obtained by the two LVDTs.

Waterflooding was initiated at 1.78% axial strain and resulted in vertical deformations up to 6.42%. Until waterflooding was initiated, the load applied to the specimen resulted in stresses below the yield stress, i.e. the specimen was in elastic state, see Figure 8.3. The 1.78% axial strain before waterflooding is referred to as bulk compaction, and is due to initial apparatus effects, closing of fractures and rearrangement of chalk lumps, but not pore collapse. The yield stress of naturally fractured, oil-saturated Hillerslev outcrop chalk has not been determined in large-scale testing, but the yield stress must be higher than 4.7 MPa, at least for a specimen with a similar fracture network as specimen 9. The significant deformation observed during waterflooding is mainly due to pore collapse, i.e. waterflooding above the yield stress for a partially water-saturated test specimen.

The injected and produced fluid volumes are shown in Figure 8.4 along with the inflow and outflow rates from the time where the specimen reached the final load step of approximately 4.7 MPa. The start of waterflooding is shown as well. Approximately 494 min. after start of waterflooding, a large, instant increase is observed in the inflow and outflow rates. This is due to the strong capillary imbibition (capillary suction) of water into the specimen, as the water reached the specimen bottom at that time. The main reason for the long period until the water reached the specimen bottom is the low hydraulic differential pressure applied initially, see Figure 8.5.

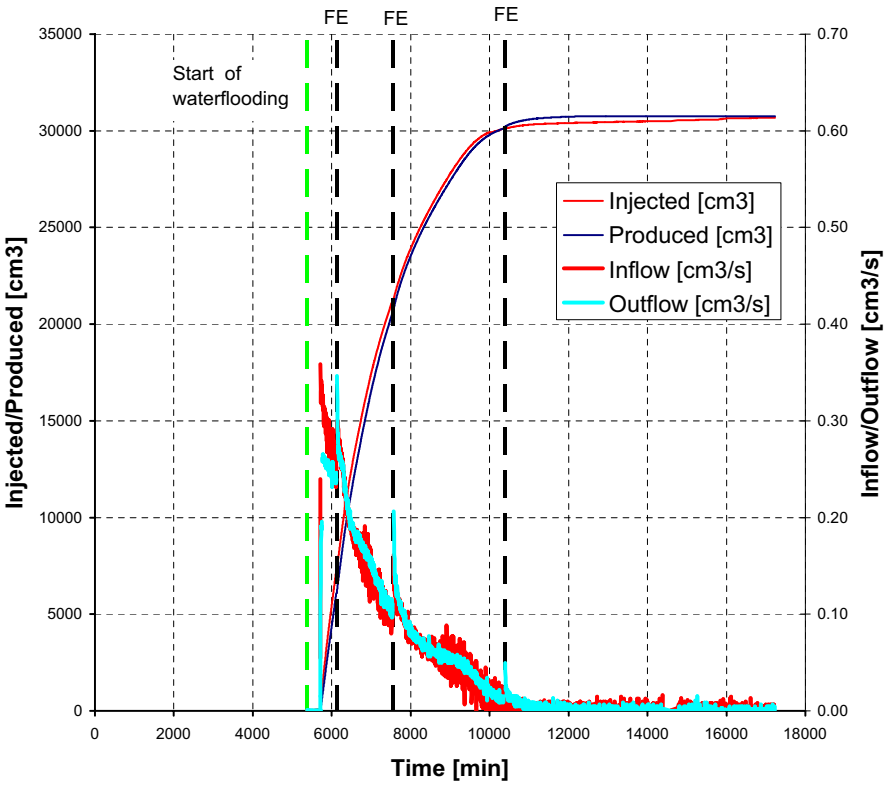

Figure 8.4 *Injected and produced fluid volumes and inflow and outflow rates vs. time from the time where specimen 9 reached the final load step of 4.7 MPa. The plot is not corrected for dead volumes.*

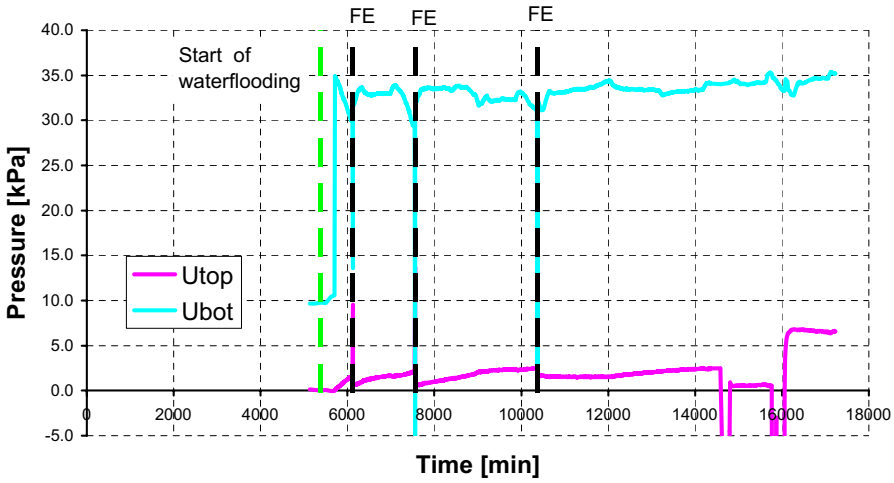

Figure 8.5 *Pore pressures measured at inflow (Ubot) and outflow (Utop) vs. time from the time where specimen 9 reached 4.7 MPa.*

During waterflooding, water was filled into the inlet container and oil was let out of the outlet container placed on weight U2. This was done three times, and is referred to as FE (fill and empty), see Figure 8.4. It is seen as an instant increase in both inflow and outflow rates.

Water breakthrough was not observed in the test. The inflow and outflow rates decreased towards zero. This was observed in spite of the refills with water and outlet of oil. As water breakthrough was not obtained, and the test was not completed, it was considered if the system was somehow blocked by fines. A vacuum pump was used to apply vacuum to the outlet tube. However, this had no effect on the flow, and the test was ended due to the low flow rates.

The inflow and outflow pressures measured by the two PPTs Ubot and Utop, respectively, are shown vs. time in Figure 8.5 from the time where specimen 9 reached the final load step of 4.7 MPa.

The large drops in the pore pressure measured by Ubot at the end of the test is due to application of vacuum. The instant drop in inflow pore pressures at FE is due to that the inlet container was lowered down for refill and elevated again. As a similar hydraulic pressure difference was applied over the specimen throughout the test, see Figure 8.5, the reduction in flow must be due a reduction in capillary suction as the waterfront moved through the specimen. In other words, the imbibition into the specimen was primarily driven by capillary forces and not the hydraulic pressure difference.

Specimen 10

The axial stress vs. axial strain during testing is plotted in Figure 8.6. The axial strain is a mean value of the axial strain obtained by the two LVDTs.

Waterflooding was initiated at 3.14% axial strain and resulted in vertical deformations up to 7.18%. Until waterflooding was initiated, the load applied to the specimen resulted in stresses below the yield stress, i.e. the specimen was in elastic state, see Figure 8.6.

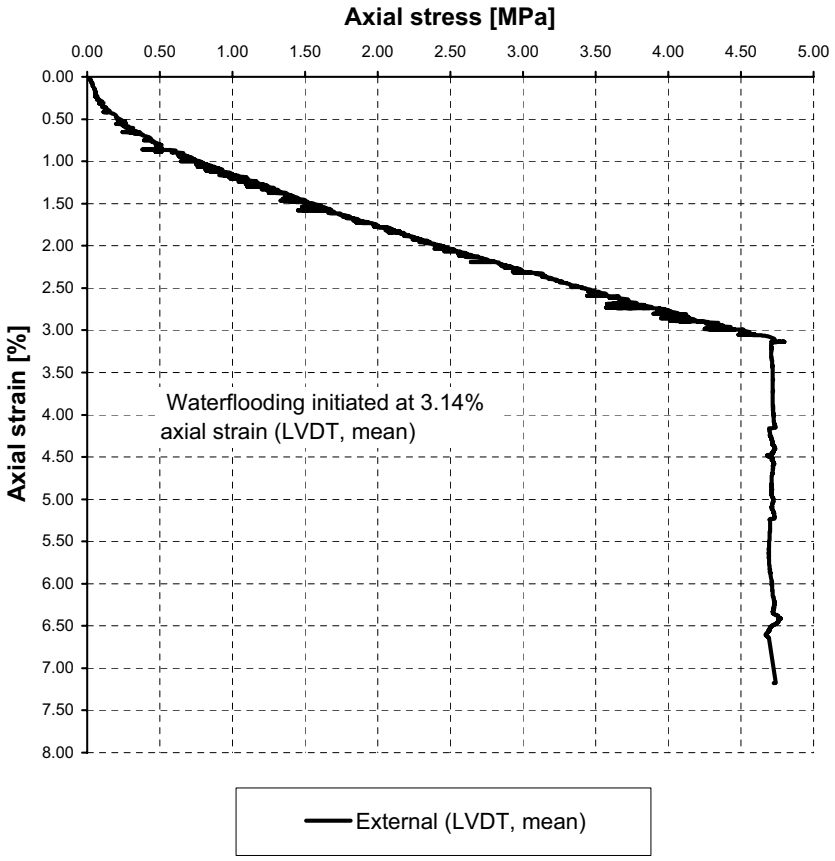

Figure 8.6 *Axial stress vs. axial strain for specimen 10.*

The 3.14% axial strain before waterflooding is referred to as bulk compaction, and is due to initial apparatus effects, closing of fractures and rearrangement of chalk lumps, but not pore collapse. Again, the yield stress must be higher than 4.7 MPa, at least for a specimen with a similar fracture network as specimen 10. The significant deformation observed during waterflooding is mainly due to pore collapse, i.e. waterflooding above the yield stress for a partially water-saturated test specimen.

The injected and produced fluid volumes are shown in Figure 8.7 along with the inflow and outflow rates from the time where the specimen reached the final load step of approximately 4.7 MPa. The start of waterflooding is shown as well. Approximately 80 min. after start of waterflooding, a large, instant increase is observed in the inflow and outflow rates. This is due to the strong capillary imbibition (capillary suction) of water into the specimen, as the water reaches the specimen bottom at that time.

During waterflooding, the valves to the inlet and outlet containers were closed for approximately 720 min., i.e. the waterflooding was stopped in that period. The closing of the valves (CV) and opening of the valves (OV) is indicated in Figure 8.7. Just before the valves were opened, more water was filled into the inlet container and oil was let out

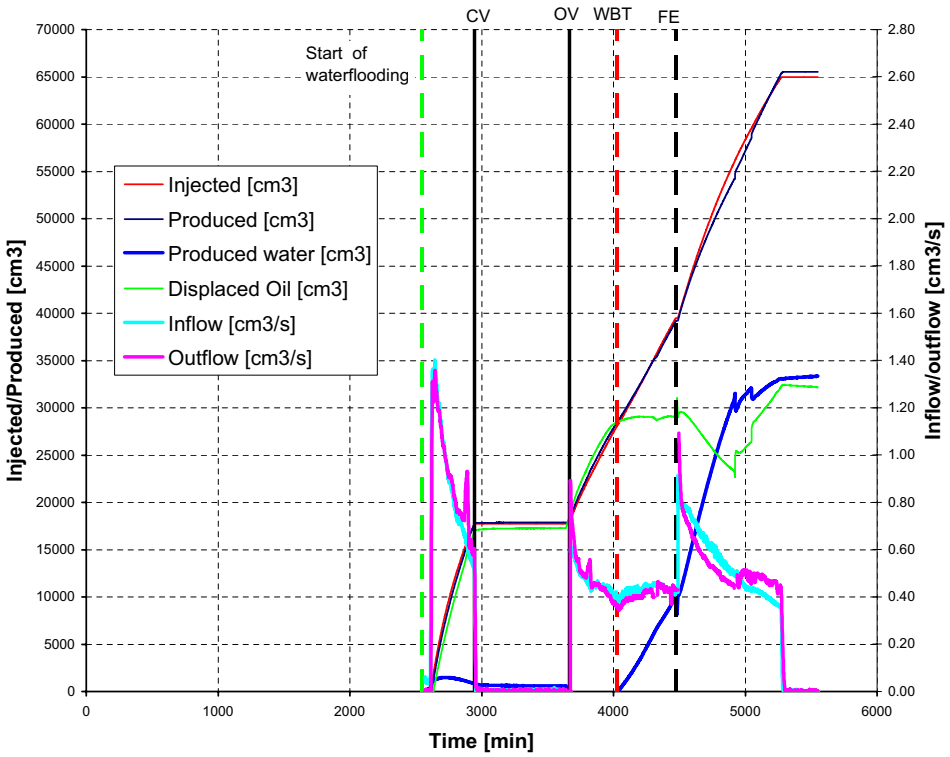

Figure 8.7 *Injected and produced fluid volumes and inflow and outflow rates vs. time from the time where specimen 10 reached the final load step of 4.7 MPa. The plot is not corrected for dead volumes.*

of the outlet container placed on weight U2. This, along with opening of the valves is seen as an instant increase in both inflow and outflow rates. Later in the test, more water was filled into the inlet container and more oil was let out of the outflow container placed on weight U2. This is referred to as FE (fill and empty) and indicated in Figure 8.7. Again, an instant increase is seen in both inflow and outflow rates.

Water breakthrough (WBT) into the outflow container placed on weight U3 is indicated in Figure 8.7.

Shortly after FE, the calculated amount of displaced oil was found to decrease during a period of approximately 390 minutes, then it increased again. A decrease in the amount of oil displaced from the specimen is of course not possible. The reason for this observation is due to problems with the weight U3 during waterflooding. Further, at the end of the test, the constant volume container on weight U3 was filled with water and consequently water was let into the total outflow container on weight U2. It was not possible to correct properly for these observations. However, based on the data, it is evaluated that the inflow data (injected water and inflow rate) are correct throughout the test, and the other data are correct until FE.

The inflow and outflow pressures measured during waterflooding by the two PPTs Ubot and Utop, respectively, are shown vs. time in Figure 8.8 from the time where the specimen reached the final load step of 4.7 MPa.

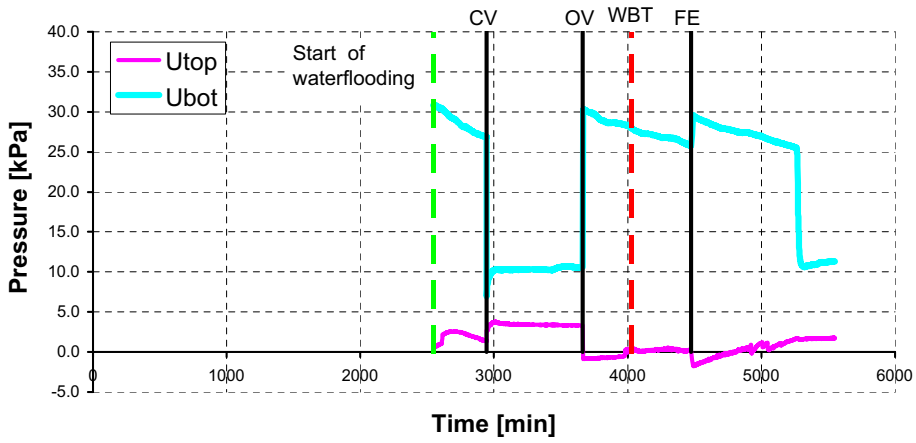

Figure 8.8 *Pore pressures measured at inflow (Ubot) and outflow (Utop) vs. time from the time where specimen 10 reached 4.7 MPa.*

Distribution of Fluids after Waterflooding

After waterflooding, the specimens were disassembled, and 42 small samples were taken from each of the two tested specimens using hammer and chisel for determination of mean saturations using Archimedes' principle for volume determination. Six samples were taken at seven different levels along the specimen. The saturation of the small samples were determined at DTU by the method described in Section 6.4.1.

The bulk fluid saturations based on mean values of the small samples are included in Table 8.2. Further, the mean values of dry density, void ratio and porosity of the small samples are included in Table 8.2, along with the standard deviations from the mean values of the porosity (in parentheses). The mean values are similar for the two specimens.

Specimen	ρ_d [g/cm^3]	e [-]	ϕ (st.dev.(ϕ)) [%]	S_o [%]	S_w [%]
9	1.463	0.847	45.8 (1.18)	26.1	73.9
10	1.463	0.847	45.8 (1.34)	29.7	70.3

Table 8.2 *Bulk fluid saturations based on mean values of the small samples taken out after waterflooding.*

The mean saturation vs. the distance to the specimen bottom are shown in Figure 8.9 for specimens 9 and 10, and in Appendix M for both specimens.

A high overall water saturation is seen in both specimens. This indicates that a waterfront moved through both specimens.

For specimen 9, water breakthrough was not obtained, i.e. no water was produced. The injected, i.e. the imbibed volume of water (Table 8.1) corresponds to a mean water saturation in the range of 72-78% based on an estimation of the pore volume after waterflooding with or without water saturation of the gypsum. This illustrates that the large amount of gypsum around the specimen has an effect on the saturation. A mean

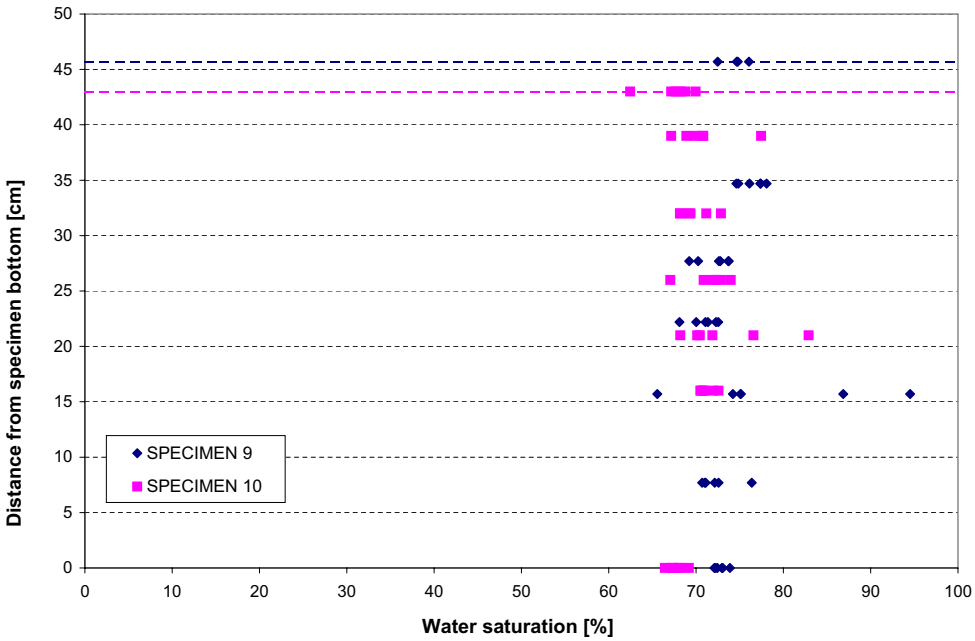

Figure 8.9 *Sketched saturation profiles based on mean saturation measured on the small samples taken from the specimens after test. The specimen heights are indicated in the plot (dotted lines).*

saturation within this range is consistent with the water saturation plot in Figure 8.9 for specimen 9. Based on the saturation plot, it is evaluated that the waterfront must have been close to the specimen top, i.e. close to water breakthrough as a high water saturation of at least 70% was encountered throughout the specimen.

The water breakthrough for specimen 10 occurred after injection of approximately 26670 cm^3 water into the specimen. This imbibed volume of water corresponds to a mean water saturation in the range of 70-75% based on an estimation of the pore volume after waterflooding with or without water saturation of the gypsum. Again, the effect of the large amount of gypsum used is illustrated. A mean saturation within this range is consistent with the water saturation plot in Figure 8.9 for specimen 10.

The mean porosity determined on basis of the small samples taken out after waterflooding is slightly lower than the mean matrix porosity of 47% used in the calculations for the large specimens, see Section 5.2. As pore collapse is evaluated to have occurred during waterflooding, the porosity is expected to be reduced. Most of the porosities of the small samples are in the range from 43-46%, i.e consistent with a porosity reduction. The reason for the mean porosity of 45.8% is due to that some of the small samples showed no signs of compaction, i.e. the determined porosities were close to 47%. The porosity vs. the distance to the specimen bottom are shown in Figure 8.10 for specimens 9 and 10.

Compaction (pore collapse) due to waterflooding happens at the first contact with the injected water, i.e. as water moves through the chalk so does the zone of highest compaction. This means that a similar compaction was expected throughout both specimens, i.e. a similar reduction in porosity, since a waterfront had moved through both specimens. However, it is clear from Figure 8.10 that instead a similar porosity profile

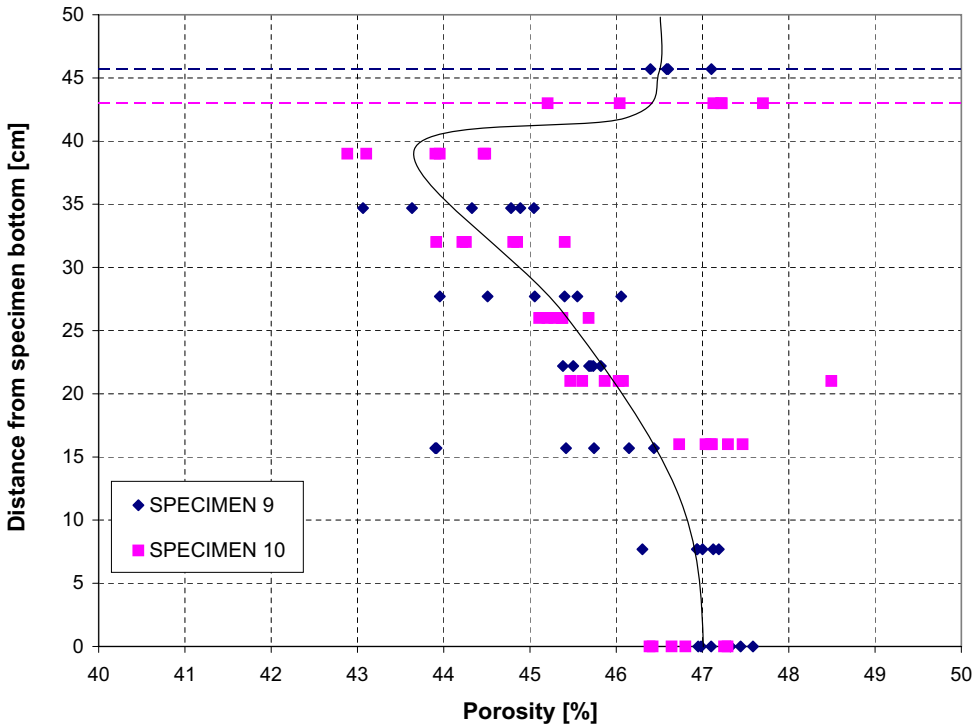

Figure 8.10 *Porosity profile for specimens 9 and 10 based on the small samples taken from the specimens after test. The specimen heights are indicated in the plot (dotted lines).*

has been introduced in both specimens. A reduced porosity is seen in the upper 2/3 of the specimen, but not in the specimen bottom.

The reason for the porosity profile obtained in the specimens is evaluated to be due to friction between the specimen and the fixed form and the gypsum resulting in transmission of stresses from the specimen to the form and from the gypsum to the form. This results in that the upper 2/3 of the specimen has been subjected to higher stresses than the lower 1/3 of the specimen. From the porosity plot it is evaluated that the specimens were above the yield stress in the upper 2/3, but not in the lower 1/3 of the specimen.

Consolidation Modulus

The elastic consolidation modulus K defining the bulk compaction below the yield stress is determined using equation (2.27) on basis of the mean axial strain obtained by the two LVDTs. The consolidation modulus is included in Table 8.3 for both specimens.

The difference in consolidation modulus is evaluated to be due to the different fracture networks in the two specimens.

For comparison, the mean consolidation modulus for large ($D \approx 50$ cm, $H \approx 50$ cm), naturally fractured, water-saturated Hillerslev outcrop chalk specimens was determined to $K_{mean} = 255$ MPa ranging from 165-470 MPa with a standard deviation of 110 MPa (Havmøller & Krogsbøll 2001). The consolidation modulus was determined for initial compaction in multiple triaxial tests.

Specimen	Consolidation modulus [MPa]
9	300
10	188

Table 8.3 *Consolidation modulus K for specimens 9 and 10.*

The consolidation modulus for the oil-saturated specimens 9 and 10 and the water-saturated specimens are similar even though Havmøller (Havmøller 1998) found that the elastic consolidation modulus decrease as the chalk change from oil-saturated to water-saturated. This expected decrease was not seen due to the problems with side friction along the oil-saturated specimens. Further, it is difficult to compare test results for oil-saturated and water-saturated specimens with different fracture networks. A comparison should be performed for test results obtained on the same specimen.

Creep and Water-Induced Compaction

A creep phase was included in the oil phase at 0.5 MPa for specimen 9. The axial strain vs. time is plotted in a log-linear plot in Figure O.1, Appendix O. For specimen 10, a creep phase was included in the oil phase at 1 MPa and just before the waterflooding at 4.7 MPa. The axial strain vs. time is plotted in a log-linear plot in Figure O.4 and O.5, Appendix O. Further, the axial strain vs. time during waterflooding is plotted in a log-linear plot in O.2 for specimen 9 and Figure O.6 for specimen 10, both in Appendix O. The data obtained from these creep phases include the load step, the initial strain $\varepsilon_{1,initial}$ and the final strain $\varepsilon_{1,final}$ for the creep phase, the additional strain per time decade during creep ε_s and the base time T_0, and are listed in Table 8.4.

Specimen	Load	$\varepsilon_{1,initial}$ [%]	$\varepsilon_{1,final}$ [%]	ε_s [%/time decade]	T_0 [min.]
9	0.5 MPa	0.2146	0.2599	0.003	0.5
	4.7 MPa (waterflooding)	1.7831	6.1931	3.6	550
10	1 MPa	1.1611	1.1659	0.002	5
	4.7 MPa	3.1358	3.1385	0.006	340
	4.7 MPa (waterflooding)	3.1385	7.1768	1.3	90

Table 8.4 *Creep data for specimens 9 and 10.*

From the data in Table 8.4, it is clear that creep is dependent on the water saturation. A much higher additional strain per time decade is seen during waterflooding than at constant load in the oil phase. This is especially clear when comparing ε_s for creep in the oil phase at 4.7 MPa for specimen 10 just before waterflooding and ε_s for waterflooding at

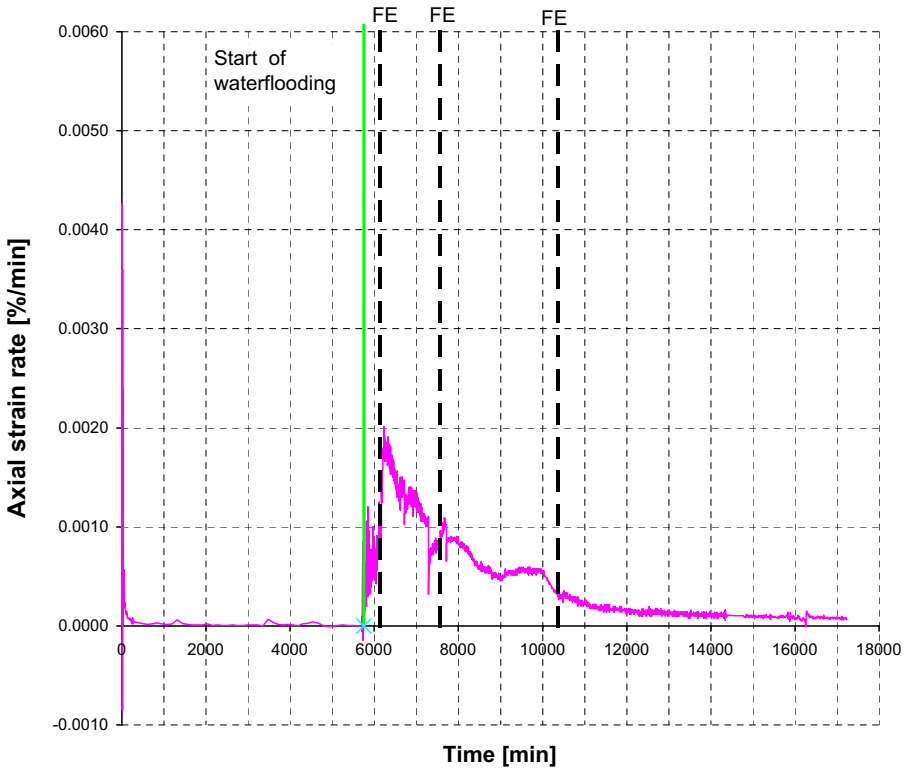

Figure 8.11 *Strain rate vs. time from the time where specimen 9 reached the final load step of 4.7 MPa. The plot is corrected for dead volumes.*

4.7 MPa. The base time T_0 at zero additional creep is relatively high for the waterflooding of specimens 9 and 10. This is may be due to effects of the side friction.

The amount of total axial strain during waterflooding is 4.64% for specimen 9 and 4.04% for specimen 10. This is plotted vs. time from the time where specimens 9 and 10 reached the final load step of 4.7 MPa in Figure O.3 and Figure O.7 in Appendix O, respectively.

The strain rate $\dot{\varepsilon}_{creep}$ vs. time from the time where specimen 9 reached the final load step of 4.7 MPa is shown in Figure 8.11. The strain rate was low initially, then the strain rate increased instantly as the water reached the specimen bottom during waterflooding. In this case a peak in strain rate was observed at the first two times of refill and emptying (FE). Otherwise, the strain rate was decreasing over time.

The strain rate $\dot{\varepsilon}_{creep}$ vs. time from the time where specimen 10 reached the final load step of 4.7 MPa is shown in Figure 8.12. Initially the strain rate was low, then the strain rate increased instantly as the water reached the specimen bottom during waterflooding. After water breakthrough an almost constant strain rate was seen for approximately 250 min., then, a peak is observed in the strain rate. The reason for this is evaluated to be due to differential compaction due to boundary effects as side friction, i.e. transmission

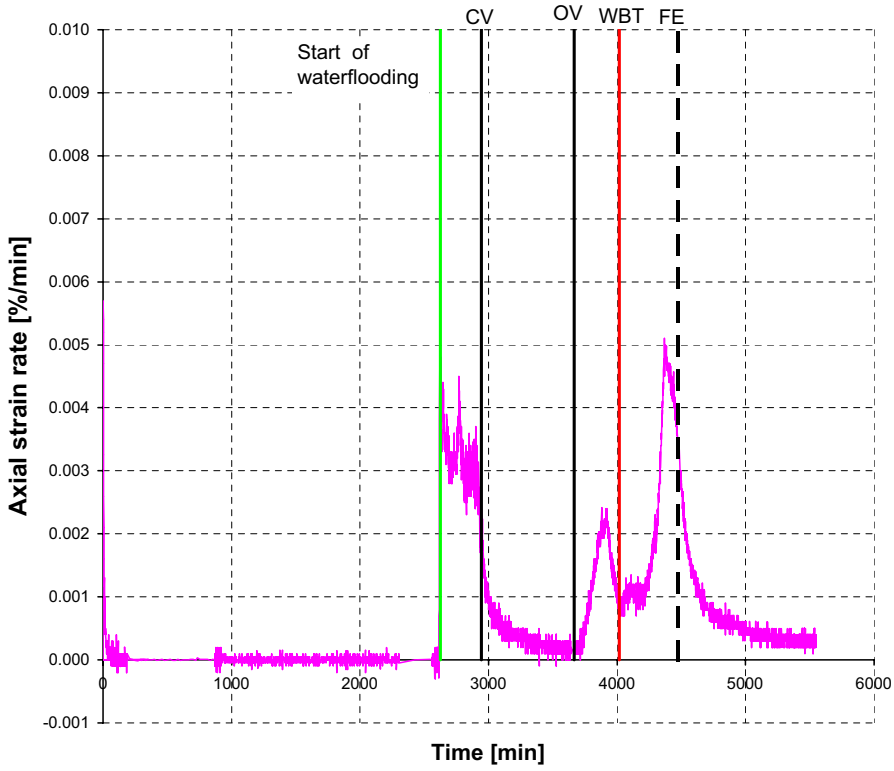

Figure 8.12 *Strain rate vs. time from the time where specimen 10 reached the final load step of 4.7 MPa. The plot is corrected for dead volumes.*

of stresses prevents the specimen from a homogeneous compaction. The side friction may have changed during the test. In other words, problems with testing in an oedometer cell and problems with the use of gypsum.

8.4 Evaluation of the Results

Displacement of oil in specimen 10 was due to a waterfront moving through the specimen, i.e. a domination of capillary imbibition. Water breakthrough was obtained due to plug flow, and consequently no oil was displaced after water breakthrough.

Specimen 9 was altered in the oil phase by fracture closing due to the high stress level. The alteration resulted in a reduction in the absolute oil permeability from 45 mD to 2 mD. However, a waterfront moved through the specimen in spite of the permeability reduction. This is due to the strong capillary imbibition (capillary suction) of water into the strongly water-wet specimen, which was reduced as the waterfront moved through the specimen. The capillary suction was reduced to zero as the waterfront approached the specimen top. Due to the reduction in permeability and capillary suction, the inflow and outflow rates decreased and water breakthrough was not obtained, even though the

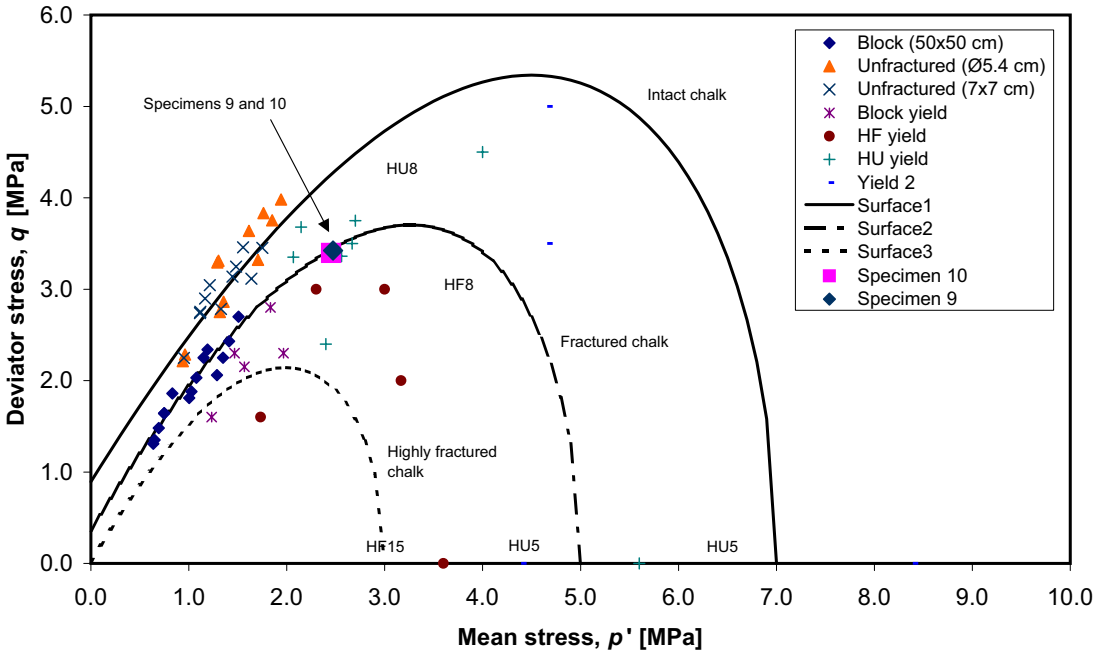

Figure 8.13 *Combined yield and failure surface for water-saturated Hillerslev outcrop chalk, from (Havmøller & Krogsbøll 2001). Data for specimens 9 and 10 are included.*

hydraulic pressure difference over specimen 9 was a little higher than over specimen 10. The reason for water breakthrough in specimen 10 and not in specimen 9 can be explained by the higher permeability in specimen 10 due to the presence of fractures at the high mean stress level. This illustrates the significance of fractures in the chalk, resulting in a more efficient (or at least faster) oil displacement upon waterflooding, especially at such low flow rates.

The yield stress was reduced in both specimens due to water weakening upon waterflooding. Both specimens showed significant deformations upon waterflooding above the yield stress, i.e. oil was also displaced due to water-induced compaction. It was seen that creep is dependent on the water saturation.

Rock Mechanics Model for Fractured Hillerslev Chalk

A rock mechanics model suggested by Papamichos et al. ((Havmøller & Krogsbøll 2001) and references therein) developed to describe chalk-water interaction was applied to test series on water-saturated Hillerslev outcrop chalk specimens (Havmøller & Krogsbøll 2001). This was explained in Section 3.4. Figure 8.13 illustrates the model for combined yield and failure surface for water-saturated Hillerslev chalk, where HF and HU refers to normal-scale tests on fractured and un-fractured Hillerslev chalk specimens, respectively. Surface 1 is for intact chalk specimens, with increasing degree of fracturing for surface 2 and surface 3.

The data for the large-scale oedometer tests on specimens 9 and 10 are included in Figure 8.13. Since the stresses in the lateral direction are unknown in an oedometer test,

the mean effective stress p' and the deviatoric stress q is found assuming that the chalk specimens are at rest, see Section 5.3.1. The mean effective stress is thus found using equation (5.3), and the deviatoric stress q is found using equation (5.4) with $K_0 = 0.28$. As seen in Figure 8.13, the specimens have reached the yield stress for fractured specimens (surface 2). This is consistent with the fact that the partly water-saturated specimens were above yield and that the specimens are fractured, but not highly fractured (surface 1).

As seen in Figure 8.13, the combined yield and failure surfaces for water-saturated Hillerslev outcrop chalk depend on the degree of fracturing. It is thus difficult to obtain a conceptual model for chalk-water interaction for fractured Hillerslev outcrop chalk in general. However, a model for chalk-water interaction may be obtained based on tests on specimens with similar fracture patterns.

8.5 Comparison of the Results

The waterflooding test results for specimens 9 and 10 in the oedometer cell are compared to the waterflooding test results for specimens 2, 5, 7, 8 and 11 in the centrifuge.

Specimen 10 was similar to specimen 7. Both specimens contained few fractures. Specimen 10 had a single, almost vertical fracture continuing from the bottom to the top. Similarly, specimen 7 had a single, almost vertical fracture continuing from the lower horizontal fracture plane to the top. Both specimens had a constant effective oil permeability with increasing mean stress of 5 mD for specimen 10 and 8 mD for specimen 7. The constant permeability was seen at high mean stress levels for specimen 10, and it is evaluated that this would also have been the case for specimen 7 at higher mean stress levels. However, the displacement processes during waterflooding were different in the two specimens. For specimen 7, flow of water in the single, almost vertical fracture continued after water breakthrough. However, a distinct waterfront was seen below the lower horizontal fracture plane due to the strong capillary imbibition potential and forced imbibition. For specimen 10, the oil displacement was dominated by capillary imbibition resulting in a waterfront moving up through the specimen. The lower flow rate along with a full capillary imbibition potential (reduced in the centrifuge) is responsible for the difference in displacement processes in the two specimens.

The oil displacement in specimen 9 was also dominated by capillary imbibition resulting in a waterfront moving up through the specimen. The reduction in permeability due to fracture closing upon loading was a problem as the oil displacement ceased before water breakthrough, i.e. the waterflooding was not completed. Further, the displacement was time consuming. Based on the observations in this test, it is evident that hydraulic fracturing along with forced imbibition may be necessary for an economic waterflood. Efficient oil displacement by waterflooding was seen especially in the extensively fractured specimens 5 and 8 in the centrifuge as a result of capillary imbibition from the fractures and forced imbibition.

The low rate waterfloods in the oedometer cell were dominated by capillary forces. The high rate waterfloods in the centrifuge were initially dominated by viscous forces, but for the three most fractured water-wet specimens, a shift towards capillary domination was observed as the flow rate decreased.

An effect of applying higher stresses to the specimens tested in the oedometer cell than in the centrifuge was seen especially since the permeability of specimen 9 was reduced. Further, a significant compaction was observed when waterflooding at a higher stress level.

Based on a comparison of the porosity plots for the specimens tested in the centrifuge shown in Figure 6.26 and the specimens tested in the oedometer cell shown in Figure 8.10, it is evaluated that the prevention of side flow using liquid rubber mass does not induce a porosity profile as was seen when using liquid gypsum. However, the main reason for using gypsum instead of rubber was that it is far more expensive to use rubber.

Further, it is evaluated that a more homogeneous porosity- and stress profile would have been obtained in the specimens in a triaxial cell than the results obtained in the oedometer cell.

Chapter 9

Waterflooding Field Evidence

9.1 Valhall Field

The Valhall reservoir was the first oil discovery in the Norwegian sector of the North Sea. Hydrocarbons were first encountered on the Valhall structure in 1969, but the field was not declared commercial until 1976. Production of oil commenced in 1982 (Leonard & Munns 1987). Valhall is operated by BP on behalf of Amerada Hess, Enterprice, TotalFinaElf and BP (Offshore Technology 2004).

A waterflood pilot was carried out from 1990 to 1993 in the highly permeable crestal area of the Valhall Tor formation. In this area, the matrix porosity was measured to 38-45% and the matrix permeability to around 4 mD. The fracture porosity was estimated to 0.3% and the effective permeability in the range of 6-45 mD (Eltvik & Settari 1992), i.e. the natural fractures enhance the matrix permeability with a factor of up to around 10. The pilot consisted of one injector A-4A, and three producers A-1, A-3A and A-8. Initially, water was injected at a low rate. However, it was necessary to inject the water above the formation parting pressure (fpp) to obtain a waterflooding rate high enough for an economic full field waterflood. The fpp is the pressure at which a fracture can grow (hydraulic fracturing). The fracture can grow, shrink or become stable depending on the rate of waterflooding, the pressure of the formation fluids, and the formation temperature. One concern with injecting water above the fpp is that the growth of the fracture shall be limited. If the fracture grows too large, the area sweep efficiency may suffer. The size of the induced fracture is dependent primarily on the waterflooding rate (Andersen 1995).

Production response to the waterflooding was observed in the three surrounding producers. However, water breakthrough in the waterflood pilot occurred in only one producer A-1 in September 1991, which was located in a fractured part of the reservoir. It was concluded that viscous displacement dominated over spontaneous imbibition and gravity drainage in displacement of oil by waterflooding in the Valhall Tor formation (Eltvik et al. 1990). This observation supported the idea that there was not a complete fracture network from the pilot injector to the producers (Andersen 1995). The above is interpreted as a domination of viscous displacement in the fractures, and forced imbibition driven by a pressure gradient in the matrix. Both in the fractures and the matrix, the viscous forces dominated due to the high rate.

Almost all the studies prior to the pilot concluded that waterflooding Valhall would

not be successful mainly due to the poor imbibition results from Valhall core tests, but also due to the weak Valhall chalk and possible effects of chalk-water interaction. Earlier measurements on Valhall Tor formation cores indicated spontaneous imbibition of only 5-10% water. These results, in addition to a wettability characteristic of neutral to slightly oil-wet did not favor waterflooding as a drive mechanism. However, later tests on cores from the waterflood pilot at Valhall indicated spontaneous water imbibition as high as 20%, and tests on the same core material showed a neutral to weakly water-wet system (Eltvik et al. 1990). As both spontaneous oil and water imbibition have been reported, the Valhall Tor formation may have a fractional-wettability. The most recent laboratory tests on Valhall Tor formation samples (personal communication with BP Norway 2004) with initial water saturations $< 10\%$ showed an increase in water saturation to 28-33% due to spontaneous water imbibition. The residual oil saturation S_{orw} after imbibition was in the range of 15-16%. Further, there were strong indications of water-wet behavior for waterfloods at reservoir conditions, but there were also indications of some oil-wet surfaces, i.e. a fractional-wettability. Low rate waterfloods ($1.1 \cdot 10^{-3}$cm^3/s) were capillary dominated, whereas high rate waterfloods (0.11 cm^3/s) were viscous dominated and drained down to a relatively low residual oil saturation.

The conclusion of the waterflood that viscous displacement dominated over spontaneous imbibition in displacement of oil by waterflooding in the Valhall Tor formation is in agreement with the observations for high rate waterfloods in the laboratory tests.

A review of the Valhall waterflood pilot was carried out in 1993 (personal communication with BP Norway 2004). The entire waterflood pilot can be divided into two periods. The first one, from the start of the pilot in January 1990 to March 1993, demonstrated that the pilot worked better than expected. The second period, from March 1993 up to end August 1993, where A-1 ceased flowing, presented a different situation in the pilot area. It was confirmed that water was injected into the Paleocene above the Tor formation, and the failure of A-1 indicated Paleocene waterflood being responsible. The Paleocene mainly consists of shale and clay stones, with very low porosities and permeabilities. However, applying a sufficient injection pressure, the Paleocene can be fractured. A likely scenario was injection through a possible well failure in A-4A into the upper zones in Paleocene. A-4 showed injection pressure anomaly, and A-1 water-cut decreased rapidly from March 1993. A-1 failed after a surge of water and solids production at the end August 1993, and shortly after the injection was stopped. The solids consisted of clay originating from upper Paleocene zones. The sudden surge of water and solids production as well as other indications point to that the upper Paleocene was waterflooded since March 1993. A-1 failure is therefore most likely due to water breakthrough from the water swollen upper Paleocene clays, i.e. clay swelling could have caused the A-1 failure.

Overall, the pilot results increased the confidence in full field waterflooding in the Valhall Tor formation, and waterflooding was initiated recently.

The Valhall field has been producing in over 20 years of primary depletion (Barkved et al. 2003). Approximately 50% of the drive has been from rock compaction. A relatively constant subsidence rate around 25 cm/year has been observed in the Valhall field from the initial measurements of 0.5 m in 1985 and until today. The platforms have subsided a total of 4.9 m since start of production. The reason for the subsidence is the reservoir compaction, which is transferred through the overburden to the seafloor as subsidence.

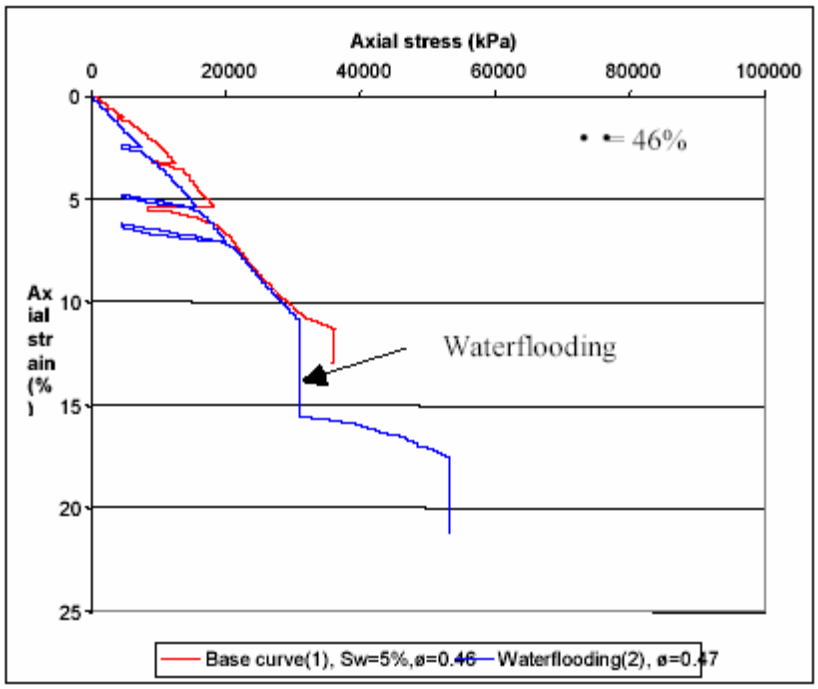

Figure 9.1 *Stress-strain curve for a typical Valhall chalk specimen. The curve shows how the chalk responds to water, from (Barkved et al. 2003).*

Due to the complicated microstructure, the chalk is strain rate sensitive. Deformations at constant stress have shown a logarithmic creep response. Due to water weakening, compaction and subsidence is expected to continue in the Valhall field after waterflooding. A stress-strain diagram of a typical Valhall chalk specimen is shown in Figure 9.1. The strain response is characterized with a close to elastic response at low stress levels. The stress-strain curve shows how chalk creeps upon waterflooding.

9.2 Comparison of the Waterflooding Tests and Field Evidence

The Valhall field observations revealed a domination of viscous displacement in the fractures, and forced imbibition driven by a pressure gradient in the matrix. Water breakthrough occurred in only one producer located in a fractured part of the reservoir. The displacement processes are evaluated to be influenced by the wettability of the Valhall Tor formation, which was earlier described as being neutral to slightly oil-wet/slightly water-wet. However, the recent laboratory tests describe the Valhall Tor formation as being fractional-wet showing water-wet behavior in waterfloods. Further, it was found that low rate waterfloods were capillary dominated, whereas high rate waterfloods were viscous dominated. The observations from the waterflood pilot is consistent with the laboratory observations of a high rate waterflood being viscous dominated. The fact that water breakthrough was only seen in one producer in a fractured part is due to the presence of fractures and may be due to a fractional wettability of the reservoir similar to what was seen in the fractional-wet specimen 2 in the centrifuge tests.

In spite the fact that specimen 2 was extensively fractured, with a well-connected fracture network, a continued flow of water in the fractures was observed in the fractional-wet specimen. As drainage is assumed to be relatively low in the oil-wet parts, flow of water in the fractures may have been able to continue, but imbibition was dominating in the water-wet parts of the specimen. Forced drainage, resulting from the applied hydraulic pressure difference, may have increased the water saturation to some degree in the oil-wet parts. Overall, a high water saturation was obtained in the specimen.

As observed in the field, see Figure 9.1, a distinct effect of waterflooding above the yield stress was also observed in specimens 9 and 10 in the oedometer cell.

Based on the sparse information on the waterflooding field evidence in the Valhall Tor formation, it is not possible provide a more detailed comparison with the present waterflooding test results.

The fracture network and the wettability are believed to be the two main factors influencing the displacement processes during waterflooding.

Chapter 10

Conclusions

Waterflooding tests were performed on seven large ($D \approx 50$ cm, $H = 43$-50 cm), oil-saturated, naturally fractured Hillerslev chalk specimens. Five of the specimens were tested in a centrifuge, and the remaining two specimens were tested in an oedometer cell.

It was found experimentally that Hillerslev outcrop chalk is strongly water-wet and that the wettability can be altered towards less water-wet by aging the chalk saturated with the laboratory oil Isopar-L added 0.5 weight% Dodekane acid. Consequently, six of the tested specimens were strongly water-wet, whereas the wettability of a single specimen was altered to a fractional-wet state to resemble Valhall Tor formation chalk best possible before testing in the centrifuge.

The oil permeability tests showed that the presence of fractures increased the matrix permeability with a factor of up to 100-130. Both constant permeability and permeability reduction was observed with increasing mean stress. The specimens with a high initial permeability (≥ 45 mD) showed a dependency on mean stress, i.e. an effect of the fracture degree. The difference in stress dependency is mainly due to different fracture patterns.

In the centrifuge tests, flow of water in the fractures, dominated initially over capillary imbibition of water from the fractures into the matrix in the four water-wet specimens, and water breakthrough was obtained by flow of water in the fractures ahead of the waterfront. However, for the three most fractured water-wet specimens, a combination of a strong capillary imbibition potential of the chalk matrix, a well connected fracture network with many branches and a reduction in the flow rate, resulted in a shift from a domination of flow of water in the fractures to a domination of capillary imbibition. This means that water in the fractures imbibed into the surrounding matrix, expelling oil into the fractures where it was displaced by water. For the least fractured water-wet specimen, a domination of flow of water in the fractures continued after water breakthrough. The continued flow of water in the fractures was due to water running in a single, almost vertical fracture connected from the lower horizontal fracture plane to the top of the specimen, with very few branches. A distinct waterfront was observed in all four specimens. In the fractional-wet specimen, a domination of flow of water in the fractures was seen, which continued after water breakthrough. This was seen in spite the specimen being extensively fractured. Imbibition dominated in the water-wet parts of the specimen, and drainage may have increased the water saturation in the oil-wet parts.

Both displacement processes: viscous displacement in the fractures and in the matrix

(forced imbibition) and capillary imbibition from the fractures into the chalk matrix were seen. Based on these tests it is concluded that the displacement processes are affected by the fracture pattern, and not just the degree of fracturing. The more extensively fractured, and the more interconnected the fracture systems were, the more capillary imbibition dominated. The displacement processes are also affected by the wettability. Further, the displacement processes are affected by the flow rate.

It was validated that the TDR principle can be used to indicate the position of water in the fractures and the waterfront during testing.

It is evaluated that the centrifuge can be used for modelling and up-scaling of waterflooding tests on the large, naturally fractured Hillerslev outcrop chalk specimens. Centrifuge scaling factors were derived for the specimens.

In the oedometer tests, the oil displacement was dominated by capillary imbibition resulting in a waterfront moving up through the specimens. A large permeability reduction was observed in one of the specimens. However, a waterfront moved through this specimen in spite of the permeability reduction. This is due to the strong capillary imbibition of water into the strongly water-wet specimen. Due to the reduced permeability and the reduction in capillary imbibition as the waterfront moved to the specimen top, the flow decreased and water breakthrough was not obtained in spite the hydraulic pressure difference over the specimen. A reduction in permeability due to fracture closing at high stresses is thus a problem for oil displacement by waterflooding increasing the displacement time. Based on the observations in these tests it is evaluated that hydraulic fracturing along with forced imbibition may be necessary for an economic waterflood.

The yield stress was reduced in the specimens due to water weakening upon waterflooding. There was a distinct effect of waterflooding above the yield stress since significant deformations were seen during waterflooding, i.e. oil was also displaced due to water-induced compaction. It was seen that creep is highly dependent on the water saturation.

It is evaluated that the prevention of side flow using liquid rubber mass does not induce a porosity profile as was seen when using liquid gypsum. Further, it is evaluated that more homogeneous porosity and stress profiles would have been obtained in the specimens in a triaxial cell than in the oedometer cell.

The difference in the displacement processes observed during waterflooding in the centrifuge and the oedometer cell is mainly due to the lower flow rate and the higher stress level in the oedometer tests. Further, the capillary imbibition potential was suppressed in the centrifuge.

Based on the test observations it is evaluated that oil displacement by waterflooding is very efficient in strongly water-wet chalk with a well-connected fracture network with many branches. Waterflooding strongly water-wet chalk containing a single almost vertical, continuing fracture with limited branching may impose a risk of continued flow of water in the fractures resulting in less efficient oil displacement. Similarly, waterflooding fractional-wet chalk may also impose a risk of continued flow of water in the fractures resulting in less efficient oil displacement, even in chalk with a well-connected fracture network with many branches.

The large-scale waterflooding tests contribute to the understanding of oil displacement by waterflooding by illustrating a number of possible waterflooding scenarios in specimens with different fracture patterns.

Chapter 11

Perspective

Based on the large-scale testing in this Ph.D. project, future work is proposed to consist of a continuation of the described waterflooding tests carried out in a centrifuge at a higher stress level. This require either a centrifuge of larger capacity and/or a modification of the test set-up to include application of an external load. Such work is believed to provide further knowledge on how the fractures affect the displacement processes in a broader range of stresses corresponding to the field behavior during waterflooding.

Future testing should also include waterflooding on a Hillerslev outcrop chalk specimen, where the wettability of the specimen is altered to a homogeneous, lesser water-wet state. This implies that the wettability alteration procedure used in the alteration of the single large, strongly water-wet test specimen should be improved. Such work is believed to provide further knowledge on how the wettability effect the displacement processes during waterflooding.

There is a need for a better way to describe the fractures inside the large chalk specimens, as the displacement processes seem to be affected mainly by the fracture network and not just on the degree of fracturing. Further, it would be valuable to perform simulations using more representative parameters and an enhanced fracture description to improve the understanding of the displacement processes during waterflooding, and especially the concept of a critical waterflooding rate.

To obtain a model for chalk-water interaction in naturally fractured chalk, future testing should include testing on oil-saturated and water-saturated chalk specimens along with waterflooding of oil-saturated chalk specimens with similar fracture patterns. These tests should be conducted in a triaxial cell instead of an oedometer cell to obtain a more homogeneous porosity- and stress profile in the tested specimens. Further, liquid rubber should be cast around the specimens instead of liquid gypsum to prevent side flow during testing.

Bibliography

Aguilera, R. (1984), *Naturally Fractured Reservoirs*, PennWellBooks.

Albrechtsen, T., Andersen, S., Dons, T., Engstrøm, F., Jørgensen, O. & Sørensen, F. (2001), 'Halfdan: Developing non-structurally trapped oil in north sea chalk', *Soc. Petr. Eng.* (SPE 71322).

Ali, N. & Alcock, T. (1992), 'Valhall field, norway - the first ten years', *Amoco Norway Oil Co. Norway* .

Allan, J. & Quing Sun, S. (2003), 'Controls on recovery factor in fractured reservoirs: Lessons learned from 100 fractured fields', *Soc. Petr. Eng.* (SPE 84590).

Andersen, M. (1995), *Petroleum Research in North Sea Chalk. Joint Chalk Research Phase IV*, Stavanger Research Center.

Andersen, M. (1996), 'Putting chalk research into context', *Proceedings at the Fifth North Sea Chalk Symposium, Reims, France, 7-9 Oct. 1996* .

Andersen, M., Foged, N. & Pedersen, H. (1992), 'The link between waterflood-induced compaction and rate-sensitive behavior in a weak north sea chalk', *Proceedings at the Fourth North Sea Chalk Symposium, Deauville, France, 21-23 September 1992* .

Anderson, W. (1986*a*), 'Wettability literature survey - part 1: Rock/oil/brine interactions and the effects of specimen handling on wettability', *SPE* .

Anderson, W. (1986*b*), 'Wettability literature survey - part 2: Wettability measurement', *SPE* .

Anderson, W. (1986*c*), 'Wettability literature survey - part 4: Effects of wettability on capillary pressure', *SPE* .

Anderson, W. (1986*d*), 'Wettability literature survey - part 5: The effects of wettability on relative permeability', *SPE* .

Anderson, W. (1986*e*), 'Wettability literature survey - part 6: The effects of wettability on waterflooding', *SPE* .

Aspenes, E., Graue, A., Baldwin, B., Moradi, A., Stevens, J. & Tobola, D. (2002), 'Fluid flow in fractures visualized by mri during waterfloods at various wettability conditions - emphasis on fracture width and flow rate', *Soc. Petr. Eng.* (SPE 77338).

Babadagli, T. (1994), 'Injection rate controlled capillary imbibition transfer in fractured systems', *Proceedings of the SPE Annual Technical Conference and Exhibition. Part 2.* (SPE 28640).

Babadagli, T. & Zeidani, K. (2004), 'Evaluation of matrix-fracture imbibition transfer functions for different types of oil, rock and aqueous phase', *Soc. Petr. Eng.* (SPE 89450).

Bagge, G., König, D., Rezzoug, A., Crancon, P., Günzel, F. & Thorel, L. (2002), 'Centrifugal modeling of capillary rise and drainage in sandy soils', *Proceedings of the International Conference on Physical Modelling in Geotechnics/ICPMG '02/ST John's/Newfoundland/Canada* .

Baldwin, B. (1988), 'Water imbibition and characterization of north sea chalk reservoir surfaces', *SPE Formation Evaluation* .

Barkved, O., Heavey, P., Kjelstadli, R., Kleppan, T. & Kristiansen, T. (2003), 'Valhall field - still on plateau after 20 years of production', *Soc. Petr. Eng.* (SPE 83957).

Bognø, T., Aspenes, E., Graue, A., Spinler, E. & Tobola, D. (2001), 'Comparison of capillary pressure measurements at various wettabilities using the direct measurement of saturation method and conventional centrifuge techniques', *Proceedings at the International Symposium of Core Analysts, Edinburgh, Scotland, 17-19 Sept. 2001* .

Brown, R. & Fatt, I. (1956), 'Measurements of fractional wettability of oilfield rocks by the nuclear magnetic relaxation method', *Trans. AIME* **207**, 262–264.

Chowdhury, T., Dabiri, G., Putra, E. & Schechter, D. (2003), 'Improving dual-porosity simulation in the naturally fractured spraberry trend area', *Prepared for presentation at the 2002 Naturally Fractured Reservoir Conference held in Oklahoma City, 3-4 June 2003* .

Christensen, H. (2001), Applicational aspects of the efp-98 study, Technical Report Report 2001-05-04, GEO.

Christensen, H. (2003), Displacement and deformation processes in fractured reservoir chalk, Efp-2000, GEO.

Christensen, H., Springer, N., Olsen, D., van den Zwaag, C. & Fabricius, I. (2000), Joint chalk research phase v. project 8.1: Chalk-water interaction, JCR Phase V Report 2000-02-18, GEO.

Christensen, H. & Vanggard, M. (1994), 'Waterflooding of oil saturated stevns outcrop chalk', *Eurock '94* .

Christoffersen, K. (1995), 'Gas/oil capillary pressure of chalk at elevated pressures', *SPE Formation Evaluation* .

Cooke, B. (2000), Centrifuge modelling of lnapl infiltration, *in* J. Garnier, L. Thorel & E. Haza, eds, 'Proceedings of the Int. Symp. on Physical Modelling and Testing in Environmental Geotechnics', NECER, LCPC.

Cuiec, L. (1987), *North Sea Oil and Gas Reservoirs*, The Norwegian Institute of Technology (Graham and Trotman), chapter 14 Wettability and Oil Reservoirs, pp. 193–207.

Cuiec, L., Bourbiaux, B. & Kalaydjian, F. (1994), 'Oil recovery by imbibition in low-permeability chalk', *Soc. Petr. Eng.* (SPE 20259).

Culligan-Hensley, P. & Savvidou, C. (1995), *Geotechnical centrifuge technology*, Blackie Academic, chapter 8. Environmental geomechanics and transport processes.

Culligan, P., Savvidou, C. & Barry, D. (1996), 'Centrifuge modelling of contaminant transport', *Electronic Journal of Geotechnical Engineering, Available:http://geotech.civen.okstate.edu/ejge/index.htm.1, 1996.* .

Dake, L. (1997), *Fundamentals of Reservoir Engineering*, number ISBN 0-444-41830-X, Elsevier Scinece Publishers B. V.

Dullien, F. (1991), *Porous Media. Fluid Transport and Pore Structure*, second edition edn, Harcourt Publishers Ltd.

Eltvik, P. & Settari, A. (1992), 'Waterflood induced fracturing in the valhall field', *Proceedings at the Fourth North Sea Chalk Symposium, Deauville, France, 21-23 September 1992* .

Eltvik, P., Skoglunn, T. & Skinnarland, O. (1990), 'Valhall waterflood pilot - a study of water injection in a fractured reservoir', *Proceedings at the Third North Sea Chalk Symposium, Copenhagen, 1990* .

Energistyrelsen (2004), Danmarks olie- og gasproduktion 2003, Årsrapport ISBN 877844-430-6. ISSN 0907-2675, Energistyrelsen.

Foged, N., Christensen, H. & Andersen, M. (1996), 'Rock mechanics and water injection', *Proceedings at the Fifth North Sea Chalk Symposium, Reims, France, 7-9 October 1996* .

Forbes, P., Chen, Z. & Ruth, D. (1994), 'Quantitative analysis of radial effects on centrifuge capillary pressure curves', *Soc. Petr. Eng.* (SPE 28182).

Fuglsang & Krebs Ovesen (1988), *The application of the theory of modelling to centrifuge studies.*

Garnier, J., Thorel, L. & Haza, E., eds (2000), *Proceedings of the Int. Symp. on Physical Modelling and Testing in Environmental Geotechnics.*, NECER, LCPC.

Graue, A., Aspenes, E., Moe, R., Bognø, T., Baldwin, B., Moradi, A. & Tobola, D. (2001b), 'Oil recovery mechanisms in fractured reservoirs at various wettabilities visualized by nuclear tracer imaging and nmr tomography', *Proceedings at the 22nd Annual Workshop and Symposium Collaborative Project on Enhanced Oil Recovery International Energy Agency., Vienna, Austria, 9-12 September 2001* .

Graue, A., Baldwin, B., Aspenes, E., Stevens, J., Tobola, D. & Zornes, D. (2003), 'Sca2003-08: Complementary imaging techniques applying nti and mri determined wettability effects on oil recovery mechanisms in fractured reservoirs', *This paper was prepared for presentation at the International Symposium of the Society of Core Analysts held in Pau, France, 21-24 September 2003.* .

Graue, A., Bognø, T., Moe, R., Baldwin, B., Spinler, E., Maloney, D. & Tobola, D. (1999), 'Impacts of wettability on capillary pressure and relative permeability', *Reviewed Proceedings of the International Symposium of Core Analysts. Golden. Co. USA. August 1999* .

Graue, A., Moe, R. & Bognø, T. (2001a), 'Oil recovery in fractured reservoirs', *Proceedings of the 6th Nordic Symposium on Petrophysics. Trondheim. May 15-16. 2001* .

Graue, A., Viksund, B. & Baldwin, B. (1999a), 'Reproducible wettability alteration of low-permeable outcrop chalk', *SPE Res. Eng. and Eval.* **2 (2)**.

Graue, A., Viksund, B., Baldwin, B. & Spinler, E. (1999b), 'Large-scale two-dimensional imaging of wettability effects on fluid movement and oil recovery in fractured chalk', *Soc. Petr. Eng.* **4 (1)**(SPE 54668).

Gudbjerg, J. (2003), Numerical modelling of oil displacement by water injection in fractured chalk, Efp-2000, ER, DTU.

Gutierrez, M. & Hansteen, H. (1994), 'Fully-coupled analysis of reservoir compaction and subsidence. europec '94', *Soc. Petr. Eng.* (SPE 28900).

Havmøller, O. (1998), Chalk-water interaction. stevns klint maastrichtian chalk. joint chalk research phase v. report 1. project 8.1, Jcr phase v, GEO.

Havmøller, O. & Krogsbøll, A. (1997), Fractures and rock mechanics. phase 1. summary report, Efp-96, DGI and GEUS.

Havmøller, O. & Krogsbøll, A. (2001), Fractures and rock mechanics. phase 2. fractures and rock mechanics., EFP-98 Report 1. ENS J. no. 1313/98-0006. GEO no. 16015027. 2001-03-23, GEO.

Homand, S. & Shao, J. (2000), 'Mechanical behaviour of a porous chalk and water/chalk interaction. part 1: Experimental study', *Oil and Gas Science and Technology - Rev. IFP* **55**(6), 591–598.

Illangasekare, T., Znidarcic, D. & Al-Sheridda, M. (1991), Multiphase flow in porous media, *in* Ko, ed., 'Centrifuge 91 - Proceedings of the International Conference Centrifuge 1991, Boulder, Colorado', Balkema, Rotterdam, ISBN 90 6191 193 1, pp. 517–523.

Jadhunandan, P. & Morrow, N. (1991), 'Spontaneous imbibition of water by crude oil/brine/rock systems', *In Situ* **15**(4), 319–345.

Jakobsen, F. (2001), Fractures and rock mechanics. phase 2. description of natural and test induced fractures in chalk, EFP-98 Report 2001/18, GEUS.

Kleppe, J. & Morse, R. (1974), 'Oil production from fractured reservoirs by water displacement', *Soc. Petr. Eng.* (SPE 5084).

Knight, M. & Mitchell, R. (1996), 'Modelling of light nonaqueous phase liquid (lnapl) releases into unsaturated sand', *Canadian Geotechnical Journal* **33**, 913–925.

Krogsbøll, A., Jakobsen, F. & Madsen, L. (1997), Fractures and rock mechanics. phase 1. geology report, EFP-96 Report 1997/63, GEUS.

Kyte, J. (1970), 'A centrifuge method to predict matrix-block recovery in fractured reservoirs', *Soc. Petr. Eng.* (SPE 2729).

Lake, L. (1989), *Enhanced Oil Recovery*, Prentice Hall. New Jersey.

Langhaar (1951), 'Dimensional analysis and the theory of models', *John Wiley, New York* .

Larsen, F., Cowie, D. & Ovens, J. (1997), 'Using 4000ft long induced fractures to water flood the dan field', *Soc. of Petr. Eng.* (SPE 38558).

Larsen, I. (2000), Water injection in oil saturated, fractured chalk samples (h×d=50×50 cm) modelling oil displacement in oil reservoirs, Master thesis, DTU.

Leonard, R. & Munns, J. (1987), *Geology of the Norwegian Oil and Gas Fields. 11. Valhall*, A. M. Spencer et al.

Lord, A. (1999), 'Capillary flow in the geotechnical centrifuge', *Geotechnical Testing Journal. GTJODJ* **22**(4), 292–300.

Madland, M., Korsnes, R. & Risnes, R. (2002), 'Temperature effects in brazilian, uniaxial and triaxial compressive tests with high porosity chalk', *Soc. Petr. Eng.* (SPE 77761).

Malmin, E. (1998), Effect of boundary conditions on chalk compaction, Master's thesis, Høgskolen i Stavanger.

Mannon, R. & Chilingar, G. (1972), 'Experiments on effect of water injection rates on imbibition rate in fractured reservoirs', *Soc. Petr. Eng.* (SPE 4101).

Mattax, C. & Kyte, J. (1962), 'Imbibition oil recovery from fractured, water-drive reservoir', *Soc. Petr. Eng.* (SPE 187).

Milter, J. (1996), Improved Oil Recovery in Chalk. Spontaneous Imbibition affected by Wettability. Rock Framework and Interfacial Tension, PhD thesis, University of Bergen.

Mitchell, R. (1998), 'The eleventh annual r. m. hardy keynote adress, 1997: Centrifugation in geoenvironmental practice and education', *Can. Geotech. J.* **35**, 630–640.

Morrow, N. (1990), 'Wettability and its effect on oil recovery', *JPT* .

Morrow, N., Lim, H. & Ward, J. (1984), 'Effect of crude-oil-induced wettability changes on oil recovery', *Soc. Petr. Eng.* (SPE 13215).

Mungan, N. (1966), 'Interfacial effects in immiscible liquid-liquid displacement in porous media', *Soc. Petr. Eng.* (SPE 1442).

Offshore Technology (2004), 'Valhall flank water injection platform, norway.', *Located July 2004 on http://www.offshore-technology.com/projects/Valhall_Flank/index.html* .

Olsen, D. B., N. Nielsen, C., If, F. & Christensen, J. (2001), Flow in fractured chalk. final report for efp-98. project no. 1313/98-0008, Efp-1998, GEUS 32.

Olufsen, K. (2002*a*), 'Application of the tdr measuring principle (in danish)', Preparatory Thesis. BYG.DTU. DTU.

Olufsen, K. (2002*b*), Using tdr during water injection in centrifuge test on hillerslev chalk. for h = 50 cm, d = 50 cm block specimen, Master's thesis, BYG.DTU. DTU.

Pantazidou, M., Abu-Hassanein, Z. & Riemer, M. (2000), 'Centrifuge study of dnapl transport in granular media', *Journal of Geotechnical and Geoenvironmental Engineering* **126**(2).

Petersen, S. & Cooke, B. (1994), Scaling concerns for immiscible multiphase flow in porous media, *in* L. Leung & Tan, eds, 'Centrifuge 94', number ISBN 90 54 10 352 3, Balkema. Rotterdam.

Pooladi-Darvish, M. & Firoozabadi, A. (2000), 'Experiments and modelling of water injection in water-wet fractured porous media', *Journal of Canadian Petroleum Technology (JCPT)* **39**(3).

Pratap, M., Kleppe, J. & Uleberg, K. (1997), 'Vertical capillary continuity between the matrix blocks in a fractured reservoir significantly improves the oil recovery by water displacement', *Soc. Petr. Eng.* (SPE 37725).

Putra, E. & Schechter, D. (1999), 'Reservoir simulation of a waterflood pilot in the naturally fractured spraberry trend', *Soc. Petr. Eng.* (SPE 54336).

Rathmell, J., Braun, P. & Perkins, T. (1973), 'Reservoir waterflood residual oil saturation from laboratory tests', *Journal of Petroleum Technology (JPT)* .

Rezzoug, A. (1999), Theoretical approach of time scaling of capillary rise and experimental verification, *in* 'Capillary Phenomena', NECER.

Risnes, R. & Flaageng, O. (1999), 'Mechanical properties of chalk with emphasis on chalk-fluid interactions and micromechanical aspects', *Oil and Gas Science and Technology - Rev. IFP* **54**(6), 751–758.

Roscoe (1968), 'Soils and model tests', *Journal of Strain Analysis* .

Ruddy, I., Andersen, M., Pattillo, P., Bishlawi, M. & Foged, N. (1989), 'Rock compressibility, compaction, and subsidence in a high-porosity chalk reservoir: A case study of valhall field', *JPT* .

Ruth, D. & Chen, Z. (1995), 'Measurement and interpretation of centrifuge capillary pressure curves - the sca survey data', *The Log Analyst* .

Salathiel, R. (1973), 'Oil recovery by surface film drainage in mixed-wettability rocks', *JPT* pp. 1216–1224.

Senneset, K., Torsæter, O., Lone, S. & Wiig, T. (1995), 'Two-phase flow and permeability of oil in porous media', *Bulletin 32. Institut for Geoteknikk. NTNU* .

Skauge, A. & Poulsen, S. (2000), 'Rate effects on centrifuge drainage relative permeability', *Soc. Petr. Eng.* (SPE 63145).

Springer, N., Olsen, D., Øyno, L., Lind, I. & Andersen, M. (1996), 'Rock mechanics and water injection: Chalk characterization and description', *Proceedings at the Fifth North Sea Chalk Symposium, Reims, France* .

Standnes, D. & Austad, T. (2000a), 'Wettability alteration in chalk. 1. preparation of core material and oil properties', *Journal of Petroleum Science and Engineering* (28).

Standnes, D. & Austad, T. (2000b), 'Wettability alteration in chalk. 2. mechanism for wettability alteration from oil-wet to water-wet using surfactants', *Journal of Petroleum Science and Engineering* (28).

Sulak, R. & Danielsen, J. (1989), 'Reservoir aspects of ekofisk subsidence', *JPT* **41**(7), 709–734.

Sylte, J., Thomas, L., Rhett, D., Bruning, D. & Nagel, N. (1999), 'Water induced compaction in the ekofisk field', *Soc. Petr. Eng.* (SPE 56426).

Tang, G. & Firoozabadi, A. (2001), 'Effect of pressure gradient and initial water saturation on water injection in water-wet and mixed-wet fractured porous media', *Soc. Petr. Eng.* (SPE 74711).

Taylor, R. (1995), *Geotechnical centrifuge technology*, Blackie Academic, chapter 2. Centrifuges in modelling: principles and scale effects.

Vanggard, M. (1993), Vandinjektion på kalkprøver (water injection in chalk specimens), Master thesis, DTU.

Viksund, B. (1998), Fluid Flow in Fractured Chalk Models at different Wettabilities, PhD thesis, University of Bergen.

Wodka, P. (1992), 'Production experience from horizontal wells in the dan field', *Fourth North Sea Chalk Symposium* .

Appendix A

Centrifuge Scaling

Model test with flow in soil between two plane-parallel surfaces with constant pressure levels

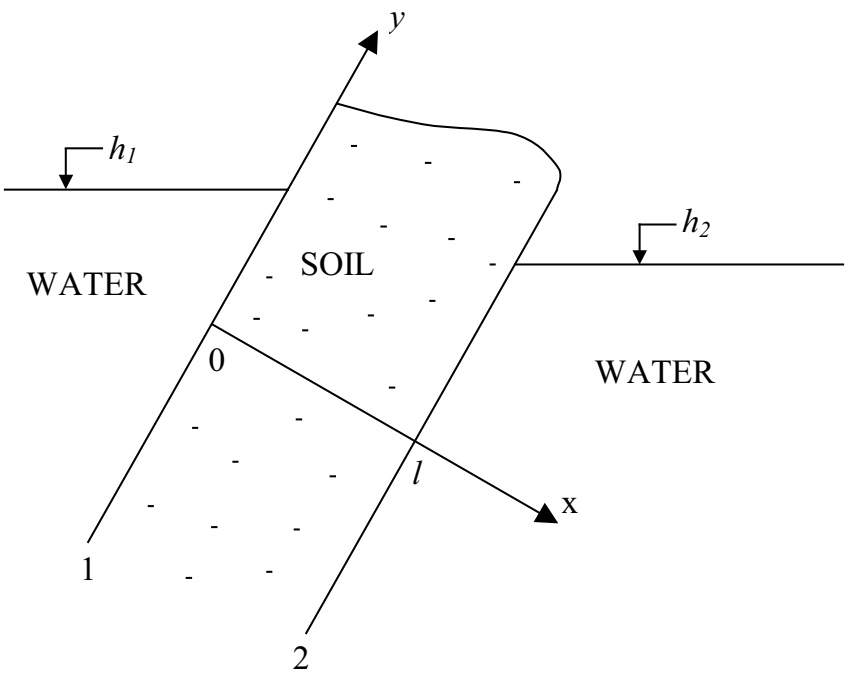

Figure A.1 *Flow in soil between two plane-parallel surfaces 1 and 2 with constant pressure levels h_1 and h_2, respectively.*

Two plane-parallel surfaces, surface 1 with constant pressure level h_1, and surface 2 with constant pressure level h_2 ($< h_1$), defines an area of soil, which is assumed to be homogeneous and isotropic. The two constant pressure levels are due to two adjacent basins with water, see Figure A.1. The pressure level difference between the two surfaces results in flow of water in the soil that is described by Laplace's equation:

$$\frac{\partial^2 h}{\partial x^2} + \frac{\partial^2 h}{\partial y^2} = 0 \tag{A.1}$$

where the x- and y-directions are shown in Figure A.1.

Linear functions in x and y are automatically solutions to Laplace's equation, such as the following linear expression in x that fulfills the boundary condition at both surfaces:

$$h = h_1 - \frac{x}{l} \cdot (h_1 - h_2) \tag{A.2}$$

where l is the thickness of the soil layer perpendicular to the surfaces, i.e. in the x-direction. This is the solution to the actual flow problem since Laplace's equation only has one solution corresponding to a given set of boundary conditions.

The flow velocities in the two axis directions are determined by Darcy's law:

$$\begin{aligned} v_x &= -k \cdot \frac{\partial h}{\partial x} = k \cdot \frac{h_1 - h_2}{l} \\ v_y &= -k \cdot \frac{\partial h}{\partial y} = 0 \end{aligned} \tag{A.3}$$

Thus, the direction of flow is perpendicular to the two boundary surfaces at any place, and the solution to the problem is independent of the inclination of the surfaces as this is not included in the equations.

A model test is performed where all lengths are divided by a factor N except for the soil, which is the same in the model and the prototype, and the gravitational acceleration is multiplied by the same factor of N. This results in the following (using subscript m for model and p for prototype):

$$\begin{aligned} v_p &= k_p \cdot \frac{h_{1p} - h_{2p}}{l_p} \\ v_m &= k_m \cdot \frac{h_{1m} - h_{2m}}{l_m} \\ &= k_m \cdot \frac{(h_{1p} - h_{2p})/N}{l_p/N} \\ &= k_m \cdot \frac{(h_{1p} - h_{2p})}{l_p} \\ &= k_m \cdot \frac{v_p}{k_p} \end{aligned} \tag{A.4}$$

The hydraulic conductivity k can be expressed as:

$$k = \frac{g}{\nu} \cdot f(\phi) \tag{A.5}$$

where g is the gravitational acceleration, ν is the kinematic viscosity of the water, and ϕ is the porosity of the soil. The value of the function $f(\phi)$ is the same in the model and the prototype when the same soil is used. This results in:

$$k_p = \frac{g_p}{\nu_p} \cdot f(\phi_p)$$

$$\begin{aligned} k_m &= \frac{g_m}{\nu_m} \cdot f(\phi_m) \\ &= \frac{N \cdot g_p}{\nu_m} \cdot f(\phi_p) \\ &= \frac{N}{\nu_m} \cdot (k_p \cdot \nu_p) \end{aligned} \tag{A.6}$$

k_m is inserted into the expression for v_m (A.4):

$$\begin{aligned} v_m &= \frac{N}{\nu_m} \cdot (k_p \cdot \nu_p) \cdot \frac{v_p}{k_p} \\ &= N \cdot \frac{\nu_p}{\nu_m} \cdot v_p \end{aligned} \tag{A.7}$$

Therefore, the flow velocity is N times faster in the model than in the prototype, except for the possible correction due to the fact that the temperature of the water can be different in the model and the prototype. This implies a ratio different from 1 between the kinematic viscosities.

Appendix B

Earlier Capillary Pressure Curves for Hillerslev Chalk

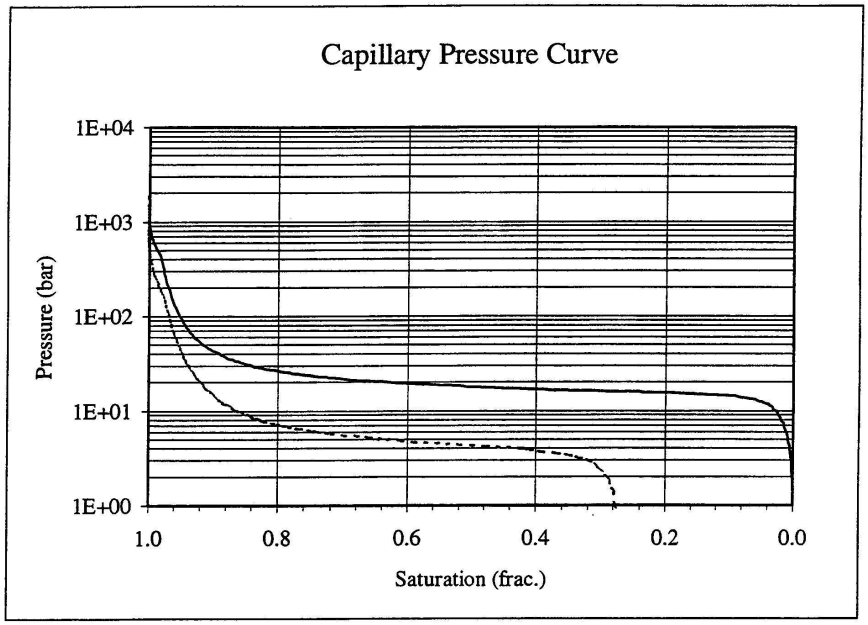

Figure B.1 *Mercury-gas capillary pressure curve for Hillerslev outcrop chalk (Krogsbøll et al. 1997). Saturation (frac.): mercury.*

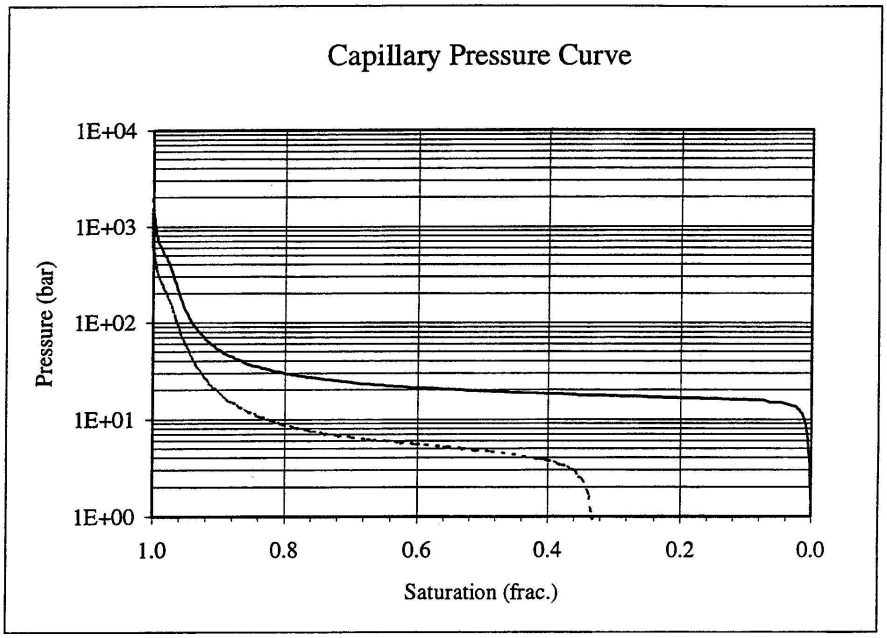

Figure B.2 *Mercury-gas capillary pressure curve for Hillerslev outcrop chalk (Krogsbøll et al. 1997). Saturation (frac.): mercury.*

Appendix C

Spontaneous Water Imbibition Tests

Spontaneous water imbibition tests were carried out on three small cylindrical Hillerslev outcrop chalk specimens. Initially, the specimens were dried in an oven at 105°C. Then, the specimens were fully saturated with the laboratory oil Isopar-L, which has a density of $\rho_o = 0.763$ g/cm^3 at 22° C. The oil saturation was carried out by placing the specimens in an exicator with Isopar-L. Underpressure was applied to the exicator by use of a vacuum pump. After the oil saturation, tape was wrapped around the specimens to ensure that fluid only enters and leaves through the end-faces of the specimens during water imbibition. Finally, the specimens were placed in glass containers, where they were fully covered by distilled water, which has a density of $\rho = 1.0$ g/cm^3 at room temperature. A millimeter measuring scale was glued onto the glass containers to measure the production of oil during water imbibition. The initial parameters for the three specimens are included in Table C.1.

Specimen	D [mm]	H [mm]	M_{dry} [g]	BV [cm^3]	ρ_{dry} [g/cm^3]	e [-]	ϕ [%]	PV [cm^3]	M_{o-sat} [g]	S_o [%]
1	54.17	26.52	86.91	61.12	1.42	0.90	47.4	28.97	108.53	97.8
2	54.02	26.85	87.95	61.54	1.43	0.89	47.1	28.99	109.63	98.0
3	54.08	26.45	85.50	60.76	1.41	0.91	47.6	28.92	107.27	98.7

Table C.1 *Initial parameters for the three specimens.*

The diameter D [mm], height H [mm], dry weight M_{dry} [g] and oil-saturated weight M_{o-sat} [g] are measured. The bulk volume BV [cm^3] is calculated as $\pi \cdot (D/2)^2 \cdot H$. The dry density ρ_{dry} [g/cm^3] is calculated as M_{dry}/BV. The void ratio e [-] is calculated as $\rho_s/\rho_{dry} - 1$, where the grain density is $\rho_s = 2.70$ g/cm^3. The porosity ϕ [%] is calculated as $e/(e+1)\cdot 100$, and the pore volume PV [cm^3] is calculated as $\phi \cdot BV$. The oil saturation S_o [%] is based on the oil uptake, i.e. $(M_{o-sat} - M_{dry})/\rho_o/PV \cdot 100$.

The parameters after water imbibition for the three specimens are included in Table C.2.

The weight after water imbibition M_{after} [g] is measured. The oil saturation after water imbibition $S_{o,a}$ [%] is calculated as $((M_{after} - M_{dry}) - \rho_w \cdot PV \cdot (1 - S_{air})/100)/(\rho_o - \rho_w)/PV \cdot$

Specimen	M_{after} [g]	$S_{o,a}$ [%]	$S_{w,a}$ [%]
1	113.43	26.4	71.4
2	114.50	27.1	70.9
3	112.19	27.1	71.6

Table C.2 *Parameters after test for the three specimens.*

100, where the air saturation S_{air} [%] is estimated to 100%-S_o. The water saturation after water imbibition $S_{w,a}$ [%] is calculated as 100%-S_o-S_{air} assuming a constant volume of air.

The measured corresponding values of time [min.] and displaced oil [mm] for the three specimens are included in Table C.3. The measured total volume of oil displaced during water imbibition [mm] is assumed to be equal to the calculated total volume of water imbibed [cm^3], which is calculated as $((M_{after} - M_{dry}) - \rho_o \cdot PV \cdot (1 - S_{air})/100)/(\rho_w - \rho_o)$. This correlation results in a slight difference between the corresponding values of displaced oil in [mm] and [cm^3] for the three specimens.

Specimen 1			Specimen 2			Specimen 3		
Time	Displaced oil		Time	Displaced oil		Time	Displaced oil	
[min.]	[mm]	[cm^3]	[min.]	[mm]	[cm^3]	[min.]	[mm]	[cm^3]
15	2.5	11.49	15	2.0	9.14	15	2.5	11.51
30	3.0	13.79	30	2.8	12.79	30	3.0	13.81
45	4.0	18.38	45	3.2	14.62	45	3.6	16.58
60	4.4	20.22	60	4.0	18.28	60	4.1	18.88
75	4.42	20.31	75	4.2	19.19	75	4.2	19.34
18.5 hrs.	4.48	20.59	90	4.3	19.65	90	4.3	19.80
24 hrs.	4.50	20.68	105	4.42	20.19	105	4.35	20.03
-	-	-	120	4.50	20.56	120	4.42	20.35
-	-	-	25.5 hrs.	4.50	20.56	25.3 hrs.	4.50	20.72

Table C.3 *Displaced oil during spontaneous water imbibition for the three specimens.*

For the three Hillerslev outcrop chalk specimens, a total water imbibition potential of 71-72% was observed with 96-98% of the imbibition completed within 1-1$\frac{1}{2}$ hours.

Appendix D

Oil Saturation

The specimens were saturated with the laboratory oil Isopar-L in the MARK-1 cell, see Figure D.1. A vacuum of 1 bar was applied to the cell, and as all the air was evacuated, the valve was opened and oil was allowed into the cell to a height approximately 1/3 above the specimen bottom. Then the valve was closed, and oil entered the specimens due to vacuum. When the level of oil had dropped again, more oil was allowed into the cell. This procedure was repeated until the specimens were saturated with oil. During the whole procedure a vacuum of 1 bar was maintained.

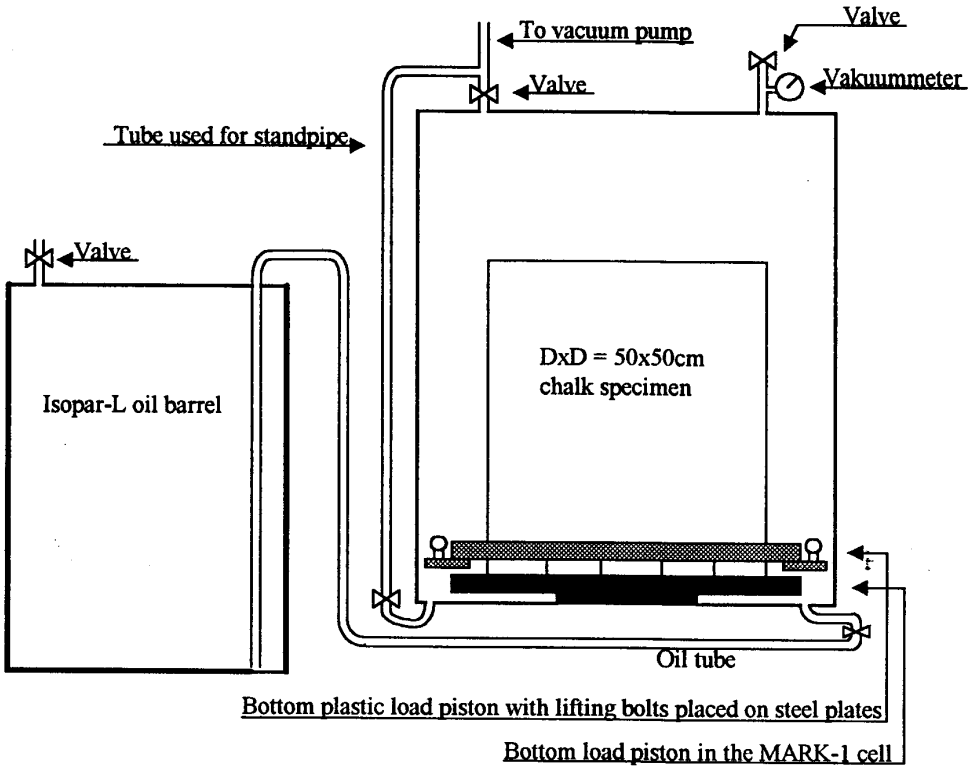

Figure D.1 *The MARK-1 cell and equipment used in the oil saturation (Larsen 2000).*

Appendix E

Sketches of the Fracture Pattern for all Seven Specimens

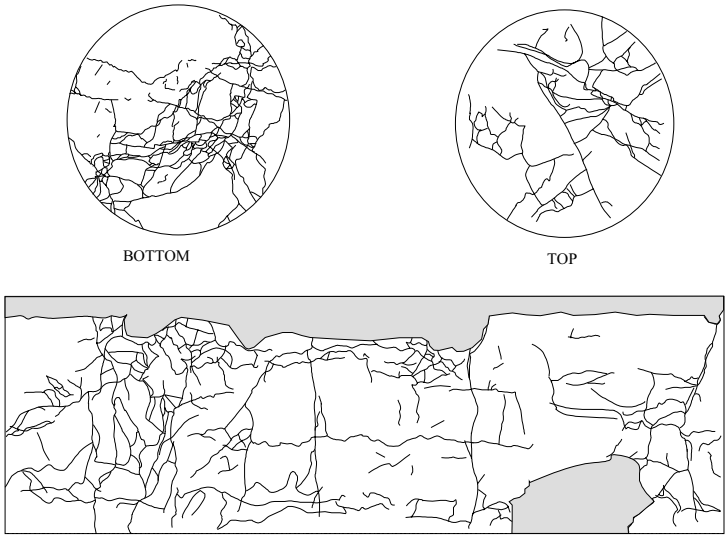

Figure E.1 *Fractures (black lines) and gypsum (light grey area) are indicated on the top, bottom and periphery of the fractional-wet specimen 2.*

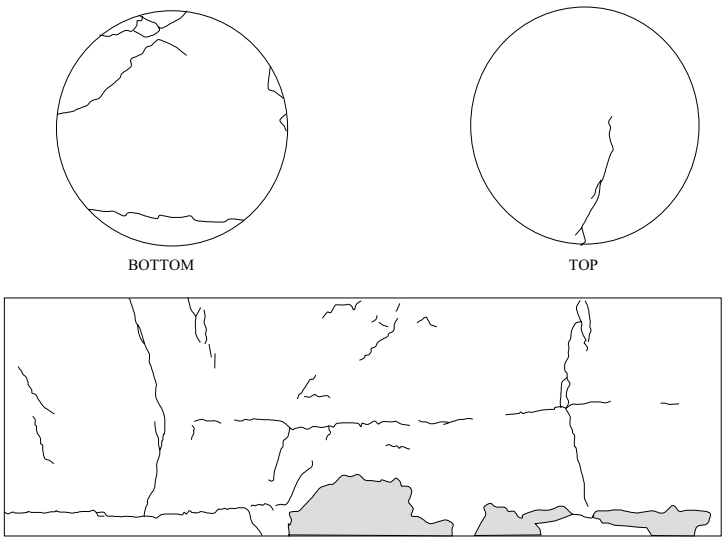

Figure E.2 *Fractures (black lines) and gypsum (grey area) are indicated on the top, bottom and periphery of the water-wet specimen 7.*

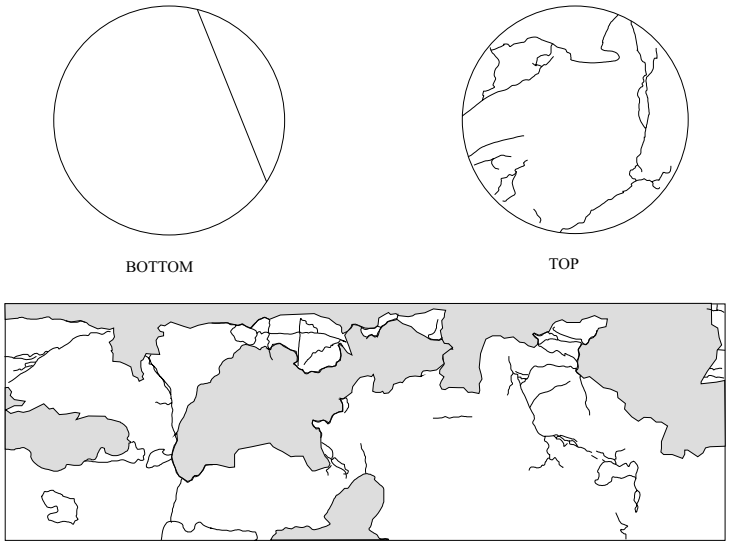

Figure E.3 *Fractures (black lines) and gypsum (grey area) are indicated on the top, bottom and periphery of the water-wet specimen 11.*

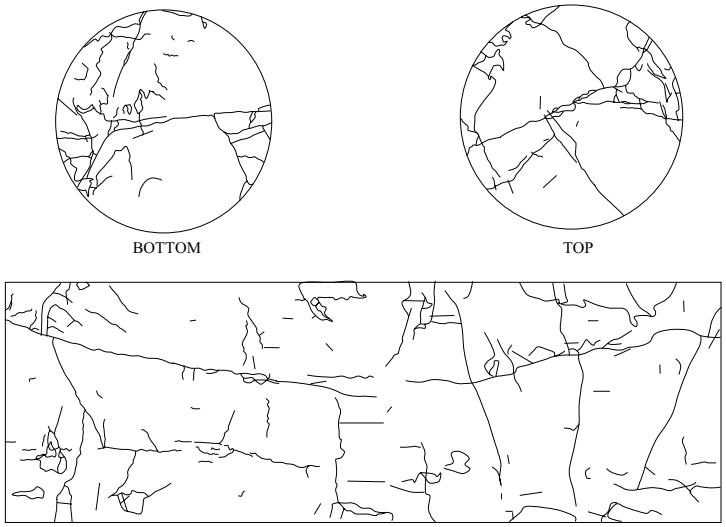

Figure E.4 *Fractures (black lines) are indicated on the top, bottom and periphery of the water-wet specimen 8.*

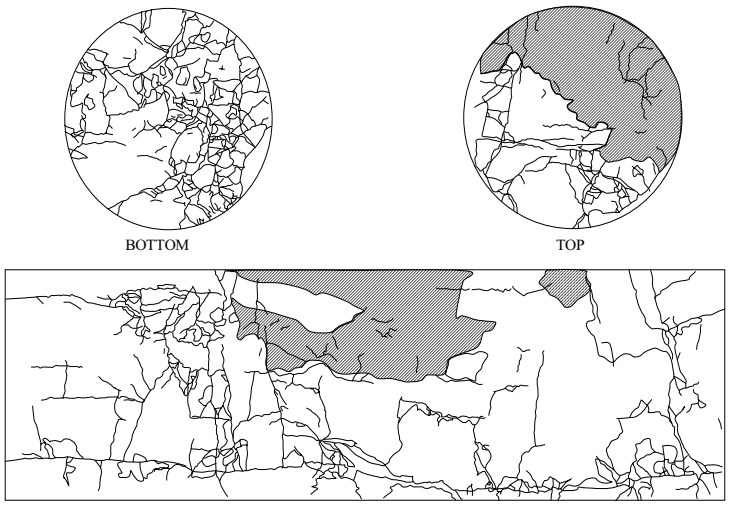

Figure E.5 *Fractures (black lines) and crushed zones (hatched areas) are indicated on the top, bottom and periphery of the water-wet specimen 5.*

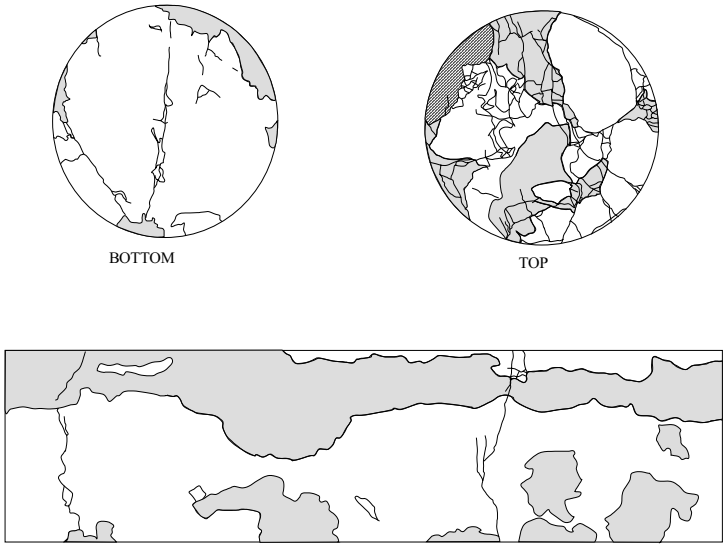

Figure E.6 *Fractures (black lines), crushed zone with gypsum (hatched, grey area) and gypsum (light grey area) are indicated on the top, bottom and periphery of the water-wet specimen 10. Only small amounts of gypsum were cast in the areas indicating gypsum on the top and bottom.*

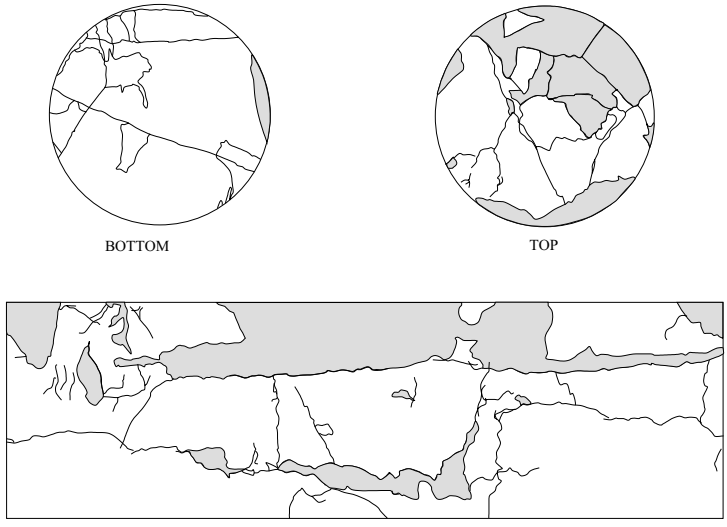

Figure E.7 *Fractures (black lines) and gypsum (grey area) are indicated on the top, bottom and periphery of the water-wet specimen 9. Only small amounts of gypsum were cast in the areas indicating gypsum on the top and bottom.*

Appendix F

Sketch of the two Test Set-up used in the Centrifuge

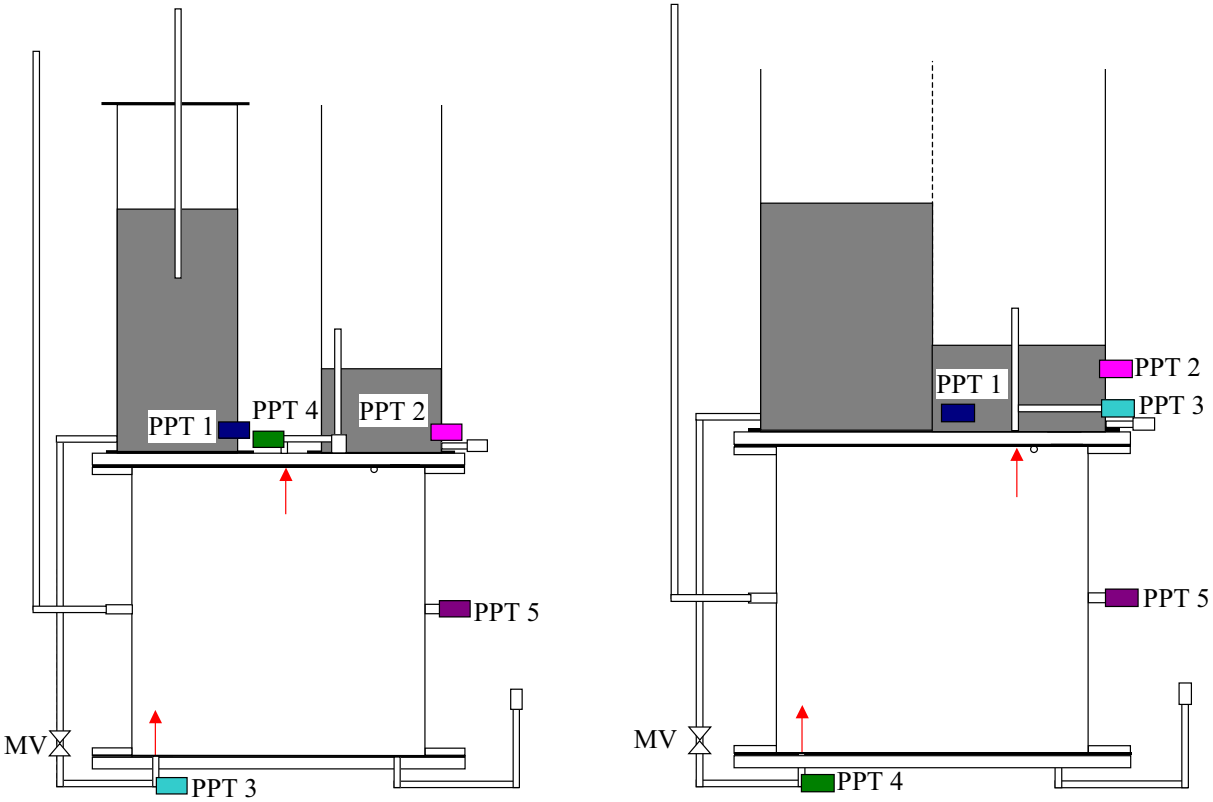

Figure F.1 *Sketch of the old test set-up (left) and the new test set-up (right) used for oil permeability tests and waterflooding in the centrifuge.*

Sketch of the two Test Set-up used in the Centrifuge

Appendix G

Pore Pressure Transducers

Pore pressures were measured by pore pressure transducers (PPTs) placed in 5 different positions. The PPTs actually measure voltage outputs, which are converted to pressure via calibration factors. The PPTs are Keller pressure transmitters with vented gauge. The PPTs were calibrated for pressures both below and above 1 bar resulting in a linear relationship $f(x) = ax+b$ with $f(x)$ in [cm water column] and x in [mV] in both intervals. The obtained calibration factors a and b are given in Table G.1.

	Pressure $<$ 1 bar		Pressure $\geq$ 1 bar	
	a [cm/mV]	b [cm]	a [cm/mV]	b [cm]
PPT 1	102.57652	-31.71987	100.03303	-29.21217
PPT 2 (old)	-	-	99.48404	offset
PPT 2 (new)	102.40789	-9.83940	100.00392	-13.34164
PPT 3	258.5125	-13.8985	250.41889	-19.32083
PPT 4	257.07603	-5.90326	250.20269	-9.39138
PPT 5 (old)	-	-	248.8878	offset
PPT 5 (new)	-	-	100.03670	-13.1596

Table G.1 *Calibration factors a and b from the calibration of the PPTs. The offset shall be calculated from the PPT measurements in the actual centrifuge test.*

PPT 2 went malfunctioning during the oil permeability test on specimen 7 and was replaced hence the PPT 2 old and new. The same was the case for PPT 5 during testing on specimen 5 resulting in a PPT 5 old and new. PPT 1, PPT 2 (old and new) and PPT 5 (new) cover the range 0-10 bar while PPT 3, PPT 4 and PPT 5 (old) cover the range 0-25 bar.

Appendix H

Test Procedure in the Oedometer Tests

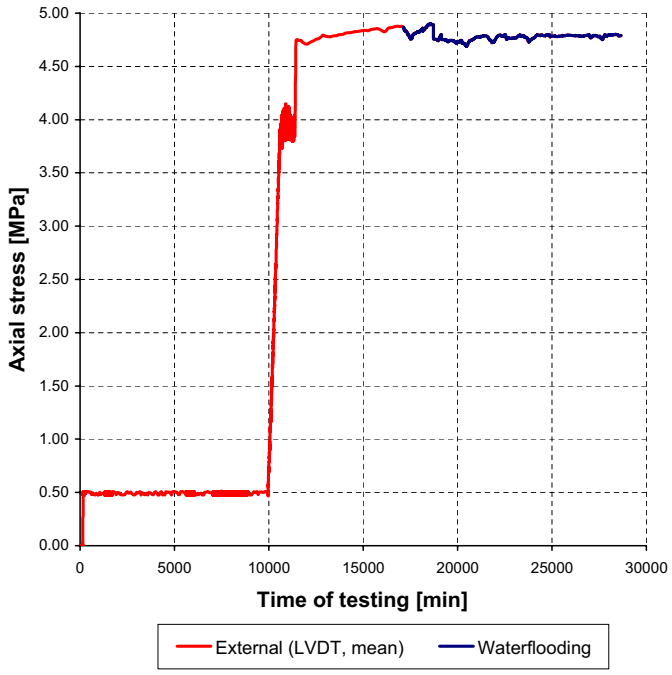

Figure H.1 *Axial stress vs. time of testing for specimen 9.*

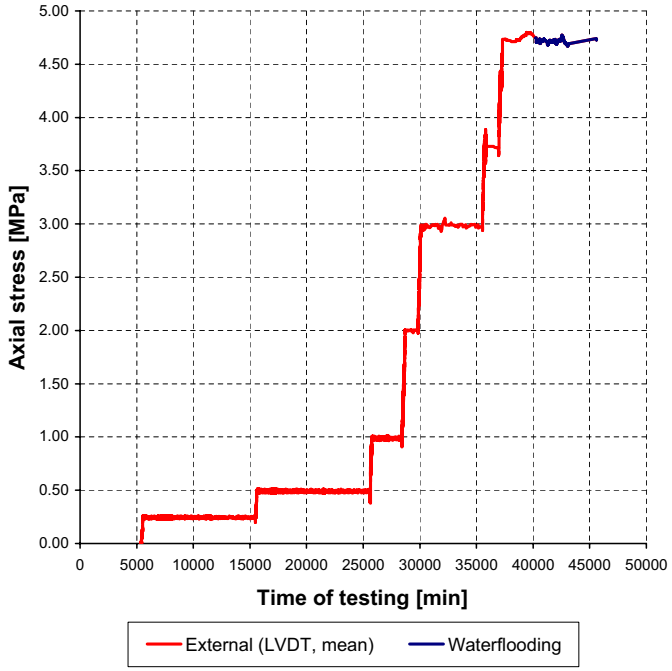

Figure H.2 *Axial stress vs. time of testing for specimen 10.*

Appendix I

Time Domain Reflectometry Probes

Eight time domain reflectomerry (TDR) probes were placed along the periphery and in the top of specimens 7, 5, 8 and 2. A photo of a TDR probe is shown in Figure I.1

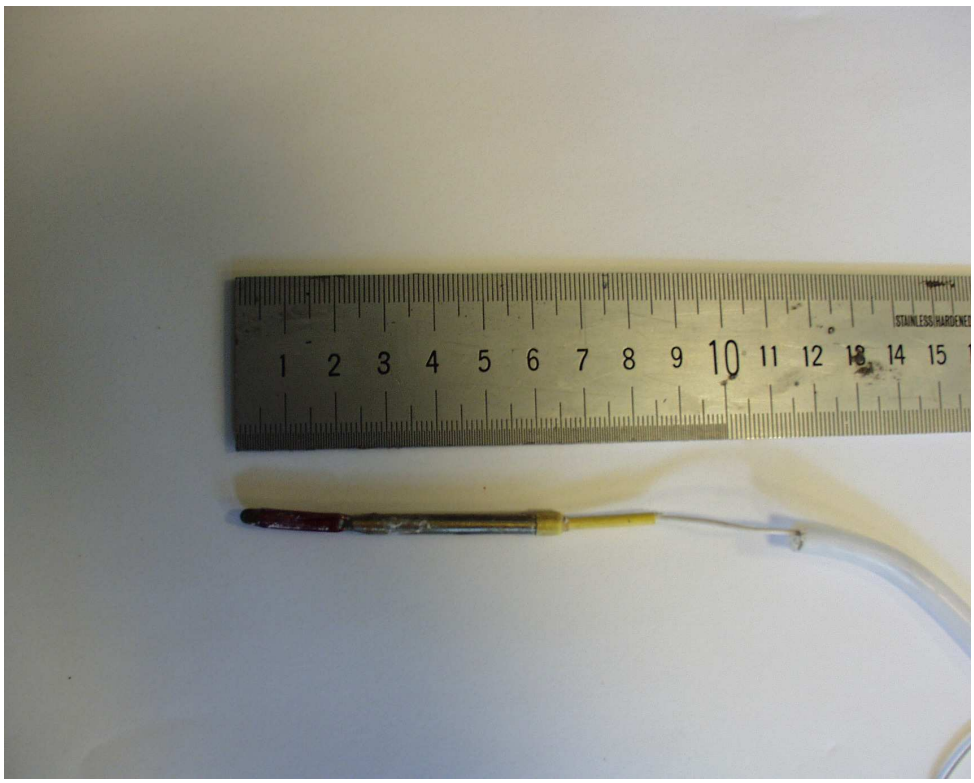

Figure I.1 *Photo of a TDR probe.*

The TDR probes measure the dielectric properties both of the surrounding material and their own core. The TDR probe output was correlated to a referenced dielectric constant obtained from output from conventional TDR probes (Olufsen 2002*b*). For determination of the raw dielectric constant, a TDR unit with build-in Campbell scientific TDR 100 reflectometer and multiplexer and software programme was used. The TDR

probes measure the apparent dielectric constant. The exact specifications for the TDR probes, a description of the measuring principle of the TDR probes and the software programme used for determination of the apparent raw dielectric constant are found in (Olufsen 2002*a*).

The TDR probes were calibrated to exclude the influence of their own core and the results were fitted to $f(x) = ax^b + ce^x$ (Olufsen 2002*b*). The obtained calibration factors a, b and c are given in Table I.1.

TDR probe	a	b	c
1	0.0388049	2.77041	$8.76807 \cdot 10^{-6}$
2	0.0185493	3.13533	$1.61613 \cdot 10^{-5}$
3	0.0089051	3.38999	$4.07577 \cdot 10^{-5}$
4	0.0177455	3.15363	$8.73051 \cdot 10^{-5}$
5	0.0564866	2.65369	$3.16649 \cdot 10^{-5}$
6	0.0101444	3.36877	$3.89825 \cdot 10^{-5}$
8	0.0479973	2.83530	$2.89222 \cdot 10^{-4}$
10	0.0481897	2.73806	$5.64563 \cdot 10^{-5}$

Table I.1 *Calibration factors a, b and c from the calibration of the TDR probes.*

Appendix J

Preparation of Specimens for Centrifuge Modelling

Figure J.1 *Specimen 7 placed on the porous filter on the bottom plate.*

Figure J.2 *Specimen 8 with holes drilled for TDR probe 1, 3, 4 and 10.*

Figure J.3 *Specimen 8 wrapped in soft plastic foil. Silicone sealant is seen along the periphery of the specimen at the bottom plate. TDR probe 1, 3, 4 and 10 are mounted in the specimen. The probe leads are secured with safety tubes, which are taken along the specimen to the top. The holes are sealed with silicone sealant.*

Figure J.4 *Specimen 11 with rubber membrane and form mounted. The membrane is kept in place by use of bolts.*

Figure J.5 *Liquid rubber mass is poured into the excess space between specimen 11 and the rubber membrane.*

Figure J.6 *Horizontally placed TDR probe down into the matrix part of the specimen 8 top. The probe is covered with a mix of pulverized chalk and Isopar-L, and covered with plastic fastened with silicone grease.*

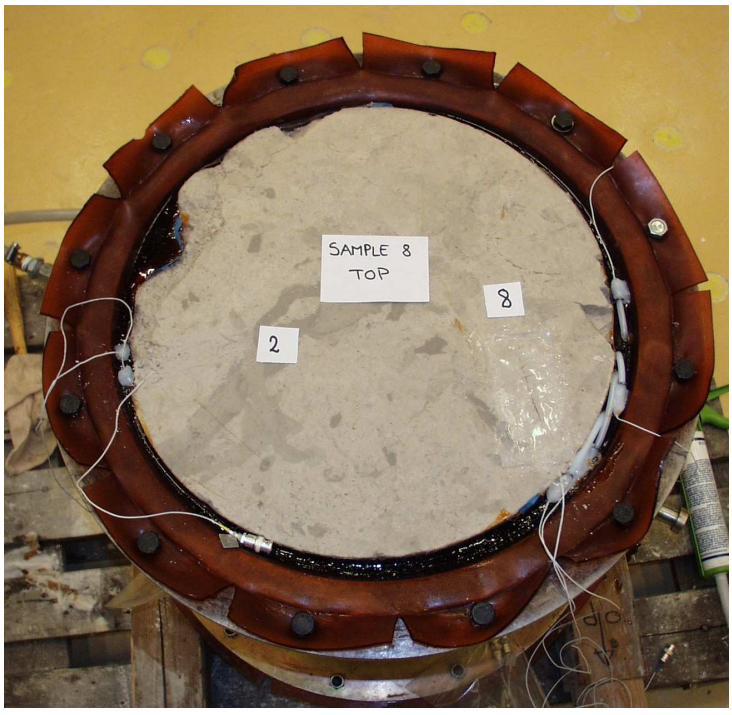

Figure J.7 *The safety tubes securing the TDR probe leads run along specimen 8 through the liquid rubber mass to the top. After hardening of the rubber mass, the safety tubes are sealed with silicone sealant.*

Appendix K

PPT Measurements during Waterflooding in the Centrifuge

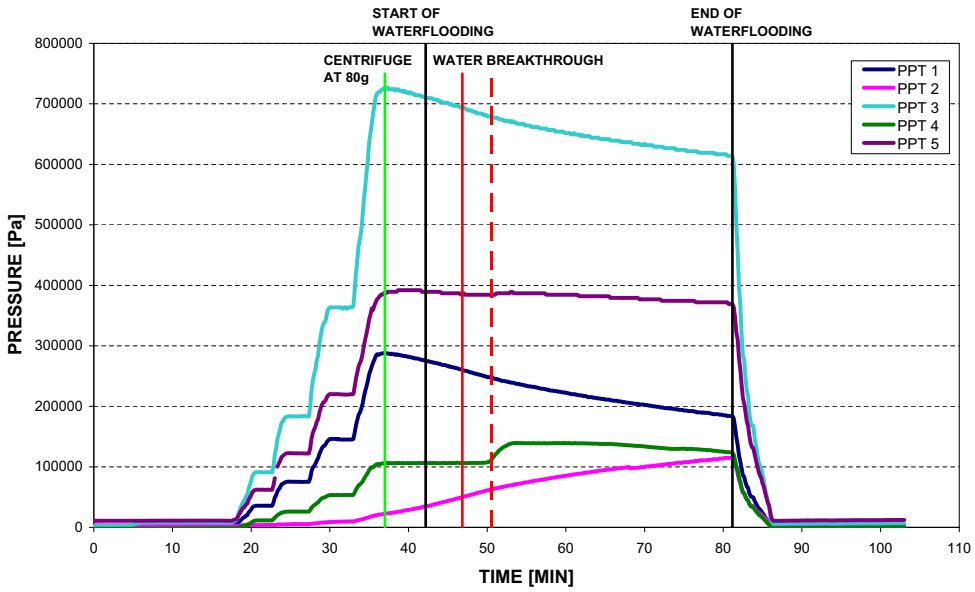

Figure K.1 *Pore pressures measured by the PPTs vs. time of testing on the water-wet specimen 11 corrected for dead volumes. Start of waterflooding = water enters the specimen bottom. Water breakthrough (full red line) = water reaches the specimen top. Water breakthrough (dotted red line) = water reaches the overflow tube in the outlet container. All based on PPT measurements.*

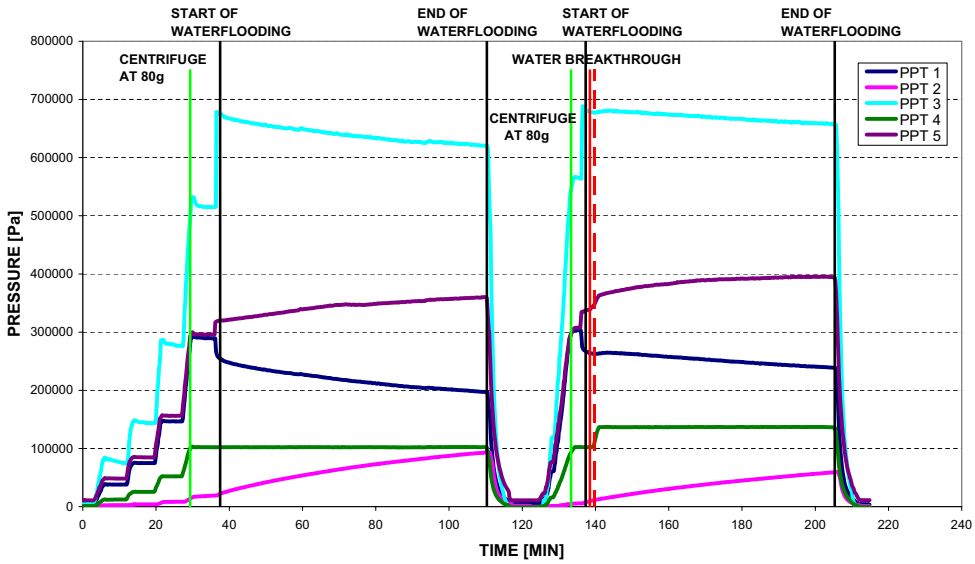

Figure K.2 *Pore pressures measured by the PPTs vs. time of testing on the water-wet specimen 7 corrected for dead volumes. Start of waterflooding = water enters the specimen bottom. Water breakthrough (full red line) = water reaches the specimen top. Water breakthrough (dotted red line) = water reaches the overflow tube in the outlet container. All based on PPT measurements except for water breakthrough (full red line), which is based on the reaction on TDR probe 8 in the top of the specimen.*

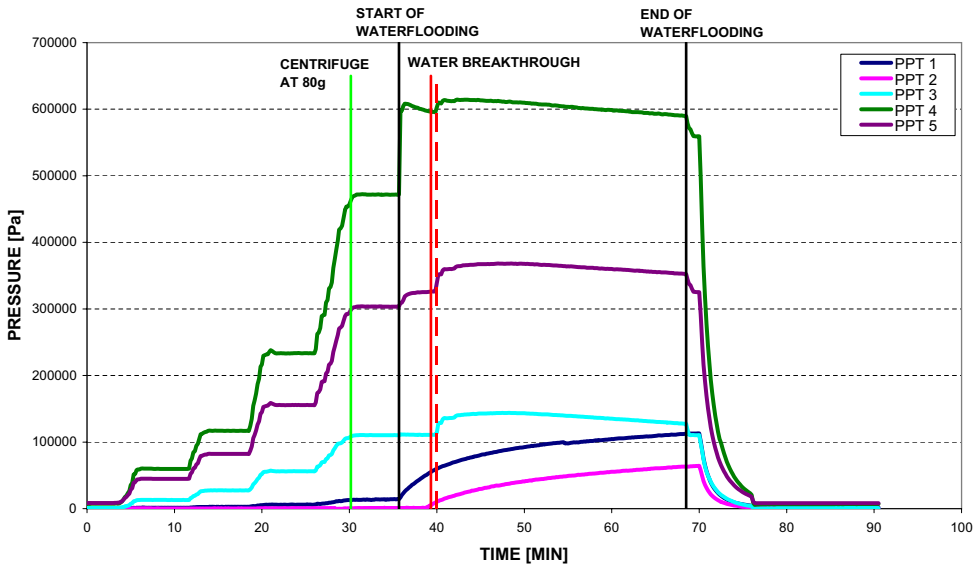

Figure K.3 *Pore pressures measured by the PPTs vs. time of testing on the water-wet specimen 5 corrected for dead volumes. Start of waterflooding = water enters the specimen bottom. Water breakthrough (full red line) = water reaches the specimen top. Water breakthrough (dotted red line) = water reaches the overflow tube in the outlet container. All based on PPT measurements.*

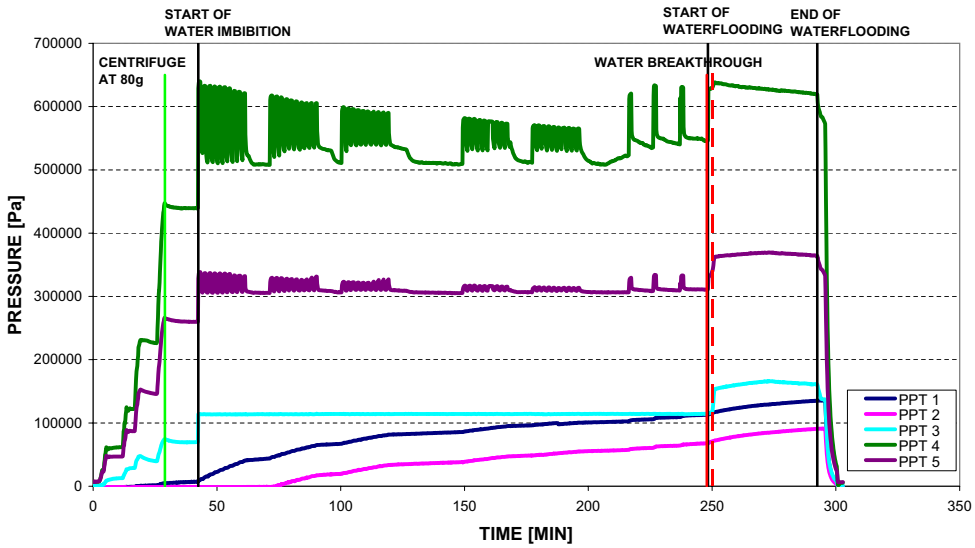

Figure K.4 *Pore pressures measured by the PPTs vs. time of testing on the water-wet specimen 8 corrected for dead volumes. Start of waterflooding = water enters the specimen bottom. Water breakthrough (full red line) = water reaches the specimen top. Water breakthrough (dotted red line) = water reaches the overflow tube in the outlet container. All based on PPT measurements.*

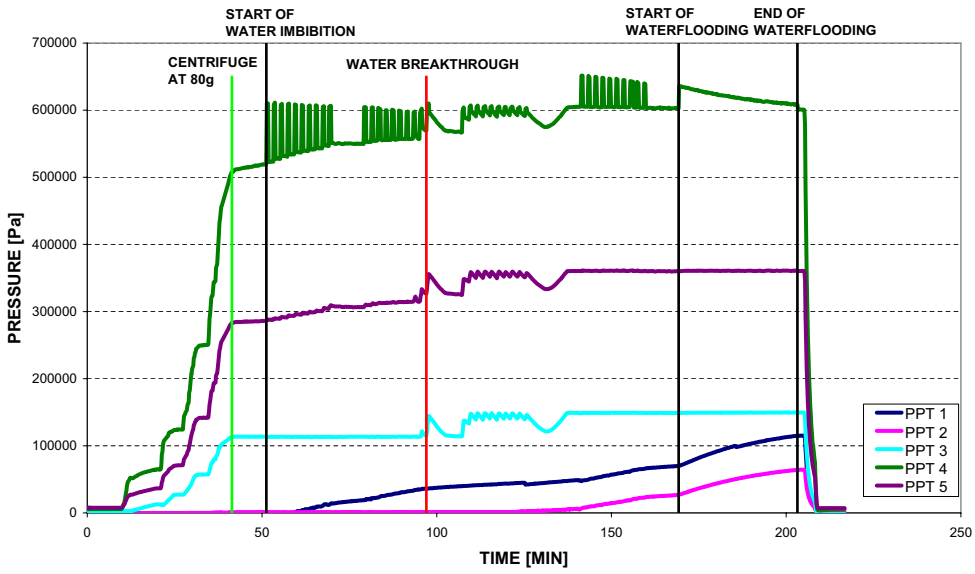

Figure K.5 *Pore pressures measured by the PPTs vs. time of testing on the fractional-wet specimen 2 corrected for dead volumes. Start of waterflooding = water enters the specimen bottom. Water breakthrough (full red line) = water reaches the specimen top. Water breakthrough (dotted red line) = water reaches the overflow tube in the outlet container. All based on PPT measurements.*

Appendix L

Disassembling of the Specimens after Waterflooding

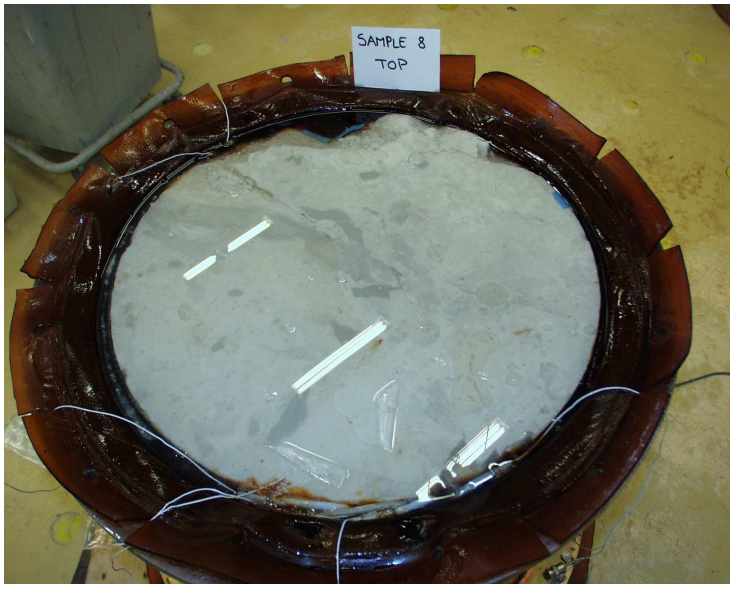

Figure L.1 *The top of specimen 8 after testing. The top plate has been removed. Approximately half of the top dead volume is oil and the other half is water.*

Figure L.2 *Specimen 8 after test. The form is removed, but the membrane is still on the specimen.*

Figure L.3 *Specimen 5 after test. The membrane has been removed, and the rubber cast around the specimen is seen.*

Figure L.4 *Specimen 8 after testing still wrapped in soft plastic foil.*

Figure L.5 *Disassembling of specimen 8 by use of a hammer and a chisel.*

Figure L.6 *The upper of the two horizontal fracture planes in specimen 8 after test.*

Figure L.7 *The lower of the two horizontal fracture planes in specimen 8 after test.*

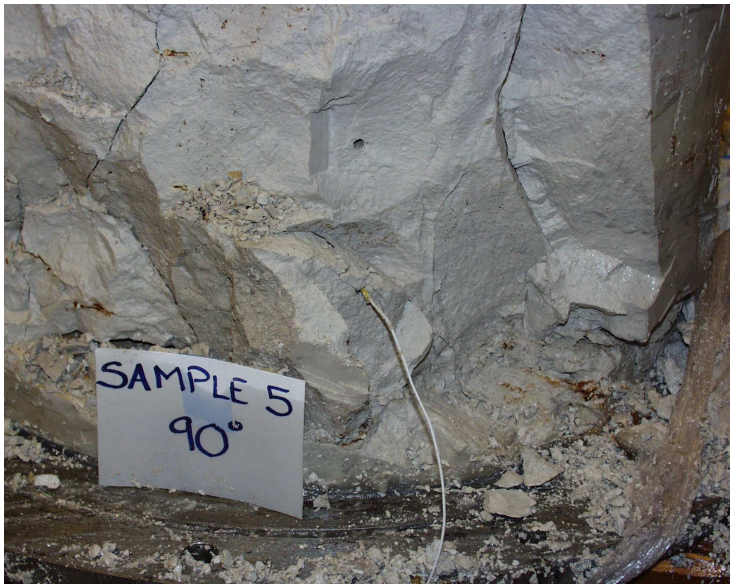

Figure L.8 *TDR probe in specimen after testing.*

Appendix M

Saturations after Waterflooding

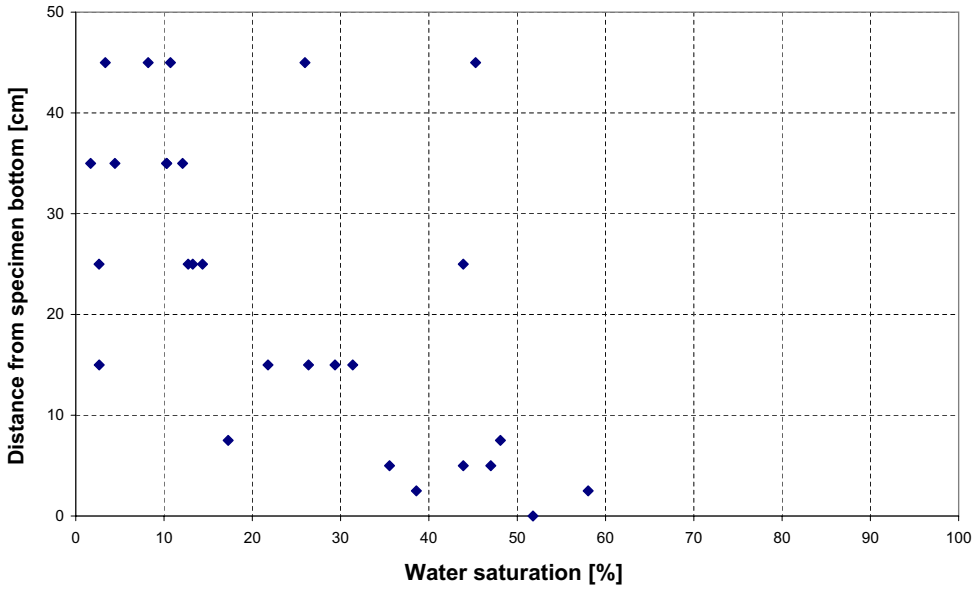

Figure M.1 *Distribution of water in the water-wet specimen 11 based on small samples taken out after waterflooding.*

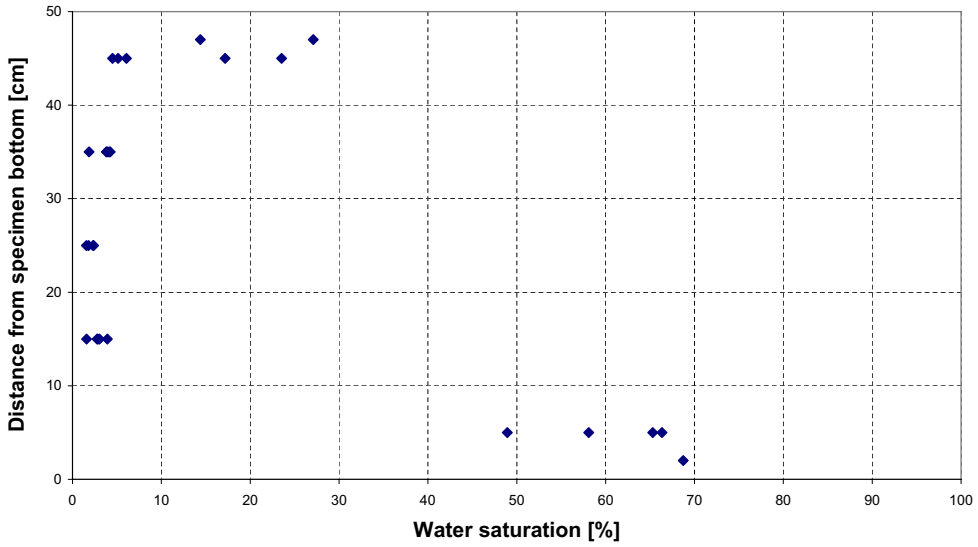

Figure M.2 *Distribution of water in the water-wet specimen 7 based on small samples taken out after waterflooding.*

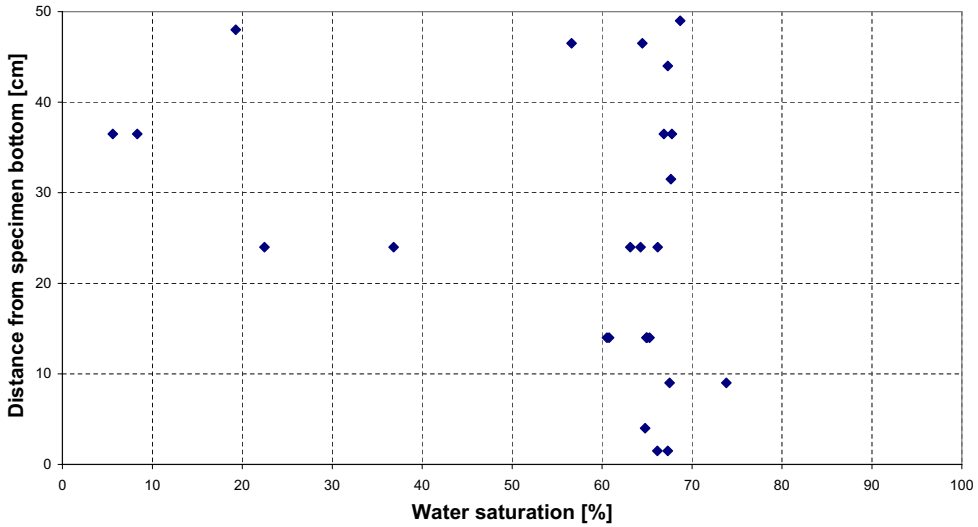

Figure M.3 *Distribution of water in the water-wet specimen 5 based on small samples taken out after waterflooding.*

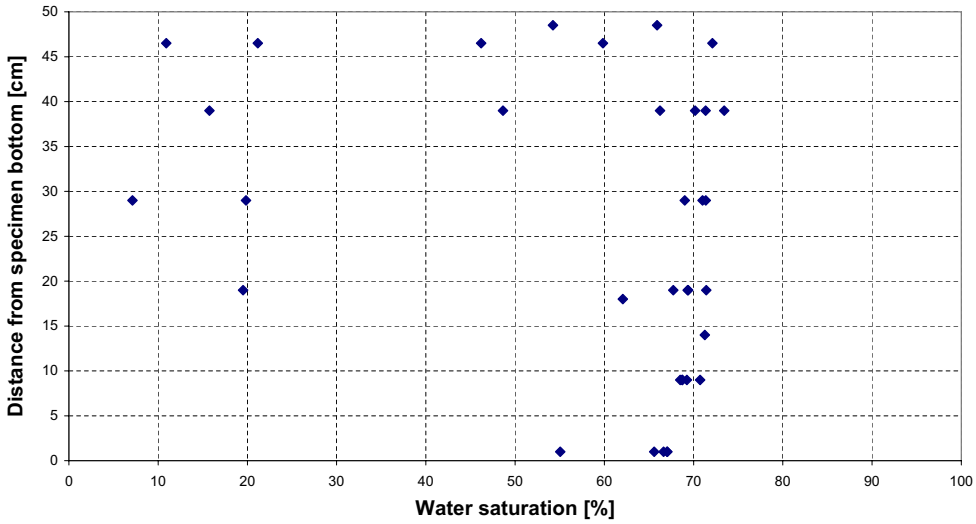

Figure M.4 *Distribution of water in the water-wet specimen 8 based on small samples taken out after waterflooding.*

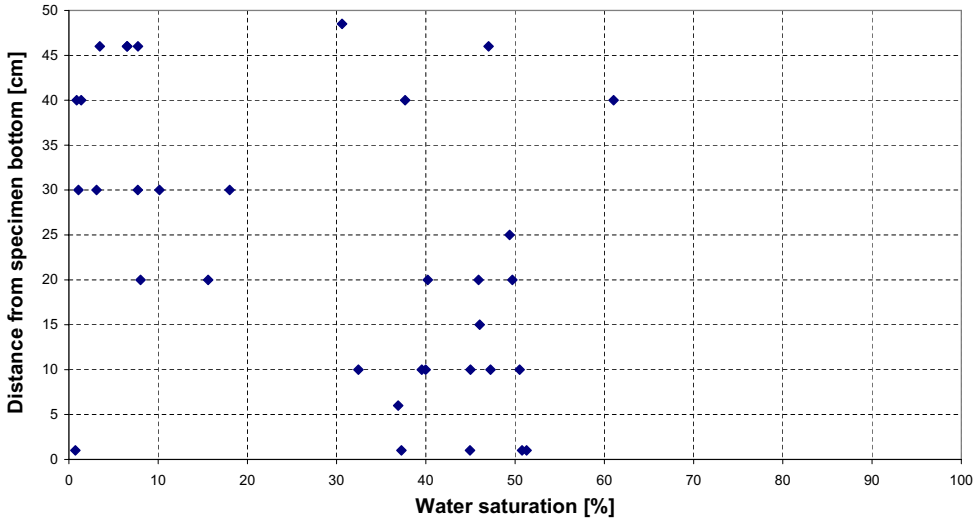

Figure M.5 *Distribution of water in the fractional-wet specimen 2 based on small samples taken out after waterflooding.*

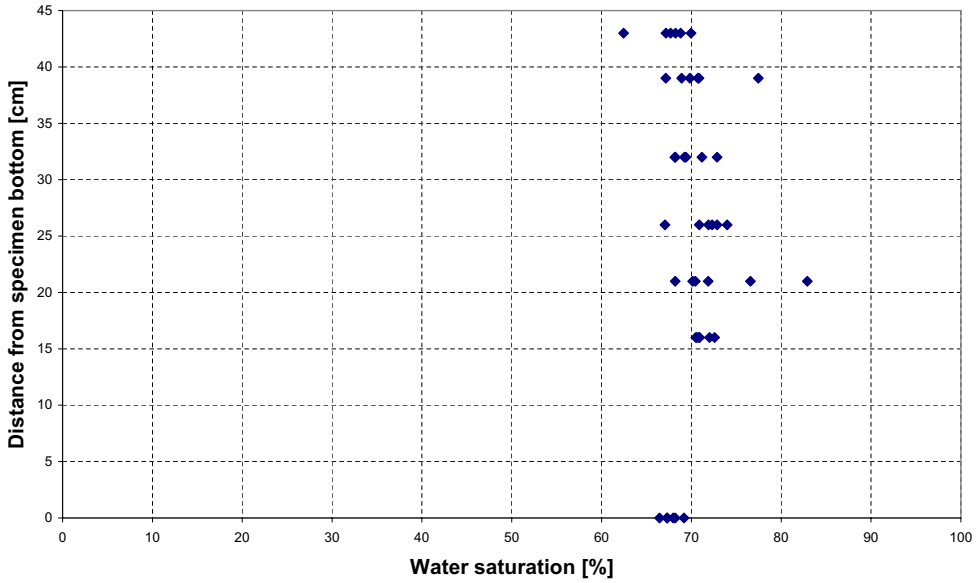

Figure M.6 *Distribution of water in the water-wet specimen 10 based on small samples taken out after waterflooding.*

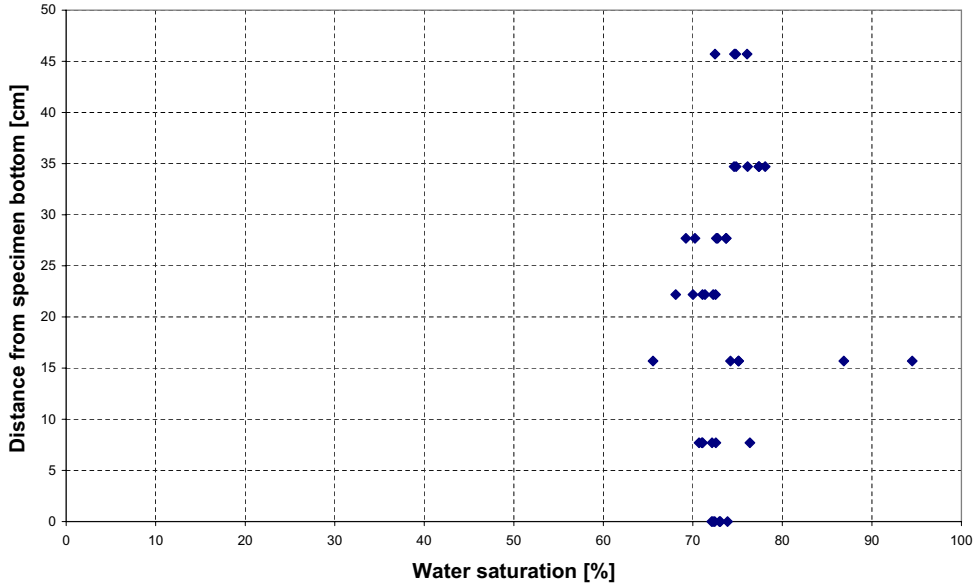

Figure M.7 *Distribution of water in the water-wet specimen 9 based on small samples taken out after waterflooding.*

Appendix N

Waterflooding Test Set-up for the Oedometer Tests

Figure N.1 *Displaced fluids recorded on a double-balance system.*

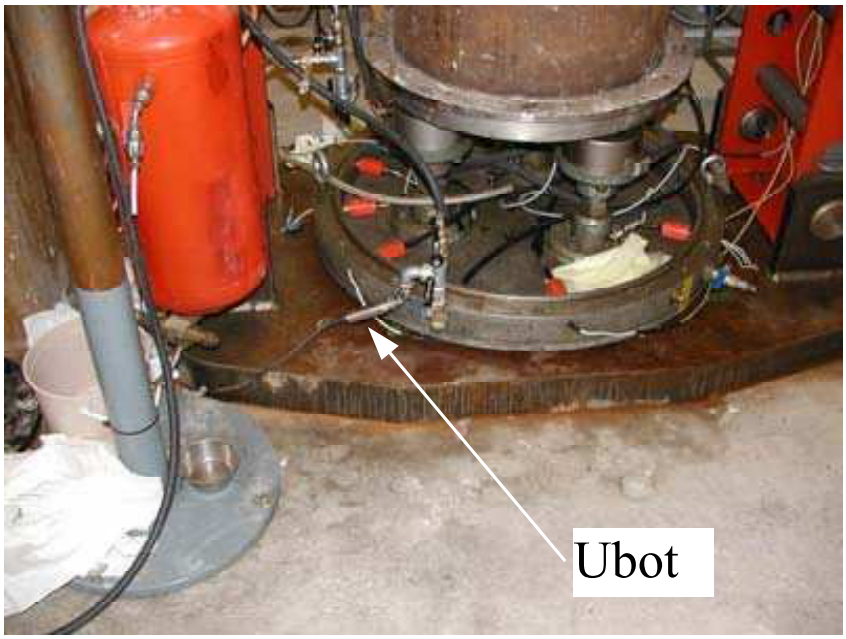

Figure N.2 *Inlet pore pressure transducer, Ubot.*

Figure N.3 *Outlet pore pressure transducer, Utop.*

Figure N.4 *Two LVDTs placed opposite each other on top of the oedometer cell treading down on the load piston. The arrow points to one of the LVDTs*

Appendix O

Waterflooding Test Results in the Oedometer Cell

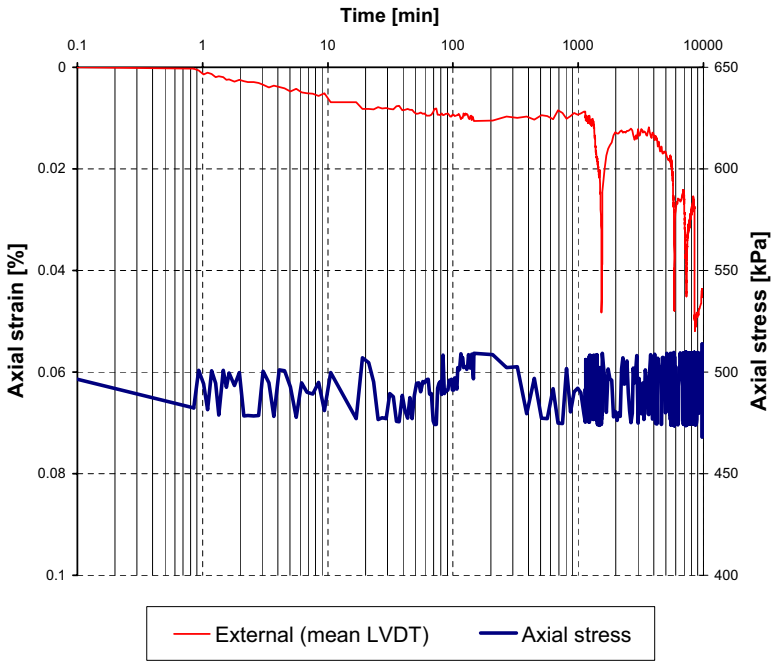

Figure O.1 *Creep at 0.5 MPa for specimen 9.*

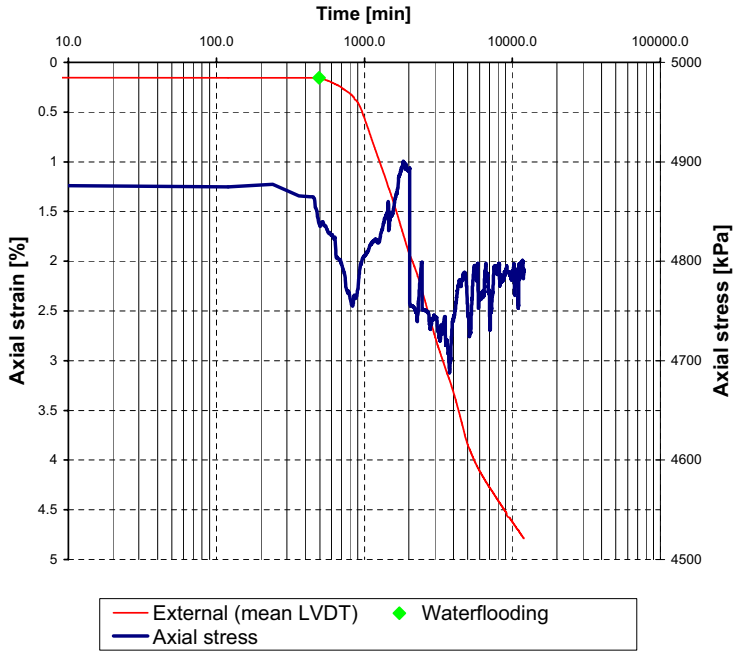

Figure O.2 *Creep at 4.7 MPa for specimen 9.*

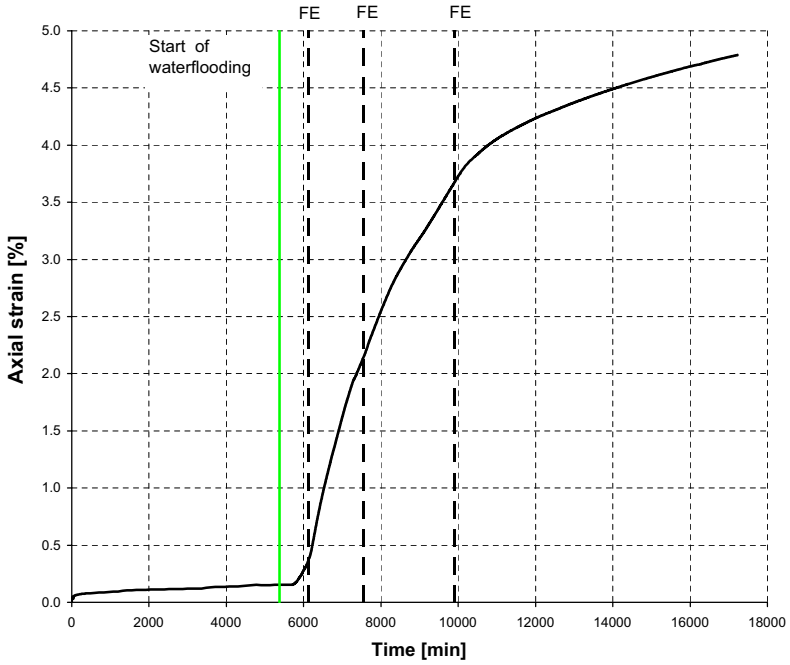

Figure O.3 *Total axial strain vs. time from the time where specimen 9 reached the final load step of 4.7 MPa. FE = fill and empty.*

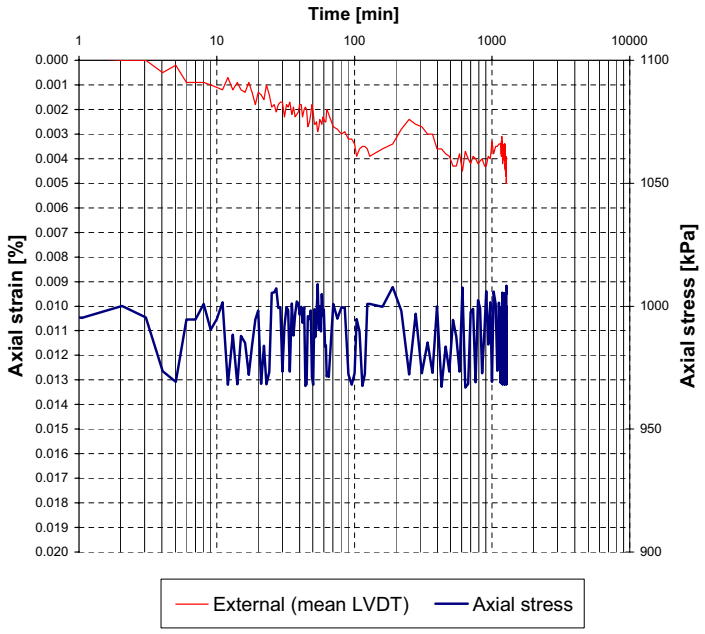

Figure O.4 *Creep at 1 MPa for specimen 10.*

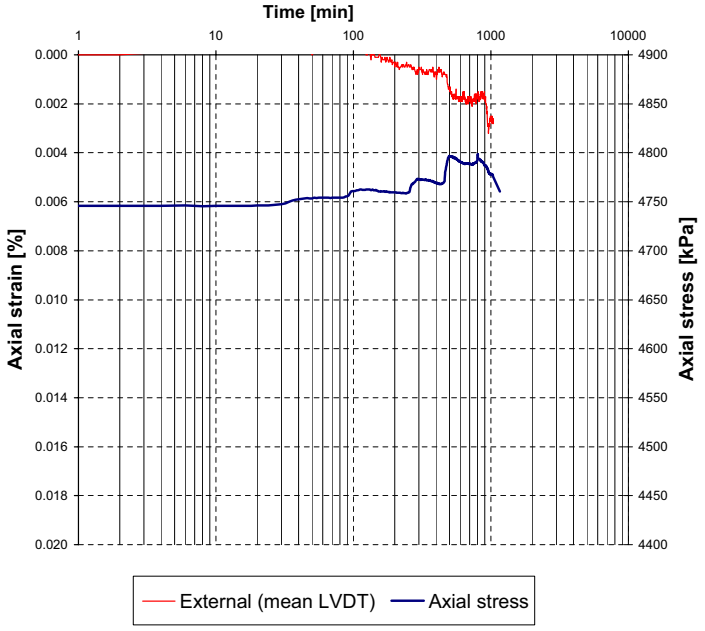

Figure O.5 *Creep at 4.7 MPa for specimen 10.*

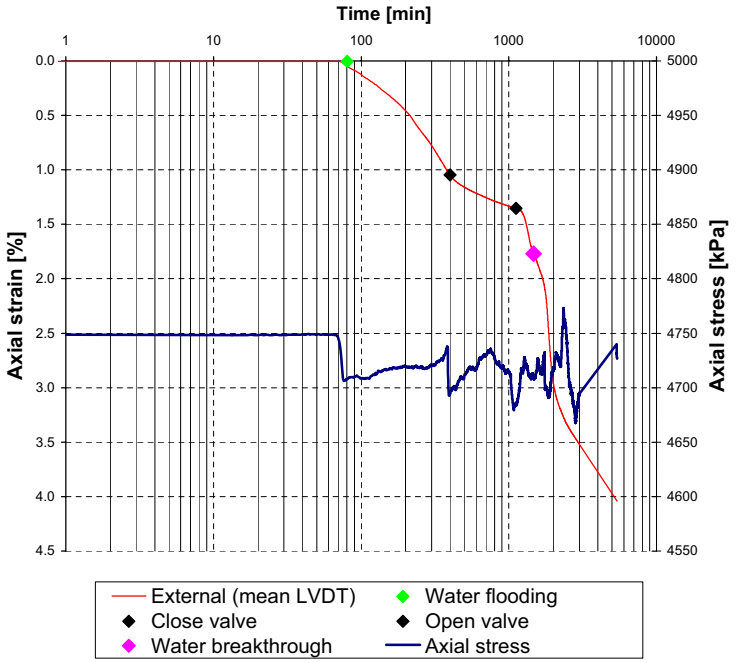

Figure O.6 *Creep at 4.7 MPa for specimen 10.*

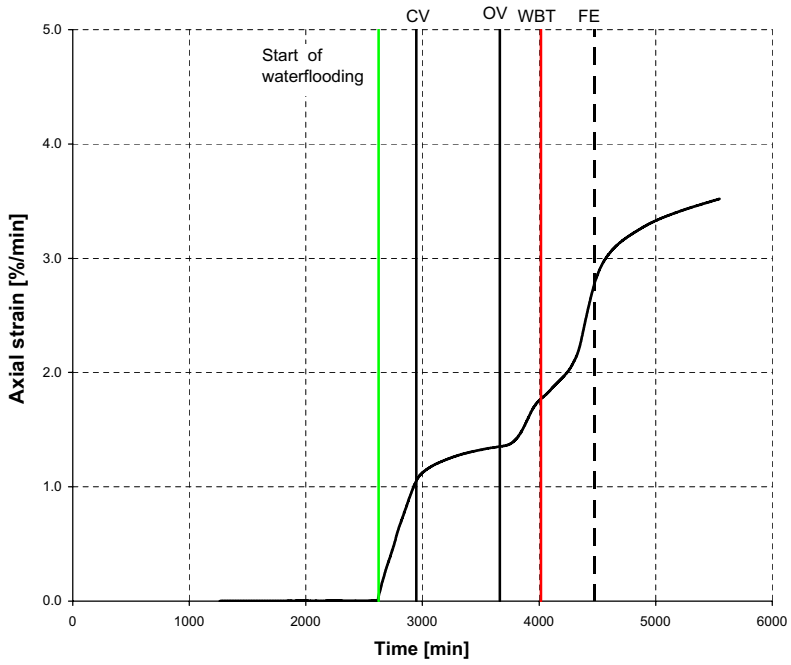

Figure O.7 *Total axial strain vs. time from the time where specimen 10 reached the final load step of 4.7 MPa. CV = close valve, OV = open valve, WBT = water breakthrough and FE = fill and empty.*

Hillerslev Outcrop Chalk

Miriam M. Lykke

Ph.D. Thesis

Department of Civil Engineering
Technical University of Denmark

2005

Hillerslev Outcrop Chalk

Printed by
Department of Civil Engineering
Technical University of Denmark

Preface

This report is part of the written documentation of the Ph.D. project: "Displacement of Oil by Waterflooding in Fractured Chalk". The Ph.D. project was coordinated with and partly financed by a Danish Energy Research Programme (EFP) project 2000. The title of this project is "Displacement and Deformation Processes in Fractured Reservoir Chalk" (Christensen 2003), and the main objective was to quantify the displacement processes in fractured reservoir chalk. The research partners were: Danish Geotechnical Institute (GEO), Geological Survey of Denmark and Greenland (GEUS), Department of Environment and Resources (ER), DTU and Department of Civil Engineering (BYG•DTU), DTU. The industrial partners were: BP Norway and Mærsk Olie og Gas AS.

I thank Senior Research Geologist Finn Jakobsen, GEUS, for help and supervision related to the work described in this report.

Lyngby, April 2005

Miriam M. Lykke

Abstract

A field trip was made to the Hillerslev outcrop chalk quarry located in the northern part of Jutland. Here, a (global) fracture description was carried out and twelve chalk block specimens were sampled. A (local) fracture description was carried out on eight Hillerslev outcrop chalk specimens.

The main orientation NNE-SSW and the secondary orientation NNW-SSE was found in all three fracture data sets in the Ph.D. project. A comparison of the measured Joint Roughness Coefficient (JRC) and fracture aperture for all Ph.D. fracture data shows that some of the fractures along the chalk wall were disturbed which apart from the influence of excavation may be due to weathering near the chalk wall.

Fracture description and sampling carried out in the Hillerslev chalk quarry during "Fractures and Rock Mechanics", phase 1 and 2 was compared to the work presented in this report (Ph.D. project). A comparison shows that the main orientation ENE-WSW is found in phase 1 and 2, and along the wall in the Ph.D. project. This orientation is also found as a secondary orientation behind the specimens. In all fracture data in the Ph.D. project and in phase 2, horizontal beds were observed, and horizontal bedding parallel fractures were common. The fracture density for all the measured fractures in the Hillerslev chalk quarry indicate almost random spacing of fractures, and the majority of all the fractures are steeply dipping with a dominance of almost vertical fractures.

All the specimens were fractured to a higher or lesser degree. In four of the specimens horizontal fracture planes were present. The most dominant fractures in the periphery of the specimens were very steeply dipping and seemed almost vertical. Zones with brittle chalk as seen in two of the specimens were also seen at the Hillerslev quarry.

Overall, the three fracture data sets in the Ph.D. project are evaluated to be similar. Further, it is evaluated that the fracture descriptions in the three research projects are similar. Finally, the local and the global fracture descriptions were in accordance, i.e. the fracture system in the specimens represents the major part of the Hillerslev chalk fracture pattern.

Table of Contents

Chapter 1

Introduction

Fractures are a great benefit to production of oil, since the matrix permeability in the oil bearing chalk reservoirs in the North Sea is low. Many of the oil fields would be marginally economic to produce without natural or induced fractures to enhance the effective permeability of the reservoirs. However, when oil is produced due to waterflooding, an important issue is the effect of fractures on the displacement processes during waterflooding.

To study the effect of fractures on the displacement processes, it is important to obtain knowledge of the fractures in the chalk, i.e. it is necessary to perform a fracture study of the chalk. A field trip was made to the Hillerslev outcrop chalk quarry located in the northern part of Jutland. Here, a (global) fracture description was carried out and twelve chalk block specimens were sampled at a chosen location in the Hillerslev quarry. A team of five including the author performed the sampling of the large specimens. However, the drilling of the specimens by use of a mobile drilling rig was performed by GEO, and staff at the Hillerslev outcrop quarry performed the rough excavation by use of a backhoe. A (global) fracture description was carried out mainly by the author with help from the group. The author performed the processing and evaluation of the fracture data. The presentation of the fracture data was carried out at GEUS with help and supervision from Senior Research Geologist Finn Jakobsen, GEUS.

For comparison of earlier work performed in the Hillerslev chalk quarry, a summary of the fracture description and sampling carried out during the earlier research project "Fractures and Rock Mechanics", phase 2 (Jakobsen 2001), and the earlier research project "Fractures and Rock Mechanics", phase 1 (Krogsbøll et al. 1997) containing even earlier work is included.

A (local) fracture description was carried out by the author on eight Hillerslev outcrop chalk specimens. One of these specimens was sampled during "Fractures and Rock Mechanics", phase 2 (Jakobsen 2001). The other seven were sampled during the Ph.D. project.

Chapter 2

Description of Hillerslev Outcrop Chalk (Earlier Work)

The Hillerslev outcrop chalk quarry is located near Thisted in the northwestern part of Jutland. The location of the Hillerslev chalk quarry is indicated on Figure 2.1.

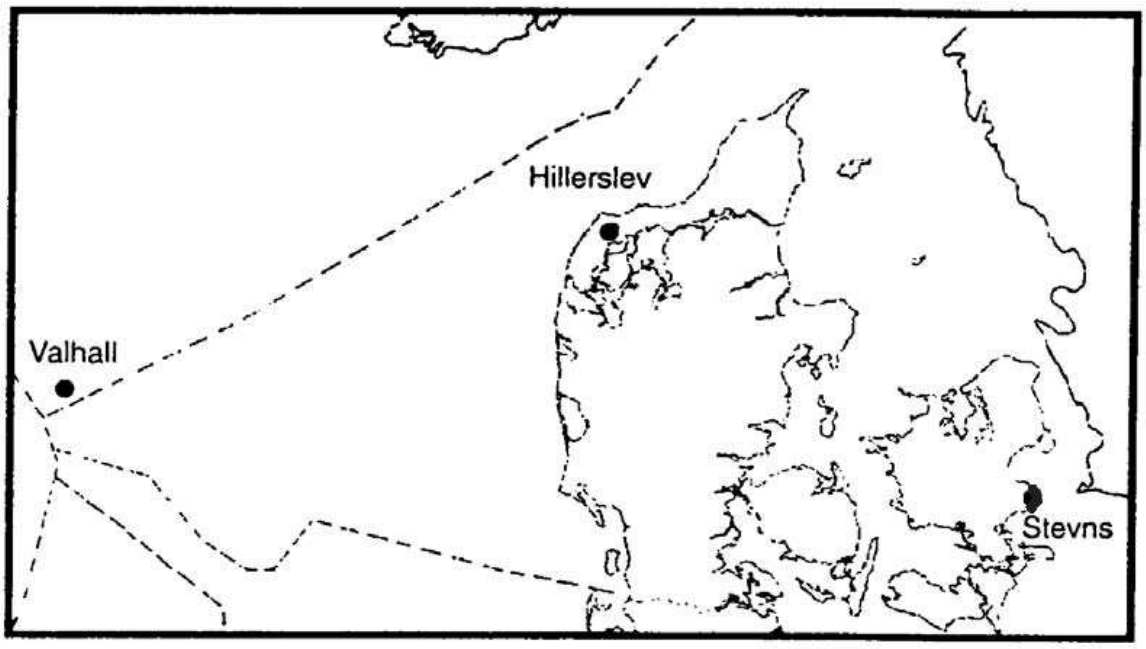

Figure 2.1 *Location of the Hillerslev chalk quarry.*

The Hillerslev chalk quarry is an active quarry located on the eastern half of the top of the Thisted dome, which is a salt-induced dome. The size of the chalk quarry is approximately 500 m × 200 m (Jakobsen 2001). The chalk at the Hillerslev quarry is heavily fractured. The fracturing of the quarry is assumed to be related to the structural

growth of the dome. The general tilt in the Hillerslev area is 4 degrees towards ESE (Krogsbøll et al. 1997).

The chalk in the quarry is of Late Maastrictian age. It is a soft, greyish white, weakly cemented mudstone/wackestone. It is composed almost exclusively of coccolithic material with subordinate amounts of skeletal material (foraminifera, bryozoans, echinoderms and molluscs). The chalk has a low content of silica, clay minerals and pyrite (Krogsbøll et al. 1997).

Analysis of Hillerslev chalk specimens indicates that the chalk is more affected by compaction (mechanical diagenesis) than chemical diagenesis. Flint concretions in the chalk only amount to a small part of the total sediment volume (Krogsbøll et al. 1997).

2.1 Earlier Research Project, Phase 1

A detailed description of the fracture system of the Hillerslev chalk quarry was carried out in an earlier chalk research project, and the main conclusions from that project are given in the earlier research project "Fractures and Rock Mechanics", phase 1, geology report (Krogsbøll et al. 1997), and summarised below.

In the northern part of the Hillerslev quarry a low chalk wall (approximately 4 m high and 45 m long) was excavated and described (Figure A.1, Appendix A). Fracture density and fracture orientations were determined along a horizontal line profile (approximately 31 m long) in the wall. The fracture description was associated with a series of one inch core specimens sampled along the horizontal line.

Analysis of more than 200 specimens sampled along the horizontal profile shows a porosity variation of 44-52% with an average of 47%. The average gas permeability is 8.1 mD, ranging from 5.1-13.4 mD. The average distribution of pore throat radius is 0.6 mm. The content of insoluble residue is low, around 4%.

As the one inch core specimens and fracture data was sampled along the same line, the possible correlation between the variation in porosity and permeability and the position of fractures was investigated. However, no clear evidence of correlation was observed.

Information on fracture density and the orientations (strike/dip) of each fracture was primarily sampled along the horizontal line profile in the excavated chalk wall, see Figure A.1, Appendix A. However, the fracture data were supplemented with measurements of fracture orientations from other locations in the quarry.

The density of the fractures along the horizontal line is evident from Figure A.2, Appendix A, where each measured fracture is marked by a vertical line. The measured fracture densities indicate almost random spacing of fractures. A rose diagram of strike (Figure A.3, Appendix A) shows that a high proportion of fractures are oriented ENE-WSW with NNW-SSE as another important direction. The dip directions are shown in a rose diagram in Figure A.4, Appendix A. The number of fractures sorted by dip is plotted as a histogram in Figure A.5, Appendix A. From Figure A.5 it is seen that the majority of the fractures are steeply dipping with a dominance of almost vertical fractures.

Three different lithotypes have been recognized along the profile. The most common lithotype found in most of the profile is burrowed massive chalk mudstone. Locally, burrowed laminated chalk mudstone is also seen and in the eastern part of the profile pebbly massive chalk mudstone (and skeletal wackestone) is dominating.

2.2 Earlier Research Project, Phase 2

In the earlier research project "Fractures and Rock Mechanics", phase 2 (Jakobsen 2001) supplementary fracture descriptions were carried out along new profiles in a re-excavation of the same wall section described in "Fractures and Rock Mechanics", phase 1. The study is thus supplementary to phase 1 and the main work is related to the descriptions and conclusions from that project. Description and fracture measurements were carried out along horizontal lines along the freshly excavated originally exposed chalk wall in the Hillerslev quarry. During the project period the chalk profile was further excavated 2 m into the wall with a temporary formation of a plateau for sampling of block specimens.

Information on fracture density and the orientations (strike/dip) of each fracture included here was sampled along a horizontal line profile along the same horizontal line profile as described in "Fractures and Rock Mechanics", phase 1, i.e. the profiles are identical except for the length. The new line profile is only approximately 25 m of the originally approximately 31 m. The new profile is referred to as the reference profile.

The density of the fractures along the reference profile is evident from Figure B.1, Appendix B. The measured fracture densities indicate almost random spacing of fractures. The orientations of the fractures were measured as strike/dip. A rose diagram of strike (Figure B.2, Appendix B) shows that a high proportion of fractures are oriented ENE-WSW and SSE-NNW with NNE-SSW and SE-NW as secondary directions. Horizontal bedding is seen, and horizontal bedding parallel fractures are common. Dip directions of fractures are plotted in a rose diagram (Figure B.3, Appendix B). The number of fractures sorted by dip is plotted as a histogram (Figure B.4, Appendix B). From Figure B.4 it is seen that the majority of fractures are steeply dipping with a dominance of almost vertical fractures.

Ten block specimens and a number of smaller irregular blocks were sampled (Havmøller & Krogsbøll 2001).

In some of the specimens hairlines were observed. Hairlines are formed by small-scale vertical shear. The induced fractures are partly controlled by the hairlines and parts of the fracture planes are coinciding with the hairlines.

Based on the sampled specimens, two chalk types were identified; a soft, greyish white bioturbated chalk mudstone characterized by a weakly laminated structure partly disturbed by burrowing organisms, and a sparse biomicritic chalk wackestone. The microfossil content in the wackestone is dominated by calcispheres. Foraminifera and echinoderm fragments are rare. The main component of the wackestone is the large amount of well-preserved coccoliths.

Chapter 3

Sampling of Large Hillerslev Chalk Specimens

At the Hillerslev outcrop chalk quarry, twelve cylindrical block specimens with the dimensions $D \approx 50$ cm and $H \approx 50$ cm were sampled successfully. A team of five including the author performed the sampling of the large specimens. However, the drilling was performed by GEO, and staff at the quarry performed the work done by backhoe.

Initially a location for fracture description and sampling at the Hillerslev chalk quarry was chosen, see Figure C.1 and C.2, Appendix C. The location is situated in the northern part of the quarry just west of the location used for fracture description and sampling in the earlier research projects "Fractures and Rock Mechanics", phase 1 and 2. The locations are indicated on Figure C.3, Appendix C.

A chalk wall (approximately 2.5 m high and 25 m long) was excavated at the chosen location, see Figure C.4, Appendix C. A fracture description including fracture density and fracture orientations (strike/dip) was performed along a horizontal line along the wall from a chosen start point (point 1) at the eastern end of the wall and approximately 9 m towards west (Figure D.1, Appendix D). The fracture description is included in Section 4.1.

A horizontal plateau (approximately 1.5 m high, 25 m long and 2 m deep) referred to as the chalk bench was made by further excavation (approximately 2 m) into the wall starting approximately 4 m above the ground, i.e. 2.5 m above the bench (Figure D.2, Appendix D). The bench is seen in Figure C.5, Appendix C. The bench was made for sampling of block specimens. A ramp of chalk was temporarily built in front of and beside the bench in order for the mobile drilling rig to be able to drill from the top of the bench (Figure C.6, Appendix C). The drilling rig is a 12 ton Unimog HY77 with a maximum torque of 900 kgm and a maximum speed of 50 rounds per minute.

Before drilling, the drill bit was mounted on the rig and the chalk surface of the drilling spot was levelled (Figure C.7, Appendix C). Water was added during drilling to cool the drill bit and flush away cuttings (Figure C.8, Appendix C). Drilling was performed using a light vertical pressure and at a speed lower than 50 rounds per minute. If the bit was pushed too hard onto the chalk surface, the chalk crushed immediately. After drilling to a depth of 60 cm below the surface, the bit was pulled up very slowly still rotating, while water was added. This procedure was performed in order to avoid tension cracks in the

specimens.

After removal of the drill bit, a metal shield was inserted in the trace left by the drill bit (Figure C.9, Appendix C). After metal shields were inserted in twelve promising out of twenty drill traces, the success criteria was fulfilled, and the drilling was ended. Then the ramp of loose chalk in front of the bench was removed. A fracture description including fracture density and fracture orientations (strike/dip) was performed along a horizontal line along the front of the bench from a chosen start point (approximately 10 m west of point 1) and approximately 10 m towards west (Figure D.2, Appendix D). The fracture description is included in Section 4.1.

A backhoe was used to perform the rough excavation in front of and beside the specimen to a distance of approximately 20 cm from the metal shield and to a depth of 30-50 cm below the estimated location of the specimen bottom. The distance to the metal shield was maintained in order to avoid possible fracturing induced by the backhoe and to avoid dragging out thin beds of hardened chalk (Figure C.10, Appendix C). As the chalk is highly fractured, most of the chalk surrounding the specimen was removed by hand using hammer and chisel or by use of an electrical Bosch hammer.

After removal of the surrounding chalk, the metal shield was removed, and the specimen was inspected. Often it was necessary to wrap blue tape around the specimen to ensure that parts of the fractured specimen did not fall of. A specimen secured with blue tape is seen in Figure C.11, Appendix C. A rubber membrane was pulled over the specimen. This is seen in Figure C.12, Appendix C. Then an additional rubber blanket and the metal shield were wrapped around the specimen. Two steel belts were fastened around the shield. The top surface was trimmed roughly by use of a chain saw. A piece of blue tape was placed on the trimmed top surface to indicate the direction of north. A plastic cap was placed on the top surface of the specimen. The top of the membrane was fitted around the cap, and a steel belt was fastened around the membrane (Figure C.13, Appendix C).

The backhoe was used to hold onto the specimen via lifting equipment fastened around the specimen while the specimen was cut free at the bottom by use of a chain saw, see Figure C.13, Appendix C. The backhoe was then used to lift up the specimen and move it from the ground and turn it upside down for a rough trimming of the bottom surface (Figure C.14, Appendix C). The trimming was performed by use of a chain saw. A plastic cap was placed on the bottom surface after trimming. The specimens were trimmed to a height a little higher that 50 cm, since the final trimming should be performed in the laboratory. The bottom of the membrane was fitted around the cap, and a steel belt was fastened around the membrane (Figure C.15, Appendix C).

The specimen was then placed upside down on a wooden pallet. The first successfully sampled specimen is shown in Figure C.15, Appendix C.

View of the bench and wall with indication of the location of the twelve specimens by yellow numbering on the wall behind the specimens is seen in Figure C.16, Appendix C. At this stage the first specimen is sampled and the surrounding chalk in front of and beside eight of the specimens is more or less removed. A sketch of the location of the twelve specimens on the bench is shown in Figure D.3, Appendix D.

A fracture description including fracture density and fracture orientations (strike/dip) was performed approximately 75 cm behind all twelve specimen stumps, i.e. the area

below the bottom of the specimens, where the specimens were cut free by use of a chain saw. The fracture description is included in Section 4.1.

Finally the specimens were transported to the laboratory at DTU on a lorry (Figure C.17, Appendix C). A number of smaller chalk blocks with fractures were also brought to the laboratory.

Chapter 4

Description of Hillerslev Outcrop Chalk (Additional Work)

4.1 Ph.D. Project

In the Ph.D. project, the fracture description was carried out along horizontal profiles in the northern part of the quarry just west of the location used for fracture description and sampling in "Fractures and Rock Mechanics", phase 1 and 2. The author mainly carried out the fracture description in the Ph.D. project with help from the group, and the author performed the processing and evaluation of the fracture data.

The fracture description includes fracture density (no. and position), fracture orientations (strike/dip), fracture roughness (JRC) and fracture aperture.

Fracture No.: The fractures are numbered for identification. The number of fractures is an alternative fracture density indication.

Strike: Strike is the orientation of the intersection line between the fracture plane and a horizontal plane, i.e. the compass orientation of the horizontal line, which can be drawn on the fracture plane. Strike is indicated in Figure 4.1.

Dip: Both dip and dip directions are included in the fracture description. Dip is the angle between the fracture plane and the horizontal plane, i.e. the angle between the vertical line that can be drawn of the fracture plane and the horizontal plane. A determination of dip direction is necessary as the fracture plane can dip to either side of the strike for the fracture plane. Dip direction is perpendicular to strike. Dip and dip direction is indicated in Figure 4.1.

Roughness: Joint Roughness Coefficient (JRC) is a quantification of fracture surface roughness (Barton 1976). A linear relationship between asperity along the dip direction and length of the measured profile is indicated as JRC values from 0-20. In this project, the fracture roughness is evaluated on basis of characteristic JRC-profiles (Appendix F).

Aperture: Maximum measurable opening of the fractures.

Position: Intersection with measuring tape (measured towards west with point 1 as zero). The position of the fractures gives opportunity to map the fracture density.

The density of the fractures and the orientations (strike/dip) are graphically represented in density maps and rose diagrams made by use of a program called SpheriStat.

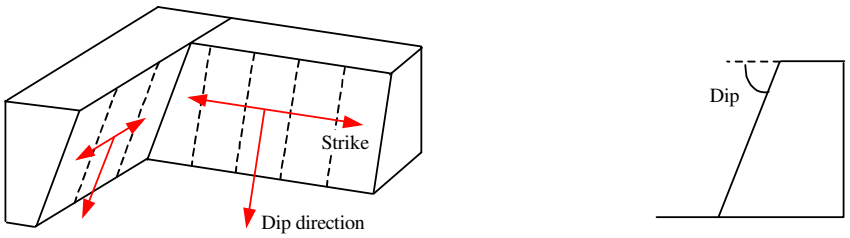

Figure 4.1 *Fracture planes with indication of strike, dip and dip direction.*

In a rose diagram strike and dip direction of a fracture can be represented. A rose diagram is seen in Figure 4.2.

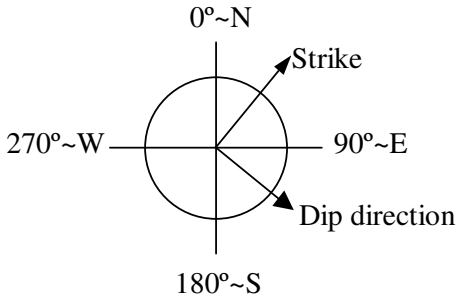

Figure 4.2 *Rose diagram with strike and associated dip direction indicated.*

The fracture density maps are based only on the measured horizontal position of the fractures, as the vertical position was not measured.

Fracture descriptions were performed along a horizontal profile along the freshly excavated chalk wall, along a horizontal profile along the front of the chalk bench made by further excavation into the chalk wall, and finally along twelve horizontal profiles - one behind each of the sampled specimens. Horizontal bedding was seen with beds of hardened chalk and horizontal bedding parallel fractures were seen along all the horizontal profiles. These fractures may be surface parallel tensional fractures due to unloading since the area has been subjected to uplift and subsequent erosion during the geological history (Jakobsen 2001). Fractures due to frost were also present since the Hillerslev formation is situated in the top of the geological profile, but such fractures were not seen and actually not expected since the fracture description is performed at least 10 m below the top of the ground, and at least 1 m of chalk material was removed in the depth, when the chalk

wall was excavated. Conjugate shear fracture sets were also seen along all the horizontal profiles. "Crushing zones", i.e. zones with brittle chalk were seen as well. The chalk at the location was identified as chalk mudstone.

Chalk Wall

The chalk wall is approximately 2.5 m high and 25 m long. A fracture description was performed along a horizontal line along the wall from a chosen start point (point 1) at the eastern end of the wall and approximately 9 m towards west (Figure D.1, Appendix D).

A map of strike/dip indicating the density of the fractures along the profile is evident from Figure E.1, Appendix E. The measured fracture densities indicate almost random spacing of fractures. A rose diagram of strike (Figure E.5, Appendix E) shows that a high proportion of fractures are oriented NNE-SSW and ENE-WSW with NNW-SSE and WNW-ESE as secondary directions. Dip directions of fractures are plotted in a rose diagram (Figure E.6, Appendix E). The number of fractures sorted by dip is plotted as a histogram (Figure E.7, Appendix E). From Figure E.7 it is seen that the majority of fractures are steeply dipping with a dominance of almost vertical fractures.

Chalk Bench

The chalk bench is approximately 1.5 m high, 25 m long and 2 m deep. The wall behind the bench is approximately 4 m above the ground, i.e. 2.5 m above the bench. A fracture description was performed along a horizontal line along the front of the bench from a chosen start point (approximately 10 m west of point 1) and approximately 10 m towards west (Figure D.2, Appendix D).

A map of strike/dip indicating the density of the fractures along the profile is evident from Figure E.2, Appendix E. The measured fracture densities indicate almost random spacing of fractures. A rose diagram of strike (Figure E.8, Appendix E) shows that a high proportion of fractures are oriented NNE-SSW and ESE-WNW with NNW-SSE as a secondary direction. Dip directions of fractures are plotted in a rose diagram (Figure E.9, Appendix E). The number of fractures sorted by dip is plotted as a histogram (Figure E.10, Appendix E). From Figure E.10 it is seen that the majority of fractures are steeply dipping with a dominance of almost vertical fractures.

Chalk Specimens

Twelve cylindrical specimens with the dimensions $D \approx 50$ cm and $H \approx 50$ cm were sampled successfully. The location of the specimens on the bench is indicated in Figure D.3, Appendix D.

Behind the Chalk Specimens

A fracture description was performed on horizontal line profiles of 0.5-2 m length approximately 75 cm behind each of the twelve specimen stumps.

A map of strike/dip indicating the density of the fractures along the line with the twelve horizontal line profiles is evident from Figure E.3, Appendix E. The measured fracture

densities indicate almost random spacing of fractures. A rose diagram of strike (Figure E.11, Appendix E) shows that a high proportion of fractures are oriented NNE-SSW and ESE-WNW with ENE-WSW and NNW-SSE as secondary directions. Dip directions of fractures are plotted in a rose diagram (Figure E.12, Appendix E). The number of fractures sorted by dip is plotted as a histogram (Figure E.13, Appendix E). From Figure E.13 it is seen that the majority of fractures are steeply dipping with a dominance of almost vertical fractures.

The location of the horizontal line profile along the wall, along the front of the bench and the location of the horizontal line along which the twelve horizontal line profiles behind the specimens are situated are sketched in Figure D.4, Appendix D.

A map of strike/dip indicating the density of all the measured fractures are shown in Figure E.4, Appendix E. In Figure E.4, the location of the centres of the twelve specimens are indicated.

Strike vs. JRC is plotted in a Schmidt projection (equal area) for measured data both for the wall, the bench and behind the specimens. The projections are seen in Figure E.14-E.16, Appendix E. The JRCs are mainly between 5-15. No clear correlation is seen between strike and JRC. However, experience from "Fractures and Rock Mechanics", phase 2 indicates that caution should be paid on determination of the JRC along fracture profiles shorter than 10 cm, which many of the measured fractures had. Further, it is important to determine the roughness along the dip direction of the fracture to obtain the most reliable values (Jakobsen 2001).

The number of fractures sorted by JRC is plotted as a histogram for measured data both for the wall, the bench and behind the specimens. The histograms are seen in Figure E.17-E.19, Appendix E. For the fractures along the chalk wall, no clear picture of JRC is seen, as all the JRCs are represented and no one more distinct than the other. For the fractures both along the chalk bench and behind the specimens, the JRC is around 9 and no smooth (JRC: 0-2) or rough (JRC: 18-20) fractures are represented.

The number of fractures sorted by aperture is plotted as a histogram for measured data both for the wall, the bench and behind the specimens. The histograms are seen in Figure E.20-E.22, Appendix E. For the fractures along the wall, apertures between $\leq$ 0.1 to 0.5 mm and 1 to 2 mm were seen, i.e. both closed to very narrow fractures and very open fractures were seen. The closed to very narrow fractures were dominating, but some very open fractures were seen. For the fractures both along the chalk bench and behind the specimens, primarily apertures $\leq$ 1 mm, were seen, i.e. the number of closed fractures were dominant and only very few very open fractures were observed.

Chapter 5

Comparison of Hillerslev Work

A comparison of the data from the "Fractures and Rock Mechanics", phase 1 and 2, and the Ph.D. project is included. In addition, a comparison of the three different sets of fracture data found in the Ph.D. project is included.

The main and secondary orientations of the measured fractures (strike) for the three research projects are included in Table 5.1.

A comparison of the main orientations of the fractures (strike) for the three research projects shows that the orientation ENE-WSW is found in "Fractures and Rock Mechanics", phase 1 and 2, and along the horizontal profile along the wall in the Ph.D. project. The orientation is also found as secondary orientation behind the specimens. It is expected to have some correlation between the measured fracture orientations from "Fractures and Rock Mechanics", phase 1 and 2, since the horizontal profile used in phase 2 is a re-excavation of the horizontal profile used in phase 1. However, the fracture data represented in phase 1 are supplemented with data from other locations in the quarry.

A comparison of the main orientations found along the wall, the bench and behind the specimens in the Ph.D. project shows that the orientation NNE-SSW is found along all three profiles, this orientation is also found as secondary orientation for phase 2. A comparison of the secondary orientations shows that the orientation NNW-SSE is found along all three profiles in the Ph.D. project. Again, it is expected to have some correlation between the measured fracture orientations from the three horizontal profiles, since the horizontal profile used is from the same location (displaced only in the northern and vertical direction).

Overall, similar fracture orientation were found along the wall, the bench and behind

	"Fractures and Rock Mechanics"				Ph.D. project					
	Phase 1		Phase 2		Wall		Bench		Behind specimens	
Main orientations	ENE-WSW	NNW-SSE	SSE-NNW	ENE-WSW	NNE-SSW	ENE-WSW	NNE-SSW	ESE-WNW	ESE-WNW	NNE-SSW
Secondary orientations	-	-	SE-NW	NNE-SSW	NNW-SSE	WNW-ESE	NNW-SSE	-	ENE-WSW	NNW-SSE

Table 5.1 *Main and secondary fracture orientations for the research projects "Fractures and Rock Mechanics", phase 1 and 2 and the Ph.D. project.*

the specimens.

The measured fracture densities indicate almost random spacing of fractures for all the measured fractures in the Hillerslev outcrop chalk quarry. The number of fractures sorted by dip is plotted as histograms for all the measured fractures in the research projects (Figure A.5, Appendix A, Figure B.4, Appendix B and Figures E.7, E.10 and E.13, Appendix E). A comparison of the histograms shows that the majority of all the measured fractures in the Hillerslev quarry are steeply dipping with a dominance of almost vertical fractures.

In both the Ph.D. project and phase 2, horizontal bedding parallel fractures are common.

The correlation between JRC and aperture for the three different sets of fracture data found in the Ph.D. project (Figures E.17-E.22, Appendix E) is interpreted as follows: The measured JRC and aperture is of the same order and distribution for the fractures both along the chalk bench and behind the specimens. This consistency indicates that the fractures here were not disturbed by etc. the excavation performed by use of a backhoe. However, when comparing the measured JRC and aperture for all three sets of fracture data, it is evaluated that the fractures along the chalk wall were disturbed. This evaluation is mainly based on the fact that some very open fractures were observed along the chalk wall, while only very few very open fractures were observed along the chalk bench and behind the specimens. Some of the included data with apertures of 1.5 to 2 mm may thus be fractures opened or induced by the backhoe. The fact that the variance in JRC for the chalk wall differs from the JRCs measured along the chalk bench and behind the specimens also supports a disturbance, which apart from the influence of excavation may be due to weathering near the chalk wall.

Chapter 6

Hillerslev Chalk Specimens

A (local) fracture description was carried out on eight Hillerslev outcrop chalk specimens used in the Ph.D. thesis. One of these specimens (specimen 11) was sampled during the "Fractures and Rock Mechanics", phase 2. The other seven (specimens 2, 3, 5, 7, 8, 9 and 10) were sampled during the Ph.D. project. For the purpose of a local fracture description, fractures, voids at the surface, gypsum and crushed zones were indicated on pieces of plastic matching the top, the bottom and the periphery of the specimens. Photos of the pieces of plastic are included in Appendix G. The location of the seven sampled specimens is indicated in Figure D.3 in Appendix D.

The specimens were described as light grey (chalk mudstone) with areas of a darker grey color (clay). Spots of rust were seen on the surfaces. There were marks on the periphery of the specimens due to the drill. There were voids at the surface (material missing) on all the specimens to a higher or lesser degree.

Small pieces of flint were seen in specimens 2, 3, 7 and 8. Few fossils were found in specimen 2 and many were found in specimen 8.

Due to the long period of storage of the specimens, long treads of fungus/roots were seen on the surface of the specimens. Further, there were traces of mould and a mouldy smell. The longer the storage, the mouldier the specimens were.

All the specimens were fractured to a higher or lesser degree. Specimen 8 was in a very good condition (the best of them all). This is due to that many of the fracture apertures were narrow (fine), and that only few voids were seen at the surface. Specimen 2 was in a very bad condition (the worst of them all) due to the many fractures and the almost brittle state of the chalk. The specimen had been cast with gypsum on the top at the Hillerslev quarry. Specimen 5 contained so-called crushed zones where the chalk was brittle, and almost plastified (reworked). In these zones, it was difficult to see fractures. This, and the many fractures were responsible for the bad condition of specimen 5 (almost as bad as specimen 2). Zones with brittle chalk as seen in specimen 2 and 5 were also seen along all the horizontal profiles at the Hillerslev quarry.

For the two best specimens 7 and 8, the fracture density was the highest observed, see Figure E.4 in Appendix E. One reason for this is that the chalk in this area does not contain crushed zones. Often, only few fractures were indicated in the crushed zone, as it was difficult to see the fractures.

It was observed that fractures opened in the specimens after being unwrapped and

exposed to air (drying), and due to the handling of the specimens.

Six of the specimens were cast with gypsum during preparation due to filling of voids at the surface (specimens 7 after drying) and due to stabilizing of the specimens (specimens 2, 3, 9 and 10 before drying). Specimen 11 had been cast with gypsum in an earlier project (Larsen 2000).

In four of the specimens horizontal fracture planes were present, two continuing ones in specimen 8, a continuing one in specimen 5, two in specimen 7 and one in specimen 9. This is in accordance with the global fracture observations.

The most dominant fractures in the periphery of the specimens are very steeply dipping and seem almost vertical. This is consistent with the overall picture from the global fracture description concluding that the majority of fractures are steeply dipping with a dominance of almost vertical fractures. The fracture density in the specimens are similar to the observations in the Hillerslev outcrop chalk quarry indicating almost random spacing of fractures.

Overall, the local and the global fracture descriptions are in accordance, i.e. the fracture system in the specimens represents the major part of the Hillerslev outcrop chalk fracture pattern.

Chapter 7

Conclusions

A field trip was made to the Hillerslev outcrop chalk quarry. Here, a global fracture description was carried out and twelve chalk block specimens were sampled. A local fracture description was carried out on eight Hillerslev outcrop chalk specimens. One of these was sampled during "Fractures and Rock Mechanics", phase 2. The other seven were sampled during the Ph.D. project. For the purpose of a local fracture description, fractures, voids at the surface, gypsum and crushed zones were indicated on pieces of plastic matching the top, bottom and periphery of the specimens.

A comparison of the main orientations found along the wall, the bench and behind the specimens shows that the orientation NNE-SSW was found in all three fracture data sets in the Ph.D. project. A comparison of the secondary orientations shows that the orientation NNW-SSE was found in all three fracture data sets.

The measured Joint Roughness Coefficient (JRC) and fracture aperture is of the same order and distribution for the fractures both along the chalk bench and behind the specimens. This indicates that the fractures here were not significantly disturbed by for instance the excavation performed by use of a backhoe. However, when comparing the measured JRC and aperture for all three sets of fracture data, it is evaluated that the fractures along the chalk wall were disturbed. The fact that the variance in JRC for the chalk wall differs from the JRCs measured along the chalk bench and behind the specimens supports a disturbance, which apart from the influence of excavation may be due to weathering near the chalk wall.

For the fractures along the wall, apertures between ≤ 0.1 to 0.5 mm and 1 to 2 mm are seen, i.e. both closed to very narrow fractures and very open fractures are seen. The closed to very narrow fractures are dominating, but some very open fractures are seen. For the fractures both along the chalk bench and behind the specimens, primarily apertures ≤ 1 mm were seen, i.e. the number of closed fractures were dominant and only very few very open fractures were observed.

Fracture description and sampling carried out in the Hillerslev chalk quarry during "Fractures and Rock Mechanics", phase 1 and 2 was compared to the work presented in this report (Ph.D. project). A comparison shows that the main orientation ENE-WSW was found in the "Fractures and Rock Mechanics", phase 1 and 2, and along the wall in the Ph.D. project. This orientation was also found as a secondary orientation behind the specimens. The main orientation NNE-SSW found in all three fracture data sets in the

Ph.D. project is also found as a secondary orientation in "Fractures and Rock Mechanics", phase 2.

In all three fracture data sets in the Ph.D. project and in "Fractures and Rock Mechanics", phase 2, horizontal beds were observed, and horizontal bedding parallel fractures were common. The fracture density for all the measured fractures in the Hillerslev chalk quarry indicate almost random spacing of the fractures. A comparison of the number of fractures sorted by dip shows that the majority of all the measured fractures in the Hillerslev chalk quarry are steeply dipping with a dominance of almost vertical fractures. Based on the comparison it is evaluated that overall, the fracture descriptions for the three research projects are similar.

All the specimens were fractured to a higher or lesser degree. In four of the specimens horizontal fracture planes were present, two continuing ones in specimen 8, a continuing one in specimen 5, two in specimen 7 and one in specimen 9. This is in accordance with the global fracture observations. The most dominant fractures in the periphery of the specimens are very steeply dipping and seemed almost vertical. This is consistent with the global fracture description. The fracture density in the specimens are similar to the observations in the Hillerslev outcrop chalk quarry indicating almost random spacing of fractures.

Zones with brittle chalk as seen in specimen 2 and 5 were also seen along all the horizontal profiles at the Hillerslev quarry.

Overall, the three fracture data sets in the Ph.D. project are evaluated to be similar. Further, it is evaluated that the fracture descriptions carried out in the three research projects are similar. Finally, the local and the global fracture descriptions are in accordance, i.e. the fracture system in the specimens represents the major part of the Hillerslev outcrop chalk fracture pattern.

Bibliography

Barton, N. (1976), *The shear strength of Rock and Rock Joints.*

Christensen, H. (2003), Displacement and deformation processes in fractured reservoir chalk, Efp-2000, GEO.

Havmøller, O. & Krogsbøll, A. (2001), Fractures and rock mechanics. phase 2. fractures and rock mechanics., EFP-98 Report 1. ENS J. no. 1313/98-0006. GEO no. 16015027. 2001-03-23, GEO.

Jakobsen, F. (2001), Fractures and rock mechanics. phase 2. description of natural and test induced fractures in chalk, EFP-98 Report 2001/18, GEUS.

Krogsbøll, A., Jakobsen, F. & Madsen, L. (1997), Fractures and rock mechanics. phase 1. geology report, EFP-96 Report 1997/63, GEUS.

Larsen, I. (2000), Water injection in oil saturated, fractured chalk samples (h×d=50×50 cm) modelling oil displacement in oil reservoirs, Master thesis, DTU.

Løset, F. (1995), Ingeniørgeologi. ingeniørgeologisk logging av borkjerner, Technical Report Report no. 540011-1, Norwegian Geotechnical Institut.

Appendix A

Fracture Description of Hillerslev Chalk (EFP-96)

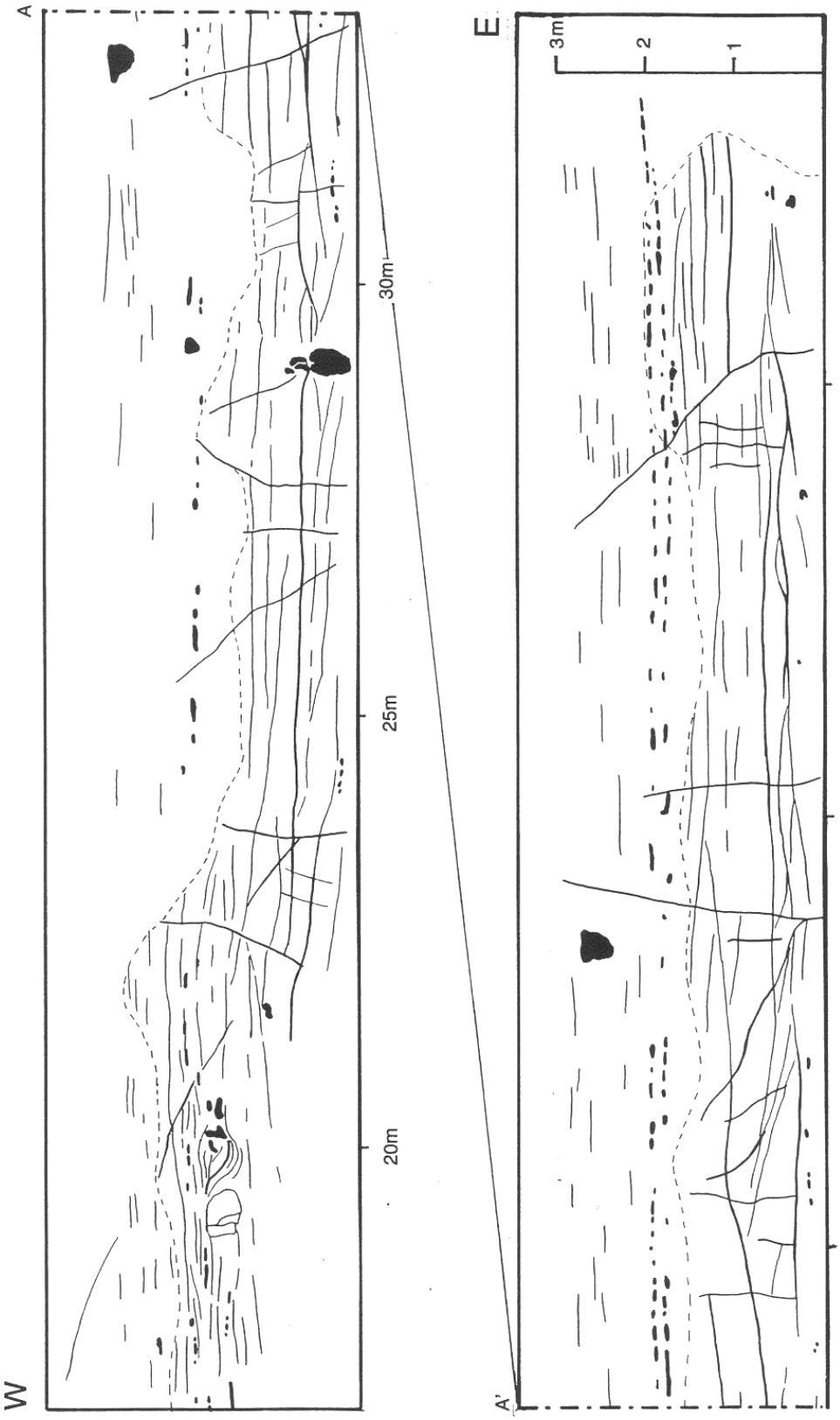

Figure A.1 *Excavated chalk wall in the northern part of the Hillerslev quarry (Krogsbøll et al. 1997).*

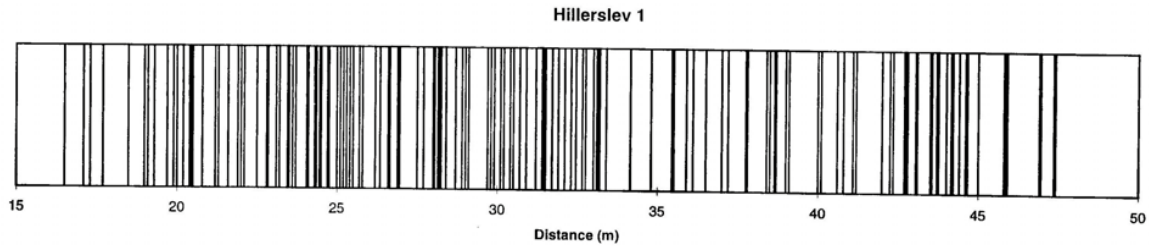

Figure A.2 *Fracture density along the horizontal line (Krogsbøll et al. 1997).*

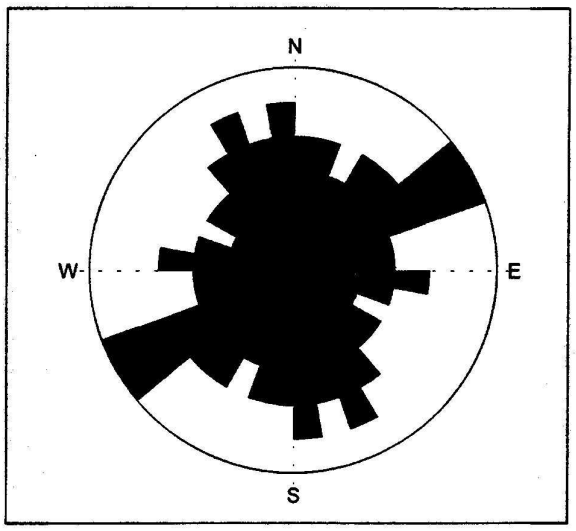

Figure A.3 *Rose diagram of strike for all measured fractures from the Hillerslev quarry (Krogsbøll et al. 1997).*

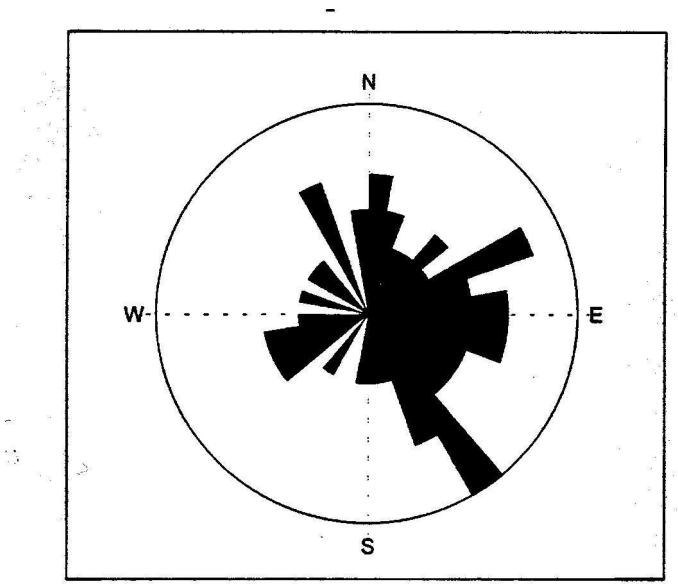

Figure A.4 *Rose diagram of dip directions for all measured fractures from the Hillerslev quarry (Krogsbøll et al. 1997).*

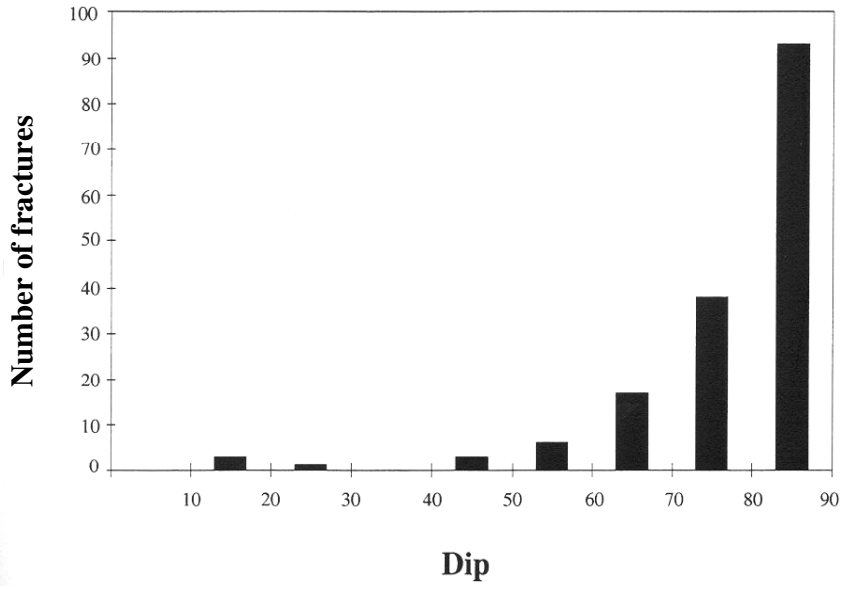

Figure A.5 *Histogram of dip for all measured fractures from the Hillerslev quarry (Krogsbøll et al. 1997).*

Appendix B

Fracture Description of Hillerslev Chalk (EFP-98)

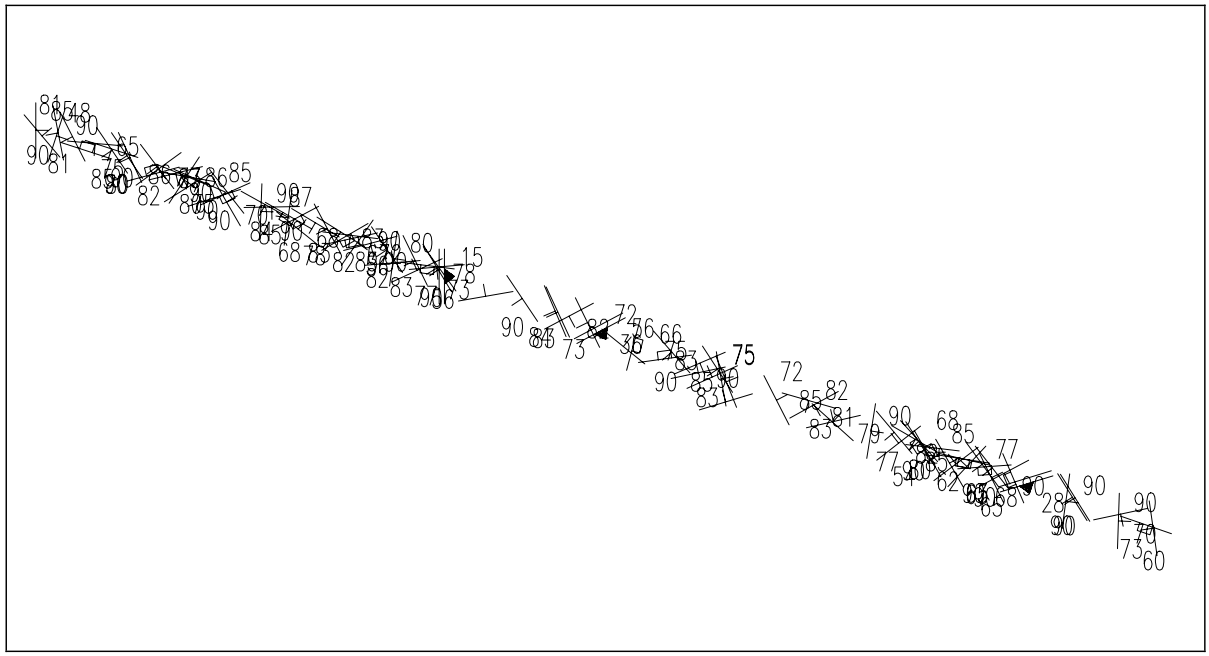

Figure B.1 *Map of strike/dip indicating the density of fractures along the same horizontal profile as described in "Fractures and Rock Mechanics", phase 1 and here referred to as the reference line (Jakobsen 2001).*

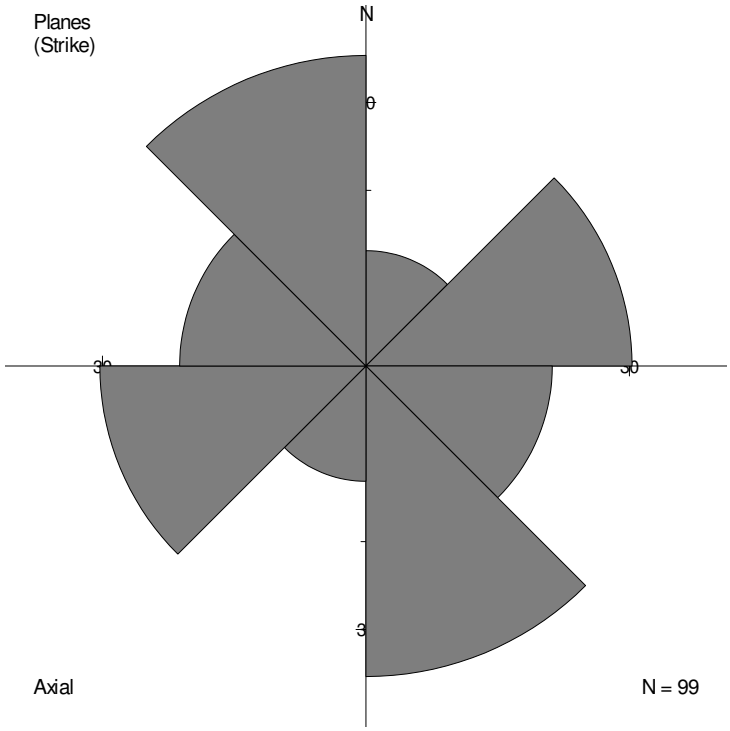

Figure B.2 *Rose diagram of strike for all measured fractures along the reference line (Jakobsen 2001).*

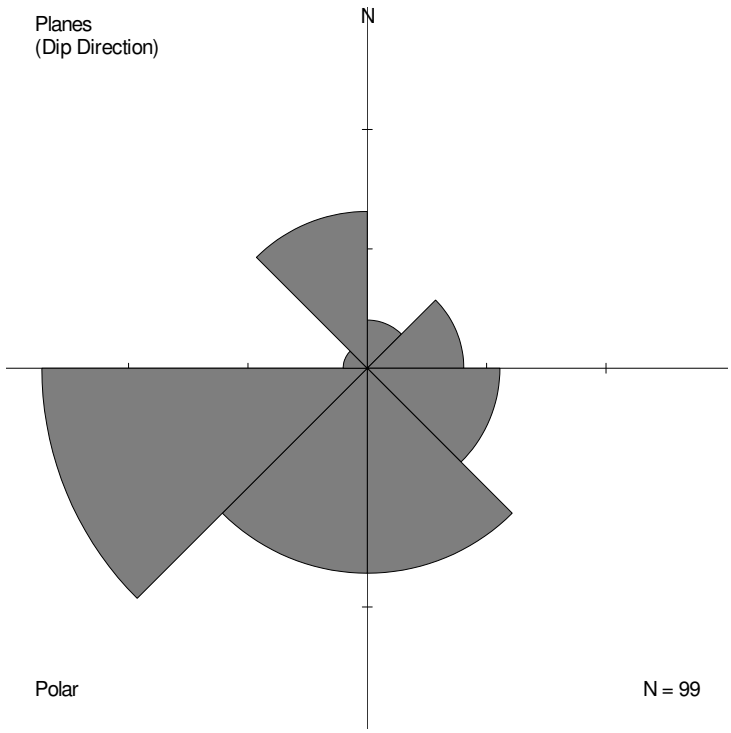

Figure B.3 *Rose diagram of dip directions for all measured fractures along the reference line (Jakobsen 2001).*

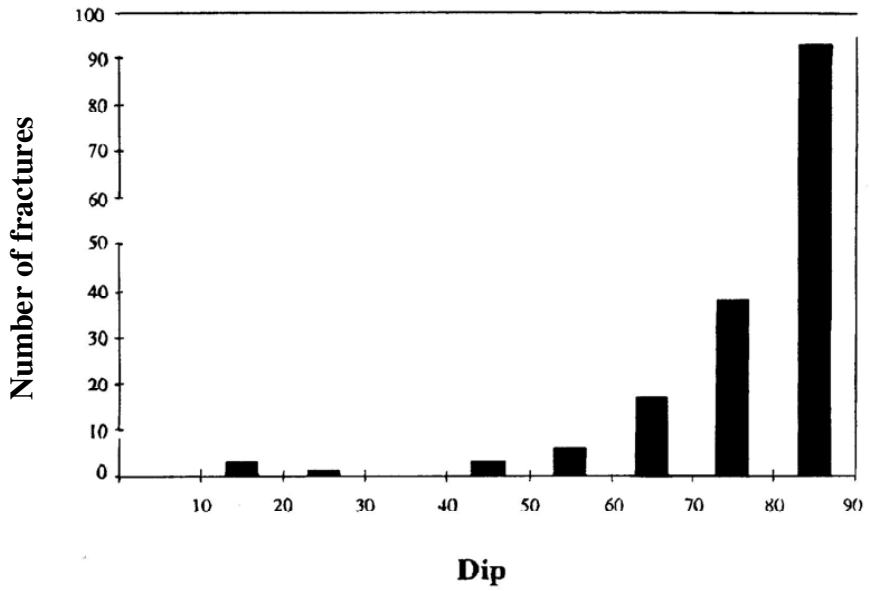

Figure B.4 *Histogram of dip for all measured fractures along the reference line (Jakobsen 2001).*

Appendix C

Field Trip to the Hillerslev Chalk Quarry (Ph.D. Project)

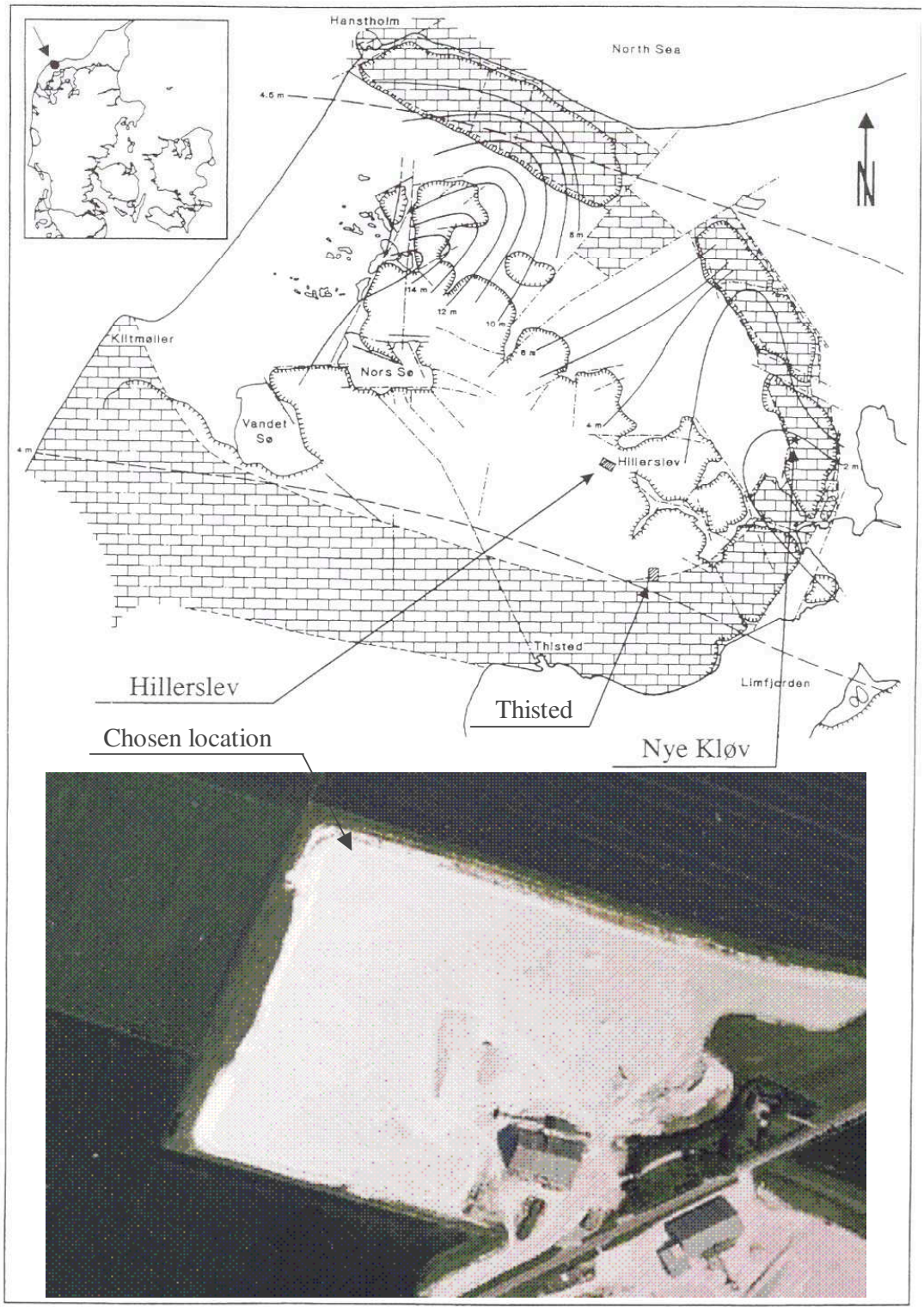

Figure C.1 *Map showing the location of the Hillerslev chalk quarry in the northern part of Jutland (Jakobsen 2001), and air photo with indication of the chosen location for fracture description and sampling in the quarry.*

Figure C.2 *Location for fracture description and sampling at Hillerslev chalk quarry.*

Figure C.3 *The area for fracture description and sampling is located just west of the area used in the earlier research projects "Fractures and Rock Mechanics", phase 1 and 2 (west ←).*

Figure C.4 *Excavated chalk wall (approximately 2.5 m high and 25 m long).*

Figure C.5 *Chalk bench (approximately 1.5 m high, 25 m long and 2 m deep).*

Figure C.6 *The mobile drilling rig on the chalk bench.*

Figure C.7 *The drill bit is mounted on the drilling rig.*

Figure C.8 *Water was used to cool the drill bit and flush away cuttings during drilling.*

Figure C.9 *Insertion of metal shield in the drill bit trace.*

Figure C.10 *Rough excavation in front of and beside the specimen performed by use of the backhoe. The excavation is supervised to prevent fracturing.*

Figure C.11 *Blue tape wrapped around the specimen to keep the fractured specimen together.*

Figure C.12 *A rubber membrane is pulled over the specimen.*

Figure C.13 *The specimen is cut free at the bottom by use of a chain saw.*

Figure C.14 *The specimen is turned upside down for a rough trimming of the bottom.*

Figure C.15 *A successfully sampled specimen placed upside down on a wooden pallet.*

Figure C.16 *View of the specimens, the bench and the wall behind. Yellow numbering on the wall indicates the location of the twelve specimens.*

Figure C.17 *Transportation of the chalk specimens to DTU by lorry.*

Appendix D

Location for Sampling at the Hillerslev Quarry (Ph.D. Project)

Chalk Wall

The chalk wall is approximately 2.5 m high and 25 m long, see Figure D.1.

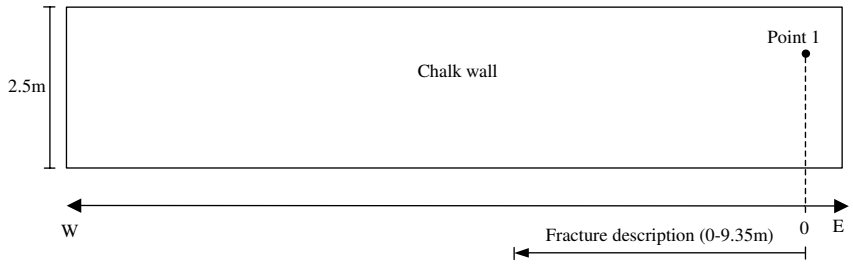

Figure D.1 *Sketch of the excavated chalk wall (2.5 m high and 25 m long).*

A fracture description was performed along a horizontal line along the wall from point 1 and 9.35 m towards west.

Chalk Bench

The chalk bench is approximately 1.5 m high, 25 m long and 2 m deep. The wall behind the bench is approximately 4 m above the ground, i.e. 2.5 m above the bench, see Figure D.2.

A fracture description was performed along a horizontal line in front of the bench from 10.35 m to 20.55 m measured from point 1 towards west.

Specimens

Twelve cylindrical specimens with the dimensions $D \approx 50$ cm and $H \approx 50$ cm were sampled successfully. The location of the specimens on the bench is indicated in Figure D.3.

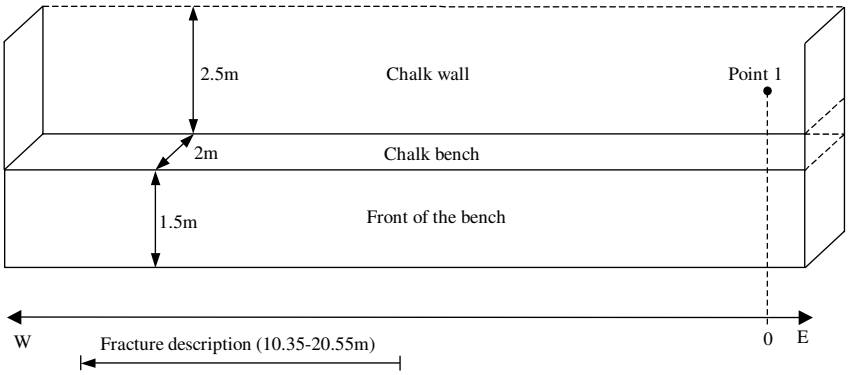

Figure D.2 *Sketch of the bench (1.5 m high, 25 m long and 2 m deep).*

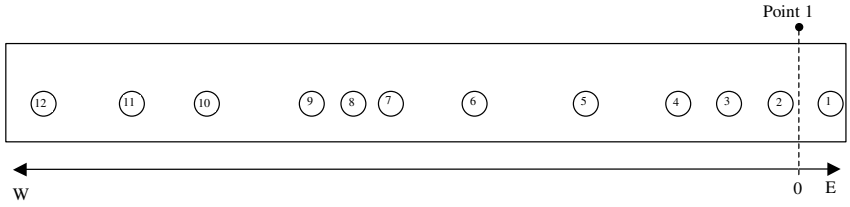

Figure D.3 *A sketch of the location of the twelve specimens in the bench.*

A fracture description was performed on horizontal line profiles of 0.5-2 m length approximately 75 cm behind each of the twelve specimen stumps, and on the stumps.

The location of the horizontal line profile along the wall, along the front of the bench and the twelve horizontal line profiles behind the specimens are sketched in Figure D.4.

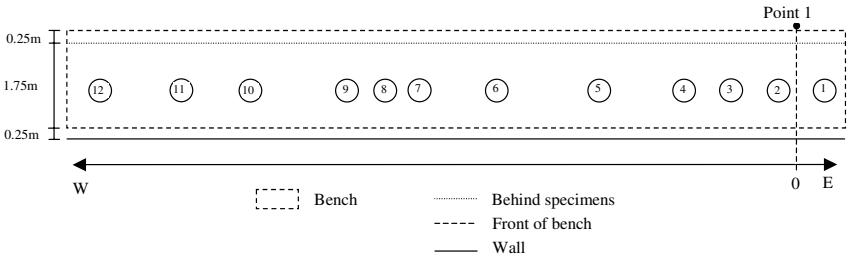

Figure D.4 *Location of the horizontal line profiles along the wall, along the bench and behind the specimens.*

Appendix E

Fracture Description of Hillerslev Chalk (Ph.D. Project)

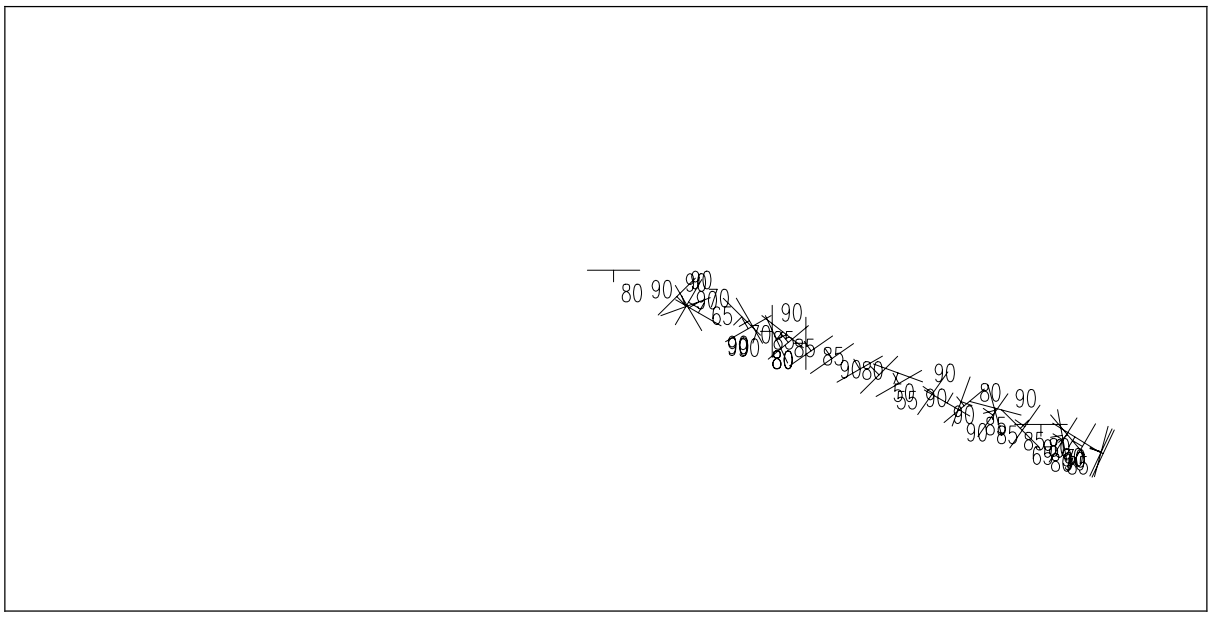

Figure E.1 *Map of strike/dip indicating the density of fractures along the horizontal profile along the chalk wall.*

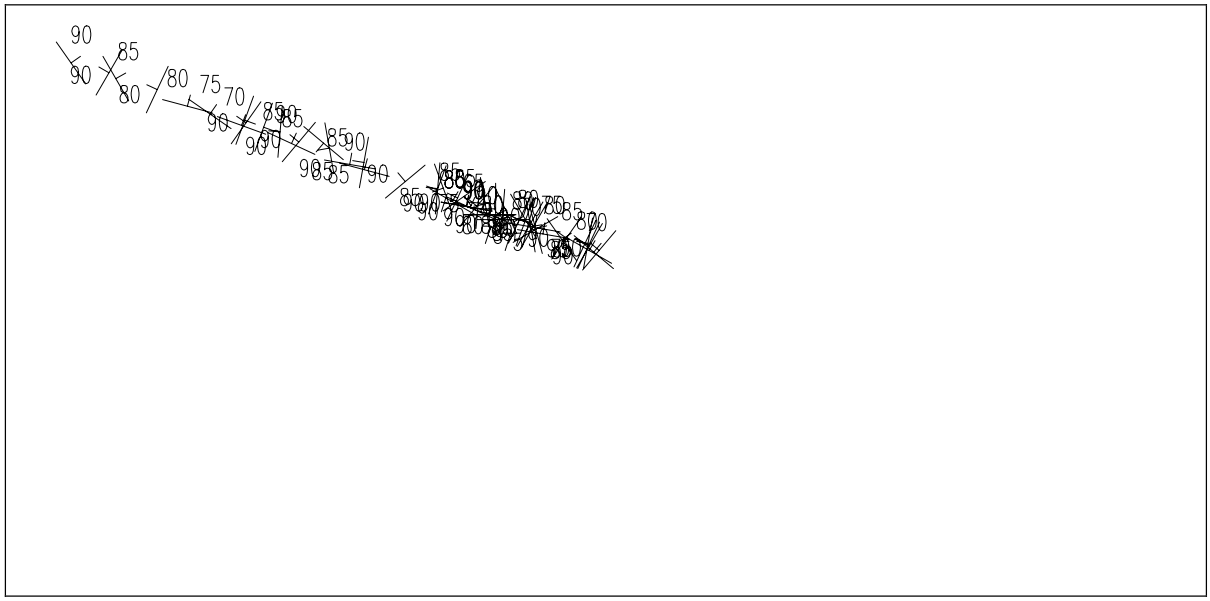

Figure E.2 *Map of strike/dip indicating the density of fractures along the horizontal profile along the chalk bench.*

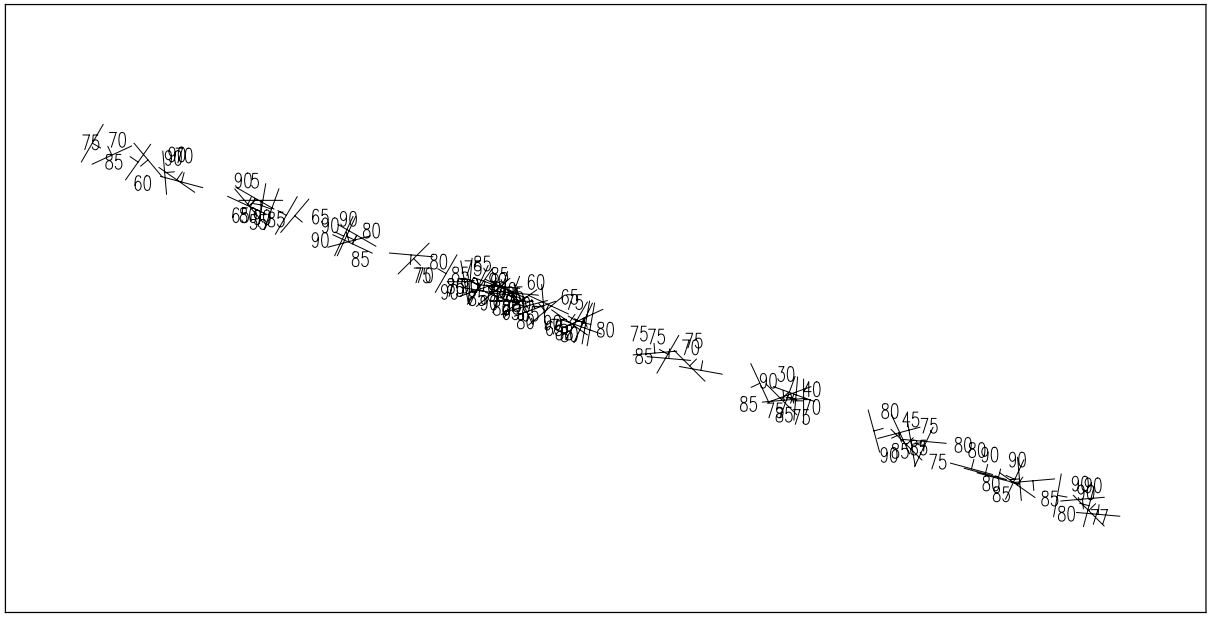

Figure E.3 *Map of strike/dip indicating the density of fractures behind each of the twelve sampled specimens.*

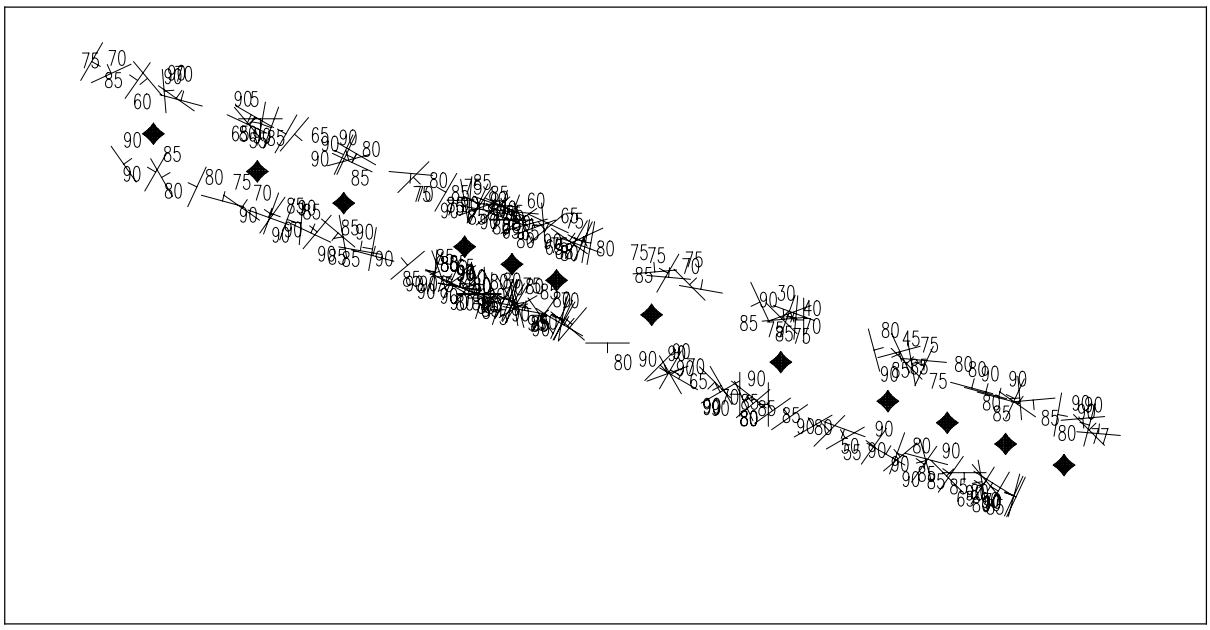

Figure E.4 *Map of strike/dip indicating the density of fractures along the profiles along the wall and the bench and behind each of the twelve sampled specimens. The centers of the specimens are indicated.*

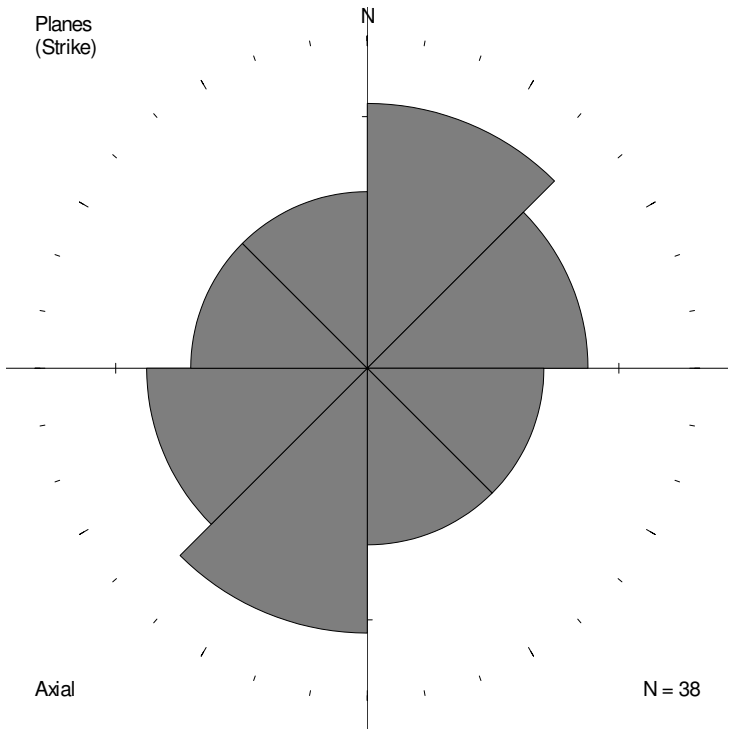

Figure E.5 *Rose diagram of strike for all measured fractures along the horizontal profile along the chalk wall.*

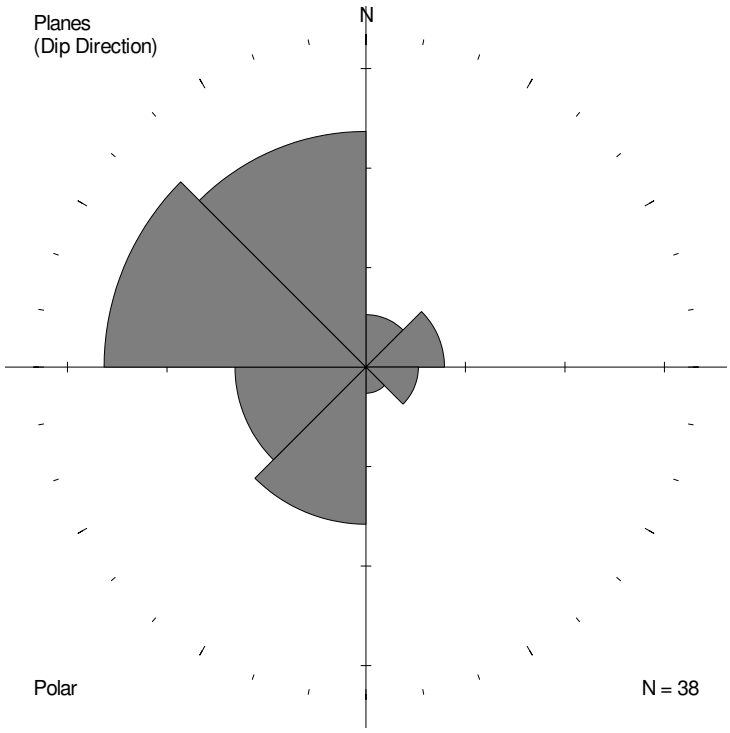

Figure E.6 *Rose diagram of dip directions for all measured fractures along the horizontal profile along the chalk wall.*

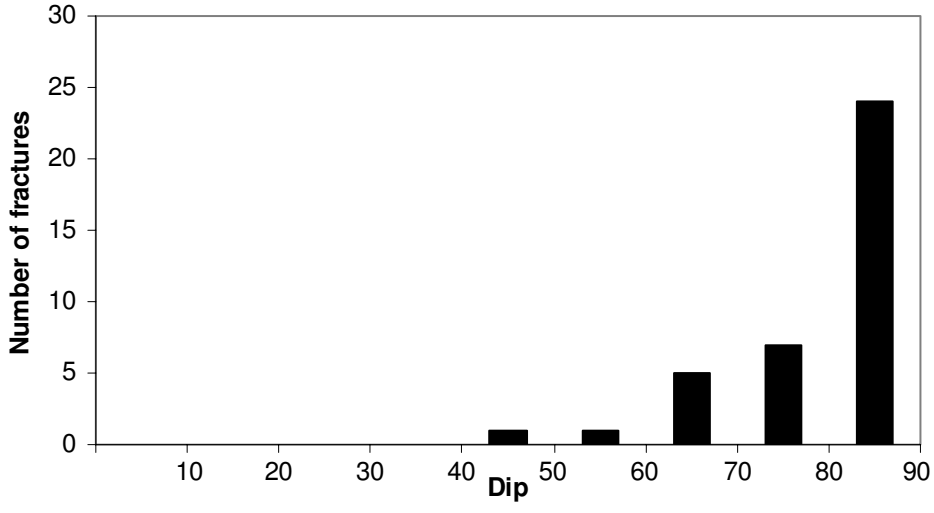

Figure E.7 *Histogram of dip for all measured fractures along the horizontal profile along the chalk wall.*

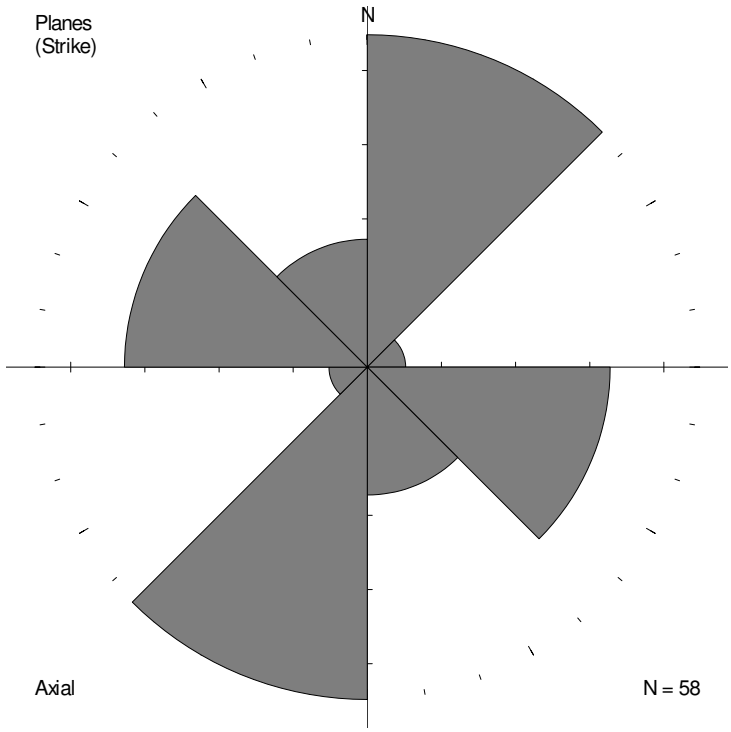

Figure E.8 *Rose diagram of strike for all measured fractures along the horizontal profile along the chalk bench.*

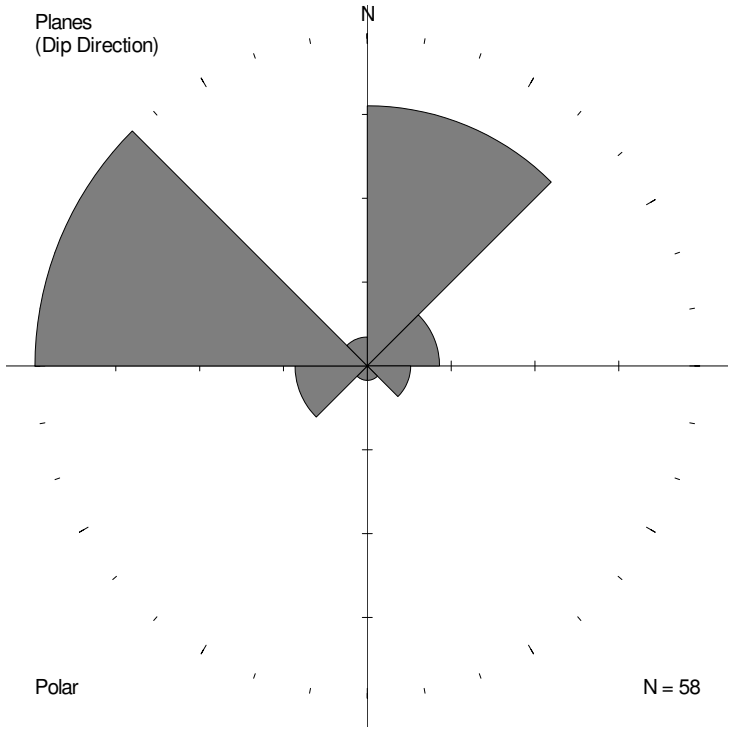

Figure E.9 *Rose diagram of dip directions for all measured fractures along the horizontal profile along the chalk bench.*

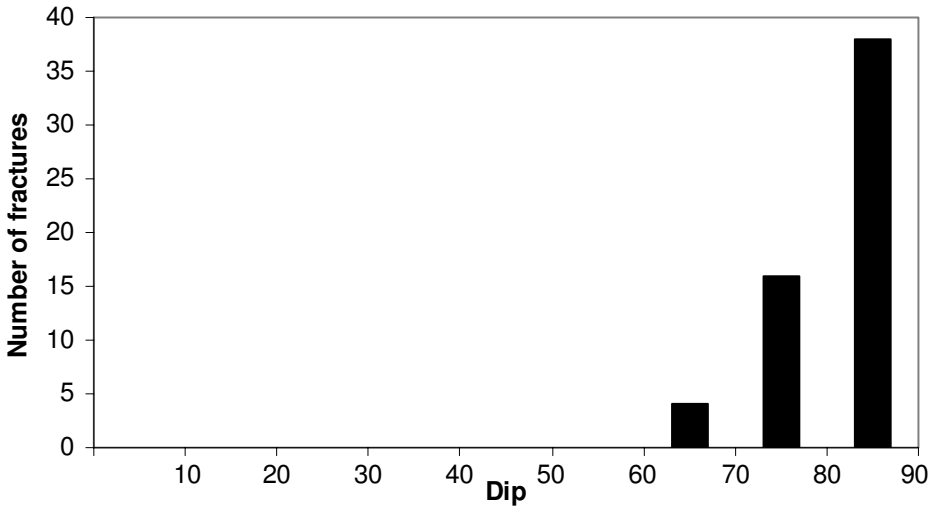

Figure E.10 *Histogram of dip for all measured fractures along the horizontal profile along the chalk bench.*

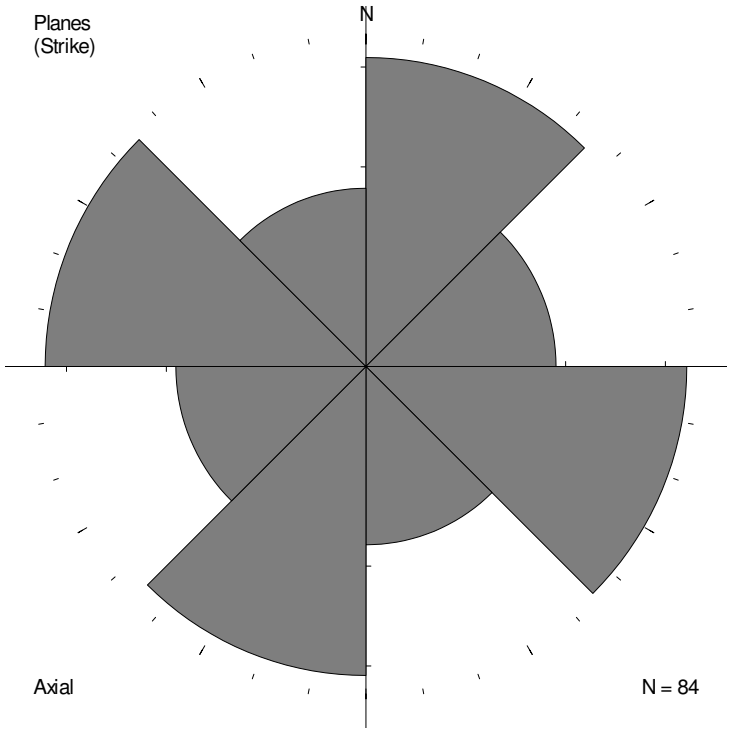

Figure E.11 *Rose diagram of strike for all measured fractures behind the twelve specimens.*

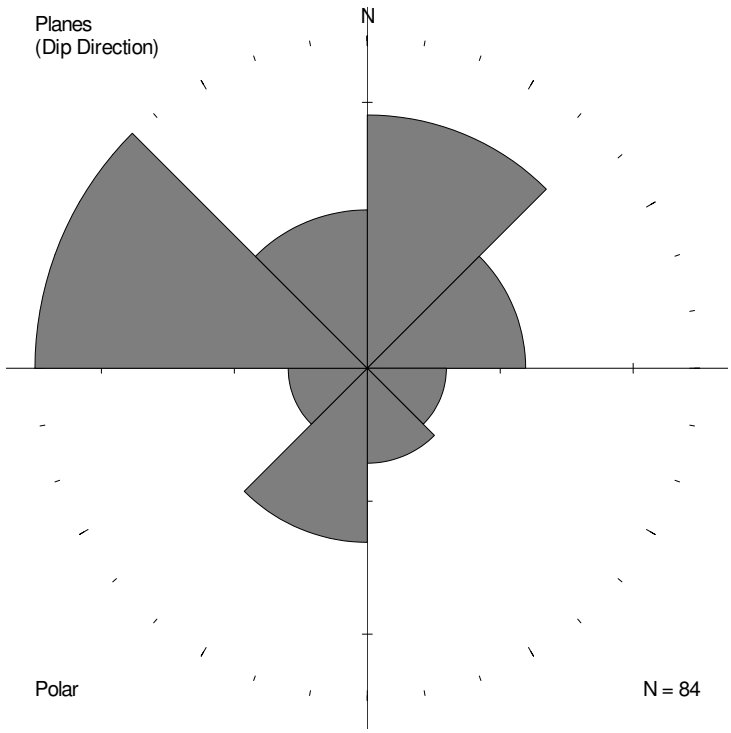

Figure E.12 *Rose diagram of dip directions for all measured fractures behind the twelve specimens.*

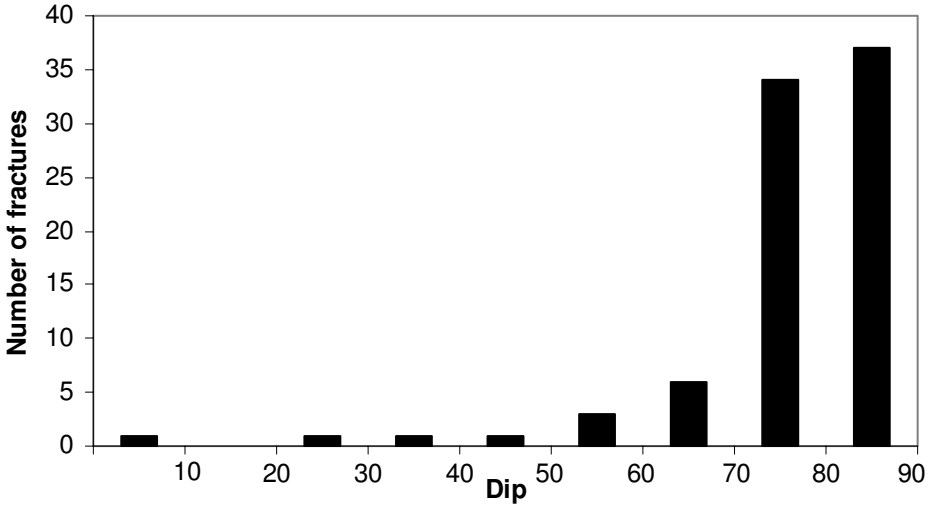

Figure E.13 *Histogram of dip for all measured fractures behind the twelve specimens.*

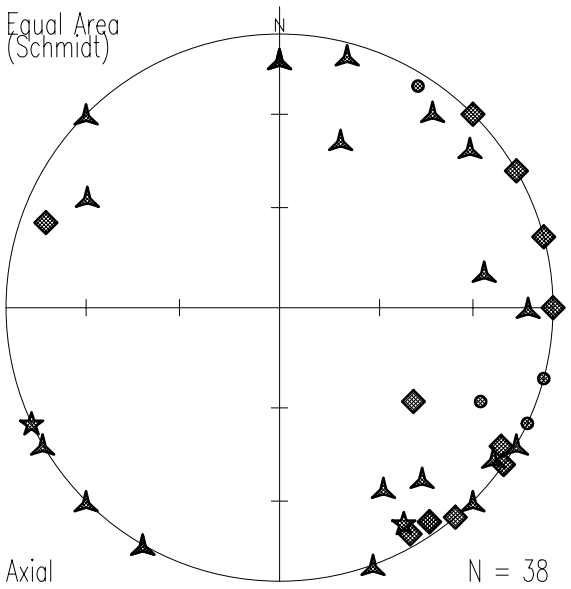

Figure E.14 *Schmidt projection of strike vs. JRC for the measured fractures along the horizontal profile along the chalk wall. Circle: JRC 0-4. Triangle: JRC 5-9. Diamond: JRC 10-15. Star: JRC > 15.*

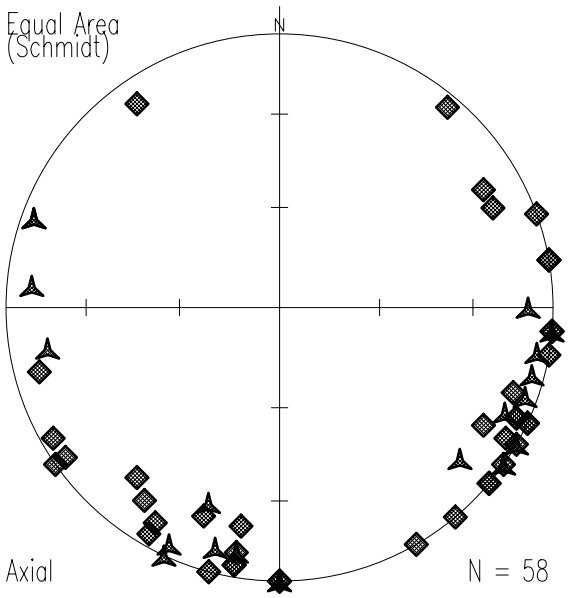

Figure E.15 *Schmidt projection of strike vs. JRC for the measured fractures along the horizontal profile along the chalk bench. Circle: JRC 0-4. Triangle: JRC 5-9. Diamond: JRC 10-15. Star: JRC > 15.*

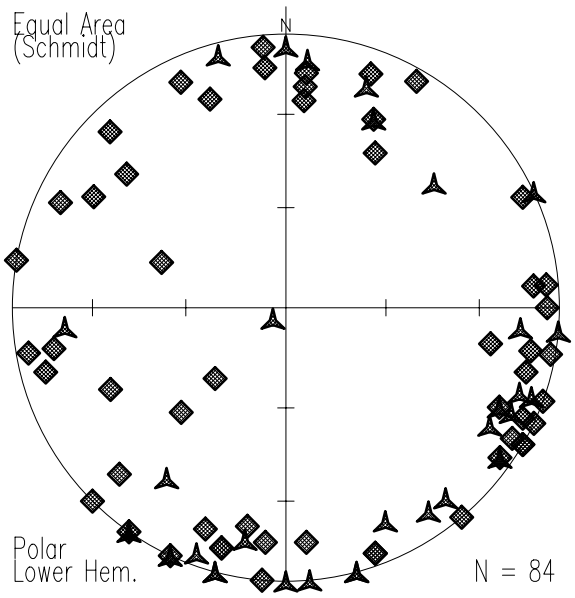

Figure E.16 *Schmidt projection of strike vs. JRC for the measured fractures behind the twelve specimens. Circle: JRC 0-4. Triangle: JRC 5-9. Diamond: JRC 10-15. Star: JRC > 15.*

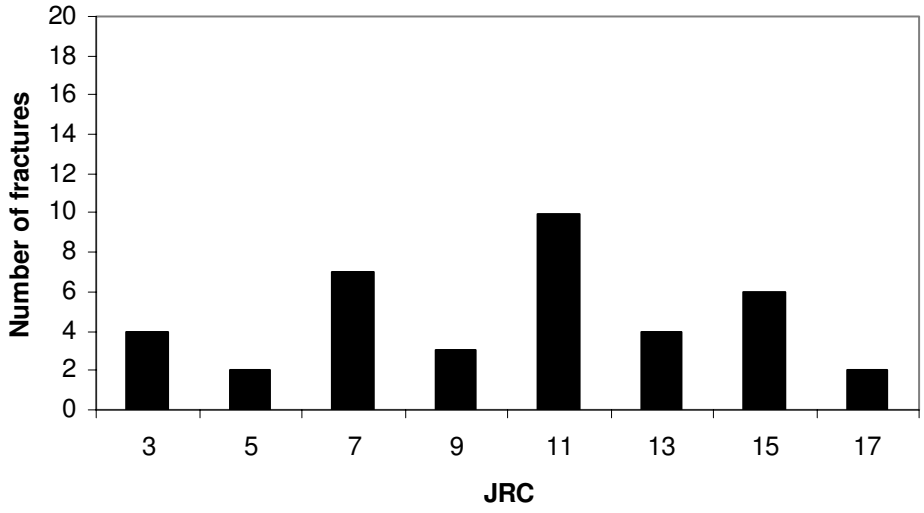

Figure E.17 *Histogram of JRC for all measured fractures along the horizontal profile along the chalk wall.*

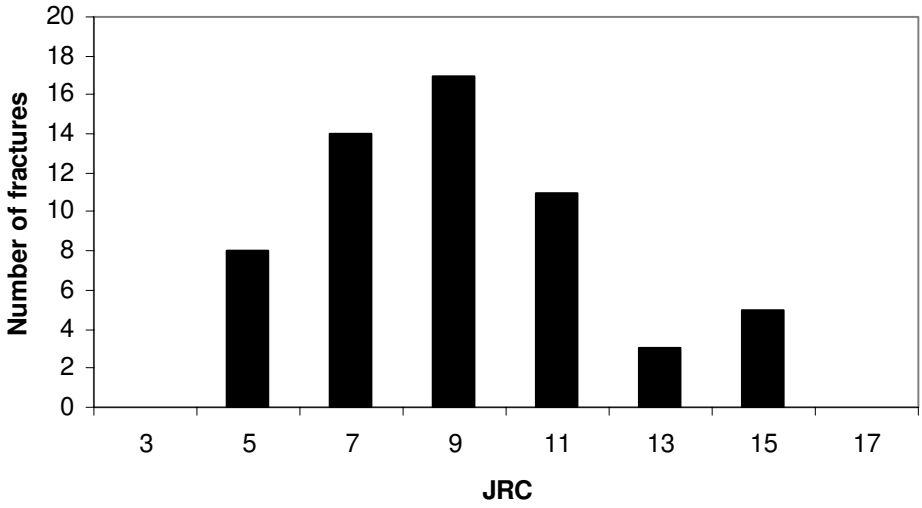

Figure E.18 *Histogram of JRC for all measured fractures along the horizontal profile along the chalk bench.*

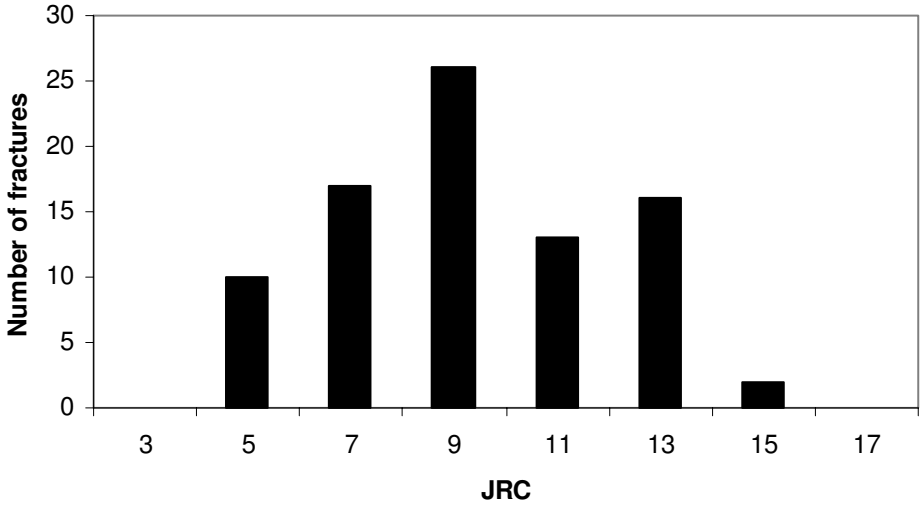

Figure E.19 *Histogram of JRC for all measured fractures behind the twelve specimens.*

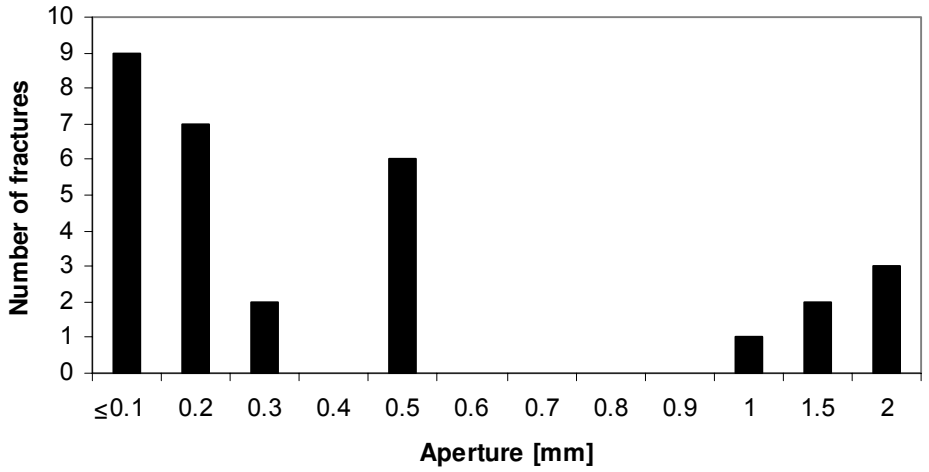

Figure E.20 *Histogram of aperture for all measured fractures along the horizontal profile along the chalk wall.*

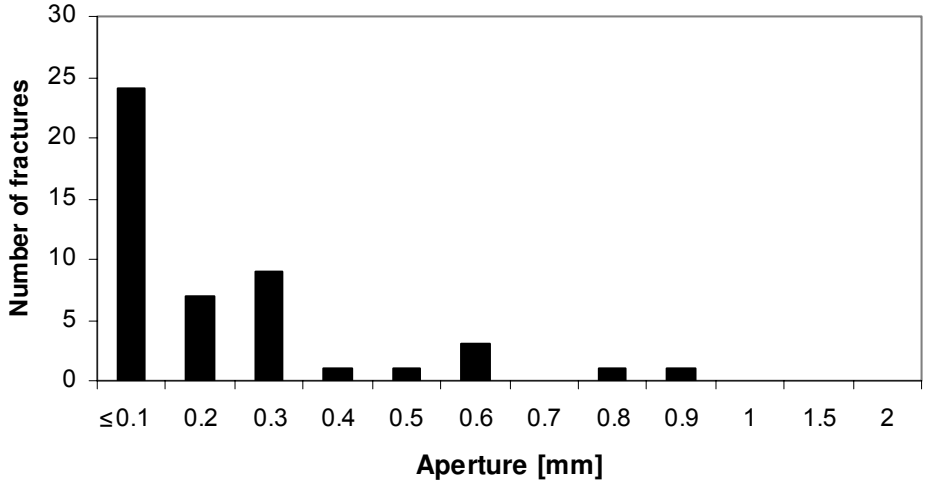

Figure E.21 *Histogram of aperture for all measured fractures along the horizontal profile along the chalk bench.*

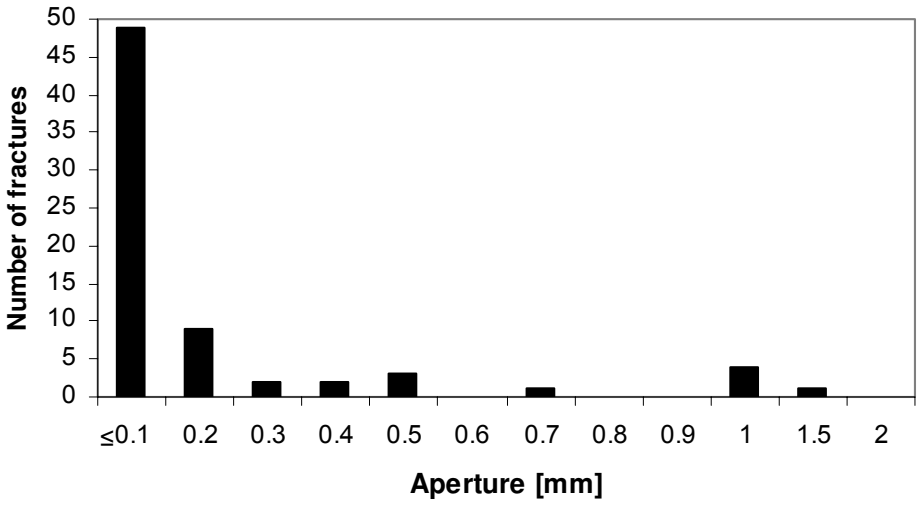

Figure E.22 *Histogram of aperture for all measured fractures behind the twelve specimens.*

Appendix F

Characteristic Joint Roughness Coefficient (JRC) Profiles

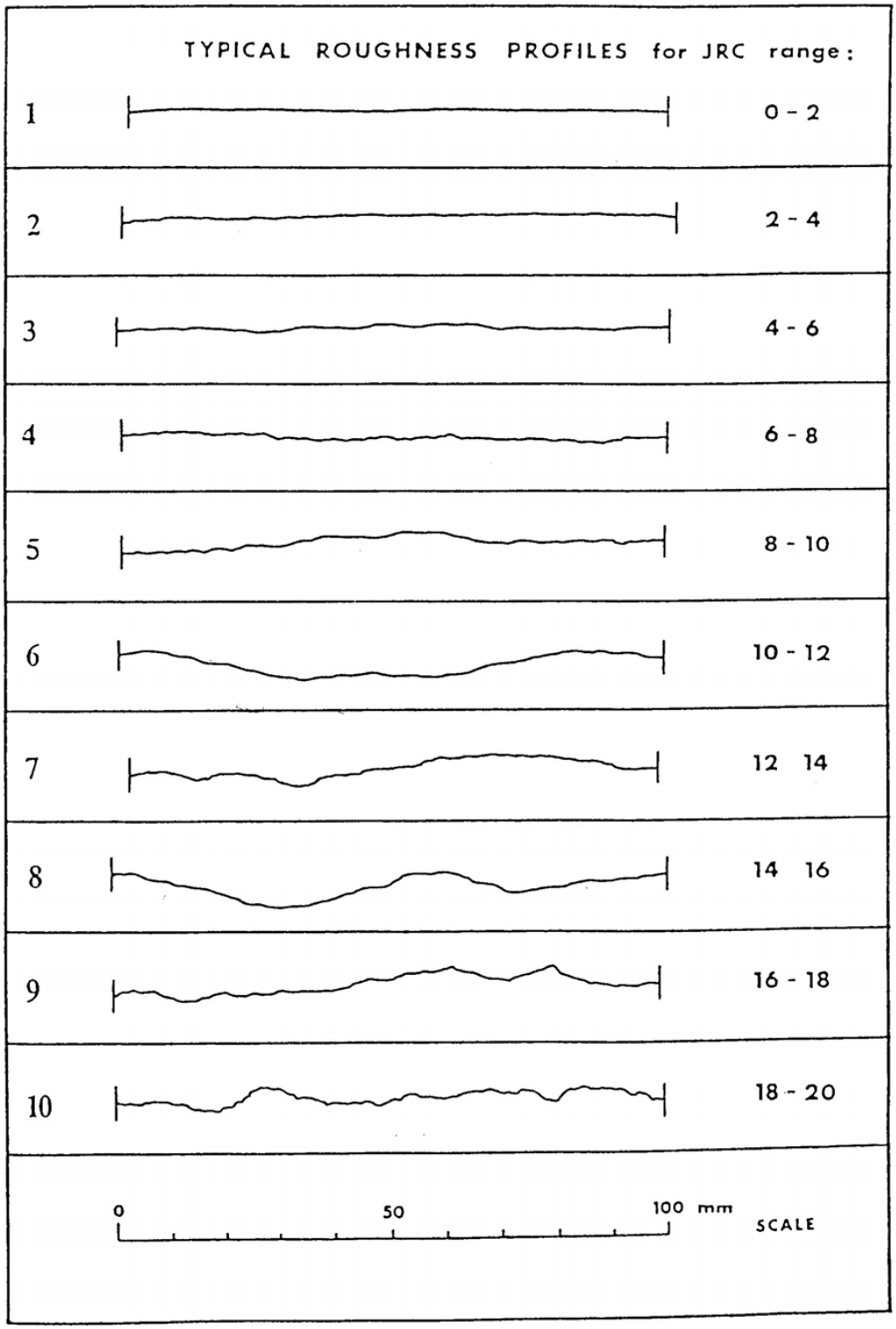

Figure F.1 *Characteristic JRC-Profiles (Løset 1995).*

Appendix G

Photographs of Fractures, Voids, Crushed Zones and Gypsum

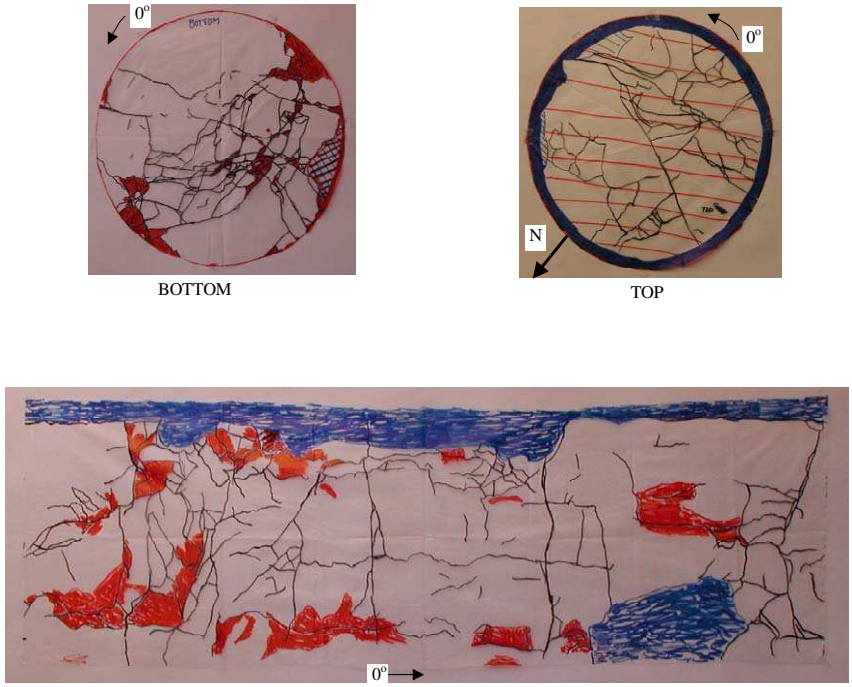

Figure G.1 *Fractures (black lines), voids at the surface (red) and gypsum (blue) indicated on plastic for specimen 2.*

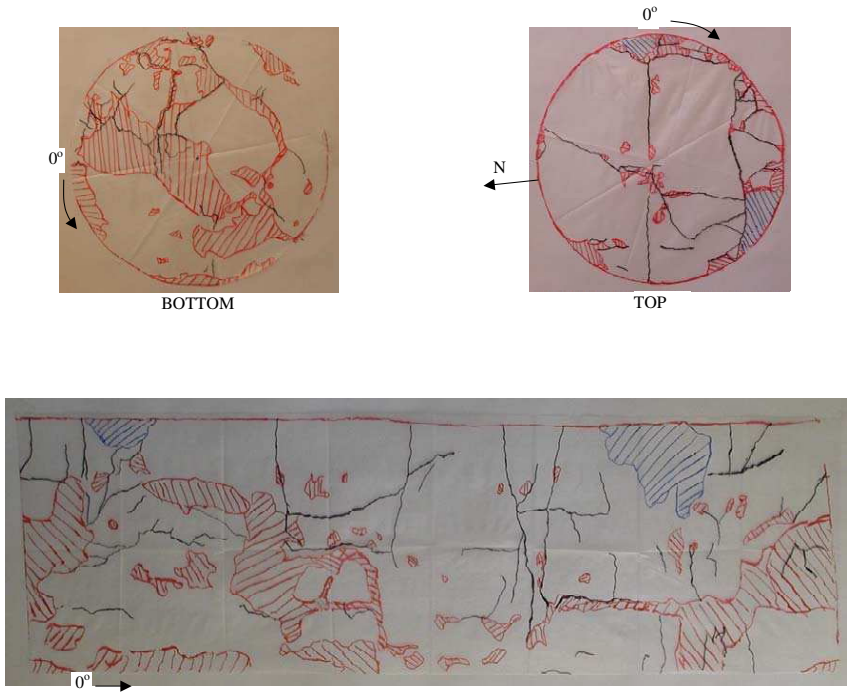

Figure G.2 *Fractures (black lines), voids at the surface (red) and gypsum (blue) indicated on plastic for specimen 3.*

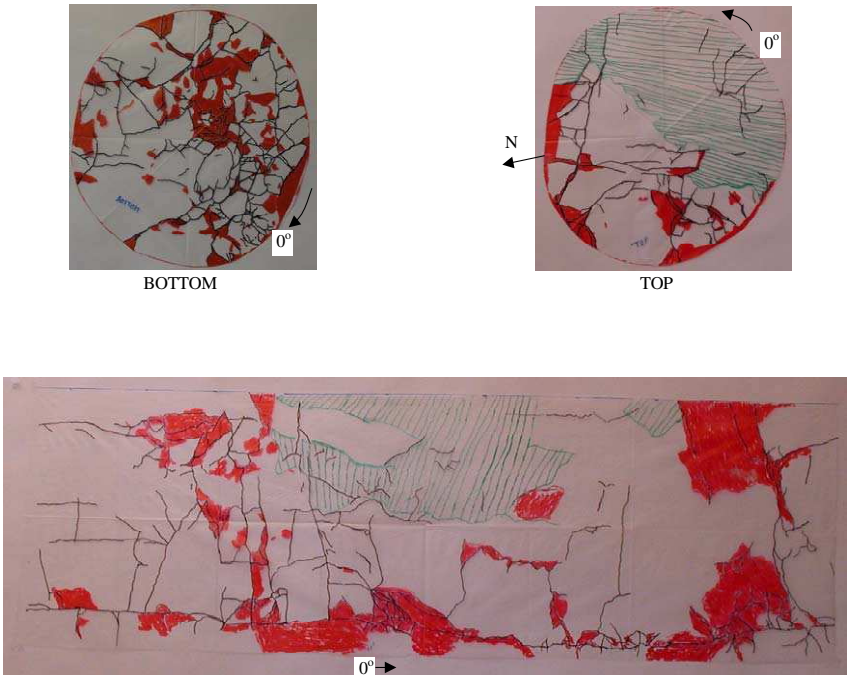

Figure G.3 *Fractures (black lines), voids at the surface (red) and crushed zones (greee) indicated on plastic for specimen 5.*

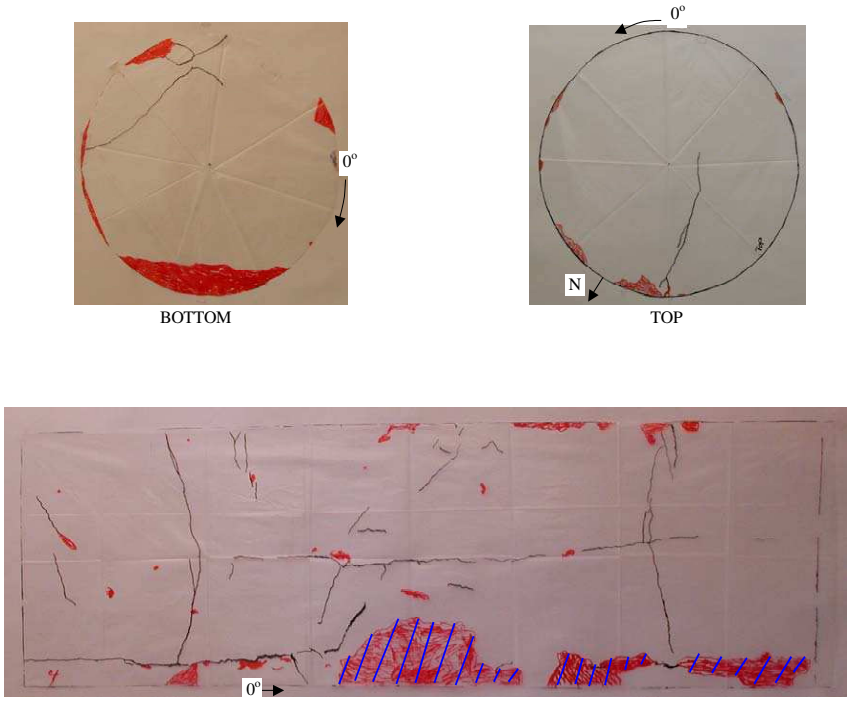

Figure G.4 *Fractures (black lines), voids at the surface (red) and gypsum (blue) indicated on plastic for specimen 7.*

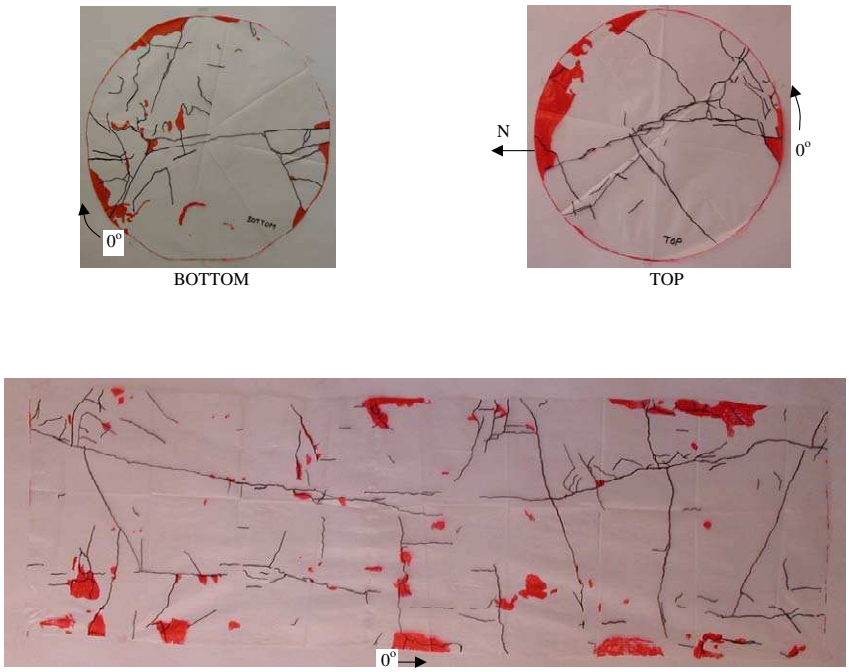

Figure G.5 *Fractures (black lines) and voids at the surface (red) indicated on plastic for specimen 8.*

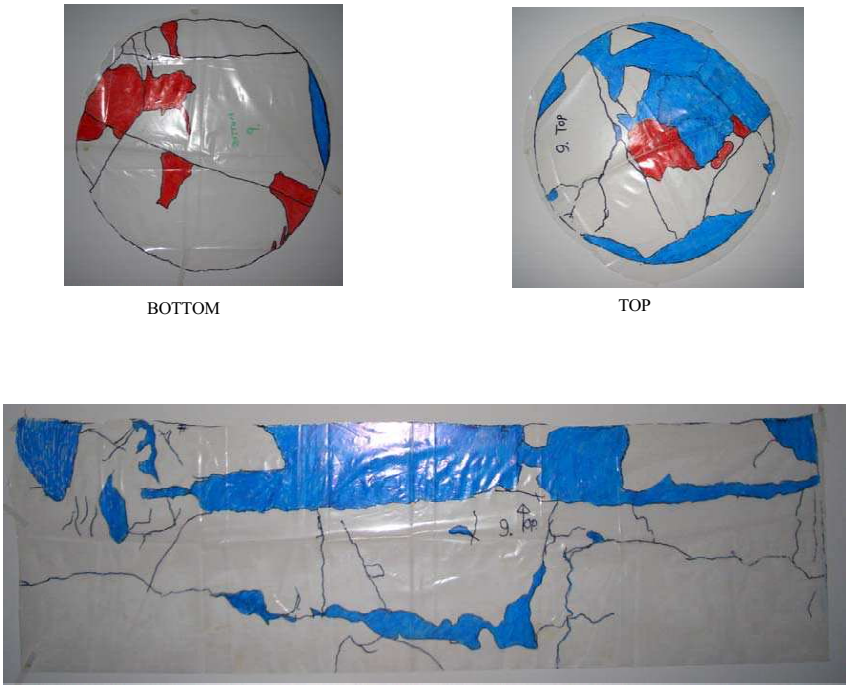

Figure G.6 *Fractures (black lines), voids at the surface (red) and gypsum (blue) indicated on plastic for specimen 9.*

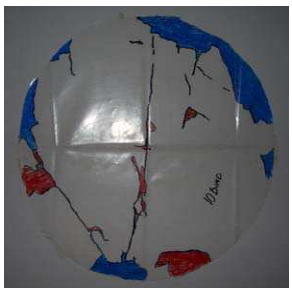

BOTTOM

TOP

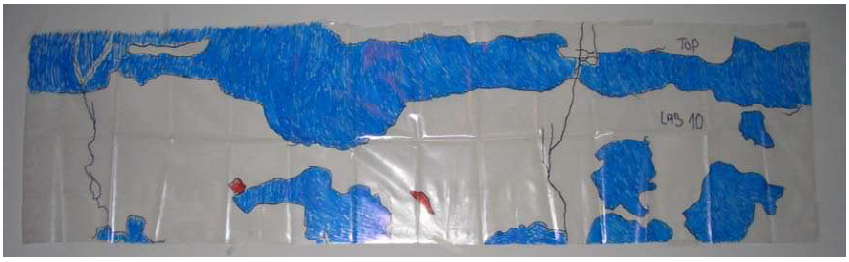

Figure G.7 *Fractures (black lines), voids at the surface (red) and gypsum (blue) indicated on plastic for specimen 10.*

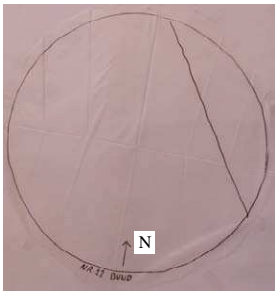

BOTTOM

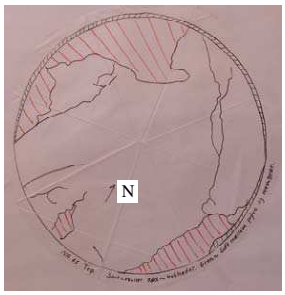

TOP

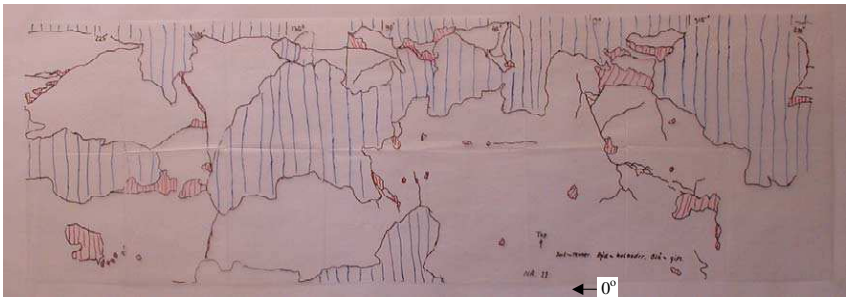

Figure G.8 *Fractures (black lines), voids at the surface (red) and gypsum (blue) indicated on plastic for specimen 11. Gab between membrane and specimen (green).*

Wettability and Capillary Pressure Measurements on Hillerslev Outcrop Chalk

Miriam M. Lykke

Ph.D. Thesis

Department of Civil Engineering
Technical University of Denmark

2005

Wettability and Capillary Pressure Measurements on Hillerslev Outcrop Chalk

Printed by
Department of Civil Engineering
Technical University of Denmark

Preface

This report is part of the written documentation of the Ph.D. project: "Displacement of Oil by Waterflooding in Fractured Chalk". The Ph.D. project was coordinated with and partly financed by a Danish Energy Research Programme (EFP) project 2000. The title of this project is "Displacement and Deformation Processes in Fractured Reservoir Chalk" (Christensen 2003), and the main objective was to quantify the displacement processes in fractured reservoir chalk. The research partners were: Danish Geotechnical Institute (GEO), Geological Survey of Denmark and Greenland (GEUS), Department of Environment and Resources (ER), DTU and Department of Civil Engineering (BYG•DTU), DTU. The industrial partners were: BP Norway and Mærsk Olie og Gas AS.

This report documents the laboratory studies of two-phase flow properties such as wettability characteristics and capillary pressure curves for Hillerslev outcrop chalk used in the integrated research project.

I am grateful to Rogaland Research, Norway for letting me perform wettability and capillary pressure measurements on three small Hillerslev outcrop chalk specimens at their premises. I wish to thank Research Engineer Jan Erik Iversen, Rogaland Research and Engineer Egil Boye Petersen, working at Rogaland Research when the measurements were initiated, for help and supervision during the measurements.

Furthermore, I wish to thank Professor Rasmus Risnes, Professor Tor Austad, Post Doctor Dag C. Standnes and Professor Svein Skjæveland at Stavanger College, Norway for fruitful discussions about wettability and capillary pressure. Stavanger College, Norway is acknowledged for a pleasant stay there.

Lyngby, April 2005

Miriam M. Lykke

Abstract

Measurement of wettability and subsequent establishment of capillary pressure curves was carried out for three small Hillerslev outcrop chalk specimens. This was done by utilizing Amott cups and an automated Beckman centrifuge at Rogaland Research, Stavanger, Norway. The dimensions of the specimens were $D = 38$ mm and $H = 50$ mm. The fluids used were synthetic Valhall formation water and the laboratory oil Isopar-L. Two of the specimens tested were originally water-wet, while the wettability of a single specimen was altered to a homogenous neutral to slightly oil-wet state. However, the wettability alteration affected the chalk, and the specimen broke in one end. Consequently, a new diameter and height were obtained, i.e. $D = 37.9$ mm and $H = 36.2$ mm.

The modified U. S. Bureau of Mines (USBM) method was used to obtain both the Amott-Harvey and the USBM wettability indices. The method consists of five steps: (1) initial oil drive, (2) spontaneous imbibition of water, (3) water drive, (4) spontaneous imbibition of oil, and (5) oil drive.

It was concluded that Hillerslev outcrop chalk is strongly water-wet and that it can be altered towards a homogeneous neutral to slightly oil-wet state using crude oil added with 1 weight% Dodekane acid. It was found that the USBM wettability index cannot be obtained for strongly water-wet Hillerslev outcrop chalk.

Water-oil capillary pressure curves were established for the specimens based on the measurements during the modified USBM method. However, due to centrifuge limitations, the capillary pressure curves were not fully completed. Further, fractures were induced during centrifuging. It is evaluated that the obtained capillary pressure curves are not fully representative for the specimens. However, a good estimate of the residual oil saturation S_{orw} was obtained, especially for the strongly water-wet specimens.

Based on the fact that the capillary pressure curves were not fully completed due to centrifuge limitations, and that fractures were induced in the specimens even at these lower centrifuge speeds, it is evaluated that capillary pressure curves cannot be obtained in the centrifuge for Hillerslev chalk.

Table of Contents

Chapter 1

Introduction

This report provides information on wettability and capillary pressure measurements for Hillerslev outcrop chalk used for large-scale waterflooding tests performed in the Ph.D. project. Hillerslev outcrop chalk was chosen for the tests as this chalk is available for sampling of large specimens and it is highly fractured. Further, the chalk can be regarded as a close analogue to the oil-producing Tor formation of the Valhall field. Like Hillerslev chalk, the Valhall Tor formation is of Late Maastrichtian age and is heavily fractured. The chalk from the Hillerslev quarry and the Valhall Tor formation has the same degree of low cementation, low hardness, high porosity and low permeability (Krogsbøll et al. 1997). The fracturing of the Valhall Tor formation and the Hillerslev chalk are considered comparable due to similar structural development (Ali & Alcock 1992). Prior to testing, Hillerslev outcrop chalk was considered water-wet whereas the Valhall Tor formation was reported neutral to slightly oil-wet (Andersen 1995) or neutral to slightly water-wet (Eltvik et al. 1990).

The success of waterflooding depends on the capillary pressure curves for the material, i.e. the relationship between saturation and capillary pressure. Wettability affects both capillary pressure and waterflooding. It is thus important to obtain knowledge about wettability and capillary pressure properties for Hillerslev outcrop chalk in order to obtain a better understanding of the displacement processes in oil-saturated Hillerslev outcrop chalk during waterflooding.

Wettability and capillary pressure measurements were performed on three small (D = 38 mm, H = 50 mm) Hillerslev outcrop chalk specimens at Rogaland Research in Stavanger, Norway. The aims of these tests were to:

- Measure the wettability of Hillerslev outcrop chalk (the degree of water-wetness)
- Establish capillary pressure curves for Hillerslev outcrop chalk
- Alter the wettability of a small Hillerslev outcrop chalk specimen towards the wettability of the Valhall Tor formation
  - To learn how to alter the wettability
  - To establish capillary pressure curves for a small wettability-altered specimen

- To obtain knowledge of the effect of the wettability of Hillerslev outcrop chalk on capillary pressure measurements
- To be able to alter the wettability of a large specimen in order to perform waterflooding test on a specimen as close an analogue to the Valhall Tor formation as possible
    - To obtain knowledge of the effect of the wettability of Hillerslev outcrop chalk on waterflooding

The specimens were prepared at Stavanger College, Norway. The tests were planned and carried out by the author with help and supervision from Research Engineer Jan Erik Iversen, Rogaland Research, and Engineer Egil Boye Petersen, earlier working at Rogaland Research. The data processing, evaluation and reporting was carried out by the author.

Chapter 2

Wettability and Capillary Pressure Measurement

2.1 Measuring Methods for Wettability

Wettability can be measured in the laboratory. Three quantitative methods are generally used: (1) contact angle measurement, (2) the Amott test, and (3) the U. S. Bureau of Mines (USBM) test. The contact-angle measures the wettability of a specific surface, while the Amott and USBM tests measure the average wettability of a specimen. The two latter methods are also used in a combined test referred to as the modified USBM test.

Contact Angle Measurement

Contact angles can be measured by submerging two smooth parallel mineral plates in water and then introduce a drop of oil between the plates. When the plates are moved relative to each other, a contact angle is formed. The maximum angle is obtained by pushing the fluid over the surface, while the minimum is obtained by pushing the fluid back. The maximum and the minimum angles measured through the same fluid are referred to as the advancing contact angle and the receding contact angle, respectively.

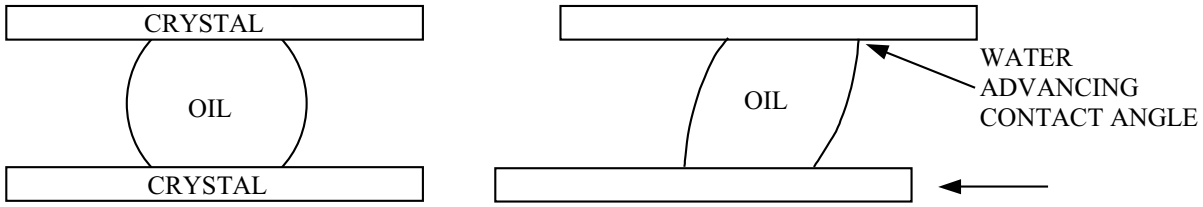

Figure 2.1 *Set-up for contact angle measurement.*

Morrow (Morrow 1990) states that water-advancing contact angles are reported as defining wettability because these are considered relevant to waterflooding. A range of

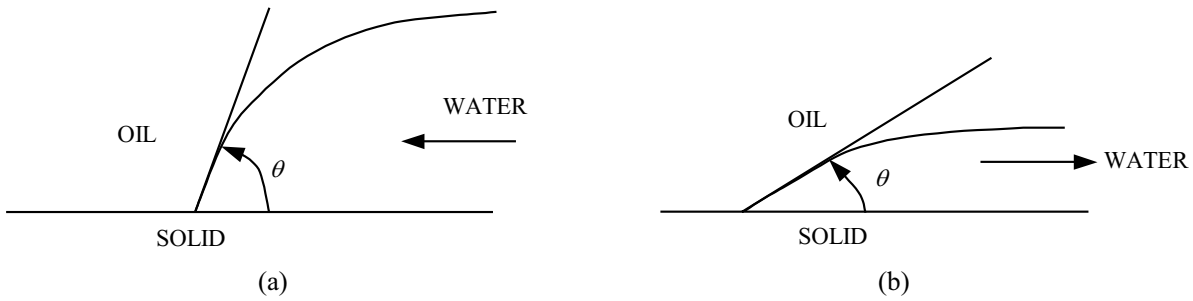

Figure 2.2 *Hysteresis in contact angle in a water-wet porous medium (a) increase in the wetting fluid (imbibition) and (b) decrease in the wetting fluid (drainage).*

contact angels will be measured in most systems, however, with relatively reproducible maximum and minimum values.

The difference between the two angles is the contact-angle hysteresis, which can be greater than 60°. There appears to be three causes of contact-angle hysteresis: surface roughness, surface heterogeneity and surface immobility on a macro-molecular scale. Contact angle hysteresis is one factor causing hysteresis between capillary pressures measured with increasing vs. decreasing wetting fluid saturations (Anderson 1986*a*). The measured value of the contact angle may also depend strongly on the time of exposure of the solid to both fluids, as alteration of the surface wettability can occur. The concept of explaining wettability based on the contact angle is not very useful, since it is based on a plane surface to measure from.

Amott Test

The Amott test combines spontaneous and forced imbibition to measure the average wettability of a specimen. The method is based on the fact that the wetting fluid will generally imbibe spontaneously into the specimen and displace the nonwetting one. The ratio of spontaneous to forced imbibition is used to reduce the influence of other factors such as relative permeability, viscosity and the initial saturation of the specimen. Based on the test, the Amott-Harvey wettability index WI can be calculated. The index compares the imbibition potential of water and oil, and varies from +1 for strongly water-wet specimens to -1 for strongly oil-wet specimens (Anderson 1986*a*).

In the first step of the Amott test, the specimen is centrifuged first in water and then in oil to reduce the specimen to the irreducible water saturation S_{wir}. Then it consists of the following four steps: (1) immerse the specimen in water, and measure the volume of oil displaced spontaneously, (2) centrifuge the specimen in water until the residual oil saturation S_{orw} is reached, and measure the amount of oil displaced under force, (3) immerse the specimen in oil, and measure the volume of water displaced spontaneously, and (4) centrifuge the specimen in oil until S_{wir} is reached, and measure the amount of water displaced under force. The specimen may be driven to S_{wir} and S_{orw} by flow rather than with a centrifuge.

The calculation of the Amott-Harvey index uses three wettability indices. The water-wetting index WWI is the displacement-by-water ratio, i.e. the ratio of the spontaneous

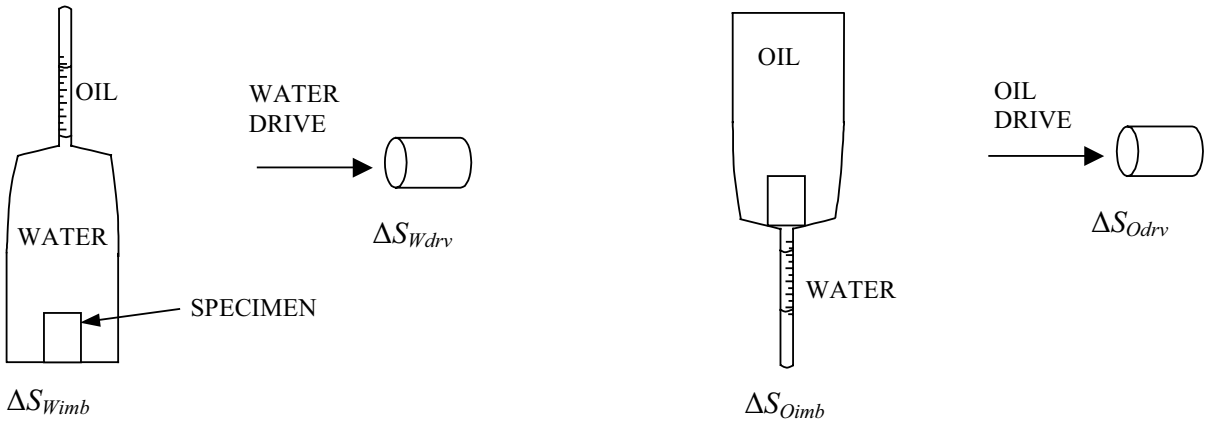

Figure 2.3 *Set-up for measurement of the Amott-Harvey wettability index.*

saturation change to the total saturation change and can be defined for spontaneous water imbibition ΔS_{Wimb} and driven water saturation change ΔS_{Wdrv} as (Andersen 1995):

$$WWI = \frac{\Delta S_{Wimb}}{(\Delta S_{Wimb} + \Delta S_{Wdrv})} \tag{2.1}$$

An oil-wetting index OWI is defined similarly for spontaneous oil imbibition, ΔS_{Oimb} and driven oil saturation change ΔS_{Odrv}, i.e. the displacement-by-oil ratio. In the Amott test, the displacement-by-water ratio is zero for neutrally and oil-wet specimens and approaches 1 as the water-wetness increases. Similarly, the displacement-by-oil ratio is zero for neutrally and water-wet specimens and approaches 1 as the oil-wetness increases.

The Amott-Harvey wettability index is the displacement-by-water ratio minus the displacement-by-oil ratio. This combines the two ratios into a single wettability index:

$$WI = WWI - OWI \tag{2.2}$$

USBM Test

The USBM test includes measurement of drainage and imbibition capillary pressure curves, usually by use of a centrifuge. The method compares the work necessary for one fluid to displace the other. Because of the favourable free-energy change, the work required for the wetting fluid to displace the nonwetting fluid from the specimen is less than the work required for the opposite displacement. It has been shown that the required work is proportional to the area under the capillary pressure curve. Based on the USBM test, the USBM wettability index can be calculated. This index is unbounded. Experimentally though, the index usually falls within -1 to +1. According to Man and Jing (Man & Jing 2000), the specimen is preferentially water-wet if the index is greater than zero. If the index is less than zero, the specimen is preferentially oil-wet. The specimen is neutral-wet if the index is approximately zero.

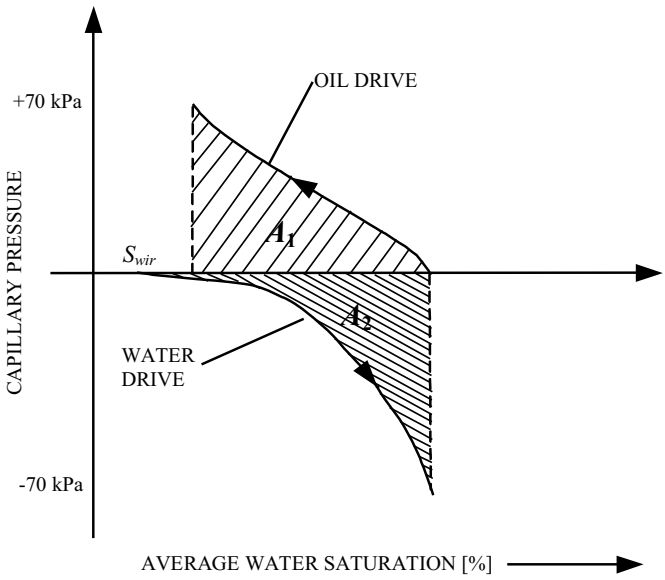

Figure 2.4 *Schematic of wettability measurements by the USBM method for a mixed-wet system.*

Before the USBM test, the specimen is prepared by centrifuging first in water and then in oil to S_{wir}. In the first step of the USBM test, the specimen is placed in water and centrifuged at incrementally increasing speeds. This step is known as the water drive because water displaces oil from the specimen. At each incremental speed, the average saturation of the specimen is calculated from the volume of expelled oil and the capillary pressure is calculated from the rotational acceleration (Section 2.2). In the second step, the specimen is placed in oil and centrifuged. During this oil drive, the capillary pressures and average saturations are calculated. Both the water drive and the oil drive are carried out until a capillary pressure of 70 kPa (10 psi) is reached. In each case (oil- and water drive), the curves are linearly extrapolated or truncated if the last pressure is not exactly 70 kPa. The USBM method uses the ratio of the areas under the two capillary pressure curves to calculate a wettability index (Anderson 1986*a*). In Figure 2.4, the schematic of the determination of the wettability index by the USBM test for a mixed-wet system is shown.

The USBM index is the log of the ratio of areas under the water and oil drive part of the capillary pressure curves for a capillary pressure between -70 kPa and 70 kPa:

$$USBM\ index = \ln(A_1/A_2) \tag{2.3}$$

where A_1 is the area under the oil drive curve, and A_2 is the area above the water drive curve.

Modified USBM Test

A modified USBM method exists which is a combined Amott and USBM test that allows for calculation of both the Amott-Harvey and the USBM wettability indices. There are two advantages of combining these tests. Firstly, the resolution of the USBM test is

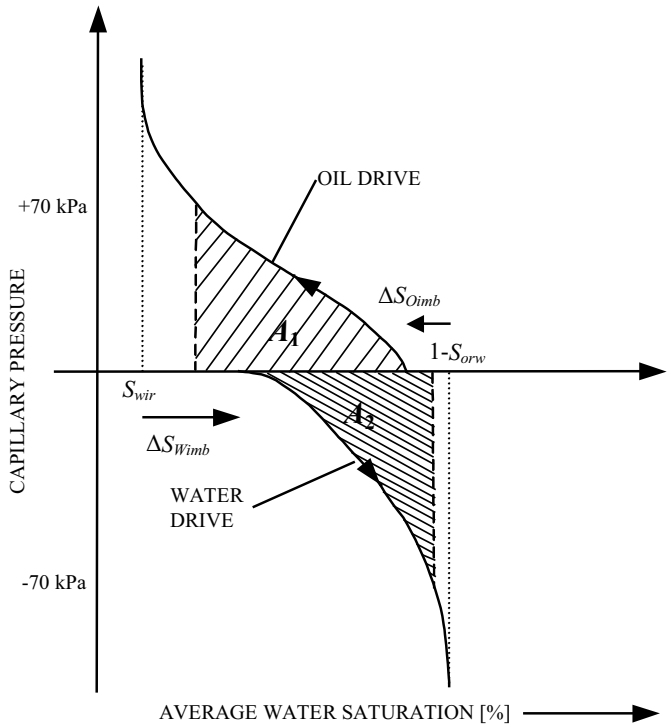

Figure 2.5 *Schematic of wettability measurements by the modified USBM method for a mixed-wet system.*

improved by accounting for the saturation changes that occur at zero capillary pressure, and secondly, the Amott-Harvey index is calculated as well. The procedure has five steps: (1) the specimen is prepared by centrifuging first in water and then in oil to S_{wir}, (2) spontaneous imbibition of water, (3) water drive, (4) spontaneous imbibition of oil, and (5) oil drive. In the second step, the specimen is immersed in water, and the volume of water that imbibes spontaneously is measured. During the water-drive, the average saturation of the specimen is determined from the volume of expelled oil at each incremental capillary pressure calculated from the rotational acceleration. At the end of the water-drive, the specimen is left at S_{orw}. In the fourth step, the specimen is immersed in oil, and the volume of oil that imbibes spontaneously is measured. The final step is the oil drive, where the specimen again is driven to S_{wir} (Anderson 1986*a*). A sketch of the wettability measurements established by the modified USBM method for a mixed-wet system is shown in Figure 2.5.

The areas under the water and oil drive curves are used to calculate the USBM index, while the Amott-Harvey index uses the volumes of spontaneous and total water and oil displacements.

The modified USBM method is best illustrated for a non-homogeneous wet system, but as the Amott-Harvey and the USBM wettability indices are a measure of the average wettability of a specimen, such indices are not very representative for specimens with non-homogeneous wettability.

For both the USBM test and the modified USBM method, the original USBM index is found from the area under the capillary pressure vs. average saturation curve. A modified

USBM index is found from the area under the capillary pressure vs. end-face saturation curve. In this report, the average saturation of the specimen is used for determination of the USBM index, i.e. the original USBM index is calculated. In contrast, the capillary pressure curves are based on the saturation at the end-face of the specimens, which is calculated from the average saturation (Section 2.2).

The USBM test appears to be superior to the Amott test, which is insensitive near neutral wettability. It is possible to have an Amott-Harvey wettability index of about zero either because the material imbibes neither water nor oil strongly, or because it imbibes quite a bit of both to the same degree. However, the USBM test cannot determine whether a system has homogeneous wettability or not, while the Amott test is sometimes sensitive. In some fractional- or mixed-wet systems, both water and oil imbibe spontaneously. The Amott test will have positive displacement-by-water and displacement-by-oil ratios, indicating that the system is non-homogeneously wetted. There are thus two advantages of the combined Amott and USBM test. It provides sensitivity near neutral wettability and will sometimes indicate if a system is non-homogeneously wetted (Anderson 1986*a*).

In Table 2.1 the approximate relationship between wettability, contact angle, and the USBM and Amott-Harvey wettability indices are included.

	Water-wet	Neutral-wet	Oil-wet
Contact angle			
Minimum	0°	60° to 75°	105° to 120°
Maximum	60° to 75°	105° to 120°	180°
USBM wettability index	W near 1	W near zero	W near -1
Amott test			
Displacement-by-water ratio	Positive	Zero	Zero
Displacement-by-oil ratio	Zero	Zero	Positive
Amott-Harvey wettability index	$0.3 \leq WI \leq 1.0$	$-0.3 < WI < 0.3$	$-1.0 \leq WI \leq -0.3$

Table 2.1 *Approximate relationship between wettability, contact angle, and the USBM and Amott-Harvey wettability indices (Anderson 1986*a*).*

According to Anderson (Anderson 1986*a*), a qualitative wettability measurement method is the imbibition method because it gives a quick but rough idea about the wettability. The imbibition method can be described as a modified form of the Amott test since the imbibition rates during the spontaneous imbibition measurements is also measured. In this test, the specimen is suspended in oil or water from an electronic balance by a small line. Weight change is monitored as a function of time as spontaneous imbibition occurs. The degree of wetness is indicated by the rate and volume of imbibition. The specimen is strongly water-wet if large volumes of water imbibe rapidly, while lower rates and smaller volumes imply a more weakly water-wet specimen. This is similar for imbibition of oil in an oil-wet specimen. If neither oil nor water imbibe spontaneously, the specimen is neutral-wet. Finally, some specimens will imbibe both water and oil spontaneously. These specimens have either fractional- or mixed-wettability. One problem with the imbibition method is that in addition to wettability, imbibition rates also depend on relative permeability, viscosity, IFT, pore structure, and initial saturation of the speci-

men. This dependence may be reduced by comparison of the measured imbibition rate with a reference rate measured when the specimen is strongly water-wet.

2.2 Establishing Capillary Pressure Curves

Capillary pressure measurements are essential for a complete characterization of an oil-bearing reservoir. Capillary pressure curves can be used for estimation of reserves, for reservoir evaluation or as input to reservoir simulation. Capillary pressure curves can be obtained in the laboratory by at least three different techniques. (1) The mercury injection method. As mercury is a nonwetting fluid for reservoir rock, drainage capillary pressure curves can be obtained. (2) The porous plate method. The specimen is placed on a diaphragm wet by the fluid to be displaced from the specimen. During increase in the displacing pressure, the corresponding saturation is determined. (3) The centrifuge method. Here, the pressure difference between the fluids results from the density difference.

Christoffersen (Christoffersen 1995) reports that the porous-plate method is considered the most accurate, whereas the mercury injection method and the centrifuge method are much faster to perform. An obvious disadvantage of the mercury injection method is that a different fluid system is used. The porous plate method directly measures the capillary pressure curve, while the centrifuge method is an indirect method and additional data processing is required to obtain a capillary pressure curve.

Earlier experimental work by Nørgaard et al. (Nørgaard et al. 1999) has shown that capillary pressure curves obtained by mercury injection lie significantly below a capillary pressure curve obtained by the centrifuge method on the same specimen of North Sea Chalk. The reason for this may lie in problems with scaling of the interfacial tension (IFT) and contact angle of the mercury liquid - mercury vapor system to the water-oil system (Anderson 1986*b*).

As mentioned, capillary pressure curves can be obtained by the centrifuge method, where the pressure difference between the fluids results from the density difference, as in the gravity-driven process in the field. The capillary pressure is not directly measured, but found from the centrifuge speed by assuming exact analogy of a centrifugal field and a gravitational field. First, centrifuge production data, i.e. corresponding values of centrifuge speed and produced volumes are measured. When the wettability of a specimen is known, these data can be transformed into capillary pressure curves.

The initial work on the centrifuge method was introduced in 1945 by Hassler and Brunner (Hassler & Brunner 1945). They introduced the theory and practice of using the centrifuge to create a pressure gradient within the specimen and presented an approximation for converting measured average saturation to end-face saturation for drainage curves. Szabo (Szabo 1974) extended the method to include imbibition curves. Over the years, various interpretation methods for improving the Hassler and Brunner derivation have been published. Forbes (Forbes 1994) concludes that the simple methods usually reduce the accuracy of the results, while the accurate ones usually require more time and must smooth, fit, or force the experimental data into a given analytical form.

The centrifuge method consists in measuring average fluid saturation versus capillary pressure P_c of a specimen at hydrostatic equilibrium during rotation at various angular

velocities ω, see Figure 2.6. The specimen is initially filled with a fluid and spun within a second fluid. Due to the rotation, the inner fluid is forced out of the specimen. The average saturation of a specimen can be determined at the different centrifuge speeds by collecting and measuring the fluid production.

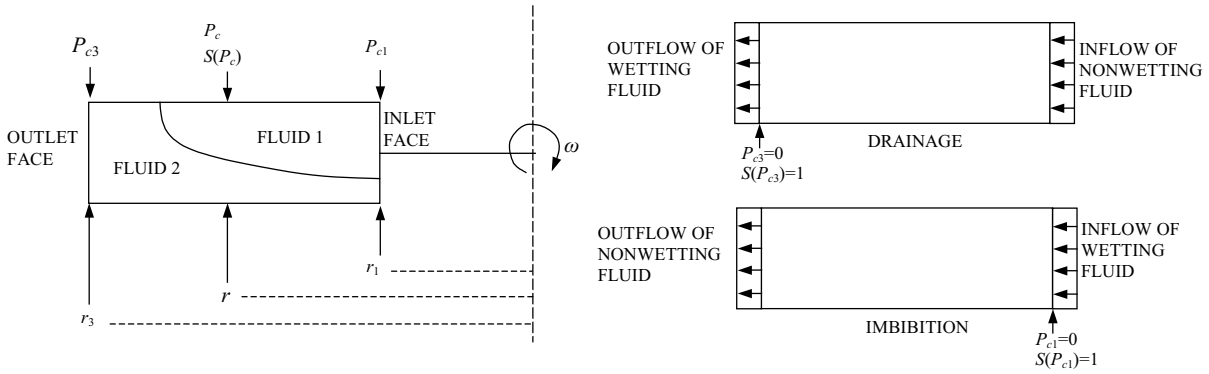

Figure 2.6 *Schematic of the centrifuge method (Forbes 1994).*

According to Hassler and Brunner (Hassler & Brunner 1945), at hydrostatic equilibrium, the capillary pressure at any position is equivalent to the difference in hydrostatic pressure between the two phases. Taking the linear variation of the centrifugal field with the distance from the axis of rotation into account, the capillary pressure P_c [Pa] for drainage is given by:

$$\int_{P_{wetting}}^{P_{nonwetting}} dP = \int_{r}^{r_3} \Delta\rho\omega^2 r dr \tag{2.4}$$

$$\Downarrow$$

$$P_c = \frac{1}{2}\Delta\rho\omega^2(r_3^2 - r^2) \tag{2.5}$$

where r [m] is the radial distance from the axis of rotation, r_3 [m] is the radius to the center of the outlet face of the specimen, ω [rad/sec] is the angular velocity of the centrifuge and $\Delta\rho$ [kg/m^3] is the density difference between the two phases defined as:

$$\Delta\rho = \rho_{wetting} - \rho_{nonwetting} \tag{2.6}$$

For drainage, it is assumed that the capillary pressure $P_c = 0$ at the outlet face (Figure 2.6), and the capillary pressure at the inlet face P_{c1} is calculated as:

$$P_{c1} = \frac{1}{2}\Delta\rho\omega^2(r_3^2 - r_1^2) \tag{2.7}$$

where r_1 [m] and r_3 [m] are the distances to the centers of the inlet and the outlet face of the specimen, respectively.

If the variation of the centrifugal field with the distance from the axis of rotation is taken into account, the average saturation for drainage of the specimen can be found from:

$$\overline{S} = \frac{1}{(r_3 - r_1)} \int_{r_1}^{r_3} S(r)dr \tag{2.8}$$

This can be rewritten into the fundamental equation for converting average wetting phase saturation for drainage into local average saturation (inlet face) formulated by Hassler and Brunner:

$$\overline{S}(P_{c1}) = \frac{1 + \sqrt{1 - B}}{2} \int_0^1 \frac{S(xP_{c1})dx}{\sqrt{1 - Bx}} \tag{2.9}$$

where x is a dimensionless integration variable, and:

$$B = 1 - \left(\frac{r_1}{r_3}\right)^2 \qquad 0 \leq B \leq 1 \tag{2.10}$$

For forced imbibition, the same equations are obtained when exchanging r_1 for r_3 (Forbes 1994). For imbibition, it is assumed that the capillary pressure $P_c = 0$ at the inlet face (Figure 2.6), and the capillary pressure at the outlet face P_{c3} is calculated as:

$$P_{c3} = \frac{1}{2}\Delta\rho\omega^2(r_1^2 - r_3^2) \tag{2.11}$$

The fundamental equation for converting average wetting phase saturation for imbibition into average local saturation (outlet face) is given by:

$$\overline{S}(P_{c3}) = \frac{1 + \sqrt{1 - B}}{2} \int_0^1 \frac{S(xP_{c3})dx}{\sqrt{1 - Bx}} \tag{2.12}$$

where:

$$B = 1 - \left(\frac{r_3}{r_1}\right)^2 \qquad B < 0 \tag{2.13}$$

The essential problem that must be solved to obtain a capillary pressure curve is to relate P_c to its appropriate end-face saturation S. For both drainage and imbibition, the problem consists therefore in inverting the fundamental average saturation equations $\overline{S}(P_{c1})$ and $\overline{S}(P_{c3})$ to obtain $S(P_{c1})$ and $S(P_{c3})$, respectively.

For drainage, Hassler and Brunner proposed the approximate solution for calculating the end-face saturation from the measured average saturation:

$$S = S_{HB} = \overline{S} + P_c \frac{d\overline{S}}{dP_{c1}} \qquad B = 0 \tag{2.14}$$

For imbibition P_{c1} is replaced by -P_{c3}. This solution is based on the assumption of a linear variation of P_c along the specimen. The solution has increasing errors outside the range of $r_1/r_3 \geq 0.7$. The solution rests on the assumption that the model is one-dimensional. Centrifugal acceleration and fluid flow are assumed to be parallel to the axis

of the core. According to Forbes (Forbes 1994), this solution is one of the worse solutions outside the range of $r_1/r_3 \geq 0.7$, but is still widely used in the oil industry.

Van Domselaar (Forbes 1994) proposed the following approximate solution for drainage:

$$S = S_D = \overline{S} + \frac{2\sqrt{1-B}}{1+\sqrt{1-B}} P_c \frac{d\overline{S}}{dP_{c1}} \tag{2.15}$$

For imbibition P_{c1} is replaced by -P_{c3}. As for the S_{HB} solution, the approximation to the correct $S(P_c)$ is accurate enough for $r_1/r_3 \geq 0.7$.

Forbes (Forbes 1994) proposed an accurate, rapid and simple method that allows for conversion of sparse and noisy experimental data without smoothing, fitting, averaging, or forcing data to a given form. Forbes believes this method to produce capillary pressure curves corresponding more closely to the centrifuge data than curves obtained from most other me-thods, and it is particularly simple for imbibition. The accurate approximate solution for drainage is given by:

$$S(P_c) \approx S_{\alpha\beta} = (1 - \frac{B}{2})S_\alpha + \frac{B}{2} S_\beta \qquad 0 \leq B \leq 1 \tag{2.16}$$

where:

$$S_\alpha(P_c) = \overline{S}(P_c) + \frac{P_c}{1+\alpha} \frac{d\overline{S}(P_c)}{dP_{c1}} \qquad \alpha = \frac{1-\sqrt{1-B}}{1+2\sqrt{1-B}} = \frac{r_3 - r_1}{r_3 + 2r_1} \tag{2.17}$$

$$S_\beta(P_c) = (1+\beta) \int_0^1 x^\beta S_{HB}(xP_c) dx \qquad \beta = \frac{2}{\alpha} \tag{2.18}$$

$$S_{HB} = \overline{S} + P_c \frac{d\overline{S}}{dP_{c1}} \tag{2.19}$$

This solution can be evaluated with high accuracy from discrete $\overline{S}$ data using a simple differencing scheme (Appendix A). Using this scheme, solution S for each step is obtained directly from the values of $\overline{S}$. No smoothing or fitting of $\overline{S}$ or averaging of S results are needed, but to prevent oscillation in processing of the experimental data, it is proposed to use physical constraints such as $S_j \leq S_{j-1}$.

The same solutions proposed for drainage can be similarly developed for imbibition, replacing:

$$B = 1 - \left(\frac{r_1}{r_3}\right)^2 \quad \text{by} \quad B = 1 - \left(\frac{r_3}{r_1}\right)^2 \tag{2.20}$$

The accurate approximate solution for imbibition is given by:

$$S(P_c) \approx S_\alpha(P_c) = \overline{S}(P_c) + \frac{P_c}{1+\alpha} \frac{d\overline{S}(P_c)}{dP_{c1}} \tag{2.21}$$

$$\alpha = \frac{1-\sqrt{1-B}}{1+2\sqrt{1-B}} = \frac{r_3 - r_1}{r_3 + 2r_1} \qquad B < 0 \tag{2.22}$$

Again, this solution can be evaluated with high accuracy from discrete $\overline{S}$ data using a simple differencing scheme (Appendix A). Using this scheme, solution S for each step

is obtained directly from the values of $\overline{S}$. No smoothing or fitting of or averaging of S results are needed, but to prevent oscillation in processing of the experimental data, it is proposed to use physical constraints such as $S_j \geq S_{j-1}$ for $P_j \leq P_{j-1}$.

Forbes (Forbes 1994) has shown analytically for both drainage and imbibition that the S_{HB} approximation is always lower, and the S_D approximation is always higher than the exact solution:

$$S_{HB} \leq S \leq S_D \tag{2.23}$$

To sum up, the capillary pressure curves are established as follows:

1. Measurement of a data set $(\overline{S}, \omega)$, $\overline{S}$ being the average saturation of the specimen and ω the corresponding rotational speed.
2. Transformation of the measured data set into a data set $(\overline{S}, P_c)$, P_c being P_{c1} in equation (2.7) for drainage and P_{c3} in equation (2.11) for imbibition.
3. $S(P_c)$ is obtained by inverting the integral equation $\overline{S}(P_c)$ defined by equation (2.9) for drainage and equation (2.12) for imbibition.

Accounting for Gravity and Radial Effects

The calculation of the capillary pressure, which is similar for the Hassler-Brunner method, the van Domselaar method and the included Forbes method, only takes into account the centrifugal effect and not the radial effect or the effect of gravity. Including these effects results in the following capillary pressure equations (Forbes 1997).

For drainage, the capillary pressure is then given by:

$$P_{c1}(r, Z, \omega) = \frac{1}{2}\Delta\rho\omega^2(r_3^2 - r_1^2) + \Delta\rho g Z + \frac{1}{2}\Delta\rho\omega^2(n+1)R^2 \tag{2.24}$$

where $n = 2(g/\omega^2)/R - 1$ if $g/\omega^2 > R$, or $n = (g/\omega^2)^2/R^2$ if $g/\omega^2 < R$.
Similarly, for imbibition, the capillary pressure is then:

$$P_{c3}(r, Z, \omega) = \frac{1}{2}\Delta\rho\omega^2(r_1^2 - r_3^2) + \Delta\rho g Z + \frac{1}{2}\Delta\rho\omega^2(n+1)R^2 \tag{2.25}$$

where $n = -2(g/\omega^2)/R - 1$.
By definition, the average saturation $\overline{S}$ of the specimen can be found as:

$$\overline{S} = \frac{1}{L\pi R^2}\int_{specimen} S_{r,Z,\omega} dv = \frac{1}{L\pi R^2}\int_{specimen} S(P_c(r, Z, \omega)) dv \tag{2.26}$$

where L is the length of the specimen, R is the radius of the specimen, r is the rotational radius, Z is the vertical coordinate and dv is the elementary volume. $\overline{S}(P_c(r, Z))$ varies inside the core, and the above equation can be normalized and re-written into an expression denoted $\overline{S}_{B,N,M}(P_c)$ (Appendix B) depending on the parameters B (centrifugal effect), N (radial effect) and M (gravity effect). For the saturation solution in the Hassler-Brunner method given in equation (2.14), the pressure field is assumed linear (neither radial nor centrifugal), and the gravity is neglected: $B = 0$, $N = 0$ and $M = 0$. The

van Domselar solution given in equation (2.15) and the included solutions by Forbes (Forbes 1994) given in equation (2.16) for drainage and equation (2.21) for imbibition neglect radial ($N = 0$) and gravity ($M = 0$) effects, but include centrifugal effects ($B \neq 0$).

To sum up, the capillary pressure curves accounting for gravity and radial effects are established as follows:

1. Measurement of a data set $(\overline{S}, \omega)$, $\overline{S}$ being the average saturation of the specimen and ω the corresponding rotational speed.
2. Transformation of the measured data set into a data set $(\overline{S}, P_c)$, P_c being P_{c1} in equation (2.24) for drainage and P_{c3} in equation (2.25) for imbibition.
3. $S(P_c)$ is obtained by inverting the integral equation $\overline{S}(P_c) = \overline{S}_{B,N,M}(P_c)$ defined in Appendix B.

Instead of performing a complicated inversion of the integral equation $\overline{S}_{B,N,M}(P_c)$, the equation is rewritten to provide an evaluation of the integral $\overline{S}_{B\neq 0,N=0,M=0}(P_c)$, for which inversion techniques are available (solutions to equation (2.9) for drainage and (2.12) for imbibition). A total correction accounting for both radial and gravity effects is then applied to the average saturation. Similarly, the total correction is applied to the calculation of P_c by equation (2.7) and (2.11) instead of using equation (2.24) and (2.25). This total correction consists of changing $(P_c, \overline{S}(P_c))$ by $(P_c/b, \overline{S}(P_c)+a_0(\overline{S}(a_0 P_c)-\overline{S}(P_c)))$ before processing the usual saturation solutions of equation (2.9) for drainage and equation (2.12) for imbibition (Forbes 1997). The correction parameters are included in Table 2.2 and Table 2.3.

	a_0	b_0
Drainage	$\frac{3/4N(1+(1-B)^{1/2})}{2(1+N)}$	$\frac{1+0.23N/(1+N)}{(1+N)}$
Imbibition	$\frac{-1/4N(1+(1-B)^{1/2})}{2}$	$\frac{1-a_0(4-(1-B)^{1/2})}{2+(1-B)^{1/2}}$

Table 2.2 *Radial correction parameters (Forbes 1997).*

	P_c	B	N	M	C	$1/b - 1/b_0$
Drainage	$\frac{1}{2}\Delta\rho\omega^2(r_3^2 - r_1^2)$	$\frac{(r_3^2-r_1^2)}{r_3^2}$	$\frac{R^2}{(r_3^2-r_1^2)}$	$\frac{g}{\omega^2 R}$	$\frac{N(4+2(1-B)^{1/2})}{(5+(1-B)^{1/2})}$	$M > 1 : (4M - 1.75)C$ $0 < M < 1 : 2.25M^{1.7}$
Imbibition	$\frac{1}{2}\Delta\rho\omega^2(r_1^2 - r_3^2)$	$\frac{(r_1^2-r_3^2)}{r_1^2}$	$\frac{R^2}{(r_1^2-r_3^2)}$	$\frac{-g}{\omega^2 R}$	$\frac{N(4+2(1-B)^{1/2})}{(5+(1-B)^{1/2})}$	$M < 0 : 4MC$

Table 2.3 *Correction parameters (Forbes 1997).*

B represents the centrifugal effects related to the fact that the capillary pressure varies with r^2 and not linearly with r. N represents the magnitude of radial effects related to

the curvature of the capillary pressure field around the rotational axis. M is "a priori" an appropriate parameter to measure the effect of gravity.

Centrifuge Bond Number

De-saturation effects, i.e. mobilization of trapped nonwetting phase (residual saturation), can cause changes in capillary pressure curves established at high flow rates. The capillary pressure curves will change as the residual saturation is changed. De-saturation effects (usually) do not occur under normal field conditions. To avoid these effects, the critical Bond number (ratio between gravitational and capillary forces) should not be exceeded (Verbruggen et al. 2000). This Bond number requirement implies an upper limit for the centrifugal acceleration due to that the gravitational (here centrifugal) forces are stronger than the capillary forces when spinning the centrifuge at high speeds.

The dimensionless centrifuge Bond number $N_{B,cen}$ describes the ratio of centrifugal to capillary forces (Skauge & Poulsen 2000):

$$N_{B,cen} = \frac{K\omega^2 r\Delta\rho}{\sigma_i} \tag{2.27}$$

where K [m^2] is the absolute permeability, ω [sec^{-1}] is the rotational speed, r [m] is the radius from the centre of the specimen to the rotational axis, $\Delta\rho$ [kg/m^3] is the fluid density difference and σ_i [mN/m] is the interfacial tension between the two fluids. This expression transforms into the conventional gravity-to-capillary Bond number, N_B, by replacing the centrifugal acceleration $\omega^2 r$ with the gravitational acceleration g.

At low centrifugal speed, the flow regime is capillary dominated, and the trapped phase is not mobilized. Above the critical centrifuge Bond number (the critical value of rotational speed), at which centrifugal forces dominates over capillary forces, the nonwetting phase is mobilized.

The dimensionless centrifuge Bond number $N_{B,cen}$ are calculated to be in the range of $9.7 \cdot 10^{-12}$ to $1.3 \cdot 10^{-9}$ for a mean absolute, permeability of $K = 2.8 \cdot 10^{-15}$ m^2 (mean value of 2.6-2.9 mD), a difference in density of oil and water of $\Delta\rho = 287$ kg/m^3 and an interfacial tension between oil and water of $\sigma_i = 60$ mN/m.

The calculated range of the centrifuge Bond number is below the critical centrifuge Bond number of 10^{-5} for Maui BD oil sands. Since the matrix permeability around 2-3 mD for Hillerslev outcrop chalk is significantly lower than for the reference low-permeable sandstone, no conclusions can be made. However, the author has located no critical centrifuge Bond number for avoiding de-saturation effects in chalk.

Chapter 3

Description of the Laboratory Tests

Wettability and capillary pressure measurements were performed on three Hillerslev outcrop chalk specimens 1, 2 and 3 at Rogaland Research, Stavanger, Norway. This was done by utilizing Amott cups and an automated Beckman centrifuge. The laboratory journal is included, see Appendix C.

All saturation calculations are based on a volume balance except for the initial fully saturation of specimens 1 and 2 with water and specimen 3 with Isopar-L, which is based on weights. In addition to the volume balance, weighing of the specimens has been performed after each step as check.

3.1 Hillerslev Chalk Specimens and Fluids

The three specimens were taken from a small block of Hillerslev outcrop chalk material from the earlier research project "Fractures and Rock Mechanics", phase 2 (Jakobsen 2001). The specimens were drilled using a water-cooled ø42 drill. The specimens were dried in an oven at 105°C.

The specimens were turned in a turning lathe to a diameter of approximately 3.8 cm and then both ends of the specimens were cut by an electric saw to a length of approximately 5.0 cm. The specimens were described, measured and sketched, see Appendix D.

Specimen 1

The aim was to obtain a less water-wet specimen containing Isopar-L and with an initial water saturation in order to resemble the conditions of the Tor formation of the Valhall field.

Hillerslev chalk is regarded as a close analogue to chalk from the Tor formation of the Valhall field. The chalk from the Tor formation is reported to be neutral- to slightly oil-wet with an initial water saturation of about 5%. The Amott-Harvey wettability index is in the range of 0 to -0.37 (Andersen, 1995). The chalk from the Tor formation is also reported to be neutral- to slightly water-wet (Eltvik et al. 1990).

Specimen 2

The aim was to obtain a water-wet specimen containing Isopar-L and with an initial water saturation in order to resemble laboratory conditions for prior tests on Hillerslev chalk.

Specimen 3

The aim was to obtain a water-wet specimen saturated with Isopar-L in order to resemble laboratory conditions for prior tests on Hillerslev chalk, and compare test results for specimens with and without initial water saturation.

Fluids

Due to the composition of the laboratory oil Isopar-L, Hillerslev outcrop chalk saturated with Isopar-L stay water-wet. The density of Isopar-L is 0.763 g/cm^3 and the viscosity is 1.41 cP, both at 22°C.

The water used was synthetic formation water, which was mixed using a recipe for the Valhall field formation water. The recipe for the water (g/2 l distilled water) is shown in Table 3.1. Small pieces of chalk were put into this mixture to prevent dissolution of the specimens. In this report, the synthetic formation water is referred to as water. The density of the water is 1.05 g/cm^3 and the viscosity is 1.0 cP, both at room temperature. The interfacial tension between Isopar-L and the water is 60 mN/m (GEUS).

NaCl	121.76 g/2 l
KCl	0.48 g/2 l
$CaCl_2$	29.5 g/2 l
$MgCl_2 \times 6H_2O$	9.1 g/2 l

Table 3.1 *Recipe for the synthetic Valhall field formation water.*

3.2 Preparation of the Specimens

The specimens were dried in an oven at 105°C. Then a shrink-fix sleeve was put around each specimen, and this was heated with a heating pistol and cut at both ends to fit the periphery of the specimen. Shrink-fix sleeves were used to ensure that fluid only enters and leaves through the end-faces of the specimens. Further, shrink-fix sleeves also makes the specimens more stabile in order to be able to withstand the rough treatment in the centrifuge.

Pressure heads and porous plates were placed in both ends of the specimen, and a rubber membrane was placed around the specimen and the pressure heads. There are channels in the pressure heads for an even distribution of injected fluids and to ease collection of displaced fluids. The length of the specimen was adjusted with rubber disks to fit the rubber membrane. The membrane was fixed at both ends with cobber wire. The specimen was then placed in an Exxon Triaxial core holder. One of the pressure

heads was fitted into the core holder and was thus a fixed part of the core holder while the other was part of a piston, see Figure 3.1. Isopar-H was sent into the core holder via a pump to obtain a pressure of 20 bar on the membrane around the specimen in order to prevent flow along the side of the specimen.

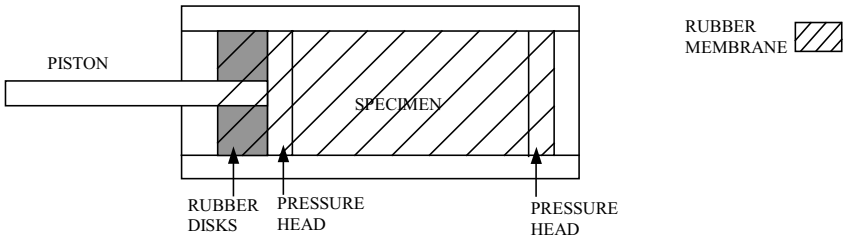

Figure 3.1 *Specimen placed in the Exxon Triaxial core holder.*

Specimens 1 and 2 were initially fully saturated with water, and specimen 3 was initially fully saturated with Isopar-L. The set-up for the initial fully saturation of the specimens is seen in Figure 3.2.

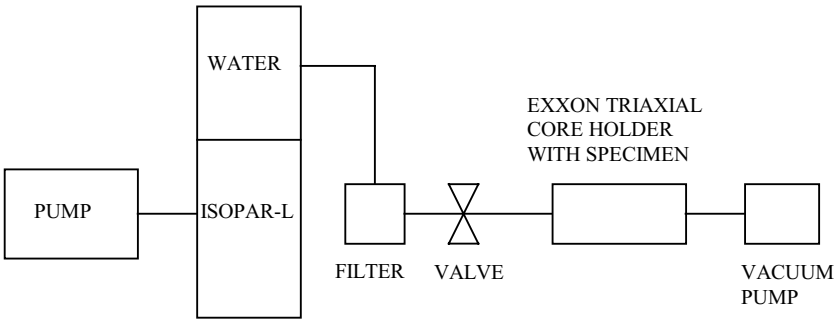

Figure 3.2 *Set-up for initial fully saturation of the specimens.*

A 10 bar reference pressure was applied for the initial fully saturation of the specimens (pump: 20 bar and vacuum pump: 10 bar). Then the specimens were flushed (0.5 ml/min.) with a backpressure of 10 bar applied in order to remove air from the specimens. A filter was put into the set-up (0.45 μm) to prevent pieces of chalk in the water above the filter size to enter the specimens. The mean absolute water permeability of specimens 1 and 2 was measured during flushing to 2.6-2.9 mD, see Appendix E.

After saturation, the specimens were taken out of the core holders and weighed. The wettability of specimen 1 was to be altered to a less water-wet state. Specimen 3 was placed in a container with Isopar-L and left until the aging period of specimen 1 was over.

To obtain low initial water saturations in specimens 1 and 2, the high viscous laboratory oil Marcol was used to displace the water, see Figure 3.3. First the specimens were flushed with the low viscous Isopar-L in order to establish a channel through the specimen

(flushing until breakthrough). This was done to avoid a high differential pressure over the specimen or a low injection rate when flushing with Marcol. The specimens were then flushed with Marcol to displace the water in place. Then the specimens were flushed with Isopar-L (0.1-0.2 ml/min.) to displace the Marcol. Specimen 2 was then placed in a container with Isopar-L and left until the aging period of specimen 1 was over.

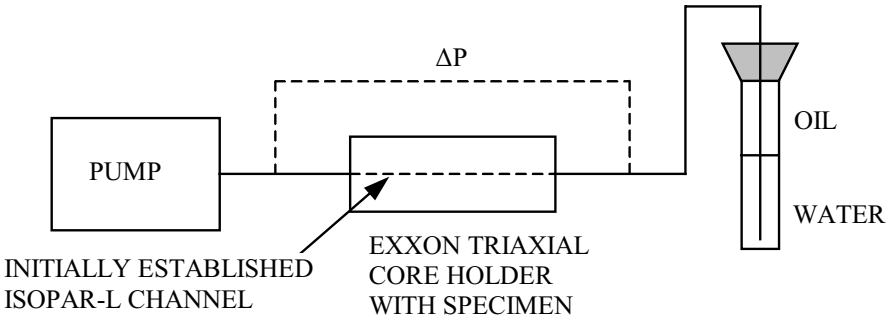

Figure 3.3 *Set-up for establishment of initial water saturation (specimens 1 and 2).*

The initial parameters for the three chalk specimens after saturation are shown in Table 3.2.

The mean diameter D [cm], height H [cm] and dry weight M_{dry} [g] are measured. The bulk volume BV [cm^3] is calculated as $\pi(D/2)^2H$. The dry density ρ_{dry} [g/cm^3] is calculated as M_{dry}/BV. The void ratio e [-] is calculated as ρ_s/ρ_{dry} -1, where the chalk grain density is $\rho_s = 2.70$ g/cm^3. The porosity ϕ [%] is calculated as $e/(e+1)\cdot 100$. The pore volume PV [cm^3] is calculated as $\phi \cdot BV$.

The fully saturation of specimens 1 and 2 with water and specimen 3 with Isopar-L is based on weights, i.e. $(M_{sat} - M_{dry})/\rho_{fluid}/PV \cdot 100$ with a water density of $\rho_w = 1.05$ g/cm^3 and an oil density of $\rho_o = 0.763$ g/cm^3. The air saturation is found as 100-S.

The initial water saturations for specimens 1 and 2 are obtained from the amount of displaced water, i.e. $(M_{sat} - M_{dry} - M_{disp})/\rho_w/PV \cdot 100$. The air saturation is assumed constant $S_a = S_{ai}$, and the initial oil saturation is found as 100-$S_{wi} - S_{ai}$.

The initial water saturation of specimen 1 is much lower than for specimen 2 although the aim was to obtain the irreducible water saturation S_{wir} in both specimens. The difference may be due to inhomogeneities in the chalk specimens or the procedure followed to obtain S_{wir}. In the following, the specimens are being referred to as having an initial water saturation S_{wi}, and not irreducible water saturations.

Wettability Alteration

The crude oil used for aging of specimen 1 was oil from the Snorre field in the North Sea (Norsk Hydro). The crude oil must have an AN in the order of 0.5-1.0 mg KOH/g oil if the chalk wettability is to be altered towards oil-wet (personal communication with Professor Tor Austad, Stavanger College, Norway). However, it was not possible to obtain information about the acid number (AN) for the Snorre oil. To ensure the ability of the oil to alter the wettability towards less water-wet, it was decided to add 1 weight%

Specimen	1	2	3
Mean diameter, D [cm]	3.81	3.80	3.81
Mean height, H [cm]	5.00	5.00	5.00
Dry weight, M_{dry} [g]	82.03	81.74	81.70
Bulk volume, BV [cm^3]	57.00	56.71	57.00
Dry density, ρ_{dry} [g/cm^3]	1.44	1.44	1.43
Void ratio, e [-]	0.88	0.88	0.89
Porosity, ϕ [%]	46.8	46.8	47.1
Pore volume, PV [cm^3]	26.68	26.54	26.85
Fully saturation with water or oil			
Weight after water or oil saturation, M_{sat} [g]	108.67	109.30	101.72
Water or oil saturation, S [%]	95.1	98.9	97.7
Air saturation, S_a [%]	4.9	1.1	2.3
Initial water saturation in specimens 1 and 2			
Displaced water, M_{disp} [g]	23.05	19.46	-
Initial water saturation, S_{wi} [%]	12.8	29.1	-
Initial oil saturation, S_{oi} [%]	82.3	69.8	97.7
Initial air saturation, S_{ai} [%]	4.9	1.1	2.3
Absolute water permeability, K [mD]	2.9	2.6	-

Table 3.2 *Initial parameters for the three Hillerslev chalk specimens.*

Dodekane acid ($C_{11}H_{23}COOH$) to the oil (personal communication with Professor Tor Austad, Stavanger College, Norway).

In order to obtain a homogenous wettability state throughout the chalk specimen, the specimen was flushed with 100 ml Snorre oil added 1 weight% Dodekane acid in each direction at a rate of 0.1-0.2 ml/min. The content of wax in crude oil can have some kind of blocking effect due to precipitation of wax in the porous media. Generally, if the temperature is above 40°C there are no problems with the wax. The flushing, though, was performed at room temperature. After flushing, the specimen was aged for 5 weeks at 90°C and 8 bar in a piston cell. The oil mixture surrounded the ends of the specimens, but it was not possible to surround the periphery of the specimens with this mixture due to the shrink-fix sleeves.

After 5 weeks of aging, specimen 1 (referred to as 1A in the following) was removed from the piston cell. The specimen broke in one end as it was removed. The specimen was now brittle, and the colour was changed to dark brown. Specimen 1A was placed in the Exxon Triaxial core holder and 20 bar pressure was applied to prevent flow along the side. The core holder was placed in the set-up shown in Figure 3.2, and the crude oil was displaced by Isopar-L. This was done at 40°C to prevent wax effect. The specimen was flushed with Isopar-L at a rate of 0.1-0.2 ml/min. After displacement of the crude oil, the periphery of specimen 1A was slightly uneven. The broken end was cut to an even surface, and the outermost layer (approximately 2 mm) of the other end was removed. A new height was measured. Under the assumption that the porosity, dry density and fluid

saturations were unchanged, a new mean diameter and thus a new bulk volume and pore volume were calculated, see Table 3.3.

Specimen	1A
Mean diameter [cm]	3.79
Mean height [cm]	3.62
Bulk volume [cm^3]	40.84
Pore volume [cm^3]	19.12

Table 3.3 *New parameters for specimen 1A.*

The wettability alteration seemed to have affected the structure of specimen 1A, and the calculation revealed a slightly lower mean diameter. However, it was chosen to use specimen 1A in the wettability and capillary pressure measurements to test a chalk specimen altered by this procedure. Further, the author was given the opportunity at Rogaland Research to carry out measurements on three chalk specimens, and no additional Hillerslev outcrop chalk specimen was available at the time.

3.3 Test Procedure

Measurement of wettability and capillary pressure was performed on the three Hillerslev outcrop chalk specimens. This was done by utilizing Amott cups and an automated Beckman centrifuge. The modified USBM method was used to obtain both the Amott-Harvey and the USBM wettability indices, and based on the measurements, water-oil capillary pressure curves were established for the three specimens. The modified USBM test procedure consists of the 5 steps listed in Table 3.4.

Step 1	Establish S_{wir} (specimens 1 and 2)
Step 2	Submerge the specimens in water and record the production of oil
Step 3	Centrifuge the specimens in water and record the production of oil
Step 4	Submerge the specimens in oil and record the production of water
Step 4	Centrifuge the specimens in oil and record the production of water

Table 3.4 *The test procedure for the wettability and capillary pressure measurements.*

Instead of establishing an irreducible water saturation S_{wir} by use of the centrifuge (step 1), an initial water saturation S_{wi} was established in specimens 1 and 2 (Section 3.2), and specimen 3 had no initial water.

After establishment of an initial water saturation S_{wi} (step 1), the specimens were immersed in water in Amott cups, and the volume of water imbibing spontaneously was measured as the volume of oil displaced (step 2). Then the specimens were centrifuged to force water into the specimens, and the average saturation of the specimens was determined from the volume of expelled oil at each incremental capillary pressure. After

centrifuging, the specimens were left at (or close to) the residual oil saturation S_{orw} (step 3). Then the specimens were immersed in oil, and the volume of oil imbibing spontaneously was measured as the volume of water displaced (step 4). Finally, the specimens were centrifuged to force oil into the specimens, and the average saturation of the specimens was determined from the volume of expelled water at each incremental capillary pressure (step 5). After centrifuging in oil, the specimens were supposed to be left at the irreducible water saturation S_{wir}, but due to centrifuge speed limitations, the water saturation after centrifuging S_w is assumed higher than S_{wir}. However, S_w was lower than S_{wi} for specimens 1 and 2.

Amott Cups

The specimens were placed in Amott cups, see Figure 2.3. A spiral made with cobber wire was placed under the specimens so that the specimens were not standing directly on the bottom, i.e. there was space under the specimens for fluid to be displaced. The amount of displaced volume was read on the calibration lines at the top of the Amott cup. The use of shrink fix sleeves delays both the imbibition and the drainage due to that these processes only take place at the end-faces of the specimens. The fluid was displaced as drops that were formed at the top and bottom ends of the specimens, and released or pushed free by use of a cobber wire.

Beckman Centrifuge

The capillary pressure measurements were performed at Rogaland Research in a Beckman L8-55M/P Ultra centrifuge using a rotor with standard or inverted buckets (Pub 1983). Three 1.5" diameter cylindrical specimens can be centrifuged simultaneously in the Beckman centrifuge. The centrifuge is automated so that there is automatic reading of produced volumes, evaluation of equilibrium, and change of speed.

This centrifuge is equipped with a strobe light assembly in the rotor chamber door. The strobe flashes once during each revolution of the rotor, so measurement of extracted volume can be made without stopping the centrifuge. The strobe can be adjusted to shine through a slit in any one of the rotor buckets. The extracted fluid is collected in a tube. A camera reads the produced fluid volume and a stroboscope light ensures that the camera obtains stable recordings in the rotation cup.

In the centrifuge, multi-step tests were performed, i.e. the angular velocity was increased in steps. The produced volumes at each step were read every 1-2 seconds initially, but as the production slowed down, the readings were every 5 minutes. At each step, the centrifuge was spun until hydrostatic equilibrium was reached. In the tests, equilibrium was defined as the point at each step for each specimen where the fluid production was ≤ 0.03 cm^3 over a 5 minutes period. However, the data processing revealed that the hydrostatic equilibrium may have been defined at too high a fluid production level, as the production curves were not constant in every step. A small production of 0.03 cm^3 or less went on for a long period of time in some of the specimens at some of the steps. These steps should have been allowed to carry on for a longer period of time. The centrifuge tests were performed at 40°C to ensure that there was no problem with wax in specimen 1A.

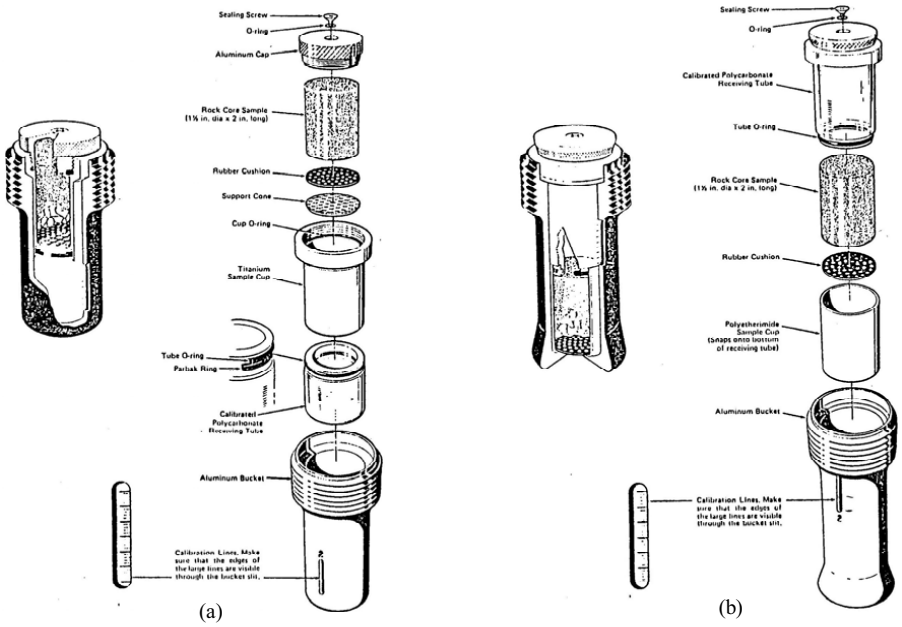

Figure 3.4 *Mounting of specimens in (a) standard buckets and (b) inverted buckets (Pub 1983).*

The specimens were mounted in the centrifuge cups, and an amount of the displacing fluid was poured into the cups. A separating disk was put into each cup to make the water and oil separation visible. As indicated in Figure 3.4, the centrifuge cups are placed inside the centrifuge buckets. The standard buckets are used for forced displacement of water by oil and the inverted buckets are used for forced displacement of oil by water.

A set-up for the centrifuge tests is shown in Figure 3.5. In the standard buckets, surrounding oil enters the specimen at the inlet face and displaces water at the outlet face. In the inverted buckets, surrounding water enters the specimen at the inlet face and displaces oil at the outlet face.

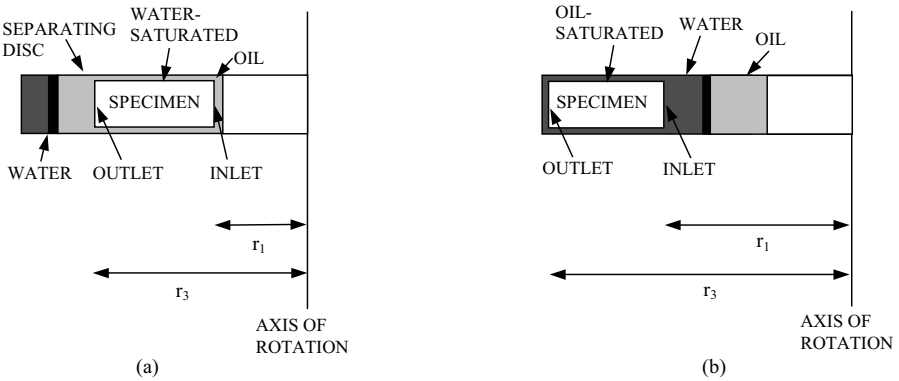

Figure 3.5 *(a) displacement of water by oil in a standard bucket (oil drive) and (b) displacement of oil by water in an inverted bucket (water drive).*

Chapter 4

Laboratory Test Results

The measured total spontaneous displaced volumes in the Amott cups and the measured total forced displaced volumes for the oil drive and the water drive in the centrifuge are included in Table 4.1. Only the total amounts of spontaneous displaced volumes are included. The production curves for the centrifuge tests, i.e. plots of the measured corresponding values of centrifuge speed and produced volumes are shown in Appendix F.

4.1 Wettability Determination

Both the Amott-Harvey and the USBM wettability indices can be determined from the modified USBM method. The capillary pressure vs. average saturation is plotted for specimens 1A, 2 and 3 to obtain the USBM wettability index, see Figure 4.1, 4.2 and 4.3, respectively. The capillary pressure is calculated using equation (2.7) for drainage and equation (2.11) for imbibition. The average water saturation is calculated as $\overline{S} = V_{water}/PV$ based on the measured production data, where V_{water} is the total volume of water present in the specimens and PV is the pore volume.

The small amount of spontaneous oil imbibition $\Delta S_{Oimb} = 0.12$ cm^3 for specimen 1A with a pore volume of 19.12 cm^3 and an initial water saturation of $S_{wi} = 12.8\%$ is indicated in Figure 4.1. The area A_1 under the oil-drive curve, and the area A_2 above the water-drive curve are indicated as well, both bounded by a capillary pressure of 70 kPa defined for the calculation of the USBM wettability index (Section 2.1). The USBM wettability index for specimen 1A is included in Table 4.1.

The spontaneous water imbibition $\Delta S_{Wimb} = 10.8$ cm^3 for specimen 2 with a pore volume of 26.55 cm^3 and an initial water saturation of $S_{wi} = 29.1\%$ is indicated in Figure 4.2.

The spontaneous water imbibition $\Delta S_{Wimb} = 19.3$ cm^3 for specimen 3 with a pore volume of 26.84 cm^3 and no initial water saturation is indicated in Figure 4.3.

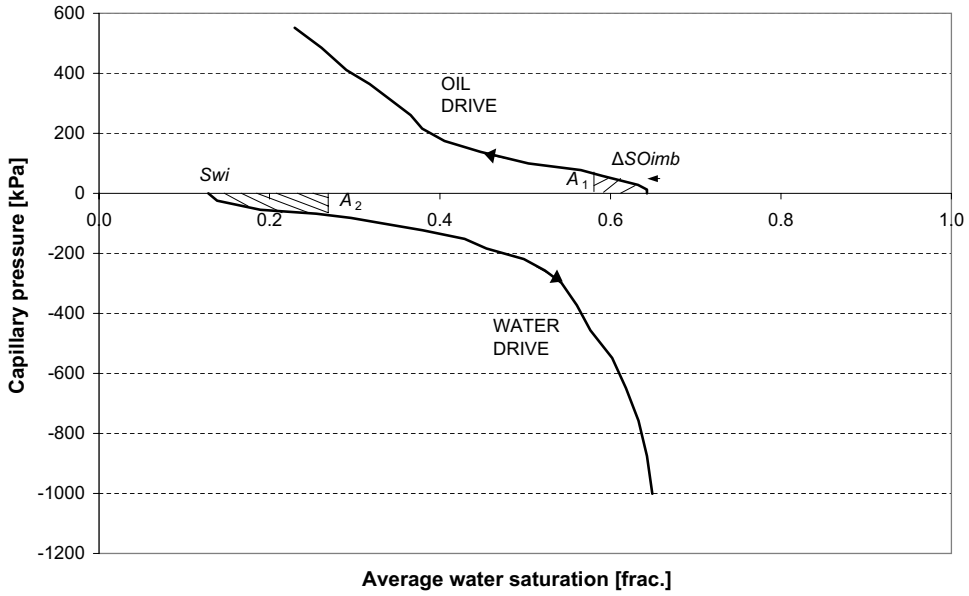

Figure 4.1 *Wettability measurement by the modified USBM method for specimen 1A.*

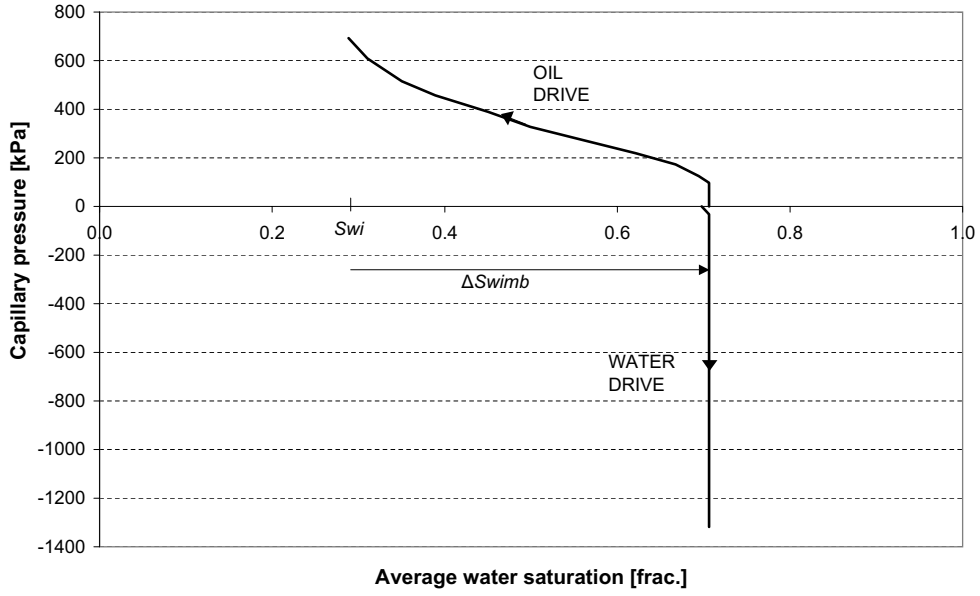

Figure 4.2 *Wettability measurement by the modified USBM method for specimen 2.*

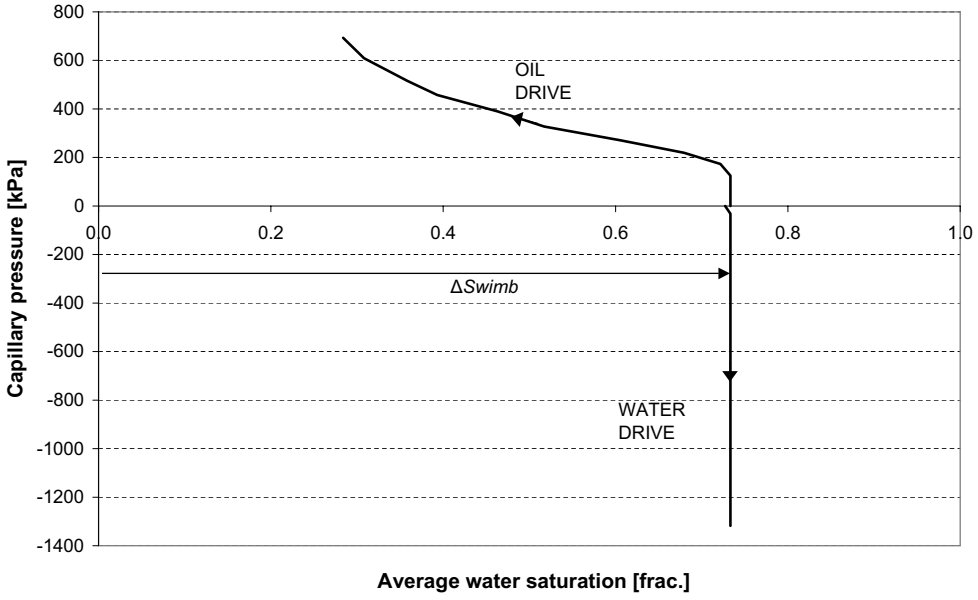

Figure 4.3 *Wettability measurement by the modified USBM method for specimen 3.*

It was not possible to calculate the USBM wettability index for specimens 2 and 3 since the minimum capillary pressure required to force oil into the specimen (oil drive) was higher than the upper boundary of 70 kPa defined for the USBM wettability index calculation, i.e. no area A_1 under the oil-drive curve can be found below the capillary pressure boundary of 70 kPa. The area A_2 above the water drive curve is zero since no water could be forced into specimens 2 and 3 after spontaneous water imbibition, see Table 4.1.

The small initial increase in S_w seen on the water drive curves for specimens 2 and 3 is calculated to be due to water displacing air in the matrix during the initial centrifuging, see Table 4.2.

The oil drive for all three specimens implies that the centrifuge test was ended at too low a capillary pressure. In other words, these capillary pressure curves were not fully completed due to centrifuge speed limitations even though the Beckman centrifuge was run to its maximum capacity of 8000 RPM. This means that the irreducible water saturation S_{wir} was not obtained in any of the specimens at the end of the test.

In the Amott test, the specimens are supposed to start at S_{wir} and end at S_{wir}. However, it is stated that the ratio of spontaneous to forced imbibition is used to reduce the influence of factors such as relative permeability, viscosity and the initial saturation of a specimen (Anderson 1986*a*). So although it is evaluated that S_{wir} was not obtained initially in any of the three specimens, the specimens are still used for the wettability measurements. Due to centrifuge speed limitations, the irreducible water saturation was also not obtained at the end of the measurements. However, the water drive for specimen 1A implies that the specimen is close to the residual oil saturation S_{orw} before the oil drive, and S_{orw} is obtained in specimens 2 and 3, since no more water could be forced

Specimen	1A	2	3
Establishment of S_{wi}			
S_{wi} (average)	12.8	29.1	-
Amott/USBM wettability test			
Amott cup step 2, oil production [cm^3]	0.0	10.8	19.3
S_w (average)	12.8	69.8	71.9
Centrifuge step 3, oil production [cm^3]	9.2	0.0	0.0
S_w (average)	63.9	70.6	73.3
Amott cup step 4, water production [cm^3]	0.12	0.0	0.0
S_w (average)	63.2	70.6	73.3
Centrifuge step 5, water production [cm^3]	7.80	11.09	12.06
S_w (average)	22.4	28.8	28.4
Amott/USBM wettability index			
$WWI = 2/(2+3)$	0	1	1
$OWI = 4/(4+5)$	0.02	0	0
Amott-Harvey $WI = WWI - OWI$	-0.02	1	1
USBM WI	-0.77	-	-

Table 4.1 *Capillary pressure measurements and wettability index determination.*

into the specimens after spontaneous water imbibition. The fact that S_{wir} was neither obtained initially nor at the end of the measurements have no influence on the Amott-Harvey wettability index for specimens 1A, 2 and 3 nor on the USBM wettability index for specimens 2 and 3. A lower S_{wi} in specimen 1A may have resulted in a larger area A_2 and thus a higher USBM wettability index, i.e. more oil-wet, since no water imbibed spontaneously.

It is obvious from the Amott cup displacement results that a wettability alteration of specimen 1A is obtained. For specimen 1A, the Amott-Harvey wettability index is calculated to -0.02, i.e. slightly oil-wet (near neutral). The produced amount of water in the Amott cup $\Delta S_{Oimb} = 0.12$ cm^3 equals less than 1% of the pore volume of specimen 1A, and this could be a result of exchange of fluids on the surface implying no spontaneous oil imbibition, and thus a neutral-wet state. However, it is evaluated that the small amount of oil imbibed. The fact that a part of one end of the specimen broke off eliminates the risk of outermost effects at that end, and 2 mm was removed at the other end.

The USBM wettability index for specimen 1A is calculated to -0.77. The USBM wettability index supports specimen 1A being oil-wet. Specimen 1A is not considered fractional-wet (at least not at the ends where the displacement takes place) as water did not imbibe spontaneously whereas a small amount of oil imbibed spontaneously. Although the USBM wettability index indicates a moderately oil-wet state, the fact that only little spontaneous oil imbibition occurred implies that the specimen is less than moderately oil-wet.

Based on these considerations, it is evaluated that the wetting state of specimen 1A is neutral to slightly oil-wet. It is thus evaluated that the USBM wettability index over-

Specimen	1A			2			3		
Average saturation	$\overline{S}_w$ [%]	$\overline{S}_o$ [%]	$\overline{S}_a$ [%]	$\overline{S}_w$ [%]	$\overline{S}_o$ [%]	$\overline{S}_a$ [%]	$\overline{S}_w$ [%]	$\overline{S}_o$ [%]	$\overline{S}_a$ [%]
Initial	12.8	82.3	4.9	29.1	69.8	1.1	0.0	97.7	2.3
Amott (water)	12.8	82.3	4.9	69.8	29.1	1.1	71.9	25.9	2.3
Centrifuge (water)	63.9	34.1	2.0	70.6	29.1	0.3	73.3	25.9	0.8
Amott (oil)	63.2	34.8	2.0	70.6	29.1	0.3	73.3	25.9	0.8
Centrifuge (water)	22.4	75.6	2.0	28.8	70.9	0.3	28.4	70.8	0.8

Table 4.2 *Average fluid saturation data throughout the test for specimens 1A, 2 and 3.*

estimates the wettability towards oil-wet for the wettability altered specimen, i.e. there is a problem using the USBM method for the wettability altered Hillerslev outcrop chalk specimen.

Hillerslev outcrop chalk and hereby specimens 2 and 3 were assumed water-wet prior to testing, but the wettability measurement can be used to determine the degree of water-wetness. For specimens 2 and 3, water imbibed rapidly, and approximately 88% of the spontaneous imbibition was completed within an hour. After spontaneous imbibition, the specimens were at the residual oil saturation S_{orw} as no water could be forced into the specimens by use of the centrifuge. This indicates, that the specimens are strongly water-wet. This is supported by the fact that the Amott-Harvey wettability index was calculated to 1.

The overestimation of the USBM wettability index for specimen 1A, and the fact that the USBM wettability index could not be obtained for the water-wet specimens 2 and 3 does not imply problems using the centrifuge for capillary pressure measurements. However, it does imply that the USBM method for obtaining the USBM wettability index cannot be used for Hillerslev outcrop chalk. To the authors knowledge, the USBM method was developed for sandstone and not chalk.

The average saturations obtained at each of the 5 steps in the combined Amott-Harvey and USBM test for all three specimens are included in Table 4.2. All saturation calculations are based on a volume balance except for the initial saturations, which are based on weights. In addition to the volume balance, weighing of the specimens has been performed after each step as check. The change in average air saturation is calculated to be due to water replacing air during the initial centrifuging of the specimens.

A comparison of the saturations for specimens 2 and 3 shows that for (these) strongly water-wet specimens, the water imbibition potential is equal, i.e. the average water saturation after spontaneous (and forced) water imbibition is approximately the same for the two specimens in spite of the difference in initial water saturation. Further, after test the specimens reach approximately the same final average water saturation.

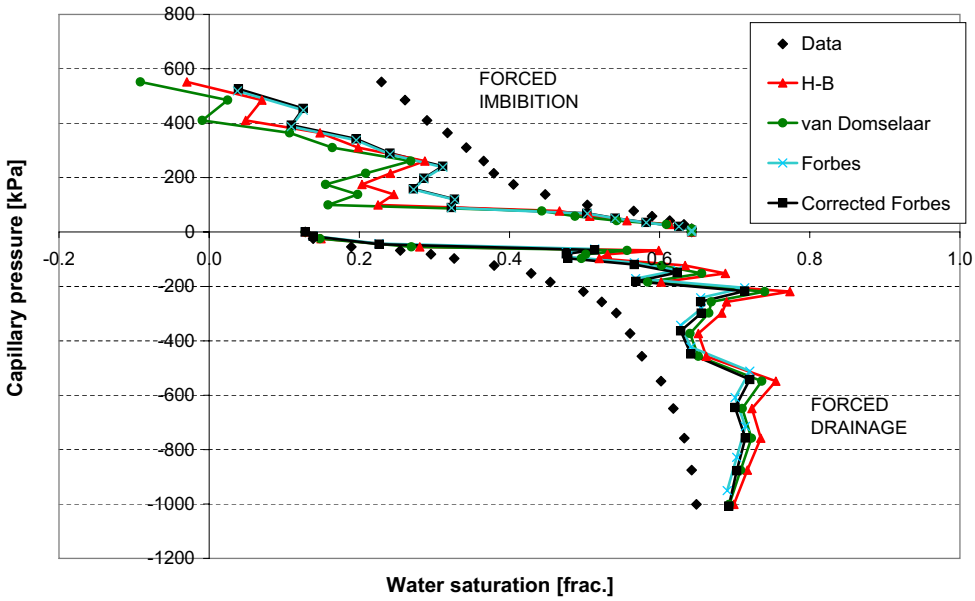

Figure 4.4 *Water-oil capillary pressure curves for specimen 1A for all data. The end-face saturations are calculated based on the Hassler-Brunner, the van Domselaar and the Forbes solutions. The corrected capillary pressure curves obtained by the Forbes method are included. The corresponding capillary pressure and average saturation are included (referred to as data).*

4.2 Capillary Pressure Curves

Since the wettability of the specimens has now been determined, the capillary pressure curves can be established from the centrifuge data obtained during the modified USBM test although to capillary pressures above 70 kPa. During the modified USBM centrifuge method, the centrifugal capillary pressures are calculated for all three specimens using equation (2.7) for drainage and equation (2.11) for imbibition.

The capillary pressure curves are based on the saturation at the end-face of the specimens, which is calculated from the average saturation. The end-face saturation is calculated on basis of the Hassler and Brunner solution (Hassler & Brunner 1945) equation (2.14), the van Domselaar solution (Forbes 1994) equation (2.15), and also the Forbes solution (Forbes 1994) equation (2.16) for drainage and equation (2.21) for imbibition. These end-face saturation solutions are uncorrected, i.e. there are not accounted for radial and gravity effects, and for the Hassler and Brunner solution there is not accounted for centrifugal effect either. The corresponding values of capillary pressure and end-face saturation obtained by the three different methods are plotted for the three specimens in Figure 4.4, 4.5 and 4.6. Only corresponding values of centrifugal capillary pressure and end-face saturation, i.e. only forced imbibition and forced drainage are included. The corresponding values of capillary pressure and average saturation are plotted as well (referred to as data). Further, the capillary pressure curves obtained by the Forbes method are corrected for radial and gravity effects, and the corrected capillary pressure curves are also included.

The capillary pressure curves for specimen 1A are plotted under the assumption that

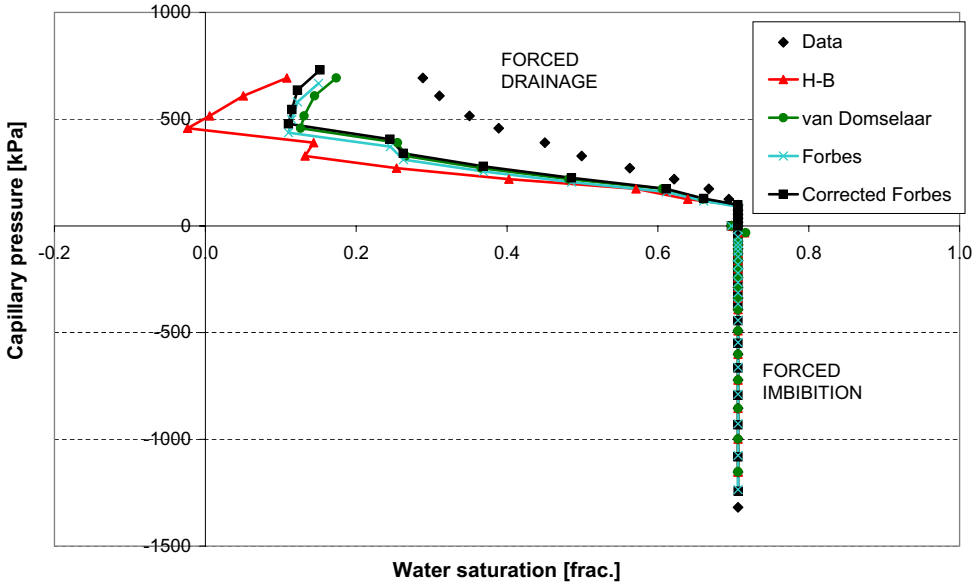

Figure 4.5 *Water-oil capillary pressure curves for specimen 2 for all data. The end-face saturations are calculated based on the Hassler-Brunner, the van Domselaar and the Forbes solutions. The corrected capillary pressure curves obtained by the Forbes method are included. The corresponding capillary pressure and average saturation are included (referred to as data).*

the specimen is neutral to slightly oil-wet. However, the capillary pressure is plotted as a function of the water saturation, i.e. the nonwetting phase saturation. The calculated capillary pressure curves consist of oscillating points. The main reason for this is that the production for some of the centrifuge steps was not constant at the defined hydrostatic equilibrium. The hydrostatic equilibrium may thus have been defined at too high a fluid production level, i.e. these steps were ended too soon.

For specimen 1A, $r_1/r_3 = 0.6$ for imbibition implies that the capillary pressure curves for the Hassler-Brunner method and the van Domselaar method ($r_1/r_3 \geq 0.7$) may not be accurate enough. For drainage, $r_1/r_3 = 0.8$ and the methods may be accurate enough.

The capillary pressure curves for specimens 2 and 3 are established knowing the specimens are strongly water-wet. The drainage part of the capillary pressure curves for both specimens 2 and 3 consists of oscillating points The main reason for this is that the production for some of the centrifuge steps was not constant at the defined hydrostatic equilibrium. For both specimens, the forced imbibition curves are straight lines as no water could be forced into the specimens after spontaneous imbibition of water.

For specimens 2 and 3, $r_1/r_3 = 0.7$ for imbibition implies that the capillary pressure curves obtained by the Hassler-Brunner method and the van Domselaar methods may be accurate enough, but $r_1/r_3 = 0.5$ for drainage implies that the methods may not be accurate enough.

The capillary pressure curves obtained by the three different methods for the three specimens all consist of oscillating points, and have similar trends, although the solution proposed by Forbes (Forbes 1994) was reported to allow for conversion of sparse and noisy experimental data without smoothing, fitting, averaging, or forcing data to a given form.

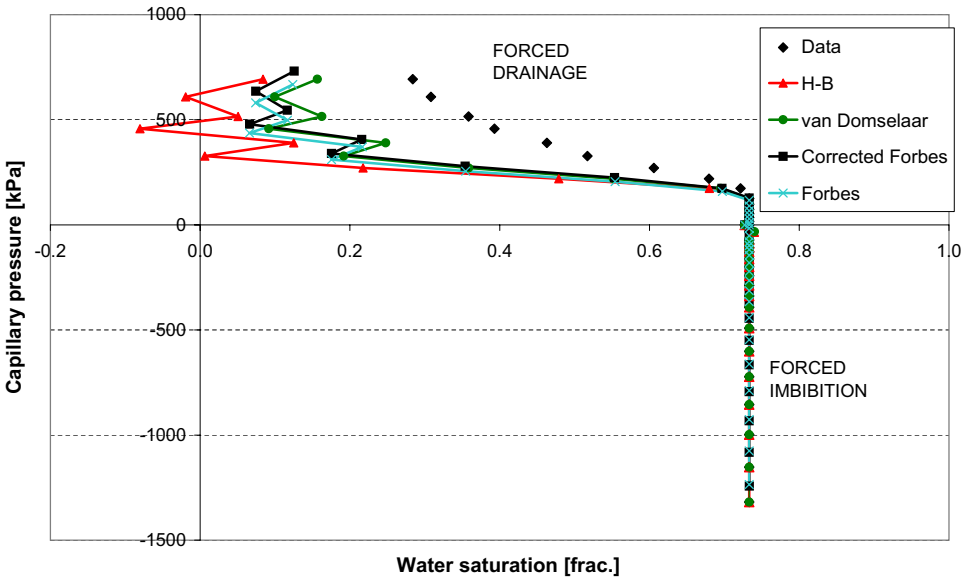

Figure 4.6 *Water-oil capillary pressure curves for specimen 3 for all data. The end-face saturations are calculated based on the Hassler-Brunner, the van Domselaar and the Forbes solutions. The corrected capillary pressure curves obtained by the Forbes method are included. The corresponding capillary pressure and average saturation are included (referred to as data).*

However, due to the problems encountered with accuracy for the Hassler-Brunner method and the van Domselaar method, the capillary pressure curves obtained by the Forbes method are used for this chalk. Further, Forbes believes this method to produce capillary pressure curves corresponding more closely to the centrifuge data than curves obtained from most other methods. Finally, the Forbes method include constraints. As can be seen from Figure 4.4, 4.5 and 4.6, there is only a small difference between the uncorrected and the corrected Forbes capillary pressure curves for Hillerslev outcrop chalk. However, it is advised (Forbes 1997) always to include the corrections, i.e. account for the radial and gravity effects in order to obtain the most accurate capillary pressure curves

The capillary pressure curves obtained by the corrected Forbes method are reduced by use of the constraints given by Forbes (Section 2.1). The reduced, corrected capillary pressure curves (final capillary pressure curves) are given in Figure 4.7, 4.8 and 4.9 for specimens 1A, 2 and 3, respectively.

The minimum capillary pressure required to force water into specimen 1A was between 0 kPa and 26 kPa, and the minimum capillary pressure required to force oil into the specimen was between 13 kPa and 28 kPa. From the form of the capillary pressure curves, it is evaluated that the obtained end-face residual oil saturation $S_{orw} = 0.34$ is close to the truth whereas S_{wir} is considered to be lower than the obtained end-face water saturation $S_w = 0.03$ due to the centrifuge limitations.

The minimum capillary pressure required to force oil into specimen 2 is between 107 kPa and 137 kPa. Since no water could be forced into specimen 2 after spontaneous imbibition, it is evaluated that the obtained end-face residual oil saturation $S_{orw} = 0.29$ is reliable. The irreducible water saturation S_{wir} is considered to be lower than the obtained

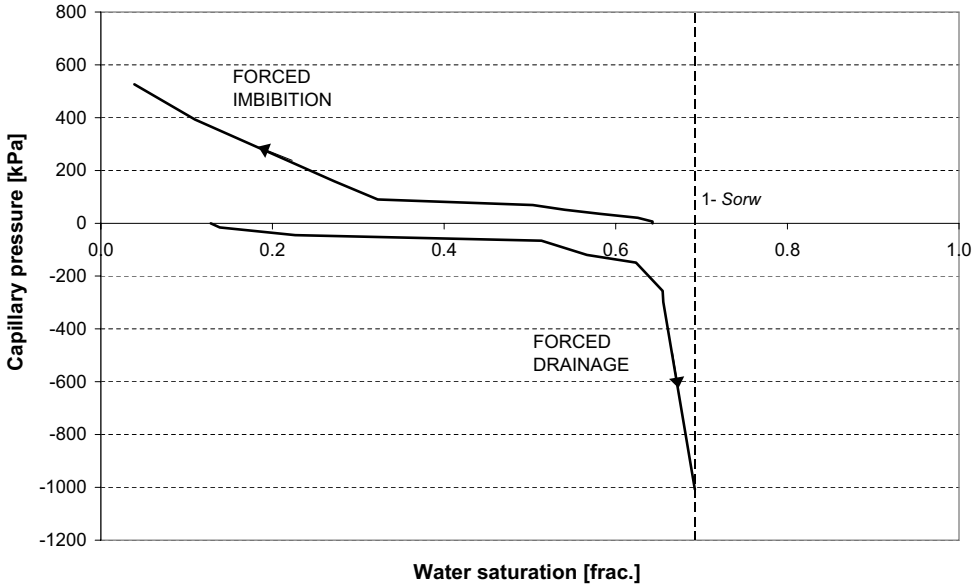

Figure 4.7 *Final water-oil capillary pressure curves for specimen 1A.*

end-face water saturation $S_w = 0.14$ due to centrifuge limitations.

The minimum capillary pressure required to force oil into specimen 3 is between 137 kPa and 190 kPa. Since no water could be forced into specimen 3 after spontaneous imbibition, it is evaluated that the obtained end-face residual oil saturation $S_{orw} = 0.27$ is reliable. Again, S_{wir} is considered to be lower than the obtained end-face water saturation $S_w = 0.09$ due to centrifuge limitations.

There were no visible fractures before the capillary pressure measurement, but distinct fractures were induced in specimens 1A and 3 during the centrifuging in water. Further, less distinct fractures may have been induced in specimen 2. This changes the fluid flow properties such as permeability of the chalk specimens, and may explain the slight difference in the capillary pressure curves for specimens 2 and 3. This also means that the capillary pressure curves were obtained on slightly fractured specimens.

In centrifuge measurements, sources of error consist of data acquisition and not waiting long enough to obtain a good estimate of equilibrium average saturation at each centrifuge step. At some of the centrifuge steps, hydrostatic equilibrium was defined at too high a production level resulting in to poor data for the capillary pressure curves. Further, interpretation of centrifuge measurement for capillary pressure curves requires a number of assumptions regarding core homogeneity and boundary conditions ($P_c = 0$).

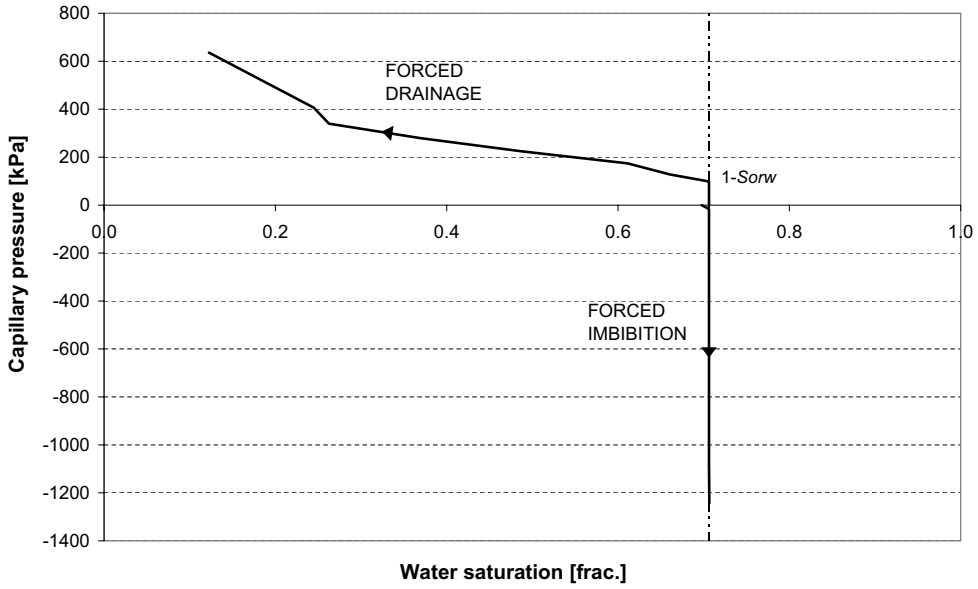

Figure 4.8 *Final water-oil capillary pressure curves for specimen 2.*

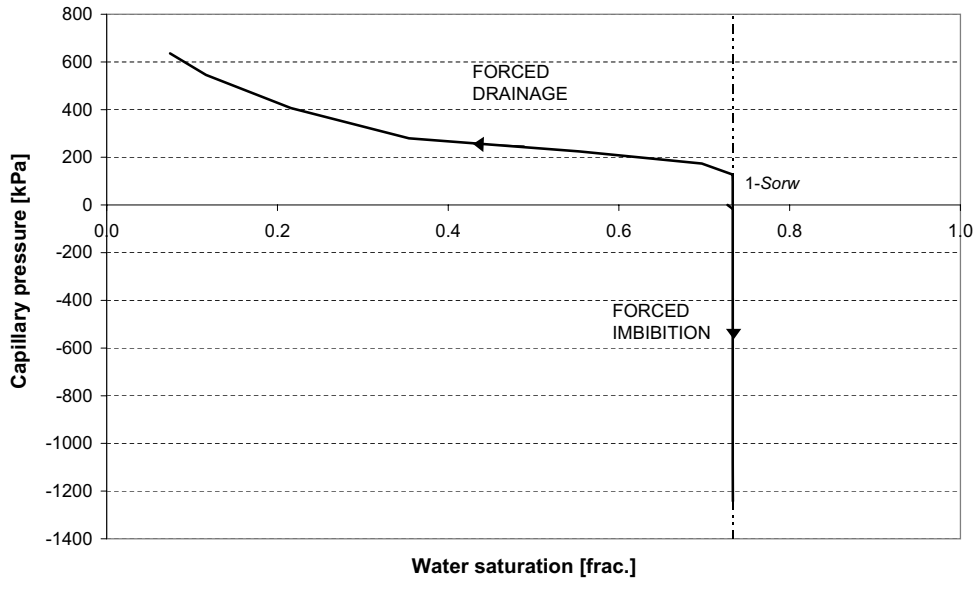

Figure 4.9 *Final water-oil capillary pressure curves for specimen 3.*

The form of the capillary pressure curves for all three specimens implies that the centrifuge test was ended at too low a capillary pressure. In other words, these capillary pressure curves were not fully completed due to centrifuge speed limitations even though the Beckman centrifuge was run to its maximum capacity of 8000 RPM. This means that the irreducible water saturation S_{wir} was not obtained in any of the specimens at the end of the test.

The form of the capillary pressure curves is affected by the fact that the production at some of the centrifuge steps was not constant at the defined hydrostatic equilibrium. Further, the capillary pressure curves were obtained on slightly fractured specimens. Evaluating this together with the fact that the capillary pressure curves were not fully completed, the obtained capillary pressure curves are not very representative for the three specimens. However, a good estimate of the residual oil saturation S_{orw} is obtained, especially for the strongly water-wet specimens.

The high capillary pressure of chalk makes it difficult to obtain the necessary high rotational speed to establish capillary pressure curves for chalk in the centrifuge. To be able to establish capillary pressure curves for Hillerslev outcrop chalk, a centrifuge of larger capacity must be used. At the same time, the low mechanical strength of chalk implies that the centrifuge speed must be limited to ensure that fractures are not induced in the chalk. Based on this it is evaluated that capillary pressure curves for Hillerslev outcrop chalk cannot be obtained in the centrifuge.

The minimum capillary pressure required to force oil into the strongly water-wet Hillerslev outcrop chalk is so high that the USBM wettability index cannot be obtained. Further, consistent Amott-Harvey and USMB wettability indices cannot be obtained for the wettability altered Hillerslev outcrop chalk specimen using the centrifuge.

This is consistent with the fact that conventional methods used for determination of saturation functions are mainly developed for rocks of lower capillary pressure and higher mechanical strength than chalk. This means that these methods may not apply for chalk. Bech (Bech et al. 2000) states that especially the centrifuge method is unsuitable due to the low mechanical strength of chalk, as well as the difficulty of obtaining the necessary high rotational speed.

Chapter 5

Conclusions

Hillerslev outcrop chalk is described as strongly water-wet. Spontaneous imbibition of water into the strongly water-wet specimens 2 and 3 was in the range of 71-73%. The water imbibed rapidly, and approximately 88% of the spontaneous imbibition was completed within an hour. No water could be forced into specimens 2 and 3 after spontaneous imbibition.

There is no clear evidence of an effect of different initial water saturations S_{wi} on the final average saturation after spontaneous (and forced) water imbibition in strongly water-wet Hillerslev outcrop chalk.

It is concluded that Hillerslev outcrop chalk can be altered towards a homogeneous neutral to slightly oil-wet state using crude oil added with 1 weight% Dodekane acid. However, the alteration affected the chalk as well.

Based on the form of the capillary pressure curves, the fact that the capillary pressure curves were obtained on slightly fractured specimens, and the fact that the capillary pressure curves were not fully completed, it is evaluated that the obtained capillary pressure curves are not fully representative for the three specimens. However, a good estimation of the residual oil saturation S_{orw} is obtained, especially for the strongly water-wet specimens.

Based on the fact that the capillary pressure curves were not fully completed due to centrifuge limitations, and that fractures were induced in the specimens even at these lower centrifuge speeds, it is evaluated that capillary pressure curves for Hillerslev outcrop chalk cannot be obtained in the centrifuge.

The minimum capillary pressure required to force oil into the strongly water-wet Hillerslev outcrop chalk is so high that the USBM wettability index cannot be obtained. Further, consistent Amott-Harvey and USMB wettability indices was not obtained for the wettability altered Hillerslev outcrop chalk specimen using the centrifuge.

Bibliography

Ali, N. & Alcock, T. (1992), 'Valhall field, norway - the first ten years', *Amoco Norway Oil Co. Norway* .

Andersen, M. (1995), *Petroleum Research in North Sea Chalk. Joint Chalk Research Phase IV*, Stavanger Research Center.

Anderson, W. (1986*a*), 'Wettability literature survey - part 2: Wettability measurement', *SPE* .

Anderson, W. (1986*b*), 'Wettability literature survey - part 4: Effects of wettability on capillary pressure', *SPE* .

Bech, N., Olsen, D. & Nielsen, C. (2000), 'Determination of oil/water saturation functions of chalk core plugs from two-phase flow experiments', *SPE Reservoir Eval. and Eng.* **3(1)**.

Christensen, H. (2003), Displacement and deformation processes in fractured reservoir chalk, Efp-2000, GEO.

Christoffersen, K. (1995), 'Gas/oil capillary pressure of chalk at elevated pressures', *SPE Formation Evaluation* .

Eltvik, P., Skoglunn, T. & Skinnarland, O. (1990), 'Valhall waterflood pilot - a study of water injection in a fractured reservoir', *Proceedings at the Third North Sea Chalk Symposium, Copenhagen, 1990* .

Forbes, P. (1994), 'Simple and accurate methods for converting centrifuge data into drainage and imbibition capillary pressure curves', *The Log Analyst* .

Forbes, P. (1997), 'Quantitative evaluation and correction of gravity effects on centrifuge capillary pressure curves', *Society of Core Analysts* (SCA-9734).

Hassler, G. & Brunner, E. (1945), 'Measurements of capillary pressure in small core samples', *Transactions AIME* **160**, 114–123.

Jakobsen, F. (2001), Fractures and rock mechanics. phase 2. description of natural and test induced fractures in chalk, EFP-98 Report 2001/18, GEUS.

Krogsbøll, A., Jakobsen, F. & Madsen, L. (1997), Fractures and rock mechanics. phase 1. geology report, EFP-96 Report 1997/63, GEUS.

Man, H. & Jing, X. (2000), 'Network modelling of mixed-wettability on electrical resistivity. capillary pressure and wettability indices', *6th International Symposium on Evaluation of Reservoir Wettability and Its Effect on Oil Recovery. Socorro. New Mexico. USA* .

Morrow, N. (1990), 'Wettability and its effect on oil recovery', *JPT* .

Nørgaard, J., Olsen, D., Reffstrup, J. & Springer, N. (1999), 'Capillary pressure curves for low permeability chalk obtained by nuclear magnetic resonance imaging of core saturation profiles', *SPE Reservoir Evaluation and Engineering 2,2* pp. 141–148.

Pub (1983), *Beckman Instruments. Instructions for using the Type PIR 16.5 Rotor in the Beckman Model L5-50P Ultracentrifuge.*

Ruth, D. & Chen, Z. (1995), 'Measurement and interpretation of centrifuge capillary pressure curves - the sca survey data', *The Log Analyst* .

Skauge, A. & Poulsen, S. (2000), 'Rate effects on centrifuge drainage relative permeability', *Soc. Petr. Eng.* (SPE 63145).

Szabo, M. (1974), 'New methods for measuring imbibition capillary pressure and electrical resistivity curves by centrifuge', *Society of Petroleum Engineers Journal* pp. 243–252.

Verbruggen, M., Farmer, R. & Adams, S. (2000), 'State-of-the-art scal experiments and interpretation', *Proceedings at New Zealand Petroleum Conference, 19-22 March 2000* .

Appendix A

Discrete Solutions for End-Face Saturation

Discrete solutions to the fundamental saturation equation for converting average specimen saturation into end-face saturation.

Drainage

The solution to the fundamental saturation equation for drainage can be evaluated with high accuracy from discrete $\overline{S}$ data using a simple differencing scheme (Forbes 1994):

$$S_{i-1/2+B/4} \approx S_{\alpha\beta i-1/2+B/4} = \left(1 - \frac{B}{2}\right) S_{\alpha i-1/2} + \frac{B}{2} S_{\beta i} \tag{A.1}$$

$$B = 1 - \left(\frac{r_1}{r_3}\right)^2 \qquad 0 \leq B \leq 1 \tag{A.2}$$

$$\alpha = \frac{1 - \sqrt{1-B}}{1 + 2\sqrt{1-B}} = \frac{r_3 - r_1}{r_3 + 2r_1} \tag{A.3}$$

$$\beta = \frac{2}{\alpha} \tag{A.4}$$

$$S_{\alpha i-1/2} = \frac{\overline{S}_i - \left(\frac{P_{i-1}}{P_i}\right)^{1+\alpha} \overline{S}_{i-1}}{1 - \left(\frac{P_{i-1}}{P_i}\right)^{1+\alpha}} \tag{A.5}$$

$$S_{\beta i} = \left(\frac{P_{i-1}}{P_i}\right)^{1+\beta} S_{\beta i-1} + \frac{1 - \left(\frac{P_{i-1}}{P_i}\right)^{1+\beta}}{1 - \left(\frac{P_{i-1}}{P_i}\right)} \left(\overline{S}_i - \left(\frac{P_{i-1}}{P_i}\right) \overline{S}_{i-1}\right) \tag{A.6}$$

Using this scheme, solution S for step i is obtained directly from the values of $\overline{S}$ at steps i and i-1 and from the value of S at step i-1. No iteration, smoothing, fitting, numerical integration or specific numerical treatment are needed.

Imbibition

The solution to the fundamental saturation equation for imbibition can be evaluated with high accuracy from discrete $\overline{S}$ data using a simple differencing scheme (Forbes 1994):

$$S_{i-1/2} \approx S_{\alpha i-1/2} = \frac{\overline{S}_i - \left(\frac{P_{i-1}}{P_i}\right)^{1+\alpha} \overline{S}_{i-1}}{1 - \left(\frac{P_{i-1}}{P_i}\right)^{1+\alpha}} \tag{A.7}$$

$$B = 1 - \left(\frac{r_3}{r_1}\right)^2 \qquad B < 0 \tag{A.8}$$

$$\alpha = \frac{1 - \sqrt{1-B}}{1 + 2\sqrt{1-B}} = \frac{r_3 - r_1}{r_3 + 2r_1} \tag{A.9}$$

Using this scheme, solution S for step i is obtained directly from the values of $\overline{S}$ at steps i and i-1 and from the value of S at step i-1. No iteration, smoothing, fitting, numerical integration or specific numerical treatment are needed.

Appendix B

Gravity and Radial Effects on Capillary Pressure

When rotating, the fluids in the specimen are subjected to the centrifugal field, $1/2\rho\omega^2 r^2$, and to the gravity field, -ρgZ, where ρ is the fluid density, g is the gravitational acceleration, ω is the angular velocity and (r, Z) refer to the cylindrical coordinates. At hydrostatic equilibrium, the pressure is (Ruth & Chen 1995):

$$P = \frac{1}{2}\rho\omega^2 r^2 - \rho gZ + Const. \tag{B.1}$$

The capillary pressure is then given by:

$$P_c(r, Z, \omega) = -\frac{1}{2}\Delta\rho\omega^2 r^2 + \Delta\rho gZ + Cons. \tag{B.2}$$

The value of the constant "$Const.$" is obtained from the boundary condition hypothesis, i.e. that $P_c = 0$, where the inner fluid is flowing out of the specimen.

By definition, the average saturation of the specimen $\overline{S}$ is:

$$\overline{S} = \frac{1}{L\pi R^2}\int_{specimen} S_{r,Z,\omega}dv = \frac{1}{L\pi R^2}\int_{specimen} S(P_c(r, Z, \omega))rdrd\theta dZ \tag{B.3}$$

where L is the length of the core, R is the radius of the core, r the rotational radius, Z is the vertical coordinate and dv is the elementary volume.

Drainage

For a cylindrical specimen in a drainage experiment: $P_c = 0$ is located at the border of the circular outflow face of the specimen, the face furthest from the axis of rotation, for $Z = -R$, if $g/\omega^2 > R$ or, for $Z = -g/\omega^2$, if $g/\omega^2 < R$, leading to:

$$P_c(r, Z, \omega) = \frac{1}{2}\Delta\rho\omega^2(r_3^2 - r^2) + \Delta\rho gZ + \frac{1}{2}\Delta\rho\omega^2(n+1)R^2 \tag{B.4}$$

where $n = 2(g/\omega^2)/R - 1$ if $g/\omega^2 > R$, or $n = (g/\omega^2)^2/R^2$ if $g/\omega^2 < R$.

$P_c(r, Z, \omega)$ varies inside the specimen, and the above equation can be normalized and re-written as:

$$\overline{S}_{B,N,M} = \frac{1+\sqrt{1-B}}{2} \int_{x=0}^{x=1} \frac{dx}{\sqrt{1-Bx}} \int_{y=0}^{y=1} \frac{2}{\pi}\sqrt{\frac{y}{1-y}}dy \int_{z=0}^{z=1} \frac{1}{2} S(P_1(x+Ny+2NMz\sqrt{y}+Nn))dz \tag{B.5}$$

using the normalized parameters:

$$\begin{aligned} B &= 1-\left(\frac{r_1}{r_3}\right)^2 \\ N &= \frac{R^2}{r_3^2-r_1^2} \\ M &= \frac{g}{\omega^2 R} \\ P_1 &= \frac{1}{2}\Delta\rho\omega^2(r_3^2-r_1^2) \end{aligned}$$

and the normalized variables:

$$\begin{aligned} x &= \frac{1-(\frac{r}{r_3})^2(\cos\theta)^2}{B} \\ y &= 1-\frac{(\frac{r}{r_3})^2(\sin\theta)^2}{NB} \\ x &= Z/R/\sqrt{y} \end{aligned}$$

Imbibition

For a cylindrical specimen in an imbibition experiment: $P_c = 0$ is located on the top of the outflow face of the specimen, the face nearest from the axis of rotation, and:

$$P_c(r,Z,\omega) = \frac{1}{2}\Delta\rho\omega^2(r_1^2-r^2) + \Delta\rho gZ + \frac{1}{2}\Delta\rho\omega^2(n+1)R^2 \tag{B.6}$$

with $n = -2(g/\omega^2)/R - 1$.

$P_c(r,Z,\omega)$ varies inside the specimen, and the above equation can be normalized and re-written as:

$$\overline{S}_{B,N,M} = \frac{1+\sqrt{1-B}}{2} \int_{x=0}^{x=1} \frac{dx}{\sqrt{1-Bx}} \int_{y=0}^{y=1} \frac{2}{\pi}\sqrt{\frac{y}{1-y}}dy \int_{z=-1}^{z=1} \frac{1}{2} S(P_3(x+Ny+2NMz\sqrt{y}+Nn))dz \tag{B.7}$$

using the normalized parameters:

$$\begin{aligned} B &= 1-\left(\frac{r_3}{r_1}\right)^2 \\ N &= \frac{R^2}{r_1^2-r_3^2} \\ M &= -\frac{g}{\omega^2 R} \\ P_3 &= \frac{1}{2}\Delta\rho\omega^2(r_1^2-r_3^2) \end{aligned}$$

and the normalized variables:

$$\begin{aligned} x &= \frac{1-(\frac{r}{r_1})^2(\cos\theta)^2}{B} \\ y &= 1-\frac{(\frac{r}{r_1})^2(\sin\theta)^2}{NB} \\ x &= Z/R/\sqrt{y} \end{aligned}$$

Appendix C

Laboratory Journal

25/04/01	Two specimens (S1 & S2) were drilled from a chalk block. S1 & S2 were drilled with a ø42 drill cooled with water. S1 & S2 were placed in an oven at 105°C overnight for drying.
26/04/01	S1 & S2 were turned in a turning lathe to a diameter of 38 mm and then cut by an electric saw at both ends to a length of 50 mm. S1 & S2 were described, sketched and photographed.
27/04/01	S1 & S2 were placed in an oven at 105°C over the weekend for drying.
30/04/01	Mixing of formation water (brine) after Valhall field recipe. A shrink fix sleeve was put around each specimen. S1 & S2 were weighed, and placed in Exxon Triaxial core holders. Isopar-H was injected into the core holders via a pump to ensure a pressure around the cores (overburden pressure). This pressure was chosen to 20 bar. S1 & S2 were then saturated with brine by applying vacuum. The brine-saturated S1 & S2 were removed from the core holders and weighed. S1 & S2 were placed in the core holders with an overburden pressure of 20 bar.
01/05/01	Rate test with brine for determination of the absolute (brine) permeability for S1 & S2. Mean brine permeabilities of 2.9 mD and 2.6 mD for specimen 1 and 2, respectively.
09/05/01	Displacement of brine by Isopar-L to S_{wi} in S1 & S2 by use of a pump. First displacement of brine by Isopar-L until breakthrough and then displacement by Marcol (displacement of Isopar-L and brine). The high viscosity Marcol is used to obtain as low S_{wi} as possible.
14/05/01	One specimen (S3) was drilled from a chalk block. S3 was drilled with a ø42 drill cooled with water. S3 was placed in an oven at 105°C for drying.
15/05/01	S3 was turned in a turning lathe to a diameter of 38 mm and then cut by an electric saw at both ends to a length of 50 mm. S3 was described, sketched and photographed. S3 was placed in an oven at 105°C for drying.
18/05/01	A shrink fix sleeve was put on the specimen. S3 was weighed, and placed in Exxon Triaxial core holder. Isopar-H was injected into the core holder via a pump to ensure a 20 bar pressure around the core (overburden pressure). S3 was then saturated with Isopar-L by applying vacuum. The Isopar-L-saturated S3 was weighed, and placed in the core holder again with an overburden pressure of 20 bar.
19/05/01	Displacement of Marcol by Isopar-L in S1 & S2. Total production of brine S1: 21.95 cm^3 & S2: 18.53 cm^3.
21/05/01	Displacement of Isopar-L by Snorre oil added 1 weight% Dodekane acid in S1. Flushing with 100 ml in each direction. S1 was placed in a piston cell at 8 bar and 90°C for aging
25/06/01	Aging of S1 was ended. S2 & S3 were taken out of the core holders and placed in cups with

	Isopar-L. S1 was removed from the piston cell, and broke in one end. S1 was placed in core holder again with 20 bar overburden pressure. Snorre oil displaced by Isopar-L at 40°C in S1.
27/06/01	S1 removed from core holder after displacement by Isopar-L. S1 now slightly uneven and greyish S1 was cut by an electric saw at both ends to a length of 36.2 mm. S1 was cut in both ends to reduce capillary end effect. S1, S2 & S3 were placed in Amott cups with brine for spontaneous production of Isopar-L. Within 1.5 hour the imbibition was almost completed.
28/06/01	Spontaneous displacement completed. S1: no Isopar-L production, S2: 10.8 cm^3 & S3: 19.3 cm^3. S1, S2 & S3 were removed from the Amott cups and placed in inverted Beckman centrifuge buckets with brine for forced production of Isopar-L. Centrifuge test initiated.
15/07/01	Centrifuge test ended at maximum capacity of the centrifuge, i.e. 7700 RPM. S1: 9.20 cm^3, S2 & S3 no production of Isopar-L. S1, S2 & S3 were placed in Amott cups with Isopar-L for spontaneous production of brine.
-	Spontaneous displacement completed. S1: 0.12 cm^3, S2 & S3: no brine production. S1, S2 & S3 were removed from the Amott cups and placed in standard Beckman centrifuge buckets with Isopar-L for forced production of brine. Centrifuge test initiated.
12/09/01	Centrifuge test ended at maximum capacity of the centrifuge, i.e. 8000 RPM. S1: 7.80 cm^3, S2: 11.09 cm^3 & S3: 12.06 cm^3.

Table C.1: Laboratory journal for specimens 1, 2 and 3.

Appendix D

Description of Specimens 1, 2 and 3

Specimen 1

Specimen 1 is very light grey with areas of a darker grey colour (clay). Small inhomogenities were seen in the surface of the specimen due to the turning in a turning lathe. A rust-coloured area was seen. A small piece of flint was observed. A sketch of specimen 1 is seen in Figure D.1.

A mean diameter of $D = 3.81$ cm and a mean height of $H = 5.00$ cm was measured.

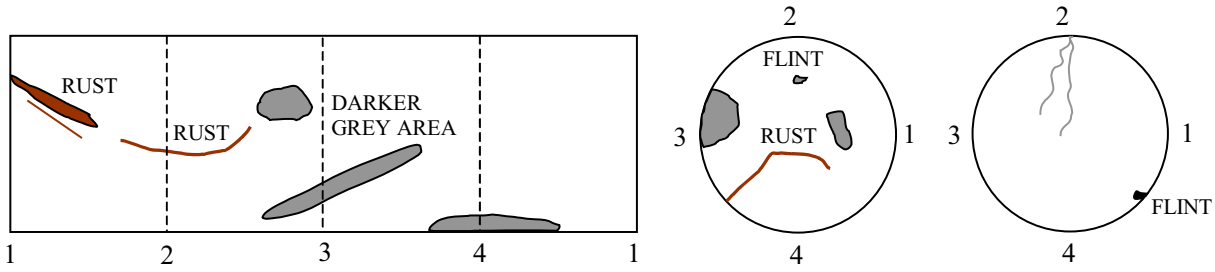

Figure D.1 *Sketch of specimen 1.*

The specimen broke in one end when removed from the cell after aging in Snorre oil added 1 weight% Dodekane acid ($C_{11}H_{23}COOH$). The specimen was cut in both ends partly to even the broken surface and partly to reduce capillary end effect in the unbroken end, where approximately 2 mm was cut off. The specimen is now referred to as specimen 1A. A new mean height was measured to $H = 3.62$ cm.

The displacement of Snorre oil with Isopar-L caused the periphery of the specimen to become uneven. Under the assumption that porosity, dry density and fluid saturations were unchanged, the mean diameter was calculated to $D = 3.79$ cm.

Specimen 2

Specimen 2 is very light grey with many areas of a darker grey colour (clay). Small inhomogenities were seen in the surface of the specimen due to the turning in a turning lathe. Flint was observed. A sketch of specimen 2 is seen in Figure D.2.

A mean diameter of $D = 3.80$ cm and a new mean height of $H = 5.00$ cm was measured.

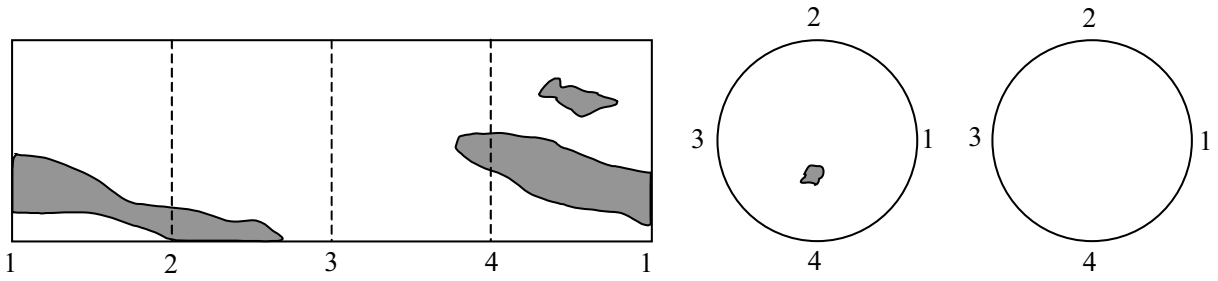

Figure D.2 *Sketch of specimen 2.*

Specimen 3

Specimen 3 is very light grey with few very small areas of a darker grey colour (clay). Small inhomogenities were seen in the surface of the specimen due to the turning in a turning lathe. A sketch of specimen 3 is seen in Figure D.3.

A mean diameter of $D = 3.81$ cm and a mean height of $H = 5.00$ cm was measured.

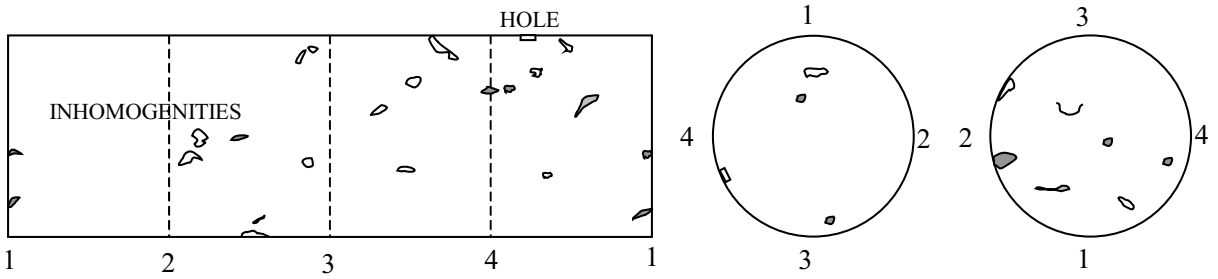

Figure D.3 *Sketch of specimen 3.*

Appendix E

Absolute Water Permeability for Specimens 1 and 2

Permeability is a measure of the ability of the porous medium to conduct one or more fluids. Provided that the porous medium is completely saturated with one fluid, the absolute, intrinsic permeability K [m^2] (1 D = $9.869 \cdot 10^{-13} m^2$) of the medium is determined as:

$$K = \frac{Q\mu L}{A\Delta P} \tag{E.1}$$

where Q [m^3/s] is the volumetric flow rate, μ [Pas] is the viscosity of the fluid, L [m] is the actual length of the specimen, A [m^2] is the cross sectional area of the specimen and ΔP [Pa] is the differential pressure over the specimen.

Corresponding values of flow and pressure difference were measured to determine the absolute water permeability of the fully water saturated specimens (specimens 1 and 2). The fluid used was synthetic Valhall formation water referred to here as water. The measurements were performed at a backpressure of 3 bar. The test set-up is shown in Figure 3.2.

Mean absolute water permeabilities for specimens 1 and 2 are 2.9 mD and 2.6 mD, respectively.

Q [$\cdot 10^{-6}\mathrm{m}^3/s$]	ΔP [kPa]	K [mD]
0.0017	26.20	2.83
0.0025	32.75	3.39
0.0033	51.50	2.88
0.0042	63.57	2.91
0.0050	74.88	2.97
0.0058	88.87	2.92
0.0050	76.26	2.91
0.0042	63.71	2.91
0.0033	51.50	2.88
0.0017	26.37	2.81
0.0013	19.79	2.81

Table E.1 *Absolute water permeability for specimen 1.*

Q [$\cdot 10^{-6}\mathrm{m}^3/s$]	ΔP [kPa]	K [mD]
0.0050	82.19	2.72
0.0042	69.15	2.69
0.0033	55.50	2.68
0.0025	41.85	2.67
0.0017	29.03	2.56
0.0008	15.48	2.40

Table E.2 *Absolute water permeability for specimen 2.*

Appendix F

Production Curves for the Centrifuge Tests

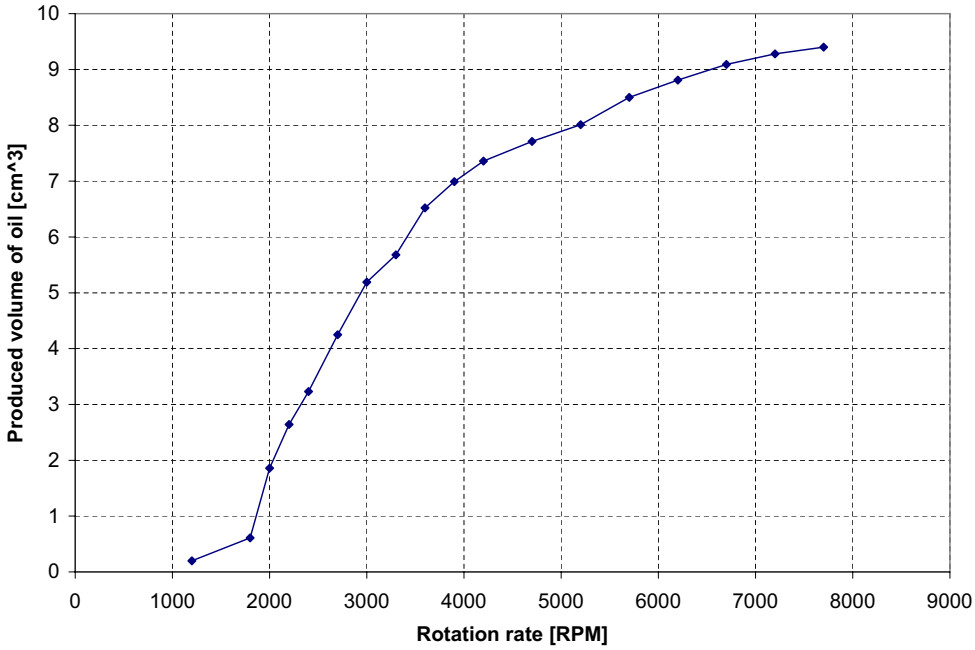

Figure F.1 *Production of oil vs. rotation rate for specimen 1A. Total oil production of 9.20 cm^3 from the pore volume of 19.12 cm^3.*

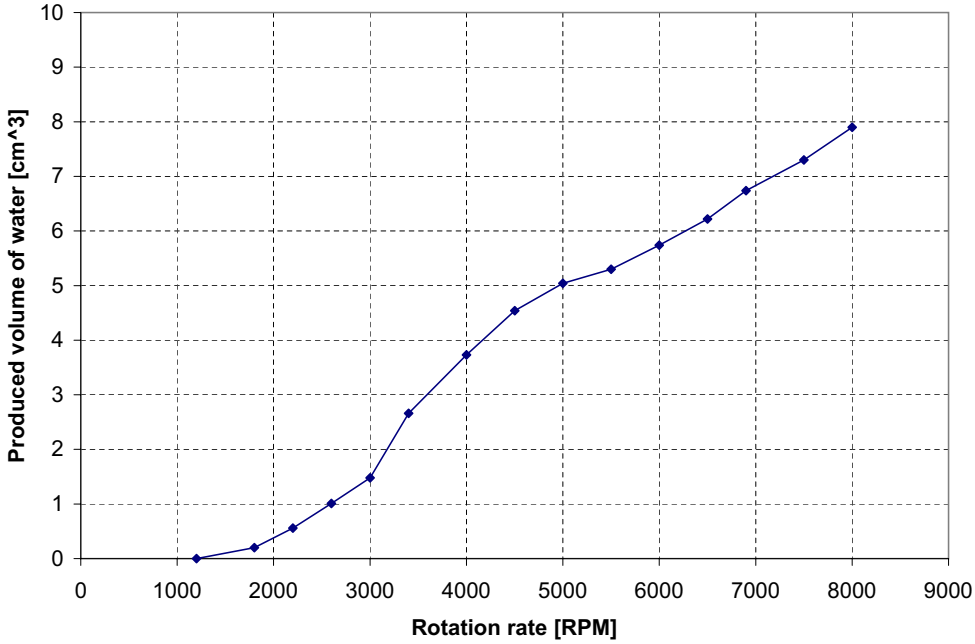

Figure F.2 *Production of water vs. rotation rate for specimen 1A. Total water production of 7.80 cm^3 from the pore volume of 19.12 cm^3.*

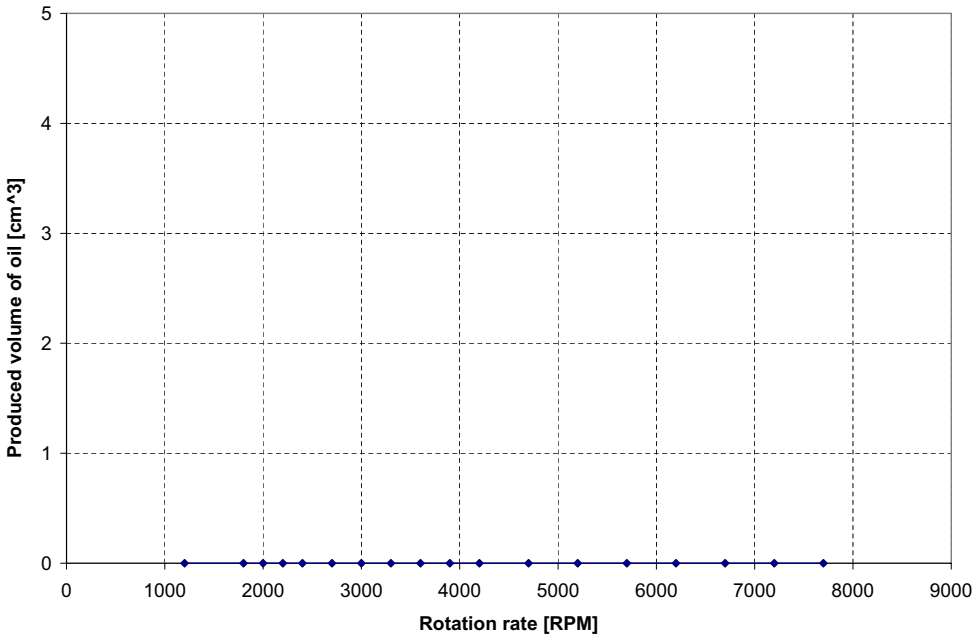

Figure F.3 *Production of oil vs. rotation rate for specimen 2. No oil production.*

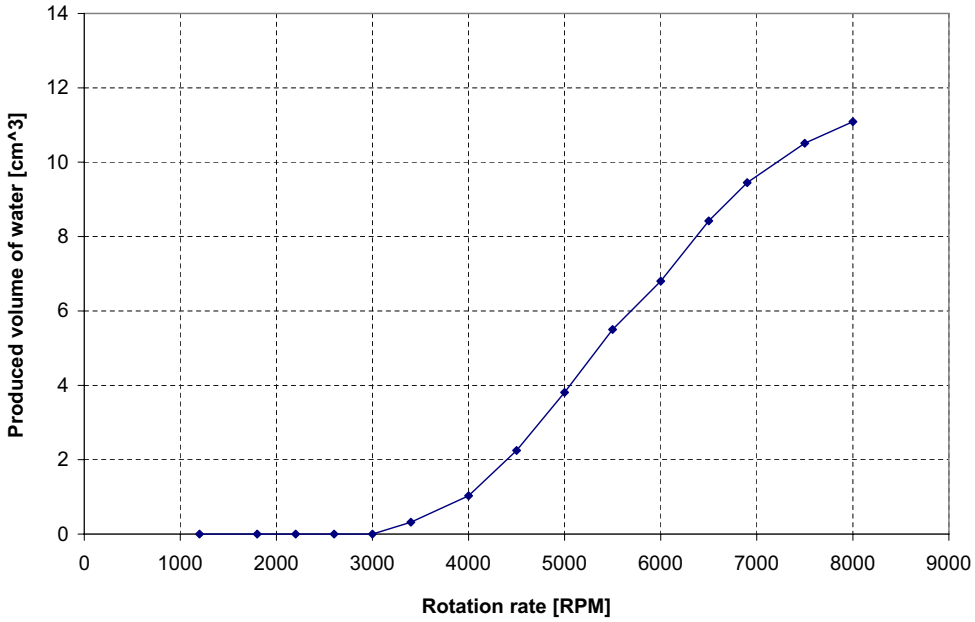

Figure F.4 *Production of water vs. rotation rate for specimen 2. Total water production of 11.09 cm^3 from the pore volume of 26.55 cm^3.*

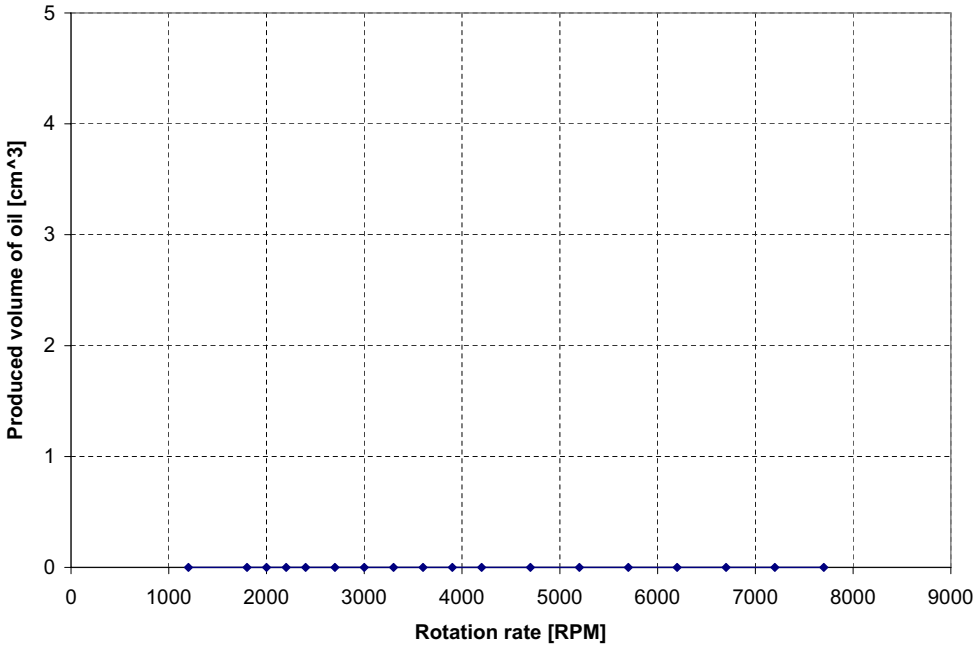

Figure F.5 *Production of oil vs. rotation rate for specimen 3. No oil production.*

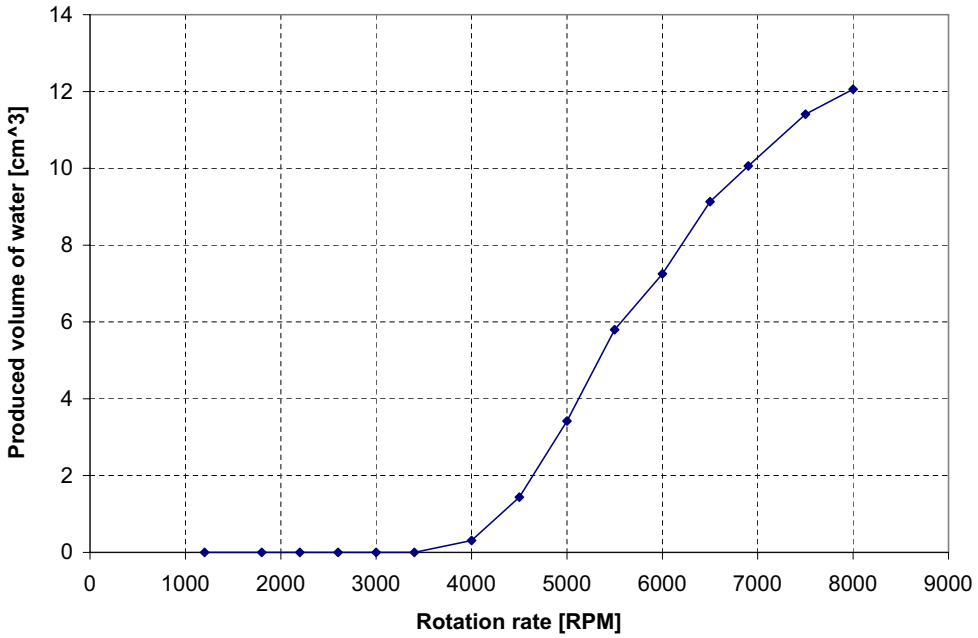

Figure F.6 *Production of water vs. rotation rate for specimen 3. Total water production of 12.06 cm^3 from the pore volume of 26.84 cm^3.*